



I. R. IRAN

ISSN: 1728-144X

e-ISSN: 1735-9244



International Journal of Engineering

Journal Homepage: www.ije.ir



TRANSACTIONS B: Applications

Volume 34, Number 08, August 2021

Materials and Energy Research Center

INTERNATIONAL JOURNAL OF ENGINEERING

Transactions B: Applications

DIRECTOR-IN-CHARGE

A. R. Khavandi

EDITOR-IN-CHIEF

G. D. Najafpour

ASSOCIATE EDITOR

A. Haerian

EDITORIAL BOARD

- | | | | |
|------|--|-------|---|
| S.B. | Adeloju, Charles Sturt University, Wagga, Australia | A. | Mahmoudi, Bu-Ali Sina University, Hamedan, Iran |
| K. | Badie, Iran Telecomm. Research Center, Tehran, Iran | O.P. | Malik, University of Calgary, Alberta, Canada |
| M. | Balaban, Massachusetts Ins. of Technology (MIT), USA | G.D. | Najafpour, Babol Noshirvani Univ. of Tech., Babol, Iran |
| M. | Bodaghi, Nottingham Trent University, Nottingham, UK | F. | Nateghi-A, Int. Ins. Earthquake Eng. Seis., Tehran, Iran |
| E. | Clausen, Univ. of Arkansas, North Carolina, USA | S. E. | Oh, Kangwon National University, Korea |
| W.R. | Daud, University Kebangsaan Malaysia, Selangor, Malaysia | M. | Osanloo, Amirkabir Univ. of Tech., Tehran, Iran |
| M. | Ehsan, Sharif University of Technology, Tehran, Iran | M. | Pazouki, Material and Energy Research Center, Meshkindasht, Karaj, Iran |
| J. | Faiz, Univ. of Tehran, Tehran, Iran | J. | Rashed-Mohassel, Univ. of Tehran, Tehran, Iran |
| H. | Farrahi, Sharif University of Technology, Tehran, Iran | S. K. | Sadrnezhaad, Sharif Univ. of Tech, Tehran, Iran |
| K. | Firoozbakhsh, Sharif Univ. of Technology, Tehran, Iran | R. | Sahraeian, Shahed University, Tehran, Iran |
| A. | Haerian, Sajad Univ., Mashhad, Iran | A. | Shokuhfar, K. N. Toosi Univ. of Tech., Tehran, Iran |
| H. | Hassanpour, Shahrood Univ. of Tech., Shahrood, Iran | R. | Tavakkoli-Moghaddam, Univ. of Tehran, Tehran, Iran |
| W. | Hogland, Linnaeus Univ, Kalmar Sweden | T. | Teng, Univ. Sains Malaysia, Gelugor, Malaysia |
| A.F. | Ismail, Univ. Tech. Malaysia, Skudai, Malaysia | L. J. | Thibodeaux, Louisiana State Univ, Baton Rouge, U.S.A |
| M. | Jain, University of Nebraska Medical Center, Omaha, USA | P. | Tiong, Nanyang Technological University, Singapore |
| M. | Keyanpour rad, Materials and Energy Research Center, Meshkindasht, Karaj, Iran | X. | Wang, Deakin University, Geelong VIC 3217, Australia |
| A. | Khavandi, Iran Univ. of Science and Tech., Tehran, Iran | | |

EDITORIAL ADVISORY BOARD

- | | | | |
|-------|--|-------|--|
| S. T. | Akhavan-Niaki, Sharif Univ. of Tech., Tehran, Iran | A. | Kheyroddin, Semnan Univ., Semnan, Iran |
| M. | Amidpour, K. N. Toosi Univ of Tech., Tehran, Iran | N. | Latifi, Mississippi State Univ., Mississippi State, USA |
| M. | Azadi, Semnan university, Semnan, Iran | H. | Oraee, Sharif Univ. of Tech., Tehran, Iran |
| M. | Azadi, Semnan University, Semnan, Iran | S. M. | Seyed-Hosseini, Iran Univ. of Sc. & Tech., Tehran, Iran |
| F. | Behnamfar, Isfahan University of Technology, Isfahan | M. T. | Shervani-Tabar, Tabriz Univ., Tabriz, Iran |
| R. | Dutta, Sharda University, India | E. | Shirani, Isfahan Univ. of Tech., Isfahan, Iran |
| M. | Eslami, Amirkabir Univ. of Technology, Tehran, Iran | A. | Siadat, Arts et Métiers, France |
| H. | Hamidi, K.N.Toosi Univ. of Technology, Tehran, Iran | C. | Triki, Hamad Bin Khalifa Univ., Doha, Qatar |
| S. | Jafarmadar, Urmia Univ., Urmia, Iran | S. | Hajati, Material and Energy Research Center, Meshkindasht, Karaj, Iran |
| S. | Hesaraki, Material and Energy Research Center, Meshkindasht, Karaj, Iran | | |

TECHNICAL STAFF

M. Khavarpour; M. Mohammadi; V. H. Bazzaz, R. Esfandiar; T. Ebadi

DISCLAIMER

The publication of papers in International Journal of Engineering does not imply that the editorial board, reviewers or publisher accept, approve or endorse the data and conclusions of authors.

AIMS AND SCOPE

The objective of the International Journal of Engineering is to provide a forum for communication of information among the world's scientific and technological community and Iranian scientists and engineers. This journal intends to be of interest and utility to researchers and practitioners in the academic, industrial and governmental sectors. All original research contributions of significant value focused on basics, applications and aspects areas of engineering discipline are welcome.

This journal is published in three quarterly transactions: Transactions A (Basics) deal with the engineering fundamentals, Transactions B (Applications) are concerned with the application of the engineering knowledge in the daily life of the human being and Transactions C (Aspects) - starting from January 2012 - emphasize on the main engineering aspects whose elaboration can yield knowledge and expertise that can equally serve all branches of engineering discipline.

This journal will publish authoritative papers on theoretical and experimental researches and advanced applications embodying the results of extensive field, plant, laboratory or theoretical investigation or new interpretations of existing problems. It may also feature - when appropriate - research notes, technical notes, state-of-the-art survey type papers, short communications, letters to the editor, meeting schedules and conference announcements. The language of publication is English. Each paper should contain an abstract both in English and in Persian. However, for the authors who are not familiar with Persian, the publisher will prepare the latter. The abstracts should not exceed 250 words.

All manuscripts will be peer-reviewed by qualified reviewers. The material should be presented clearly and concisely:

- *Full papers* must be based on completed original works of significant novelty. The papers are not strictly limited in length. However, lengthy contributions may be delayed due to limited space. It is advised to keep papers limited to 7500 words.
- *Research notes* are considered as short items that include theoretical or experimental results of immediate current interest.
- *Technical notes* are also considered as short items of enough technical acceptability with more rapid publication appeal. The length of a research or technical note is recommended not to exceed 2500 words or 4 journal pages (including figures and tables).

Review papers are only considered from highly qualified well-known authors generally assigned by the editorial board or editor in chief. Short communications and letters to the editor should contain a text of about 1000 words and whatever figures and tables that may be required to support the text. They include discussion of full papers and short items and should contribute to the original article by providing confirmation or additional interpretation. Discussion of papers will be referred to author(s) for reply and will concurrently be published with reply of author(s).

INSTRUCTIONS FOR AUTHORS

Submission of a manuscript represents that it has neither been published nor submitted for publication elsewhere and is result of research carried out by author(s). Presentation in a conference and appearance in a symposium proceeding is not considered prior publication.

Authors are required to include a list describing all the symbols and abbreviations in the paper. Use of the international system of measurement units is mandatory.

- On-line submission of manuscripts results in faster publication process and is recommended. Instructions are given in the IJE web sites: www.ije.ir-www.ijeir.info
- Hardcopy submissions must include MS Word and jpg files.
- Manuscripts should be typewritten on one side of A4 paper, double-spaced, with adequate margins.
- References should be numbered in brackets and appear in sequence through the text. List of references should be given at the end of the paper.
- Figure captions are to be indicated under the illustrations. They should sufficiently explain the figures.
- Illustrations should appear in their appropriate places in the text.
- Tables and diagrams should be submitted in a form suitable for reproduction.
- Photographs should be of high quality saved as jpg files.
- Tables, Illustrations, Figures and Diagrams will be normally printed in single column width (8cm). Exceptionally large ones may be printed across two columns (17cm).

PAGE CHARGES AND REPRINTS

The papers are strictly limited in length, maximum 6 journal pages (including figures and tables). For the additional to 6 journal pages, there will be page charges. It is advised to keep papers limited to 3500 words.

Page Charges for Papers More Than 6 Pages (Including Abstract)

For International Author ***	\$55 / per page
For Local Author	100,000 Toman / per page

AUTHOR CHECKLIST

- Author(s), bio-data including affiliation(s) and mail and e-mail addresses).
- Manuscript including abstracts, key words, illustrations, tables, figures with figure captions and list of references.
- MS Word files of the paper.

CONTENTS:

S. Lotfi; M. Ghasemzadeh; M. Mohsenzadeh; M. Mirzarezaee	The Construction of Scalable Decision Tree based on Fast Splitting and J-Max Pre-Pruning on Large Datasets	1810-1818
M. Pourabdoli; Z. Sahebi Hamrah; M.H. Doost Mohammadi; V. A. Lashgari	New Application of Electrically Conductive Adhesive as a Transistor-based Electrical Circuit under AC and DC Currents	1819-1826
R. Rahmi; S. Lubis; N. Az-Zahra; K. Puspita; M. Iqhrammullah	Synergetic photocatalytic and adsorptive removals of metanil yellow using TiO ₂ /grass-derived cellulose/chitosan (TiO ₂ /GC/CH) film composite	1827-1836
V. Vasiya; C. H. Solanki	An Experimental Investigation on Black Cotton Soil using Terrazyme	1837-1844
A. Gholami; S.A. Jazayeri; Q. Esmaili	Investigating Behavior of VLCC Ship's Diesel Engine on Handling Stormy Waters	1845-1855
H. Hassanpour; M. Ghasemi	A Three-stage Filtering Approach for Face Recognition	1856-1864
I. S. Al-Haydari; H. S. Al-Haidari; H. Mohammed-Noor Khudhur; N. Waleed Jummah; M. Abd Al-Hamza	Durability and Aging Characteristics of Sustainable Paving Mixture	1865-1873
N. Rakhshani; N. Hassanzadeh Nemati; A. Ramezani Saadatabadi; S.K. Sadrnezhaad	Fabrication and evaluation of controlled release of Doxorubicin loaded UiO-66-NH ₂ metal organic frameworks	1874-1881
S. H. Abd- Awn; H. O. Abbas	Behavior of Gypseous Soil under Static and Dynamic Loading	1882-1887
E. Darezereshki; A. Behrad Vakylabad; M. Yousefi	Chemical process of synthesizing zinc oxide (ZnO) with nanorod and spherical morphologies	1888-1897

M. Alemi-Rostami; G. Rezazadeh	Selective Harmonic Elimination of a Multilevel Voltage Source Inverter Using Whale Optimization Algorithm	1898-1904
K. Gunasekaran; S. Choudhury	Experimental Study on Single Bay Reinforced Coconut Shell Concrete Portal Frame under Lateral and Cyclic Load	1905-1912
Y. Pourasad; A. Afkar	A study on the modified algorithm for image processing in Tracking Seam Welding	1913-1922
S. Mohsenzadeh; A. Maleki; M.A. Lotfollahi-Yaghin	Strengthening of RC Beams Using SCC Jacket Consisting of Glass Fiber and Fiber-Silica Fume Composite Gel	1923-1939
A. M.J. Alhassani	Analysis of Under-Reamed Piles Subjected to Different Types of Load in Clayey Soil	1940-1948
H. Tiwan; M. N. Ilman; K. Kusmono	Effect of Pin Geometry and Tool Rotational Speed on Microstructure and Mechanical Properties of Friction Stir Spot Welded Joints in AA2024-O Aluminum Alloy	1949-1960
S. Behzad Rahimi; A. Jalali; S. Mohammad Mirhoseini; E. Zeighami	Experimental Comparison of Different Types of FRP Wrapping in Repairing of RC Deep Beams with Circular Openings	1961-1973
S. Motahar	A Neural Network Approach to Estimate non-Newtonian Behavior of Nanofluid Phase Change Material Containing Mesoporous Silica Particles	1973-1981
S. Valizadeh; A. Mahmoodi; I. Nakhai Kamalabadi	Price and Service Competition Between Two Leader-Follower Retailer-Stackelberg Supply Chains	1982-1993
S. Esmaili; S.J. Hosseinipour; A. Shamsi-Sarband	Numerical analyses of Manufacturing of an AA8111 Pin-shaped Bipolar Plate by Hot Metal Gas Forming	1994-2001
N. Arish; H. Yaghobi	Analysis of a New Linear Dual Stator Consequent Pole Halbach Array Flux Reversal Machine	2002-2009
M. Tabasi; M. Ojaghi; M. Mostafavi	Analyzing Vibration as a Useful Domain for Getting Bearing Fault Signals in Induction Motors	2010-2020
N. F. Soliman; D. O. Ramadan; J. A. Yagoob	Influence of Mould Thickness on Microstructure, Hardness and Wear of AL-Cu Cast Alloys	2021-2027
A. Zohrevand; Z. Imani	Holistic Persian Handwritten Word Recognition Using Convolutional Neural Network	2028-2037
M. Taheri; A. Mahdavi; H. Safikhani	Multi objective optimization of multi-hole orifices using FSI analysis and NSGA II algorithm	2038-2044



The Construction of Scalable Decision Tree based on Fast Splitting and J-Max Pre Pruning on Large Datasets

S. Lotfi^a, M. Ghasemzadeh^{*b}, M. Mohsenzadeh^a, M. Mirzarezaei^a

^a Department of Computer Engineering, Science and Research Branch, Islamic Azad University, Tehran, Iran

^b Computer Department, Engineering Campus, Yazd University

PAPER INFO

Paper history:

Received 03 March 2021

Received in revised form 18 April 2021

Accepted 24 April 2021

Keywords:

Fuzzy Decision Trees

Large Dataset

Fuzzy Entropy

Fuzzy Partitioning

Incremental Approach

ABSTRACT

The decision tree is one of the most important algorithms in the classification which offers a comprehensible model of data. In building a tree we may encounter a memory limitation. The present study aims to implement an incremental scalable approach based on fast splitting, and employs a pruning technique to construct the decision tree on a large dataset to reduce the complexity of the tree. The proposed algorithm constructs the decision tree without storing the entire dataset in the primary memory via employing a minimum number of parameters. Furthermore, the *J*-max Pre pruning method was used to reduce the complexity with acceptable results. Experimental results show that this approach can create a balance between the accuracy and complexity of the tree and overcome the difficulties of the complexity of the tree. In spite of the appropriate accuracy and time, the proposed algorithm could produce a decision tree with less complexity on a large dataset.

doi: 10.5829/ije.2021.34.08b.01

1. INTRODUCTION

Today, a large amount of data is stored in a variety of information sources which can be used as valuable knowledge. In order to analyze and process the data and extract the knowledge, the data mining process is used in different ways [1]. Classification is one of the most widely used methods for data mining in order to provide a model for specifying the label of different samples based on their characteristics. In this regard, the decision tree is one of the most widely used algorithms which can produce understandable human descriptions of relationships in a dataset [2]. Further, this algorithm is one of the most widely used algorithms in pattern recognition domain due to its simplicity and interpretation, rule representation in a hierarchical format, cost and time of proper construction, the ability to work with continuous and discrete data, the need for prior knowledge and accurate presentation.

The C4.5, ID3, and CART are regarded as the most common decision tree algorithms. These algorithms have

two phases: growth, pruning. In the growth phase, the dataset is recursively divided so that all records within a section can have the same class while the nodes are repeatedly pruned to prevent overfitting phenomena in the pruning phase [1]. Recently, an algorithm was developed to construct a decision tree focusing on the construction time presented to maximize accuracy. The strength of this algorithm is the construction of the tree in a limited time. In other words, when there is enough time to build a tree, the algorithm should choose the feature to split having the most benefit while it chooses the most effective feature in terms of time when the time is limited. However, the method has not been implemented for big data with respect to the complexity of the resulting tree [3].

1.1. Complexity of Decision Tree The interpretation ability is one of the most important benefits of the decision tree. However, there is a negative relationship between the tree dimensions and interpretation ability. In other words, an increase in the

*Corresponding Author Institutional Email:
m.ghasemzadeh@yazd.ac.ir (M. Ghasemzadeh)

complexity of the tree results in decreasing the interpretation ability [4]. It is worth noting that the complexity of the tree is measured by some criteria such as the total number of nodes, the tree levels, the depth of the tree, and the number of traits used. Nevertheless, the complexity of the tree can be controlled by specifying the appropriate stop condition or using the pruning method on the tree. The growth phase continues until a stop condition occurs. The pre-and post-pruning methods are regarded as the two basic pruning approaches. In the first approach, several limitations are applied during the construction of the tree while it is simplified after the construction of the whole tree. The calculations of the entire data can be regarded as the traditional criteria for determining the best attribute for the split. Some of them utilized discrete methods to select numerical features while some used costly evaluations. However, none of these methods are appropriate for dealing with large dataset. Data integration in an incremental form through using all dataset is another method for constructing decision trees. However, this method disregards the complexity of the tree, and interpretation ability of DTFS algorithms are more efficient than all other methods due to the use of all trained data, the lack of computational overhead, as well as the use of a quick criterion for splitting continuous variables [5]. Ignoring the tree complexity and the effect of pruning on the accuracy of the tree are considered as two disadvantages of this method.

1. 2. Incremental Scalable Method The present study proposes an incremental scalable approach based on fast splitting and pruning for the decision tree construction in order to reduce the complexity of the tree. In this regard, the decision tree is constructed from all the trained data, without storing all data in memory. The use of all training data results in increasing the reliability of the model. In the proposed method, the data are incrementally entered into the tree and accordingly the decision tree is developed. In order to control the complexity of the tree, the *J*-Max pre-pruning is used [6]. The proposed approach focuses on both challenges of identifying the best attribute for development and losing interpretation capability, despite a large amount of data. The simulation results indicate that the proposed algorithm can balance the accuracy and complexity of the tree.

The present study is organized as follows: Section 2 presents the general issues related to the decision tree. In Section 3, the decision-making tree works on large datasets are reviewed and a new category is provided for these algorithms. In Section 4, an algorithm is proposed based on using an incremental and pre-pruning method to construct a tree. Section 5 indicates the data analysis results and are compared with other algorithms. Finally, the conclusion is explained in Section 6.

2. BACKGROUNDS

2. 1. Decision Tree

The decision tree has a hierarchical structure and supervised learning that implemented using divide and conquer strategy. In this method, features are used for data classification as a tree structure. Tree nodes are connected by edges. Edges are conditions that are split at each node. Each extracted rules are a unique path from the root to leaf nodes.

The growth phase is the primary phase of making the decision tree by which, the training dataset is recursively partitioned until all records within a section have the same class. Each partition adds a new node to the tree. For a set of records inside P , the condition t is determined for further segmentation of the set into $P1, P2, \dots Pm$. Then, the new nodes $P1$ to Pm are created and inserted as the children of P . The node P is labeled with the condition t and the nodes $P1$ to Pm are recursively split. They are not split up if all records within a section represent a class. The node is considered as a leaf and is labeled with the same class. After constructing the decision tree, the tree starts to scroll from the root to the end of one of the leaves for classifying a new record. Finally, the leaf label is returned as the result [7].

2. 2. Splitting Measures

Selecting the attribute for branching is one of the main problems in the decision tree. Based on the type of data, the split in each node can be binary or multiple. The branch type is most often binary if the values of the attributes are continuous. However, the split may be binary or multiple if the attribute values are discrete. In order to select the best attribute in node branching, the degree of purity and distribution of the homogeneous class in each category should be considered. In order to determine the degree of purity and select the appropriate attribute for node expansion, various criteria such as the Gini's criterion and Entropy are implemented. The following formula is used for calculating each of these values [8]:

Entropy determines the purity of a set of data, which represents the qualitative division of the training examples based on a feature. If the target feature includes c different values, the occurrence probability of each is P_i , and the entropy I is defined as :

$$Entropy(I) = \sum_{i=1}^c -p_i \log_2 p_i \quad (1)$$

Based on the irregularities as impurities in a set of training examples, the effectiveness of an attribute is defined in data classification. The criterion is regarded as the expected reduction in irregularity, which is obtained by separating the examples based on this attribute. The information gain of a feature is the amount of entropy reduction, which is obtained by separating the samples through this feature. The information gain of a feature such as A , for the value of I , is defined as Equation (2):

$$Gain(I, A) = Entropy(I) - \sum_{v \in values(A)} \frac{|I_v|}{|I|} Entropy(I_v) \quad (2)$$

In the above equation, the first item is the amount of data entropy and the second item is the expected entropy value after the data separation. Value A represents a set of all possible values for attribute A . I_v indicates a subset of I , in which the values of attribute A is v . With respect to feature A , the uncertainty of the entity is obtained from Equation (3):

$$SplitInfo(A) = - \sum_{i=1}^c \frac{\#classj}{I} \log_2 \frac{\#classj}{I} \quad (3)$$

Equation (4) is used to calculate the ratio of information gain. The Gain Ratio indicates how much the feature separates the data uniformly. The denominator eliminates those features having large amounts of uniform distribution values.

$$GainRatio(A) = \frac{Gain(I, A)}{SplitInfo(A)} \quad (4)$$

2. 3. Stopping Criteria Stopping condition in the growing phase is regarded as another important variable for decision tree algorithms. The growth phase is completed when the resolution is no longer useful, or a category can be applied to all instances in the subset [9]. The general rules for stopping are as follows:

- All examples of training data sets belong to a same class.
- The tree has reached the maximum depth.
- The number of samples in a leaf node is less than the minimum number of parent samples.
- The number of records in the current node is less than the threshold value.
- The selection criterion is less than one threshold.

2. 4. Decision Tree Pruning In general, the interpretation ability is one of the distinguishing features of the decision tree which are considered more than other tree features by researchers. Importantly, a decrease in tree complexity leads to a decrease in interpretation ability. By increasing the complexity of the decision tree, a considerable increase takes place in the occurrence probability of overfitting. In addition, the training error decreases while the test error increases [2]. The reason for the occurrence of this phenomenon is the noise in the training dataset or inappropriate selection of training data.

Pruning approach is regarded as one of the most common ways to reduce the complexity, overcome the overfitting, and finding the appropriate tree size. Further, the pruning can reduce the decision tree size by removing those parts of the tree having little power for

classification. Furthermore, pruning leads to a reduction in the complexity of the final classification and an improvement in the prediction accuracy. The pruning aims to extract those sub-trees which prevent the occurrence of overfitting phenomena.

In general, pruning methods are divided into two pre and post-pruning groups. Pre-pruning is implemented during the tree development in the growth phase in order to prevent excessive tree growth, useless branching, and rapid tree stopping in the growth phase. In addition, this method is utilized to reduce the time and memory required. However, the early stop of the tree is the main disadvantage of this method, which may obtain better results during the continuation of tree expansion. As for the post-pruning approach, a number of branches are removed by using statistical tests after building the entire tree. This method is used to create a balance between the accuracy and complexity of the tree. However, the computational overhead due to the processing after the tree construction is regarded as the main limitation [10]. Since the tree must be completely constructed and a lot of time and memory should be allocated to the tree construction despite a large amount of data during the post-pruning methods, the pre-pruning method was implemented in the present study. As building a complete tree is not necessary for pre-pruning techniques, it can be useful for large-scale applications.

The J-measure is one of the pre-pruning methods, used as an information theory tool to measure the content of the rules extracted from the tree [11]. Assuming that the form of the rules extracted from the tree is in the form if $Y=y$ Then $X=x$, the value of the information content of the rules is calculated by using Equation (5) :

$$J(X;Y=y) = p(y) j(X;Y=y) \quad (5)$$

$p(y)$ represents the probability which the preceding rule occurs, and $j(X;Y=y)$ is calculated by Equation (6):

$$j(X;Y=y) = p(x|y) \log_2 \left(\frac{p(x|y)}{p(x)} \right) + (1-p(x|y)) \log_2 \left(\frac{1-p(x|y)}{1-p(x)} \right) \quad (6)$$

J pruning method is presented based on the J measurement criterion for reducing the overfitting. In this way, the value of j is calculated for each tree node. If j -value of a node was less than its father value, the branch should be pruned accordingly. Otherwise, the process will continue. The reduction of the number of rules or nodes with acceptable accuracy which reduces the occurrence of overfitting is the main advantage of using this pruning method. However, the j -pruning technique may be locally optimal since the value of a node pruned due to the less value of j for its father may increase in subsequent branches and accordingly reduces the tree efficiency.

In order to overcome the problem at hand, j -pruning was developed, by which a new approach called " J -max" was presented. Based on this method, in addition to the J -value, the J -max value of that node is computed by using Equation (7). The J -max value is checked if the j -value of a node is less than its father's value. In addition, the tree growth continues because the J -value may increase again if the J -max value of that node is greater than its previous j -values. The growth continues until the j -value and J -max are equal. In order to calculate the J -max value, the following formula is used [6]:

$$J_{Max} = p(y), \max\{p(x|y), \log_2\left(\frac{1}{p(x)}\right), (1-p(x|y))\log_2\left(\frac{1}{1-p(x)}\right)\} \quad (7)$$

Based on the results, compared to the j -pruning technique, this approach can reduce the number of rules or nodes and improve accuracy in most cases. Therefore, j -max pruning method was used in the proposed algorithm.

3. RELATED WORKS

Generally, the algorithms used to construct decision trees from large datasets are classified into sampling, data list, and incremental categories.

3. 1. Sampling Algorithm Based on sampling category, the samples are first selected from the main collection. Then, the decision tree algorithm is applied to the selected sample. In order to prevent the storage of all data in the main memory, ICE and BOAT, divide the training data into some sections. For each section, a decision tree is created by using a traditional algorithm such as C4.5 or CART, and the likes. In the next stage, the decision tree of each segment is individually processed or combined without any need to get all the data in memory. High flexibility in dealing with increasing or decreasing data in partitions is regarded as the major benefit of this method although the reliability of the model is low due to the lack of the use of the entire data in this method. The timing of the sampling algorithm, the dependence of the results on the sampling technique and the time required to construct the tree for a set of different data are some challenges of this method [12,13].

3. 2. Data List Algorithm In order not to store all data in the main memory, this approach implements a list of structures for each feature which is mainly stored in the disk memory and it is used for devising and developing, instead of using the records. The SLIQ is considered as one of the algorithms for this method, which creates a list structure for each attribute storing in

the disk space [14]. In addition, the algorithm creates an additional list, including a class of each instance, along with the number of tree nodes, which saved the sample and keeps it in the main memory. Given that the magnitude of this list relies on the number of records, it may create some problems in a large dataset. Further, the SPRINT algorithm is an improved SLIQ method. Storing a separate list in the main memory is not essential when a column is added to the list structure for the maintenance class of each instance. However, the entire list should be read from the disk memory for each expansion. A dual space of the training data is essential as the magnitude of the list structure is proportional to the number of records in each branch in both of the above-mentioned methods. Despite a large amount of data and reading from the disk, the implementation time of the algorithm is high. Thus, list structure processing is performed in a multiprocessor or parallel manner in order to solve the problem at hand [15]. Further, the Rainforest algorithm uses the list to display the features, while the different values of the attributes are only kept, which results in decreasing the number of records. The present algorithm aims to reduce the space occupied by memory, due to the type of list structure of the related feature. However, the list should be kept in memory as an increase takes place on the list size if various values of a variable are available. All the data must be read twice and written once when a list is made, which is not appropriate for large datasets [16].

3. 3. Incremental Algorithm Based on the incremental algorithm, the data contributes to the tree structure in order to make the decision tree by using the entire dataset [17]. The VFDT algorithm included in this category makes the decision tree constantly, irrespective of the number of samples. First, the records should be randomly selected in order to create the original tree. Then, all the records are entered into the tree incrementally and scrolled through. In the next stage, the information gain is calculated when the number of records in a leaf reaches a certain number. The VFDT algorithm must compute all the different classification conditions for all numerical attributes, which is very time-consuming due to the diverse data [18]. DTFS is another algorithm which adds data to the tree incrementally in order to exclude the training data in the main memory and solve the computational overhead problem. Based on this algorithm, the Gain Ratio is used to select the best feature for branching. Only the s stored record in the node is considering for development and accordingly, the best split ratio is searched among the s records. Then, the mean values for all records in a class are calculated for each variable as the split criterion. As a result, Gain Ratio is calculated based on the obtained values, upon which the best feature is selected. Selecting the split property using the s records accelerates the process of branching [4]. Table 1 indicates a comparison

TABLE 1. Comparison of decision tree construction algorithms in the face of large datasets

Method	Advantages	Disadvantages
SLIQ	The basis for the development of many algorithms Speed up training time	
SPRINT	Reducing memory overhead than SLIQ	Needing extra space
CLOUDS [19]	Decreasing the time of selection	Keeping definition lists
RainForest	Providing a storage method Reducing memory overhead	
BOAI [20]	Speeding up the training time	
BOAT	Building a tree with a double-scanned data	Using a small subset of data
ICE	Having high flexibility in dealing with increasing or decreasing data in partitions	Wasting time due to data selection
		Needing preprocess
VFDT	High speed	Needing to set many parameters Wasting time due to the calculation of all branching states
DTFS	High speed Lacking memory overhead Splitting fast continuous data	The complexity of the tree Needing to preprocess

of the decision tree algorithms for large datasets. In this table, the algorithms are compared in terms of criteria such as the speed of decision tree construction, overcoming the challenge of memory limitation, the need for re-scanning the dataset, using all or part of the dataset, and the need to adjust multiple parameters.

Due to this, the DTFS is selected as the basis for the proposed algorithm. The details of this algorithm are discussed further. The use of all training data in the tree construction, lack of memory and time overload due to the lack of using a special data structure, the simplicity of implementation, and an appropriate timeframe are regarded as some advantages of the DTFS algorithm. In addition to all these benefits, the following points should be taken into consideration in the basic approach:

- In the DTFS method, no preprocessing is used to determine the order of data entry unless the records are uniform in terms of class variables. However, it is

essential to consider the time of making the main body of the tree and using the appropriate data to increase performance. For this purpose, it is important to consider pre-processing on the data in order to determine the priority of entering the tree.

- The time to develop the decision tree in the DTFS method is based on the parameter s , and the node is developed if the number of records stored in the node is greater than the parameter s , which is constant from beginning to the end of tree construction. Naturally, the behavior of tree development in the roots should not be similar to the leaves of the final stages. In addition, in a large tree, it may be stored in a large number of leaves, less than s records. In this case, there are many leaves which never meet the development conditions. Further, the total records stored in these leaves can be regarded as a limiting factor for memory.

- In the DTFS, the size of the tree and its complexity is deemphasized. The results of some studies indicated that changing the value of the parameter s does not play a significant role in the runtime and accuracy of the algorithm. However, the effect of this parameter on the complexity of the tree has not been addressed yet.

4. PROPOSED METHOD

In the present study, a new method was presented for constructing a decision tree based on the incremental method which can create a balance between accuracy and complexity, in addition to overcoming the challenge of the large dataset. In decision tree construction, all the data should be simultaneously present in the memory in order to determine the best attribute for development. Memory restrictions may prevent the calculation of the best feature by increasing the number of records. In addition, reducing the interpretation ability and increasing the error rate are regarded as the main challenge for high data. In order to overcome the problems of not locating training data in main memory, along with computational overhead, the algorithm incrementally injects the training data into the tree. In this way, each record is scrolled in the tree and stored in the leaves. When the algorithm decides to develop a node, only the label of the input edge of the leaf is updated if all the records in the leaf belong to the same class while the leaf begins to develop if the classes are different. The J -max measure is used to decide on the branching in order to reduce the complexity of the developmental leaves. In the present study, the proposed method focuses on both the main memory challenge and the complexity of the tree. The principles of the proposed method are summarized as follows:

4. 1. Determining the Priority of Entering Records into the Tree

First, the similarity criteria, based on the type of input data, are used for determining the

priority of entering the records into the tree. Then, the amount of similarity between different records is calculated and accordingly a number indicating the similarity of a record with other records is obtained. In the next stage, the records are sorted by the descending order of similarity. Finally, based on the results, those data having the most similarity with others are placed at the beginning, while those having the least similarity with others are placed at the end. Based on this approach, those records having better quality are used in the early stages of tree construction.

4. 2. Selecting a Feature for Branching Gain Ratio is regarded as one of the most important criteria for splitting a decision tree in traditional algorithms. This method is time-consuming because each branch should compute all available states for all the features, and select the features with the highest Gain Ratio value. Given the timeliness of calculating this criterion, the proposed algorithm only uses the records stored in that node to compute and select the best feature while deciding to split a node. In categorical variables, each value is calculated as the split criterion while the mean values appearing for all records of a class are regarded for calculating the split criterion in continuous variables. Finally, the best feature is selected as the Gain Ratio values. Choosing the best feature for branching based on using records within a node accelerates the process of branching.

4. 3. Reducing Complexity The algorithm starts constructing the tree with an empty node called root. At the beginning, the root of the tree is a leaf. The training records are entered into the root, and scrolled through the tree to the end of a leaf and stored in the leaf. When the number of records stored in one sheet reaches its maximum number, the algorithm can follow one of the following alternatives:

- If all records stored within a node are in the same class, the leaf is not expanded, and only the edge of that node is updated while the records stored in this node are deleted.
- If the included records in this leaflet belong to different classes, an edge should be created for each attribute value after selecting the appropriate branching attribute based on the aforementioned formulas. J and J -max values are calculated by using Equations (6) and (7) for each of the possible edges in the developmental leaf. Then, the conditions for creating the new node are studied as follows:
 - 1) If the j -value of a node is greater than its father's value, the node development is performed.
 - 2) If the j -value of a node is less than its father's value, the J -max value of that node is checked.
 - 3) If the J -max of that node is greater than its previous J -values, the tree node development is performed. If node

j -value is equal to J -max, the node development is stopped.

The records for each edge are stored inside the leaf related to that edge. The mean values in that class are assigned as the edge label. The previous level node is converted to an internal node and accordingly, the records stored in this node are deleted. Then, the inference phase is completed after scrolling and processing all records. Finally, the majority class is assigned as a label to all leaves. If a node is empty, the majority of the parent class is given to.

For example, assume that based on the records in a node, the Y attribute is chosen as the best attribute for the branch, and the values of this property are y_1, y_2, y_3 . There are three possible branches for this node. Each tree rule is as follows:

If $X = x_1$ then Class C1
(J -value = 0.00113, J max = 0.02315)

If $X = x_1$ and $Y = y_1$ then Class C1
(J -value = 0.0013, J max = 0.01157)

If $X = x_1$ and $Y = y_2$ then Class C1
(J -value = 0.00032, J max = 0.0116)

If $X = x_1$ and $Y = y_3$ then Class C2
(J -value = 0.0032, J max = 0.001)

As for the rule 2, the branching is created as the node j -value is greater than father j -value, based on rule 3, the value of j is less than the value of j of his father, but since the J -max value is greater than the value of j in the previous step, this split occurs. In the case of rule 4, none of the branching conditions has been established.

4. 4. Scrolling Trees and Classifying Samples

The tree scroll starts from the root and extends to the depths of the tree to reach a leaf, based on the split characteristics and the edge values. A path is selected for scrolling, and the difference of the value of the property with the average value calculated for that edge is the lowest value. The classification process in the decision tree algorithm for a new record involves scrolling the tree from root to reach a leaf. Then, the class corresponding to that leaf is determined as the class to the desired sample.

4. 5. Analyzing Time Complexity The time complexity of the algorithm for a dataset with record m , feature d , and maximum value k for each attribute consists of three parts as follows:

- The similarity of records is calculated with each other and the records are sorted based on their similarity,

which uses a sorting algorithm of $O(m \log m)$ in the worst case.

- The scrolling cost for each record is equal to the maximum depth of the tree, $O(\log m)$, and the cost for the entire dataset is equal to $O(m \log m)$.

- The Gain Ratio should be calculated to select the best attribute for splitting in each node with the s record for all attributes and the time allocated $O(s, d)$. As this

criterion is calculated $\frac{m}{s}$ times, the cost of this part of

the algorithm is $O(s, d, \frac{m}{s} = d, m)$. The j and J -max values for each selected feature should be computed at most k times and the execution time for this part of the algorithm equals to $O(d, k, m)$.

- In sum, the time complexity of the algorithm is equivalent to $O(2m \log m + dkm) = O(m \log m)$.

5. EXPERIMENTAL RESULTS

In the present study, a method was presented for constructing a decision tree with an incremental approach and J -max pruning. The records of training dataset were entered into the decision tree and accordingly the decision tree was developed in an appropriate time. In the proposed method, the records were entered into the tree based on the priorities specified and placed in the appropriate leaf. Gain Ratio was used to determine the split priority in each node. Finally, the J -max approach was implemented to balance the accuracy and complexity of the developmental leaves. In this section, the proposed method is evaluated and compared with C4.5 and DTFS algorithms in terms of accuracy, runtime, and complexity.

In order to implement the proposed method and other tree algorithms, a system with a RAM of 6GB, CPU 2.1 GHz, 64-bit Win10 operating system was used. During the implementation and comparison of algorithms, the same conditions were used for execution. Table 2 displays the dataset used for testing, taken from UCI [21], without any missing value. Then, the Hold Out method was used to divide the data. At each run, 70% of the dataset was considered for training and 30% of the total were implemented for evaluation. In the next stage, in order to validate the results, the Hold Out method was repeated 10 times and the average results were reported. In all experiments, the algorithms C4.5, C4.5 through applying J -max pruning, DTFS with different values of s , and the proposed method were compared.

Table 3 illustrates the depth of the tree and the accuracy of the algorithms on the MagicGamma set. The tree depth, which is regarded as a criterion for tree complexity, was modified in DTFS for various s values.

In addition, the tree complexity is high in C4.5, and the driller could not play a significant role in reducing complexity. The proposed algorithm was obtained by creating a balance between the accuracy and complexity.

As for the DTFS algorithm, the accuracy decreases when s is low. As shown in Table 5, in the Poker dataset, for $s = 10$, the precision of the algorithm is 50%, which increased by increasing s . However, this is not always true. For example, the accuracy is decreased again at $s = 600$. The decision tree is very complicated, although the C4.5 algorithm has the highest output accuracy. The results indicated that the proposed algorithm could obtain a balance between the accuracy and complexity. Other parameters indicating the complexity of the tree, including the number

TABLE 2. Dataset used in the experiments.

Dataset	Number of attributes	Number of records
Magic Gamma	11	19020
Statlog(Shuttle)	9	58000
Poker	11	1025010

TABLE 3. Accuracy, Depth and Nodes of decision trees for the MagicGamma dataset

Algorithm	Test Accuracy	Tree Depth	Number of Nodes
C4.5	69.96	191	12292
C4.5+Jmax	70.8	186	7378
DTFS(S=10)	67.72	110	3208
DTFS(S=100)	68.5	59	343
DTFS(S=200)	67.64	44	172
DTFS(S=400)	69.34	27	82
DTFS(S=600)	71	19	55
Proposed Method	68.48	30	103

TABLE 4. Accuracy, Depth and Nodes of decision trees for the Poker dataset

Algorithm	Test Accuracy	Tree Depth	Number of Nodes
C4.5	54.28	85	8256
C4.5+Jmax	53.78	69	2580
DTFS(S=10)	50.18	30	1171
DTFS(S=100)	53.16	24	598
DTFS(S=200)	53.82	25	310
DTFS(S=400)	53.77	28	235
DTFS(S=600)	54.24	18	107
Proposed Method	53.41	30	231

TABLE 5. Accuracy, Depth and Nodes of decision trees for the Shuttle dataset

Algorithm	Test Accuracy	Tree Depth	Number of Nodes
C4.5	81.25	105	2548
C4.5+Jmax	80.78	87	1899
DTFS(S=10)	81.34	31	781
DTFS(S=100)	79.23	17	196
DTFS(S=200)	79.01	15	115
DTFS(S=400)	78.69	11	64
DTFS(S=600)	78	13	85
Proposed Method	78.65	15	126

of nodes and the number of leaf nodes, which in fact represents the number of rules derived from the decision tree, are given in the table for the three test datasets.

6. CONCLUSION

In this paper, an algorithm was developed to construct decision trees on large datasets. In the proposed approach, the record entry priority is assigned to the tree. Then, the set of training data is based on the specified priorities of the record entered into the decision tree and placed in the appropriate leaf. For each node, its complexity is calculated at appropriate times, and it is decided whether to split it or not. Gain ratio has been used to determine the best feature for branching. Finally, to avoid the complexity of the tree and to balance the precision and complexity, the developmental leaves are pruned using the J -max criteria.

In general, the most important components of the proposed framework are: achieving a balance between the precision and complexity using the pre-pruning approach, solving the memory limitation problem for a large dataset by entering data incrementally into the decision tree, increasing reliability of the model by making decision tree of all training data, lacking of memory and time overload due to the non-use of especial data structure. One of the unfortunate results in our algorithm is that the number of nodes and tree depth is slightly higher when it reaches the same accuracy as the DTFS algorithm. Of course, we have eliminated the dependence of the results on the value of the s parameter, and it is important to strike a balance between the accuracy and complexity of the tree. Also, with the use of a pruning method, the development of nodes is largely prevented so that the tree's complexity is kept to an acceptable level. Other decision criteria for nodal branching can be considered for further work. Also, using parallel computing can increase speed of the algorithm.

7. REFERENCES

- Agarwal, S., "Data mining: Data mining concepts and techniques" In 2013 International Conference on Machine Intelligence and Research Advancement, (2013), 203-207, IEEE, doi: 10.1109/ICMIRA.2013.45.
- Qolipour, F., Ghasemzadeh, M. and Mohammad-Karimi, N., "The Predictability of Tree-based Machine Learning Algorithms in the Big Data Context." *International Journal of Engineering, Transactions A: Basics*, Vol. 34, No. 01, (2021), 82-89, doi: 10.5829/ije.2021.34.01a.10.
- Chen, Y.L., Wu, C.C. and Tang, K. "Time-constrained cost-sensitive decision tree induction." *Information Sciences*, Vol. 354, (2016), 140-152, doi: 10.1016/j.ins.2016.03.022.
- Priyanka and Kumar, D., "Decision tree classifier: a detailed survey." *International Journal of Information and Decision Sciences*, Vol. 12, No. 3, (2020), 246-269, doi: 10.38094/jastt20165.
- Franco-Arcega, A., Carrasco-Ochoa, J.A., Sánchez-Díaz, G. and Martínez-Trinidad, J.F., "Decision tree induction using a fast splitting attribute selection for large datasets." *Expert Systems with Applications*, Vol. 38, No. 11, (2011): 14290-14300, doi: 10.1016/j.eswa.2011.05.087
- Stahl, F. and Bramer, M., "Jmax-pruning: A facility for the information theoretic pruning of modular classification rules." *Knowledge-Based Systems*, Vol. 29, (2012), 12-19, doi: 10.1016/j.knsys.2011.06.016.
- Grossi, V., Romei, A. and Turini, F., "Survey on using constraints in data mining." *Data Mining and Knowledge Discovery*, Vol. 31, No. 2, (2017): 424-464, doi: 10.1007/s10618-016-0480-z.
- Chandra, B., Kothari, R. and Paul, P., "A new node splitting measure for decision tree construction." *Pattern Recognition*, Vol. 43, No. 8, (2010), 2725-2731, doi: 10.1016/j.patcog.2010.02.025.
- Lomax, S. and Vadera, S., "A survey of cost-sensitive decision tree induction algorithms." *ACM Computing Surveys (CSUR)*, Vol. 45, No. 2, (2013), 1-35, doi: 10.1145/2431211.2431215.
- Brunello, A., Marzano, E., Montanari, A. and Sciacovico, G., "Decision tree pruning via multi-objective evolutionary computation." *International Journal of Machine Learning and Computing*, Vol. 7, No. 6, (2017), 167-175, doi: 10.18178/IJMLC.2017.7.6.641.
- Bramer, M., "Using J-pruning to reduce overfitting in classification trees." *In Research and Development in Intelligent Systems XVIII*, Springer, London, (2002), 25-38, doi: 10.1007/978-1-4471-0119-2_3.
- Manapragada, C., Webb, G. I., and Salehi, M., "Extremely fast decision tree." In Proceedings of the 24th ACM SIGKDD International Conference on Knowledge Discovery & Data Mining, (2018), 1953-1962, doi: 10.1145/3219819.3220005.
- Gehrke, J., Ganti, V., Ramakrishnan, R. and Loh, W.Y., "BOAT-optimistic decision tree construction." *ACM*, Vol. 28, No. 2, (1999), doi: 10.1145/304182.304197.
- Mehta, M., Agrawal, R. and Rissanen, J., "SLIQ: A fast scalable classifier for data mining" International conference on extending database technology, Springer, Berlin, Heidelberg, (1996), 18-32, doi: 10.1007/BFb0014141.
- Zaki, M. J. "Parallel and distributed data mining: An introduction." In Large-scale parallel data mining, Springer, Berlin, Heidelberg. (2000), 1-23, doi: 10.1007/3-540-46502-2_1.
- Gehrke, J., Ramakrishnan, R. and Ganti, V., "RainForest—a framework for fast decision tree construction of large datasets." *Data Mining and Knowledge Discovery*, Vol. 4, No. 2, (2000), 127-162, doi: 10.1023/A:1009839829793.

17. Hulten, G. and Domingos, P., "Mining Decision Trees from Streams." In *Data Stream Management*, Springer, Berlin, Heidelberg, (2016), 189-208, doi: 10.1007/978-3-540-28608-0_9.
18. Domingos, P. and Hulten, G., "Mining high-speed data streams." In Proceedings of the sixth ACM SIGKDD international conference on Knowledge discovery and data mining, (2000), 71-80, doi: 10.1145/347090.347107.
19. Ranka, S. and Singh, V., "CLOUDS: A decision tree classifier for large datasets." In Proceedings of the 4th Knowledge Discovery and Data Mining Conference, Vol. 2, No. 8, 1998.
20. Yang, B., Wang, T., Yang, D. and Chang, L., "BOAI: Fast alternating decision tree induction based on bottom-up evaluation." In Pacific-Asia Conference on Knowledge Discovery and Data Mining, Springer, Berlin, Heidelberg, (2008), 405-416, doi: 10.1007/978-3-540-68125-0_36.
21. Blake, C.L. and Merz, C.J., "UCI Repository of machine learning databases [http://www.ics.uci.edu/~mlearn/MLRepository.html]. Irvine, CA: University of California." Department of Information and Computer Science 55 (2008).

Persian Abstract

چکیده

درخت تصمیم یکی از مهمترین الگوریتم‌های طبقه‌بندی است که مدل قابل درکی از داده‌ها ارائه می‌دهد. در ساخت درخت تصمیم ممکن است با محدودیت حافظه روبرو شویم. در مطالعه حاضر رویکرد مقیاس‌پذیر افزایشی بر مبنای تقسیم سریع و هرس، جهت ساخت درخت تصمیم بر روی داده‌های حجیم ارائه شده است به نحوی که پیچیدگی ساخت درخت کاهش یابد. الگوریتم ارائه شده درخت تصمیم را بدون نیاز به ذخیره‌سازی کل مجموعه داده در حافظه اصلی و با حداقل تعداد پارامتر لازم مهیا می‌سازد. همچنین جهت کاهش پیچیدگی و دستیابی به دقت قابل قبول از روش پیش هرس مبتنی بر J-Max استفاده شده است. نتایج آزمایش بر روی مجموعه داده‌ها نشان می‌دهد با استفاده از این رویکرد می‌توان به موازنه‌ای میان دقت و پیچیدگی درخت دست‌یافت و بر مشکلات حاصل از پیچیدگی درخت غلبه کرد. الگوریتم ارائه شده با وجود دقت و زمان اجرای مناسب، درخت تصمیمی با پیچیدگی‌های کمتر بر روی داده‌های حجیم می‌سازد.



New Application of Electrically Conductive Adhesive as a Transistor-based Electrical Circuit under AC and DC Currents

Z. Sahebi Hamrah^a, M. H. Doost Mohammadi^b, M. Pourabdoli^{*a}, V. A. Lashgari^c

^a Department of Materials Science and Engineering, Hamedan University of Technology, Hamedan, Iran

^b Department of Electrical Engineering, Hamedan University of Technology, Hamedan, Iran

^c Department of Materials Science and Engineering, University of Bonab, Bonab, Iran

PAPER INFO

Paper history:

Received 18 April 2021

Received in revised form 28 May 2021

Accepted 03 July 2021

Keywords:

Conductive Adhesive

Silver-coated Copper

Filler

Transistor Circuit

Electrical Resistivity

A B S T R A C T

Electrically conductive composite adhesives containing 70, 75 and 85 wt% of filler particles (Cu@Ag) and polymer matrix were prepared. Thermal stability and morphology of the prepared adhesives were examined using TG (Thermo-Gravimetry), DSC (Differential Scanning Calorimetry), and SEM (Scanning Electron Microscope) techniques. In the next step, a transistor-based electrical circuit using self-biased common-emitter combination was made from the prepared conductive adhesive as well as a copper board. All of the prepared boards were subjected to DC (8-30 V) and AC (1 kHz) currents to evaluate their performance. For these circuits, parameters such as transistor operating points and the voltage gain of the amplifier, were measured. TG and DSC analyses showed that increasing the filler amount from 70 to 85 wt%, reduces the weight loss of the adhesive from 15.48 to 11.35 wt%. Also, effect of increasing the silver amount in Cu@Ag particles on the thermal stability of adhesives at temperatures below 350 °C showed that by increasing of the amount of silver from 20 to 40 wt%, has a negligible effect on weight change (about 2 wt% at 250 °C). Both samples showed almost the same overall weight loss at 350 °C. Evaluation of circuit performance showed that the changes in circuit width (1, 1.5, and 2 mm) has no significant effect on the V-I characteristics and voltage gain. The value of these two parameters for all three circuits and also the copper board circuit were the same which indicates the high conductivity of the prepared conductive adhesive.

doi: 10.5829/ije.2021.34.08b.02

NOMENCLATURE

V_{CC}	Supply voltage	I_c	Collector-emitter current (operating point current)
V_B	Base pin voltage	V_{RC}	Dropped voltage across Rc
V_E	Emitter pin voltage	V_{CE}	Collector-emitter voltage (operating point voltage)

1. INTRODUCTION

One of the outcomes of rapid growth of technology is the short lifetime of electronic devices and consequently, generating avalanche of electronic scraps. These electronic scraps contain large amounts of lead due to the lead-containing materials (lead-tin solders) in them. Lead in these scraps can be released into the environment if stored improperly. Lead is a toxic metal and can cause irreparable damage on the environment and living creatures. For this reason, the use of lead-containing solders has been severely banned in many European countries, and especially in Japan. Electrically

conductive adhesive is a suitable alternative to lead-based solders. The adhesive composed the components of a polymer matrix, conductive filler, curing agent, catalyst, and additives. Performance of a conductive adhesive depends on the amount, type of filler and polymer matrix. Due to the variety of components mentioned, there are many different types of conductive adhesives [1-3]. Electrically conductive adhesives can be used in a variety of electronic equipments. Some of these adhesives are designed only for the specific applications, while others have more general applications. For example, high temperature thermal stability is not very important for ordinary computers, but it is very critical

*Corresponding Author Institutional Email: mpourabdoli@hut.ac.ir
(M. Pourabdoli)

for avionics, sensors, and car engine electronics. Adhesives are divided into isotropic and anisotropic conductive adhesives. Isotropic conductive adhesives are used in electronic packaging, circuits and electronic devices. applications of anisotropic conductive adhesives include flat panel displays, fine pitch interconnection, highly reliable flip chip assemblies, high frequency inter-connection, high current density inter-connection and wafer level packages [4-6]. Various aspects of type, preparation, and characterization of electrically conductive adhesive such as effect of silver content on shear mechanical properties [7], using recycled resources for development of electrically conductive adhesives [8], effect of graphene filler structure on electrically conductive adhesive [9], properties of graphene based epoxy adhesive [10], DTT functionalization of Ag particles for conducting adhesive [11], adhesives prepared from epoxy and silver-coated copper particles [12], adhesives prepared from mixture of silver nanowires and nano-silver-coated copper [13], novel electrically conductive epoxy/reduced graphite oxide/silica hollow microspheres adhesive [14], silver nanostructures for high-performance composite conductive adhesive [15], stretchable conductive adhesives [16], silver coated nano-graphite filled conductive adhesive [17], and conductive adhesive prepared with silver coated graphite nano-sheets [18] have been studied. An important category of electronic circuits is amplifier circuits whose main task is to amplify the amplitude of the input signals and convert them into larger signals. Amplifier circuits can exhibit specific AC performance under DC operating conditions. Therefore, using these amplifying circuits, the performance of DC and AC can be simultaneously evaluated. One of the basic transistor-based amplifier circuits is the self-biased common-emitter circuit that is capable of amplifying both the voltage and the current signals [19]. Transistor is sensitive to its operating point (DC parameters), that is an important point in using transistor-based amplifiers. If its operating point changes, its amplification parameters will also change. Therefore, it can be said that they are sensitive to environmental factors. This type of circuit to evaluate the performance of conductive adhesives can be very valuable because performance of this circuit is very sensitive to environmental parameters. Therefore, the difference in the performance of conductive adhesive in comparison with copper wire can be evaluated. On the other hand, if the performance of the conductive adhesive is acceptable, it can greatly help electronic circuit designers in terms of prototype design and fabrication speed. Also, using conductive adhesives instead of printed circuit boards (PCBs) results in achieving prototypes of many circuits and systems with lower fabrication costs, higher production rates and improved flexibility.

In the present study, an electrically conductive adhesive was made using epoxy resin and Cu@Ag particles as a polymer matrix and a conductive filler, respectively. Then it was practically used to build an emitter-joint circuit. The innovation of current research is the practical use of electrically conductive adhesive to make a self-biased common-emitter amplifier circuit and evaluating its performance with respect to the similar circuit made on a copper board.

2. MATERIALS AND MEHTODS

2. 1. Raw Materials and Method of Preparing Conductive Adhesive

All chemicals were of analytical grade and used as received without any further purification. To prepare the conductive adhesive, Cu@Ag particles ($< 30 \mu\text{m}$) were washed with the alkaline solution (mixture of 0.5 M ammonium sulfate and 1 M sodium hydroxide solutions) for 2 minutes to remove possible surface impurities. Then, 1.4 wt% stearic acid was dissolved in ethanol and added to the filler and placed in an oven at 50 °C until its ethanol completely evaporated. Subsequently, the epoxy resin (Epoxiran 8126 equivalent to Epon 826) with ethanol (0.5 ml per 1 g of adhesive) was added to the filler particles and thoroughly mixed to obtain an almost homogeneous mixture. After this step, the resulting material was placed in an oven at 80 °C for complete ethanol removal from the resin. Then, a hardener (curing agent:3895 epoxiran equivalent to LS-81K) was added to the resin and mixed. The prepared conductive adhesive was cured in an oven at 77 °C for 30 minutes [2]. Table 1 summarizes the specifications of the prepared adhesives. To study the structure and morphology of adhesives, JEOL JSM-840A Scanning Electron Microscope (SEM) was employed.

2. 2. Thermal Stability of Conductive Adhesives

The thermal stability of conductive adhesives was studied using Thermo-Gravimetry (TG) and Differential Scanning Calorimetry (DSC) analyses with TA Instruments model SDT Q600 in the temperature range

TABLE 1. Specification of prepared adhesives

Code	Filler wt%	Ag in filler wt%	Epoxy wt%	Curing agent wt%
CA7520	75	20	15.7	7.9
CA7530	75	30	15.7	7.9
CA7540	75	40	15.7	7.9
CA7030	70	30	19.1	9.5
CA8530	85	30	9.1	4.5

of 25-350 °C and heating rate of 10 °C/min in laboratory air atmosphere.

2. 3. Performance of Conductive Adhesive as a Transistor Circuit under AC and DC Currents

To study the practical application of prepared adhesives, a circuit according to Figure 1 was assembled from CA7530 adhesive in three different widths of 1, 1.5, and 2 mm and with the same thickness of 0.5 mm. Then, the performance of the prepared circuits was evaluated under DC and AC currents. For this purpose, a circuit was used that is capable of evaluating the AC and DC parameters. This is important since the adverse environmental parameters, commonly referred to as ambient noise, have different effects on the AC and DC parameters of the electrical circuits. Also, due to the different nature of the AC and DC parameters, the conductive adhesive might have been appropriate for one parameter and inappropriate for another. Since the main application of this adhesive is in the electrical and electronic industries, its performance in all possible situations and under real environmental conditions should be considered. The used circuit was a single-stage transistor-based electronic circuit and a bipolar junction transistor (BJT). With 3 terminals assigned to a BJT, it becomes possible to configure these devices in 3 unique ways in a circuit depending on the application requirement. These configurations are called common-emitter (C.E.), common-base (C.B) and common-collector (C.C.) configurations. The main characteristics of a BJT in the three configurations (single stage) are given in Table 2.

The common emitter amplifier construction delivers the very best current and power gain among the 3 bipolar transistor designs which is, therefore, the widely used type [19, 20]. It should be noted that there are much more powerful multi-stage amplifiers (Darlington, Cascade, Differential, Power, etc.) which are also designed and built based on these three single-stage configurations. For this reason, one of these three basic configurations (BJT-based) is used in this work [21-23]. So, the used circuit was a single-stage BJT-based circuit known as the self-biased Common Emitter Amplifier. This circuit can amplify the input signal (AC parameter) based on a specific operating point (DC parameter). A practical pre-designed circuit was used in this study because the aim

TABLE 2. Transistor Configuration Summary

BJT Configurations	C.E (bypassed/un-bypassed)	C.B	C.C
Voltage Gain	High/Medium	High	Low
Current Gain	High	Low	High
Power Gain	High	Low	Medium
Input Resistance	Medium/High	Low	High
Output Resistance	Medium	High	Low

was the performance test of the prepared conductive adhesive. To observe and measure the input and output parameters of the circuit, a digital multimeter GW Instek model GDM-8145 and an oscilloscope GW Instek model GOS-653G were used. Furthermore, a DC power supply (Azma Electronic model JPS-303D) and an AC signal source (GW Instek model SFG-1013) were employed to supply direct and alternating currents, respectively. As shown in Figure 1, this circuit consists of an NPN transistor (with the part number 2SC945), a 10 kΩ resistance attached to the collector pin, a 1 kΩ resistance attached to the emitter pin, and two resistances, namely 10 kΩ and 1 kΩ attached to the base. A DC power supply is used to create the desired operating point of the transistor. The adhesive performance was evaluated by applying a variable DC voltage of 8 to 30 V to the circuit as a power supply. Since this is a DC test, the most important parameters to consider are the collector current (I_C) and the collector-emitter voltage (V_{CE}), which indicate the operating area of the transistor (Active linear, Saturation, Cut off). The calculation of these two parameters is based on Equations (1) to (3) [19]. Writing Kirchhoff's voltage equation in the clockwise direction for the input loop, we obtain:

$$V_B = \frac{R_1}{R_1 + R_2} \times V_{CC} \quad (1)$$

$$V_B - (R_1 \parallel R_2) \times I_B - V_{BE} - R_E I_E = 0 \quad (2)$$

$$I_B = \frac{I_E}{(1 + \beta)} \quad (3)$$

where I_E is the collector current, V_{BE} is the base-emitter voltage with a practical value of 0.62 V, and the β is *common-emitter, forward-current, amplification factor*, since the collector current is usually the output current for the CE configuration and the base current is the input current. For practical devices, the level of β typically ranges from about 50 to over 400, with the most in the midrange. This parameter can be determined at a particular operating point on the BJT characteristics [19]. The practical value of the β was 270 for 2SC945 transistor at room temperature.

Substituting for I_B in Equation (2) result in:

$$V_B - \frac{(R_1 \parallel R_2)}{(1 + \beta)} I_E - V_{BE} - R_E I_E = 0 \quad (4)$$

Grouping terms then provides the following:

$$V_B - V_{BE} - \left[\frac{(R_1 \parallel R_2)}{(1 + \beta)} + R_E \right] \times I_E = 0 \quad (5)$$

and solving for I_E gives:

$$I_E = \frac{V_B - V_{BE}}{R_E + \frac{(R_1 \parallel R_2)}{(1 + \beta)}} \quad (6)$$

if β times the value R_E is at least 10 times the value of R_2 , the approximate approach can be applied with a high degree of accuracy. Once V_B is determined, the I_E can be calculated from Equation (7):

$$I_E \cong \frac{V_B - V_{BE}}{R_E} \tag{7}$$

The collector-to-emitter voltage is determined by Equation (8) as follow:

$$V_{CE} = V_{CC} - (R_C + R_E)I_C \tag{8}$$

where I_C is the collector current, V_{CE} is the collector to emitter voltage [19]. The obtained results of these parameters using the variable power supply (from 8 to 30 V) for the circuit's root width of 1, 1.5, and 2 mm were recorded. The reference circuit for checking the operation of these circuits was the same circuit implemented on a copper board. The results of the copper board implemented circuit are presented in Table 4. The active linear is the main area of transistor performance evaluation. Therefore, according to the combination of circuit resistors in Figure 1, the minimum supply voltage required to set the transistor within the active linear area was 8 V. Hence, the circuit test started using 8 V as the initial voltage.

The second step in the evaluation of the conductive adhesive performance was to figure out the AC performance of the circuit. To achieve this goal, the signal generator was connected to the transistor's base pin using a capacitive connection. The use of capacitors is to prevent any undesired change of the DC operating point after applying the AC input. The AC output of this circuit is the collector pin, which is shown in Figure 2.

Using the hybrid equivalent circuit of the BJT, the ratio of the output to the input signals of this circuit known as the voltage gain factor, is obtained from Equation (9) [19].

$$A_v = \frac{-h_{fe}R_C}{h_{ie} + (1+h_{fe})R_E} \tag{9}$$

where h_{fe} is the AC form of the β and it can be referred to as β_{ac} , and h_{ie} is the input resistance of the hybrid equivalent circuit of the BJT. The value of h_{fe} has ranged

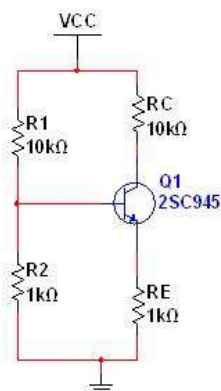


Figure 1. Schematic of the self-biased common-emitter circuit used for the DC performance test of CA7530 adhesive

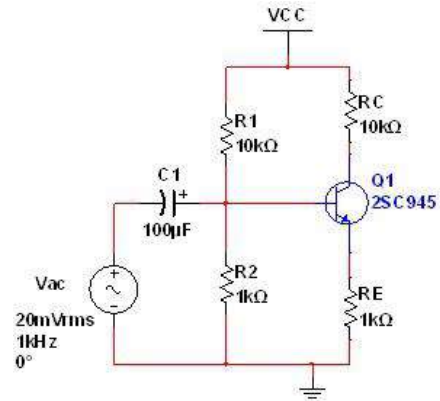


Figure 2. Schematic of the common-emitter amplifier circuit used to evaluate the AC performance of CA7530 adhesive

from about 50 to over 400. The practical value of the h_{fe} was 270 for 2SC945 transistor at room temperature. The value of h_{ie} is calculated using Equation (10) [19].

$$h_{ie} = \frac{\eta V_T \beta}{I_c} \tag{10}$$

where η is an internal value of BJT (1.05 at this work), and the V_T is the thermal voltage with the value of about 26mV at room temperature. Equation (11) can be used to calculate the voltage gain factor from an oscilloscope using observed signals.

$$A_v = \frac{v_o}{v_i} = \frac{\text{peak-peak of the output voltage signal}}{\text{peak-peak of the input voltage signal}} \tag{11}$$

A real illustration of a circuit made with conductive adhesive, the devices used, and the components connected to the circuit are shown in Figure 3.

The input and output signals of the three circuits based on conductive adhesive and the reference circuit are shown in Figure 4. As shown in Figure 4, the voltage gain can be obtained from the amplitude of the input and

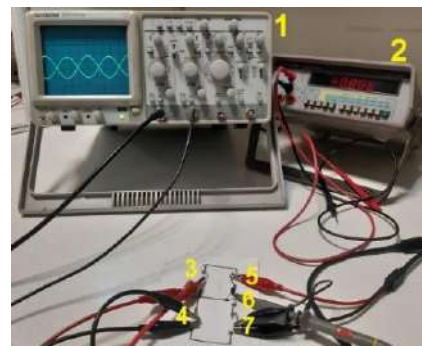


Figure 3. Implemented circuit with CA7530 adhesive and equipments used to assess its performance. 1-Oscilloscope, 2-Multimeter, 3- Oscilloscope channel 1, 4- Input from signal generator, 5-Positive terminal of Vcc, 6-Oscilloscope Channel 2, 7-Negative terminal of Vcc

output voltage signals. To this end, the amplitude of each signal was measured based on the cells and sub-cells of the screen and then multiplied by the value indicated by the voltage divider volume (volt \ div). The values of this volume are shown in Figure 4 (a-d) with green arrows. In all pictures of Figure 4, channel 1 and 2 represents the input and output signals, respectively. Comparing the pictures of Figure 4 shows that the amplitude of the input and output voltage signals are very close to each other. This is while the ratio of the volume volt \ div of channel 2 (output) to the volume volt \ div of channel 1 (input) is 10. This means that the voltage gain is approximately 10. It should be noted that the difference in the amplitude of the signals in pictures Figure 4 (a to d) is due to the different inputs applied to each of the four different circuits. The exact amount of voltage gain can be calculated with the stated method (Equation (11)). These values are given in Table 3.

3. RESULTS AND DISCUSSION

3. 1. Morphology of Conductive Adhesives

Figure 5 illustrates SEM images of the cross-section of CA7520, CA7530 and CA7540 adhesives. In these images, Cu@Ag particles have surrounded by black epoxy phase. As can be seen, with increasing silver amount from 20 to 30 and 40 wt%, the average thickness of silver coating around copper particles increases. Consequently, electrical resistivity of the adhesive is reduced due to the decrease in contact resistance between particles [24].

3. 2. Thermal Stability of Adhesives

Figures 6 and 7 show the TG/DSC results of conductive adhesives. According to the TG curves in Figure 6, which indicate

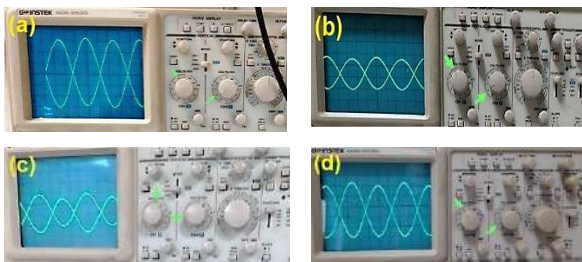


Figure 4. Oscilloscope graphs obtained after connecting circuits made of (a) copper board and CA7530 adhesive with a thickness of 0.5 mm and a width of (b) 1 mm, (c) 1.5 mm and (d) 2 mm under AC current

TABLE 3. Voltage gain of various circuits

Circuit type	Copper board	1 mm	1.5 mm	2 mm
Voltage gain	9.5	9.6	9.7	9.4

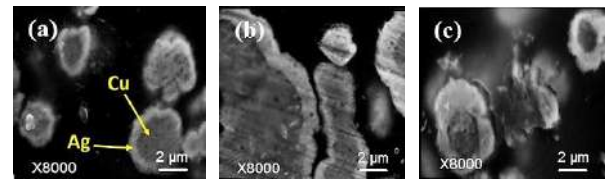


Figure 5. SEM images of conductive adhesives: a) CA7520, b) CA7530, c) CA7540

the effect of filler amount on the thermal stability of the conductive adhesive, temperature rising has reduced weight of both samples. The corresponding weight loss of CA7030 sample (15.48 wt%) is more than that of CA8530 sample (11.35 wt%) at 350 °C. Reason is that the CA7030 sample has more epoxy that decomposes with temperature rising. Two exothermic peaks at 210 and 330 °C are clearly evident in DSC curves of Figure 6. The first peak is related to residual cure and the second peak is related to the epoxy degradation [25].

According to TG curves in Figure 7, it is evident that the CA7540 sample (40 wt% Ag) showed greater thermal stability than CA7520 sample (20 wt% Ag). Therefore, increasing the silver amount from 20 to 40% improves the thermal stability of the conductive adhesives.

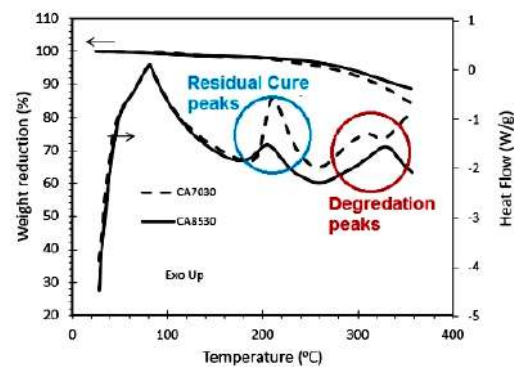


Figure 6. TG and DSC curves of CA7030 and CA8530 conductive adhesives

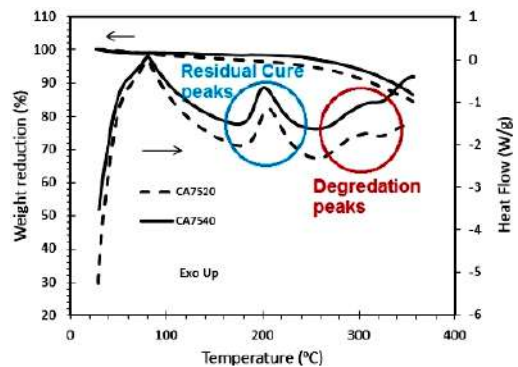


Figure 7. TG and DSC curves of CA7520 and CA7540 conductive adhesives

According to the DSC curves in Figure 7, it is clear that the samples have almost the same behavior in terms of exothermic peak position and area (calorific value). The reason for the similar behavior of the samples is that both samples have the same amount of epoxy/filler and the same amount of Cu@Ag particles.

3. 3. Performance of the Conductive Adhesive as a Transistor Circuit under DC and AC Currents

3. 3. 1. DC Current The performance results of the circuits with copper board and CA7530 adhesive with a width of 1, 1.5, and 2 mm (Figure 1) for CA7530 adhesive under DC supply are listed in Tables 4-7 and plotted in Figures 8a-8d, respectively. As can be seen, as the supply voltage increases, the current (Ic) increases, and all three curves follow a linear pattern with almost similar positive slopes. This observation indicates the similar V-I characteristic of the circuits according to Ohm's law ($V = RI$). This means that changing the width of the circuits has no significant impact on the obtained results. Comparing Figure 8a with Figures 8b-8d showed that the same results were obtained from circuits made of conductive adhesives. As a result, it can be said that the performance of these adhesives is the same as that of the copper board.

3. 3. 2. AC Current AC sinusoidal signal was used as the input voltage signal to calculate the voltage gain. Since the high amplitude of the input signal may lead to output signal distortion, then the amplitude of the input signal is set within the range of 1 mV to 100 mV. Voltage gain was calculated using Equations (4) and (5). The voltage gain for all three circuits prepared from adhesive

TABLE 4. Circuit Data related to the copper board

$V_{cc}(V)$	10	20	30
$V_B(V)$	0.888	1.776	2.283
$V_E(V)$	0.288	1.143	2.041
$I_c(mA)$	0.292	1.159	2.070
$V_{RC}(V)$	3.011	11.667	20.74
$V_{CE}(V)$	6.725	7.120	7.220

TABLE 5. Circuit data for a width of 1 mm

$V_{cc}(V)$	8	10	15	20	25	30
$V_B(V)$	0.709	0.892	1.334	1.774	2.220	2.666
$V_E(V)$	0.126	0.329	0.701	1.208	1.654	2.103
$I_c(mA)$	0.127	0.334	0.711	1.225	1.677	2.133
$V_{RC}(V)$	1.646	3.353	7.893	12.263	16.789	21.35
$V_{CE}(V)$	6.161	6.350	6.382	6.480	6.146	6.568

TABLE 6. Circuit data for a width of 1.5 mm

$V_{cc}(V)$	8	10	15	20	25	30
$V_B(V)$	0.720	0.896	1.334	1.768	2.235	2.268
$V_E(V)$	0.122	0.305	0.697	1.129	1.567	1.989
$I_c(mA)$	0.124	0.309	0.707	1.145	1.589	2.017
$V_{RC}(V)$	1.398	2.960	7.064	11.442	15.855	20.029
$V_{CE}(V)$	6.537	6.750	7.040	7.214	7.445	7.572

TABLE 7. Circuit data for a width of 2 mm

$V_{cc}(V)$	8	10	15	20	25	30
$V_B(V)$	0.634	0.904	1.345	1.795	2.249	2.695
$V_E(V)$	0.078	0.301	0.721	1.159	1.602	2.043
$I_c(mA)$	0.079	0.305	0.731	1.175	1.625	2.072
$V_{RC}(V)$	0.749	3.032	7.283	11.695	16.165	20.61
$V_{CE}(V)$	6.247	6.730	7.020	7.168	7.268	7.350

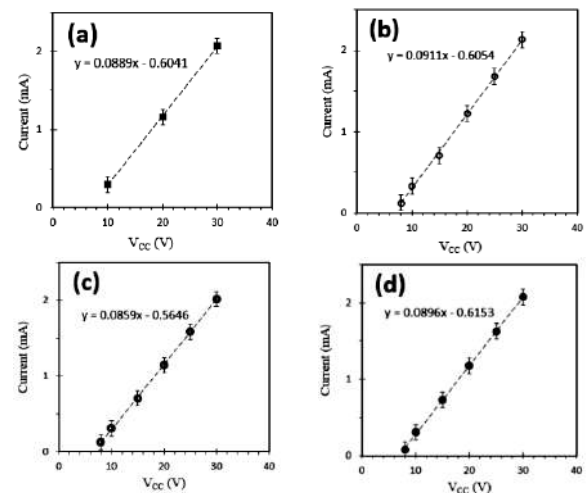


Figure 8. The V–I characteristic of the implemented circuits (Operating frequency of 1 kHz). a) copper board, b) CA7530 adhesive with a thickness of 1 mm, c) CA7530 adhesive with a thickness of 1.5 mm, d) CA7530 adhesive with a thickness of 2 mm

was approximately the same as 9.5. Consequently, the circuit width did not affect the voltage gain significantly. Then, to compare the circuit made of conductive adhesives with the copper board, the voltage gain from the graph in Figure 4a was recalculated for the copper board and the same results were obtained.

4. CONCLUSIONS

The most important results of this research are as follows:

- SEM images showed that changing the silver amount from 20 to 30 and to 40 wt% increases the average thickness of the silver coating on copper particles from 0.5 to 1 and to 1.5 μm , respectively.
- TG and DSC analyses showed that when the filler amount increases from 70 to 85 wt%, the adhesive weight loss reduces from 15.48 to 11.35 wt%.
- Adhesive prepared from Cu@Ag particles containing 40 wt% silver had more thermal stability than adhesive prepared from Cu@Ag particles containing 20 wt% silver.
- Performance evaluation of circuit made of conductive adhesives under DC and AC currents showed that changing the circuit width (1, 1.5, and 2 mm) has no significant effect on the V-I characteristic and also on the voltage gain of the circuit. The voltage gain of all three circuits was 9.5.
- It was found that the circuit made from conductive adhesive indicates the behavior quite similar to the behavior of the circuit made on the copper board.

5. ACKNOWLEDGMENTS

The authors are thankful to Mr. Ahmad Nasri and Mr. Ehsan Zamanian for their assistance during the experiments. This work was supported by Hamedan University of Technology under grant No. 18-94-1-361.

6. REFERENCES

- Trinidad, E., "Evaluation of hybrid electrically conductive adhesives", University of Waterloo, (2016).
- Massoumi, B., Hosseinzadeh, M. and Jaymand, M., "Electrically conductive nanocomposite adhesives based on epoxy or chloroprene containing polyaniline, and carbon nanotubes", *Journal of Materials Science: Materials in Electronics*, Vol. 26, No. 8, (2015), 6057-6067, doi: 10.1007/s10854-018-9284-9.
- Licari, J.J. and Swanson, D.W., "Adhesives technology for electronic applications: Materials, processing, reliability, William Andrew, (2011).
- Zhang, R. and Wong, C., "Low cost copper-based electrically conductive adhesives", in 2010 12th Electronics Packaging Technology Conference, IEEE. (2010), 715-720.
- Yim, M.J. and Paik, K.W., "Review of electrically conductive adhesive technologies for electronic packaging", *Electron Mater Lett.* Vol. 2, No. 3, (2006), 183-194, doi.
- Aradhana, R., Mohanty, S. and Nayak, S.K., "A review on epoxy-based electrically conductive adhesives", *International Journal of Adhesion and Adhesives*, Vol. 99, (2020), 102596, doi: 10.1016/j.ijadhadh.2020.102596.
- Ji, X., Jin, X., Hou, C., Xiao, G., Fan, X. and Shu, X., "Loading rate response on shear mechanical properties of conductive adhesive with different silver contents", *Journal of Adhesion Science and Technology*, Vol. 34, No. 18, (2020), 1935-1946, doi: 10.1080/01694243.2020.1749405.
- Ali, A., Baheti, V., Khan, M.Z., Ashraf, M. and Militky, J., "Development of electrically conductive composites based on recycled resources", *The Journal of The Textile Institute*, Vol. 111, No. 1, (2020), 16-25, doi: 10.1080/00405000.2019.1644121.
- Szeluga, U., Pusz, S., Kumanek, B., Olszowska, K., Kobylukh, A. and Trzebicka, B., "Effect of graphene filler structure on electrical, thermal, mechanical, and fire retardant properties of epoxy-graphene nanocomposites-a review", *Critical Reviews in Solid State and Materials Sciences*, Vol. 46, No. 2, (2021), 152-187, doi: 10.1080/10408436.2019.1708702.
- Meng, Q., Han, S., Araby, S., Zhao, Y., Liu, Z. and Lu, S., "Mechanically robust, electrically and thermally conductive graphene-based epoxy adhesives", *Journal of Adhesion Science and Technology*, Vol. 33, No. 12, (2019), 1337-1356, doi: 10.1080/01694243.2019.1595890.
- de Oliveira, C.S., Quispe, L.T., Pla Cid, C.C., Sierra, J.A., de Barros, S., Mello, A. and Pasa, A.A., "Dtt functionalization of ag particles for conducting adhesives", *The Journal of Adhesion*, Vol. 94, No. 6, (2018), 473-485, doi: 10.1080/00218464.2017.1288113.
- Zhang, X.M., Yang, X.-L. and Wang, B., "Electrical properties of electrically conductive adhesives from epoxy and silver-coated copper powders after sintering and thermal aging", *International Journal of Adhesion and Adhesives*, Vol. 105, (2021), 102785, doi: 10.1016/j.ijadhadh.2020.102785.
- Wang, Q., Zhang, S., Liu, G., Lin, T. and He, P., "The mixture of silver nanowires and nanosilver-coated copper micronflakes for electrically conductive adhesives to achieve high electrical conductivity with low percolation threshold", *Journal of Alloys and Compounds*, Vol. 820, (2020), 153184, doi: 10.1016/j.jallcom.2019.153184.
- Aradhana, R., Mohanty, S. and Nayak, S.K., "Novel electrically conductive epoxy/reduced graphite oxide/silica hollow microspheres adhesives with enhanced lap shear strength and thermal conductivity", *Composites Science and Technology*, Vol. 169, (2019), 86-94, doi: 10.1016/j.compscitech.2018.11.008.
- Chen, Y., Li, Q., Li, C., Dai, Z., Yan, H., Zhu, M., Zhang, Y., Yao, Y. and Li, Q., "Regulation of multidimensional silver nanostructures for high-performance composite conductive adhesives", *Composites Part A: Applied Science and Manufacturing*, Vol. 137, (2020), 106025, doi: 10.1016/j.compositesa.2020.106025.
- Dou, J., Tang, L., Mou, L., Zhang, R. and Jiang, X., "Stretchable conductive adhesives for connection of electronics in wearable devices based on metal-polymer conductors and carbon nanotubes", *Composites Science and Technology*, Vol. 197, (2020), 108237, doi: 10.1016/j.compscitech.2020.108237.
- Lin, W., Xi, X. and Yu, C., "Research of silver plating nanographite filled conductive adhesive", *Synthetic Metals*, Vol. 159, No. 7-8, (2009), 619-624, doi: 10.1016/j.synthmet.2008.12.003.
- Zhang, Y., Qi, S., Wu, X. and Duan, G., "Electrically conductive adhesive based on acrylate resin filled with silver plating graphite nanosheet", *Synthetic Metals*, Vol. 161, No. 5-6, (2011), 516-522, doi: 10.1016/j.synthmet.2011.01.004.
- Boylestad, R.L. and Nashelsky, L., "Electronic devices and circuit theory 11th ed", (2018).
- Fathi, A., Azizian, S. and Sharifan, N., Sensors and amplifiers: Sensor output signal amplification systems, in Handbook of research on nanoelectronic sensor modeling and applications. 2017, IGI Global.423-504.
- Rashtian, M. and Vafapour, M., "Gain boosted folded cascode op-amp with capacitor coupled auxiliary amplifiers", *International Journal of Engineering, Transactions B: Applications*, Vol. 34, No. 5, (2021), 1233-1238, doi: 10.5829/ije.2021.34.05b.16.
- Chauhan, D.S., Tomar, R. and Singh, S., "A new trans-admittance-mode biquad filter suitable for low voltage operation", *International Journal of Engineering, Transactions C: Aspects*,

- Vol. 28, No. 12, (2015), 1738-1745, doi: 10.5829/idosi.ije.2015.28.12c.06.
23. Dehghanian, R. and Salimi, A., "A hysteretic two-phase supply modulator for envelope tracking rf power amplifiers", *International Journal of Engineering, Transactions C: Aspects*, Vol. 27, No. 12, (2014), 1832-1840, doi: 10.5829/idosi.ije.2014.27.12c.05.
24. Zhao, J. and Zhang, D., "Epoxy-based adhesives filled with flakes ag-coated copper as conductive fillers", *Polymer Composites*, Vol. 38, No. 5, (2017), 846-851, doi: 10.1002/pc.23645.
25. Abenojar, J., Enciso, B., Pantoja, M., Velasco, F. and Martínez, M.-A., "Thermal characterization and diffusivity of two mono-component epoxies for transformer insulation", *International Journal of Adhesion and Adhesives*, Vol. 103, (2020), 102726, doi: 10.1016/j.ijadhadh.2020.102726.

Persian Abstract

چکیده

چسب های کامپوزیت رسانای الکتریکی از ۷۰، ۷۵ و ۸۵ درصد وزنی ذرات پرکننده (پودر مس پوشش داده شده با نقره) و ماتریس پلیمری تهیه شدند. پایداری حرارتی و مورفولوژی چسب های تهیه شده با استفاده از روشهای ترموگراویمتری (TG)، کالریمتری ریشی تفاضلی (DSC) و میکروسکوپ الکترونی ریشی (SEM) بررسی شدند. در مرحله بعدی، یک مدار الکترونیکی مبتنی بر ترانزیستور (مدار امیتر- مشترک خود بایاس) از چسب رسانا و نیز به طور جداگانه از یک بورد مسی ساخته شد. جهت بررسی عملکرد مدارهای ساخته شده، همه آنها تحت جریان DC (۳۰-۸ ولت) و جریان AC (یک کیلو هرتز) قرار گرفتند. برای این مدارها، پارامترهایی مانند نقطه کار ترانزیستور و بهره ولتاژ اندازه گیری شدند. نتایج آنالیزهای TG و DSC نشان داد که افزایش مقدار پرکننده از ۷۰ تا ۸۵ درصد وزنی، اتلاف وزنی چسب ها را از ۱۵/۴۸ به ۱۱/۳۵ درصد وزنی کاهش می دهد. همچنین، بررسی اثر افزایش مقدار نقره در ذرات پرکننده روی پایداری حرارتی چسب ها در دماهای زیر ۳۵۰ درجه سانتیگراد، نشان داد که افزایش مقدار نقره از ۲۰ به ۴۰ درصد وزنی تاثیر کمی روی تغییر وزن چسب ها (در حدود ۲ درصد وزنی در دمای ۲۵۰ درجه سانتیگراد) دارد و هر دو نمونه در دمای ۳۵۰ درجه سانتیگراد اتلاف وزنی تقریباً یکسانی از خود نشان دادند. ارزیابی عملکرد مدارها نشان داد که تغییر در عرض مدار (۱، ۱/۵ و ۲ میلیمتر) تاثیری قابل توجهی روی مشخصه V-I و بهره ولتاژ ندارد. مقدار این دو پارامتر برای هر سه نوع مدار و نیز مدار تهیه شده از بورد مسی یکسان بودند که نشان دهنده هدایت بالای چسب های رسانا است.



Synergetic Photocatalytic and Adsorptive Removals of Metanil Yellow using TiO₂/Grass-derived Cellulose/Chitosan Film Composite

Rahmi^{*a}, S. Lubis^a, N. Az-Zahra^a, K. Puspita^b, M. Iqhrammullah^{a,c}

^a Department of Chemistry, Faculty of Mathematics and Natural Sciences, Universitas Syiah Kuala, Kopelma Darussalam, Indonesia

^b Department of Chemistry Education, Faculty of Education and Teacher Training, Universitas Syiah Kuala, Kopelma Darussalam, Indonesia

^c Graduate School of Mathematics and Applied Sciences, Universitas Syiah Kuala, Kopelma Darussalam, Indonesia

PAPER INFO

Paper history:

Received 23 April 2021

Received in revised form 16 May 2021

Accepted 04 June 2021

Keywords:

Chitosan

Cellulose

Photocatalyst

Nanoparticle

TiO₂

ABSTRACT

Chitosan (CH) and cellulose are the most abundant biopolymers which could be utilized for hazardous dye removal. By incorporating TiO₂ onto cellulose/CH matrix, our research aimed to achieve high metanil yellow removal by means of synergetic adsorption/photodegradation mechanism. The cellulose particles were extracted from wild grass (*Imperata cylindrica* L.) to obtain grass-derived cellulose (GC). Simple blending method was used to prepare TiO₂/GC/CH, in which the composition was determined by simple additive weighting method (SAW). TiO₂/GC/CH was characterized by means of tensile strength test (also used for SAW), Fourier Transform-Infrared (FT-IR), X-ray diffraction (XRD), differential scanning calorimetry (DSC), and scanning electron microscopy (SEM). Metanil yellow removal using TiO₂/GC/CH works very well at acidic pH range. The removal follows the pseudo-second-order kinetic ($R^2 = 0.997$) and Langmuir isotherm ($R^2 = 0.998$) modellings. High q_m obtained from the metanil yellow removal under UV irradiation ($q_m = 171.527$) proves the synergism between adsorption and photodegradation. The developed TiO₂/GC/CH could be potentially used in the wastewater treatment for azo dye removal.

doi: 10.5829/ije.2021.34.08b.03

1. INTRODUCTION

Chitosan (CH) has been recognized by scientific communities for its excellent properties in removing hazardous contaminants from water, either they are heavy metals or dyes [1, 2]. For practical aspect, CH adsorbent can be prepared in a form of film. In such form, the adsorbent could be easily filtered from the water after the adsorption has been completed. Unfortunately, CH could be easily ruptured by mechanical force and dissolved by acidic solution. To overcome, some studies have prepared CH-based composite using various fillers [3-5].

Cellulose is a good filler candidate, especially because of its high adsorptive performance and rich abundance in nature [6-8]. Some research groups have developed Cellulose/CH-based composite to improve

the inherent properties of CH [5, 9, 10]. Our research group focuses on utilizing widely available biomass as the source of cellulose. Previously, we had successfully prepared CH film composite with cellulose derived from oil palm empty fruit bunches [11, 12], and applied it to remove Cd²⁺ from water. Others have used biopolymers as the reinforcement including leaf fibre [13], cassava starch [14], and cellulose [15]. In this research, we used wild grass (*Imperata cylindrica* L.) – or locally known as *alang-alang*, as the source for the cellulose filler.

Adsorptive removal could be synergized with photo-induced degradation facilitated by TiO₂ photocatalyst. As a photocatalyst, TiO₂ can be triggered by UV irradiation to produce pairs of electron and holes leading to the generation of hydroxyl radicals [16, 17].

There have been extensive reports regarding the effective photodegradation performed by TiO₂ [18, 19]. Agglomeration is one of the challenges in the

*Corresponding Author Email: rahmi@fmipa.unsyiah.ac.id (Rahmi)

application of nanoparticles due to the loss of contact surface. Our groups had used TiO₂ for dye removal with various modifications to prevent agglomeration of the nanoparticles [20-22]. Herein, we expected that the cellulose/CH matrix could prevent the agglomeration by fine distribution of the nanoparticles on the matrix surface. Moreover, addition of TiO₂ onto polymeric matrix can improve the physical properties of the material [23, 24].

Indeed, CH, cellulose, and TiO₂ blends have been widely investigated for its performance on removing dyes, but mostly those reported studies used cellulose derivative – cellulose acetate [24-27]. On contrary, we used non-valuable and widely abundant source – grass, as the source to obtain grass-derived cellulose (GC) filler. To test the performance of TiO₂/GC/CH film composite, we chose metanil yellow as a model for azo dye pollutant which occupies 50% of world's dye production [28]. At the end of the day, we expect that our TiO₂/GC/CH film composite can be applied to treat wastewater produced in azo dye-related industries.

2. MATERIALS AND METHODS

2. 1. Materials and Cellulose Extraction

Chitosan (CH) as the feed material for the matrix polymer was purchased from Tokyo Chemical Industry Co., Ltd. (Japan) with acetyl degree of 75-85%. Glacial acetic acid, TiO₂ powder, metanil yellow, H₂SO₄, H₂O₂, and pH adjusters (NaOH and HNO₃) were purchased from Sigma-Aldrich (Missouri, United States).

Grass-derived cellulose (GC) had been priorly obtained and its characteristics had been reported [29]. Briefly, powdered grass was hydrolyzed in H₂SO₄ 40% and bleached in H₂O₂ 30% (at 45°C; 90 min), followed by washing and oven-drying at 40°C.

2. 2. Preparation of TiO₂/GC/CH CH was dissolved in 100 mL glacial acetic acid (20% v/v) and stirred at 250 rpm for 2 h to obtain a matrix solution. GH and TiO₂ were priorly homogenously dispersed in distilled water before they were sequentially added into the matrix solution and stirred at 250 rpm for another 2 and 3 h, respectively. The casting solution was then poured onto a glass mold (17.5 x 12.5 cm) and dried at room temperature for 48 h to obtain the film composite as depicted in Figure 1.



Figure 1. A visual appearance of TiO₂/GC/CH composite film

2. 3. Selection of the Best Film Composite To select the best composite we employed simple additive weighting method (SAW) [30]. The decision making analysis was based on the tensile strength of the film and the % removal of metanil yellow, with % priority of 40% and 60%, respectively. Tensile strength was measured by using Universal Testing Machine (UTM) Huang Ta with strain rate of 20 mm/s, where the film's shape followed ASTM D638. Meanwhile, the % removal of metanil yellow from aqueous solution (20 mL) was determined from batch adsorption at equilibrium and pH 6.5 in dark condition using 0.01 g of the film samples, which will be further explained later. Afterward, the data were normalized by dividing each value with the maximum value of all samples. This calculation produced normalized tensile strength (N_a) and normalized removal percentage (N_b). The priority index (N_{pi}) was then calculated by Equation (1):

$$N_{pi} = (40\% \times N_a) + (60\% \times N_b) \quad (1)$$

Film composite with N_{pi} closest to 1 was selected for characterization and further metanil yellow removal studies.

2. 4. Characterization Characterizations of the prepared materials were conducted in Shimadzu Fourier transform – infrared (FT-IR) 8400 (Kyoto, Japan), Jeol. Jsm-6510 LA scanning electron microscope (SEM) (Tokyo, Japan), Shimadzu X-ray diffractometer (XRD)-700 (Kyoto, Japan), and Shimadzu differential scanning calorimetry (DSC)-60 (Kyoto, Japan). The characterization procedures followed our previous reports [6, 31].

2. 5. Batch Adsorption/Photodegradation

Metanil yellow removal by TiO₂/GC/CH film composite was conducted (at 250 rpm; 30°C) in two conditions, with and without the presence of UV irradiation for adsorption and synergetic adsorption/photodegradation studies, respectively. The final concentration (C_e (mg/L)) of metanil yellow was calculated employing Shimadzu UV-Vis spectrophotometer (Uvmini-1240, Shimadzu, Kyoto, Japan) at λ_{max} = 432 nm after the pH adjustment into 6, as suggested previously [32]. For the contact time studies, the procedure was carried out at pH 6.5 using 0.05 g TiO₂/GC/CH in 25 mL metanil yellow (100 mg/L). The adsorption parameters followed the suggestion of previous reports [33, 34]. All the following studies employed the optimum adsorption parameters obtained earlier (100 minutes contact time; pH 3). Adsorption capacity at *t* time (q_t (mg/g)), adsorption capacity at equilibrium (q_e (mg/g)), and removal percentage (%) were calculated based on the equations we had used in the previous reports [35-37]. For the photodegradation using UV irradiation, a UV lamp (6 W; λ = 365 nm) was used and positioned 10 cm away from the batch container.

3. RESULTS AND DISCUSSION

3. 1. Effect of Filler Addition on the Tensile Strength and Metanil Yellow Uptake

Addition of GC and TiO₂ promotes adhesive force, resulting in higher tensile strength than neat CH (Table 1). The addition of fillers prevents the slipping effect and reduces the void in the matrix. Our findings are consistent with the previously reported studies [3, 4, 38, 39].

However, adverse effect of GC and TiO₂ fillers incorporation onto chitosan matrix on metanil yellow removal was observed. It is presumably because of the blockage of the binding sites in the chitosan. Yet, TiO₂ embedment was expected to provide synergetic adsorptive and photocatalytic removal. In determining the optimum composite, the removal was merely based on the adsorption since it was conducted in dark condition.

The aim of preparing this composite is not only to obtain a material that performs the highest dye removal. For practical purposes, the composite film should possess a good endurance against mechanical stress from the water flow. Therefore, mechanical properties of the material should also be taken into account. Combinations of TiO₂, GC, and CH yield complex interaction, resulting in unpredictable tensile strength and metanil yellow removal performance. Therefore, selection of the most optimum composite was determined through SAW method, where composite with the composition of 0.9 g CH, 0.05 g GC, and 0.05 g TiO₂ was selected due to its possession of the highest Npi value (Table 1).

3. 2. Characteristics The purposes of analyzing FT-IR spectra (Figure 2) are: a) Investigating the success of GC and TiO₂ fillers addition, and b) Identifying functional groups that can act as active sites,

namely O- and N-containing groups [35, 40]. Overlapping of O-H and N-H stretching vibration was observed at a range of around 3500 – 3000 cm⁻¹ in all samples. Within the same wavenumber range, GC/CH and TiO₂/GC/CH showed broader spectral bands indicating the addition of O-H from GC [41] and TiO(OH)₂ nanoparticles [42]. Amide I bands (N-H deformation and C-O stretching) of typical CH were observed at 1638 cm⁻¹; shifted to lower wavenumber 1632 cm⁻¹ stem from the effect of GC and TiO₂ addition. Transmittance peaks at 1147 and 888 cm⁻¹ from CH are assigned to C-O-C and C=O stretching, respectively. These peaks were shifted to higher wavenumber associated with the successful immobilization of GC and TiO₂ [43, 44]. The immobilization of TiO₂ into GC/CH could also be proven by the appearance of transmittance peak of O-Ti-O stretching vibration, which is similar to the previously reported study [45].

Based on the diffractogram of CH (Figure 3a), the appearance of amorphous peak at 2θ = 20.00° is typical for hydrophilic chitosan crystalline lattice [46]. Previously, GC had been characterized using XRD where the typical peaks at 15.24° and 21.96° (2θ) were found [46]. In this study, those peaks were not observable in GC/CH composite. Moreover, the addition of GC resulted in the disappearance of several peaks in CH matrix (2θ = 37.79, 57.90, 64.73, and 77.68), indicating the change in polymer crystallinity. A new peak at 24.85 in TiO₂/GC/CH corresponds to the immobilization of TiO₂. Significant decrease at 20.00° (2θ) in GC/CH and TiO₂/GC/CH is ascribed to the addition of those GC and TiO₂ as fillers. Depression of crystalline lattice of CH may occur due to the presence of those fillers induced by both hydrogen bonds and steric effect [45]. It is then confirmed by quantitatively calculate the crystallinity of the samples using the proposed method [12, 47]; crystalline peaks divided by noises of the entire diffractogram and multiplied by

TABLE 1. Results of SAW analysis based on the tensile strength and q_e

Composition	Criteria		Npi
	Tensile Strength (kgf/mm ²)	Removal (%)	
CH (1 g)	12.33	99.07	0.90
CH : GC (0.9 g : 0.1 g)	14.00	98.82	0.94
CH : TiO ₂ (0.9 g : 0.1 g)	15.42	98.88	0.98
CH : GC : TiO ₂ (0.9 g : 0.025 g : 0.075 g)	14.25	99.13	0.95
CH : GC : TiO ₂ * (0.9 g : 0.05 g : 0.05 g)	16.17	98.80	1.00
CH : GC : TiO ₂ (0.9 g : 0.075 g : 0.025 g)	14.25	99.04	0.95

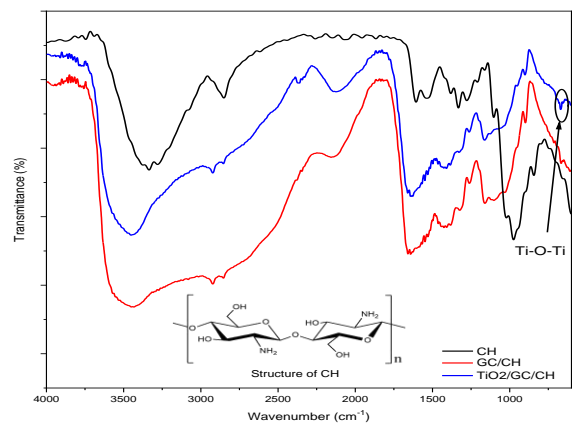


Figure 2. FT-IR spectra of CH, GC/CH, and TiO₂/GC/CH

100%. CH, GC/CH, and TiO₂/GC/CH have crystallinity indices of 63.86%, 30.32%, and 27.96%, respectively.

DSC analysis aims to see the endothermic and exothermic temperatures of the chitosan-cellulose-TiO₂ composite film, which in principle measures the difference in heat that enters with that of reference temperature. Endothermic shoulder at 115.67°C in CH thermogram (Figure 3b) is ascribed to the presence of water evaporation, where higher temperature was needed to evaporate the water in GC ($T_{\text{peak}} = 156.36^\circ\text{C}$). It is probably due to the higher hydrophilicity of GC, as opposed to CH, resulting in stronger binding of water molecules. Interestingly, the endothermic shoulder return to lower temperature after the embedment of TiO₂. There have been reports where TiO₂ embedment can increase the hydrophobicity of a material [48, 49].

Exothermic peak at 338.97°C is ascribed to the decomposition of CH, whereas in GC/CH and TiO₂/GC/CH, the decomposition was observed by two identical exothermic peaks (at 319 and 395°C). The thermal profile of GC/CH with two exothermic decomposition peaks explains two different polymers in the composites (GC and CH). The inherent decomposition temperature of CH decreased in the composite, which can be attributed to the reduction of intermolecular interaction of chitosan caused by the presence of GC particles. It is corroborated by the XRD

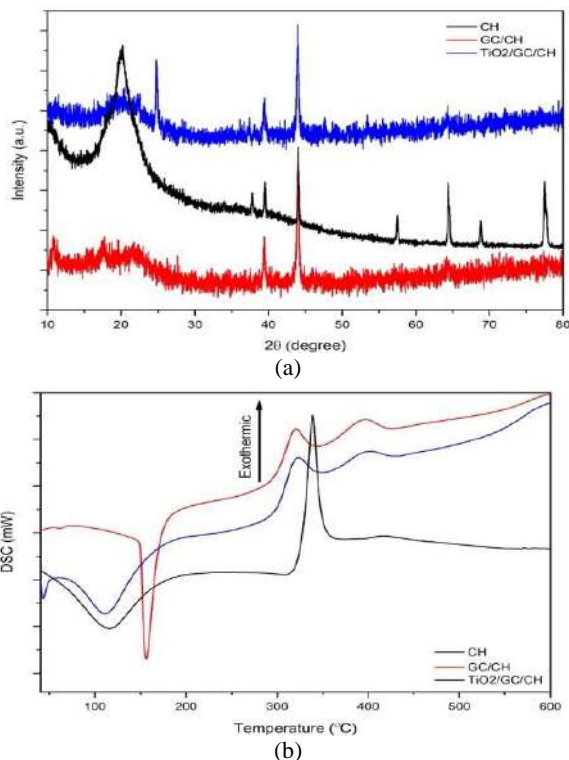


Figure 3. XRD patterns and DSC thermogram of CH, GC/CH, and TiO₂/GC/CH

thermogram, where GC addition resulted in the deformation of CH crystalline structure. Meanwhile, the addition of TiO₂ appeared to contribute to slower decomposition, where broader exothermic peak at 395°C is observed and ascribed to the degradation of not only the polysaccharide and but also the O-H from TiO₂ [43].

SEM images of CH, GC, GC/CH, and TiO₂/GC/CH (Figure 4) are used to examine the surface morphology of the samples. SEM image of CH shows a smooth surface which indicates its homogenous mixing in the solvent – in line with a previously reported study [50]. Diverse sizes of GC particles are observed with fibrous shape and a diameter of 10 to 50 μm. The difference may be influenced by the hydrolysis and bleaching process. GC/CH composite is observed to be having rougher surface than CH. From the image, we can see that GC was totally enveloped with CH layer indicating the compatible composite. TiO₂ nanoparticles can be observed to be very well dispersed on the GC/CH surface, suggesting the successful embedment polymer [25]. However, several agglomerations of TiO₂ were observed as shown by the red arrow.

3. 3. Metanil Yellow Removal

3. 3. 1. Optimum Adsorption Parameters

Two important parameters for metanil yellow removal via adsorption or photodegradation, namely contact time and pH, had been studied (Figure 4). Rapid increment of the adsorption capacities from the 20th to 60th minute

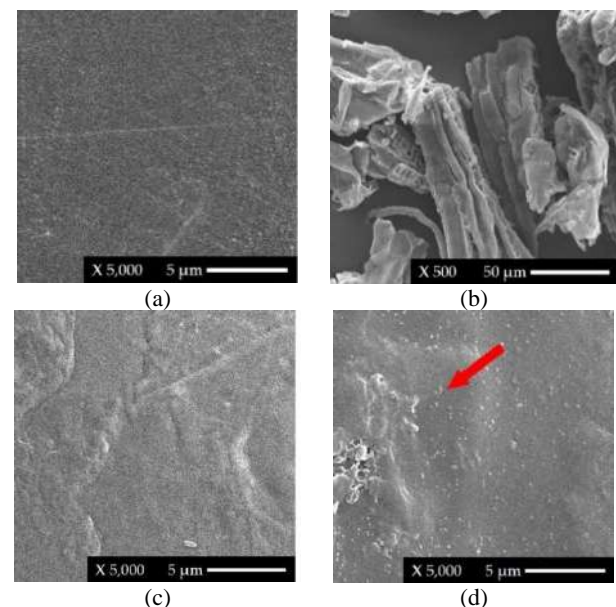


Figure 4. SEM images of (a) CH film, (b) GC particles, (c) GC/CH film, and (d) TiO₂/GC/CH film with 5,000 x magnification. The red arrow indicated the presence of TiO₂ agglomeration.

was observed to be 135% and 202% for the adsorption and adsorption/photodegradation, respectively (Figure 5a). It is due to the high diffusion force as at the initial phase, the vacant binding sites is still numerous. On contrary, at longer contact time the adsorption is governed by chemical interaction between adsorbate and adsorbent surface. Higher adsorption capacity from the adsorption/photodegradation, especially at 60th minute, may indicate the synergetic mechanism. However, further studies using isothermal modelling were used to substantiate the synergism. As the metanil yellow pollutant attaches to the TiO₂/GC/CH surface, the pollutant will be photodegraded by TiO₂ – providing extra vacant site. This process reached equilibrium at 100th minute indicated by the saturation of adsorption capacity in the following contact times. At equilibrium, the adsorption capacity for adsorption and adsorption/photodegradation were 47.84 and 48.28 mg/g, respectively. Therefore, the following investigations were carried out for 100 minutes.

Metanil yellow is an acid dye which forms negative ions in aqueous solution – anionic dye [51]. When the anionic dye interacted with positively charged adsorbent, the adsorption would increase due to electrostatic interaction between the opposite charges.

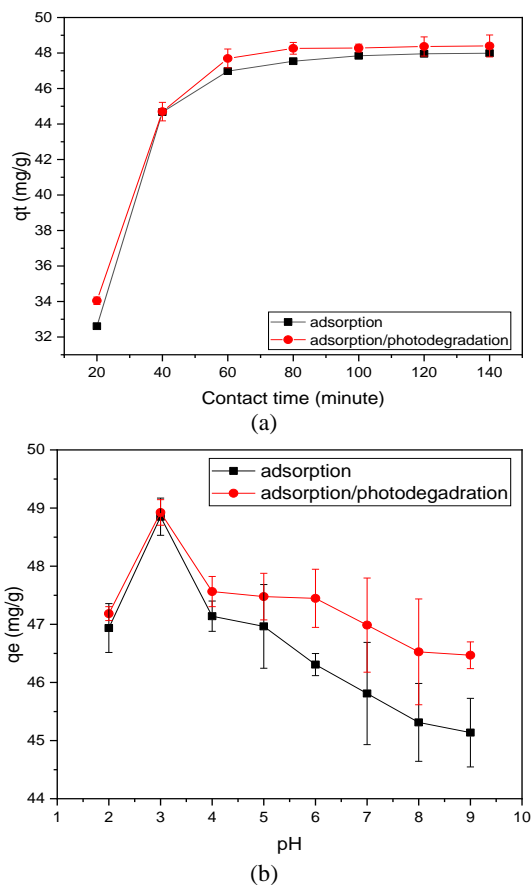


Figure 5. Effects of (a) contact time and (b) pH on the removal of metanil yellow by TiO₂/GC/CH film composite

When $\text{pH} > 3$, the adsorption capacity of metanil yellow decreased reciprocally with the increase of pH (Figure 5b). It stems from the fact that CH matrix from TiO₂/GC/CH composite was protonated in acidic solution producing positively charged surface [51, 52]. Furthermore, in acidic solution, TiO₂ may produce hydroxyl radicals via hole trapping mechanism [16, 53]. Nonetheless, at high pH value, the adsorption/photodegradation process performed higher adsorption capacity than the adsorption alone. It suggests that at high pH, the removal was not only dependant on the electrostatic attraction-based adsorption, but rather on the photodegradation mechanism. In basic solution, the formation of OH[•] can still occur via electroreduction of dissolved O₂ [16, 53]. Therefore, the working pH range can be broadened by incorporating TiO₂ which can benefit the removal process without decreasing the solution pH, in addition to its practical aspect. However, since pH 3 facilitated the highest removal of metanil yellow, the pH value was selected for further investigations.

3. 3. 2. Kinetic and Isotherm Studies

The adsorptive behavior of methanyl yellow using TiO₂/GC/CH composite film was investigated by the kinetic modeling. Therefore, two kinetic models were employed, namely pseudo-first-order (Equations (2)) and pseudo-second-order (Equation (3)), as used in previous studies [23, 40].

$$\log(q_e - q_t) = \log q_e - \frac{k_1}{2.303} t \quad (2)$$

$$\frac{t}{q_t} = \frac{1}{k_2 q_e^2} + \frac{t}{q_e} \quad (3)$$

where k_1 and k_2 are the constant rate of pseudo-first-order and pseudo-second-order, respectively.

Kinetic model for adsorption and adsorption/photodegradation of metanil yellow using TiO₂/GC/CH has been presented based on the linear equations of pseudo-first-order (Figure 6a) and pseudo-second-order (Figure 6b). The adsorption and adsorption/photodegradation fit the pseudo-second-order equation the most with $R^2 = 0.997$ and 0.9975 , respectively (Table 2).

Another statistical parameter that could be considered is the values of Root-Mean-Square-Errors (RMSE) that are lower in pseudo-second-order. Thus, we concluded that the adsorption and adsorption/photodegradation follows the assumption of pseudo-second-order, in which the rate-limiting step depends on the chemisorption [40, 54]. Nonetheless, since the data solely rely on the modelling approach, we suggest further study to confirm the chemisorption dominance.

Isotherm modellings were used to study the interaction phenomenon in the adsorption and

TABLE 2. Kinetic parameters for adsorption and adsorption/photodegradation of metanil yellow using TiO₂/GC/CH.

Kinetic models	Parameters	Adsorption	Adsorption/ photodegradation
Pseudo-first-order	R ²	0.98856	0.95852
	RMSE	0.10349	0.20684
	K ₁ (g/mg.min)	0.0593	0.0615
	q _e (mg/g)	43.1728	37.3534
Pseudo-second-order	R ²	0.99699	0.9975
	RMSE	0.04638	0.04206
	K ₁ (g/mg.min)	0.0026	0.0028
	q _e (mg/g)	51.2033	51.3611

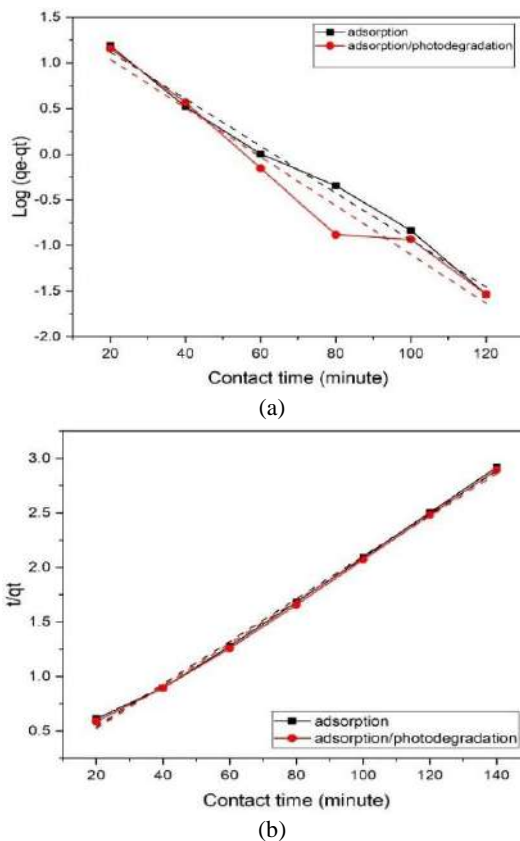


Figure 6. Kinetic modelling with (a) pseudo-first-order and (b) pseudo-second-order equations for metanil yellow removal using TiO₂/GC/CH film composite

adsorption-photodegradation process. Herein, we employed the common Langmuir and Freundlich isotherm models. The linearized equations for Langmuir (Equation (3)) and Freundlich (Equation (4)) are shown below:

$$\frac{1}{q_e} = \frac{1}{q_m} + \frac{1}{K_L q_m C_e} \tag{4}$$

$$\text{Log } q_e = \text{Log } K_F + \frac{1}{n} \text{Log } C_e \tag{5}$$

These equations have been used in the previous works [7, 55], where q_m (mg/g) is the maximum adsorption capacity, K_L is Langmuir constant, and K_F and n are Freundlich constants. K_L and K_F represent the free energy and removal capacity, respectively, meanwhile n is for adsorption intensity.

The isotherm modellings of metanil yellow removal via adsorption and adsorption/photodegradation based on linearized Langmuir (Figure 6a) and Freundlich (Figure 6b) equations have been presented. The study revealed that both adsorption and adsorption/photodegradation of metanil yellow in our work are Langmuir-dependent with R² = 0.998 and 0.9865, respectively (Table 3).

The RMSE are also 7.5 and 5 times lower in Langmuir than in Freundlich modelling for the adsorption and adsorption/photodegradation, respectively. Therefore, the adsorptive interaction between metanil yellow and TiO₂/GC/CH, either with or

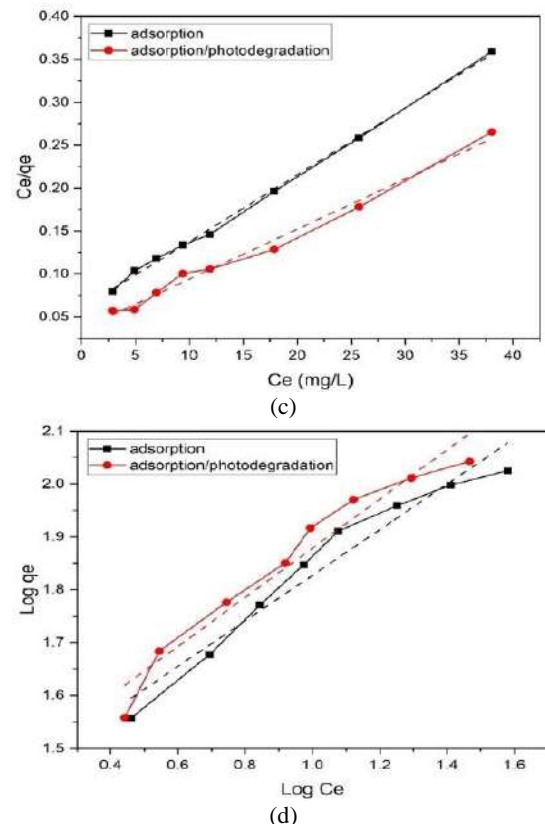


Figure 7. isotherm modelling with (a) Langmuir and (b) Freundlich equations for metanil yellow removal using TiO₂/GC/CH film composite

TABLE 3. Isotherms parameters for adsorption and adsorption-photodegradation of metanil yellow using TiO₂/GC/CH.

Kinetic models	Parameters	Adsorption	Adsorption/photodegradation
Langmuir	R ²	0.99786	0.98649
	RMSE	0.00432	0.00817
	K _L (L/mg)	0.1299	0.1628
	q _m (mg/g)	128.5347	171.5266
Freundlich	R ²	0.94663	0.94114
	RMSE	0.03807	0.04108
	K _F (mg/g)	24.917	25.939
	n	2.320	2.152

without light exposure, follows the assumptions that each active site shares the same binding energy and the adsorption occurs in monolayer.

Maximum adsorption capacity from the Langmuir equation revealed that the metanil yellow removal via adsorption has a higher value (128.5347 mg/g) as opposed to that of adsorption/photodegradation (171.527 mg/g). Neat TiO₂ nano powder is reported to have q_m = 2.79 x 10⁻⁴ mg/g [18], which is far smaller compared with TiO₂/GC/CH in our work. It confirms that the higher q_m was obtained due to the synergism between adsorption and photodegradation in reducing the level of metanil yellow from water. Comparatively, other studies have used chitosan-based adsorbent and achieved higher q_m for metanil yellow adsorption. A research group led by Tural has accomplished q_m = 625 mg/g [32], Tehrani-Bagha with q_m = 910 mg/g [56], and Lee with q_m = 558.18 mg/g [57]. But they used adsorbents in a form of nanoparticles [32, 56] and aerogels [57] which are less practical than film adsorbent due to their separation difficulty. Additionally, the Langmuir constants of more than 0.01 (0.132 and 0.239 for adsorption and adsorption/photodegradation, respectively) can be associated with intense adsorbate-adsorbent interaction [58].

4. CONCLUSION

We have successfully prepared TiO₂/GC/CH with improved mechanical properties and synergistic adsorption/photodegradation ability for metanil yellow removal. Characterization using FT-IR proves the successful attachment of TiO₂ onto GC/CH matrix and the presence of N- and O-containing groups. Through XRD analysis, we have observed the loss of crystallinity of CH upon the addition of TiO₂ nanoparticles and GC

particles. SEM images confirm the distribution of embedded TiO₂ nanoparticles on the GC/CH, with the presence of several agglomerations. DSC analysis revealed that GC addition can increase bonding intensity between water molecules and adsorbents, while TiO₂ reduce the bonding intensity. The performance in metanil yellow removal suggests the synergistic adsorption and photodegradation mechanism of TiO₂/GC/CH that follows pseudo-second-order kinetic and Langmuir isotherm modellings. Additionally, the role of TiO₂ photocatalyst can broaden the working pH range for the metanil yellow removal which improves the practical aspect of our material. However, the agglomeration was still a challenge in this study which might be responsible for the low photodegradation activities.

5. REFERENCES

- Zhang, L., Zeng, Y. and Cheng, Z., "Removal of heavy metal ions using chitosan and modified chitosan: A review", *Journal of Molecular Liquids*, Vol. 214, (2016), 175-191. DOI: 10.1016/j.molliq.2015.12.013.
- Vakili, M., Deng, S., Cagnetta, G., Wang, W., Meng, P., Liu, D. and Yu, G., "Regeneration of chitosan-based adsorbents used in heavy metal adsorption: A review", *Separation and Purification Technology*, Vol. 224, (2019), 373-387. DOI: 10.1016/j.seppur.2019.05.040.
- Kavimani, V., Soorya Prakash, K., Thankachan, T. and Udayakumar, R., "Synergistic improvement of epoxy derived polymer composites reinforced with graphene oxide (GO) plus titanium di oxide(TiO₂)", *Composites Part B: Engineering*, Vol. 191, (2020). DOI: 10.1016/j.compositesb.2020.107911.
- Shirkavand, S. and Moslehifard, E., "Effect of TiO₂ nanoparticles on tensile strength of dental acrylic resins", *Journal of Dental Research, Dental Clinics, Dental Prospects*, Vol. 8, No. 4, (2014), 197-203. DOI: 10.5681/joddd.2014.036.
- Valizadeh, S., Naseri, M., Babaei, S., Hosseini, S.M.H. and Imani, A., "Development of bioactive composite films from chitosan and carboxymethyl cellulose using glutaraldehyde, cinnamon essential oil and oleic acid", *International Journal of Biological Macromolecules*, Vol. 134, (2019), 604-612. DOI: 10.1016/j.ijbiomac.2019.05.071.
- Iqhrammullah, M., Marlina, M., Khalil, H., Kurniawan, K.H., Suyanto, H., Hedwig, R., Karnadi, I., Olaiya, N.G., Abdullah, C.K. and Abdulmadjid, S.N., "Characterization and performance evaluation of cellulose acetate-polyurethane film for lead II ion removal", *Polymers (Basel)*, Vol. 12, No. 6, (2020). DOI: 10.3390/polym12061317.
- Santoso, S.P., Kurniawan, A., Soetaredjo, F.E., Cheng, K.-C., Putro, J.N., Ismadji, S. and Ju, Y.-H., "Eco-friendly cellulose-bentonite porous composite hydrogels for adsorptive removal of azo dye and soilless culture", *Cellulose*, Vol. 26, No. 5, (2019), 3339-3358. DOI: 10.1007/s10570-019-02314-2.
- Shen, S.S., Yang, J.J., Liu, C.X. and Bai, R.B., "Immobilization of copper ions on chitosan/cellulose acetate blend hollow fiber membrane for protein adsorption", *RSC Advances*, Vol. 7, No. 17, (2017), 10424-10431. DOI: 10.1039/c7ra00148g.
- Alni, A., Puspita, K. and Zulfikar, M.A., "Biosorbent from chinese cabbage (*Brassica pekinensis* L.) for phenol contaminated waste water treatment", *Key Engineering*

- Materials**, Vol. 811, (2019), 71-79. DOI: 10.4028/www.scientific.net/KEM.811.71.
10. Zheng, X., Li, X., Li, J., Wang, L., Jin, W., Liu, J., Pei, Y. and Tang, K., "Efficient removal of anionic dye (congo red) by dialdehyde microfibrillated cellulose/chitosan composite film with significantly improved stability in dye solution", *International Journal of Biological Macromolecules*, Vol. 107, No. Pt A, (2018), 283-289. DOI: 10.1016/j.ijbiomac.2017.08.169.
 11. Rahmi, Lelifajri, Julinawati and Shabrina, "Preparation of chitosan composite film reinforced with cellulose isolated from oil palm empty fruit bunch and application in cadmium ions removal from aqueous solutions", *Carbohydrate Polymers*, Vol. 170, (2017), 226-233. DOI: 10.1016/j.carbpol.2017.04.084.
 12. Rahmi, Iqhrammullah, M., Audina, U., Husin, H. and Fathana, H., "Adsorptive removal of Cd (ii) using oil palm empty fruit bunch-based charcoal/chitosan-edta film composite", *Sustainable Chemistry and Pharmacy*, Vol. 21, (2021). DOI: 10.1016/j.scp.2021.100449.
 13. Jumaidin, R., Diah, N.A., Ilyas, R.A., Alamjuri, R.H. and Yusuf, F.A.M., "Processing and characterisation of banana leaf fibre reinforced thermoplastic cassava starch composites", *Polymers (Basel)*, Vol. 13, No. 9, (2021). DOI: 10.3390/polym13091420.
 14. Jumaidin, R., Khiruddin, M.A.A., Asyul Sutan Saidi, Z., Salit, M.S. and Ilyas, R.A., "Effect of cogon grass fibre on the thermal, mechanical and biodegradation properties of thermoplastic cassava starch biocomposite", *International Journal of Biological Macromolecules*, Vol. 146, (2020), 746-755. DOI: 10.1016/j.ijbiomac.2019.11.011.
 15. Omran, A.A.B., Mohammed, A., Sapuan, S.M., Ilyas, R.A., Asyraf, M.R.M., Rahimian Koloor, S.S. and Petru, M., "Micro- and nanocellulose in polymer composite materials: A review", *Polymers (Basel)*, Vol. 13, No. 2, (2021). DOI: 10.3390/polym13020231.
 16. Schneider, J., Matsuoka, M., Takeuchi, M., Zhang, J., Horiuchi, Y., Anpo, M. and Bahnemann, D.W., "Understanding TiO₂ photocatalysis: Mechanisms and materials", *Chemical Reviews*, Vol. 114, No. 19, (2014), 9919-9986. DOI: 10.1021/cr5001892.
 17. Rostami, M., Joshaghani, A.H., Mazaheri, H. and Shokri, A., "Photo-degradation of p-nitro toluene using modified bentonite based nano-TiO₂ photocatalyst in aqueous solution", *International Journal of Engineering*, Vol. 34, No. 4, (2021), 756-762. DOI: 10.5829/IJE.2021.34.04A.01.
 18. Chakraborty, D. and Sen Gupta, S., "Decolourisation of metanil yellow by visible-light photocatalysis with n-doped TiO₂ nanoparticles: Influence of system parameters and kinetic study", *Desalination and Water Treatment*, Vol. 52, No. 28-30, (2013), 5528-5540. DOI: 10.1080/19443994.2013.808594.
 19. Nguyen, C.H., Tran, M.L., Tran, T.T.V. and Juang, R.-S., "Enhanced removal of various dyes from aqueous solutions by UV and simulated solar photocatalysis over TiO₂/ZnO/RGO composites", *Separation and Purification Technology*, Vol. 232, (2020). DOI: 10.1016/j.seppur.2019.115962.
 20. Irwan, I., Lubis, S., Ramli, M. and Sheilatina, S., "Photocatalytic degradation of indigo carmine by TiO₂/activated carbon derived from waste coffee grounds", *Journal Natural*, Vol. 16, No. 1, (2016), 21-26. DOI: 10.24815/jn.v16i1.4640.
 21. Lubis, S., Sheilatina and Murisna, "Synthesis, characterization and photocatalytic activity of α -Fe₂O₃/bentonite composite prepared by mechanical milling", *Journal of Physics: Conference Series*, Vol. 1116, (2018). DOI: 10.1088/1742-6596/1116/4/042016.
 22. Lubis, S., Maulana, I. and Masyithah, "Synthesis and characterization of TiO₂/ α -Fe₂O₃ composite using hematite from iron sand for photodegradation removal of dye", *Journal Natural*, Vol. 18, No. 1, (2018), 38-43. DOI: 10.24815/jn.v18i1.8649.
 23. Razzaz, A., Ghorban, S., Hosayni, L., Irani, M. and Aliabadi, M., "Chitosan nanofibers functionalized by tio₂ nanoparticles for the removal of heavy metal ions", *Journal of the Taiwan Institute of Chemical Engineers*, Vol. 58, (2016), 333-343. DOI: 10.1016/j.jtice.2015.06.003.
 24. Shi, X., Zhang, X., Ma, L., Xiang, C. and Li, L., "TiO₂-doped chitosan microspheres supported on cellulose acetate fibers for adsorption and photocatalytic degradation of methyl orange", *Polymers (Basel)*, Vol. 11, No. 8, (2019). DOI: 10.3390/polym11081293.
 25. Mafirad, S., Mehrmia, M.R., Zahedi, P. and Hosseini, S.N., "Chitosan-based nanocomposite membranes with improved properties: Effect of cellulose acetate blending and TiO₂ nanoparticles incorporation", *Polymer Composites*, Vol. 39, No. 12, (2017), 4452-4466. DOI: 10.1002/pc.24539.
 26. Yu, H., Liu, H., Yuan, X., Ding, W., Li, Y. and Wang, J., "Separation of oil-water emulsion and adsorption of Cu(II) on a chitosan-cellulose acetate-TiO₂ based membrane", *Chemosphere*, Vol. 235, (2019), 239-247. DOI: 10.1016/j.chemosphere.2019.06.060.
 27. ZabihiSahebi, A., Koushkbaghi, S., Pishnamazi, M., Askari, A., Khosravi, R. and Irani, M., "Synthesis of cellulose acetate/chitosan/SWCNT/Fe₃O₄/TiO₂ composite nanofibers for the removal of Cr(VI), As(V), methylene blue and congo red from aqueous solutions", *International Journal of Biological Macromolecules*, Vol. 140, (2019), 1296-1304. DOI: 10.1016/j.ijbiomac.2019.08.214.
 28. Chung, K.T., "Azo dyes and human health: A review", *Journal of Environmental Science and Health, Part C: Toxicology and Carcinogenesis*, Vol. 34, No. 4, (2016), 233-261. DOI: 10.1080/10590501.2016.1236602.
 29. Az-Zahra, N., Rahmi, R. and Lubis, S., "Reinforcement of chitosan film using cellulose isolated from grass (*Imperata cylindrica*)", *Journal of Physics: Conference Series*, Vol. 1402, (2019). DOI: 10.1088/1742-6596/1402/5/055039.
 30. Hwang, C.-L. and Yoon, K., "Multiple attribute decision making, Lecture notes in economics and mathematical systems, Berlin, Heidelberg, Springer Berlin Heidelberg, Vol. 186, (1981). DOI: 10.1007/978-3-642-48318-9.
 31. Rahmi, Lelifajri and Nurfatimah, R., "Preparation of polyethylene glycol diglycidyl ether (PEDGE) crosslinked chitosan/activated carbon composite film for Cd²⁺ removal", *Carbohydrate Polymers*, Vol. 199, (2018), 499-505. DOI: 10.1016/j.carbpol.2018.07.051.
 32. Tural, S., Tarhan, T. and Tural, B., "Removal of hazardous azo dye metanil yellow from aqueous solution by cross-linked magnetic biosorbent; equilibrium and kinetic studies", *Desalination and Water Treatment*, Vol. 57, No. 28, (2015), 13347-13356. DOI: 10.1080/19443994.2015.1056842.
 33. Davarnejad, R. and Karimi Dastnayi, Z., "Cd (II) removal from aqueous solutions by adsorption on henna and henna with chitosan microparticles using response surface methodology", *Iranian Journal of Chemistry and Chemical Engineering*, Vol. 38, No. 3, (2019), 267-281. DOI: 10.30492/IJCCE.2019.30929.
 34. Davarnejad, R., Karimi Dastnayi, Z. and Kennedy, J.F., "Cr(VI) adsorption on the blends of henna with chitosan microparticles: Experimental and statistical analysis", *International Journal of Biological Macromolecules*, Vol. 116, (2018), 281-288. DOI: 10.1016/j.ijbiomac.2018.04.189.
 35. Marlina, Iqhrammullah, M., Saleha, S., Fathurrahmi, Maulina, F.P. and Idroes, R., "Polyurethane film prepared from ball-milled algal polyol particle and activated carbon filler for NH₃-N

- removal", *Heliyon*, Vol. 6, No. 8, (2020), e04590. DOI: 10.1016/j.heliyon.2020.e04590.
36. Rahmi, Fathurrahmi, Lelifajri and PurnamaWati, F., "Preparation of magnetic chitosan using local iron sand for mercury removal", *Heliyon*, Vol. 5, No. 5, (2019), e01731. DOI: 10.1016/j.heliyon.2019.e01731.
 37. Arahman, N., Fitri, R.A., Wirakusuma, A., Fahrina, A. and Bilad, M.R., "Adsorption performance of low-cost java plum leaves and guava fruits as natural adsorbents for removal of free fatty acids from coconut oil", *International Journal of Engineering*, Vol. 32, No. 10, (2019), 1372-1378. DOI: 10.5829/ije.2019.32.10a.06.
 38. Guo, S.-Y., Zhang, X., Ren, J., Chen, J.-Z., Zhao, T.-J., Li, T.-W. and Zhang, L., "Preparation of tio₂/epoxy resin composite and its effect on mechanical and bonding properties of opc mortars", *Construction and Building Materials*, Vol. 272, (2021). DOI: 10.1016/j.conbuildmat.2020.121960.
 39. Vosough, M., Sharafi, S. and Khayati, G.R., "Co-tio₂ nanoparticles as the reinforcement for fe soft magnetic composites with enhanced mechanical and magnetic properties via pulse electrodeposition", *International Journal of Engineering*, Vol. 33, No. 10, (2020), 2030-2038. DOI: 10.5829/ije.2020.33.10a.21.
 40. Iqhrammullah, M., Marlina and Nur, S., "Adsorption behaviour of hazardous dye (methyl orange) on cellulose-acetate polyurethane sheets", *IOP Conference Series: Materials Science and Engineering*, Vol. 845, (2020). DOI: 10.1088/1757-899x/845/1/012035.
 41. Luzi, F., Puglia, D., Sarasini, F., Tirillo, J., Maffei, G., Zuurro, A., Lavecchia, R., Kenny, J.M. and Torre, L., "Valorization and extraction of cellulose nanocrystals from North African grass: *Ampelodesmos mauritanicus* (diss)", *Carbohydrate Polymers* Vol. 209, (2019), 328-337. DOI: 10.1016/j.carbpol.2019.01.048.
 42. León, A., Reuquen, P., Garín, C., Segura, R., Vargas, P., Zapata, P. and Orihuela, P., "FTIR and Raman characterization of TiO₂ nanoparticles coated with polyethylene glycol as carrier for 2-methoxyestradiol", *Applied Sciences*, Vol. 7, No. 1, (2017). DOI: 10.3390/app7010049.
 43. Behera, S.S., Das, U., Kumar, A., Bissoyi, A. and Singh, A.K., "Chitosan/TiO₂ composite membrane improves proliferation and survival of 1929 fibroblast cells: Application in wound dressing and skin regeneration", *International Journal of Biological Macromolecules*, Vol. 98, (2017), 329-340. DOI: 10.1016/j.ijbiomac.2017.02.017.
 44. Terán, E.J., Montes, M.L., Rodríguez, C., Martino, L., Quiroga, M., Landa, R., Torres Sánchez, R.M. and Díaz Pace, D.M., "Assessment of sorption capability of montmorillonite clay for lead removal from water using laser-induced breakdown spectroscopy and atomic absorption spectroscopy", *Microchemical Journal*, Vol. 144, (2019), 159-165. DOI: 10.1016/j.microc.2018.08.047.
 45. Montaser, A.S., Wassel, A.R. and Al-Shaye'a, O.N., "Synthesis, characterization and antimicrobial activity of schiff bases from chitosan and salicylaldehyde/tio₂ nanocomposite membrane", *International Journal of Biological Macromolecules*, Vol. 124, (2019), 802-809. DOI: 10.1016/j.ijbiomac.2018.11.229.
 46. Tsai, H.-S. and Wang, Y.-Z., "Properties of hydrophilic chitosan network membranes by introducing binary crosslink agents", *Polymer Bulletin*, Vol. 60, No. 1, (2007), 103-113. DOI: 10.1007/s00289-007-0846-x.
 47. de Queiroz Antonino, R., Lia Fook, B.R.P., de Oliveira Lima, V.A., de Farias Rached, R.I., Lima, E.P.N., da Silva Lima, R.J., Peniche Covas, C.A. and Lia Fook, M.V., "Preparation and characterization of chitosan obtained from shells of shrimp (*Litopenaeus vannamei boone*)", *Marine Drugs*, Vol. 15, No. 5, (2017). DOI: 10.3390/md15050141.
 48. Li, C., Sun, Y., Cheng, M., Sun, S. and Hu, S., "Fabrication and characterization of a TiO₂/polysiloxane resin composite coating with full-thickness super-hydrophobicity", *Chemical Engineering Journal*, Vol. 333, (2018), 361-369. DOI: 10.1016/j.cej.2017.09.165.
 49. Lou, L., Kendall, R.J. and Ramkumar, S., "Comparison of hydrophilic PVA/TiO₂ and hydrophobic PVDF/TiO₂ microfiber webs on the dye pollutant photo-catalyzation", *Journal of Environmental Chemical Engineering*, Vol. 8, No. 5, (2020). DOI: 10.1016/j.jece.2020.103914.
 50. Salari, M., Sowti Khiabani, M., Rezaei Mokarram, R., Ghanbarzadeh, B. and Samadi Kafil, H., "Preparation and characterization of cellulose nanocrystals from bacterial cellulose produced in sugar beet molasses and cheese whey media", *International Journal of Biological Macromolecules*, Vol. 122, (2019), 280-288. DOI: 10.1016/j.ijbiomac.2018.10.136.
 51. Guo, X., Wei, Q., Du, B., Zhang, Y., Xin, X., Yan, L. and Yu, H., "Removal of metanil yellow from water environment by amino functionalized graphenes (NH₂-G) – influence of surface chemistry of NH₂-G", *Applied Surface Science*, Vol. 284, (2013), 862-869. DOI: 10.1016/j.apsusc.2013.08.023.
 52. Santra, A.K., Pal, T.K. and Datta, S., "Removal of metanil yellow from its aqueous solution by fly ash and activated carbon produced from different sources", *Separation Science and Technology*, Vol. 43, No. 6, (2008), 1434-1458. DOI: 10.1080/01496390701885729.
 53. Hoffmann, M.R., Martin, S.T., Choi, W. and Bahnemann, D.W., "Environmental applications of semiconductor photocatalysis", *Chemical Reviews*, Vol. 95, No. 1, (2002), 69-96. DOI: 10.1021/cr00033a004.
 54. Robati, D., Mirza, B., Rajabi, M., Moradi, O., Tyagi, I., Agarwal, S. and Gupta, V.K., "Removal of hazardous dyes-br 12 and methyl orange using graphene oxide as an adsorbent from aqueous phase", *Chemical Engineering Journal*, Vol. 284, (2016), 687-697. DOI: 10.1016/j.cej.2015.08.131.
 55. Akl, M.A.A., "Efficient removal of phenol from water samples using sugarcane bagasse based activated carbon", *Journal of Analytical & Bioanalytical Techniques*, Vol. 5, No. 2, (2014). DOI: 10.4172/2155-9872.1000189.
 56. Momenzadeh, H., Tehrani-Bagha, A.R., Khosravi, A., Gharanjig, K. and Holmberg, K., "Reactive dye removal from wastewater using a chitosan nanodispersion", *Desalination*, Vol. 271, No. 1-3, (2011), 225-230. DOI: 10.1016/j.desal.2010.12.036.
 57. Lai, K.C., Hiew, B.Y.Z., Lee, L.Y., Gan, S., Thangalazhy-Gopakumar, S., Chiu, W.S. and Khiew, P.S., "Ice-templated graphene oxide/chitosan aerogel as an effective adsorbent for sequestration of metanil yellow dye", *Bioresource Technology* Vol. 274, (2019), 134-144. DOI: 10.1016/j.biortech.2018.11.048.
 58. Costa, T.d.S., Rogez, H. and Pena, R.d.S., "Adsorption capacity of phenolic compounds onto cellulose and xylan", *Food Science and Technology (Campinas)*, Vol. 35, No. 2, (2015), 314-320. DOI: 10.1590/1678-457x.6568.

Persian Abstract

چکیده

کیتوزان و سلولز فراوانترین بیوپلیمرهایی هستند که می توانند برای حذف رنگ های خطرناک استفاده شوند. با استفاده از TiO_2 بر روی ماتریس سلولز- کیتوزان ، تحقیق ما با هدف دستیابی به حذف بالا متانیل زرد با استفاده از مکانیسم جذب هم افزایی / تجزیه نوری ، انجام شده است. ذرات سلولز برای بدست آوردن سلولز مشتق شده از چمن وحشی (*Imperata cylindrica L.*) استخراج شد. برای تهیه $TiO_2 / GC / CH$ از روش ترکیبی ساده استفاده شد که در آن ترکیب با روش توزین ساده افزودنی تعیین شد. $TiO_2 / GC / CH$ با استفاده از آزمون مقاومت کششی (همچنین برای SAW نیز استفاده می شود) ، مادون قرمز تبدیل فوریه (FT-IR) ، پراش اشعه (XRD) ، کالریمتری اسکن دیفرانسیل (DSC) و میکروسکوپ الکترونی روبشی (SEM) حذف متانیل زرد با استفاده از $TiO_2 / GC / CH$ در محدوده pH اسیدی بسیار خوب عمل می کند. حذف به دنبال مدل های شبه نظم جنبشی مرتبه دوم $0.997 (R^2)$ و ایزوترم لانگمویر $0.998 (R^2)$ می باشد. qm زیاد حاصل از حذف متانیل زرد تحت تابش اشعه ماورا بنفش ($qm = 171.5266$) هم افزایی بین جذب و تجزیه نوری را اثبات می کند. $TiO_2 / GC / CH$ توسعه یافته می تواند به طور بالقوه در تصفیه فاضلاب برای حذف رنگ آزو استفاده شود.



An Experimental Investigation on Black Cotton Soil using Terrazyme

V. Vasiya*, C. H. Solnki

Civil Engineering Department S.V.N.I.T. Surat Gujarat India

PAPER INFO

Paper history:

Received 01 February 2021

Received in revised form 11 May 2021

Accepted 15 May 2021

Keywords:

Terrazyme

Black Cotton Soil

Unconfined Compressive Strength

Consolidation

ABSTRACT

The application of biodegradable substances for the improvement of weak soil has given better results in the field of geotechnical engineering. These substances are fermented and extracted from vegetation. It reduced the void ratio, thickness of absorbed water and maximize the compaction. Terrazyme contains natural protein. It is non-toxic and eco-friendly. It is soluble in water. The black cotton soil is highly plastic with swelling potential. Reduction in moisture causes shrinking, leads to differential settlement of the foundation. This will result in damage to the structure. This paper presents experimental work on black cotton soil reinforced with Terrazyme. Various proportions of Terrazyme were mixed with black cotton soil to evaluate the engineering properties of soil. The change in index properties and strength parameters were assessed by experiments on treated and untreated soil. Atterberg limits, free swell index, compaction test, triaxial tests were performed. Experimental results show a reduction in liquid limit, plasticity index, free swell index, optimum moisture content, and compression index. Triaxial tests showed improvement in cohesion and angle of shearing resistance. The optimum dosage of Terrazyme was found 2% by weight of dry soil.

doi: 10.5829/ije.2021.34.08b.04

1. INTRODUCTION

Black cotton soil covers more than a one-fifth area of India. Higher compressibility with swelling and shrinking is the main attributes of the black cotton soil. It is known for its black color and suitable for growing cotton. Engineering properties are changed with water content. Its swell by 200 to 300% to its original volume leads to exert in swelling pressure up to 10 kg/cm². It poses high strength in dry conditions but loses strength in a saturated condition. Its shrinking characteristics lead to differential settlement further progress in damaging of structure.

Eco-friendly materials have taken a significant role to enhance the engineering properties of weak soil. Nontraditional materials which are fulfilling the criteria for the improvement of soil are applied wholly or partially. Terrazyme is a nontoxic, nonflammable, noncorrosive organic liquid extracted from vegetation. It is soluble in water and rich in natural protein. The organic cations of the Terrazyme are exchanged with soil cations.

This exchange meant accelerates the bonding of soil particles.

Sen and Singh [1] stabilized black cotton soil at a dosage of 200 ml for 3m³ and found improvement in the California Bearing Ratio (CBR) value and reduction in pavement thickness by 25 to 40%. Umar et al. [2] studied the biological process of soil improvement and suggested that it is a practicable technique. Athira et al. [3] mixed the Laterite soil of Kerala with Terrazyme and found an improvement of 139% in CBR value and 281 % in Unconfined compressive strength (UCS) at 28 days of curing. Agrawal [4] mixed 1 ml Terrazyme in 5 kg of Black Cotton soil and found 200 % increases in UCS. Khan et al. [5] performed the experiments on clayey soil treated with three different enzymes and found an enhancement in unconfined compressive strength (UCS) and reduction in Swelling and shrinking. They further confirm dense packing of clayey soil through field emission scanning electron microscopy (FESEM). Thomas [6] prepared the blend of soil from Kaloor, Kochi, and enzymatic cement-treated clay to study the

*Corresponding Author Institutional Email:

d15am001@amd.svnit.ac.in (V. Vasiya)

UCS value. During the test, the stress-strain curve shows peak stress than the virgin soil at 28 days of curing with an improvement of 200 to 281% in UCS value. Greeshma et al. [7] experimented on high liquid limit clayey soil and Terrazyme, and 12 times enhancement in UCS value was found when Terrazyme mixed at the content of 210-230 ml/m³ of soil. Enhancement in compressive strength and reduction in compaction effort was reviewed by Taha et al. [8] when soil is mixed with bio-enzymes. Increases in the density of the soil and reduction in permeability were also confirmed. Suresh et al. [9] mixed Terrazyme with local soil and found improvement in Specific gravity from 2.45 to 2.96 plastic limit from 27.7 to 32.22, CBR from 6.16 to 8.81 with a reduction in liquid limit was found when black cotton soil was mixed with Terrazyme at 0.5 ml per 100 ml of water. Sravan. and Nagaraj [10] mixed soil, cement lime, and enzymes to prepare compressed earth blocks. 50% improvement in wet compressive strength was found in the block comparing the block prepared without enzymes. Muguda [11] applies 200 ml of Terrazyme in 1.5m³, to 3m³ soil at 0.5m³ intervals and found that there is a decrease in a liquid limit. Increases in the plastic limit, and shrinkage limit resulting in the reduction of plastic and shrinkage indices. Volumetric stability and resistance against crake formation were also found. Significant increase in CBR value found in stabilization process of soil with D1-14 (Bio-enzyme). An increase in CBR value leads to a reduction in the thickness of the subgrade [12, 13]. Consistency limit, UCS, and CBR tests were performed by Greeshma et al. [14] on soil north of Calicut, India. Inferred was made from test results that enzymatic lime is more efficient than the lime only. Mekaideche et al. [15] conducted an experimental study on calcareous Tufa with 4 % Lime and found a reduction in thermal conductivity. Obinayo [16] studied the efficiency of horizontal and vertical baffle walls at 5 levels for the 5k fractional design model and conclude that horizontal baffle walls better than vertical baffle walls in a sedimentation tank. Jafer et al. [17] stabilized fine-grained soil with calcium carbide residue and rice husk ash and found interesting growth in UCS test, reduction in PI at the curing of 90 days. Suresh and Murugaiyan [18] improved the engineering properties of expansive soil with 6 % ultra-fine slag and 1% CaCl₂. Experimental results showed a reduction in PI, swelling pressure, and increase in dry unit weight and UCS value. Local basalt in Vietnam was stabilized with cement and DZ33 (a type of enzyme) by Tran et al. [19] and found suitability in the construction of a rural road. Sandy soil was stabilized at various water content and different percentage of epoxy resin by Rahmannejad and Toufigh [20]; they found significant improvements in (UCS) of sandy soil.

All the existing literature demonstrates that extensive experiments were conducted on the blend of soil and Terrazyme focusing on improvement in Atterberg limit,

unconfined compressive strength, and CBR value. Very few studies are available that show the application of Terrazyme in clayey soil to improve unlined waterways with low discharge potential. Unlined water conveying systems are still available at the tail ends in the irrigation system, and slum water carrier in small towns of India. The water conveying system gets deteriorates as they are consist of clayey soil and unlined.

This paper demonstrates the experiments on water retention and water discharge through a laboratory model prepared for unlined waterways after evaluating the engineering properties of black cotton soil. Experimental results showed major improvements in unlined waterways when black cotton soil is stabilized with Terrazyme.

2. MATERIALS

2. 1. Soil The black cotton soil sample for the study was collected from village Bhatpore on the bank of river Tapi, Dist Surat. The soil was collected at the depth of 4-5 meters. The soil sample was collected through auger boring, sealed in a watertight plastic bag for the retention of the moisture. Collected soil was transferred to SVNIT Surat for assessing the index and engineering characteristics.

The soil was kept in the oven at temperature 60-70°C for 72h, for retention of ingredients of the clay. Lumps of the oven-dried soil were powdered and sieved through a 4.75 mm size I.S. Sieve. Table 1 represents the properties of the soil.

2. 2. Terrazyme Terrazyme is an organic liquid extracted from the vegetation. Terrazyme is a nonflammable, noncorrosive, and nontoxic eco-friendly

TABLE 1. Properties of soft soil

No	Property	Value
01	Field moisture content	49 %
02	Specific gravity	2.53
03	Shrinkage limit	14%
04	Plastic limit	21%
05	Liquid limit	73%
06	Plasticity index	52%
07	MDD with OMC	15.58kN/m ³ at 24%
08	Unit weight	14.0 kN/m ³
09	Classification (ISC)	CH
10	Fine Sand content	11%
11	Silt content	18%
12	Clay content	71%

liquid. The unit weight is equal to or nearer to that of water. Their odor does not affect. Handling does not necessitate the use of gloves or masks, but it can irritate the eyes. A temperature less than 55°C must be maintained if they are to be preserved for long periods without losing any of their properties. It has no danger of decay. Oxidizing agents interfere with the terrazyme. Terrazyme was specifically developed to improve the engineering properties of soil. For appropriate application, it must be diluted in water. Terrazyme helps to decrease absorbed water in the soil and reduce voids between soil particles for optimum compaction. This lowers permeability and decreases the swelling pressure of the soil particles. Terrazyme enhances the weather resistance of soils and increases their strength. These characteristics are particularly noticeable in fine-grained soils such as clay, where formulation affects swelling and shrinking behavior. The formula can change the soil matrix to prevent the soil from losing its reabsorption of water after compaction, and even when water is re-applied to the compacted soil, the mechanical benefits of compacted soil are not lost. The change is permanent and the product biodegradable once the enzyme reacts with soil. Terrazyme used in this experimental work was provided by Dhara Biotech (Manufacturer) village Sarasa, near Vasad, District Vadodara, Gujarat, India. The physical and chemical characteristics of the Terrazyme are listed in Tables 2 and 3, respectively.

3. EXPERIMENTAL WORK

In the first attempt, the experimental work was performed on untreated soil.

TABLE 2. Physical Property of Terrazyme

No	Property	Value
01	Water solubility	Infinite
02	Specific Gravity	1.00-1.08
03	Melting point	Liquid
04	PH value	2.8-3.5
05	Colour	Brown
06	Boiling Point	190° F- 200° F

TABLE 3. Chemical Properties of Terrazyme

No	Name of Element	Concentration (mg/L)
01	Ca	685
02	Al	2.78
03	Fe	23.79
04	K	7659
05	Mg	298
06	Si	332

3. 1. Atterberg Limits and Free Swell Test The liquid limit and plastic limit were determined as per IS 2720 part 5. The liquid limit was determined through the Casagrande apparatus.

Free swell indexed test was performed as per IS 2720 part 40. A soil sample was placed in the two measuring cylinders, one with distilled water and one with kerosene. An increase in the volume of soil was recorded and the free swell index was determined on untreated soil.

3. 2. Permeability Test Falling head permeability test was performed as per IS 2720 part 17. A sample with Optimum moisture content (OMC) and maximum dry density (MDD) was prepared with a 50 cm² cross-sectional area and 6 cm height. Discharge through the soil was recorded after complete saturation of the soil.

3. 3. Standard Procter Test About more than 100 kg of air-dried soil passing from IS sieve, 4.75 was taken for the test. The soil was divided into 2.5 kg for each test, a total of 40 compaction tests were done. Water was mixed into the soil with different water content and kept in an airtight container for 24 hours, for maturing. Standard Procter test was performed according to I S 2720 part 8.

3. 4. Consolidation Test Consolidation test was performed on remolded soil with 20 mm thickness and 60 m diameter as per IS 2720 part 15. The void ratio was determined at each loading and unloading.

3. 5. Triaxial Test Triaxial tests were performed on black cotton soil- Terrazyme mixture as per IS 2720 Part 11 to evaluate strength parameters. Real stress conditions can be simulated through a triaxial test. The specimen with 38 mm diameter and 76 mm height were prepared at MDD corresponding OMC obtained from the compaction test. For each horizontal stress (Called cell pressure), Vertical stress (called deviator stress) was applied through the loading frame, up to a failure of the specimen.

3. 6. Water Retention and Discharge Test Water retention and discharge over the soil slab were performed in the transparent model with a 6 mm thick acrylic sheet.

In the second attempt, all the tests were performed on the blend of black cotton soil and Terrazyme, aiming to decide suitable content for strengthening the soil.

4. RESULT AND DISCUSSION

4. 1. Atterberg Limits and Free Swell Test The blend of black cotton soil and Terrazyme was tested for Atterberg Limits. Table 4 represents the effects of

Terrazyme on consistency limits of Black cotton soil. Drastic reduction in the liquid limit from 83% to 45% was found at 2% Terrazyme. A further marginal increment was found with the addition of Terrazyme at 3% and 4%. The plastic limits remain almost stagnant at all the content of Terrazyme. Maximum variation of 3% found in water content at 2% Terrazyme content with untreated soil. Clay with less content of Terrazymes attracts the moisture and makes soil wetter. But this future of Terrazyme is valid up to a specific limit until moisture-holding capacity. Beyond this stage, soil behaves like water soil with a reduction in a liquid limit. The liquid limit in black cotton soil in the presence of 2% was found to be reduced by 41% by LL of virgin soil. Untreated soil shows a plasticity index of 62%, which 27% by 2% Terrazyme. The drop in consistency limit of soil and terrazyme blends leads to improvement in shear parameters. Figure 1 illustrates the clay particles with free and adsorbed water. Figure 2 shows a free swell index. Experimental results show a reduction in the free well index up to 2% Terrazyme content. Further increase in Terrazyme content results in an increment of a free swell index. Table 4 shows Atterberge limits at various content of Teraazyme.

4. 2. Permeability Test 5 cm fall in a head was measured for the soil with and without Terrazyme. Soil without Terrazyme gives a co-efficient of permeability 3.18×10^{-7} cm/s.

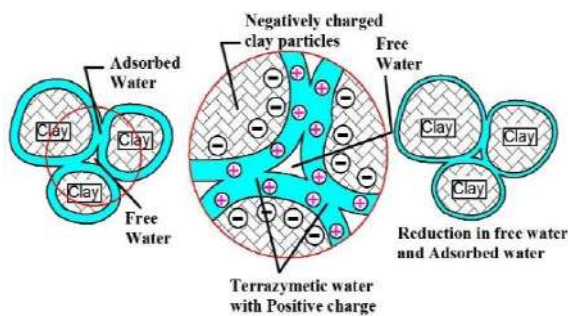


Figure 1. Clay particles with free and adsorbed water

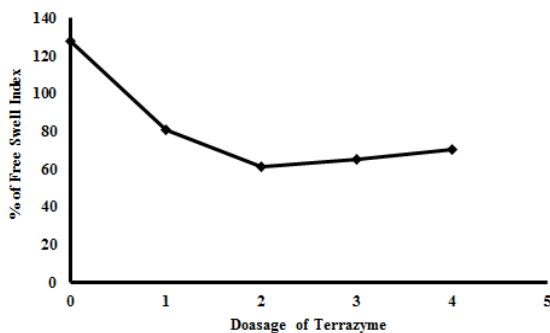


Figure 2. Free swell index at Different Terrazyme dosage

TABLE 4. Atterberg Limits at Different content of Terrazyme

Terrazyme, %	Shrinkage Limit, %	Plastic Limit, %	Liquid Limit, %	Plasticity Index, %
0	14	21	83	62
1	14	21	51	30
2	14	18	45	27
3	14	19	47	28
4	14	19	47	28

As Terrazyme diluted in water blend with soil, a reduction in permeability was found. 1 and 2% Terrazyme blended with black cotton soil gives coefficient of permeability 2.82×10^{-7} cm/sec and 2.58×10^{-7} cm/sec respectively. At 3 and 4% content of Terrazyme, marginal increases were found in the coefficient of permeability.

4. 3. Compaction Test Oven-dried pulverized soil was tested under the lightweight compaction test as per IS 2720 part 8 at 1, 2, 3, and 4% of Terrazyme. The blend of Black cotton soil, Terrazyme, and water was kept in a desiccator for 1-day curing. MDD and OMC were obtained for each dosage of Terrazyme. The effect of terrazyme addition was observed as a reduction in the electrical charge of water molecules and pressure from negatively charged ions on positively charged metal ions in adsorbed water.

The metal ions must move from the adsorbed water to free water, and the electrostatic barrier occurs by breaking down. Thus terrazyme treats adsorbed water with organic cations and neutralize the negative charge on clay particles. The organic cations also trim down the thickness of the electrical double layer. This process makes the soil structure friable with the adsorbed thinner water layer, resulting in dense packing, and allows treated soil to compact easily. Untreated soil gives the MDD of 15.58 kN/m^3 at 24% OMC. The 2% Terrazyme content gives MDD of 16.47 kN/m^3 at 20% OMC. Further increases in terrazyme content reduce the MDD and increase the OMC. Figure 3 shows the reduction in adsorbed water thickness through the ionic exchange process. Figure 3 Shows the Compaction curve for all samples.

4. 4. Consolidation Test The one-dimensional consolidation test was performed on all samples prepared with black cotton soil and Terrazyme. Soil without Terrazyme gives a void ratio of 0.652 at a pressure of 10 kPa. The pressure was increased double of the previous pressure and up to 640 kPa. Unloading for all the tests was done up to 40 kPa. The void ratio was determined by the height of solids method at every increment of the load as well as unloading. Untreated soil shows a reduction in

the void ratio of 0.24 while 1 and 2% Terrazyme treated black cotton soil shows a reduction of 0.227 and 0.191. Figure 4 depicted the consolidation curves for all treated and untreated soil. The consolidation test gives a C_c value of 0.094 for untreated soil. At 1% and 2% Terrazyme content the C_c value of the soil is 0.088 and 0.076 respectively, demonstrate improvement in resistance. At 3% and 4%, content marginal increase found in C_c value leads to a decrease in resistance. Figure 3 shows Mechanism behind the process of reduction in adsorbed water thickness.

4. 5. Triaxial Test All the tests were performed as consolidated drained tests. The untreated soil gives a cohesion value of 36 kPa with an angle of shearing resistance of 14° . The improvement in shear parameters was found as the soil is blended with Terrazyme. The 2% terrazyme gives cohesion of 59 kPa, with 63% higher than untreated soil. the angle of shearing resistance also increased 19° from 14° . A reverse trend in C and ϕ was observed at 3% and 4% terrazyme. Table 5 shows details of all triaxial tests.

Untreated soil and soil blended with different content of Terrazyme are tested for a basic test of soil. All these

TABLE 5. Summary of Triaxial Tests

No	Soil and Terrazyme content	Cell pressure (kPa)	Deviator stress (kPa)	C (kPa)	(ϕ)
1		50	124		
2	Soil +TR ₀	80	143.21	36	14°
3		110	162.36		
4		40	169.55		
5	Soil +TR ₁	60	187.44	48.6	18°
6		85	209.81		
7		60	238.71		
8	Soil +TR ₂	75	255.46	59	21°
9		90	272.22		
10		60	238.71		
11	Soil +TR ₃	75	255.46	55	20°
12		90	272.22		
13		60	202.4		
14	Soil +TR ₄	80	221.35	51.4	19°
15		100	239.22		

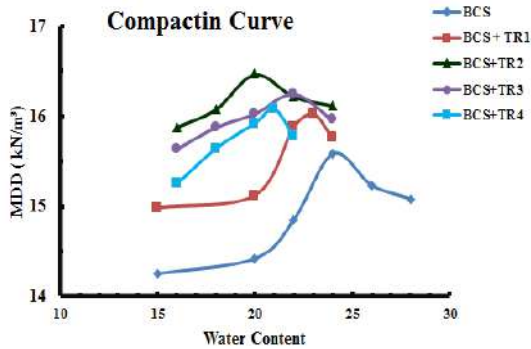


Figure 3. Compaction Curve

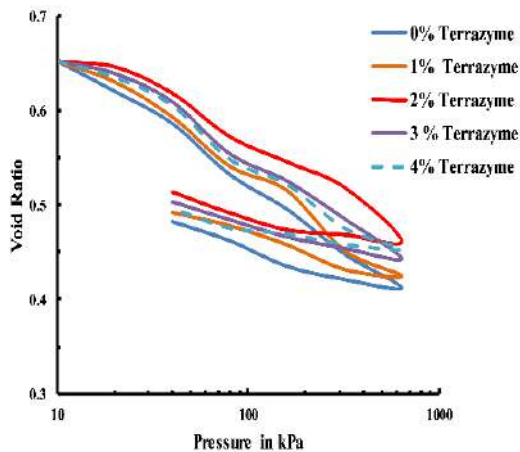


Figure 4. Consolidation Curve

tests have shown improvements in the engineering properties of black cotton soil. From experimental results, the water retention and water discharge tests were carried out.

4. 6. Water Retention and Discharge Test

4. 6. 1. Water Retention Test A working model with a clear width of 30 cm was prepared from a 6 mm thick transparent acrylic sheet. the depth and length of the model were kept at 20 cm and 60 cm respectively. A 30 cm X 10 Cm slab with 5 cm thickness was prepared from the blend of soil and Terrazyme. Slab kept vertically in the model with great care as shown in Figure 5. On the upstream of the soil slab, water was poured gently. Different heights of the water upstream are filled and downstream kept free. The time required for the percolation of the water is recorded. An experimental result shows no seepage found up to 3 cm water depth even up to 7 days. 4 cm of water depth gives the seepage at a rate of 3 ml/s after 5 days. 5 cm depth of water gives 5 ml/sec after 3 days. 6 cm depth of water gives seepage at 7 ml/s after 2 days.

4. 6. 2. Discharge Test Discharge tests were conducted on rectangular and trapezoidal sections. In the first attempt same model of 30 X 20 X 60 cm and soil slab with the same dimension of 30 X 10 was used. The flow of water is regulated in such a way that water height on the soil slab is maintained 1 to 4 cm at the interval of 1 cm, as shown in Figure 6. The flow of water was

adjusted in such a way so 1 cm height of water flow was obtained at the discharge of 265 ml/s. the blend of soil and terrazyme resists this discharge for 45 hours and 15 minutes. The water depth of 2 cm on the soil slab gives the water flow of 750 ml/s, up to 36 hours before the failure of the slab. 1.38 lit/s discharge was obtained when 3 cm depth on soil slab was maintained for 22 hours 27 minutes. Overflow through the slab with 4 cm water thickness and 2.12 lit/s discharge rate was registered for 16 hours. Overflow with 5 cm height gives 2.5 lit/s but the resistance period was only 4.5 hours.

In the second attempt the same model was used but a section is changed from rectangular to trapezoidal. The base width was kept 15 cm. the special wooden templet is prepared to provide an inclination of 45°. The soil at

MDD and OMC was laid first at an inclination of 45°. 2 cm thick Terrazyme treated soil was placed to create the trapezoidal section as per the required dimension. Figure 7 demonstrates the schematic diagram of the trapezoidal section for the discharge test.

Flow in the trapezoidal section was adjusted to maintain a constant depth of water. 2 cm depth gave the discharge of 831 ml/s. The cross-section resists this flow for 57 hours. Flow at 3 cm depth gives discharge of 1.6 lit/s and resistance for 42 hours. 2.6 lit/s discharge was obtained at 4 cm depth. The soil resists this flow for 27 hours. At a 5 cm depth, of 3.6 lit/sec discharge was obtained for a resistance period of 18 hours.

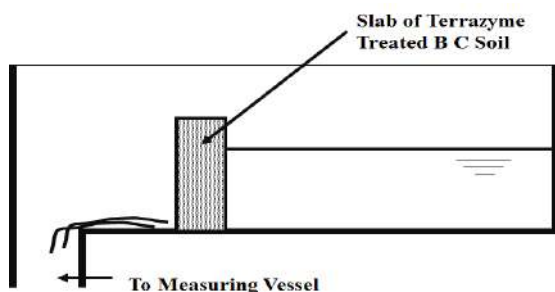


Figure 5. Schematic diagram for water retention test

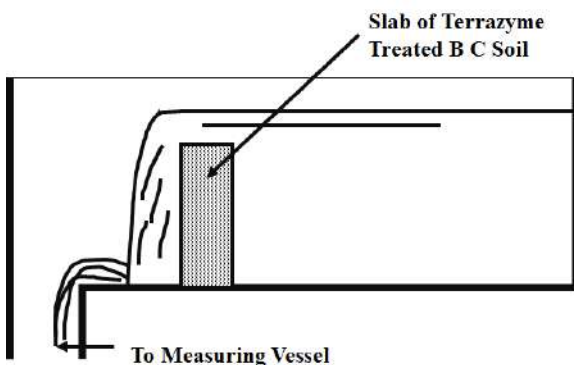


Figure 6. Schematic diagram for discharge through a rectangular section

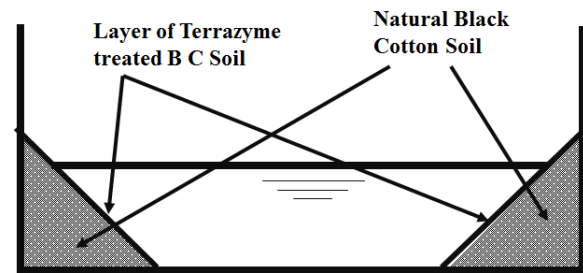


Figure 7. Schematic diagram for discharge through a trapezoidal section

5. CONCLUSIONS

Laboratory experiments were performed on the black cotton soil with and without Terrazyme. An effort was made to explain the mechanism for improvements in the engineering properties of the black cotton soil. A novel material introduced in this paper can be used as an alternative stabilizing black cotton soil. From the experimental results, the following conclusion can be made.

- As the clayey soil blended with Terrazyme drastic reduction in liquid limit was found. Significant improvement in other Atterberg limits was also obtained.
- From the experimental results, it is found that a blend of black cotton soil and Terrazyme generates dens packing through a reduction in adsorbed water thickness, results in a reduction in permeability.
- The addition of terrazyme makes clayey soil stiffer hence MDD increases and OMC decreases.
- Both shear parameters cohesion and friction angle of the treated soil was improved 1.5 times comparing with untreated soil.
- Free swell index reduced noticeably as a thickness of an adsorbed layer decreases.
- In the case where clayey soil is sensitive to high compressibility blend of terrazyme and clay reduces the compressibility up to 19%.
- The treated clayey soil behaves as an impervious barrier that retains the water for a considerable time.
- The black cotton soil with 2% diluted in water generates the best resistance in organic soil.
- The seepage rate increases as the height of retain water increases.
- As the rate of flow increases duration of resistance decreases for both sections.
- Trapezoidal sections support higher discharge with a longer duration compare to rectangular sections.

When compared to traditional stabilizers, non-traditional stabilizers like Terrazyme can be used successfully. This would reduce the erosion of unlined waterways, resulting in benefits in maintenance prevention. Since soil conditions vary by site, an

evaluation of basic soil properties on treated and untreated soil is needed before applying terrazyme to clayey soil for optimum content. Present clayey soil requires 2% terrazyme for better improvements. As result research parameters are significant for commercial applications.

6. FUTURE SCOPE

The blend of Terrazyme and black cotton soil can be design to support high discharge. In addition to this, the thickness of the layer can be design, which will reduce the permeability of unlined water bodies, and store the water for a higher duration.

7. REFERENCES

- J. Sen and J. P. Singh, "Stabilization of Black Cotton Soil using Bio- Enzyme for a Highway Material," *International Journal of Innovative Research in Science, Engineering and Technology*, Vol. 4, No. 12, (2015), 12453-12459, doi: 10.15680/IJRSET.2015.0411146
- M. Umar, K. A. Kassim, and K. T. Ping Chiet, "Biological process of soil improvement in civil engineering: A review," *Journal of Rock Mechanics and Geotechnical Engineering*, Vol. 8, No. 5, (2016), 767-774, doi: 10.1016/j.jrmge.2016.02.004.
- Athira S, B K Safana, and Keerthi Sabu, "Soil Stabilization using Terrazyme for Road Construction," *International Journal of Engineering Research & Technology* Vol. V6, No. 03, (2017), 547-549, doi: 10.17577/ijertv6is030515.
- P. Agarwal, "Effect of Bio-Enzyme Stabilization on Unconfined Compressive Strength of Expansive Soil," *International Journal of Engineering Research & Technology*, Vol. 03, No. 05, (2014), 30-33, doi: 10.15623/ijret.2014.0305007.
- T.A. Khan and M. R. Taha, "Effect of three bio enzymes on compaction, consistency limits, and strength characteristics of a sedimentary residual soil," *Advances in Materials Science and Engineering*, Vol. 2015, (2015), doi: 10.1155/2015/798965.
- A. G. Thomas and B. K. Rangaswamy, "Strength behavior of enzymatic cement-treated clay," *International Journal of Geotechnical Engineering*, Vol. 13, No. 03, (2021), 259-272, doi: doi.org/10.1080/19386362.2019.1622854
- G. Nizy Eujine, L. T. Somervell, S. Chandrakaran, and N. Sankar, "Enzyme stabilization of high liquid limit clay," *Electronic Journal of Geotechnical Engineering*, Vol. 19, (2014), 6989-6995.
- M. R. Taha, T. A. Khan, I. T. Jawad, A. A. Firoozi, and A. A. Firoozi, "Recent experimental studies in soil stabilization with a bio-enzymes-a review," *Electronic Journal of Geotechnical Engineering*, Vol. 18 R, (2013), 3881-3894.
- S. T. B. Y, and N. K3, "Improving the Properties of Black Cotton Soil Using Terrazyme as an Admixture," *International Journal of Engineering Technology*, Vol. 3, No. 1, (2017), 96-105.
- M. V. Sravan and H. B. Nagaraj, "Potential use of enzymes in the preparation of compressed stabilized earth blocks", *Journal of Materials in Civil Engineering*, Vol. 29, No. 9. (2017), 1-8.
- S. Muguda and H. B. Nagaraj, "Effect of enzymes on plasticity and strength characteristics of an earthen construction material," *International Journal of Geo-Engineering*, Vol. 10, No. 1, (2019), doi: 10.1186/s40703-019-0098-2.
- C. Venkatasubramanian and G. Dhinakaran, "Effect of bio-enzymatic soil stabilisation on unconfined compressive strength and California Bearing Ratio," *Journal of Engineering and Applied Sciences*, Vol. 6, No. 5, (2011), 295-298, doi: 10.3923/jeasci.2011.295.298.
- Y. J. Li, L. Li, and H. C. Dan, "Study on application of TerraZyme in road base course of road," *Applied. Mechanics and Materials.*, Vol. 97-98, (2011), 1098-1108, doi: 10.4028/www.scientific.net/AMM.97-98.1098.
- G. N. Eujine, S. Chandrakaran, and N. Sankar, "The engineering behaviour of enzymatic lime stabilised soils," *Proceedings Institution of Civil Engineering Ground Improvement*, Vol. 170, No. 1, (2017), 1-11, doi: 10.1680/jgrim.16.00014.
- K. Mekaideche, F.-E. M. Derfouf, A. Laimeche, and N. Abou-Bekr, "Influence of the Hydric State and Lime Treatment on the Thermal Conductivity of a Calcareous Tufa," *Civil Engineering Journal*, Vol. 7, No. 3, (2021), 419-430, doi: 10.28991/cej-2021-03091663.
- J. I. Obianyo and J. C. Agunwamba, "Efficiencies of horizontal and vertical baffle mixers," *Emerging Science Journal*, Vol. 3, No. 3, (2019), 130-145, doi: 10.28991/esj-2019-01176.
- H. Jafer, Z. H. Majeed, and A. Dulaimi, "Incorporating of two waste materials for the use in fine-grained soil stabilization," *Civil Engineering Journal*, Vol. 6, No. 6, (2020), 1114-1123, doi: 10.28991/cej-2020-03091533.
- H. Jafer, Z. H. Majeed, and A. Dulaimi, "Incorporating of two waste materials for the use in fine-grained soil stabilization," *Civil Engineering Journal*, Vol. 6, No. 6, (2020), 1114-1123, doi: 10.28991/cej-2020-03091533.
- B. H. Tran, B. V. Le, V. T. A. Phan, and H. M. Nguyen, "In-situ Fine Basalt Soil Reinforced by Cement Combined with Additive DZ33 to Construct Rural Roads in Gia Lai Province, Vietnam," *International Journal of Engineering, Transactions B Applications*, Vol. 33, No. 11, (2020), 2137-2145, doi: 10.5829/ije.2020.33.11b.03.
- M. Rahmnejad and V. Toufigh, "Influence of curing time and water content on unconfined compressive strength of sand stabilized using epoxy resin," *International Journal of Engineering, Transactions B Applications*, Vol. 31, No. 8, 1187-1195, (2018), doi: 10.5829/ije.2018.31.08b.05.

Persian Abstract

چکیده

استفاده از مواد زیست تخریب پذیر برای بهبود خاک ضعیف نتایج بهتری در زمینه مهندسی ژئوتکنیک داده است. این مواد تخمیر شده و از پوشش گیاهی استخراج می شوند. این باعث کاهش نسبت باطل ، ضخامت آب جذب شده و به حداکثر رساندن تراکم می شود. Terrazyme حاوی پروتئین طبیعی است غیر سمی و سازگار با محیط زیست است. در آب قابل حل است. خاک پنبه سیاه بسیار پلاستیکی و دارای قابلیت تورم است. کاهش رطوبت باعث کوچک شدن ، منجر به نشست دیفرانسیل پی می شود. این باعث آسیب به ساختار می شود. در این مقاله کار آزمایشی روی خاک پنبه سیاه تقویت شده با Terrazyme ارائه شده است. بخشهای مختلف Terrazyme با خاک پنبه سیاه مخلوط شد تا خصوصیات مهندسی خاک را ارزیابی کند. تغییر در خصوصیات شاخص و پارامترهای مقاومت توسط آزمایشات روی خاک تصفیه شده و تصفیه نشده ارزیابی شد. محدوده های آتربریگ ، شاخص تورم آزاد ، آزمون تراکم ، آزمایشات سه محوری انجام شد. نتایج تجربی کاهش محدودیت مایع ، شاخص انعطاف پذیری ، شاخص تورم آزاد ، رطوبت مطلوب و شاخص فشرده سازی را نشان می دهد. آزمایش های سه محوری بهبود انسجام و زاویه مقاومت برشی را نشان می دهد. دوز مطلوب % Terrazyme 2 از نظر وزن خاک خشک حاصل گردید.



Investigating Behavior of Very Large Crude Oil Carrier Ship's Diesel Engine on Handling Stormy Waters

A. Gholami^a, S. A. Jazayeri^{*b}, Q. Esmaili^c

^a Department of Mechanical Engineering, Ayatollah Amoli Branch, Islamic Azad University, Amol, Iran

^b Department of Mechanical Engineering, K. N. Toosi University of Technology, Tehran, Iran

^c School of Engineering Technology, University of Special Modern Technologies, Amol, Iran

PAPER INFO

Paper history:

Received 07 April 2021

Received in revised form 21 May 2021

Accepted 21 June 2021

Keywords:

Diesel Engine

Very Large Crude Oil Carrier

Fuel Consumption

Emissions

Sea Wave and Wind

Mean Value Engine Model

ABSTRACT

The behavior of ship engine encountering stormy waters with different sea wavelengths has been investigated. In this study, a mathematical model is developed using governing equations for various parts of the ship, that is the hull, engine, power transmission shafts from the engine to the propeller also the propeller of the ship itself were implemented in MATLAB/ Simulink software environment. The model consists of the torsional vibrations of the transmission shafts; this enables a more accurate analysis of the engine behavior which is the source of power generation in the ship's propulsion system. The simulation results showed that the wavelength of sea waves has a significant effect on the dynamic performance of the engine. In this research, the effect of different ratios of wavelength to ship length (λ/L_{PP}) including 0.5, 1, 1.5 and 2 in violent stormy sea conditions with a wave height of 11.5 m and wind speed of 28.5 m/s has been investigated. The results showed that with the exception of λ/L_{PP} of 1.5, at another ratios of λ/L_{PP} , changes in engine performance parameters such as torque, fuel and air consumption, CO₂ emission and power are decreasing with increasing wavelength. Most variations in engine speed are related to λ/L_{PP} of 2. The results showed that by reducing the wavelength, the period of oscillations is reduced. As the ratio of wavelength to ship length increases, the number of oscillating points in the engine behavior increases and the lowest number of oscillating points can be seen at λ/L_{PP} of 1.5. This study highlights the importance of effects of sea wavelengths as one of the most important physical parameters of the sea which should not be ignored in the design phase of the ship propulsion system and engine selection.

doi: 10.5829/ije.2021.34.08b.05

1. INTRODUCTION

Today, ship efficiency, energy consumption and strict environmental regulations taking a major impact on marine company's performance [1-3]. Ship propulsion systems are commonly designed to be effective in calm waters. Usually 15-30% of the power required in

calm waters is considered as the sea margin to provide the extra power needed in the face of adverse weather conditions [4]. However, due to the uncertain behavior of the waves [5-9] and its effect on the performance of the ship, it is difficult to choose a sea margin, which is reliable and provides the minimum power required in all adverse weather conditions. Waves does affect the size selection of the main engine which adds resistance on the ship or changing the operating point of the main engine, which affects both fuel consumption and emissions. It is common practice that the ship's engine loses some of its torque when

* Corresponding Author Institutional Email: jazayeri@kntu.ac.ir (S. A. Jazayeri)

dealing with waves, so it is vital important to study the behavior of the engine such as torque, power and fuel consumption in the face of sea waves at earlier stages of ship design or engine selection. Taskar et al. [10, 11] investigated the propeller's emergence and submergence in the face of waves and its effects on the load applied to the engine. Their studies indicated an increase in engine fuel consumption and power in unsteady flows.

Kyrtatos et al. [12] studied the dynamics of the ship and the propeller to optimize the machinery control strategy of the ship's propulsion system. Full scale experiments carried out by Kayano et al. [13] showed that the amount of power delivered by the engine in the face of waves and wind was greater than the amount previously considered at the design stage.

It is very important to have a detail knowledge of the engine performance, as the prime part of the ship's propulsion system. Among the various models such as transfer function models [14], zero or one-dimensional models [15], and multi-zone phenomenological models [16] and cycle Mean Value Engine Models (MVEMs) [12, 17-19] capable of evaluating the engine performance, the mean value engine model (MVEM) has least complexity, much less input data requirements and an adequate calculation execution time. In a transfer function model, which usually represents the relationship of fuel consumption to engine speed, the essential characteristics of the system does not reflect. On the other hand, more accurate results can be achieved using

multidimensional models, but achieving these results will be much more time consuming and computationally costly. The basic assumption in the MVEM modeling method is that the air and fuel flows to the cylinder are continuous, so the periodic trend of the engine is ignored and therefore this model can be used to calculate the average time value of engine parameters with a very reasonable accuracy, while the in-cycle variation (e.g. per degree of crank angle) cannot be determined.

In this study, the performance behavior of a very large crude oil carrier (VLCC) ship in the face of sea regular waves of different wavelengths has been investigated using mean value engine model (MVEM). The ship propulsion system model is modularly designed and implemented in Simulink software. As shown in Figure 1, the various components of the ship are defined and implemented as specific blocks in the software environment. Finally, in this research, engine performance parameters such as torque, power, fuel consumption and emissions at different wavelengths have been calculated and examined.

The difference between this paper and other researches is that unlike previous studies in which power transmission shafts were considered only as a rigid body, in the relevant calculations only the mass moment of inertia was considered, but in the present study the power transmission shafts from the engine to the propeller are considered as distributed systems in which the geometric and mechanical properties of

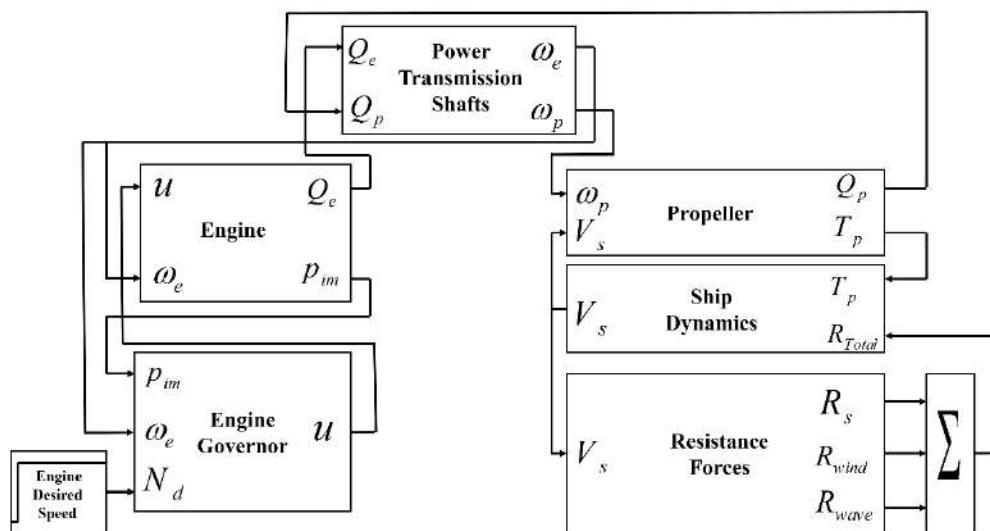


Figure 1. Schematic ship model in Simulink

the shaft such as length, diameter, shear modulus and moment of inertia are applied and coupled to the general model of the ship system. Given the importance of the power-train system in ships, especially in adverse weather conditions, providing a more accurate model of this system will more accurately predict the behavior of the system, especially the ship propulsion engine, in the design or optimization stage.

2. SHIP MODEL

As mentioned earlier, the modular method has been used to model the ship system. Each part of the ship system is a separate block that are interconnected to each other via interfaces. The solver selected in the Simulink environment is ODE45 because it has a high ability to solve ordinary differential equations. The implemented model can be used for low-speed and medium-speed ships, including oil carriers, container ships, bulk carriers and etc.; so the performance parameters of the ship such as speed, power, forces on the ship, fuel consumption, emissions and etc. are calculated.

2. 1. Engine Model

The mean value engine model is used to model the engine behavior. In this method, the inflow of air and fuel into the cylinders are assumed continuous and the scavenging and exhaust receivers are assumed thermodynamically open systems [20]. This model includes scavenging and exhaust receivers, cylinders, turbochargers, air cooler, exhaust pipe and engine controller. The governing equations for calculating engine performance are as follows [20, 21]:

$$Q_e = \frac{p_b V_D}{2\pi rev_{cy}}; P_b = \frac{\pi Q_e N_e}{30}; p_b = \frac{60P_b}{z_{cyl} V_D N_e} \quad (1)$$

where P_b is the engine brake power (watts), p_b is the engine brake mean effective pressure (BMEP), N_e is the engine crankshaft rotational speed (rpm), Q_e is the engine torque, rev_{cy} is revolutions per cycle (2 is for four-stroke engine) and V_D is the engine volume displacement.

The mass flow rate (kg/s) of fuel injected is calculated as follows:

$$\dot{m}_f = \frac{z_{cyl} m_{f_{cycle}} N_e}{(60 rev_{cy})} \quad (2)$$

where z_{cyl} is the number of engine cylinders, $m_{f_{cycle}}$ is

the mass of the fuel injected per cylinder per cycle.

A proportional-integral (PI) controller is used to model the engine governor:

$$u = u_0 + k_p \Delta N + k_i \int \Delta N dt \quad (3)$$

where $\Delta N = N_d - N_e$, N_d is the engine desired speed and N_e is the actual speed, k_i and k_p are the integral and proportional constant, and u_0 is the initial rack position.

The fuel assumed in this model is heavy fuel oil (HFO). The amount of emissions due to combustion can be calculated from the following equation in which EF is the emission factor and can be seen in Table 1 for different emissions [22]:

$$m_{f_{total}} = \dot{m}_f \Delta t; \dot{m}_i = \dot{m}_f EF_i \quad (4)$$

where Δt is the time interval, m and \dot{m} are mass and mass flowrate, respectively.

To calculate the amount of air passing through the cylinders, considering that the engine is considered to be a two-stroke type, the following equation has been used [20]:

$$\dot{m}_a = C_V A_{V_{eq}} \frac{p_{SC}}{\sqrt{R_{air} T_{SC}}} \left(\frac{2\gamma_A}{\gamma_A - 1} \left(pr_{cyl}^{\frac{2}{\gamma_A}} - pr_{cyl}^{\frac{\gamma_A + 1}{\gamma_A}} \right) \right)^{0.5}; \quad (5)$$

$$pr_{cyl} = \frac{p_{ER}}{p_{SC}}$$

where C_V is air flow resistance coefficient, $A_{V_{eq}}$ is equivalent effective area, p_{SC} and p_{ER} are scavenging and exhaust receiver's pressures, respectively, pr_{cyl} is cylinder pressure ratio and γ_A is air specific heat ratio. To model the turbocharger behavior, curve fitting and interpolation methods on compressor and turbine performance maps have been used. In the compressor, the volume flow rate of air is a function of the compressor pressure ratio and the rotational speed of the turbocharger, and in the turbine, the gas volume flow rate is a function of the turbine pressure ratio.

The temperature of air exiting the air cooler is calculated as follows:

$$T_{AC} = T_c - \varepsilon(T_c - T_w) \quad (6)$$

TABLE 1. Emission factors [23]

CO ₂ (g/g fuel)	NO _x (g/g fuel)	PM (g/g fuel)	SO _x (g/g fuel)
3.114	0.07846	0.00728	0.053

where T_c is the temperature of air exiting the compressor, T_w is the cooling water temperature, and ε is the air cooler effectiveness.

2. 2. Propeller Model The ship propeller is fixed pitch and the relationships of Wageningen propeller type B are used to calculate the dimensionless coefficients of thrust (T_p) and torque (Q_p) [23];

$$\begin{aligned} T_p &= K_T \rho_w N_p^2 D_p^4 \beta; \\ Q_p &= K_Q \rho_w N_p^2 D_p^5 \beta^{0.8} \end{aligned} \quad (7)$$

where K_T and K_Q are the dimensionless coefficients of thrust and torque, respectively, ρ_w is sea water density, N_p (rev/s) and D_p are the propeller rotational speed and the propeller diameter, respectively and β is thrust diminution factor.

The propeller average wake inflow velocity is affected by ship surge and pitch motions and the waves, based on the available data as follows [24, 25]:

$$V_{Total} = \left(\begin{array}{l} (1-w_p) \\ \{V_s - \omega_e \xi_a \sin(\omega_e t - \zeta_\xi)\} \\ + \alpha \omega h_a \exp(-kz_p) \\ \cos X \cos(\omega_e t - kx_p \cos X) \end{array} \right) \sqrt{\left(1 - \frac{\Delta \bar{p}}{0.5 \rho_w V_s^2} \right)} \quad (8)$$

where w_p is effective wake fraction, V_s is ship speed, ω_e is wave encounter circular frequency, ξ_a is surge amplitude, ζ_ξ is phase delay, ω is wave circular frequency, h_a is wave amplitude, k is wave number, z_p is the immersion depth of the propeller shaft, x is the longitudinal distance of the propeller from the center of gravity of the ship, x_p is the position of the propeller section with reference to the center of gravity of the vessel, $\Delta \bar{p}$ is pressure gradient below the bottom of the ship due to pitching motion, X is wave encounter angle (0 for following sea; 180 for head sea), ρ_w is density of seawater, t is time, η_s is pitch amplitude.

2. 3. Power Transmission Shafts It is assumed that the ship's power transmission shafts from the engine to the propeller are distributed elements. The flywheel and the propeller of the ship are considered lumped elements. The schematic layout of the ship powertrain system is shown in Figure 2. The governing equations of the transmission shafts are as follows [26]:

$$\begin{bmatrix} \omega_1(z_1^{-1}) \\ \omega_2(z_1^{-1}) \end{bmatrix} = 1/\xi_1 \times \begin{bmatrix} \frac{1+z_1^{-1}}{1-z_1^{-1}} & -2\frac{z_1^{-1/2}}{1-z_1^{-1}} \\ \frac{z_1^{-1/2}}{1-z_1^{-1}} & \frac{1+z_1^{-1}}{1-z_1^{-1}} \end{bmatrix} \begin{bmatrix} T_1(z_1^{-1}) \\ T_2(z_1^{-1}) \end{bmatrix}; \quad (9)$$

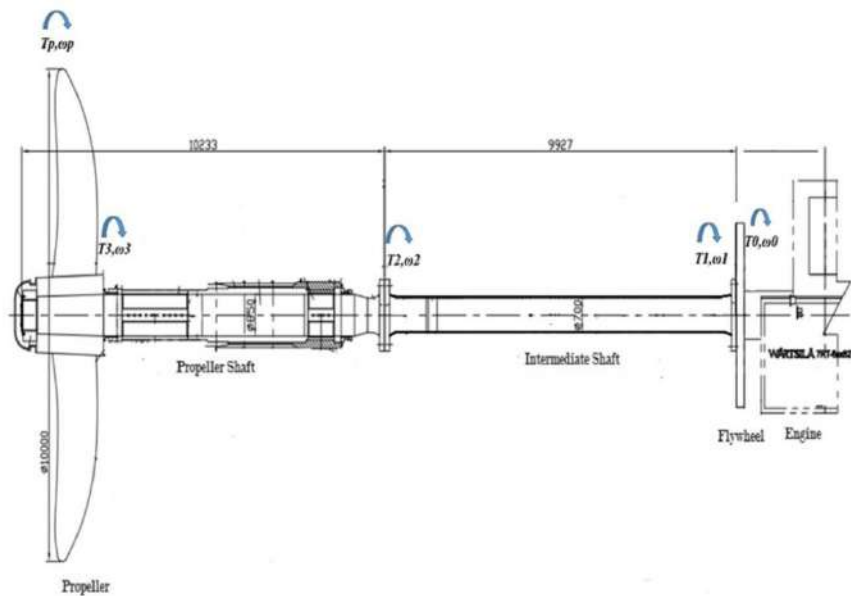


Figure 2. Schematic layout of powertrain system [31]

$$\begin{bmatrix} T_2(z_2^{-1}) \\ T_3(z_2^{-1}) \end{bmatrix} = \xi_2 \begin{bmatrix} 1+z_2^{-1} & -\frac{1}{z_2} \\ \frac{1-z_2^{-1}}{1-z_2} & \frac{1}{1-z_2} \end{bmatrix} \begin{bmatrix} \omega_2(z_2^{-1}) \\ \omega_3(z_2^{-1}) \end{bmatrix}; \tag{10}$$

$$z_1^{-1} = e^{(-2l_1\sqrt{L_1C_1})}; z_2^{-1} = e^{(-2l_2\sqrt{L_2C_2})}; \xi_1 = \sqrt{\frac{L_1}{C_1}}; \xi_2 = \sqrt{\frac{L_2}{C_2}}$$

$$C_j = \frac{1}{G_j J_{sj}}; L_j = J_{sj} \rho_j \quad j = 1, 2$$

The governing equations of the flywheel and propeller as lumped elements are as follows:

$$\begin{aligned} \frac{\omega_f}{T_f}(z_1) &= \frac{\beta_f z_1}{z_1 + \alpha_f}; \beta_f = \frac{1 - \alpha_f}{B_f}; \\ \alpha_f &= \exp\left(-\frac{B_f}{J_f} 2l_1 \sqrt{\rho_1 / G_1}\right) \\ \frac{\omega_p}{T_p}(z_2) &= \frac{\beta_p z_2}{z_2 + \alpha_p}; \beta_p = \frac{1 - \alpha_p}{B_p}; \\ \alpha_p &= \exp\left(-\frac{B_p}{J_p} 2l_2 \sqrt{\rho_2 / G_2}\right) \end{aligned} \tag{11}$$

where ω_f and ω_p are flywheel and propeller angular speeds, respectively; T_f and T_p are flywheel and propeller torques, respectively. In this case there is not any intermediary parts between intermediate shaft and flywheel; therefore $\omega_e = \omega_0 = \omega_1 = \omega_f$, where ω_e is engine angular speed. on the other hand, since there is not any intermediary parts between propeller shaft and propeller, therefore $\omega_3 = \omega_p$.

2. 4. Ship Dynamic

In this research, for modeling the ship motion, only movement in the longitudinal direction is considered. Hence, the governing equation is as follows:

$$\frac{dV_s}{dt} = \frac{(1-t_d)T_p - (R_s + R_{Add})}{m_{ship} + m_{add}} \tag{12}$$

where V_s is the ship's longitudinal velocity, T_p is the effective propeller thrust, R_s is the ship's resistance which is calculated by the Holtrop method for calm water conditions [27], t_d is the thrust deduction factor, m_{ship} is the ship's mass, m_{add} is the added virtual mass to consider the hydrodynamic force owing to the acceleration of a body in a fluid. The total added resistance (R_{Add}) due to the weather conditions (wave and wind) is estimated using the proposed formula by Liu et al. [28];

$$R_{Add} = R_{AW} + R_{AA} \tag{13}$$

R_{AW} and R_{AA} are added resistance components due to wave and wind, respectively.

3. VALIDATION

The whole ship system was implemented in Simulink environment based on the formulations expressed above. For the model validation, a 12-day VLCC ship fuel consumption measurements report [29] has been used. As shown in Figure 3, there is a good agreement between the simulation results and the

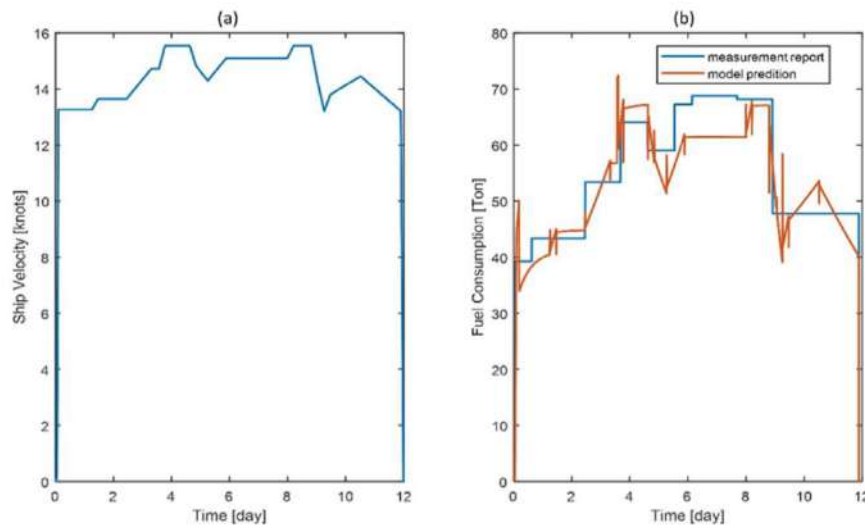


Figure 3. (a) VLCC voyage cycle;(b) fuel consumption

measured report. The maximum difference between the value predicted by the model and the measurement value was 10.82 tons, which is equivalent to 16.1% of the error. The daily average fuel consumption predicted by the model is 49.91 tons and, on the other hand, the measured value is 51.65 tons, which indicates a very good accuracy within 3.5% error.

4. RESULTS AND DISCUSSION

In this section, it is assumed that the ship is facing rough weather conditions. The sea is considered as violent storm with a wave height of 11.5 m and a wind speed of 28.5 m/s according to the ITTC 2017.

The wavelength to the length of ship between perpendicular ratio (λ/L_{PP}) will be 0.5, 1, 1.5 and 2. The ship is in full load condition. It is assumed that the engine desired speed at time 2 s changes from 45 rpm to 80 rpm, which is considered as an input step signal to the model implemented in Simulink. The simulation time is 150 seconds. Using the data in Table 2, simulations were performed at different sea wavelengths. The simulation results including speed, torque, fuel consumption, emitted CO₂ and power are calculated and presented in Figures 4 to 8.

At λ/L_{PP} of 0.5, as shown in Figure 4, the range of engine speed fluctuations at steady-state is between 74.5 and 77.5 rpm. The number of oscillation points is 6. Engine torque fluctuations range is from 2.2 to 3.6 MNm with 9 oscillation points. Fuel consumption

TABLE 2. Ship specifications [30]

Engine		Intermediate shaft	
7RT-flex82T	2-stroke	Diameter(d_i)	0.7 [m]
Cylinders no.	7 In-line	Length(l_i)	9.927 [m]
Output (CMCR)	31640 [Kw]	Inertia	1376 [kgm ²]
Propeller		Ultimate-tensile strength (UTS)	590 [N/mm ²]
Blades no.	4	Shear modulus(G_i)	81.4 [GPa]
Diameter (d_p)	9.86 [m]	Density(ρ_i)	7850 [kg/m ³]
Damping (B_p)	467580 [Nms/rad]	Propeller shaft	
Load inertia (J_p)	429250 [kgm ²]	Diameter(d_2)	0.85 [m]
Flywheel		Length(l_2)	10.233 [m]
Inertia (J_f)	13600 [kgm ²]	Inertia	3454 [kgm ²]
Damping (B_f)	9115 [Nms/rad]	Ultimate tensile strength(UTS)	590 [N/mm ²]
Ship		Shear modulus(G_2)	81.4 [GPa]
Length (L)	320 [m]	Density (ρ_2)	7850 [kg/m ³]
Breadth (B)	58 [m]		
Displacement volume (V)	312600 [m ³]		
Area of maximum transverse section exposed to the wind (A_{XV})	1161 [m ²]		

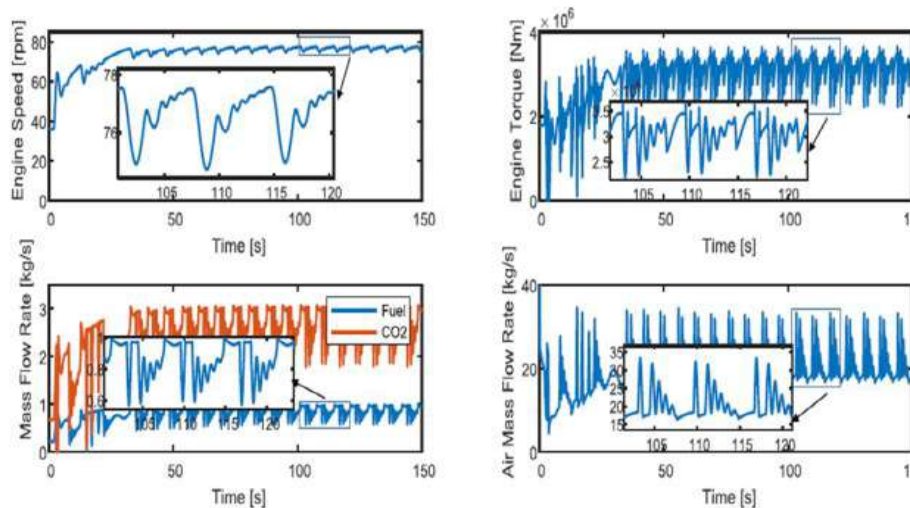


Figure 4. Predicted system response at $\lambda/L_{PP}=0.5$

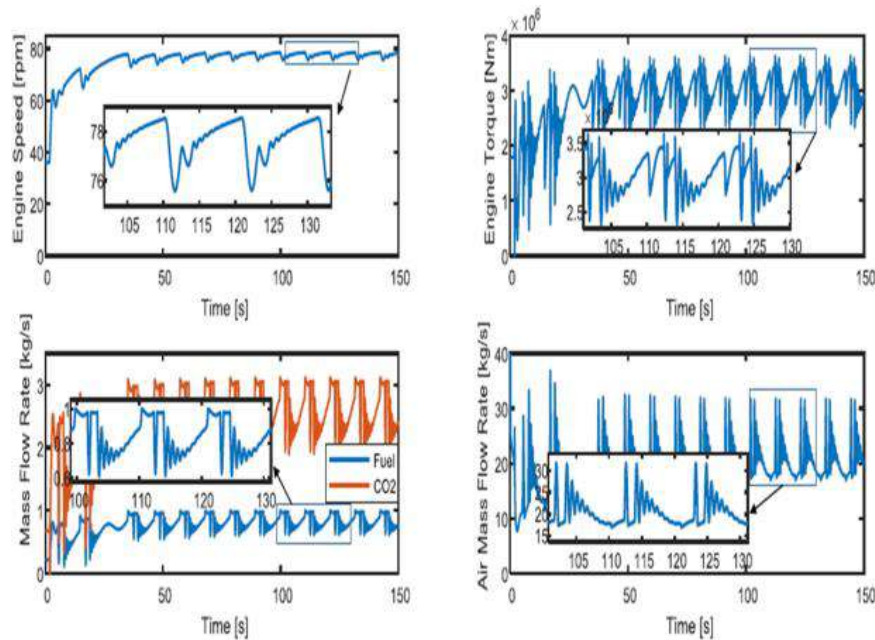


Figure 5. Predicted system response at $\lambda/L_{PP}=1$

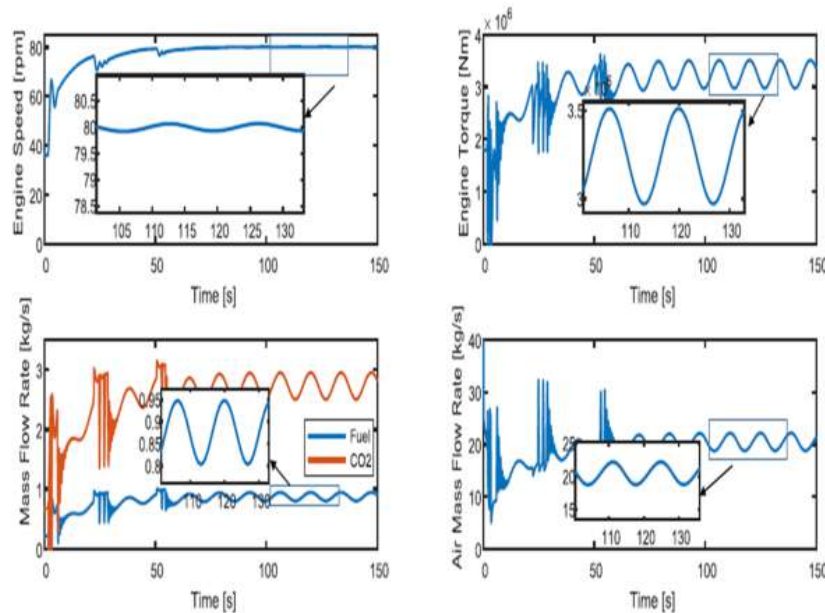


Figure 6. Predicted system response at $\lambda/L_{PP}=1.5$

and CO₂ emission are in the range of 0.57 to 0.98 kg/s and 1.77 to 3.05 kg/s, respectively, which is accompanied by 7 oscillation points. Air consumption is between 16.6 to 33.4 kg/s with 6 oscillation points. As shown in Figure 8, the amplitude of engine power fluctuations in the steady

state is from 17.6 to 29.1 MW. In addition, the number of oscillation points is 7.

At λ/L_{PP} of 1, as can be seen in Figure 5, the amplitude of the engine speed fluctuations in the steady state is from 75.6 to 78.5 rpm. The number of oscillating points is 8. Torque oscillations range is of

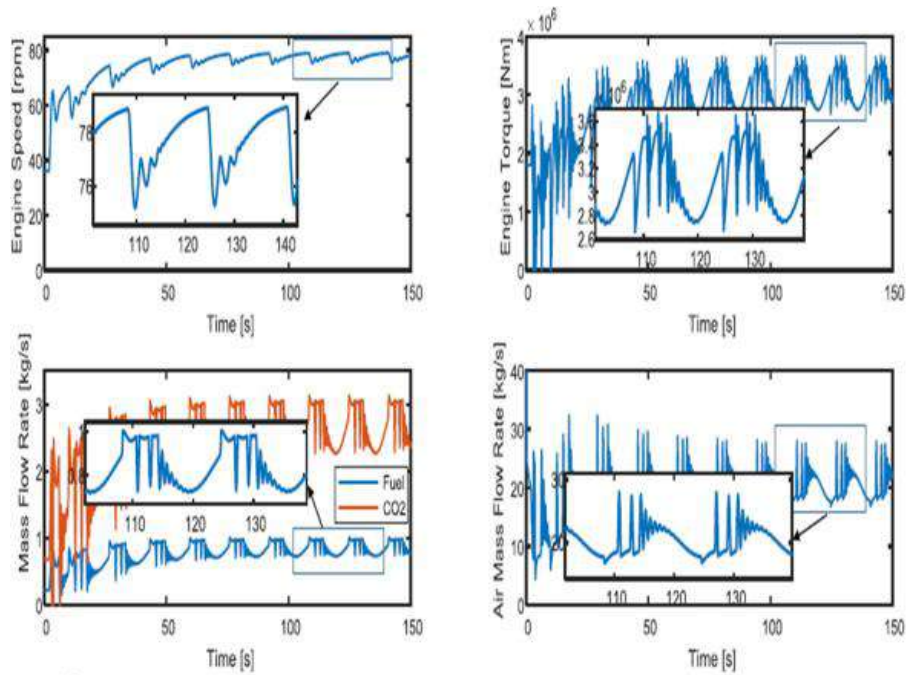


Figure 7. Predicted system responses at $\lambda/L_{PP}=2$

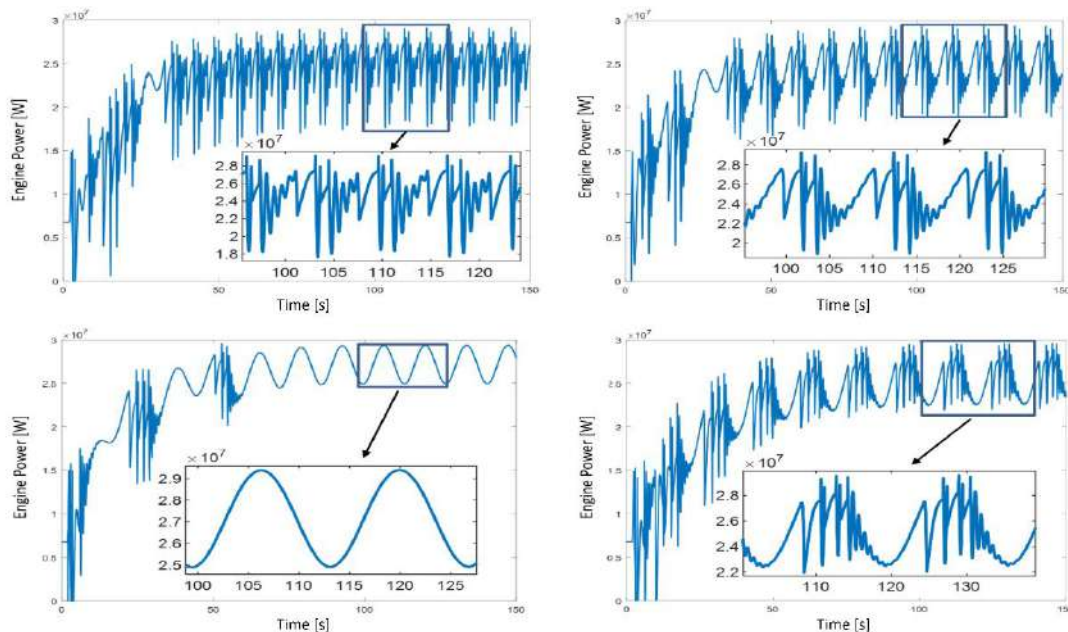


Figure 8. Predicted engine power at: (a) $\lambda/L_{PP}=0.5$; (b) $\lambda/L_{PP}=1$; (c) $\lambda/L_{PP}=1.5$; (d) $\lambda/L_{PP}=2$

2.3 to 3.6 MNm with 13 oscillation points. Fuel consumption and CO₂ emission are in the range of 0.60 to 0.99 kg/s and 1.86 to 3.08 kg/s, respectively, with 12 oscillation points. Air consumption is

between 16.9 to 31.7 kg/s with 11 oscillation points. As can be seen in Figure 8, the range of power fluctuations in the steady state is from 18.8 to 29.2 MW. The number of oscillation points is 11.

At λ/L_{PP} of 1.5, as shown in Figure 6, the range of engine speed fluctuations is changed from 79.9 to 80 rpm. As can be seen the number of oscillation points is 2. Torque fluctuations range is 2.97 to 3.51 MNm with 2 oscillation points. Fuel consumption and CO₂ emission are in the range of 0.80 to 0.94 kg/s and 2.49 to 2.92 kg/s, respectively, which are accompanied by 2 oscillation points. Air consumption is between 18.75 to 22.17 kg/s with 2 oscillating points. As shown in Figure 8, the range of power fluctuations in the steady state is from 24.9 to 29.3 MW with number of 2 oscillation points.

At λ/L_{PP} of 2, as can be seen in Figure 7, the amplitude of the engine speed fluctuations in the steady state is 75.18 to 78.92 rpm. The number of oscillation points is 8. Torque fluctuations interval is from 2.66 to 3.67 MNm with 15 oscillation points. Fuel consumption and CO₂ emission are in the range of 0.72 to 1 kg/s and 2.24 to 3.114 kg/s, respectively, which are accompanied by 14 oscillation points. Air consumption is from 16.7 to 28.1 kg/s with 11 oscillation points. As can be seen in Figure 8, the interval of engine power fluctuations in the steady state is from 21.9 to 29.5 MW. The number of oscillation points is 14.

As shown in these figures, when fuel consumption increases, the air flow does not increase simultaneously, and the air consumption diagram shows a delay, which is due to the inertia of the turbocharger system and its response. When the propeller coming out of the water, an increase in propeller speed occurs and as a result the torque will decrease and the power has a decreasing trend. As soon as the ship's propeller is completely submerged in the water, the torque increases and the speed decreases. As a result, the decreasing trend of power becomes an increasing trend. The results related to changes in engine performance parameters and the number of oscillation points can be seen in Table 3. As can be seen, there is the highest number of oscillation points and on the other hand the highest changes in engine speed at λ/L_{PP} of 2. At λ/L_{PP} of 0.5, the largest changes in torque, fuel consumption, CO₂ emission and air consumption are observed. On the other hand, the smallest changes in engine speed, torque, fuel consumption, CO₂ emission and air consumption can be seen at λ/L_{PP} of 1.5. By comparing the results, it can be seen that as the λ/L_{PP} ratio increases, the period of oscillations and the number of fluctuations in each period will also increase. At λ/L_{PP} of 1.5, as can be seen from the

TABLE 3. Changes in engine performance parameters

λ/L_{PP}	0.5	1	1.5	2
Speed changes (rpm)/ number of oscillation points	3/ 6	2.9/ 8	0.1/ 2	3.74/ 8
Torque changes (MNm)/ number of oscillation points	1.4/9	1.3/13	0.54/ 2	1.01/ 15
Fuel consumption changes (kg/s)/ number of oscillation points	0.41/7	0.39/12	0.14/ 2	0.28/ 14
CO ₂ changes (kg/s)/ number of oscillation points	1.28/7	1.22/12	0.43/ 2	0.874/14
Air consumption changes (kg/s)/ number of oscillation points	16.8/6	14.8/11	3.42/ 2	11.4/ 11
Power changes (MW)/ number of oscillation points	11.5/7	10.4/11	4.4 / 2	7.6/ 14

responses, the graph is smooth and no fluctuations are seen in this case.

5.CONCLUSION

A very large crude oil carrier ship is successfully modeled and through implementation of Simulink environment, the behavior of the engine such as power, fuel consumption and the amount of emissions in dealing with waves at different wavelengths have been investigated. The validity and accuracy of the model were examined through the voyage report of a VLCC available. The accuracy of the model results with good compliance with the VLCC report shows that the model is reliable. In the modeling process, the various components of the ship, including the hull and forces on it, the engine and its components, the power transmission shafts and the propeller were considered. The study shows that the effect of waves with different wavelength on engine behavior cannot be ignored. The effect of changing the wavelength can be seen as fluctuations in the behavior of the engine, which can cause problems in the ship's powertrain system if repeated. The results of the effect of λ/L_{PP} of 0.5, 1, 1.5 and 2 in violent stormy sea conditions on the engine show, with the exception of λ/L_{PP} of 1.5, in other cases with increasing λ/L_{PP} , the number of oscillating points in

the behavior of the engine performance parameters increases. The least changes in engine performance parameters are seen at λ/L_{PP} of 1.5, while with the exception of λ/L_{PP} of 2, where the speed variations are higher than other λ/L_{PP} values, the trend of changes in other engine performance parameters is decreasing with increasing λ/L_{PP} values. As a result, the effects of waves with different wavelengths should not be neglected in the design phase of the ship's propulsion system.

6. REFERENCES

- Molina, S., Guardiola, C., Martín, J. and García-Sarmiento, D., "Development of a control-oriented model to optimise fuel consumption and nox emissions in a di diesel engine", *Applied Energy*, Vol. 119, (2014), 405-416, <https://doi.org/10.1016/j.apenergy.2014.01.021>
- Liu, J., Yang, F., Wang, H., Ouyang, M. and Hao, S., "Effects of pilot fuel quantity on the emissions characteristics of a cng/diesel dual fuel engine with optimized pilot injection timing", *Applied Energy*, Vol. 110, (2013), 201-206, <https://doi.org/10.1016/j.apenergy.2013.03.024>
- Rutherford, D. and Comer, B., "The international maritime organization's initial greenhouse gas strategy", (2018).
- Diesel, M. and Turbo, S., "Basic principles of ship propulsion", *MAN Diesel & Turbo Publication*, (2004).
- Naghipour, M., "Estimation of hydrodynamic force on rough circular cylinders in random waves and currents (research note)", *International Journal of Engineering*, Vol. 14, No. 1, (2001), 25-34.
- Mirbagheri, S., RAJAEI, T. and MIRZAEI, F., "Solution of wave equations near seawalls by finite element method", *International Journal of Engineering, Transactions A: Basics*, Vol. 21, No. 1, (2008), 1-16.
- Farhadi, A., "Investigating the third order solitary wave generation accuracy using incompressible smoothed particle hydrodynamics", *International Journal of Engineering, Transactions C: Aspects*, Vol. 29, No. 3, (2016), 426-435, doi: 10.5829/idosi.ije.2016.29.03c.17.
- Bayani, R., Farhadi, M., Shafaghat, R. and Alamian, R., "Experimental evaluation of irwecl, a novel offshore wave energy converter", *International Journal of Engineering*, Vol. 29, No. 9, (2016), 1292-1299, doi: 10.5829/idosi.ije.2016.29.09c.15.
- Yazdi, H., Shafaghat, R. and Alamian, R., "Experimental assessment of a fixed on-shore oscillating water column device: Case study on oman sea", *International Journal of Engineering, Transactions C: Aspects*, Vol. 33, No. 3, (2020), 494-504, doi: 10.5829/ije.2020.33.03c.14.
- Taskar, B. and Steen, S., "Analysis of propulsion performance of kvlcc2 in waves", in Proceedings of the Fourth International Symposium on Marine Propulsors (Volume I), International Symposiums on Marine Propulsors Texas. (2015).
- Taskar, B., Yum, K.K., Steen, S. and Pedersen, E., "The effect of waves on engine-propeller dynamics and propulsion performance of ships", *Ocean Engineering*, Vol. 122, (2016), 262-277, <https://doi.org/10.1016/j.oceaneng.2016.06.034>
- Kyrtatos, N., Theodosopoulos, P., Theotokatos, G. and Xiros, N., "Simulation of the overall ship propulsion plant for performance prediction and control", *Transactions-Institute of Marine Engineers Series C*, Vol. 111, (1999), 103-114, doi.
- Kayano, J., Yabuki, N., Sasaki, N. and Hiwatashi, R., "A study on the propulsion performance in the actual sea by means of full-scale experiments", *TransNav: International Journal on Marine Navigation and Safety of Sea Transportation*, Vol. 7, No. 4, (2013), 521-526, <https://doi.org/10.12716/1001.07.04.07>
- Larroude, V., Chenouard, R., Yvars, P.-A. and Millet, D., "Constraint based approach for the steady-state simulation of complex systems: Application to ship control", *Engineering Applications of Artificial Intelligence*, Vol. 26, No. 1, (2013), 499-514, <https://doi.org/10.1016/j.engappai.2012.07.003>
- Scappin, F., Stefansson, S.H., Haglind, F., Andreasen, A. and Larsen, U., "Validation of a zero-dimensional model for prediction of nox and engine performance for electronically controlled marine two-stroke diesel engines", *Applied Thermal Engineering*, Vol. 37, (2012), 344-352, doi. <https://doi.org/10.1016/j.applthermaleng.2011.11.047>
- Bazari, Z., "Diesel exhaust emissions prediction under transient operating conditions", *SAE Transactions*, (1994), 1004-1019, <https://doi.org/10.4271/940666>
- Hendricks, E., "Mean value modelling of large turbocharged two-stroke diesel engines", *SAE Transactions*, (1989), 986-998, <https://doi.org/10.4271/890564>
- Yum, K.K., Taskar, B., Pedersen, E. and Steen, S., "Simulation of a two-stroke diesel engine for propulsion in waves", *International Journal of Naval Architecture and Ocean Engineering*, Vol. 9, No. 4, (2017), 351-372, doi. <https://doi.org/10.1016/j.ijnaoe.2016.08.004>
- Theotokatos, G. and Tzelepis, V., "A computational study on the performance and emission parameters mapping of a ship propulsion system", *Proceedings of the Institution of Mechanical Engineers, Part M: Journal of Engineering for the Maritime Environment*, Vol. 229, No. 1, (2015), 58-76, <https://doi.org/10.1177/1475090213498715>
- Xiros, N., "Robust control of diesel ship propulsion, Springer Science & Business Media, (2012).
- Heywood, J.B., "Internal combustion engine fundamentals, McGraw-Hill Education, (2018).
- IMO, T.I., "Greenhouse gas study", Executive Summary and Final Report, London, (2014).
- Minsaas, K., Faltinsen, O. and Persson, B., "On the importance of added resistance, propeller immersion and propeller ventilation for large ships in a seaway", (1983).
- Faltinsen, O.M., "Prediction of resistance and propulsion of a ship in a seaway", in Proceedings of the 13th symposium on naval hydrodynamics, Tokyo, 1980. (1980).
- Ueno, M., Tsukada, Y. and Tanizawa, K., "Estimation and prediction of effective inflow velocity to propeller in waves", *Journal of Marine Science and Technology*, Vol. 18, No. 3, (2013), 339-348, <https://doi.org/10.1007/s00773-013-0211-8>
- Gholami, A., Jazayeri, S.A. and Esmaili, Q., "Marine powertrain simulation for design and operational performance evaluation", *International Journal of*

- Powertrains*, Vol. 9, No. 4, (2020), 289-314, doi: 10.1504/IJPT.2020.111232.
27. Holtrop, J. and Mennen, G., "An approximate power prediction method", *International Shipbuilding Progress*, Vol. 29, No. 335, (1982), 166-170.
28. Liu, S., Shang, B. and Papanikolaou, A., "On the resistance and speed loss of full type ships in a seaway", *Ship Technology Research*, Vol. 66, No. 3, (2019), 161-179, <https://doi.org/10.1080/09377255.2019.1613294>
29. Safaei, A.A., Ghassemi, H. and Ghiasi, M., "Correcting and enriching vessel's noon report data using statistical and data mining methods", *European Transport*, Vol. 67, (2018).
30. Yasukawa, H., Zaky, M., Yonemasu, I. and Miyake, R., "Effect of engine output on maneuverability of a vlcc in still water and adverse weather conditions", *Journal of Marine Science and Technology*, Vol. 22, No. 3, (2017), 574-586, doi: 10.1007/s00773-017-0435-0.

Persian Abstract

چکیده

در این تحقیق، به بررسی تاثیر طول موج های مختلف موج دریا بر رفتار موتور کشتی پرداخته شده است. برای این منظور یک مدل از سیستم کشتی با استفاده از روابط حاکم بر بخشهای مختلف کشتی اعم از بدنه، موتور، شفت های انتقال قدرت از موتور به پروانه و پروانه کشتی در محیط نرم افزار Matlab/Simulink پیاده سازی گردیده است. در این تحقیق، ارتعاشات پیچشی شفت های انتقال قدرت در مدل لحاظ شده تا بتوان تحلیل دقیقتری از رفتار موتور به عنوان المان تولید قدرت سیستم پیشران کشتی ارائه کرد. نتایج نشان می دهد تغییر طول موج می تواند بر عملکرد دینامیکی موتور تاثیر چشمگیر داشته باشد. در این تحقیق، تأثیر نسبت های مختلف طول موج به طول کشتی (λ/LPP) برابر ۰.۵، ۱، ۱.۵ و ۲ در شرایط طوفانی دریا با ارتفاع موج ۱۱.۵ متر و سرعت باد ۲۸.۵ متر بر ثانیه بررسی شده است. نتایج نشان می دهد به استثنای λ/LPP برابر ۱.۵، در نسبتهای دیگر λ/LPP تغییرات در پارامترهای عملکرد موتور مانند گشتاور، مصرف سوخت و هوا، میزان انتشار CO_2 و توان با افزایش طول موج، کاهش می یابد. بیشترین تغییرات در سرعت موتور مربوط به λ/LPP برابر ۲ است. نتایج نشان می دهد با کاهش طول موج، دوره نوسانات کاهش می یابد. با افزایش نسبت طول موج به طول کشتی، تعداد نقاط نوسانی در رفتار موتور افزایش می یابد و کمترین تعداد نقاط نوسانی را میتوان در λ/LPP برابر ۱.۵ مشاهده نمود. این مطالعه اهمیت تاثیرات طول موج دریا به عنوان یکی از مهمترین پارامترهای فیزیکی دریا را برجسته می کند که نباید در مرحله طراحی سیستم پیشران کشتی و انتخاب موتور نادیده گرفته شود.



A Three-stage Filtering Approach for Face Recognition using Image Hashing

M. Ghasemi, H. Hassanpour*

Computer Engineering and IT Department, Shahrood University of Technology, Shahrood, Iran

PAPER INFO

Paper history:

Received 15 April 2021
Received in revised form 21 May 2021
Accepted 21 June 2021

Keywords:

Face Recognition
Image Hashing
Local Sensitive Hashing
Large Datasets

ABSTRACT

Face recognition has become a crucial topic in recent decades, which offers important opportunities for applications in security surveillance, human-computer interaction, and forensics. However, it poses challenges, including uncontrolled environments, large datasets, and insufficiency of training data. In this paper, a face recognition system is proposed to iron out the above problems with a new framework based on a hashing function in a three-stage filtering approach. At the first stage, candidate subjects are chosen using the Locality-Sensitive Hashing (LSH) function. We employ a voting system to select candidates via disregarding a large number of dissimilar identities considering their local features. At the second stage, a robust image hashing based on Discrete Cosine Transform (DCT) coefficients is used to further refine the candidate images in terms of global visual information. Finally, the test image is recognized among selected identities using other visual information, resulting in further accuracy gains. Extensive experiments on FERET, AR, and ORL datasets show that the proposed method outperforms with a significant improvement in accuracy over the state-of-the-art methods.

doi: 10.5829/ije.2021.34.08b.06

1. INTRODUCTION

Within the past decade, face recognition has become one of the most powerful applications of image processing and visual surveillance systems [1]. Although face recognition systems have seen striking improvements, they are remarkably affected by several issues such as uncontrolled pose and illumination conditions, large volume of data, and computational complexity optimization [2,3].

Performance of face recognition systems is significantly affected by its feature extraction step. Several feature extraction methods have been introduced in literature for face recognition, such as handcrafted feature like histogram of oriented gradients (HOG) [4], local binary patterns (LBP) [5], and learned feature like Fisher Vectors Faces [6] and learning-based (LE) descriptor [7]. However, they may not achieve a suitable performance in uncontrolled scenarios and large volume of dataset.

Image hashing is considered as an approach to cope with the limitations of face recognition [8]. Using

hashing functions, one can map high-dimensional data into low-dimensional codes. Because of their low memory usage and low computational cost, many hashing approaches have been proposed in literature to form compact codes for image representation. Modern hashing methods can be divided into two categories: data-dependent and data-independent. In data-dependent hashing methods, hashing functions are learned from data by preserving the data structure. Data-independent hashing methods, such as LSH [9], generate codes by using random projections.

In this work, a new face recognition method is proposed using a multi-stage filtering framework. Our basic intuition is that if we disregard dissimilar identities to the query image using different visual information at different stages, a better result will be achieved. To solve the time complexity of the search strategy, an image hashing function is used in each stage. The performance of the proposed method is evaluated in several face recognition scenarios: face recognition in semi-

*Corresponding Author Email: h.hassanpour@shahroodut.ac.ir (H. Hassanpour)

uncontrolled conditions, aging condition, limitation in training data, and large datasets².

Indeed, the proposed method applies a cascaded filtering in three stages for analyzing different visual information in each stage using image hashing. A large number of dissimilar identities in terms of local visual information are disregarded in the first stage using the Locality-Sensitive Hashing (LSH) function. Then, image candidates are further refined by comparing their global features with the corresponding global feature from the query image, using an image hashing applied on Discrete Cosine Transform (DCT) coefficients of the images. Finally, by comparing the LBP features of the refined identities and the query image, the best matching candidate was chosen to recognize the query image from the database. Performance of the proposed face recognition method was evaluated using different datasets. Experimental results in this manuscript showed that the proposed method improves face recognition's performance.

Image hashing is useful for saving a remarkable amount of computational power by reducing features space [8,10]. In addition, the use of LSH in the first stage can also reduce the execution time of the search [9]. Another advantage of our three-stage filtering framework is that it analyses different visual information of face images in each stage. The proposed method, with its low computational cost and high accuracy is suitable for face recognition in a large dataset.

The rest of paper is organized as follows: section 2 briefly reviews related works in face recognition. The proposed method is explained in section 3. Experimental results are illustrated in section 4. Finally conclusions are drawn in section 5.

2. BACKGROUND

One of the most crucial steps in designing a face recognition system is feature extraction. Existing descriptors referring to facial images are generally in two categories: global appearance descriptors and local image descriptors for face recognition [11]. While global features represent the whole appearance features in a vector, the local features consider fiducial points like the nose, eyes, and mouth and inherently possess orientation selectivity and spatial locality. Common local descriptors for face recognition include scale-invariant feature transform (SIFT) [12], LBP [5], and Gabor Wavelets [13]. The Principal Component Analysis (PCA) [14] and the Linear Discriminant Analysis (LDA) [15] are two

common methods to employ global descriptors for face recognition.

Several promising face recognition approaches have been developed in literature using image hashing [16-18]. LSH is a classic hashing algorithm that generates hash code by random projection functions [19]. LSH is helpful when training data is insufficient. In this regard, some researchers have proposed various models using LSH. An efficient hashing method has been introduced by Cassio et al. [20]. They employed LSH along with Partial Least Squares (PLS) to achieve a high recognition rate with a high speed for face recognition. Recently, Dehghani et al. [21] have evaluated different versions of LSH according to different hash families. Also, many hashing based approaches have been proposed in face recognition. For example, a novel method for face recognition called Bayesian Hashing was proposed by Dai et al. [22]. They achieved competitive performance with low memory cost by generating binary codes. In order to obtain hash codes from face images, common techniques can be used such as DCT which is an exceptionally good way to express the visual contents of the image. Tang et al. [23] introduced a robust image hash code by hashing the DCT coefficients into a compact feature vector.

Many face recognition methods have been proposed in recent years to cope with uncontrolled conditions [2,24,46,47]. These methods have achieved a high recognition rate under unconstrained conditions. Recently, some methods have been proposed for robust face recognition where each of them focused on a particular challenge for face recognition. Li et al. [25] proposed a framework called Recurrent Regression Neural Network (RRNN) to address sequential changes of images, including poses, by unifying two classic tasks of cross-pose face recognition. Extended Sparse Representation-based Classification (ESRC) was proposed by Deng et al. [26] to overcome occlusion and non-occlusion challenges leading to a high recognition result. Chakraborti et al. [27] proposed a novel feature selection method for face recognition using binary adaptive weights based on Gravitational Search Algorithm (GSA). They overcome several challenges of face recognition using local gradient patterns, the modified census transform, and LBP. A hybrid approach was introduced by Ouyang et al. [28] based on a combination of the Probabilistic Neural Networks (PNNs) and the Improved Kernel Linear Discriminant Analysis (IKLDA), resulting in encouraging recognition performance in face recognition. In another work, Dora et al. [29] extracted Gabor energy feature vectors from face images by introducing an Evolutionary Single Gabor

² MATLAB codes of the proposed method are available at <https://www.dropbox.com/sh/jkn33y8pjgkzk7b/AAAir4-hxmvZhA1wPOEGV-da?dl=0>.

Kernel (ESGK) based filtering approach. Liao *et al.* [30] applied the Subspace ESRC (SESRC) and the Discriminative Feature Learning (LDF) in order to address some challenges in face recognition.

In many face recognition approaches when the number of identities increases, the recognition rate considerably drops. Since the size of training data affects the performance of face recognition, many researchers focused on tackling this challenge in face recognition by considering a single sample per person for training [31], [32]. Zeng *et al.* [33] introduced a well-trained deep convolutional neural network (DCNN) model for face recognition using combining traditional and deep learning methods. Fisher Linear Discriminant Analysis (FLDA) was developed by Gao *et al.* [34] to estimate the intra-class variance in datasets with a single sample per person. Also, Lu *et al.* [35] introduced a patch-based face recognition method called Discriminative Multi-Manifold Analysis (DMMA). They achieved a high performance on a large dataset via segmenting the training samples to obtain patches and using them to learn discriminative features.

Multiple feature extraction generally leads to high recognition performance. High-dimensional facial features can be extracted using several feature extractors. In this regard, some methods have been proposed to improve face recognition performance by employing multiple feature extractors. Schwartz *et al.* [36] employed a large set of feature descriptors for face identification and achieved a high recognition rate across varying conditions. Also, Liu *et al.* [37] presented a face recognition technique that extracts multiple features and acquired a good recognition rate.

3. THE PROPOSED APPROACH

In this paper, we proposed a new multi-stage filtering framework based on image hashing for face recognition. As mentioned before, the proposed method consists of feature extraction and recognition phases. In this section, initially, the feature extraction phase is explained. Then, the proposed face recognition method is described.

3.1. Feature Extraction Phase

In this phase, we first adjust the brightness and size of images to a normal standard. In order to detect the face area, the Multi-Task Cascaded Convolutional (MTCNN) algorithm is used [38]. This approach can precisely detect faces from a wide range of poses. To detect face and landmark locations, this framework implements a cascaded architecture with carefully designed deep convolutional networks. Then, the captured face is analyzed using different visual information in parallel. Figure 1 shows the feature extraction phase. The SURF and LBP descriptors are used to extract local visual

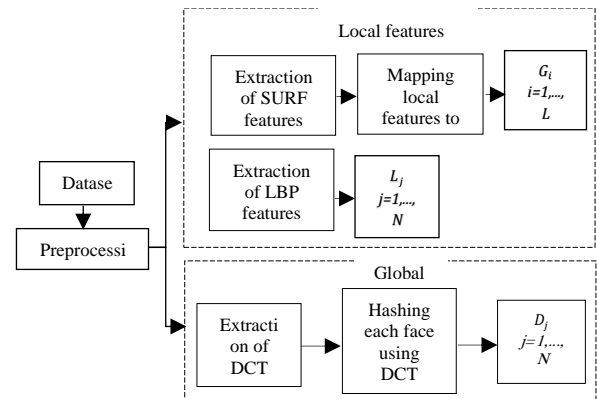


Figure 1. Diagram of the feature extraction phase for the proposed method

information from the image. The DCT is also applied based on hashing functions to extract global feature associated with the image.

The SURF descriptor extracts local features, which is robust to image scaling, translation, rotation, and to some extent is robust to 3D projection and illumination changes [39]. The SURF feature descriptor is a vector and its length is 64 in this research. Using local feature vectors from the gallery set, a set of randomized LSH tables are built. In this case, a query feature vector can be mapped to a set of buckets in which nearest neighbor candidates with the corresponding identity can be found. Therefore, feature vectors from all the images are mapped to L randomized hash tables $G_i, i=1, \dots, L$. In this regard, we employ P-stable LSH [9] which approximates the high-dimensional similarity search without any sub-linear dependence on the size of data. This scheme is a hashing framework that maps close feature vectors to the same buckets with high probability, and keeps dissimilar features to different buckets of the table. P-stable LSH is a development version of LSH. It can be employed in d -dimensional Euclidean space and has a better query response [9]. The following notation belongs to the extended P-stable LSH. We indicate the space R^d with the Euclidean norm l_2 , and data set X , in any metric space with the point $v \in X$. $B(v, r) = \{q \in X | D(v, q) \leq r\}$ is the ball of radius r centered at v .

Definition 1. A LSH family $H = \{h: S \rightarrow U\}$ is called (r, cr, p_1, p_2) -sensitive for a distance measure if for any $v, q \in S$

$$\begin{cases} \text{if } v \in B(q, r) \text{ then } P_r[h(q) = h(v)] \geq p_1 \\ \text{if } v \notin B(q, cr) \text{ then } P_r[h(q) = h(v)] \leq p_2 \end{cases}$$

where $p_1 \geq p_2$ and $c = 1 + \varepsilon$.

The process of making a hash table is the process of applying a hash operation on each vector. Local feature hash tables in P-stable LSH are made using $h_j(v) = \left\lfloor \frac{a \cdot v + b}{r} \right\rfloor$, in which v is a feature point, $j = 1, \dots, n$ and a is a d -dimensional vector with entries selected randomly

and independently from a stable distribution; b is a real number selected uniformly from the range $[0, r]$. First, the high-dimension vector v is projected onto a real line which is cleaved into equal parts of size r . Then, regarding the segment it projects onto, the vector v is assigned as a hash value. The reader can find more information regarding the P-stable LSH in literature [9].

The LBP captures the spatial structure of the local image texture [40]. The basic LBP operator labels the pixels of an image and uses the histogram of the labels as a texture descriptor. The idea behind using this descriptor is that we can see the images as a combination of micro-patterns that are robust to illumination and rotation variations. A global description of the image is achieved by combining these micro-patterns. LBP feature of each face is stored in $l_j, j=1, \dots, N$, which N is the number of images in dataset.

Also, image hashing is applied on DCT coefficients of the images to extract global features. Low-frequency DCT coefficients are more essential than high-frequency coefficients in describing the image because they have larger values and contain the main part of the signal energy [41]. Hence, via the hashing, the less important frequencies are removed and the most important frequencies of the image are kept. For more information about this algorithm, we refer the reader to the work introduced by Tang et al. [23]. Similarly, each hash code is stored in $D_j, j = 1, \dots, N$, which N is the number of images in dataset. Following the feature extraction phase for all cropped faces, the query face images can be recognized through the multi-stage filtering.

3. 2. Recognition Phase In order to recognize a query face, after resizing and cropping, the image is imported to a three-stage filtering framework. The three stages of this framework are as follows.

(1) In the first stage, local features are extracted from a query image, using the SURF descriptor. The similarity of extracted local features, between each feature of the query image and those from the gallery images, is specified using LSH. For each feature from the query image, its reverse normalized distances with the selected features using the LSH are considered as their associated weight to match with the gallery images. The votes to each feature from the query image are computed via summation of its weights to the features associated with the gallery images [42]. Finally, a small percentage of identities with the highest number of votes are considered as similar candidate identities which are sent to the second stage to analyze their other visual information. For example, as it can be seen in Figure 2, we found identities whose local features are most similar to the local features of the query image.

(2) Middle-stage refinement is believed to be extremely beneficial to find identities that are similar to the test image in terms of global visual information. Firstly, this

level converts high-dimensional features of the query face into a much more compact representation using DCT coefficients. Then, it further refines the output result from the first level according to their extracted hash codes. The best matching candidates' gallery for the test image are found by the k-nearest neighbors (KNN).

(3) At the last stage, the query face is analyzed by another visual information. In this case, we apply the LBP algorithm to extract robust features from the images. Finally, the query face is recognized among the remaining subjects from the previous stages by using this information. The overall pipeline of the recognition phase is shown in Figure 3. For a given query image, a considerable number of the gallery images are filtered out in each stage, which saves the computational cost.

4. EXPERIMENTAL RESULTS

In this section, first, we introduce the face image datasets, including FERET, ORL, and AR. Then, the performance

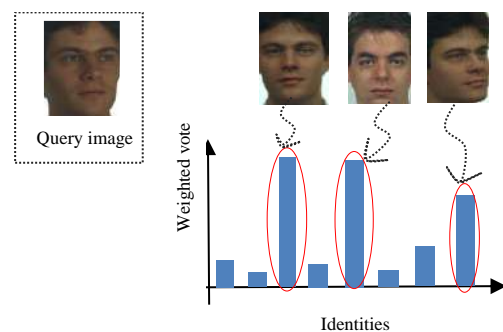


Figure 2. Most similar identities to the query image

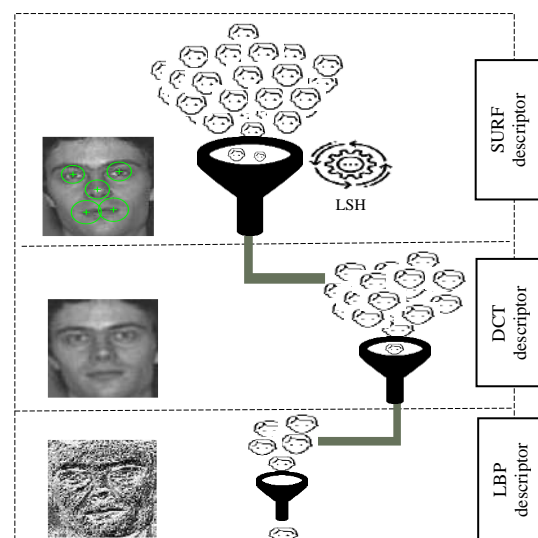


Figure 3. Overview of the recognition phase of the proposed method

of our method is evaluated by conducting several experiments. Finally, the running time of the proposed method is examined to estimate its computational cost in face recognition.

4. 1. Datasets: AR This dataset includes over 4000 faces corresponding to 70 males and 56 females. The pictures were captured in two different sessions which contain various illumination conditions, facial expressions, and occlusions. Sample images from the AR dataset are shown in Figure 4.

ORL: This dataset contains 400 frontal face images from 40 people photographed at different times with differing illuminations, facial expressions, facial details and somewhat pose variation. Samples from the ORL dataset are illustrated in Figure 5.

FERET: The FERET dataset contains 14,126 facial images from 1199 individuals. This dataset consists of different subsets of frontal images, quarter left, quarter right, profile left, profile right, half left, half right, and rotated images. The images were taken at different times and demonstrate variation including expressions, lighting, facial expressions, pose variation, and ages. Figure 6 demonstrates a number of sample images from this dataset.

Combinatorial dataset: To evaluate the proposed method on a large dataset, we collected identity images from several available datasets and provided a combinatorial dataset. For this purpose, images were collected from FERET, MUCT, PICS, FEI, and Face 94 datasets. Faces in the collected dataset are mostly frontal, but they may differ in facial expressions and brightness.



Figure 4. Sample images from the AR dataset



Figure 5. Sample images from the ORL dataset



Figure 6. Sample images of the second subset from FERET dataset

The total number of identities in this collection is 1684 with two samples per person. A number of samples from the data are shown in Figure 7.

4. 2. Parameters Setting The number of hash tables and the hash length of each bucket in the LSH algorithm are equal to 5. Likewise, the width of each bucket is 2. The number of nearest neighbors considered in each entry point is 10. In the DCT-based image hashing method, a 3×3 Gaussian filter is considered. As mentioned earlier, in the first stage of the recognition step, identifiers that are not similar to the filtered out test image. In this regard, the identities whose vote value is more than 65 percent of the highest voting value are considered for the next stage of recognition.

4. 3. Recognition Rate Here, different scenarios are considered and the proposed method is evaluated using the three datasets (i.e. AR, ORL, and FERET), and the results are compared with those from other recently developed face recognition methods.

In order to evaluate the effects of the number of images per person on the recognition rate, we have conducted two different experiments on the AR and ORL datasets. In Experiment 1, we randomly chosen 50 percent of the images from each identity for the feature extraction step, and the remaining were used for testing. But, in Experiment 2, 60 percent of the images from each identity were randomly selected for the feature extraction step and the rest for testing. Table 1 compares results of



Figure 7. Sample images from the combinatorial dataset

different face recognition methods in Experiments 1 and 2. The reason behind considering these two experiments is that we can train our method with a different number of data. In this case, the result can be more trustable. As can be seen, the proposed method achieved the highest recognition rates compared to other existing methods in both of the experiments. In addition, the results showed more robustness of the proposed method compared to other methods in terms of reducing the number of training sample per person in the dataset. The hyphen (-) in the table indicates that no result was reported in the literature for the associated method in that experiment.

Also, our proposed method is evaluated using the two different image subsets of the FERET dataset. The first subset contains 990 identities with 1980 face images which each individual has two samples that are frontal with two different expressions. Using this subset, our method can easily be assessed when only a single sample per person is available. We obtained the highest recognition rate on the first subset of FERET dataset which can be seen in Table 2. In the second subset, the performance of the proposed method is evaluated using 4017 face images from 994 individuals. This subset includes more images with challenges of variation including lighting, facial expressions, pose variation of $\pm 15^\circ$, $\pm 25^\circ$, and ages. Table 3 shows the comparison results on the second subset. Other existing approaches have considered a subset with a less number of identities. In order to compare the performance of our method with them, we achieved the result with their subset too.

Also, our method obtained a 96.62 percent recognition rate in the combined dataset. Figure 8 shows the variation of the recognition rate with a number of identities using the proposed method on this dataset.

4. 4. Running Time Next, we evaluate the running time of our proposed method on the second subset of the FERET dataset. The experimental set-up is on a 64-bit

TABLE 1. Recognition rate of different methods on ORL and AR

Name of method	Experiment 1 (%)		Experiment 2 (%)	
	AR	ORL	AR	ORL
SVM [42]	87.31	78.47	85.68	75.77
SRC [43]	96	-	95	-
LBP [40]	-	88	-	83
LGP+BAW-GSA [27]	-	92.5	-	90.7
IKLDA + PNN [28]	97.46	93.95	95.86	91.44
PLSH [9]	80	94.16	78	92.33
ESGK [29]	-	97.5	-	96
Proposed method	98	100	96.08	100

TABLE 2. Recognition rate of different methods on the first subset of FERET

Method	Number of images in dataset	Number of identities	Accuracy (%)
ESRC [26]	1400	200	51.60
LBP [5]	1400	200	74.90
RRNN [25]	1400	200	77.90
PCA [44]	1400	200	83.16
ESGK [29]	1400	200	84.5
PCA & LDA [45]	1400	200	86.10
SESRC & LDF [30]	1400	200	93.75
Proposed	1400	200	95.04
Proposed	4017	994	93.29

TABLE 3. Recognition rate of different methods on the second subset of FERET

Method	Number of images in dataset	Number of identities	Accuracy (%)
FLDA-SVD [34]	400	200	90.5
DMMA [35]	400	200	93
TDL [33]	400	200	93.9
Proposed	400	200	98
NNMF [32]	1980	990	92.73
Proposed	1980	990	97.29

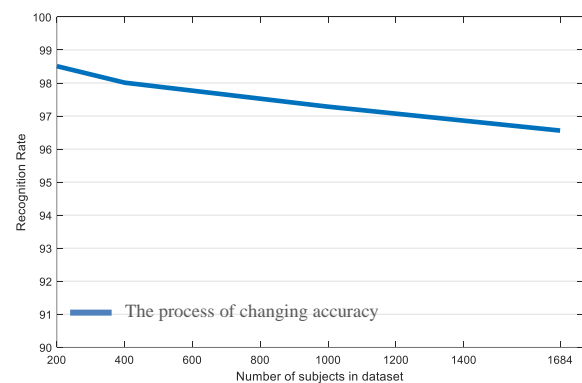


Figure 8. Recognition rate of the proposed method regarding to the number of identities in the combinatorial dataset

Windows operating system using the Intel Core i5 with 4 GByte RAM. All the programs were performed in MATLAB. In some cases, the test image is recognized in the first stage, hence there is no need to analyze them in the other stages. Figure 9 shows the impact of increasing the number of identities on recognition time. As shown

in the figure, when the number of identities increases, the recognition time increases almost linearly.

Figure 10 shows samples of wrong recognition using the proposed method. As can be seen, even humans may consider the faces shown in each row to be similar.

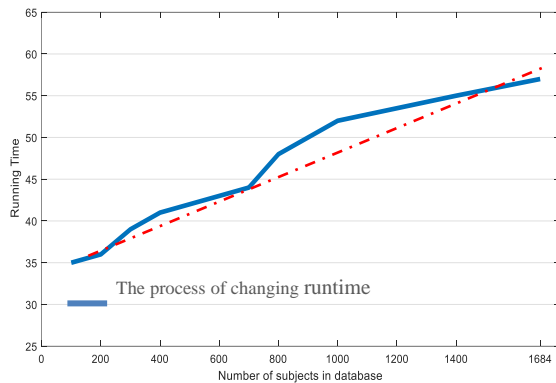


Figure 9. Running time of the proposed method regarding to the number of identities in the combinatorial dataset

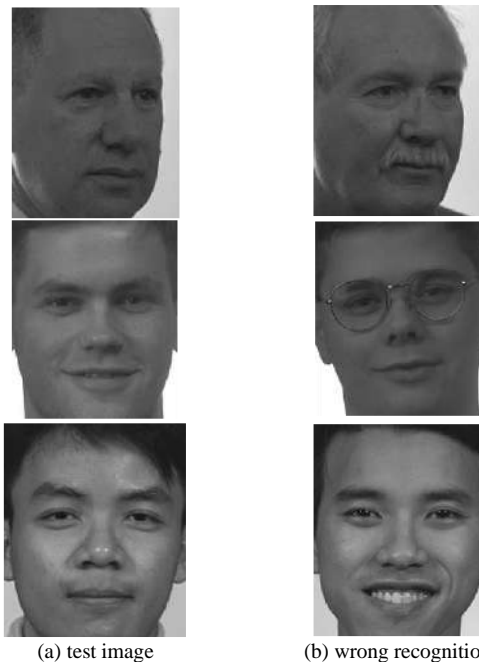


Figure 10. Some samples of wrong recognition in the proposed method. The left hand images were applied to the method and the right hand images were wrongly retrieved

5. CONCLUSION

In this paper, we have proposed a novel three-stage filtering framework for human face recognition. In this approach, different feature extraction methods are used to analyze different visual information in each stage. A

hashing function is used for feature extraction to reduce computational cost and improve accuracy of the proposed face recognition system. The merits of the proposed method are: (i) easy implementation; (ii) better performance than state-of-the-art methods across various face recognition scenarios; (iii) good performance when a single sample per person is available; (iv) scalable to the incremental enrollment of identities in the gallery; (v) significantly reduced the time complexity in face recognition. Several experiments were conducted on different datasets to evaluate the performances of the proposed face recognition in terms of changes in facial expressions, illuminations and pose variation, and perspective variations. The result shows that the proposed method outperforms current state-of-the-art methods.

6. REFERENCES

1. Lahasan, B., Lutfi, S. L., and San-Segundo R., "A survey on techniques to handle face recognition challenges: occlusion, single sample per subject and expression." *Artificial Intelligence Review*, Vol. 52, No. 2, (2019), 949-979, DOI:10.1007/s10462-017-9578-y.
2. Oloyede, M. O., Hancke, G. P., and Myburgh, H. C., "A review on face recognition systems: recent approaches and challenges", *Multimedia Tools and Applications*, (2020), 27891-27922, DOI:10.1007/s11042-020-09261-2.
3. Adjabi, I., Ouahabi, A., Benzaoui, A., and Taleb-Ahmed, A., "Past, present, and future of face recognition: A review", *Electronics*, Vol. 9, No. 8, (2020), 1-53, DOI: 10.3390/electronics9081188.
4. Surasak, T., Takahiro, I., Cheng, C. H., Wang, C. E., Sheng and P. Y., "Histogram of oriented gradients for human detection in video" *International Conference on Business and Industrial Research*, (2018), 172-176, DOI: 10.1109/ICBIR.2018.8391187.
5. Ahonen, T., Member, S., Hadid, A., Member, S., and Pietika M., "Face Description with Local Binary Patterns: Application to Face Recognition", *IEEE Transactions on Pattern Analysis and Machine Intelligence*, Vol. 28, No. 12, (2006), 2037-2041, DOI: 10.1109/TPAMI.2006.244.
6. Simonyan, K., Parkhi, O. M., Vedaldi, A., "Fisher vector faces in the wild", *BMVC*, (2013), DOI: 10.5244/C.27.8.
7. Cao, Z., Yin, Q., Tang, X., and Sun, J., "Face recognition with learning-based descriptor", *Proceedings of the IEEE Computer Society Conference on Computer Vision and Pattern Recognition*, (2010), 2707-2714, DOI:10.1109/CVPR.2010.5539992.
8. Vadlamudi, L., Vaddella, R. "A Review Of Robust Hashing Methods For Content Based Image Authentication based on DWT", *IEEE Transactions on Information Forensics and Security*, Vol. 3, No. 4, (2017), DOI: 10.1109/TIFS.2012.2223680.
9. Datar, M., Immorlica, N., and Indyk, P., "Locality-Sensitive Hashing Scheme Based on p-Stable Distributions", *Proceedings of the twentieth annual symposium on Computational geometry*, (2004), 253-262, DOI: 10.1145/997817.997857.
10. Shi, Q., Li, H., and Shen, C., "Rapid face recognition using hashing", *Proceedings of the IEEE Computer Society Conference on Computer Vision and Pattern Recognition*, (2010), 2753-

- 2760, DOI: 10.1109/CVPR.2010.5540001.
11. Stan, Z. Li., Anil, K. Jain., " Local Representation of Facial Features ", *Handbook of Face Recognition*, (2011), DOI:10.1007/978-0-85729-932-1_4.
 12. Lowe, D. G., "Distinctive image features from scale-invariant keypoints", *International Journal of Computer Vision*, Vol. 60, No. 2, (2004), 91-110, DOI: 10.1023/B:VISI.0000029664.99615.94.
 13. Liu, C. and Wechsler, H., "Gabor Feature Based Classification Using the Enhanced Fisher Linear Discriminant Model for Face Recognition", *IEEE Transactions on Image Processing*, vol. 11, no. 4, pp. 467-476, 2002, DOI: 10.1109/TIP.2002.999679.
 14. Zafaruddin, G. M. and Fadewar, H. S., "Face recognition using eigenfaces", *Advances in Intelligent Systems and Computing*, Vol. 810, (2018), 855-864, DOI: 10.5120/20740-3119.
 15. Belhumeur, P. N., Hespanha, J. P., and Kriegman, D. J., "Eigenfaces vs. Fisherfaces: Recognition using class specific linear projection", *Lecture Notes in Computer Science*, Vol. 1064, No. 7, (1996), 45-58, DOI:10.1109/34.598228.
 16. Luo, Y., Yang, Y., Shen, F., Huang, Z., Zhou, P., and Shen, H. T., "Robust discrete code modeling for supervised hashing", *Pattern Recognition*, Vol. 75, (2018), 128-135, DOI: 10.1016/j.patcog.2017.02.034.
 17. Shiyuan, H., Bokun, W., "Bidirectional Discrete Matrix Factorization Hashing for Image Search", *IEEE Transactions on Cybernetics*, Vol. 50, No. 9, (2020), 4157-4168, DOI: 10.1109/tcyb.2019.2941284.
 18. Lu, X., Zhu, L., Li, J., Zhang, H., and Shen, H. T., "Efficient Supervised Discrete Multi-View Hashing for Large-Scale Multimedia Search", *IEEE Transactions on Multimedia*, Vol. 22, No. 8, (2020), 2048-2060, DOI: 10.1109/TMM.2019.2947358.
 19. Paulevé, L., Jégou, H., and Amsaleg, L., "Locality sensitive hashing: A comparison of hash function types and querying mechanisms", *Pattern Recognition Letters*, Vol. 31, No. 11, (2010), 1348-1358, DOI: 10.1016/j.patrec.2010.04.004.
 20. Dos Santos, C. E., Kijak, E., Gravier, G., and Schwartz, W. R., "Partial least squares for face hashing", *Neurocomputing*, Vol. 213, (2016), 34-47, DOI: 10.5753/ctd.2016.9132.
 21. Dehghani, M., Moeni, A., and Kamandi, A., "Experimental Evaluation of Local Sensitive Hashing Functions for Face Recognition", *5th IEEE International Conference on Web Research*, (2019), 184-195, DOI: 10.1109/ICWR.2019.8765276.
 22. Dai Q., J. Li, Wang, J., Chen, Y., and Jiang, Y. G., "A Bayesian Hashing approach and its application to face recognition", *Neurocomputing*, Vol. 213, (2016), 5-13, DOI: 10.1016/j.neucom.2016.05.097.
 23. Tang, Z., Yang, F., Huang, L., and Zhang, X., "Robust image hashing with dominant DCT coefficients", *Optik*, Vol. 125, No. 18, (2014), 5102-5107, DOI: 10.1016/j.ijleo.2014.05.015.
 24. Akhlaghi, S. and Hassanpour, H., "Frontal face modeling using morphing-based averaging and Low-rank decomposition", *Multimedia Tools and Applications*, (2020), 7125-7144, DOI: 10.1007/s11042-020-09878-3.
 25. Li, Y., Zheng, Cui, W., Z., and Zhang, T., "Face recognition based on recurrent regression neural network", *Neurocomputing*, Vol. 297, (2018), 50-58, DOI: 10.1016/j.neucom.2018.02.037.
 26. Deng, W., Hu, J., and Guo, J., "Extended SRC: Undersampled face recognition via intraclass variant dictionary", *IEEE Transactions on Pattern Analysis and Machine Intelligence*, Vol. 34, No. 9, (2012), 1864-1870, DOI: 10.1109/TPAMI.2012.30.
 27. Chakraborti, T. and Chatterjee, A., "Engineering Applications of Artificial Intelligence A novel binary adaptive weight GSA based feature selection for face recognition using local gradient patterns, modified census transform , and local binary patterns", *Engineering Applications of Artificial Intelligence*, Vol. 33, (2014), 80-90, DOI: 10.1016/j.engappai.2014.04.006.
 28. Ouyang, A., Liu, Y., Pei, S., Peng, X., He, M., and Wang, Q., "A hybrid improved kernel LDA and PNN algorithm for efficient face recognition", *Neurocomputing*, Vol. 393, (2020), 214-222, DOI: 10.1007/s11042-020-08997-1.
 29. Dora, L., Agrawal, S., Panda, R., and Abraham, A., "An evolutionary single Gabor kernel based filter approach to face recognition", *Engineering Applications of Artificial Intelligence*, Vol. 62, (2017), DOI: 286-301, 10.1016/j.engappai.2017.04.011.
 30. Liao, M. and Gu, X., "Face recognition approach by subspace extended sparse representation and discriminative feature learning" *Neurocomputing*, 2019, DOI: 10.1016/j.neucom.2019.09.025.
 31. Xie, X. and Lam, K. M., "Gabor-based kernel PCA with doubly nonlinear mapping for face recognition with a single face image", *IEEE Transactions on Image*, Vol. 15, No. 9, (2006), 2481-2492, DOI: 10.1109/TIP.2006.877435.
 32. Nikan, F. and Hassanpour, H., "Face recognition using non-negative matrix factorization with a single sample per person in a large database", *Multimedia Tools and Applications*, (2020), 28265-28276, DOI: 10.1007/s11042-020-09394-4.
 33. Zeng, J., Zhao, X., Gan, J., Mai, C., Zhai, Y., and Wang, F., "Deep Convolutional Neural Network Used in Single Sample per Person Face Recognition", *Computational Intelligence and Neuroscience*, (2018), DOI: 10.1155/2018/3803627.
 34. xue Gao, Q., Zhang, L., and Zhang, D., "Face recognition using FLDA with single training image per person", *Applied Mathematics and Computation*, Vol. 205, No. 2, (2008), 726-734, DOI: 10.1016/j.amc.2008.05.019.
 35. Lu, J., Tan, Y., and Wang, G., "Discriminative Multi-Manifold Analysis for Face Recognition from a Single Training Sample per Person", *IEEE International Conference on Computer Vision*, (2011), 1943-1950, DOI: 10.1109/ICCV.2011.6126464.
 36. Schwartz, W. R., Guo, H., Choi, J., and Davis L. S., "Face identification using large feature sets," *IEEE Transactions on Image Processing*, Vol. 21, No. 4, (2012), 2245-2255, DOI: 10.1109/TIP.2011.2176951.
 37. Liu, Z., Yang, J., and Liu, C., "Extracting multiple features in the CID color space for face recognition", *IEEE Transactions on Image Processing*, Vol. 19, No. 9, (2010), 2502-2509, DOI:10.1109/TIP.2010.2048963.
 38. Zhang, K., Zhang, Z., Li, Z., Member, S., Qiao, Y., and Member, S., "(MTCNN) Multi-task Cascaded Convolutional Networks" *IEEE Signal Processing Letters*, Vol. 23, No. 10, (2016), 1499-1503, DOI:10.1109/LSP.2016.2603342.
 39. Bay, H., Ess, A., Tuytelaars, T., and Van Gool, L., "Speeded-Up Robust Features (SURF)", *Computer Vision and Image Understanding*, Vol. 110, No. 3, (2008), 346-359, DOI: 10.1016/j.cviu.2007.09.014.
 40. Ojala, D., Pietikainen, T., Harwood, M., "A comparative study of texture measures with classification based on feature distributions", *Pattern Recognition*, (1996), 51-59, DOI: 10.1016/0031-3203(95)00067-4.
 41. Fridrich, G. M., "Robust hash functions for digital watermarking", International Conference on Information Technology: Coding and Computing (ITCC'00), USA, (2000), 27-29, DOI: 10.1109/ITCC.2000.844203.
 42. Vapnik, V. and Corinna, C., "Support-vector networks," *Machine Learning*, (1995), 273-297, DOI: 10.1007/BF00994018.
 43. Wright, J., Member, S., Yang, A. Y., Ganesh, A., and Sastry, S. S., "Robust Face Recognition via Sparse Representation", *IEEE Transactions on Pattern Analysis and Machine Intelligence*,

- Vol. 31, No. 2, (2009), 210-227, DOI: 10.1109/TPAMI.2008.79.
44. Martinez, A. M. and Kak, A. C., "PCA versus LDA," *IEEE Transactions on Pattern Analysis and Machine Intelligence*, Vol. 23, No. 2, (2001), 228-233, DOI: 10.1109/34.908974.
45. Marian, B., Javier, R., Terrence, J., "Face Recognition by Independent Component Analysis", *IEEE Transactions on Neural Networks.*, Vol. 13, No. 6, (2002), 296-338, DOI: 10.1109/TNN.2002.804287.
46. Taskiran, M., Kahraman, N., ErogluErdem, C., "Face recognition: Past, present and future (a review) ", *Digital Signal Processing*, Vol. (2020), 106, DOI: 10.1016/j.dsp.2020.102809.
47. Shavandi, M. and Afrakoti, I. E. P., "Face Recognition in Thermal Images based on Sparse Classifier". *International Journal of Engineering, Transactions A: Basics*, 32, 1, 2019, 78-84, DOI: 10.5829/ije.2019.32.01a.10.

Persian Abstract

چکیده

سیستم شناسایی چهره به عنوان یکی از مهم ترین زمینه های تحقیقاتی، کاربردهای فراوانی در حوزه های مختلف از جمله تعامل انسان و کامپیوتر، پزشکی قانونی و نظارت امنیتی دارد. اما این سیستم ها با چالش هایی از جمله شرایط محیطی کنترل نشده، مجموعه داده های بزرگ و ناکافی بودن داده های آموزشی مواجه هستند. در این مقاله، با بهره گیری از یک چارچوب شناسایی چهره جدید و به کمک فیلترگذاری سه مرحله ای مبتنی بر درهم سازی تصویر به مشکلات فائق می آیم. در مرحله اول این روش، تعدادی از هویت ها از طریق عملکرد درهم سازی حساس به مکان (LSH) انتخاب می شوند. به طوریکه با استفاده از یک سیستم رأی گیری، تعداد زیادی از افراد غیرمشابه با تصویر آزمون از نظر دیدگاه بصری جزئی نگر حذف می شوند. در مرحله دوم، از یک تابع درهم سازی تصویر قوی بر اساس ضرایب تبدیل گسسته کسینوس (DCT) برای بررسی بیشتر کاندیدهای مرحله اول از نظر دیدگاه بصری کلی نگر استفاده می کنیم. در آخرین مرحله، با استفاده از یک دیدگاه بصری کلی نگر دیگر، تصویر آزمون از بین افراد باقی مانده شناسایی می شود. نتایج آزمایش بر روی مجموعه داده های AR, FERET و ORL نشان می دهد که روش پیشنهادی عملکرد بهتری نسبت به روش های موجود دارد.



Durability and Aging Characteristics of Sustainable Paving Mixture

I. S. Al-Haydari^a, H. S. Al-Haidari^b, H. Mohammed-Noor Khudhur^a, N. Waleed Jummah^a, M. Abd Al-Hamza^a

^a Highway and Transportation Department, College of Engineering, Mustansiriyah University, Baghdad, Iraq

^b Civil Engineering Department, Al-Nahrain University, Baghdad, Iraq

PAPER INFO

Paper history:

Received 12 May 2021

Received in revised form 12 June 2021

Accepted 18 June 2021

Keywords:

Durability

Short-term Aging

Economic Assessment

Sustainable Paving Mixture

Recycling of Waste Plastic

ABSTRACT

With the industrial revolution, many inventions have been introduced with many solid waste materials in return. This study investigates the potential recycling of waste plastic sheets, made from low-density polyethylene, as asphalt modifier in the paving mixture. The shredded plastic sheet was used in the asphalt mixture via the wet process. The dosage rate was set up to 9 % by weight of asphalt binder (0,3,6, and 9)%. The experimental program was designed to assess the mechanical properties (Marshall stability and flow, and volumetric properties), durability, and short-term aging of asphalt mixtures, in addition to economical assessment. The test results revealed the applicability of using this solid waste material in paving construction as a surface layer, since its usage enhances the pavement performance by increasing stability, index of retained strength, and volumetric characteristics before and after aging as well as saving in cost. The best enhancement can be achieved with 6% of recycled low-density polyethylene.

doi: 10.5829/ije.2021.34.08b.07

1. INTRODUCTION

Works on the polymer-modified asphalt mixture have been increased in recent years [1-6]. Researchers recommended using polymers to enhance pavement performance to accommodate local traffic and weather conditions and avoid the common types of distresses. With the industrial revolution and the advance of material science, more materials and polymers have been introduced and used in every detail of life. Some of these materials are non-biodegradable like plastics. In other words, it would be stuck in dump places for hundreds of years and cause real risks to the environment as land and marine pollution. The presence of microplastic in the seawater threatens the aquatic organisms, thereby disrupting the bio-system [7]. Moreover, soil contamination with microplastics may damage the health of the flora-fauna ecosystem. And these plastic particles would intake by the human body through food chains [8]. To alleviate these concerns, these materials are recycled by crushing and using again as secondary paving materials. Apart from virgin polymers, incorporating

waste polymers has also been revealed to improve the asphalt pavement properties to a level similar to that observed with virgin polymers besides its potential sustainable practice [9]. Researchers in the field of pavement engineering used recycled expanded polystyrene as Al-Haydari and Masued [10]. They noticed a reduction in Marshall properties and increasing moisture resistance with the inclusion of this recycled polymer. Whereas, Ramadan et al. [11] enhanced binder performance in terms of rutting resistance to achieve mixtures that can sustain up to 64°C temperatures with styrofoam incorporation. Additionally, Al-Haydari and Al-Haidari [12] and Naghawi et al. [13] utilized recycled polyethylene terephthalate to enhance the mechanical properties, tensile strength, and moisture damage resistance of the hot mix asphalt. Mosa et al. [14] also used this type of additive to modify the warm mix asphalt performance in terms of rutting resistance in addition to other mechanical properties.

Plastic bags, characterized as low-density polyethylene (LDPE), are widespread plastic polymers that can be shredded to 5 mm× 5mm particles or smaller

*Corresponding Author Institutional Email:

israasaed@uomustansiriyah.edu.iq (I. S. Jawad Al-Haydari)

Please cite this article as: I. S. Al-Haydari, H. S. Al-Haidari, H. Mohammed-Noor Khudhur, N. Waleed Jummah, M. Abd Al-Hamza, Durability and Aging Characteristics of Sustainable Paving Mixture, International Journal of Engineering, Transactions B: Applications, Vol. 34, No. 08, (2021) 1865-1873

and used in paving layers. It can be used in form of pellets or flakes. However, Angelone et al. [15] recommended using LDPE as flakes in the paving mixture. Singh et al. [16] stated that the inclusion of shredder polyethylene to the asphalt mixture enhances the volumetric properties, Marshall stability, and flow for the mixture. Also, it improves the recovered asphalt binder in terms of complex modulus and phase angle. Similarly, El-saikly [17] recommended using waste plastic bags as a modifier for pavement mixture as well as a sustainable practice. To sum up, Wu and Montalvo [9] summarized most of the studies conducted on the utilization of recycled LDPE on asphalt mixture. They stated that there is a common consensus among researchers that recycled LDPE can enhance the mixture resistance to rutting, fatigue, and moisture susceptibility. However, resistance against thermal cracking is still problematic. To solve this problem, using waste oil as facilitator can possibly improve the aging resistance and reduce thermal cracks, as well as enable the engineers to use an extra amount of the recycled LDPE, as stated by Nouali et al. [18], even with reclaimed asphalt pavement [19].

In Iraq, it is estimated that the population provides 31000 tons of solid waste daily with the capacity to dispose of 4000 tons per day only [20]. Most of the trash is waste plastics. This discrepancy in solid waste production and disposing necessitates the local government to find a suitable management system to overcome these challenging environmental tasks. Moreover, most of the LDPE-modified pavement mixtures studies did not take into consideration the change in mixture properties during the mixing and construction process. The plastic is affected by temperature change during mixing and compacting for the surface paving layer. This change in behavior would affect the pavement mixture performance. Thereby this research aims to investigate the short-term aging to simulate the mixture behavior when mixed, placed, and compacted in the field. In addition, the effect of weather through moisture susceptibility on this layer (durability) of hot mix asphalt containing recycled plastic sheets, made from LDPE, besides its cost-effectiveness are the main focus of this study.

2. MATERIALS

2.1. Conventional Paving Mixture The materials used for asphalt concrete pavement are natural quartz aggregate with a maximum nominal aggregate size of 12.5mm, limestone dust with a 2.78 specific gravity of mineral filler, and (40-50) penetration grade of asphalt binder. All these materials were individually tested following ASTM C127 and C128 procedures for coarse and fine aggregate respectively, to ensure that it complies with Iraqi's specifications for roads and bridges [21].

Test results are reported in Table 1. Besides, aggregate gradation is presented in Figure 1.

2.2. Recycled LDPE Polymers The used modifier is the shredded plastic bags, made from low-density polyethylene, which is globally available and non-biodegradable material. Thermoplastic monomer ethylene, recycled low-density polyethylene LDPE polymers, have been used in this study from shredded plastic sheets, in a wet process as partial replacement of asphalt binder. The dosage rates, used in this investigation, are 0, 3, 6, and 9% of asphalt weight. Material descriptions are presented in Table 2.

3. EXPERIMENTAL PROGRAM

The initial stage of the experimental program is to find the optimum asphalt content that satisfies most of the

TABLE 1. Physical properties of aggregate

Property	Coarse Aggregate	Fine Aggregate
Apparent specific gravity	2.69	2.68
Bulk specific gravity	2.62	2.63
water absorption, %	0.49	0.61
Los-Angeles abrasion, %	27.1	---

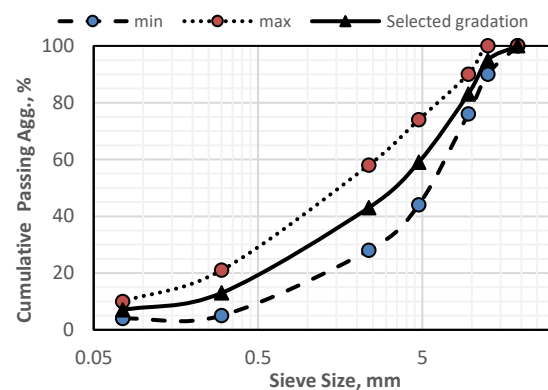


Figure 1. Gradation of aggregate in wearing layer III

TABLE 2. Properties of the LDPE waste material

Property	Measure
Chemical formation	(-CH ₂ -CH ₂)-n
Tensile strength (N/mm ²)	0.2 – 0.4
Density (gm/cm ³)	0.91 - 0.94
Thermal expansion coefficient	100 – 220 × 10 ⁻⁶
Softening point (°c)	100-120 °c
Melting point (°C)	110

desirable characteristics of the asphalt concrete mixture. Triplicate samples were prepared in accordance with ASTM D 6926 [22] at varying asphalt content (4-6) % of mixture weight with 0.5% interval, and tested in accordance with ASTM D 6927 [23]. From test results, 5% is found the optimum binder content the revealed higher stability and bulk density, lower flow, with accepted range of voids ratio.

To study the effect of the recycled LDPE on durability and aging of HMA, three sets were prepared as illustrated in Figure 2. The HMA samples were prepared by heating aggregate and asphalt binder at (160, and 150) °C, respectively. Then, it was mixed together for approximately two minutes to ensure wetting and covering of all aggregate particles. The first two sets were compacted by Marshall hammer for 75 blows for each side. While the third set was placed in the oven before the compaction stage to prepare the mixture for short-term aging.

The work plan for this research is presented in Figure 2.

3. 1. Durability in bituminous mixes can be assessed through water sensitivity. Index of retained strength (IRS), the loss of pavement serviceability due to the presence of moisture is usually used for durability estimation. IRS is the stability ratio of water-conditioned samples to the unconditioned ones. [24]

$$IRS = \frac{S_2}{S_1} \times 100\% \quad (1)$$

where, IRS: Index of Retained Strength, %, S_1 : Marshall stability of the standard specimens, (S wet, 60°C, and 30 min.) KN, and S_2 : Marshall stability of the wet specimens, (S wet, 60°C, and 24 hrs.) KN.

The higher IRS value is the more resistance to water damage mixture.

A total of 8 sets of Marshall specimens of Hot Mix Asphalt stabilized with recycled LDPE additives (0, 3, 6,

and 9) % by weight of asphalt, were prepared and divided into two groups (4 specimens each). The first group was immersed in a water bath at 60°C, for 24 hours (conditioned sample). The samples were then removed from the water bath to be tested for Marshall Stability at 60°C. Another set of samples (unconditioned sample) are immersed in a water bath at 60°C for a half-hour, then tested at 60°C.

3. 2. Aging The short-term aging of the asphaltic paving mixture is used to simulate the effect of plant mixing and construction on the mechanical properties of the asphalt mixture. This test was conducted under AASHTO R30 [25] designation.

The same procedure that has been adopted to prepare the control mixture was used except the oven- condition stage. The loose mixtures were spread in a pan to an even thickness of 20-50mm. The pans containing the loose mixtures were conditioned in the oven at 135°C temperature for 4 hours. During the condition period, the loose mixtures were stirred every 60 minutes to ensure uniform conditioning. After the conditioning periods, the mixtures were removed from the oven and compacted by a Marshall hammer in the same procedure that has been adopted for the control mixture.

4. RESULTS AND DISCUSSION

4. 1. Analysis of Modified Bitumen The properties of the standard and LDPE-modified asphalt binder were investigated through the traditional tests for the asphalt, like penetration [26], ductility [27], and softening point [28] tests. The blending dosage rate was limited to 9% as a partial replacement by the weight of the asphalt. Through visual observation, an extra amount requires more heating and energy during blending, which is not a cost-effective solution. Thereby, the mixes were prepared

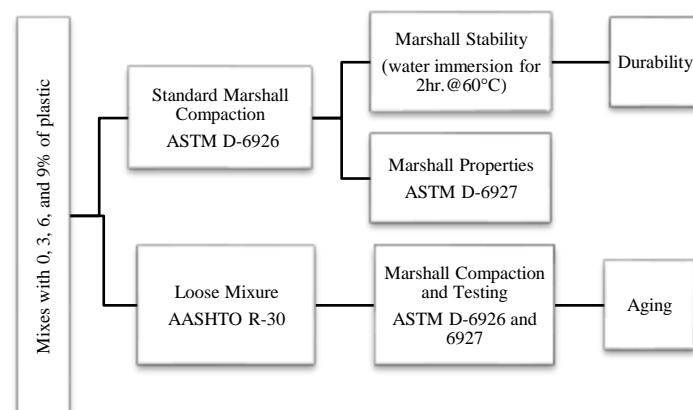


Figure 2. Flow-chart for the experimental program

and tested with a concentration of (0, 3, 6, and 9) % by weight of asphalt. The test results are summarized in Table 3.

The chemical function of asphalt is similar to plastic which is a hydrocarbon. When the plastic polymers are induced to asphalt, it works as modifiers. This modifier does not chemically react with base asphalt, but it is dispersed and absorbed by the asphalt component. So, compatibility is the main requirement to ensure homogeneity in the asphalt medium without stratification or cohesion, or separation from each other [9].

Table 3 summarized the penetration and ductility of modified binders substantially decrease with an increase of blending dosage rate. This resulted in losing workability, thus required more heating to reach the required viscosity that can cover all aggregate particles. This behavior is also noted by Nouali et al. [18]. However, adding plastic to the asphalt binder increase the plasticity and toughness of the mixture. It is also noticed an increase in penetrability index which indicates that the mixture would have higher temperature stability [29]. That means less affected by temperature variations.

4. 2. Analysis of the Modified Mixture All the essential tests were performed according to ASTM D6927 [23], ASTM D 2726 [30], and ASTM D [31] to highlight the physio-mechanical behavior of the LDPE-modified mixture. The test results are illustrated in Figure 3. Obviously, addition of recycled LDPE enhance the mixture properties by increasing stability and bulk density and reducing the flow value besides keeping other volumetric properties with the prescribed limits recommended by Iraqi's specifications for roads and bridges [21].

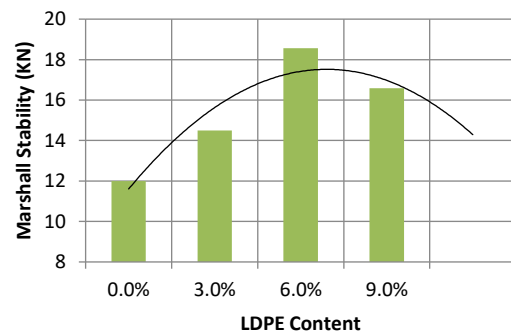
This enhancement may be attributed to the bonding ability of the recycled plastic polymer. Since recycled polyethylene works as a "glue" [16] to bond aggregate particles and strengthens the aggregate-binder matrix.

TABLE 3. Physical properties of the standard and modified asphalt binders

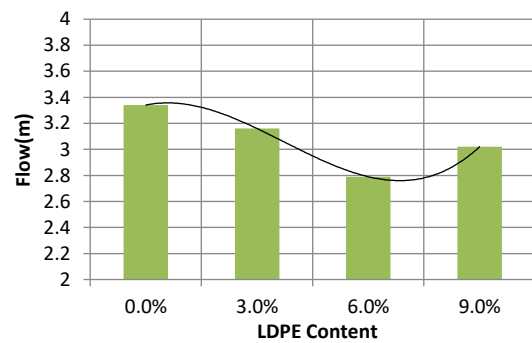
LDPE-dosage	Penetration	Ductility	Softening point	Penetration Index
Test methods [units]	25°C, 100g, 5 s [0.1mm]	25°C [0.1 cm]	°C [1°C]	
0%	43	125	56	-0.16
3%	39	101	60	0.43
6%	31	87	69	1.52
9%	26	63	73	1.76
Iraqi's specification*	40-50	>100	50-60	----

* Iraqi specification of roads and bridges SCRB [21]

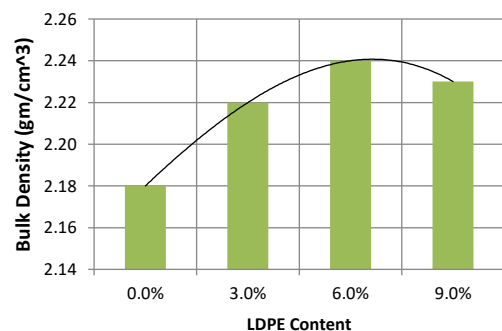
Although, there is a reduction in pavement performance with a 9% of LDPE rate as compared to the previous rate. However, the laboratory test results are still within the required limit of the Iraqis specifications [21] and better when compared with the reference mixture. This reduction in performance of the 9% mixture could be attributed to the reduction in LDPE-modified asphalt characteristics as penetration and ductility values. This means that the binder is stiffer and having higher viscosity that could not cover all aggregate particles. These deficiencies in the aggregate covering cause improper compaction that can be inferred from other volumetric characteristics as lower density, and higher air voids.



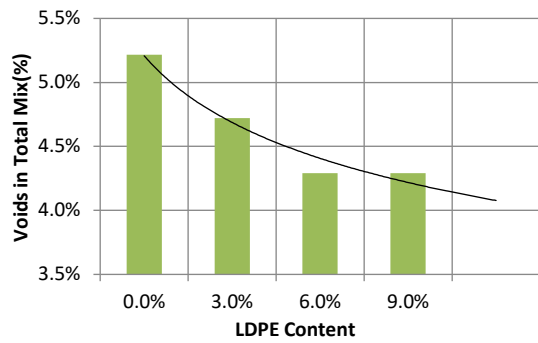
A: Marshall Stability



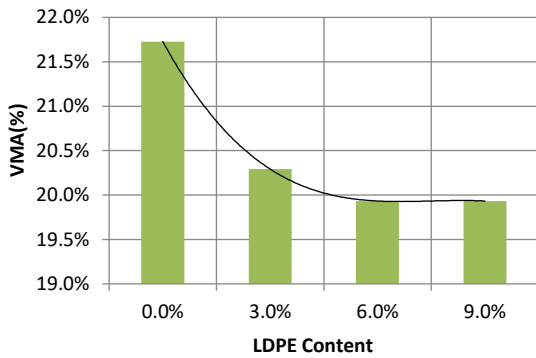
B: Marshall Flow



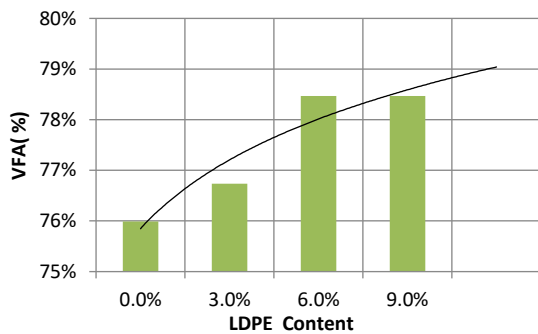
C: Bulk density



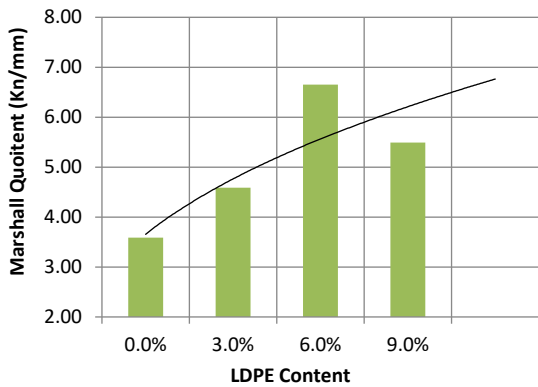
D: Air voids



E: Voids in mineral aggregate



F: Voids filled with asphalt



G: Marshall Quoitent

Figure 3. Effect of LDPE on Phsiomechanical properties of Asphalt Mixtures

4. 3. Durability

is the ability of a material to sustain weather conditions [32]. For pavements, moisture is a fundamental parameter that causes pavement deterioration in a form of moisture damage (stripping) distress [33]. The moisture sensitivity of the control and the recycled LDPE-modified mixtures was evaluated following ASTM D 6927 [23] specification. This test assesses the loss in cohesion resulted from water ingress through the mixture. The Marshall stability of the conditioned and unconditioned samples with the selected LDPE dosage rates with the corresponding Index of retained strength IRS are presented in Figure 4. The test results indicates that the IRS increase with increasing LDPE ratio, and the rate of increase in the index of retained strength is improving significantly with 9% of recycled LDPE material. This behavior is also remarked by other researchers [16]. They attributed this behavior to the bonding ability of the polyethylene polymer with aggregates particles, acting as glue to bind the aggregate particles together and reduce waste ingress. Since the moisture damage depends not only on the aggregate mineralogy but also on asphalt-aggregate interaction as well as other volumetric properties and the layer film thickness [12]. Enhancing these characteristics would result in improving the moisture resistance of the paving mixture. Noticeably, the addition of any type of recycled plastic polymer enhances the pavement properties against moisture damage [12, 34], especially when using the wet method of mixing.

4. 4. Short-term Aging

Volumetric properties of the mixture are essential in predicting the performance of the pavement service life since they affect durability. After the aging process, the asphalt binder loses the volatile materials through oxidation and volatilization, thereby reducing its volume, and increase its viscosity [35]. Subsequently, decreasing the mixture weight, and density. This behavior is clearly noticed in Figure 5.

Figure 6 shows the effect of short-term aging on Marshall stability, flow, and quotient which is the ratio

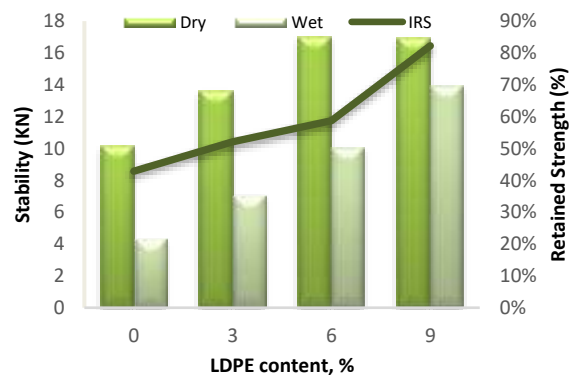


Figure 4. Marshall stability, and retained stability for control and conditioned samples

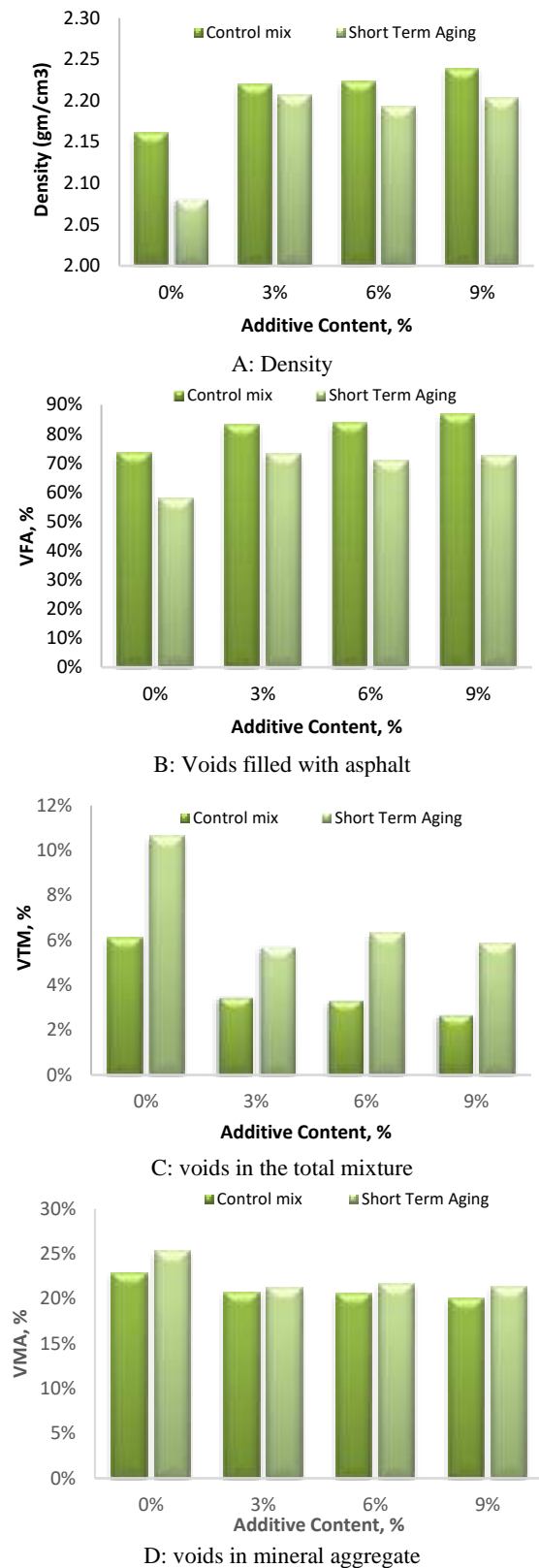


Figure 5. Effect of recycled LDPE and short-term aging on volumetric properties of asphalt mixture

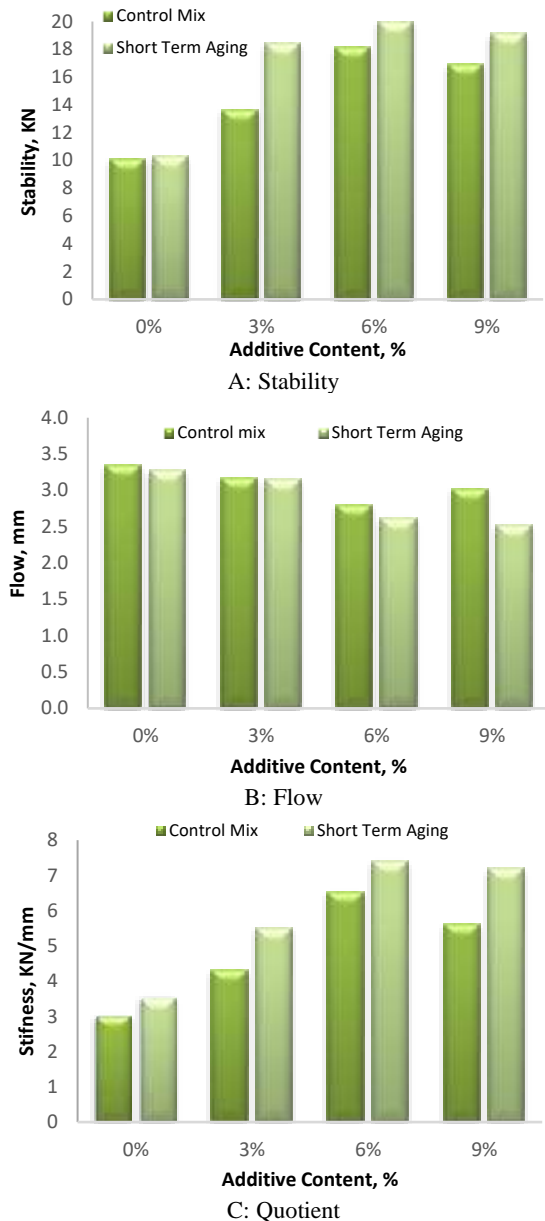


Figure 6. Effect of recycled LDPE and short-term aging on Marshall stability and flow of asphalt mixture

of Marshall stability to flow [15]. The aging process causes loss of volatiles that makes the asphalt binder and mixture stiffer and can resist deformation. This behavior is inferred from increasing Marshall stability, and quotient values, and decreasing flow values. Moreover, the percent change in the modified mixture is less than that observed in the control mix. The LDPE, when mixed with asphalt binder, disperses and absorbed by its components [9] making the maltene phase stiffer and less susceptible to aging. This behavior has been also inferred from the penetrability index, presented in Table 3, which

shows an increase in this value with increasing dosage rate of LDPE. So, it can be concluded that the LDPE-modified paving mixture is less susceptible to temperature. Especially, at high temperature that causes rutting, which is the common type of distress in Iraq [36].

4. 5. Economic Analysis The important aspect of sustainable production is the economic assessment to show the cost-effectiveness of a specific intervention. Therefore, a quantity calculation and cost analysis were implemented and explained in Table 5. The assumptions were set as 1 km of a four-lane highway, with a surface thickness of 50 mm. The savings are presented in Table 6 in terms of the quantity of materials per m³ of the mixture with their corresponding cost.

A cheaper and eco-friendlier material could be achieved by incorporating recycled LDPE in the paving mixture as a surface layer.

TABLE 5. Design parameters for the assumed road section

Design Parameters	Values
Length of pavement section	1 km
Number of lanes	4
Width of lane	3.6 m
Thickness of surface layer	5 cm
Volume of pavement mixture	length × width × thickness = 720 m ³
Approximate density of surface layer	2400 kg/m ³
Percentage of asphalt binder	5%
Quantity of asphalt binder	volume × mix density × binder percentage = 86400 kg = 86.4 ton
Quantity of asphalt binder for 1m ³	86400 kg/720 m ³ = 120 kg
Bitumen cost	0.5\$/kg

TABLE 7. Description of saving in binder volume and cost

LDPE rate	The required quantity of bitumen (kg/ m ³)	Quantity of bitumen saving (kg/ m ³)	Saving cost (\$/m ³)
0 %	120	0	0
3 %	116.4	3.6	1.8
6 %	112.8	7.2	3.6
9 %	109.2	10.8	5.4

5. CONCLUSION

The hot mix asphalt with different percentages of recycled low-density polyethylene had been prepared and tested for Marshall stability and flow and other

volumetric properties. Another set was immersed in water to measure its durability, whereas the other set was conditioned in the oven before compaction to test the short-term aging. Based on test results, the main conclusions can be highlighted as:

- The partial replacement of asphalt binder by recycled LDPE enhances Marshall properties and maintains other volumetric properties to the specified limits. Additionally, the resistance to moisture damage increases.
- The addition of LDPE to asphalt mixture via the wet process improves the aging characteristics of the short-term aged mixture.

To sum up, utilization of waste materials as plastic bags or sheets, made from low-density polyethylene, extends pavement service life by enhancing pavement properties in terms of mechanical, and physical properties, durability, aging, and provides an economical and eco-friendly paving material and maintain a sustainable environment.

5. ACKNOWLEDGMENT

Authors would like to thank Mustansiriyah University (www.uomustansiriyah.edu.iq) Baghdad-Iraq, for providing the necessary support to carry out the present work.

6. REFERENCES

1. A. I. Al-Hadidy, "Engineering behavior of aged polypropylene-modified asphalt pavements," *Construction and Building Materials*, Vol. 191, (2018), 187-192, <https://doi.org/10.1016/j.conbuildmat.2018.10.007>.
2. A. H. Abed and H. U. Bahia, "Enhancement of permanent deformation resistance of modified asphalt concrete mixtures with nano-high density polyethylene," *Construction and Building Materials*, Vol. 236, (2020), 117604, <https://doi.org/10.1016/j.conbuildmat.2019.117604>.
3. A. H. Abed, Z. I. Qasim, H. Al-mosawe, H. H. Norri, and F. G. Pratico, "The effect of hybrid anti-stripping agent with polymer on the moisture resistance of hot-mix asphalt mixtures," *Cogent Engineering*, Vol. 6, (2019), 1-15, doi: 10.1080/23311916.2019.1659125.
4. E. N. Ezzat and A. H. Abed, "The influence of using hybrid polymers , aggregate gradation and fillers on moisture sensitivity of asphaltic mixtures," *Materials Today: Proceedings*, Vol. 20, (2020), 493-498, doi: 10.1016/j.matpr.2019.09.176.
5. M. A. Al-Jumaili and H. A. Al-Jameel, "Reducing Rutting in Flexible Pavement Using Specified Polymers with HMA," *IOP Conference Series: Material Science Engineering*, Vol. 978, No. 1, (2020), 012006, doi: 10.1088/1757-899X/978/1/012006.
6. A. A. Abdulmawjoud and L. S. Thanoon, "Evaluation of SBR and PS-Modified Asphalt Binders and HMA Mixtures Containing Such Binders," *Applied Research Journal*, Vol. 1, No. 9, (2015).
7. M. N. Issac and B. Kandasubramanian, "Effect of microplastics in water and aquatic systems," *Environmental Science and Pollution Research*, Vol. 28, No. 16, (2021), 19544-19562, doi: 10.1007/s11356-021-13184-2.

8. Y. Zhou, J. Wang, M. Zou, Z. Jia, S. Zhou, and Y. Li, "Microplastics in soils: A review of methods, occurrence, fate, transport, ecological and environmental risks," *Science Total Environment*, Vol. 748, (2020), 141368, doi: 10.1016/j.scitotenv.2020.141368.
9. S. Wu and L. Montalvo, "Repurposing Waste Plastics into Cleaner Asphalt Pavement Materials: A Critical Literature Review," *Journal of Clean. Production*, (2020), 124355, doi: 10.1016/j.jclepro.2020.124355.
10. I. S. Al-Haydari and G. G. Masued, "Benefit of Using Expanded Polystyrene Packaging Material to Improve Pavement Mixture Properties," *Applied Research Journal*, Vol. 11, (2017).
11. K. Z. Ramadan, G. G. Al-khateeb, and M. M. Taamneh, "Mechanical properties of styrofoam-modified asphalt binders," *Int. J. Pavement Res. Technol.*, (2019), <https://doi.org/10.1007/s42947-019-0102-4>.
12. [12] I. S. Al-Haydari and H. S. Al-Haidari, "Mechanical Properties of Polyethylene Terephthalate-Modified Pavement Mixture," *IOP Conference Series Material Science Engineering*, Vol. 870, (2020), 012073, doi: 10.1088/1757-899X/870/1/012073.
13. H. Naghawi, R. Allouzi, A. Alklub, and K. Masarwah, "Plastic Waste Utilization as Asphalt Binder Modifier in Asphalt Concrete Pavement," *World Academy of Science, Engineering and Technology International Journal of Civil and Environmental Engineering*, Vol. 12, No. 5, (2018), 566-571.
14. A. M. Mosa, I. T. Jawad, and L. A. Salem, "Modification of the Properties of Warm Mix Asphalt Using Recycled Plastic Bottles," *International Journal of Engineering, Transactions C: Aspects*, Vol. 31, No. 9, (2018), 1514-1520, doi: 10.5829/ije.2018.31.09c.06.
15. S. Angelone, M. C. Casaux, M. Borghi, and F. O. Martinez, "Green pavements: reuse of plastic waste in asphalt mixtures," *Materials and Structures*, Vol. 49, No. 5, (2015), 1655-1665, doi: 10.1617/s11527-015-0602-x.
16. P. Singh, A. Tophel, and A. K. Swamy, "Properties of asphalt binder and asphalt concrete containing waste polyethylene," *Petroleum Science and Technology*, Vol. 35, No. 5, (2017), 495-500, doi: 10.1080/10916466.2016.1265559.
17. M. A. El-saikaly, "Study of the Possibility to Reuse Waste Plastic Bags as a Modifier for Asphalt Mixtures Properties (Binder Course Layer)," The Islamic University of Gaza, (2013).
18. M. Nouali, Z. Derriche, and E. Ghorbel, "Effect of Used Engine Oil Addition on the Rheological Properties of a Plastic Bag Waste - Modified 40/50 Grade Bitumen," *Journal of Materials in Civil Engineering*, Vol. 33, No. 3, (2021), 1-10, doi: 10.1061/(ASCE)MT.1943-5533.0003533.
19. C. Rodrigues, S. Capitão, L. Picado-Santos, and A. Almeida, "Full recycling of asphalt concrete with waste cooking oil as rejuvenator and LDPE from urban waste as binder modifier," *Sustainability*, Vol. 12, No. 19, (2020), 8222, doi: 10.3390/su12198222.
20. H. Caliendo, "City in Iraq Opens its First Recycling, Production Plant," *Recycled Materials*, (2016). <https://www.ptonline.com/blog/post/city-in-iraq-opens-its-first-recycling-production-plant-> (accessed Dec. 25, 2020).
21. SCRB, "Materials Specification and Construction Works." State Corporation of Roads and Bridges, Ministry of Housing and Construction, Iraq, (2009).
22. ASTM D6926, "Standard Practice for Preparation of Asphalt Mixture Specimens Using Marshall Apparatus," *ASTM International, West Conshohocken, PA*, (2020).
23. ASTM D6927, "Standard Test Method for Marshall Stability and Flow of Asphalt Mixtures." ASTM International, West Conshohocken, PA, (2015).
24. Laboratory Testing Manual, "Method of Test for Resistance to Stripping of Asphalt Cement in Bituminous Mixture by Marshall Immersion," No. 17. Ministry of Transportation, Ontario, (1998).
25. AASHTO R 30-02, "Standard Practice for Mixture Conditioning of Hot Mix Asphalt," *American Association State Highway Transportation Office*, (2019).
26. ASTM D5 / D5M, "Standard Test Method for Penetration of Bituminous Materials," *ASTM International West Conshohocken*, (2020).
27. ASTM D113, "Standard Test Method for Ductility of Asphalt Materials," *ASTM International West Conshohocken, PA*, (2017).
28. ASTM D36 / D36M - 14, "Standard Test Method for Softening Point of Bitumen (Ring-and-Ball Apparatus)," *ASTM International West Conshohocken, PA*, (2020).
29. M. Ghasemi and S. M. Marandi, "Laboratory studies of the effect of recycled glass powder additive on the properties of polymer modified asphalt binders," *International Journal of Engineering, Transactions A: Basics*, Vol. 26, No. 10, (2013), 1183-1190, doi: 10.5829/idosi.ije.2013.26.10a.08.
30. ASTM D 2726, "Standard Test Method for Bulk Specific Gravity and Density of Non- Absorptive Compacted Bituminous Mixtures." ASTM International, (2014).
31. ASTM D2041, "Standard Test Method for Theoretical Maximum Specific Gravity and Density of Bituminous Paving Mixture." ASTM International, (2011).
32. N. G. Ahmed, Y. M. Al-Badran, and D. M. Azeez, "Laboratory Evaluation of Moisture Damage and Durability of Hot Mix Asphalt (HMA)," *Journal of Engineering and Sustainable Development*, Vol. 21, No. 2, (2017), 149-162.
33. G. L. S. Babu, P. S. Kandhal, N. M. Kottayi, R. B. Mallick, and A. Veeraragavan, *Pavement Drainage: Theory and Practice*. Taylor & Francis Group, (2020).
34. S. Haider, I. Hafeez, Jamal, and R. Ullah, "Sustainable use of waste plastic modifiers to strengthen the adhesion properties of asphalt mixtures," *Construction and Building Materials*, Vol. 235, (2020), 117496, doi: 10.1016/j.conbuildmat.2019.117496.
35. S. I. Sarsam and S. M. Abdulmajeed, "Influence of Aging Time on Asphalt Pavement Performance," *Journal of Engineering*, Vol. 20, No. 12, (2014), 1-12.
36. A. H. A. Al-Haddad and I. S. J. Al-Haydari, "Modeling of flexible pavement serviceability based on the fuzzy logic theory," *Journal of Transportation Engineering, Part B: Pavements*, Vol. 144, No. 2, (2018), doi: 10.1061/JPEODX.0000026.

Persian Abstract

چکیده

با انقلاب صنعتی ، بسیاری از اختراعات با بسیاری از مواد زائد جامد در ازای آن ارائه شده است. این مطالعه بازیافت بالقوه ورق های پلاستیکی زباله ، ساخته شده از پلی اتیلن با چگالی کم ، به عنوان اصلاح کننده آسفالت را در مخلوط روسازی بررسی می کند. ورق پلاستیکی خرد شده از طریق فرآیند مرطوب در مخلوط آسفالت استفاده شد. میزان دوز تا ۹ از وزن چسب آسفالت تنظیم شد. این برنامه آزمایشی علاوه بر ارزیابی اقتصادی ، برای ارزیابی خصوصیات مکانیکی ، دوام و پیری کوتاه مدت مخلوط های آسفالت نیز طراحی شده است. نتایج آزمون کاربرد استفاده از این مواد زائد جامد در ساخت روسازی را نشان داد زیرا استفاده از آن با افزایش پایداری ، شاخص مقاومت حفظ شده و خصوصیات حجمی قبل و بعد از پیری و همچنین صرفه جویی در هزینه ، عملکرد روسازی را افزایش می دهد. با ۶٪ پلی اتیلن با چگالی کم بازیافت شده ، بهترین پیشرفت را می توان بدست آورد.



Fabrication and Evaluation of Controlled Release of Doxorubicin Loaded UiO-66-NH₂ Metal Organic Frameworks

N. Rakhshani^a, N. Hassanzadeh Nemati^{*a}, A. Ramazani Saadatabadi^b, S. K. Sadrnezhaad^c

^a Department of Biomedical Engineering, Science and Research Branch, Islamic Azad University, Tehran, Iran

^b Department of Chemical and Petroleum Engineering, Sharif University of Technology, Tehran, Iran

^c Department of Materials Science and Engineering, Sharif University of Technology, Tehran, Iran

P A P E R I N F O

Paper history:

Received 18 March 2021

Received in revised form 18 May 2021

Accepted 12 June 2021

Keywords:

Metal Organic Framework

UiO-66-NH₂

Doxorubicin

Controlled Release

Biocompatibility

A B S T R A C T

The metal-organic frameworks (MOFs) due to their large specific surface area and high biocompatibility are suitable as carriers for drug delivery systems (DDS). In the present study, doxorubicin (DOX) as an anticancer drug was loaded into UiO-66-NH₂ MOFs to decrease the adverse side effects of pristine DOX use and to increase its efficiency through the controlled release of DOX from MOFs. The MOFs were synthesized via microwave heating method and characterized using X-ray diffraction, scanning electron microscopy, and Brunauer-Emmett-Teller analysis. The drug loading efficiency, drug release profiles from synthesized MOFs and pharmacokinetic studies were investigated. The biocompatibility of drug-loaded-UiO-66-NH₂ MOFs was also evaluated by their incubation in L929 normal fibroblast cells. The average particle sizes of UiO-66-NH₂ MOFs and DOX loaded-MOFs were found to be 175 nm, and 200 nm respectively. The Brunauer-Emmett-Teller surface area of UiO-66-NH₂ MOFs and DOX (100 µg mL⁻¹) loaded-UiO-66-NH₂ MOFs were estimated to be 1052 m²g⁻¹, and 121 m²g⁻¹, respectively. The synthesized MOFs exhibited high capability for the controlled release of DOX from MOFs as a pH sensitive carrier. The DOX release data were best described using Korsmeyer-Peppas pharmacokinetic model (R²≥0.985). The cell viability of synthesized MOFs against fibroblast normal cells was found to be higher than 90%. It could be concluded that the UiO-66-NH₂ MOFs could be used as an effective pH sensitive carrier for loading anticancer drugs.

doi: 10.5829/ije.2021.34.08b.08

1. INTRODUCTION

The main challenges of traditional drug delivery systems are their poor controlled release and low dosage of anticancer agents in targeted tissue [1]. Furthermore, the use of pristine anticancer drugs due to their high toxicity and adverse effect on normal tissues is limited [2]. For example, although doxorubicin (DOX) as an anticancer agent has been applied for the various cancers treatment such as lung, brain, prostate, breast, and skin; its use is associated with many limitations such as toxic side effects and the low therapeutic efficiency due to its low half time of 1.8 h [3]. To reduce the adverse effects of DOX to patients and to increase the chemotherapy efficacy, various drug delivery systems such as hydrogels [3], liposomes [4], micelles [5], nanofibers [6], and

inorganic materials [7] have been developed for controlled release of DOX. Among inorganic materials used in biomedical applications such as carbon based-materials [8], metal oxides [9], zeolites [7], silver [10], and metal-organic frameworks (MOFs) [11-14], MOFs as a new class of crystalline porous materials due to their higher specific surface area, and large porosity in compare to other inorganic materials have been developed for biomedical applications. The nanosized-MOFs (NMOFs) exhibited unique physicochemical properties such as the higher specific surface area in compare to the micrometer scale of MOFs which provide the high loading of drugs and high chemotherapeutic efficacy [14, 15]. Various NMOFs such as ZIF-8 [16], MIL 101 [17] and UiO-66 [18, 19] have been used for drug delivery systems. UiO-66 consisted of [Zr₆O₄(OH)₄

*Corresponding Author Institutional Email: hasanzadeh@srbiau.ac.ir
(N. Hassanzadeh Nemati)

octahedral (11 Å) and tetrahedral (8 Å) cages in 1:2 ratio and 1,4-benzenedicarboxylic acid (H₂bdc) ligands is synthesized by various methods such as hydrothermal, solvothermal, microwave and microreactor technology [20]. The heterogeneous reaction takes place under high pressure and high temperature conditions in the hydro/solvothermal methods which could be resulted in generation of large crystals with micro-sized particles [21]. The ultrasonic method provides the changes in the physicochemical properties of molecules under ultrasonic irradiation ranging from 20 kHz–10 MHz. However, the rate of sonochemical reduction completely depends on the ultrasonic frequency and thus, the heat-sensitive materials cannot withstand the acoustic cavitation at higher ultrasonic frequency [22, 23]. The microwave heating method has advantages over other synthetic methods such as the use of lower temperature, shorter reaction time, control of morphology and phase as well as the synthesis of finer particles with higher specific surface area [24]. Furthermore, the uniform absorption of energy throughout the entire volume of MOFs compared to conventional oven heating methods leads to homogeneous nucleation and reduction in crystallization time followed by production of the microporous MOFs for loading of the high content of drug [25]. Whereas, the longer time of conventional methods for MOFs synthesis leads to the production of micro-sized-MOF particles with lower high specific surface area [26].

UiO-66 as a zirconium-based MOF has unique properties such as high mechanical properties and water stability which facilitate its use for environmental and biomedical applications [27-29]. UiO-66 MOFs due to having high stability in aqueous solutions and bloodstream as well as high biocompatibility could be considered as an ideal candidate for drug delivery of anticancer drugs such as DOX, paclitaxel, etc. [29, 30]. Moreover, the presence of open cavities in the UiO-66 MOF matrix led to incorporate the high content of drug molecules. Furthermore, UiO-66 MOF could be considered as a pH-sensitive carrier for the controlled release of anticancer agents into the cancer tissues [29]. The delivery of calcein as a hydrophilic drug into the UiO-66 MOF was studied by the Orellana-Tavra et al. [30]. Nasrabadi et al. [19] synthesized the UiO-66 metal-organic framework nanoparticles via a solvothermal method for the controlled release of ciprofloxacin. In the present study, DOX anticancer drug was loaded into UiO-66-NH₂ MOFs synthesized by the microwave heating method. The synthesized UiO-66-NH₂ MOFs and DOX loaded-UiO-66-NH₂ MOFs were characterized using XRD, SEM, and BET analysis. The drug loading efficiency, drug release, and kinetic studies were investigated.

2. MATERIALS AND METHODS

2.1. Materials 2-Aminoterephthalic acid (BDC-NH₂, purity ≥ 99.9%), and zirconium chloride (ZrCl₄, purity ≥ 99.9%) were supplied from Sigma-Aldrich (Germany). N,N Dimethylformamide (DMF, purity ≥ 99.0%), and hydrochloric acid (HCl, 37%) were purchased from Fluka (Switzerland). Doxorubicin was provided by Sobhan Darou Co. (Iran).

2.2. Synthesis of UiO-66-NH₂ The UiO-66-NH₂ MOF particles were synthesized by microwave method as described previously by Jamshidifard et al. [31]. Briefly, 125 mg ZrCl₄, 134 mg BDC-NH₂, 15 mL DMF and 1 mL HCl were mixed under sonication for 1 h. Then, the mixture was poured into the glass bottle. The microwave heating was proceeded into a microwave oven (CE1110 C, Samsung, Korea) with 900 W power and wavelength of 2.45 GHz at 130°C for 1 h. The temperature of the glass bottle was measured by a Teflon-coated thermocouple (TC4Y, Autonics, Korea). Then, the product was washed with DMF and methanol three times and dried at 60 °C for 6 h [32].

2.3. Loading of DOX into the UiO-66-NH₂ To load DOX molecules into the UiO-66-NH₂ MOFs, 5 mg UiO-66-NH₂ NMOFs were dispersed into 10 mL DOX solutions (10, 50, and 100 µg mL⁻¹) for 24 h under stirring. Then, the prepared UiO-66-NH₂/DOX NMOFs were washed with ethanol and distilled water three times. Then, the prepared products were centrifuged at 12000 rpm for 20 min. The final DOX loading efficiency (%) in NMOFs samples was determined after centrifugation of NMOFs using UV-Vis spectrophotometer at the wavelength of 481 nm as follow:

$$DEE (\%) = \frac{\text{Final content of drugs in samples}}{\text{Initial content of drugs doped - samples}} \times 100 \quad (1)$$

2.4. Characterization Tests To confirm the structure and crystallinity of NMOFs, the X-ray diffraction (XRD) patterns of MOF samples were recorded at 25 °C using Philips X'pert diffractometer ranging from 10–80° with Cu-Kα radiation. The functional groups of DOX, UiO-66-NH₂, and UiO-66-NH₂/DOX were determined using Fourier-transform infrared spectroscopy (FTIR) on an Equinox 55 FTIR spectrometer ranging from 4000–400 cm⁻¹. The morphology of NMOFs was investigated using scanning electron microscopy (TESCAN, VEGA 3SB) and field emission scanning electron microscopy (FESEM, MIRA3TESCAN-XMU). The specific surface area of NMOFs was determined using Brunauer-Emmett-Teller (BET) method. The concentration of DOX was

determined using UV-Vis spectrophotometer (JAS.CO V-530, Japan) at wavelength of 481 nm. The hydrodynamic diameter and size distribution of the UiO-66-NH₂ MOFs and DOX loaded-MOFs were determined using dynamic light scattering (DLS) by a Malvern Zetasizer Nano (Malvern Instruments, Worcestershire).

2. 5. Drug Release and Kinetic Studies

To achieve the DOX release from synthesized MOFs, 50 mg drug-loaded-MOFs were incubated at 37 °C in 2 mL Phosphate-buffered saline (PBS) and then sealed into a dialysis bag (molecular cut off 50 kD). Then, the samples were soaked in 20 mL of 0.1M PBS (pH values of 7.4 and 5.5). The suspensions were transferred into a thermostated shaking water bath (Hidolff) at 37 °C and 100 rpm for 3 days. At certain times (0.5 h, 1 h, 2h, 3h, 6h, 9 h, 12 h, 24h, 30 h, 36 h, 42 h, 48 h, 60 h and, 72 h), 2.0 mL of released solution was taken from the dissolution medium, while 2 mL of fresh buffer solution was added to the incubation medium. The final content of DOX was determined using UV-Vis spectroscopy. The DOX release percentage was calculated based on the actual drug content in the UiO-66-NH₂ MOFs. The DOX release data were analyzed using zero-order, Higuchi and Korsmeyer-Peppas pharmacokinetic models [6]. The experiments were repeated five times and the average values were reported.

2. 6. Cell Viability

To investigate the biocompatibility of MOFs samples, the synthesized nanoparticles were incubated in the L929 normal fibroblast cells (Institute Pasteur of Iran, IPI, Tehran, Iran) cultured in RPMI with 10% fetal calf serum and 1% penicillin-streptomycin at 37°C in a humidified atmosphere of 5% CO₂. The experiments were repeated three times and the average values were reported.

2. 7. Statistical Analysis

The statistical analysis was performed by one-way analysis of variance using SPSS version 18 to define the statistically significant values as $P < 0.05$.

3. RESULTS AND DISCUSSION

3. 1. Characterization of UiO-66-NH₂ and DOX Loaded- UiO-66-NH₂

The XRD patterns of DOX, UiO-66-NH₂, and DOX loaded- UiO-66-NH₂ NMOFs are illustrated in Figure 1. The presence of sharp diffraction peaks at $2\theta = 7.5^\circ$ and 8.5° corresponding to (111), and (002) planes indicated the formation of pure UiO-66-NH₂ MOF nanoparticles [31]. It can be seen that there are sharp peaks in the XRD pattern of DOX, which demonstrated the crystalline form of pristine DOX. Incorporation of DOX into the MOF resulted in the weakening of diffraction peaks of UiO-66-NH₂ MOF due

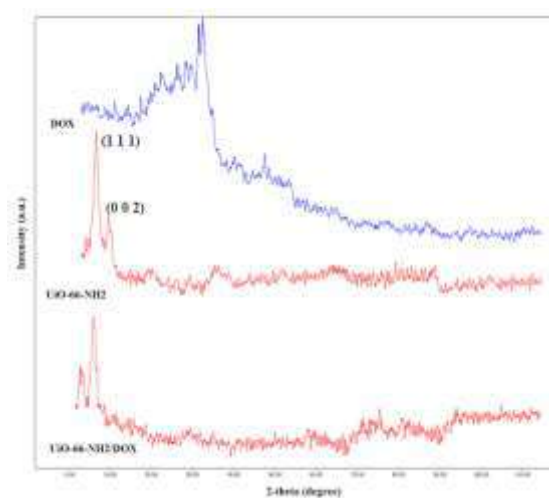


Figure 1. XRD patterns of DOX, UiO-66-NH₂ and DOX loaded- UiO-66-NH₂ NMOFs

to decreasing the X-ray contrast of MOF pore cages. Furthermore, no diffraction peaks were detected in the XRD pattern of UiO-66/DOX MOF nanoparticles, which indicated the amorphous status of DOX after loading DOX into the UiO-66-NH₂ MOF particles in comparison with the crystalline form of pristine DOX, which is consistent with the pores' size being small scale not supporting aggregation into a crystalline form [33]. A similar trend was reported by Farboudi et al. [32] for doxorubicin and folic acid/UiO-66-NH₂ loaded-nanofibers.

The SEM images of UiO-66-NH₂ NMOFs and DOX loaded- UiO-66-NH₂ NMOFs are illustrated in Figure 2. As shown, the uniform nanoparticles ranging from 100-300 nm were obtained for UiO-66-NH₂ MOF particles. The average particle sizes of UiO-66-NH₂ NMOFs and DOX loaded- UiO-66-NH₂ NMOFs were found to be 175 nm and 200 nm, respectively. The FESEM image of the synthesized UiO-66-NH₂ MOF nanoparticles revealed the presence of various shapes including spherical and polyhedral shapes of UiO-66-NH₂ MOF (Figure 1C). An increase in the particle sizes of DOX loaded- UiO-66-NH₂ NMOFs may be attributed to the aggregation of some UiO-66-NH₂ particles during the incorporation of DOX into the UiO-66-NH₂ matrix. An increase in particle sizes was further confirmed by the dynamic light scattering (DLS) measurement. As shown, the average hydrodynamic sizes of UiO-66-NH₂ NMOFs and DOX loaded- UiO-66-NH₂ NMOFs were found to be about 230 nm and 275 nm, respectively. The average particle sizes of synthesized NMOFs reported by SEM were lower than that of DLS. The hydrodynamic radius of MOFs was found to be higher than that of particle size of dried nanoparticles. Similar trends were reported by other researchers [34, 35].

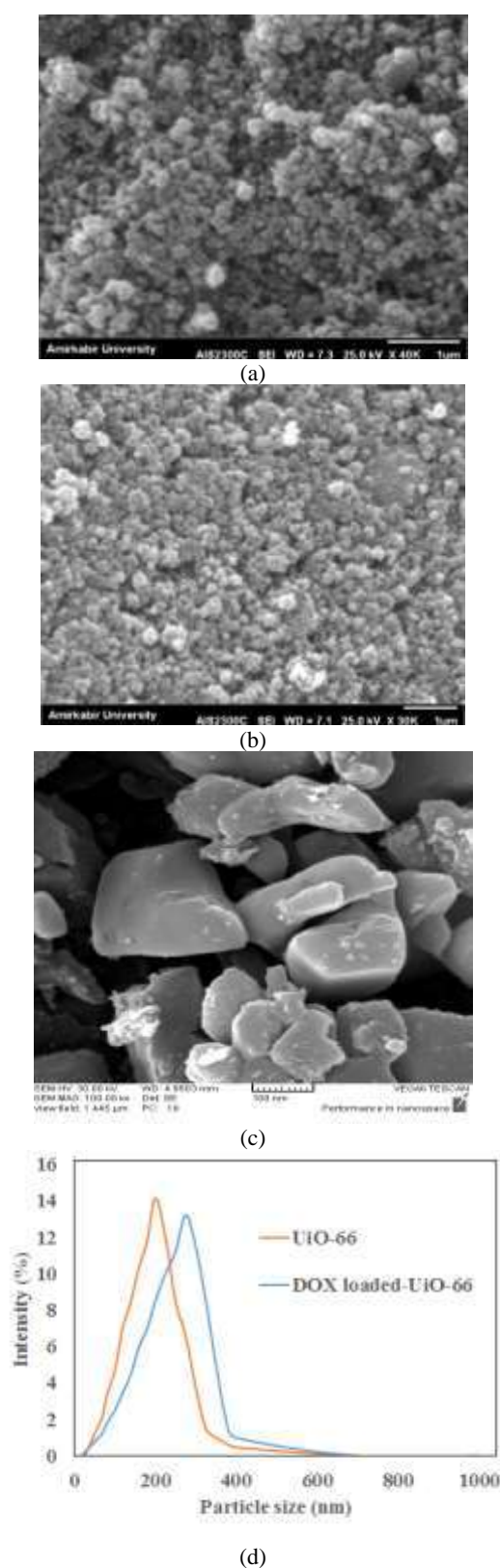


Figure 2. SEM images of (A) UiO-66-NH₂ NMOFs, (B) DOX loaded-UiO-66-NH₂ NMOFs, (C) FESEM image of UiO-66-NH₂ NMOFs, and (D) DLS of synthesized UiO-66-NH₂ NMOFs and DOX loaded-UiO-66-NH₂

The FTIR spectra of UiO-66-NH₂ and DOX loaded-UiO-66-NH₂ are illustrated in Figure 3. For UiO-66-NH₂ MOFs, the observed peaks at 3450 cm⁻¹ and 3360 cm⁻¹ were assigned to the stretching vibrations of OH and NH, respectively. The detected peaks at 1575 cm⁻¹ and 1390 cm⁻¹ were due to the carboxylate groups of BDC-NH₂. The Zr(μ₃) O bands of MOF were detected at wavenumbers of 730 cm⁻¹, 665 cm⁻¹, and 560 cm⁻¹. After loading of DOX into the MOFs, the observed new peaks at 1710 cm⁻¹ and 1610 cm⁻¹ corresponding to the C=O and C=C groups of DOX demonstrated the successful doping of DOX into the MOFs. A similar trend was reported by Farboudi et al. [32] after loading DOX into the nanofibers. The BET surface area and pore volume of UiO-66-NH₂ NMOFs vs. DOX loaded-UiO-66-NH₂ NMOFs were found to be 1052 m²g⁻¹ and 0.58 cm³g⁻¹ vs. 121 m²g⁻¹ and 0.12 cm³g⁻¹, respectively. The obtained results demonstrated the high loading of DOX molecules into the MOF particle pores. The blockage of NMOFs pores by the DOX molecules resulted in significant decrease in specific BET surface area after loading of DOX into the NMOFs. Chowdhuri et al. [29] indicated that the surface area of UCNP@UiO-66-NH₂/FA was decreased from 932 m²g⁻¹ to 186 m²g⁻¹ after loading of DOX into the MOFs.

3. 2. Drug Encapsulation Efficiency, Drug Release and Kinetic Studies

The DOX encapsulation efficiency for NMOFs incubated at 10 μg mL⁻¹, 50 μg mL⁻¹ and 100 μg mL⁻¹ DOX is presented in Table 1. As shown, the maximum drug encapsulation efficiency (DEE %) was found to be 53.5% from NMOFs containing 10 μg mL⁻¹ DOX. By increasing DOX concentration, the DEE was gradually decreased. The

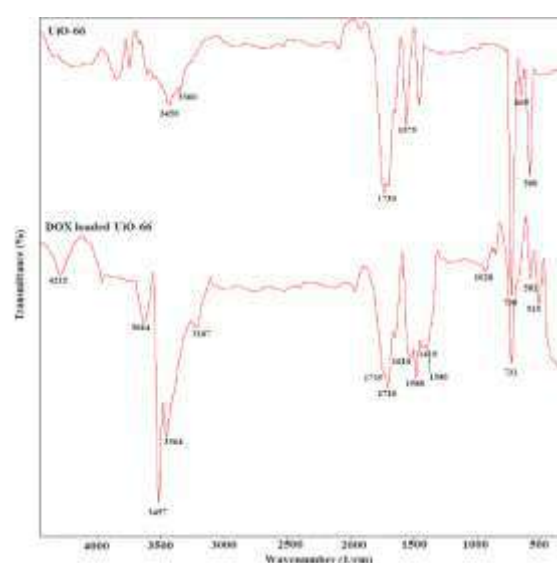


Figure 3. FTIR spectra of UiO-66-NH₂ and DOX loaded-UiO-66-NH₂ NMOFs

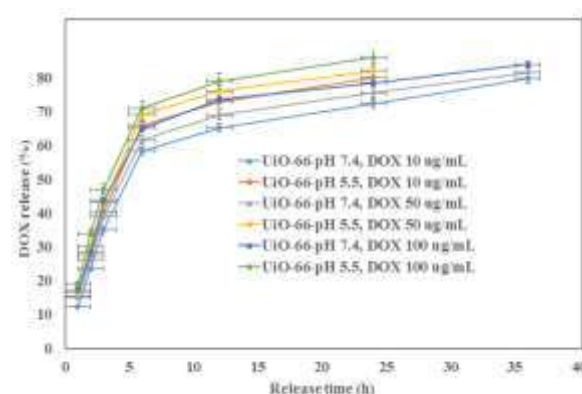
TABLE 1. Drug encapsulation efficiency of synthesized UiO-66-NH₂/DOX (n=5)

DOX concentration ($\mu\text{g mL}^{-1}$)	Drug loading efficiency (%)
10	53.5 \pm 1.5
50	51.3 \pm 1.7
100	50.2 \pm 1.8

higher percentage of drug lost in the loading medium by increasing DOX concentration resulted in a decrease in DEE. A similar trend is reported by Kamba et al. [36] for controlled release of doxorubicin against bone cancer treatment.

The DOX release profiles of NMOFs containing 10 $\mu\text{g mL}^{-1}$, 50 $\mu\text{g mL}^{-1}$ and 100 $\mu\text{g mL}^{-1}$ DOX under pH values of 5.5 and 7.4 are illustrated in Figure 4. As shown, the decrease in pH from physiological pH to acidic pH resulted in faster release of DOX from NMOFs. About 80% DOX release occurred from NMOFs containing 10 $\mu\text{g mL}^{-1}$ after 24 h, and 36 h at pH values of 5.5, and 7.4, respectively. After that, the cumulative release of DOX did not significantly change. Therefore, 24 h and 36 h could be considered as equilibrium times of the DOX release from NMOFs at pH values of 5.5, and 7.4, respectively under an initial concentration of 10 $\mu\text{g mL}^{-1}$ DOX. Whereas, the increase in drug content in samples resulted in the gradual increase in the release rate of DOX due to the lower distance of DOX molecules. The loss of some interactions between Zr-O clusters and DOX molecules resulted in the faster release of DOX from NMOFs at pH of 5.5 in comparison to DOX release at pH of 7.4. Nasrabadi et al. [19] reported the higher release percentage of ciprofloxacin from UiO-66 at pH 5 (87%) in comparison with its release from UiO-66 at pH 7.4 after 3 days (80%). Chowdhuri et al. [29] indicated that the DOX release from UCNP@ UiO-66-NH₂/FA MOF was increased from 30 and 40% to 65 and 72 % at pH 5.5 in compare to the DOX release at physiological pH after 12 h and 24 h, respectively. Due to the large specific surface area of UiO-66-NH₂ MOFs, the majority of DOX molecules have been released from the surface of the MOFs which were adsorbed on the MOF surface during loading of DOX into the UiO-66-NH₂ MOFs via electrostatic interaction. The drug release from NMOFs occurred during two stages including the faster release from surface and pores near the surface in the first stage and the second stage was the DOX molecules diffusion from inner pores and cages of NMOFs.

The pharmacokinetic parameters and correlation coefficients of pharmacokinetic models are summarized in Table 2. Based on correlation coefficient values, the DOX release data were best described using Korsmeyer-Peppas model ($R^2 > 0.98$) in compare to zero order ($R^2 > 0.88$) and Higuchi ($R^2 > 0.94$) kinetic

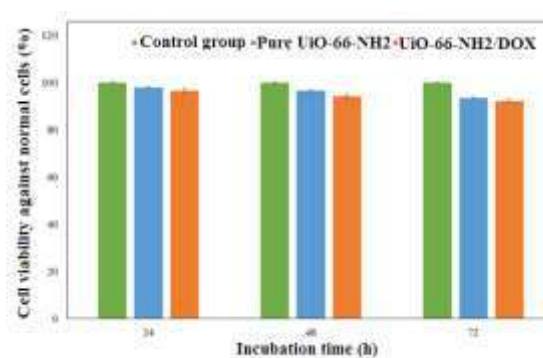
**Figure 4.** DOX release from UiO-66-NH₂ NMOFs containing 10, 50 and 100 $\mu\text{g mL}^{-1}$ DOX**TABLE 2.** Pharmacokinetic parameters of DOX release from UiO-66-NH₂ NMOFs

pH	DOX ($\mu\text{g/mL}$)	Zero-order		Higuchi		Korsmeyer-Peppas		
		K_0 (hr^{-1})	R^2	K_H ($\text{hr}^{-0.5}$)	R^2	n	K_{KP}	R^2
7.4	10	0.253	0.901	3.342	0.947	0.712	4.34	0.989
7.4	50	0.260	0.910	3.677	0.934	0.752	4.56	0.991
7.4	100	0.267	0.895	4.123	0.944	0.778	5.44	0.988
5.5	25	0.274	0.907	4.811	0.945	0.801	5.55	0.985
5.5	37	0.291	0.903	4.854	0.950	0.844	5.62	0.992
5.5	25	0.305	0.888	4.944	0.949	0.865	5.68	0.990

models (Table 2). The “n” values of Korsmeyer-Peppas equation indicated the non-Fickian diffusion of the DOX release from MOFs under both pH values of 5.5 and 7.4.

3. 3. Biocompatibility of NMOFs

The biocompatibility of UiO-66-NH₂ and DOX loaded-UiO-66-NH₂ was investigated by their incubation in normal fibroblast cells which results are illustrated in Figure 5.

**Figure 5.** Cell viability of UiO-66-NH₂, and DOX loaded-UiO-66-NH₂ against L929 normal fibroblast cells

The gradual decrease in the cell viability of pure UiO-66-NH₂ by time could be attributed to the Zr-O clusters release into the medium which increased the cytotoxicity of fibroblast cells treated with UiO-66-NH₂ NMOFs. The cell viability higher than 90% for NMOF samples demonstrated the good biocompatibility of NMOFs for in vivo studies. Orellana-Tavra et al. [30] also indicated that the UiO-66 as a biocompatible and water-stable MOF could be considered as a good candidate for drug delivery applications.

4. CONCLUSION

The UiO-66-NH₂/DOX NMOFs were successfully synthesized via microwave heating method for controlled release of DOX. The BET surface area and average particle size of UiO-66-NH₂ NMOFs and DOX loaded-UiO-66-NH₂ NMOFs were found to be 1052 m²g⁻¹, 175 nm and, 121 m²g⁻¹, 200 nm, respectively. The maximum DOX encapsulation efficiency was found to be 53.5% for NMOFs containing 10 µg mL⁻¹ DOX. The cumulative release percentage of DOX from NMOF containing 10 µg mL⁻¹ was about 80% after 24 h, and 36 h at pH of 5.5, and 7.4, respectively. The non-Fickian diffusion mechanism was achieved by fitting DOX release data with the Korsmeyer-Peppas model. In addition, the high biocompatibility, controlled release manner and high content of DOX in the UiO-66-NH₂ NMOFs demonstrated the high capability of the synthesized NMOFs for various cancer treatments.

5. REFERENCES

- Zamboni. W. C, "Liposomal, nanoparticle, and conjugated formulations of anticancer agents", *Clinical Cancer Research*, Vol.11, No. 23, (2005), 8230-8234, doi: 10.1158/1078-0432.
- Dizaji. B. F, Khoshbakht. S, Farboudi. A, Azarbaijan. M. H, and Irani. M, "Far-reaching advances in the role of carbon nanotubes in cancer therapy", *Life Sciences*, Vol. 257, (2020), 118059, doi: 10.1016/j.lfs.2020.118059.
- Fathi. M, Alami-Milani. M, Geranmayeh. M. H, Barar. J, Erfan-Niya. H, and Omid. Y, "Dual thermo-and pH-sensitive injectable hydrogels of chitosan/(poly (N-isopropylacrylamide-co-itaconic acid)) for doxorubicin delivery in breast cancer", *International Journal of Biological Macromolecules*, Vol. 128, (2019), 957-964, doi:10.1016/j.ijbiomac.2019.01.122.
- Pirouz. F, Najafpour. G, Jahanshahia. M, and Sharifzadeh Baei. M, "Plant-based calcium fructoborate as boron-carrying nanoparticles for neutron cancer therapy", *International Journal of Engineering, Transactions A: Basics*, Vol. 32, No. 4, (2019), 460-466. doi: 10.5829/ije.2019.32.04a.01.
- Ma. B, Zhuang. W, Wang. Y, Luo. R, and Wang. Y, pH-sensitive doxorubicin-conjugated prodrug micelles with charge-conversion for cancer therapy. *Acta Biomaterialia*, Vol. 70, (2018), 186-196, doi: 10.1016/j.actbio.2018.02.008.
- Abasian. P, Radmansouri. M, Jouybari. M. H, Ghasemi. M. V, Mohammadi. A, Irani. M, and Jazi. F. S, Incorporation of magnetic NaX zeolite/DOX into the PLA/chitosan nanofibers for sustained release of doxorubicin against carcinoma cells death in vitro. *International Journal of Biological Macromolecules*, Vol. 121, (2019), 398-406, doi: 10.1016/j.ijbiomac.2018.09.215.
- Rezaei. S, Mohammadi. M, Najafpour. G, D, Moghadamnia. A, Kazemi. S, and Nikzad M, "Separation of curcumin from curcuma longa L. and its conjugation with silica nanoparticles for anti-cancer activities". *International Journal of Engineering, Transactions B: Applications*, Vol.31, No. 11, (2018), 1803-1809, doi:10.5829/ije.2018.31.11b.01.
- Bagheri. M, Sangpour. P, Badiei. E, and Pazouki. M, Graphene oxide antibacterial sheets: Synthesis and characterization (research note). *International Journal of Engineering, Transactions C: Aspects*, Vol. 27, No. 12, (2014), 1803-1808, doi: 10.5829/idosi.ije.2014.27.12c.01
- Hassanzadeh Nemati. N, and Mirhadi. S. M, "Synthesis and characterization of highly porous TiO₂ scaffolds for bone defects", *International Journal of Engineering, Transactions A: Basics*, Vol. 33, No. 1, (2020), 134-140, doi: 10.5829/ije.2020.33.01a.15.
- Rozilah. A, Jaafar. C. N, Sapuan, S. M, Zainol. I, and Ilyas. R. A, "The effects of silver nanoparticles compositions on the mechanical, physiochemical, antibacterial, and morphology properties of sugar palm starch biocomposites for antibacterial coating", *Polymers*, Vol.12, (2020), 2605, doi: 10.3390/polym12112605
- Huxford. R. C, Della Rocca. J, and Lin. W, "Metal-organic frameworks as potential drug carriers", *Current Opinion in Chemical Biology*, Vol. 14, No. 2, (2010), 262-268, doi: 10.1016/j.cbpa.2009.12.012.
- Zheng. H, Zhang. Y, Liu. L, Wan. W, Guo. P, Nyström. A. M, and Zou. X, "One-pot synthesis of metal-organic frameworks with encapsulated target molecules and their applications for controlled drug delivery", *Journal of the American Chemical Society*, Vol. 138, No. 3, (2016), 962-968, doi: 10.1021/jacs.5b11720.
- Beg. S, Rahman. M, Jain. A, Saini. S, Midoux. P, Pichon. C, and Akhter. S, "Nanoporous metal organic frameworks as hybrid polymer-metal composites for drug delivery and biomedical applications". *Drug Discovery Today*, Vol. 22, No. 4, (2017), 625-637, doi: 10.1016/j.drudis.2016.10.001.
- Pirzadeh. K, Ghoreyshi. A. A, Rohani. S, and Rahimnejad. M, "Strong Influence of Amine Grafting on MIL-101 (Cr) Metal-Organic Framework with Exceptional CO₂/N₂ Selectivity", *Industrial & Engineering Chemistry Research*, Vol. 59, No. 1, (2019), 366-378, doi: 10.1021/acs.iecr.9b05779.
- Wang. L, Zheng. M, Xie. Z, "Nanoscale metal-organic frameworks for drug delivery: a conventional platform with new promise", *Journal of Materials Chemistry B.*, Vol. 6, No. 5, (2018), 707-717, doi: 10.1039/C7TB02970E.
- Zheng. C, Wang. Y, Phua. S. Z. F, Lim. W. Q, and Zhao. Y, "ZnO-DOX@ ZIF-8 core-shell nanoparticles for pH-responsive drug delivery", *ACS Biomaterials Science & Engineering*, Vol. 3, No. 10, (2017), 2223-2229, doi: 10.1021/acsbomaterials.7b00435.
- Gordon. J, Kazemian. H, and Rohani. S, "MIL-53 (Fe), MIL-101, and SBA-15 porous materials: potential platforms for drug delivery", *Materials Science and Engineering: C*, Vol. 47, (2015), 172-179, doi: 10.1016/j.msec.2014.11.046.
- Jarai. B. M, Stillman. Z, Attia. L, Decker. G. E, Bloch. E. D, and Fromen. C. A, "Evaluating UiO-66 metal-organic framework nanoparticles as acid-sensitive carriers for pulmonary drug delivery applications. *ACS Applied Materials & Interfaces*, Vol. 12, No. 35, (2020), 38989-39004, doi: 10.1021/acami.0c10900.
- Nasrabadi. M, Ghasemzadeh. M. A, and Monfared. M. R. Z, "The preparation and characterization of UiO-66 metal-organic

- frameworks for the delivery of the drug ciprofloxacin and an evaluation of their antibacterial activities”, *New Journal of Chemistry*, Vol. 43, No. 40, (2019), 16033-16040, doi: 10.1039/C9NJ03216A.
20. Katz. M. J, Brown. Z. J, Colón. Y. J, Siu. P. W, Scheidt. K. A, Snurr. R. Q, and Farha, O. K. A, “facile synthesis of UiO-66, UiO-67 and their derivatives”, *Chemical Communications*, Vol. 49, No. 82, (2013), 9449-9451, doi:10.1039/C3CC46105J.
 21. Gangu. K. K, Maddila. S, Mukkamala. S. B, and Jonnalagadda. S. B. “A review on contemporary metal–organic framework materials”, *Inorganica Chimica Acta*, Vol. 446, (2016) 61-74, doi: 10.1016/j.ica.2016.02.062.
 22. Jamkhande. P. G, Ghule. N. W, Bamer. A. H, and Kalaskar. M. G, “Metal nanoparticles synthesis: An overview on methods of preparation, advantages and disadvantages, and applications”, *Journal of Drug Delivery Science and Technology*, Vol. 53, (2019), 101174, doi: 10.1016/j.jddst.2019.101174
 23. Rane. A. V, Kanny. K, Abitha. V. K, and Thomas. S, “Methods for synthesis of nanoparticles and fabrication of nanocomposites”. In *Synthesis of inorganic nanomaterials* (pp. 121-139). (2018). Woodhead Publishing. doi: 10.1016/B978-0-08-101975-7.00005-1.
 24. Taddei. M, Dau. P. V, Cohen. S. M, Ranocchiar. M, van Bokhoven. J. A, Costantino. F, and Vivani. R, “Efficient microwave assisted synthesis of metal–organic framework UiO-66: optimization and scale up”, *Dalton Transactions*, Vol. 44, No. 31, (2015), 14019-14026, doi: 10.1039/C5DT01838B.
 25. Choi. J. S, Son. W. J, Kim. J, and Ahn. W. S, “Metal–organic framework MOF-5 prepared by microwave heating: Factors to be considered”, *Microporous and Mesoporous Materials*, Vol. 116, No. 1-3, (2008), 727-731, doi: 10.1016/j.micromeso.2008.04.033.
 26. Ni. Z, and Masel. R. I, “Rapid production of metal– organic frameworks via microwave-assisted solvothermal synthesis”, *Journal of the American Chemical Society*, Vol. 128, No. 38, (2006), 12394-12395, doi: 10.1021/ja0635231.
 27. Pirzadeh. K, Esfandiari. K, Ghoreyshi. A. A, and Rahimnejad, M, “CO₂ and N₂ adsorption and separation using aminated UiO-66 and Cu₃ (BTC) ₂: A comparative study”, *Korean Journal of Chemical Engineering*, Vol. 37, No.3, (2020), 513-524, doi: 10.1007/s11814-019-0433-5.
 28. Pirzadeh. K, Ghoreyshi. A. A, Rahimnejad. M, and Mohammadi. M, “Electrochemical synthesis, characterization and application of a microstructure Cu₃ (BTC) ₂ metal organic framework for CO₂ and CH₄ separation”, *Korean Journal of Chemical Engineering*, Vol. 35, No. 4, (2018), 974-983, doi: 10.1007/s11814-017-0340-6
 29. Chowdhuri. A. R, Laha. D, Chandra. S, Karmakar. P, and Sahu. S. K, “Synthesis of multifunctional upconversion NMOFs for targeted antitumor drug delivery and imaging in triple negative breast cancer cells”, *Chemical Engineering Journal*, Vol. 319, (2017), 200-211, doi: 10.1016/j.cej.2017.03.008.
 30. Orellana-Tavra. C, Baxter. E. F, Tian. T, Bennett. T. D, Slater. N. K, Cheetham. A. K, and Fairen-Jimenez. D, “Amorphous metal–organic frameworks for drug delivery”, *Chemical Communications*, Vol. 51, No. 73, (2015), 13878-13881, doi: 10.1039/C5CC05237H
 31. Jamshidifard. S, Koushkbaghi. S, Hosseini. S, Rezaei. S, Karamipour. A, and Irani. M, “Incorporation of UiO-66-NH₂ MOF into the PAN/chitosan nanofibers for adsorption and membrane filtration of Pb (II), Cd (II) and Cr (VI) ions from aqueous solutions”, *Journal of Hazardous Materials*, Vol. 368, (2019), 10-20, doi: 10.1016/j.jhazmat.2019.01.024.
 32. Farboudi. A, Mahboobnia. K, Chogan. F, Karimi. M, Askari. A, Banihashem. S, and Irani. M, “UiO-66 metal organic framework nanoparticles loaded carboxymethyl chitosan/poly ethylene oxide/polyurethane core-shell nanofibers for controlled release of doxorubicin and folic acid”, *International Journal of Biological Macromolecules*, Vol. 150, (2020), 178-188, doi: 10.1016/j.ijbiomac.2020.02.067.
 33. Suresh. K, and Matzger. A. J, “Enhanced drug delivery by dissolution of amorphous drug encapsulated in a water unstable metal–organic framework (MOF)”, *Angewandte Chemie*, Vol. 131, No. 47, (2019), 16946-16950, doi: 10.1002/ange.201907652.
 34. You. J, Li. W, Yu. C, Zhao. C, Jin. L, Zhou. Y, and Wang. O, “Amphiphilically modified chitosan cationic nanoparticles for drug delivery”, *Journal of Nanoparticle Research*, Vol. 15, No. 12, (2013), 1-10, doi: 10.1007/s11051-013-2123-2.
 35. Guo. S, Qiao. Y, Wang. W, He. H, Deng. L, Xing. J, and Dong. A, “Poly (ε-caprolactone)-graft-poly (2-(N, N-dimethylamino) ethyl methacrylate) nanoparticles: pH dependent thermo-sensitive multifunctional carriers for gene and drug delivery”, *Journal of Materials Chemistry*, Vol. 20, No. 33 (2010) 6935-6941. DOI: 10.1039/C0JM00506A.
 36. Kamba. S. A, Ismail. M, Hussein-Al-Ali. S. H, Ibrahim. T. A. T, and Zakaria. Z. A. B, “In vitro delivery and controlled release of doxorubicin for targeting osteosarcoma bone cancer”, *Molecules*, Vol. 18, No. 9, (2013), 10580-10598, doi: 10.3390/molecules180910580.

Persian Abstract

چکیده

چهارچوب‌های آلی-فلزی به علت داشتن سطح ویژه بزرگ و زیست سازگاری بالایشان به عنوان جامل‌های مناسب سیستم‌های رهایش دارو هستند. در این مطالعه، دوکسوروبیسین به عنوان یک داروی ضد سرطان داخل چهارچوب آلی-فلزی $UiO-66-NH_2$ سنتز شده به روش مایکروویو بارگذاری شد تا اثرات منفی استفاده از دوکسوروبیسین خالص را کاهش داده و بازده آن از طریق رهایش کنترل شده دارو از چهارچوب آلی فلزی افزایش یابد. سپس چهارچوب آلی فلزی بدون دارو و همچنین با دارو بوسیله آزمون‌های پراش اشعه ایکس، میکروسکوپ الکترونی روبشی، میکروسکوپ الکترونی روبشی نشر میدانی، طیف سنجی مادون قرمز و اندازه گیری سطح ویژه به روش برنور-ایمیت-تله مورد ارزیابی قرار گرفت. بازده بارگذاری دارو، پروفایل‌های رهایش دارو و مطالعات فارماکوکینتیکی حاصل از داده‌های رهایش دوکسوروبیسین از نانوذرات چهارچوب آلی-فلزی $UiO-66-NH_2$ بررسی شد. زیست سازگاری نانوذرات سنتز شده نسبت به سلول‌های فیبروبلاست L929 مورد ارزیابی قرار گرفت. اندازه ذرات بدون دارو ۱۷۵ نانومتر و ذرات حاوی دارو ۲۰۰ نانومتر اندازه گیری شد. سطح ویژه برای ذرات بدون دارو ۱۰۵۲ متر مربع بر گرم و برای ذرات حاوی دارو ۱۲۱ مترمربع بر گرم توسط آزمون برنور-ایمیت-تله اندازه گیری شد. چهارچوب آلی-فلزی سنتز شده توانایی بالایی را برای رهایش کنترل شده دوکسوروبیسین به عنوان یک حامل حساس به pH نشان داد. داده‌های رهایش دوکسوروبیسین توسط مدل فارکوکینتیکی کورسمیر-پیاس به خوبی تحلیل شد (ضریب همبستگی بیشتر از ۰.۹۸۵). همچنین زیست سازگاری ذرات به وسیله آزمون MTT از طریق غوطه وری آنها در سلول‌های فیبروبلاست بالای ۹۰ درصد حاصل شد. می‌توان نتیجه گرفت که چهارچوب آلی-فلزی $UiO-66-NH_2$ می‌تواند به عنوان یک حامل محرک پاسخ حساس به pH برای بارگذاری داروهای ضد سرطان استفاده شود.



Behavior of Gypseous Soil under Static and Dynamic Loading

S. H. Abid Awn*, H. O. Abbas

Department of Transportation and Airports Engineering, University of Diyala, Iraq

PAPER INFO

Paper history:

Received 28 March 2021

Received in revised form 28 June 2021

Accepted 01 July 2021

Keywords:

Dynamic Loading

Gypseous Soil Behavior

Earthquake

Vibration

ABSTRACT

This study is concerned with the soaking and leaching of gypseous soil at both static and dynamic conditions. The soil used was Natural gypseous soil with 50% gypsum. Three parameters were studied (deformation ratio, dissolve gypsum salts, and hydraulic conductivity) in both static and dynamic conditions. 20 tests were carried using laboratory model. A platform base connected to the loading frame was designed in a manner that allows free movement provided for dynamic test, as an earthquake. Results of experimental work revealed that the deformation ratio S/B (settlement /footing width) for the sample subjected to 10 seconds vibration was twice that of sample without vibration, while the deformation ratio was 15 times that of the sample without vibration when subjected to 30 seconds. On the other hand, 70% of hydraulic conductivity was achieved at the first 10 minutes of leaching for the model subjected to 30 seconds of vibration. That reflects the effect of earthquakes on structures constructed on such problematic soil.

doi: 10.5829/ije.2021.34.08b.09

1. INTRODUCTION

One of the biggest problems facing humanity is climate change and construction. 58% of the climate change indicators are critical and give evidence of the negative outlook that housing building organizations have in terms of sustainability. This can contribute to designing strategies to promote sustainable building by the local government, and thus achieve more sustainable organizations that contribute to reducing their impact on climate change [1].

The presence of problematic soil like gypseous soils cause structural problems for the buildings built on them especially when exposed to moisture from any water source. When such soil is subjected to sudden earthquakes it becomes more dangerous. Lack of information or studies on some variables such as permeability, rate of dissolved salts, and subsidence with time during exposure of such soil to an earthquake. This study was needed because of its practical and applied importance to study the behavior of these soils which are spread in large areas of the continent of Asia. Structures constructed on gypseous soil including buildings, roads,

bridges, harbors, and railways have always been associated with settlement problems [2].

The problem appears when water table or rainfall fluctuates and/or infiltrates into the gypseous soil and dissolution of gypsum occurs, causes loss of cementation between soil particles [3]. Another problem appears for hydraulic structures and irrigation channels which are presented by the leaching problem for gypseous soil below these structures [4]. The presence of water in these structures and the difference in heads between the upper and lower stream of dam structures causes seepage of water, also it causes washing of the dissolved gypsum between soil particles [5]. This washing process led to what we call cavities, inside the soil mass below the heavy hydraulic structure which is filled with water and the dissolved gypsum. At this stage, sudden failure of hydraulic structure constructed on such soil may happen [6]. The problem appears at the first moment of soaking the soil with water [7]. While the other problem presented by leaching the dissolved gypsum inside soil structure, as in the hydraulic structures like dams and irrigation channels [8].

This issue becomes more serious when the soil

*Corresponding Author Email: dr.safaalshamary@gmail.com (S. H. Abid Awn)

subjects to earth quickly or any dynamic excitation like the offshore or retaining wall structure [9]. The dynamic effect of an earthquake depends on the amplitude and duration time of the wave the acceleration and the velocity of the locomotor system causing the vibration to simulate the earthquake presentation in the laboratory [10]. Shaking table, the rotor-mounted disk with eccentric gravity is one of the means of representing the dynamic effect on the soil model .

Till now there is no obvious evidence about the presentation of the behavior of such soil by a standard laboratory test, as other soils. The common method of measuring failure of gypseous soils is by using the oedometer test device by a single or double oedometer test [9]. This method is unrealistic to the natural behavior for this soil because of the disturbance of soil sample which may happen when placing the sample of soil inside the ring of the oedometer cell and the small size of the ring and using large scale model is more real.

The strongest earthquake that struck the world is in the Chilean region, with a magnitude of 9.5 on the Richter scale, and it occurred in the city of Valdivia in southern Chile on May 22, 1960, and its duration was 10 minutes². The effect of earthquakes on the structures built on collapsing soils is shown in Figure 1.

The aim of this study to simulate the effect of an earthquake on a big scale gypseous soil sample and study the variation of total dissolved salts, permeability and deformation with time in both static and dynamic cases using a big scale laboratory model.

2. EXPERIMENTAL WORK

2. 1. Soil Used The soil used in the study was brought from Tikrit City (North of Iraq), with 50% gypsum. The testing program is shown in Figure 2. The engineering properties including chemical and physical properties of soil used are shown in Tables 1 and 2. All laboratory tests were carried out on such soil; also



Figure 1. The earthquakes on the structures built on collapsing soils

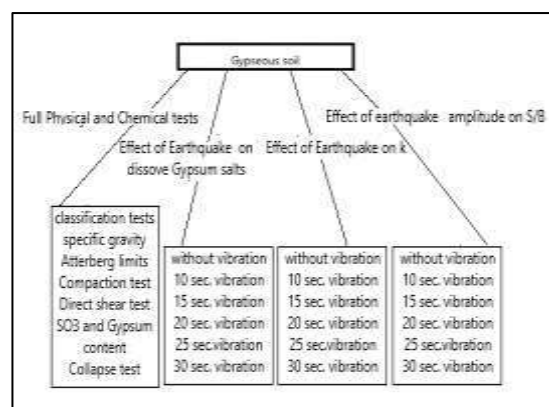


Figure 2. Experimental work program flow chart

TABLE 1. Chemical test for soil used

Soil composition	Value (%)
Dissolve salts	45.6
Sulphate content	20.5
Organic material	0.23
Gypsum content	50
Chloride content	0.08
pH	6.9

TABLE 2. Physical properties of gypseous soil used in the study brought from Salah-Alden governorate in Iraq

Test type	Property	Value
Grain size	D10 mm	0.06
	D30 mm	0.07
	D60 mm	0.19
Coefficient of Uniformity, Cu	Coefficient of Uniformity, Cu	3.02
	Coefficient of Curvature, Cc	0.4
	Passing sieve no. 200	38
Soil Type	Soil Type	SM
	Specific gravity	2.42
Atterberg limits	Liquid limit (L.L) %	24
	Plastic Limit (P.L) %	none
Shear test	friction angle (ϕ) (dry soil)	34
	cohesion (c) (kN/m ²) (dry soil)	5
	Friction angle (ϕ) (soaked soil)	30
Void ratio	cohesion for soaked soil (kN/m ²)	8
	Void ratio	0.63
Water content	Water content	7.3
	Compaction test	Dry unit weight (kN/m ³)
Optimum moisture content%		14
Field density kN/m ³		15.1

² <https://www.arabiaweather.com/content>

relative density was carried according to (ASTM D4254), the temperature for the initial water content determination test is (40 - 50°C) to obviate losing crystal of gypseous soil. The gypseous soil is classified as moderate and moderately severe according to (ASTM D 5533-2003).

2. 2. Laboratory Model Preparation and Test Methodology

A steel model consists of a steel tank with dimensions 300*300*600mm and stiffened at sides and the entire face painted to reduce friction with the soil. A graded fine aggregate was placed at the lower 150mm of the steel model to allow for the leaching water infiltration out of the gypseous soil specimen in the leaching test. Natural gypseous soil with 50% gypsum was used in this study. The density of soil was controlled using the raining technique. A steel footing with 100mm diameter was placed at the center of the soil specimen. Fix weights were fitted over the circular footing with the aid of a vertical shaft connected to the loading frame from its tip to prevent overturning. The soaking process was controlled by feeding water from a water tank as shown in Figure 3.

The leaching process was controlled by making two openings at the bottom of the plastic container opened at the beginning of the leaching test. The head at both upstream and downstream sides was fixed all over the leaching process.

The platform base of the loading frame was designed in a manner that allows free movement using slotting spindles and holes provided for dynamic excitation simulating the earthquake as shown in Figure 3.

A mechanical Oscillator fixed to the platform base. It is composed of steel wheel with a small mass placed on its edge. A digital tachometer (DT-2234At) was used to control and fix the Oscillator speed at a frequency of 10Hz which was obtained by rotating the wheel 600 revolution per minute with 2.63 mm/s velocities and 1.72 m/s² acceleration which kept constant during the dynamic test.

To ensure the fixity of these values, a device called Piezoelectric Accelerometer connected to digital wave velocity model (HG-6360) use to measure velocity and acceleration and can connect to a computer. All accessories used in the study are shown in Figure 2. The valves in the lower part of the models have opened the dissolved salt liquid collected after a limited period to measure the cumulative water and hydraulic conductivity k and dissolve salts.

3. RESULTS AND DISCUSSION

3. 1. Dynamic Response of Gypseous Soil

3. 1. 1. Deformation of Gypseous Soil The relationship between stress and strain was studied for models of gypsum soils subjected to a static dynamic vibration of 10 Hz and at different vibration times (10, 15, 20, 25, 30 seconds) and they were compared with a static model as shown in Figure 4. It can be seen that the footing deformation for gypseous soil sample exposed to 30-second vibration increased about 18 times compared with the static model. While the increase was twice for the model exposed to the same vibration frequency for 10 seconds, especially after the immersion of gypsum from the soil model compared with the static model. This may be due to the effect of gypsum melting inside the soil and restructuring the grains, and this condition increases with an increase in the vibration time; which leads to large deformation of the foundation, while the deformation was less for the foundation based on the gypsum soil model subjected to less vibration. It can recognize that the problem of leaching is not less dangerous than the problem of soaking and it is more serious for models subjected to dynamic excitation. This behavior is more pronounced as with vibration time. With continuous feeding of water, the excitation of saturated gypseous soil model rearrange soil particles and increase footing settlement for soaking and leaching tests in addition that the pores between soil particles increase with continuous flooding of water because gypsum dissolution causes sudden collapse of gypseous soil.

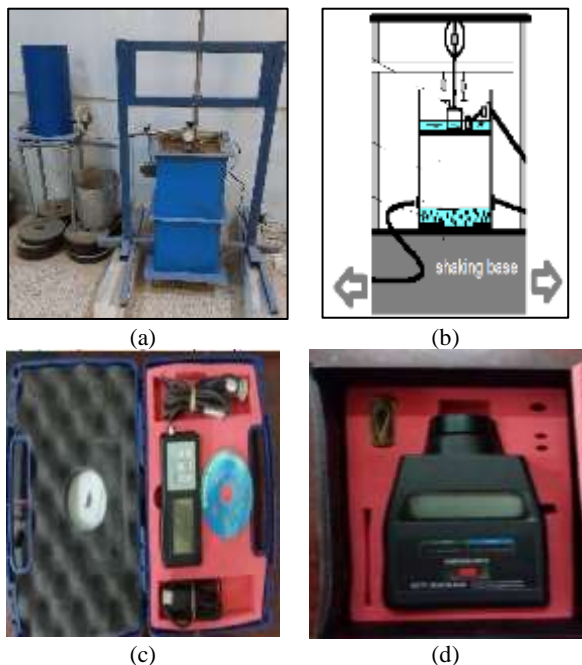


Figure 3. (a) Loading frame and water control system (b) Set up of laboratory model and preparation of soaking (c) Vibration measuring device (d) Digital Tachometer

3. 1. 2. Permeability and Solubility of Gypseous Soil

Figure 5 shows the hydraulic conductivity (k) relation with leaching time for the gypseous soil model subjected to different vibration time amplitudes (5, 10, 15, 20, 25, and 25 s). At the beginning of the leaching test, high values of coefficient of permeability were recorded this may be due to the pressure release of collected water from the previous soaking stage and not from chemical changes. An increase in shaking time for the laboratory model subjected to a dynamic vibration reduces permeability due to an increase in the pore water pressure for saturated gypseous soil due to the disturbance movement of particles inside soil specimen so the permeability decreases.

Figure 6 shows the relation between leaching time and coefficient of permeability k for laboratory model tested at different vibration amplitudes. The undissolved gypsum from the first stage (immersion stage) begins to dissolve during the washing process due to the low concentration of solvent water inside the model and to allow the dissolved gypsum to exit outside the model, so gaps are formed which filled with water and begins to form gaps between the soil grains of the laboratory model which made the soil becomes more permeable.

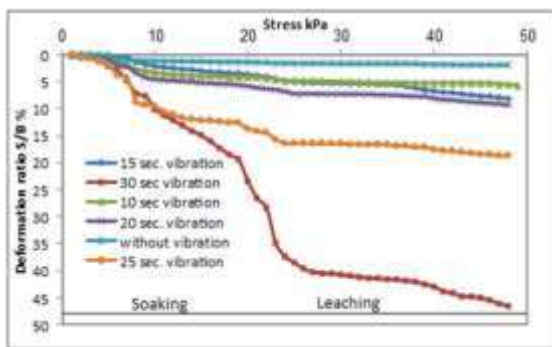


Figure 4. Effect of soaking and leaching on the deformation of footing constructed on gypseous soil of big-scale laboratory model subjected to 10Hz vibration with different vibration times (gypsum content=50%)

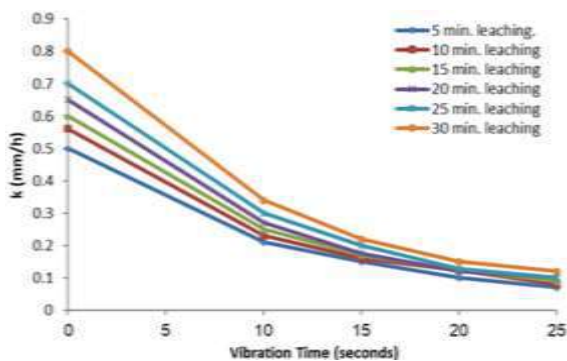


Figure 5. Relation between hydraulic conductivity and vibration time amplitude for different leaching periods

Figure 7 shows the dissolve salt-leaching time relation for gypseous soil models tested at different vibration periods. The dissolve salts vary with leaching time and fluctuate in a randomly descending order until reaching the steady-state condition after 10 days of leaching, this may attribute to the rearrangement of soil particles with vibration time which led to the reduction in pores between soil particles. It was also observed that after 12 days of continuous washing of the gypseous soil model with water after conducting a dynamic examination, the percentage of dissolved salts decreases with an increase in the shaking time. Therefore, the dissolved salts of the model subjected to 25 seconds of vibration reduced 16% from the static model.

4. CONCLUSION AND SUMMARY

In this study, a sample of gypseous soil was exposed to the same conditions and frequency as in the highest earthquake that struck the world in Valencia, southern Chile on 22 May 1960. different vibration periods were investigated (0, 10, 15, 20, 25, 30 seconds). The longest time for earthquakes that hit the world was 10 seconds. The effect of earthquakes on the deformation of a foundation constructed on high contaminated gypseous

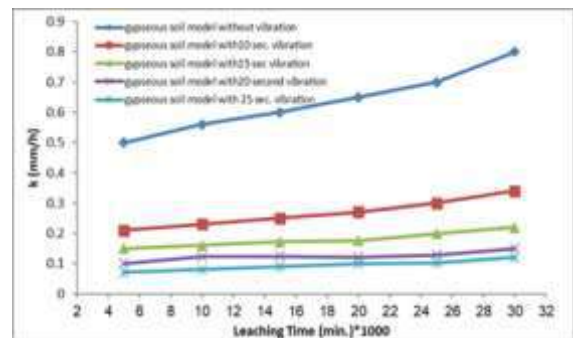


Figure 6. Leaching time and permeability relationship

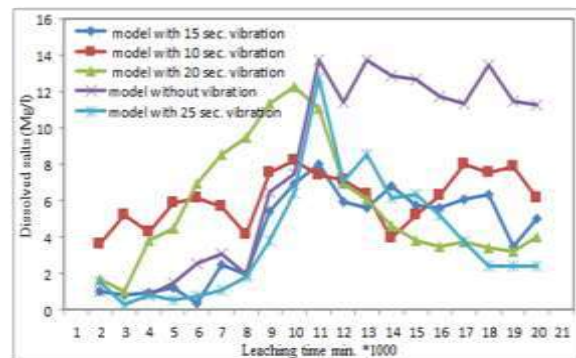


Figure 7. Effect of leaching time on the dissolve salts of gypseous soil mode tested at different vibration time, 10, 15, 20, 25 s and sample without vibration

soil, in addition, to change in the solubility of salts and permeability with time in cases of immersion and washing of gypsum, was also investigated.

1. It is recommended to use large model tests rather than the conventional oedometer tests for both soaking and leaching on gypseous soil at dynamic tests.

2. The danger caused by the exposure of saturated gypseous soil to dynamic vibration increases with an increase in time of the vibration. The deformation of foundation constructing on these soils increases to more than 200% if it is subjected to 10 minutes of vibration. compared to the static model.

3. It may be dangerous to construct heavy structures with a high-stress level on such kind of problematic soil without suitable treatment. In addition to that, the problem of the collapse was more pronounced for the gypseous soil model subjected to 30 seconds excitation, the deformation ratio increased 25 times compared with that for the static model.

4. An increase in shaking time reduces the permeability of the soil, which leads to the retention of water inside the soil as a result of the dynamic activity because of the earthquake, which leads to an increase in pore water pressure and thus has a significant impact on soil behavior.

5. From the results of the dynamic leaching test, 70% of the hydraulic conductivity was achieved at the first 10 min leaching for the model subjected to 30 seconds vibration. On the other hand, the deformation ratio at the leaching process was continued especially for the model subjected to 30 seconds vibration.

6. It can be recognized that the percentage of dissolved salts in leaching of the gypsum soil decreases with the increase in the time of vibration, which delays the dissolution of the gypsum salts inside the soil. The dissolve salts vary with time and fluctuate in a randomly descending order until reaching the steady-state condition after 12 days of continuous leaching.

7. It is recommended to take caution when constructing buildings beside any dynamic soars, especially in gypseous soil.

8. It is recommended to study the possibility of using a laboratory model and its realistic representation and to identify the dynamic behavior of gypsum soils with different gypsum ratios and the possibility of treating them using chemical additives such as cement or lime or

physical treatments such as aggregate columns or soil reinforcement to ward off construction hazards.

5. REFERENCES

- Burciaga, U.M., "Sustainability assessment in housing building organizations for the design of strategies against climate change", *HighTech Innovation Journal*, Vol. 1, No. 4, (2020), 136-147, doi: 10.28991/HIJ-2020-01-04-01 .
- Al-Badran, Y.M., Al-Muftly, A.A.A.-A. and Nashat, I.H., "Leaching behavior of gypseous soils", *ournal of Engineering Sustainable Development*, Vol. 22, No. 02 Part-5, (2018), 119-126, doi: 10.31272/jeasd.2018.2.73 .
- Zhou, W.-H., Liu, F., Yi, S., Chen, Y.-Z., Geng, X. and Zheng, C., "Simultaneous stabilization of pb and improvement of soil strength using nzvi", *Science of The Total Environment*, Vol. 651, (2019), 877-884, doi: 10.1016/j.scitotenv.2018.09.146 .
- Fattah, M.Y. and Dawood, B.A., "Time-dependent collapse potential of unsaturated collapsible gypseous soils", *World Journal of Engineering*, (2020), doi: 10.1108/WJE-09-2019-0276 .
- Kounaves, S.P., Hecht, M.H., Kapit, J., Quinn, R.C., Catling, D.C., Clark, B.C., Ming, D.W., Gospodinova, K., Hredzak, P. and McElhoney, K., "Soluble sulfate in the martian soil at the phoenix landing site", *Geophysical Research Letters*, Vol. 37, No. 9, (2010), doi: 10.1029/2010GL042613 .
- Shukla, J., Mehta, M.J. and Kumar, A., "Effect of ionic liquid additives on the solubility behavior and morphology of calcium sulfate dihydrate (gypsum) in the aqueous sodium chloride system and physicochemical solution properties at 30°C", *Journal of Chemical Engineering Data*, Vol. 63, No. 8, (2018), 2743-2752, doi: 10.1021/acs.jced.8b00093 .
- Almashhadany, O.Y. and Albusoda, B.S., "Experimental study of seismic response of the square tunnel in granular soil", *Journal of Engineering Sustainable Development*, Vol. 24, No. 02, (2020), doi: 10.31272/jeasd.24.2.6 .
- Shukla, J., Mehta, M.J. and Kumar, A., "Solubility behavior of calcium sulfate dihydrate (gypsum) in an aqueous sodium chloride system in the presence of hydroxyalkyl ammonium acetate ionic liquids additives: Morphology changes and physicochemical solution properties at 35°C", *Journal of Chemical Engineering Data*, Vol. 64, No. 12, (2019), 5132-5141, doi: 10.1021/acs.jced.9b00354 .
- Gritto, R., Korneev, V., Elobaid, E., Mohamed, F. and Sadooni, F., "Seismic detection of subsurface karst-like structures", in Qatar Foundation Annual Research Conference Proceedings Volume 2014 Issue 1, Hamad bin Khalifa University Press (HBKU Press). Vol. 2014, No. 1, (2014), EEPP0551.
- Safaa, J., "Geotechnical study of baghdad soil with evaluation of liquefaction potential", M. Sc. Thesis, University of Technology, Building and Construction, (2017)

Persian Abstract

چکیده

این مطالعه مربوط به خیساندن و شسته شدن خاک گچ در هر دو شرایط استاتیک و دینامیکی است. خاک مورد استفاده خاک گچی طبیعی با گچ ۵۰٪ بود. سه پارامتر (نسبت تغییر شکل، حل نمک های گچ و هدایت هیدرولیکی) در هر دو حالت استاتیک و دینامیکی مورد بررسی قرار گرفت. ۲۰ آزمون با استفاده از مدل آزمایشگاهی انجام شد. یک پایه سکو متصل به قاب بارگیری به شکلی طراحی شده است که امکان حرکت آزاد را برای آزمایش پویا فراهم می کند، به عنوان یک زلزله. نتایج کار آزمایشی نشان داد که نسبت تغییر شکل (S/B) نشتی / عرض پایه) برای نمونه مورد آزمایش ۱۰ ثانیه لرزش دو برابر نمونه بدون لرزش بود، در حالی که نسبت تغییر شکل ۱۵ برابر نمونه بدون لرزش هنگام قرار گرفتن در معرض بود ۳۰ ثانیه. از طرف دیگر، ۷۰ درصد هدایت هیدرولیکی در ۱۰ دقیقه اول شستشو برای مدل تحت ۳۰ ثانیه لرزش به دست آمد. این نتایج نشان دهنده تأثیر زلزله بر روی سازه های ساخته شده در چنین خاک مشکل دار است.



Chemical Synthesis of Zinc Oxide Nanoparticles with Nanorod and Spherical Morphologies

E. Darezereshki^a, A. B. Vakylabad^b, M. Yousefi*^a

^a Department of Materials Engineering, Shahid Bahonar University of Kerman, Kerman, Iran

^b Department of Materials, Institute of Science and High Technology and Environmental Sciences, Graduate University of Advanced Technology, Kerman, Iran

PAPER INFO

Paper history:

Received 26 April 2021

Received in revised form 27 May 2021

Accepted 21 June 2021

Keywords:

Thermal Decomposition

Semiconductor

Phase Transformation

Zinc Oxide Nanoparticles

Chemical Synthesis

ABSTRACT

ZnO nanoparticles were prepared by direct thermal decomposition of the precursor [contain: $Zn_4(SO_4)(OH)_6 \cdot H_2O$ and ZnO] in air for 1 h at 875°C. The pH of the precursor solution was set at 6 and 11 by the controlled addition of the $NH_3 \cdot H_2O$ solution. The as-prepared materials were characterized by X-ray diffraction (XRD), infrared spectrum (FTIR), scanning electron microscopy (SEM), and transmission electron microscopy (TEM). According to the analyses, the ZnO nanoparticles were pure with both rod-like and spherical shapes which were synthesized using chloride and sulfate solutions, respectively. Moreover, the average diameter of synthesized spherical ZnO at pH=6 was around 85 ± 5 nm; while, an average diameter of the nanorods was 980 nm and 2.2 μm in length. The average nanorods diameter at pH=11 was 760 nm and 3.3 μm in length; while the average particle size of spherical shape was around 112 ± 5 nm. The TEM and SEM image showed the morphology of spherical and nanorods particles. The reaction temperature of all steps during the synthesis of ZnO nanopowders shifted to high temperature, as the pH of the starting solution increased from 6 to 11. Due to the simplicity, the present method could be proposed as a convenient approach to produce pure ZnO nanoparticles by means of $ZnSO_4$ and $ZnCl_2$ solutions without using any toxic and organic chemicals.

doi: 10.5829/ije.2021.34.08b.10

1. INTRODUCTION

Zinc oxide (ZnO) is an important material for applications in catalytic luminescent and electronic (e.g., varistors, semiconductors, and gas sensors) devices, pigments, rubber, ceramics, chemical and components for the pharmaceutical and cosmetic industries [1-4]. Additionally, ZnO nanostructures were used as nanoadsorbent to remove heavy metals that the removal efficiency depends on the shapes of ZnO nanoparticles [5, 6]. Different morphologies of ZnO including nanospheres, nanorods, nanoflowers, nanotubes, nanoplates and nanotripods have been reported [7]. The literature showed that microstructures and chemical properties of ZnO depend on the synthesis method, synthesis parameters, and also the used starting

precursor. Different synthesis methods were used to prepare ZnO particles of different size and morphology. Table 1 summarized a description of different morphologies obtained under various synthesis conditions and methods [8-21]. Among these methods, precipitation and thermal decomposition are low cost techniques which can provide large scale production without expensive raw materials and complicated equipment. Moreover, different zinc salts such as zinc acetate dehydrate ($Zn(C_2H_3O_2)_2 \cdot 2H_2O$), zinc nitrate hexahydrate ($Zn(NO_3)_2 \cdot 6H_2O$) zinc sulfate ($Zn(SO_4)_2 \cdot 7H_2O$) and zinc chloride ($ZnCl_2$) as precursor have been used. ZnO nanoparticles prepared using $Zn(NO_3)_2 \cdot 6H_2O$ precursor was mixture of nano-prisms and nanorods shape with an average crystallite size of 18.91 nm [22].

Synthesis of ZnO crystalline-structures from $ZnSO_4$ solution with carbonate solutions such as Na_2CO_3 , NH_4HCO_3 , etc. often leads to the occurrence of a

* Corresponding Author Institutional Email: m.yousefi@eng.uk.ac.ir (M. Yousefi)

TABLE 1. Methods for preparing ZnO nano-structures with different size and morphologies

Reaction	Explanation	Reference
$Zn_4SO_4(OH)_6 \cdot xH_2O \rightarrow ZnSO_4 \cdot 3Zn(OH)_2 \cdot xH_2O$ $2[ZnSO_4 \cdot 3Zn(OH)_2] \rightarrow 5ZnO + Zn_3O(SO_4)_2 + 6H_2O$ $Zn_3O(SO_4)_2 \rightarrow 3ZnO + 2SO_2 + O_2$	Chemical reaction at 70 °C to form the precursor of $Zn_4(SO_4)(OH)_6 \cdot 0.5 H_2O$, then, thermal decomposition for the synthesis of ZnO nanoparticles in air for 1 h at 825 °C, with the 92 nm nanoparticles.	[8]
$Zn_2B_6O_{11} + 3H_2O \rightarrow Zn_2B_6O_{11} + 3H_2O$ (at room temperature) $Zn_2B_6O_{11} \rightarrow (900^\circ C) 2ZnO + 3B_2O_3$	Decomposing zinc borate nanoplatelets at 900°C, average diameters of perfect spherical shape of nanoparticles was 50 nm.	[9]
$Zn(NH_3)_4^{2+} + 2OH^- \rightarrow ZnO + 4NH_3 + H_2O$	Transformation of $Zn(NH_3)_4^{2+}$ complexes as a precursor in the presence of sodium oleate and hydrazine at 80 °C, ZnO nanoparticles with 30–60 nm	[10]
$Zn(CH_3COO)_2 + 2NaOH \rightarrow Zn(OH)_2 + 2CH_3COONa$ $Zn(OH)_2 \rightarrow \text{Hydrothermal ZnO} + H_2O$	Hydrothermal method at 100-200°C for different periods from 5 - 10 h, nano-particles size of ZnO in the range of 55–110 nm	[11]
$Zn^{2+} + 2OH^- \rightarrow Zn(OH)_2$ $Zn(OH)_2 \rightarrow ZnO + H_2O$ $Zn(OH)_2 + 2OH^- + TEA \rightarrow [Zn(OH)_4]^{2-} + TEA$	Aqueous solution of zinc acetate dehydrate ($Zn(CH_3COO)_2 \cdot 2H_2O$, 0.1 M) and 2.0 mL of triethanolamine (TEA) as a surfactant; 1 M ammonia (NH_4OH) as a reduction agent. Hydrothermal treatments at 95 °C for 2 h. ZnO microcrystals with length of 2.2 μm and diameter of 1.8 μm, a single crystal wurtzite structure.	[12]
 $NH_3 \cdot H_2O \rightarrow NH_4^+ + OH^-$ $Zn^{2+} + 2OH^- \rightarrow Zn(OH)_2$ $Zn(OH)_2 + 2OH^- \rightarrow [Zn(OH)_4]^{2-}$ $Zn(OH)_2 + 4NH_3 \cdot H_2O \rightarrow [Zn(NH_3)_4]^{2+} + 2OH^- + 4H_2O$ $[Zn(NH_3)_4]^{2+} + 4H_2O \rightarrow ZnO + 3NH_4^+ + 2NH_3 \cdot H_2O$ $Zn(OH)_4^{2-} \rightarrow ZnO + H_2O + 2OH^-$	Hydrothermal process at 180°C for 20 h. uniform pencil-like crystals with the average diameter of 300 nm and length of about 10 μm	[13]
$ZnSO_4 + 2NH_4OH \rightarrow Zn(OH)_2 + (NH_4)_2SO_4 \rightarrow ZnO (s) + 4NH_3(aq) + 2H_2O(l)$	Synthesized through a novel low-temperature aqueous solution route (90–95°C) and rapid thermal processing (300-850°C). One-dimensional (1D) ZnO nanorod arrays and branched two-dimensional (2D), three-dimensional (3D) – nanoarchitectures.	[14]
$Zn(CH_3COO)_2 + H_2O \rightarrow ZnO + 2CH_3COOH$ $HOCH_2CH_2OH \leftrightarrow CH_3CHO + H_2O$ $CH_3CHO + 2AgNO_3 + H_2O \rightarrow 2Ag + 2HNO_3 + CH_3COOH$ $C_6H_{12}N_4 + 6H_2O \rightarrow 6CH_2O + 4NH_3$ $NH_3 + H_2O \rightarrow NH_4^+ + OH^-$ $Zn(CH_3COO)_2 + 2NH_4^+ + 2OH^- \rightarrow 2CH_3COONH_4 + Zn(OH)_2$ $Zn^{2+} + 2OH^- + 2H_2O \rightarrow Zn(OH)_4^{2-} + 2H^+$ $Zn(OH)_4^{2-} + 2H^+ \rightarrow ZnO_{cluster} + 3H_2O$	Fabrication of the Ag/ZnO microspheres via a “one-pot” process in ethylene glycolmedium. heating the solution to 160 °C at the rate of 5 °C/min.	[15]
$Zn_5(CO_3)_2(OH)_6 \rightarrow 5ZnO + 3H_2O \uparrow + 2CO_2 \uparrow$	The chemical growth of ZnO nanorod arrays in the solution on the ITO substrates by a two- step chemical bath deposition (CBD) method with an average of 1.83 μm in length and 87 nm in diameter. The reaction temperature from 25 to 95 °C	[16]
$CO(NH_2)_2(s) + 3H_2O(l) \rightarrow CO_2(g) + 2NH_3 \cdot H_2O(aq)$ $2NH_3 \cdot H_2O(aq) + CO_2(g) \rightarrow 2NH_4^+(aq) + CO_3^{2-}(aq)$ $NH_3 \cdot H_2O(aq) \rightarrow NH_4^+(aq) + OH^-(aq)$ $Zn^{2+}(aq) + CO_3^{2-}(aq) + 4OH^-(aq) + 3H_2O(l) \rightarrow ZnCO_3 \cdot 2Zn(OH)_2 \cdot H_2O(s)$ $ZnCO_3 \cdot 2Zn(OH)_2 \cdot H_2O(s) \rightarrow 3ZnO(s) + 3H_2O(g) + CO_2(g)$	Precipitation of the precursor using $ZnCl_2$ and Na_2CO_3 by heating; calcinations at 300-400°C.	[17]
$5ZnSO_4(aq) + 10NH_4HCO_3(aq) \rightarrow Zn_5(CO_3)_2(OH)_6(s) + 5(NH_4)_2SO_4(aq) + 8CO_2(g) + 2H_2O(l)$ $Zn_5(CO_3)_2(OH)_6(s) \rightarrow 5ZnO(s) + 2CO_2(g) + 3H_2O(g)$ $(CH_2)_6N_4 + 6H_2O \rightarrow 6HCHO + 4NH_3$ $NH_3 + H_2O \rightarrow NH_4OH$ $Zn^{2+} + 2OH^- \rightarrow ZnO + H_2O$	Mean sizes of nano-particles, ranging from 8 nm to 80 nm.	[18]
$CO(NH_2)_2(s) + 3H_2O(l) \rightarrow CO_2(g) + 2NH_3 \cdot H_2O(aq)$ $2NH_3 \cdot H_2O(aq) + CO_2(g) \rightarrow 2NH_4^+(aq) + CO_3^{2-}(aq)$ $NH_3 \cdot H_2O(aq) \rightarrow NH_4^+(aq) + OH^-(aq)$ $Zn^{2+}(aq) + CO_3^{2-}(aq) + 4OH^-(aq) + 3H_2O(l) \rightarrow ZnCO_3 \cdot 2Zn(OH)_2 \cdot H_2O(s)$ $ZnCO_3 \cdot 2Zn(OH)_2 \cdot H_2O(s) \rightarrow 3ZnO(s) + 3H_2O(g) + CO_2(g)$	The industrial preparation of ZnO nanoparticles using a stirring tank reactor containing the zinc nitrate solution under 95 °C conditions, direct precipitation method.	[19]
$5ZnSO_4(aq) + 10NH_4HCO_3(aq) \rightarrow Zn_5(CO_3)_2(OH)_6(s) + 5(NH_4)_2SO_4(aq) + 8CO_2(g) + 2H_2O(l)$ $Zn_5(CO_3)_2(OH)_6(s) \rightarrow 5ZnO(s) + 2CO_2(g) + 3H_2O(g)$ $(CH_2)_6N_4 + 6H_2O \rightarrow 6HCHO + 4NH_3$ $NH_3 + H_2O \rightarrow NH_4OH$ $Zn^{2+} + 2OH^- \rightarrow ZnO + H_2O$	direct precipitation method at room temperature; precursor dried at 100°C, and calcinations at 300, 350, 400, and 500° C. ZnO nano-particles with average crystal size of about 9.4 nm	[20]
$(CH_2)_6N_4 + 6H_2O \rightarrow 6HCHO + 4NH_3$ $NH_3 + H_2O \rightarrow NH_4OH$ $Zn^{2+} + 2OH^- \rightarrow ZnO + H_2O$	Totally 20 cycles for the deposition of ZnO nanorods at 95°C. The well-defined hexagonal facet, the side length of about 150 nm, the aspect ratio of 2:3.	[20]
$Zn^{2+} + 4NH_3 \rightarrow Zn(NH_3)_4^{2+}$ $Zn(NH_3)_4^{2+} + 2OH^- \rightarrow ZnO + 4NH_3 + H_2O$	First, reaction of the Zn ions in $Zn(NO_3)_2 \cdot 6H_2O$ solution with ammonia to form amine complexes ($Zn(NH_3)_4^{2+}$), second, reaction of the complex with OH^- to produce ZnO crystals; hydrothermal growth of the ZnO nanorods in an oven at 90°C for 1–3 h.	[21]

carbonate compound of Zn as precursor $[Zn_5(CO_3)(OH)_6]$ [23]. Depending on the concentration of the precursor, the nanostructures prepared through breakdown and recombination of ionic bonds [24] may exhibit itself in composition of ZnO particles. For instance, $ZnCl_2$ as precursor results in a mixture of ZnO and $Zn_5(OH)_8Cl_2 \cdot H_2O$ phases [22]. The presence of these phases in the final product indicates that the conversion of reactants into the desired ZnO product is not complete. However, it is established that different zinc salts have little or no effects on the crystallite size of ZnO nanoparticles [5].

Precise control of the size and shape of nanocrystals results in desired chemical and physical properties [25]. In hydrothermal synthesis, the effect of pH is crucial because OH^- is strongly related to the series of reactions that produced ZnO [26, 27]. The flower-like ZnO nanostructures are synthesized by decomposing $Zn(OH)_2$ in which the zinc nitrate is used as a precursor. The size of the ZnO is altered with pH of the solution [7]. In addition, the reaction temperature and the concentration of salt precursors play a critical role in the crystallite size [28]. There is still considerable uncertainty regarding the factors affecting end-product properties and the mechanism by which the high purity ZnO nanoparticles form within a simple and cost-effective method.

Herein, we report an innovative and simple method to synthesize ZnO nano-structures through thermal decomposition of the precursor [contain: $Zn_4(SO_4)(OH)_6 \cdot H_2O$ and ZnO] which prepared at the room temperature from $ZnSO_4$, $ZnCl_2$ and NH_4OH . The preparation procedure is to be conducted without using any organic and toxic solvents. Among many parameters affecting the nanostructures' growth, the pH of the precursor preparation is to be investigated in relation to the morphological changes of the ZnO nanostructures. Moreover, changes in dimensions as the pH changes are also expected to be observed.

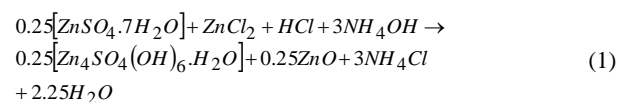
2. MATERIALS AND METHOD

All of the reagents used in these experiments including zinc sulfate heptahydrate ($ZnSO_4 \cdot 7H_2O$), zinc chloride ($ZnCl_2$), ammonium solution (NH_4OH), hydrochloric acid (HCl) and ethanol (CH_3CH_2OH) were of analytical grade. All these starting chemicals were supplied by Merck Chemicals Company (Darmstadt, Germany). Distilled water was used as solvent. Precursor powders were synthesized using the following methods:

First, $ZnCl_2$ and $ZnSO_4 \cdot 7H_2O$ were dissolved in a 2 M hydrochloric acid to form a solution with the concentration of 2 M for $ZnCl_2$ and 1 M for $ZnSO_4 \cdot 7H_2O$. After complete mixing by a magnetic

stirrer, the $NH_3 \cdot H_2O$ solution (1 M (final pH=6.12) and 2 M (final pH=11.23)) dropwise added to the solution with vigorous mixing at room temperature for 2 h. The obtained precursor, the preparation pH of which was 6.12 will be referred hereafter as "precursor #1", and that was 11.23 will be named as "precursor #2". The obtained ZnO powders after calcinations of them will be referred hereafter as "powder #1" (from precursor #1) and "powder #2" (from precursor #2).

The white precipitate precursors (1 and 2) were collected by filtration. They were then rinsed four times with deionized water and absolute ethanol; then, dried at 70 °C overnight. In the precipitation process, the ZnO powder was formed according to Equation (1):

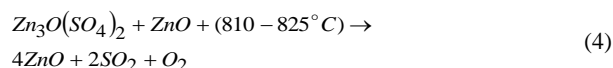
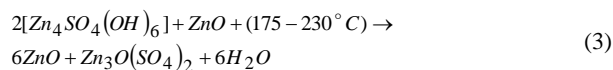
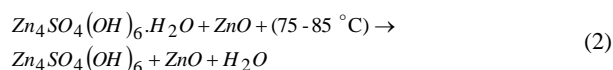


Finally, the precursors were calcinated in a muffle furnace at 875 °C for 1 h under atmospheric air pressure. The crystalline structure of the nanoparticles was characterized by X-Ray diffraction (XRD, PHILIPS, X'pert-MPD system) using $Cu K\alpha$ ($\lambda=1.54 \text{ \AA}$) radiation. The thermal behavior of the precursors was studied by thermogravimetry (TG), under air flow. 35 mg of samples were heated with the heating rate of 10 °C/min at temperature range of 35–900 °C. Infrared (IR) spectra were recorded on a Bruker tensor 27 Fourier Transform infrared (FTIR) spectrometer with RTDLATGS detector, in the range of 400 to 4000 cm^{-1} with a spectral resolution of 4 cm^{-1} in transmittance mode. The morphology and average particle size of ZnO nanoparticles were also determined with scanning electron microscopy (SEM, Tescan Vega-II) and a transmission electron microscopy (TEM, PHILIPSCM20).

3. RESULTS AND DISCUSSIONS

Figure 1 (a and b) shows the TG-DSC analysis for the prepared precursors at pH=6.12 and pH=11.23 in the air flow, respectively. Three endothermic peaks (75.5 °C and 85°C; 175.5°C and 230 °C; 810 °C and 825 °C) were found in the heating process. The peaks correspond to the crystal water decomposition reaction (Equation (2)), dehydroxylation of the basal hydroxide layer (Equation (3)), and the decomposition of sulfate groups (Equation (4)). Due to the large number of disk-like $Zn_4SO_4(OH)_6$ in the precursor at pH=11.23, temperature of dehydroxylation of the basal hydroxide layer (230 °C) was higher than the precursor at pH=6.12 (175 °C).

In the decomposition process, the white powder ZnO was formed from the following reactions [Equations (2)-(4)]:



The results confirmed the scheme of decomposition [8,14,19], including the three sequential stages, which led to the formation of ZnO as the final product.

These reactions were governed by the pH of the solution. As observed by increasing the pH, the reaction temperature of all steps during the synthesis of ZnO nano-powders shifted to the higher temperature.

Figure 2 shows X-ray diffraction patterns of the precursor #1 (a), precursor #2 (b), ZnO powder #1, (c), and the powder #2 (d). All the diffraction peaks in Figures 2a and 2b are consistent with the $\text{Zn}_4\text{SO}_4(\text{OH})_6 \cdot \text{H}_2\text{O}$ phase (JCPDS card no. 00-039-0690) and hexagonal phase ZnO which was reported in JCPDS card (No. 00-036-1451). As summarized in Table 2, the ZnO nano-rods which was prepared from the precursor synthesized at pH=6.12, displayed the stronger diffraction peaks than pH=11.23. It revealed that the nano-rods pertaining to pH=6.12 possessed well-aligned growth and high crystal quality [29-32]. Moreover, the crystallinity of ZnO nanostructures was improved after annealing.

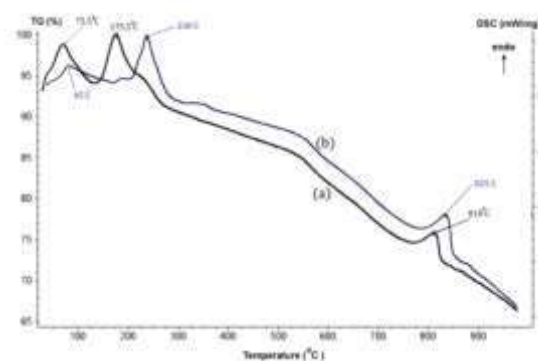


Figure 1. TGA–DSC curves of the ZnO precursors prepared at (a) pH=6 and (b) pH=11 from 35 to 900 °C

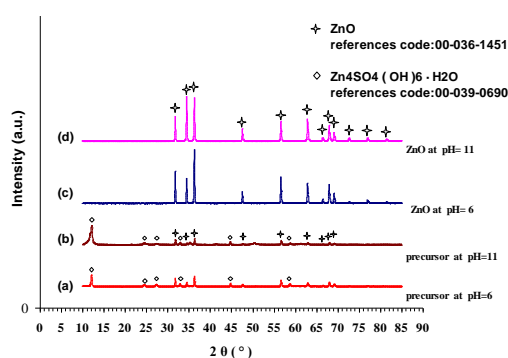


Figure 2. X-ray patterns of the precursor #1 (a), precursor #2 (b), ZnO powder #1 (c), and powder #2 (d) synthesized by direct thermal decomposition of the precursors at 875 °C for 1 h

TABLE 2. Representative X-ray of Zinc oxide powder diffraction data in the prepared precursor at pH=6.12 and pH=11.23

h	k	l	ZnO crystals in the synthesized precursor at pH= 6.12			ZnO crystals in the synthesized precursor at pH=11.23		
			d _{cal.}	d _{meas.}	Peak height (cts)	d _{cal.}	d _{meas.}	Peak height (cts)
1	1	0	2.811	2.814	431	2.810	2.814	261
0	0	2	2.601	2.603	196	2.599	2.603	90
1	0	1	2.474	2.476	518	2.472	2.475	292
1	0	2	1.910	1.911	92	1.907	1.911	39
1	1	0	1.624	1.625	310	1.624	1.624	194
1	0	3	1.477	1.477	162	1.476	1.477	77
2	0	0	1.406	1.407	52	1.406	1.407	29
1	1	2	1.378	1.378	187	1.378	1.378	92
2	0	1	1.358	1.358	110	1.358	1.358	66
0	0	4	1.303	1.301	13	1.305	1.301	3
2	0	2	1.238	1.238	26	1.239	1.238	22
1	0	4	1.184	1.181	10	1.186	1.181	9.6

Disk and hexagonal shapes of $\text{Zn}_4\text{SO}_4(\text{OH})_6\cdot\text{H}_2\text{O}$ and ZnO , respectively, were detected in the SEM images (Figure 3). The stability of zinc hydroxy-sulfate decreases in acidic conditions ($\text{pH}<7$) [33], which leads to more ZnO precipitating from the solution phase. As shown in Figure 3 (a, b) and (c, d), the amount of hexagonal rod shapes of ZnO in the precursor #1 are more than the precursor #2, which agrees well with the XRD analysis.

According to the FTIR spectra shown in Figure 4(A), the absorption peaks at 441, 597.68, 961.74, and 1125.93 cm^{-1} are attributed to SO_4^{2-} and 417 cm^{-1} is assigned to ZnO [8,34]. The peak at 769.73 cm^{-1} is the stretching mode of Zn-OH vibrations. The results of IR analyses confirmed that the produced precursor was $\text{Zn}_4\text{SO}_4(\text{OH})_6\cdot\text{H}_2\text{O}$ and ZnO , that is in agreement with the results of XRD. When the precursors were heated at $875\text{ }^\circ\text{C}$ for 1 h, they decomposed into ZnO crystallite phase (JCPDS card no. 00-036-1451) (Figure 2 c and d). In this case, the ZnO nano-crystals were hexagonal with the lattice parameters: $a = 3.24\text{ \AA}$, $b = 3.24\text{ \AA}$, $c = 5.20\text{ \AA}$ (space group= $\text{P6}_3\text{mc}$). Representative X-ray ZnO powder diffraction data are shown in Table 3. Sharp peaks indicated elevated crystallinity of ZnO . Figure 4(B) shows the FTIR spectrum of the ZnO nanopowders prepared through thermal decomposition at 875°C . The absorption band at 430.06 and 507.45 cm^{-1} (Figure 4B) are attributed to Zn-O , and the band at 3428.27 cm^{-1} is attributed to $-\text{OH}$ stretching [34]. The

band at 1635.99 cm^{-1} is due to the OH bending of water. Finally, the tiny dip in the spectra at 2369.67 cm^{-1} is due to atmospheric CO_2 [35-38]. In general, the IR peaks intensities at $\text{pH}=6.12$ are higher than those at $\text{pH}=11.23$. It could be postulated that the higher IR peaks intensity are due to the higher ZnO structures particles during the thermal decomposition [39]. The average diameter and the length of the nanorods in the powder #1 were 980 nm and $2.2\text{ }\mu\text{m}$, respectively; while, in the powder #2, the diameter and length were 760 nm and $3.3\text{ }\mu\text{m}$, respectively. Generally, the aspect ratio of the ZnO nanorods increased with the enhanced concentration of OH^- . It is worth noting that an increase in concentration of OH^- ions could partially suppress the growth of as-deposited ZnO nanocrystallines [16]. Thus, the diameter of nanorods decreased when the concentration of OH^- increased from $\text{pH } 6.12$ to 11.23 (see Figure 5).

Figures 6 and 7 show TEM images of powder #1 and powder #2, respectively. Figures 8a and 9a show that the spherical ZnO nanoparticles have a wide size distribution with the average diameter of $85\pm 5\text{ nm}$ and $112\pm 5\text{ nm}$, respectively. The Rosin-Rammler (RR) distribution function (Equation (5)) is the most commonly used equation for describing the particle size distribution (PSD) [40]:

$$Q(x) = 1 - \exp\left[-(x/d_0)^n\right] \quad (5)$$

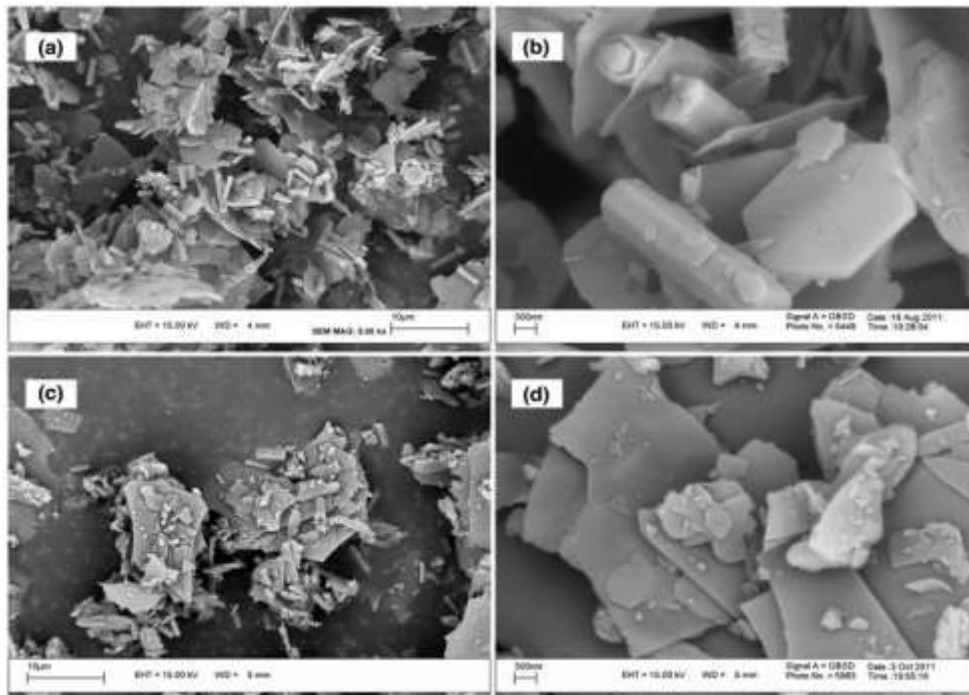


Figure 3. SEM images of the (a, b) precursor #1 (prepared at $\text{pH}=6$), and (c, d) precursor #2 (prepared at $\text{pH}=11$) at two different magnifications

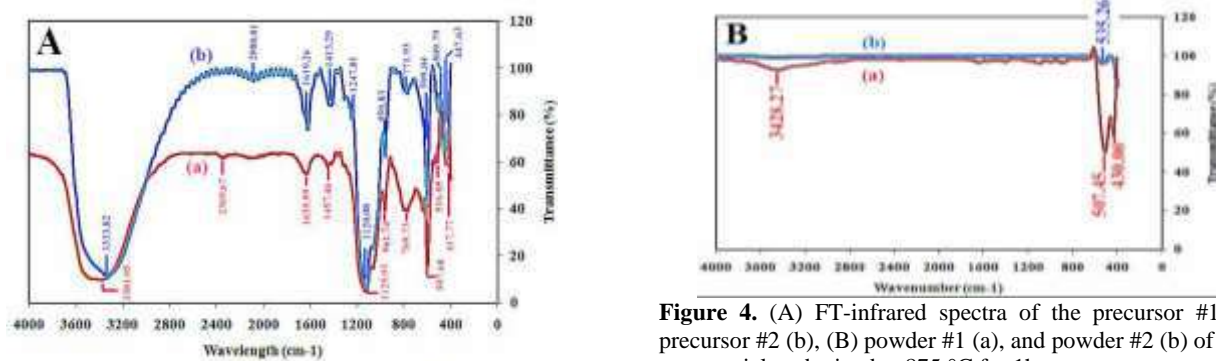


Figure 4. (A) FT-infrared spectra of the precursor #1 (a), precursor #2 (b), (B) powder #1 (a), and powder #2 (b) of ZnO nanoparticles obtained at 875 °C for 1h

TABLE 3. Representative X-ray Zinc oxide powder (#1 and #2) diffraction data

h	k	l	ZnO crystals in powder #1			ZnO crystals in powder #2		
			d cal.	d meas.	Peak Height [cts]	d cal.	d meas.	Peak Height [cts]
1	1	0	2.812	2.814	1569	2.812	2.814	1204
0	0	2	2.601	2.603	1193	2.600	2.603	2180
1	0	1	2.474	2.475	2615	2.474	2.476	2096
1	0	2	1.910	1.911	575	1.910	1.911	599
1	1	0	1.623	1.624	1284	1.623	1.625	959
1	0	3	1.476	1.477	956	1.476	1.477	1063
2	0	0	1.406	1.407	202	1.406	1.407	151
1	1	2	1.377	1.378	918	1.377	1.378	741
2	0	1	1.357	1.358	502	1.357	1.358	396
0	0	4	1.300	1.301	84	1.300	1.301	144
2	0	2	1.237	1.238	151	1.237	1.238	135
1	0	4	1.180	1.181	73	1.180	1.181	90

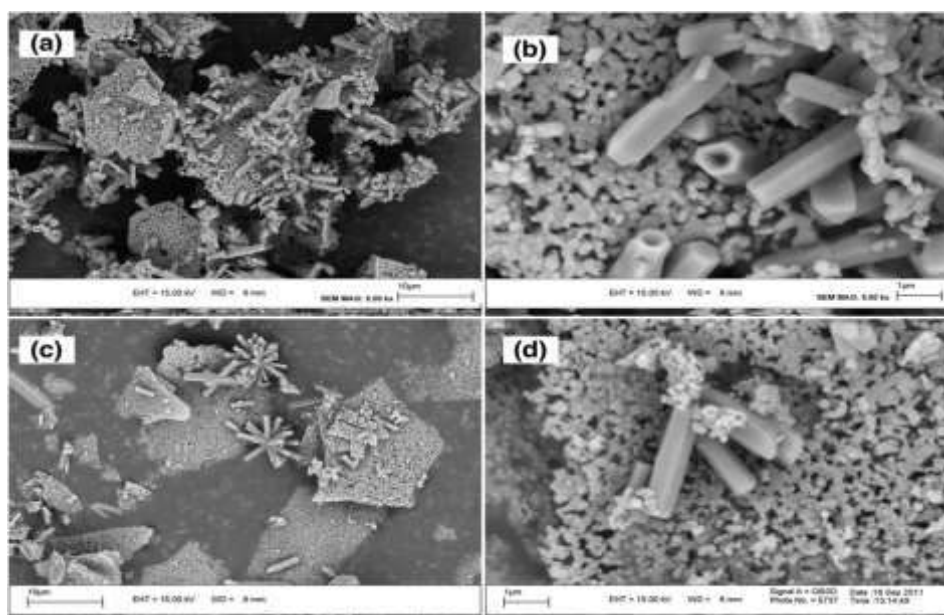


Figure 5. SEM images of (a, b) powder #1 (prepared at pH=6), and (c, d) powder #2 (prepared at pH=11) at two different magnifications

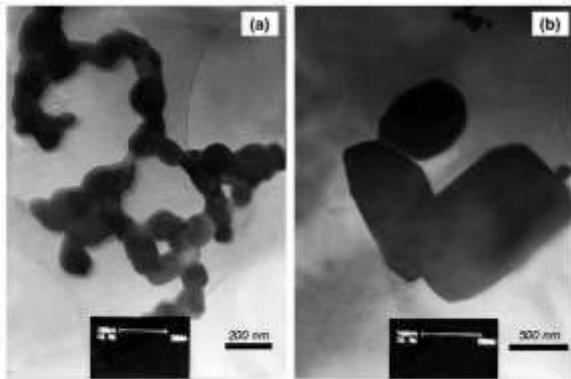


Figure 6. TEM images of the ZnO nano-architectures (powder #1)

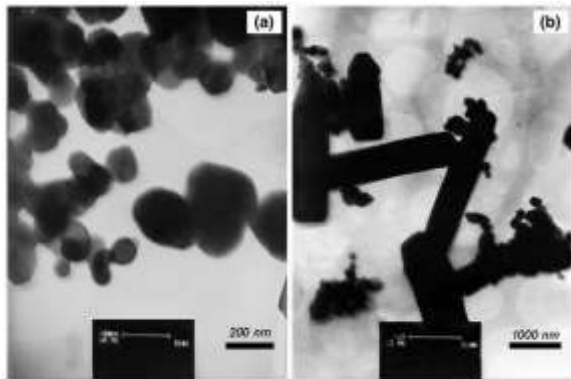


Figure 7. TEM images of the ZnO nano-architectures (powder #2)

where, x is the measured particle size, $Q(x)$ is the cumulative fraction passing function, d_0 is the size factor, and n is the spread factor. The size factor, d_0 , is a characteristic of the PSD. In the function, the size factor indicates the fineness of powder. So, the smaller d_0 , the finer is the powder. On the other hand, the spread factor, n , is a measure of the uniformity. It is larger for narrower distribution. That is, the higher the n value the more uniform is the distribution.

The parameters of the PSD of the sphere-like ZnO by using the Rosin–Rammler model is illustrated in Table 4. The factor of d_0 is 74.67 for the spheres of powder #1 while it is 106.50 for powder #2. It indicated that the average size of the sphere-like particles of the ZnO in powder #1 was lower than that of powder #2. It established a direct relationship between the reaction temperature and particle sizes. Increasing the reaction temperature leads to either an increase in the formation of nuclei, which would promote smaller particles in the end-product, or a faster rate of decomposition of zinc-hydroxo- complexes to ZnO, which results in the growth and coarsening of the end-products [33]. In this case, however, the growth of particles seems to

dominate as the temperature of the reaction is increased in this series of reactions by increasing pH value (Figure 1). According to Figures 8, 9 and Table 4, the lower n values in both powders indicate the wider particle-size distributions [40].

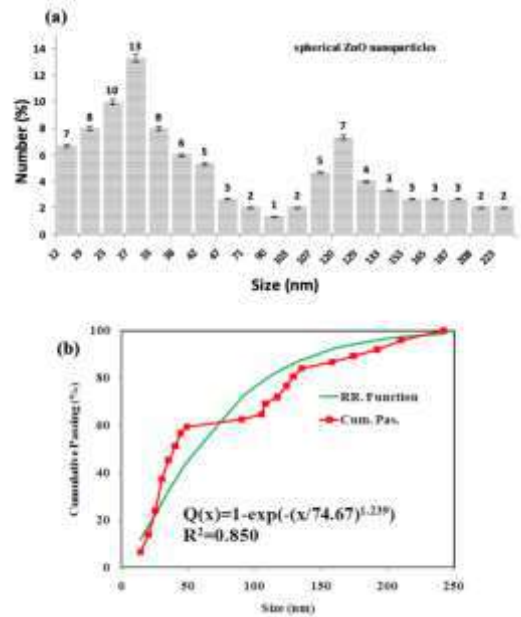


Figure 8. (a) Particle size distribution and (b) fitting of the Rosin–Rammler equation into the ZnO nanospheres of powder #1 data by using TEM analysis

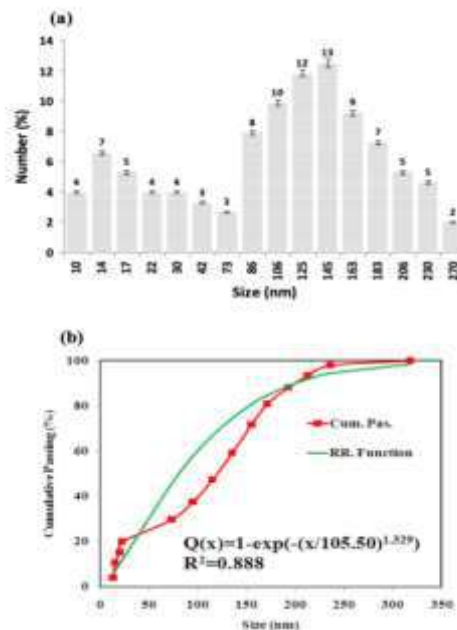


Figure 9. (a) Particle size distribution and (b) fitting of the Rosin–Rammler equation into the ZnO nanospheres of powder #2 data by using TEM analysis

TABLE 4. Rosin–Rammler equation parameters for TEM data from spherical ZnO nanoparticles

Factor	Powder	
	Powder #1	Powder #2
d_0	74.67	106.50
n	1.239	1.329

4. CONCLUSIONS

Pure ZnO nanoparticles have been successfully produced with a simple thermal decomposition method without using organic solvents, expensive raw materials, and complicated equipment. Then, the SEM and TEM images showed that the ZnO nanoparticles were of rod and spherical shapes. The following major conclusions were made.

- The sequential occurrence of ZnO nanoparticles was included nanorods and nanosphere. Nanorods were obtained in the earliest stage when $ZnCl_2$ was used as a zinc ion source, which implied that the source of Zn ions affected the morphology of the synthesized ZnO nanoparticles.
- The average particles size of ZnO nanoparticles increased with increasing pH of the reaction media.
- As the pH of the starting solution increased from 6 to 11, the reaction temperature of all steps during the synthesis of ZnO nanopowders including the water decomposition, dehydroxylation and decomposition of sulfate groups were shifted to the higher amounts.
- A direct relationship was observed between the reaction temperature and particle sizes. As if, raising the reaction temperature increased the average particle size of ZnO.
- The diffraction peaks decreased in intensity with the increasing pH value.

Finally, the facile protocol can be proposed for synthesis of zinc oxide nano-materials with rod and spherical shapes. Again, future programs have been designed to control the operational parameters to obtain ZnO nano-structures with desired size, shape, and alignment.

5. ACKNOWLEDGEMENTS

This work was supported by the science-based company, Engineers of Nano & Bio Advanced Company (ENBASCo).

6. REFERENCES

1. Gondal, M.A., Drmosh, Q.A., Yamani, Z.H. and Saleh, T.A., "Synthesis of ZnO_2 nanoparticles by laser ablation in liquid and

- their annealing transformation into ZnO nanoparticles", *Applied Surface Science*, Vol. 256, (2009), 298-304, doi: [10.1016/j.apsusc.2009.08.019](https://doi.org/10.1016/j.apsusc.2009.08.019)
2. [2] Bigdeli, F. and Morsali, A., "Synthesis ZnO nanoparticles from a new Zinc(II) coordination polymer precursor", *Materials Letters*, Vol. 64, (2010), 4-5, doi: [10.1016/j.matlet.2009.09.038](https://doi.org/10.1016/j.matlet.2009.09.038)
3. [3] Music, S., Drag, D., Popovic, S. and Ivanda, M., "Precipitation of ZnO particles and their properties", *Materials Letters*, Vol. 59, (2005), 2388-2393, doi: [10.1016/j.matlet.2005.02.084](https://doi.org/10.1016/j.matlet.2005.02.084)
4. Janet Priscilla, S., Andria Judi, V., Daniel R. and Sivaji, K., "Effects of Chromium Doping on the Electrical Properties of ZnO Nanoparticles", *Emerging Science Journal*, Vol. 4, (2020), 82-88, doi: [10.28991/esj-2020-01212](https://doi.org/10.28991/esj-2020-01212)
5. Shaba, E.Y., Jacob, J.O., Tijani, J.O. and Suleiman, M.A.T., "A critical review of synthesis parameters affecting the properties of zinc oxide nanoparticle and its application in wastewater treatment", *Applied Water Science*, Vol. 11, (2021), 1-41, doi: [10.1007/s13201-021-01370-z](https://doi.org/10.1007/s13201-021-01370-z)
6. Durguti, V., Aliu, S., Laha, F. and Feka, F., "Determination of Iron, Copper and Zinc in the Wine by FAAS", *Emerging Science Journal*, Vol. 4, (2020), 411-417, doi: [10.28991/esj-2020-01240](https://doi.org/10.28991/esj-2020-01240)
7. Heidari, A., Younesi, H. and Zinatizadeh, A.A.L., "Controllable Synthesis of Flower-like ZnO Nanostructure with Hydrothermal Method", *International Journal of Engineering Transactions B: Applications*, Vol. 22, (2009), 283-290.
8. Darezereshki, E., Alizadeh, M., Bakhtiari, F., Schaffie, M. and Ranjbar, M., "A novel thermal decomposition method for the synthesis of ZnO nanoparticles from low concentration $ZnSO_4$ solutions", *Applied Clay Science*, Vol. 54, (2011), 107-111, doi: [10.1016/j.clay.2011.07.023](https://doi.org/10.1016/j.clay.2011.07.023)
9. Tian, Y., Ma, H., Shen, L., Wang, Z., Qu, Y. and Li, Sh., "Novel and simple synthesis of ZnO nanospheres through decomposing zinc borate nanoplatelets" *Materials Letters*, Vol. 63, (2009), 1071-1073, doi: [10.1016/j.matlet.2009.02.009](https://doi.org/10.1016/j.matlet.2009.02.009)
10. Li, M., Bala, H., Lv, X., Ma, M., Sun, F., Tang, L. and Wang, Z., "Direct synthesis of monodispersed ZnO nanoparticles in an aqueous solution", *Materials Letters*, Vol. 61, (2007), 690-693, doi: [10.1016/j.matlet.2006.05.043](https://doi.org/10.1016/j.matlet.2006.05.043)
11. Ismail, A.A., El-Midany, A., Abdel-Aal, E.A. and El-Shall, H., "Application of statistical design to optimize the preparation of ZnO nanoparticles via hydrothermal technique", *Materials Letters*, Vol. 59, (2005), 1924-1928, doi: [10.1016/j.matlet.2005.02.027](https://doi.org/10.1016/j.matlet.2005.02.027)
12. Zeng, Y., Zhang, T. and Qiao, L., "Preparation and gas sensing properties of the nutlike ZnO microcrystals via a simple hydrothermal route", *Materials Letters*, Vol. 63, (2009), 843-846, doi: [10.1016/j.matlet.2009.01.012](https://doi.org/10.1016/j.matlet.2009.01.012)
13. Dai, K., Zhu, G, Liu, Z., Liu, Q., Chen, Z. and Lu, L., "Facile preparation and growth mechanism of zinc oxide nanopencils", *Materials Letters*, Vol. 67, (2012), 193-195, doi: [10.1016/j.matlet.2011.09.079](https://doi.org/10.1016/j.matlet.2011.09.079)
14. Lupan, O., Chow, L., Chai, G., Roldan, B., Naitabdi, A., Schulte, A. and Heinrich, H., "Nanofabrication and characterization of ZnO nanorod arrays and branched microrods by aqueous solution route and rapid thermal processing", *Materials Science and Engineering B*, Vol. 145, (2007), 57-66, doi: [10.1016/j.mseb.2007.10.004](https://doi.org/10.1016/j.mseb.2007.10.004)
15. Tian, C., Li, W., Pan, K., Zhang, Q., Tian, G., Zhou, W. and Fu, H., "One pot synthesis of Ag nanoparticle modified ZnO microspheres in ethylene glycol medium and their enhanced photocatalytic performance", *Journal of Solid State Chemistry*, Vol.183, (2010), 2720-2725, doi: [10.1016/j.jssc.2010.09.020](https://doi.org/10.1016/j.jssc.2010.09.020)

16. Lee, Y.M. and Yang, H.W., "Optimization of processing parameters on the controlled growth of ZnO nanorod arrays for the performance improvement of solid-state dye-sensitized solar cells", *Journal of Solid State Chemistry*, Vol. 184, (2011), 615-623, doi: [10.1016/j.jssc.2011.01.021](https://doi.org/10.1016/j.jssc.2011.01.021)
17. Han, Y.X., Ding, Y.Z., Yin, W.Z. and Ma, Z.X., "Preparation of homogeneous ZnO nanoparticles via precipitation-pyrolysis with $ZnS(CO_3)_2(OH)_6$ as precursor", *Transactions Nonferrous Metals Society of China*, Vol. 16, (2006), 1205-1212, doi: [10.1016/S1003-6326\(06\)60402-0](https://doi.org/10.1016/S1003-6326(06)60402-0)
18. Wang, Y., Zhang, Ch., Bi, S. and Luo, G., "Preparation of ZnO nanoparticles using the direct precipitation method in a membrane dispersion micro-structured reactor", *Powder Technology*, Vol. 202, (2010), 130-136, doi: [10.1016/j.powtec.2010.04.027](https://doi.org/10.1016/j.powtec.2010.04.027)
19. Wang, Y., Zhang, C., Bi, S. and Luo, G., "Preparation of ZnO nanoparticles using the direct precipitation method in a membrane dispersion micro-structured reactor", *Powder Technology*, Vol. 202, (2010), 130-136, doi: [10.1016/j.powtec.2010.04.027](https://doi.org/10.1016/j.powtec.2010.04.027)
20. Gao, X.D., Li, X.M., Yu, W.D., Li, L. and Qiu, J.J., "Seed layer-free synthesis and characterization of vertically grown ZnO nanorod array via the stepwise solution route", *Applied Surface Science*, Vol. 253, (2007), 4060-4065, doi: [10.1016/j.apsusc.2006.09.002](https://doi.org/10.1016/j.apsusc.2006.09.002)
21. Lee, D., Yoo, M., Seo, H., Tak, Y., Kim, W.G., Yong, K., Rhee, S.W. and Jeon, S., "Enhanced mass sensitivity of ZnO nanorod-grown quartz crystal microbalances", *Sensors and Actuators B*, Vol. 135, (2009), 444-448, doi: [10.1016/j.snb.2008.10.026](https://doi.org/10.1016/j.snb.2008.10.026)
22. Gusattia, M., Barrosoa, G.S., Maduro de Camposb, C.E., Souza, D.A. and Rosário, J.A., "Effect of Different Precursors in the Chemical Synthesis of ZnO Nanocrystals", *Materials Research*, Vol. 14, (2011), 264-267, doi: [10.1590/S1516-14392011005000035](https://doi.org/10.1590/S1516-14392011005000035)
23. Alhawi, T, Rehana, M, York, D and Lai, X., "Hydrothermal Synthesis of Zinc Carbonate Hydroxide Nanoparticles", *Procedia Engineering*, Vol. 102, (2015), 356 - 361, doi: [10.1016/j.proeng.2015.01.158](https://doi.org/10.1016/j.proeng.2015.01.158)
24. Trang, G.T.T., Linh, N.H., Linh, N.T.T. and P. H. Kien, "The Study of Dynamics Heterogeneity in SiO_2 Liquid", *HighTech and Innovation Journal*, Vol. 1, (2020), 1-7, doi: [10.28991/HIJ-2020-01-01-01](https://doi.org/10.28991/HIJ-2020-01-01-01)
25. Gharibshahian, E., "The Effect of Polyvinyl Alcohol Concentration on the Growth Kinetics of $KTiOPO_4$ Nanoparticles Synthesized by the Co-precipitation Method", *HighTech and Innovation Journal*, Vol. 1, (2020), 187-193, doi: [10.28991/HIJ-2020-01-04-06](https://doi.org/10.28991/HIJ-2020-01-04-06)
26. Jaejin, S, Seonghoon, B., Jonghyuck, L. and Sangwoo, L., "Role of OH⁻ in the low temperature hydrothermal synthesis of ZnO nanorods", *Journal of Chemical Technology and Biotechnology*, Vol. 83, (2008), 345-350, doi: [10.1002/jctb.1817](https://doi.org/10.1002/jctb.1817)
27. Zare, E., Pourseyedi, Sh., Khatami, M. and Darezereshki, E., "Simple biosynthesis of zinc oxide nanoparticles using nature's source, and it's in vitro bio-activity", *Journal of Molecular Structure*, Vol. 1146, (2017), 96-103, doi: [10.1016/j.molstruc.2017.05.118](https://doi.org/10.1016/j.molstruc.2017.05.118)
28. Purwaningsih, S.Y., Zainuri, M., Triwikantor, T., Pratapa, S. and Darminto, D., "Structural, Optical and Defect State Analyses of ZnO Nanoparticle Films", *International Journal of Engineering Transactions B: Applications*, Vol. 33, (2020), 852-860, doi: [10.5829/ije.2020.33.05b.17](https://doi.org/10.5829/ije.2020.33.05b.17)
29. Liang, H.Q., Pan, L.Z. and Liu, Z.J., "Synthesis and photoluminescence properties of ZnO nanowires and nanorods by thermal oxidation of Zn precursors", *Materials Letters*, Vol. 62, (2008), 1797-1800, doi: [10.1016/j.matlet.2007.10.010](https://doi.org/10.1016/j.matlet.2007.10.010)
30. Li, Z., Huang, X., Liu, J., Li, Y. and Li, G., "Morphology control and transition of ZnO nanorod arrays by a simple hydrothermal method", *Materials Letters*, Vol. 62, (2008), 1503-1506, doi: [10.1016/j.matlet.2007.09.011](https://doi.org/10.1016/j.matlet.2007.09.011)
31. Wang, M., Na, E.K., Kim, J.S., Kim, E.J., Hahn, S.H., Park, C. and Koo, K.K., "Photoluminescence of ZnO nanoparticles prepared by a low-temperature colloidal chemistry method", *Materials Letters*, Vol. 61, (2007), 4094-4096, doi: [10.1016/j.matlet.2007.01.026](https://doi.org/10.1016/j.matlet.2007.01.026)
32. Chang, W.Y., Fang, T.H., Weng, C.I. and Yang, S.S., "Flexible piezoelectric harvesting based on epitaxial growth of ZnO", *Applied Physics A: Materials Science & Processing*, Vol. 102, (2011), 705-711, doi: [10.1007/s00339-010-5962-z](https://doi.org/10.1007/s00339-010-5962-z)
33. Moezzi, A., Cortie, M. and McDonagh A., "Aqueous pathways for the formation of zinc oxide nanoparticles", *Dalton Transactions.*, Vol. 40, (2011), 4871-4878, doi: [10.1039/C0DT01748E](https://doi.org/10.1039/C0DT01748E)
34. Darezereshki, E., Behrad Vakylabad, A. and Koohestani, B., "A Hydrometallurgical Approach to Produce Nano-ZnO from Electrical Arc Furnace Dusts", *Mining, Metallurgy & Exploration*, (2021), 1-11, doi: [10.1007/s42461-021-00412-z](https://doi.org/10.1007/s42461-021-00412-z)
35. [35] Darezereshki, E., "One-step synthesis of hematite (α - Fe_2O_3) nano-particles by direct thermal-decomposition of maghemite", *Materials Letters*, Vol. 65, (2011), 642-645, doi: [10.1016/j.matlet.2010.11.030](https://doi.org/10.1016/j.matlet.2010.11.030)
36. Darezereshki, E., "Synthesis of maghemite (γ - Fe_2O_3) nanoparticles by wet chemical method at room temperature", *Materials Letters*, Vol. 64, (2010), 471-472, doi: [10.1016/j.matlet.2010.03.064](https://doi.org/10.1016/j.matlet.2010.03.064)
37. Mostafaei, A. and Zolriasatein, A., "Synthesis and characterization of conducting polyaniline nanocomposites containing ZnO nanorods", *Progress in Natural Science: Materials International*, Vol. 22, No. 4, (2012), 273-280, doi: [10.1016/j.pnsc.2012.07.002](https://doi.org/10.1016/j.pnsc.2012.07.002)
38. Darezereshki, E. and Bakhtiari, F., "A novel technique to synthesis of tenorite (CuO) nanoparticles from low concentration $CuSO_4$ solution", *Journal of Mining and Metallurgy, Section B: Metallurgy*, Vol. 47, No. 1, (2011), 73-78, doi: [10.2298/JMMB1101073D](https://doi.org/10.2298/JMMB1101073D)
39. Koohestani, B., Darban, A.K., Mokhtari, P., Darezereshki, E., Yilmaz, E., and Yilmaz, E., "Influence of hydrofluoric acid leaching and roasting on mineralogical phase transformation of pyrite in sulfidic mine tailings", *Minerals*, Vol. 10, No. 6, (2020), 513-527, doi: [10.3390/min10060513](https://doi.org/10.3390/min10060513)
40. Darezereshki, E., Bakhtiari, F., Alizadeh, M., Behrad Vakylabad, A. and Ranjbar, M., "Direct thermal decomposition synthesis and characterization of hematite (α - Fe_2O_3) nanoparticles", *Materials Science in Semiconductor Processing*, Vol. 15, (2012), 91-97, doi: [10.1016/j.mssp.2011.09.009](https://doi.org/10.1016/j.mssp.2011.09.009)

Persian Abstract

چکیده

نانوذرات اکسید روی از طریق فرایند تجزیه حرارتی مستقیم پیش ماده [شامل: ZnO و $\text{Zn}_4(\text{SO}_4)(\text{OH})_6\cdot\text{H}_2\text{O}$] در هوا به مدت ۱ ساعت و در دمای ۸۷۵ درجه سانتی‌گراد سنتز شدند. مقدار pH محلول از طریق افزودن محلول $\text{NH}_3\cdot\text{H}_2\text{O}$ روی دو مقدار ۶ و ۱۱ تنظیم شد. مشخصه یابی نمونه‌ها با استفاده از آنالیز پراش پرتو ایکس (XRD)، طیفسنجی مادون قرمز (FT-IR)، میکروسکوپ الکترونی روبشی (SEM) و میکروسکوپ الکترونی عبوری (TEM) انجام شد. نتایج نشان داد نانو ذرات خالص اکسید روی، با دو مورفولوژی کروی و میله‌ای، به ترتیب در محلول‌های کلریدی و سولفاتی تشکیل شدند. میانگین قطر نانوذرات کروی ZnO که از تجزیه حرارتی پیش ماده تهیه شده در $\text{pH} = 6$ سنتز شد، حدود 5 ± 85 نانومتر بود، در حالی که نانومیله‌های ZnO به طور میانگین دارای قطر ۹۸۰ نانومتر و طول ۲/۲ میکرومتر بودند. در شرایط $\text{pH} = 11$ نانومیله‌ها دارای قطر میانگین ۷۶۰ نانومتر و طول ۳/۳ میکرومتر بوده، در حالی که اندازه ذرات متوسط نانوذرات با مورفولوژی کروی حدود 5 ± 112 نانومتر بود. تصاویر حاصل از SEM و TEM حضور نانو ذرات میله‌ای و کروی را نشان داد. با افزایش pH محلول از ۶ به ۱۱ دمای واکنش مربوط به تمام مراحل ساخت نانوذرات ZnO افزایش یافت. با توجه به نتایج حاصل، روش حاضر می‌تواند به عنوان روشی ارزان و مناسب برای تولید نانوذرات ZnO خالص با استفاده از محلول‌های ZnSO_4 و ZnCl_2 و بدون استفاده از هرگونه مواد شیمیایی سمی و آلی اعمال شود.



Selective Harmonic Elimination of a Multilevel Voltage Source Inverter using Whale Optimization Algorithm

M. Alemi-Rostami^{*a}, G. Rezazadeh^b

^a Department of Electrical Engineering, Aerospace Research Institute (ARI) of Ministry of Science, Research and Technology, Tehran, Iran

^b Department of Electrical Engineering, Sharif university of Technology, Tehran, Iran

PAPER INFO

Paper history:

Received 14 April 2021

Received in revised form 01 June 2021

Accepted 06 July 2021

Keywords:

Genetic Algorithm

Multilevel Inverter

Optimization Method

Selective Harmonic Elimination

Whale Optimization Algorithm

Pulse Width Modulation

ABSTRACT

In this paper, the whale optimization algorithm is proposed for harmonics elimination in a cascaded multilevel inverter. In selective harmonic elimination pulse width modulation, the selected low-order harmonics are eliminated by solving nonlinear equations, while the fundamental of output waveform is adjusted to a desired value. In this paper, whale optimization algorithm is applied to a 7-level cascaded H-bridge inverter to solve the equations. Also, it was validated by experimental results, since this algorithm has an ability to search in entire solution space, the probability of catching a global best solution is very high. This method has higher accuracy and probability of convergence than the genetic algorithm. The optimization and comparison of whale optimization algorithm and genetic algorithm have been done in MATLAB software. A 1 kW prototype of this converter is built and the results are presented. The effectiveness and the theoretical analysis of this method are verified through both simulation and experimental results.

doi: 10.5829/ije.2021.34.08b.11

1. INTRODUCTION

Multilevel voltage source inverters (MVSIs) have been widely applied in medium voltage (MV) and high power industry applications such as AC power supply, motor drives, HVDC, interconnection of distributed generation (DG) units to a grid and wind energy systems [1-3]. MVSIs have several advantages compared to the traditional two-level inverter such as low harmonic contents, low switching stresses and losses, low electromagnetic interface (EMI), and high system efficiency. Owing to have low total harmonic distortion (THD), MVSIs can follow the target signal more accurately. Moreover, the smaller harmonic filters are required and the insulation requirements are reduced [4]. For improving MVSIs performance and quality of the output waveforms, different methods have been proposed such as sinusoidal pulse Width modulation (SPWM) [5], optimal minimization of THD [6, 7], space-vector modulation (SVM) [8], and selective harmonic elimination pulse width modulation (SHEPWM) [9, 10].

SHEPWM has been paid a great attention for its ability to eliminate the specific low-order harmonic contents, and to leave triple harmonics uncontrolled to facilitate the advantages of the three phase system. Several works have been done to solve the nonlinear equations related to SHEPWM with different optimization methods such as genetic algorithm [11, 12], particle swarm optimization (PSO) [13], ant colony systems [14]. In these works, the objective function is defined and minimized. GA is widely used which is simpler and more applicable.

One of the best methods for solving optimization problems is whale optimization algorithm (WOA) which is proposed by several researchers [15-18]. Whale optimization algorithm is inspired by the bubble-net hunting strategy of the humpback whale. The trajectory path of the bubble-net attack mechanism of WOA is based on the shrinking circling mechanism on the spiral track. As a result, the probability of catching the global best solution is very high as it covers total space. The motion of the whale in the WOA is divided in two parts:

*Corresponding Author Institutional Email: alemi@ari.ac.ir (M. Alemi-Rostami)

A linear direction (in shrinking part) with 50% probability and circled spiral direction by other 50% probability. Selection between these two parts is done or decided by a random number.

Some valuable reaserch works are published related to the presented work in the current. WOA is implemented to decide optimum switching angles for three-phase Voltage Source Inverter of eliminating some high order harmonics while providing the required voltage [19]. Moreover, authors show that WOA gives faster and more accurate results in terms of decreasing THD than PSO algorithm in SHE applications. Unfortunately, no experimental results is reported in this paper to approve the claim. The selective harmonic elimination of an eleven level inverter using WOA was investigated by Dash et al. [16] and the results are satisfying the proposed method. However, the obtained results are not compared with the results from using another optimization method. A modified WOA is presented for harmonic elimination of a 11-level three-phase VSI [17]. The results showed a superior performance compared to the simple WOA results. An original asymmetrical half-cascaded multilevel inverter structure that its half-cascaded part has operated as zero-positive step creator, and then, H-bridge part provides the perfect staircase quasi-sinusoidal voltage [18]. The novel VSI has been optimized using WOA.

In this study, WOA is utilized to solve the nonlinear equations to eliminate the low-order harmonics while adjusting the fundamental harmonic to a desired value. The optimization results with WOA including the probability of catching a global minimum and optimum value of objective functions in three-phase and single-phase Cascaded Half-Bridge (CHB) inverters are compared with the results of GA. The results show the superiority of WOA to GA.

The features of the presented research work can be listed as:

- 1) Investigating a 7-level VSI structure,
- 2) Implementing selective harmonic elimination using WOA,
- 3) Comparing the WOA results with the GA results using Cumulative Distribution Function (CDF),
- 4) Investigating the WOA results for single-phase and three-phase MVSI structures,
- 5) Obtaining satisfying results for harmonic elimination using WOA in the proposed structures,
- 6) Implementing the optimum inverter to obtain the experimental results for evaluation purpose.

The main goal of presenting all the aforementioned features in the current study is to find an appropriate approach to reduce the size of the output filter for the MVSI especially in ultrasonic converter application.

The rest of this paper is organized as follows. The whale optimization algorithm is described at section II. section III contains the problem formulation for

multilevel inverters, the optimization results, and comparison of WOA with GA. Section V reports the experimental results of WOA algorithm for single-phase and three-phase 7-level cascaded H-bridge inverters.

2. METHOD

2. 1. Whale Optimization Analysis

One of the nature-inspired meta-heuristic algorithm, which can be utilized in optimization problems, is whale optimization algorithm (WOA) that mimics the hunting behavior of humpback whales. The foraging behavior of these whales is called bubbled net feeding method. In this foraging method, the whale creates distinctive bubbles along a “9” shaped path around the prey and swims up toward the surface to capture it as illustrated in Figure 1. The process of hunting consists of three steps, 1) encircling, 2) bubble-net attacking, and 3) searching of a prey. In the following section, the mathematical model is briefly discussed.

2. 1. 1. Encircling of a Prey

The humpback whale can recognize the location of a prey and encircle it. After defining the best search agent, the whale tries to move toward this best agent. The mathematical description of this step is as follows [18]:

$$\vec{D} = |\vec{C} \cdot \vec{X}^*(i) - \vec{X}(i)| \tag{1}$$

$$\vec{X}(i + 1) = |\vec{X}^*(i) - \vec{A} \cdot \vec{D}| \tag{2}$$

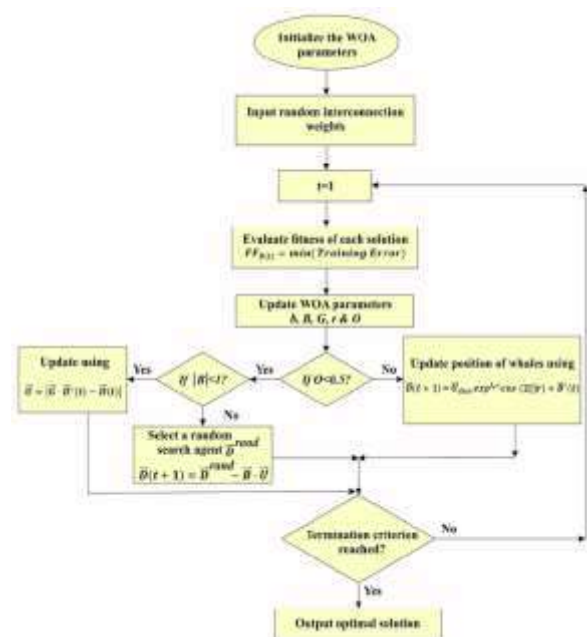


Figure 1. Flowchart of whale optimization algorithm for optimally selecting [20]

where i is the iteration's number, \vec{A} and \vec{C} are coefficient vectors, \vec{X} is the position vector, \vec{X}^* is the position of the best agent, $||$ is the absolute value of the vector, and \cdot is an element by element multiplication. The vectors \vec{A} and \vec{C} are obtained as follows [18]:

$$\vec{A} = 2\vec{a} \cdot \vec{r} - \vec{a} \tag{3}$$

$$\vec{C} = 2\vec{r} \tag{4}$$

where \vec{a} is linearly decreased from 2 to 0 over the iteration and \vec{r} is a random vector in $[0, 1]$.

2. 1. 2. Bubble-net Attack Method (Exploitation Phase)

The whale swims around the prey within a shrinking circle and along a “9” shaped path simultaneously with 50% percent probability. The mathematical model for this attacking behavior is as follows [18]:

$$\vec{X}(i+1) = \begin{cases} \vec{X}^*(i) - \vec{A} \cdot \vec{D} & \text{if } p < 0.5 \\ \vec{D} \cdot e^{bl} \cdot \cos(2\pi l) + \vec{X}^*(i) & \text{if } p > 0.5 \end{cases} \tag{5}$$

where \vec{D} indicates the distance between the whale to the prey (best agent obtained so far), b is a constant value, and l is a random number in $[-1, 1]$.

2. 1. 3. Search for Prey (Exploration Phase)

According to the random coefficient vector \vec{A} , WOA forces to search on a global level. When $|\vec{A}| > 1$, humpback whale starts foraging in the entire region. This step mathematically described as follows [18]:

$$\vec{D} = |\vec{C} \cdot \vec{X}_{rand}(i) - \vec{X}(i)| \tag{6}$$

$$\vec{X}(i+1) = \vec{X}_{rand}(i) - \vec{A} \cdot \vec{D} \tag{7}$$

where \vec{X}_{rand} is a random position vector (a random whale) chosen from the current population. The WOA starts with a set of random solution. In every iteration, the search agents update their positions based on a randomly chosen search agent or the best solution so far.

2. 2. Harmonic Elimination using a WOA

2. 2. 1. Problem Formulation

In this paper, without loss of generality, single-phase and three-phase 7-level CHB inverters are chosen as a case study which consists of three series connected H-bridge cells (shown in Figure 2) in each phase. Three different voltage levels ($-V_{dc}, 0$, and V_{dc}) can be generated by each cell. In order to implement SHEPWM, three switching angles (α_1, α_2 , and α_3) are utilized as illustrated in Figure 3. The frequency of each cell is equal to the fundamental frequency (f_s). By these definitions, the output phase voltage of the 7-level CHB inverter (V_o) can be expressed using Fourier Transform as follows [17]:

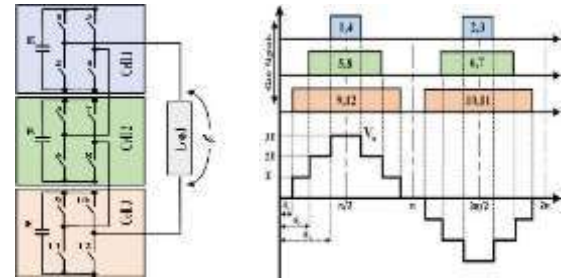


Figure 2. CHB inverter (a) a 7-level CHB single-phase inverter structure (b) switching pattern of SHEPWM for a 7-level CH.

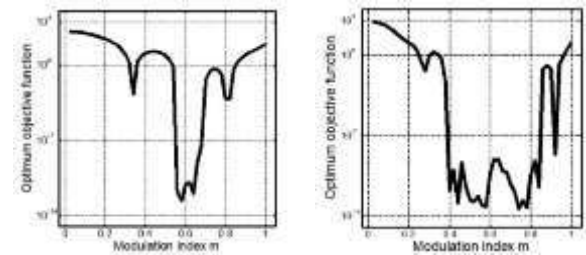


Figure 3. Optimum value of the objective function versus modulation index m (a) F_{SP} (b) F_{TP} .

$$V_o = \sum_{n=1}^{\infty} (A_n \cos(n\omega t) + B_n \sin(n\omega t)) \tag{8}$$

where ω is the output angular frequency, and A_n and B_n are the coefficients of Fourier series. As it is shown in Figure 3, it can be concluded that the even harmonics are absent owing to the symmetry of the waveforms. Consequently, the coefficient A_n is zero. Therefore, Equation (8) declines to [18]:

$$V_o = \sum_{n=1}^{\infty} B_n \sin(n\omega t) \tag{9}$$

The coefficient B_n can be calculated as Equation (9) [16]:

$$B_n = \left(\frac{4E}{n\pi}\right) \sum_{k=1}^3 \cos(n\alpha_k), \quad n = \text{odd} \tag{10}$$

where E is the DC bus voltage of each cell, and α_k is the switching angle of k^{th} cell. The modulation index is defined to be a representative value of the fundamental harmonic V_1 [17]:

$$m = \frac{\pi V_1}{12E} \quad (0 \leq m \leq 1) \tag{11}$$

In this study, the switching angles are found such that low-order harmonics are eliminated and the magnitude of the fundamental harmonic reaches to the desired value. In a single-phase CHB, the low-order harmonics are third and fifth harmonics. Therefore, a general objective function $F_{SP}(\alpha)$ of the optimization problem is defined as follows:

$$F_{SP} = \left|100 \frac{B_{1-m}}{m}\right|^4 + \frac{1}{3} \left|50 \frac{B_3}{B_1}\right|^2 + \frac{1}{5} \left|50 \frac{B_5}{B_1}\right|^2 \tag{12}$$

In three-phase CHB, the triple harmonics are not existed in line voltages. In this case, the objective function can be written to eliminate the fifth and seventh harmonics as below:

$$F_{TP} = \left| 100 \frac{B_1 - m}{m} \right|^4 + \frac{1}{5} \left| 50 \frac{B_5}{B_1} \right|^2 + \frac{1}{7} \left| 50 \frac{B_7}{B_1} \right|^2 \quad (13)$$

The objective function F_{SP} and F_{TP} are subjected to the following constraint:

$$0 \leq \alpha_k \leq \frac{\pi}{2}, \quad k = 1,2,3 \quad (14)$$

According to Equations (12) and (13), for any variation of fundamental component form desired value lower than %1, the first term gets a negligible value. Although, if its variation is more than %1, the first term of these equations fines it by a power of 4. Other terms neglect harmonics under 2 % of the fundamental. If any harmonic gets value more than this limit, the objective function fines it by power of 2. Finally, by weighting each harmonic by inverse of its order, elimination of low-order harmonics gets higher importance. The more detailed mathematical model for harmonic elimination using WOA is presented in previous published research works [15-18].

3. RESULTS

3.1. Solving SHEPWM Equations As mentioned in the previous section, the whales search for the prey with random initial positions. Then they move toward the best or random search agent in the search area. The WOA is considered as a global optimizer because it has the exploring and exploiting abilities. In addition, this algorithm defines a search space in the nearby of the best solution which allows other search agents to exploit the current best solution inside this domain. To solve the optimization problem discussed in the previous section, WOA is written in MATLAB software. The size of population is 100. For each run the number of iteration is 100.

Figure 3 shows the optimum objective functions for different values of m by step of 0.01 applied in 7-level single-phase and three-phase CHB inverters. The objective functions are defined in a way that the variation of fundamental harmonic from desired value is lower than 1% and two low-order harmonics are lower than 2% of the fundamental. As a result, if the objective function has a low value, the result is satisfactory and acceptable. As it is illustrated in Figure 3, for a range of [0.3, 0.85], the optimum objective functions have small values. Therefore, WOA can successfully find the optimum switching angles. For other range of m , the SHEPWM does not have perfect results.

Optimum switching angles are illustrated in Figure 4. As the desired fundamental harmonic increases (m

increases), switching angles are shifted to the origin so that regulates the fundamental harmonic to desired value. For low value of modulation index, all switching angles have a value close to 90 degree. In addition, as it is illustrated in Figure 4, for all set of switching angles the constraint of optimization problem is satisfied. Therefore, it can be concluded that WOA is a reliable algorithm for solving SHE equations.

Low-order harmonics and THD level are calculated by Equation (10) and the results are depicted in Figure 5. It is expected that fundamental harmonic regulates completely due to. using a penalty for first harmonic. Other harmonics and THD level have a negligible value when objective function is closed to zero. Although, WOA is not able to eliminate harmonics in a low value of m .

3.2. Comparison

As mentioned in the previous section, WOA is considered as a global optimizer. In order to show this ability, results of WOA algorithm are compared with the results of GA for solving SHEPWM equations. Figure 6(a) shows the optimum values of F_{SP} obtained by these algorithms. It can be noted that, in a range of [0.55, 0.7], WOA algorithm has suitable results. For three-phase applications, Figure 6(b) shows that WOA finds better solutions for a range of [0.4, 0.85]. As a matter of fact, it is pointed out that WOA can find the global minimum. In these cases, GA finds the local minimum. In order to compare the probability of finding global minimum using WOA and GA, the cumulative distribution function (CDF) is defined as follows [19]:

$$CDF(x) = P(X < x) \quad (15)$$

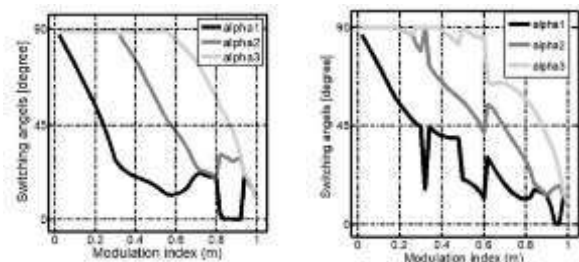


Figure 4. Switching angles versus modulation index m (a) for a single-phase structure (b) for a three-phase structure

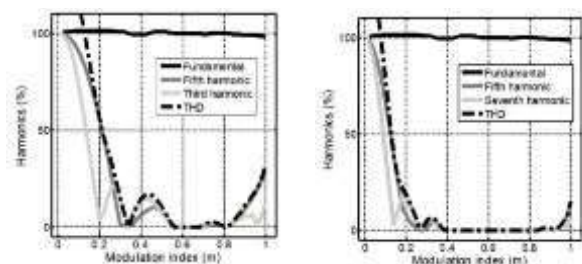


Figure 5. Fundamental, two low-order harmonics and THD versus m (a) single-phase CHB (b) three-phase CHB.

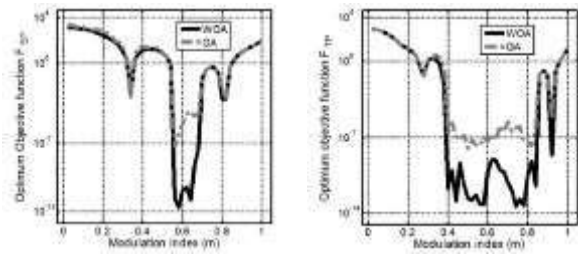


Figure 6. Comparison between the answers of WOA and GA versus m: (a) to minimize F_{sp} , (b) to minimize F_{tp} .

For a given probability distribution, the probability of having a value less than or equal to x for a random variable X is called cumulative distribution function (CDF). The CDF curve shows the probability of reaching to a value lower or equal to a specified level of objective function. Figure 7 illustrates CDF curve of WOA and GA to solve Equations (12) and (13). It is clear that CDF of WOA is above of CDF of GA. Therefore, WOA is more likely to converge comparing to GA. As a case in point, CDF (10^{-7}) of WOA is 14% and CDF (10^{-7}) of GA is 2% for a single-phase CHB, and CDF (10^{-7}) of WOA is 48% and CDF (10^{-7}) of GA is 22% for a three-phase CHB.

3. 3. Experimental Results A 1kW 7-level CHB inverter is constructed in laboratory as illustrated in Figure 8. It consists of three H-bridge inverter that are connected in series. The main parameters of the systems are shown in Table 1. It is assumed that each cell has a

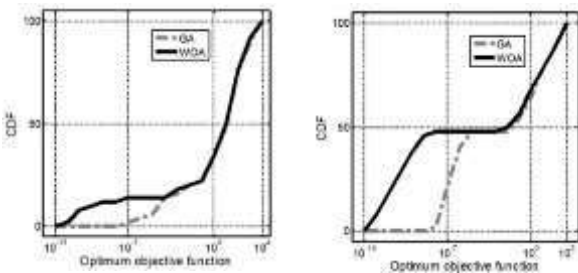


Figure 7. Cumulative distribution function curves of WOA and GA to solve SHE-PWM equations: (a) for a single-phase CHB inverter (b) for a three-phase CHB inverter

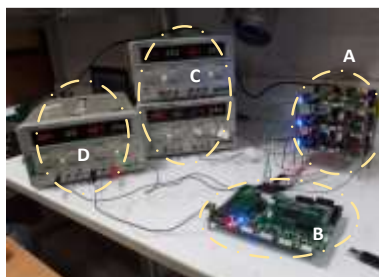


Figure 8. The constructed 7-level CHB inverter: A- CHB inverter B- FPGA processor and interface C- DC voltage sources D-auxiliary voltage sources

TABLE 1. Parameters of the 7-level CHB inverter

Parameters	Sym.	Value
Number of cell per phase	N	3
DC voltage of cell	E	25 [V]
Switching frequency	f_{sw}	50 kHz
IGBT switches	S	IKW40N120H3

constant DC voltage 25V. The output voltage frequency is 50Hz. Isolated-gate bipolar transistor (IGBT) switches have been employed as power switches in this structure. In this prototype, the SHEPWM modulation is implemented over a Spartan-3 field-programmable gate array (FPGA). The switching angles which are obtained offline by WOA, are loaded in a FPGA processor as a lookup table. Therefore, for each modulation index m , the processor finds the optimum switching angles from this lookup table. For isolation of the power circuit from the control board, optocoupler 6N137 have been used. At the end, the isolated signals are reached to the power switches by IGBT driver HCPL-3120 to provide the amount of charges required to turn on IGBT switches.

In order to validate the results of WOA, two operation points are implemented in single-phase and three-phase CHB inverters when the modulation index are $m=0.6$ and $m=0.8$. The switching angles for each case are tabulated in Table 2. Figures 9 and 10 show the output phase voltage of CHB inverter and frequency spectrum in the single-phase and three-phase CHB inverters. It can be noted that, the third and fifth harmonics in single-phase CHB, and fifth and seventh harmonics in three-phase CHB, are completely eliminated that confirms the results of WOA. Figure 11 shows the phase voltage of single-phase CHB when a step change in the modulation index is applied.

TABLE 2. Switching angles for $m = 0.8$

7-level CHB	α_1	α_2	α_3
Single phase	19.998297	20.183009	58.349913
Three phase	11.504323	28.713562	57.104075

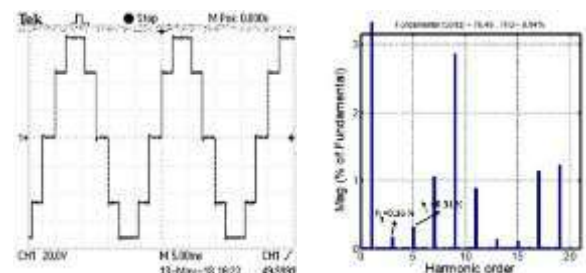


Figure 9. Experimental results of SHE-PWM for a CHB inverter in $m=0.8$: (a) phase voltage, (b) harmonic spectrum in a single-phase structure

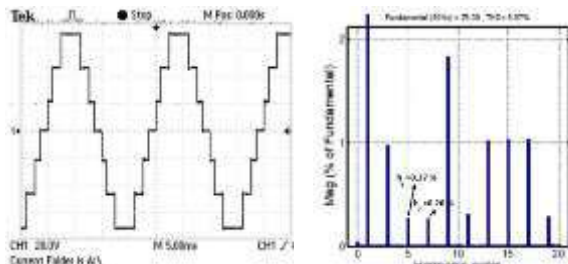


Figure 10. Experimental results of SHE-PWM for a CHB inverter in $m=0.8$: (a) phase voltage, (b) harmonic spectrum in a three-phase structure

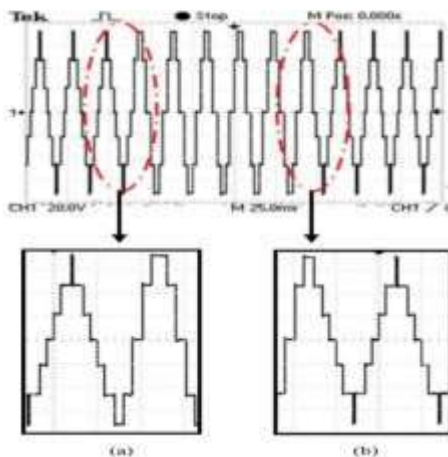


Figure 11. Experimental results of SHE-PWM for a single-phase CHB inverter: (a) when m increases form 0.6 to 0.8, (b) when modulation index decreases from 0.8 to 0.6

5. CONCLUSION

In this paper, the whale optimization algorithm has been used to solve nonlinear equations of SHEPWM for multilevel inverters. It is shown that WOA has an ability to find a global solution for two objective functions. Comparison of the optimization results of WOA and the results of GA proves that this method has higher accuracy and probability of convergence than GA and shows the superiority of WOA to GA. A 1 kW prototype of 7-level CHB inverter is built and the results are presented. The low-order harmonics are eliminated completely and the first harmonic is adjusted to the specific value.

6. REFERENCES

- Zarepor Ashkezari, A., and H. Mosalman Yazdi. "Location Allocation of Earthquake Relief Centers in Yazd City Based on Whale Optimization Algorithm." *International Journal of Engineering, Transactions B: Applications*, Vol. 34, No. 5, (2021), 1184-1194. doi: 10.5829/ije.2021.34.05b.12.
- Ouni S. "Improvement of Post-Fault Performance of a Cascaded H-bridge Multilevel Inverter." *IEEE Transactions on Industrial Electronics*, Vol. 64, No. 4, (2017), 2779-2788. doi: 10.1109/TIE.2016.2632058
- Rodriguez J., Lai J., and Zheng F., "Multilevel inverters: a survey of topologies, controls, and applications," *IEEE Transactions on Industrial Electronics*, Vol. 49, No. 4, (2002), 724-738 . doi: 10.1109/TIE.2002.801052
- M., Saadati Vahidi J., Seydi V., and Sheikholharam P. "Proposing a New Image Watermarking Method Using Shearlet Transform and Whale Optimization Algorithm." *International Journal of Engineering, Transactions A: Basics*, Vol. 34, No. 4 (2021), 843-853. doi: 10.5829/ije.2021.34.04a.10
- Narimani M., Wu B. and Zargari N. R., "A Novel Five-Level Voltage Source Inverter with Sinusoidal Pulse Width Modulator for Medium- Voltage Applications," *IEEE Transactions on Power Electronics*, Vol. 31, No. 3, (2016) 1959-1967. doi: 10.1109/TPEL.2015.2440656
- Khamooshi R. and Namadmalan A., "Converter utilisation ratio assessment for total harmonic distortion optimisation in cascaded H-bridge multi-level inverters," *IET Power Electronics*, Vol. 9, No. 10, (2016), 2103-2110, 8 17. doi: 10.1049/iet-pel.2015.0787
- Yousefpoor N., Fathi S. H., Farokhnia N. and Abyaneh H. A., "THD Minimization Applied Directly on the Line-to-Line Voltage of Multilevel Inverters," *IEEE Transactions on Industrial Electronics*, Vol.59, No. 1, (2012), 373-380 doi: 10.1109/TIE.2011.2143373
- Kirankumar B., Siva Reddy Y. V. and Vijayakumar M., "Multilevel inverter with space vector modulation: intelligence direct torque control of induction motor," *IET Power Electronics*, Vol. 10, No. 10, (2017), 1129-113. doi: 10.1049/iet-pel.2016.0287
- Buccella C., Cecati C., Cimatoroni M. G., Kulothungan G., Edpuganti A. and Rathore A. K., "A Selective Harmonic Elimination Method for Five-Level Converters for Distributed Generation," *IEEE Journal of Emerging and Selected Topics in Power Electronics*, Vol. 5, No. 2, (2017), 775-783. doi: 10.1109/JESTPE.2017.2688726
- Ozpineci B., Tolbert L. M. and Chiasson J. N., "Harmonic optimization of multilevel converters using genetic algorithms," *IEEE Power Electronics Letters*, Vol. 3, No. 3, (2015), 92-95. doi: 10.1109/PESC.2004.1355167
- Wenyi Z, Meng X., and Jiang L. "Genetic Algorithm for Selective Harmonic Elimination PWM Control." *Foundations of Intelligent Systems*, 799-809. Springer, Berlin, Heidelberg, 2014. doi: 10.1007/978-3-642-54924-3_75
- Kavousi A., Vahidi B., Salehi R., Bakhshizadeh M. K., Farokhnia N. and Fathi S. H., "Application of the Bee Algorithm for Selective Harmonic Elimination Strategy in Multilevel Inverters," *IEEE Transactions on Power Electronics*, Vol. 27, No. 4, (2012), 1689-1696. doi: 10.1109/TPEL.2011.2166124
- Mohamed A., "Harmonic elimination in three-phase voltage source inverters by particle swarm optimization." *Journal of Electrical Engineering and Technology*, 6, No. 3, (2011), 334-341. doi: 10.5370/JEET.2011.6.3.334
- Sundareswaran K., Jayant K. and Shanavas T. N., "Inverter Harmonic Elimination Through a Colony of Continuously Exploring Ants," *IEEE Transactions on Industrial Electronics*, Vol. 54, No. 5, (2017), 2558-2565. doi: 10.1109/TIE.2007.899846
- Seyedali M, and Lewis A. "The whale optimization algorithm." *Advances in Engineering Software*, Vol. 95, (2016), 51-67. doi.org/10.1016/j.advengsoft.2016.01.008
- Dash, S.K., Nayak, B. and Sahu, J.B., "Selective Harmonic Elimination of an Eleven Level Inverter Using Whale Optimization Technique." *International Journal of Power Electronics and Drive Systems*, Vol. 9, No. 4, (2018), 1944. doi: 10.11591/ijpeds.v9.i4.pp1944-1951
- Routray A, Singh RK, Mahanty R. "Selective harmonic elimination in hybrid cascaded multilevel inverter using modified

- whale optimization.” *International Transactions on Electrical Energy Systems*, Vol. 30, No. 4, (2020), 12298. doi.org/10.1002/2050-7038.12298
18. Falehi A. D. “Optimal harmonic mitigation strategy based on multiobjective whale optimization algorithm for asymmetrical half-cascaded multilevel inverter.” *Electrical Engineering*. 102 (3), (2020), 1639-50. doi.org/10.1007/s00202-020-00983-y
19. Nalcaci G., Ermis M., “Selective harmonic elimination for three-phase voltage source inverters using whale optimizer algorithm,” 5th International Conference on Electrical and Electronic Engineering (ICEEE), (2018) 1-6. [doi: 10.1109/ICEEE2.2018.8391290](https://doi.org/10.1109/ICEEE2.2018.8391290)
20. Rathore, R., Sangwan S., Adhikari k. “Modified Echo State Network Enabled Dynamic Duty Cycle for Optimal Opportunistic Routing in EH-WSNs,” *Electronics*, Vol. 9, No. 1, (2020), 98. doi.org/10.3390/electronics9010098

Persian Abstract

چکیده

در این مقاله، الگوریتم بهینه سازی نهنگ برای حذف هارمونیک در یک اینورتر چند سطحی آبشار ارائه شده است. در مدولاسیون پالس حذف هارمونیک انتخابی، هارمونیک های کم مرتبه انتخاب شده با حل معادلات غیر خطی حذف می شوند، در حالی که بنیاد شکل موج خروجی به مقدار دلخواه تنظیم می شود. در این مقاله، الگوریتم بهینه سازی نهنگ بر روی یک اینورتر پل H آبشاری ۷ سطح برای حل معادلات اعمال می شود. همچنین، با نتایج تجربی تأیید گردید، از آنجا که این الگوریتم توانایی جستجو در کل فضای محلول را دارد، احتمال گرفتن بهترین راه حل جهانی بسیار زیاد است. این روش از دقت و احتمال همگرایی بالاتری نسبت به الگوریتم ژنتیک برخوردار است. بهینه سازی و مقایسه الگوریتم بهینه سازی نهنگ و الگوریتم ژنتیک در نرم افزار MATLAB انجام شده است. نمونه اولیه ۱ مبادله از این مبدل ساخته شده و نتایج ارائه می شود. اثربخشی و تجزیه و تحلیل نظری این روش از طریق نتایج شبیه سازی و تجربی تأیید می گردد.



Experimental Study on Single Bay Reinforced Coconut Shell Concrete Portal Frame under Lateral and Cyclic Load

K. Gunasekaran^a, S. Choudhury^{*b}

^a Professor, Department of Civil Engineering, SRM Institute of Science and Technology, Kattankulathur Tamil Nadu, India

^b M. Tech Structural Engineering, Department of Civil Engineering, SRM Institute of Science and Technology, Kattankulathur Tamil Nadu, India

PAPER INFO

Paper history:

Received 27 May 2021

Received in revised form 25 June 2021

Accepted 02 July 2021

Keywords:

Coconut Shell

Concrete

Single Bay

Reinforced Cement Concrete

Portal Frame

ABSTRACT

As a natural stone aggregate, resources are reducing at a high rate due to the large concrete use. For the search of substitute material for natural aggregates, in recent years coconut shells are used in the concrete field. Reinforced cement concrete (RCC) portal frames are a very common structural element and used for resisting lateral loads. In this research single bay, RCC portal frames made with coconut shell concrete (CSC) are tested under lateral load and cyclic push-pull load. The results are compared with frames made with conventional concrete (CC). Four prototype bare frames cast in that two frames made with CSC and two with CC. Behavior and characteristics like load capacity, deflection, crack formation, concrete strain, stiffness, and ductility are studied. It was found that under cyclic push-pull load CSC frames are comparable with CC frames rather than under lateral load. The amount of deflection and strains are observed in the CSC frame is comparatively more than in CC frames. Stiffness and ductility also observed more in CSC frames than CC frames.

doi: 10.5829/ije.2021.34.08b.12

1. INTRODUCTION

In recent times lightweight concrete has a great impact on the concrete production field and has been used in reinforced concrete. By using lightweight concrete (LWC) cost can save up to 15-20 % of that of normal weight concrete. As a result of the growing population and industrialization, the use of concrete is increasing at a high rate. This caused a drastic reduction in natural stone recourses, as aggregate plays a significant role in concrete production. In this situation search for a substitute material for crushed stone aggregate (CSA) is significant. Many agriculture wastes and by-products are already in use as aggregate in the concrete field. Recently in LWC production lightweight aggregates (LWA) used are pumice, perlite, expanded clay, coal slag, sintered fly ash, rice husk, straw, sawdust, cork granules, wheat husk, oil palm shell, and coconut shell (CS) [1-4]. With the help of these LWAs, LWC with the required strength can be produced [5]. Studies found

that the basic properties of coconut shell concrete (CSC), mechanical properties of CSC, bond properties of CSC [2] and long term performance of CSC are coming in the similar range as required for the structural applications of LWC [3]. In previous researches behaviors of reinforced CSC beam under flexure, shear, and torsion had been already studied [6-8], hence this study investigated an experimental study of reinforced CSC portal frames under lateral and cyclic load, then compared with the conventional concrete (CC). Reinforced cement concrete (RCC) portal frames are a very commonly used structure in the construction field. RCC frames generally consist of two structural element beams and columns, in which beams are fixed to the columns, and columns are strongly made that they can give stability to the entire portal frame [9]. In the case of framed structures, lateral loads are having more effects than the gravity loadings like dead load and vertical imposed loadings [10].

It is found that in previous studies the use of many structural elements were analyzed using CSC but none of them have used CSC in portal frames. Therefore, the study on CSC used portal frame is found to be very

*Corresponding Author: sc9352@srmist.edu.in (S. Choudhury)

limited. In that case study, the analyzing the characteristics of single bay reinforced portal frame by using CSC under lateral loads is the need of the hour. This research is focusing on the use of CS as a suitable replacement material to substitute the natural stone as coarse aggregate in the case of concrete portal frames. This includes the comparisons of behavioral characteristics such as deflection, strain characteristics, stiffness, and ductility of CSC frame with CC frame under lateral and cyclic loads. This analysis can provide significant insight into the performance of bare portal frame structure.

1. 1. Coconut Shell Aggregate The making process of aggregate from CS, which is thrown as an environmental waste is already discussed and presented in earlier researches and studies [2-3]. Some of the important properties of CS aggregates have been found in previous studies. The CS having average moisture content and water absorption were 04.20% and 24.00%, respectively. The average specific gravity of CS found as 1.05-1.20 respectively, it is comparatively less than the normal aggregates. This justified that, if CS as aggregate is used in concrete it will fall in the LWC category. The average bulk densities of CS in loose and compacted conditions are 550 kg/m^3 and 650 kg/m^3 , respectively. CS aggregates will produce concrete of less unit weight compared to normal weight aggregate concrete and that falls under the category of producing LWC [2-3].

1. 2. Coconut Shell Concrete In the making of two types of concrete, ordinary Portland cement, river sand, water, and crushed granites are the ingredients for making CC. But for making CSC crushed granites are replaced by CS as coarse aggregates. The concrete grade is selected as M25 concrete, for both CC and CSC. CS are collected and crushed by the crushing machine available on the University premises. Figure 1 showing the process pictures of CSC from the collection of CS to cast specimen under curing. Trail mix proportions are collected from previous studies [6-8]. Table 1 showing the trail mixes and properties of the CC and CSC found in preliminary tests.

2. EXPERIMENTAL TEST

2. 1. Frame Size and Detailing

The overall portal frame size was decided with respect to the feasibility of accommodating the same into the loading from provision available to apply both static and push-pull load in the structural testing laboratory of the university premises.

Since the maximum size in height is 1650 mm and the provision to hold the base is 1500 mm and hence the

maximum base width of 1400 mm and the column height of 1500 mm were fixed. The sectional detailing is provided based on the Indian Standard IS 456: 2000 [11] (i.e) it recommended for column minimum diameter of reinforcement bar should be 12 mm and the



(a) Collected



(b) CS crusher



(c) CS size segregation



(d) Crushed CS



(e) Material batching



(f) Materials loading



(g) CSC



(h) Specimen before casting



(i) Specimen after casting

Figure 1. Process pictures of CSC

TABLE 1. Trail mixes and concrete properties

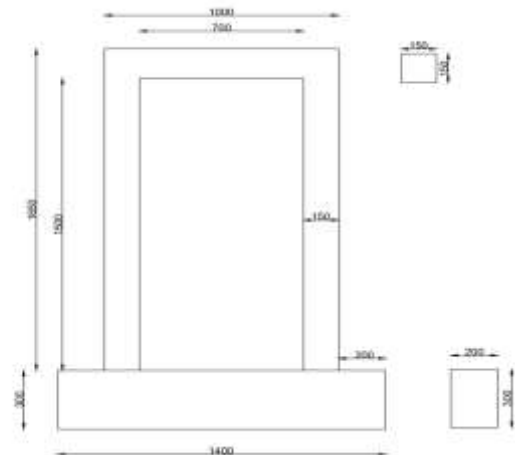
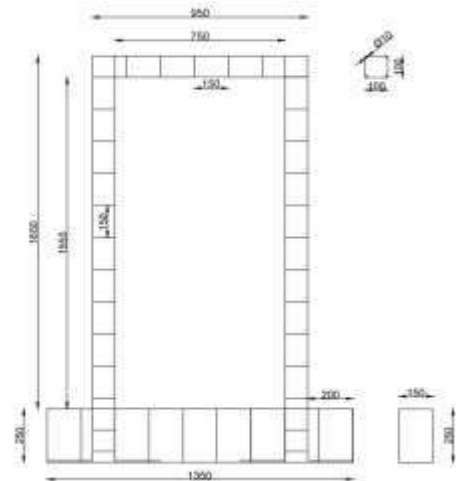
Description	Conventional concrete (CC)	Coconut shell concrete (CSC)
Mix ratio	1:2.22:3.66 (cement: sand: CSA)	1:1.47:0.65 (cement: sand: CS)
Water/Cement	0.55	0.42
Cement content	320 kg/m ³	510 kg/m ³
Slump	11 mm	7 mm
Compaction factor	0.89	0.93
28 days dry density	2496 kg/m ³	1982 kg/m ³
28 days compressive strength	27.85 N/mm ²	26.16 N/mm ²

CS minimum four number bars should be provided. In this aspect, it was adopted. Since most of the research studies on structural elements size, shape, and reinforcement detailing are fixed at first and tested for their capacity and behavior rather than designed for resisting particular applied load [12-15] which is normally adopted for field execution. Therefore, the size of the beam ((150 × 150 × 1000 mm), size of the column (150 × 150 × 1500 mm), and size of the base (200 × 300 × 1400 mm) is adopted for the prototype frames, in this study.

Totally four frames were cast in that two for CC and two for CSC. Four numbers of steel bars having a diameter of 12 mm are provided for the beam, column, and base of the frames. The schematic diagram of the cross-section and reinforcement detailing are showing in Figure 2 and Figure 3, respectively.

2. 2. Casting Process For casting process the plywood moulds and the reinforcement are made as per the size and detailing. Before placing the reinforcements a thin coat of crude oil was coated inside of the frames. All materials are collected and mixed. Concretes are placed into the moulds very carefully and compacted using a needle vibrator. Right after the casting frames are covered with plastic sheets. Only after 24 h moulds are removed from the frames and the curing process is started for the next 28 days.

2. 3. Loading Setup The testing of the frames was carried out in a self-straining loading frame of a capacity of 200 kN. Only after 28 days of curing the frames are placed and rigidly fixed to the frame base with clamps and bolt nuts for avoiding any kind of displacement during testing. The setup is showing in Figure 4, where a hydraulic jack of 200 kN is fixed in such a way it can give the loading to the beam-column joint of the frame. A linear variable displacement transducer (LVDT) was placed to the opposite beam-column connection for measuring deflection to the

**Figure 2.** Cross section of frame**Figure 3.** Reinforcement detailing of frame

(1) Hydraulic jack 200 kN capacity, (2) LVDT, (3) Deflection indicator, (4) Load indicator, (5) Multi-channel data logger, and (6) Strain gauges on the surface

Figure 4. Loading set-up

corresponding load. Strain gauges were pasted to the frame surface and connected to the multi-channel data logger for concrete strain readings.

2. 4. Loading Protocol In the case of lateral static loading, a load applied on the increment of 2 kN. But in the case of cyclic loading because of the application of load in both push and pull to minimize the number of cycles it was applied in 4 kN increment. That is, it was applied to one direction positive (push) 4 kN, then brought to neutral position and then applied to the opposite direction negative (pull) 4 kN for the first cycle. The same way was followed for cycle two for 8 kN and then 12 kN for cycle three and so on till the ultimate. This is how the loading protocol was followed for both lateral and cyclic load application in this study.

3. RESULTS AND DISCUSSIONS

3. 1. Ultimate Loads In lateral loading the ultimate failure load for the CC portal frame was found to be 62 kN and for the CSC frame, it was 40 kN. For cyclic push load the ultimate failure load for CC portal frame was found to be 40 kN and for the CSC frame, it was 38 kN. Similarly, for cyclic pull load, the ultimate failure load for the CC portal frame was found to be 40 kN and for the CSC frame, it was 38 kN.

The ultimate failure load in lateral loading is found less in CSC frame compared to CC frame. It's approximately 34% lesser in CSC than the CC portal frame. But in the case of cyclic push-pull loading, the ultimate loads are much more same in both CC and CSC frames. It's only 5% lesser in CSC compared to the CC portal frame. It shows that CSC frames are having similar strength as CC frames under cyclic loads rather than lateral loading.

3. 2. Load vs Deletion Behavior The load-deflection patterns are much more similar in both CC and CSC portal frames. In both cases, CC and CSC portal frames, the pattern of load-deflection the curve is similar parabolic type. But it was found that the CSC portal frames are showing more deflection than CC portal frames for a similar amount of aping load. This is happening because of the porous nature, low density of CS that results in lower elastic modulus of CSC as found in previous works CSC [10].

In both CC and CSC the deflection curve is initially linear than it's followed by a parabolic curve. During lateral loading, there is no deflection up to 10 kN for both CC and CSC. But in the case of cyclic loading deflection was started from the initial load of 4 kN. But in both loading cases deflection was found more in the CSC frame compared to the CC portal frame on a similar amount of load. Figures 5, 6 and 7 are showing

the load versus deflection curve for both CC and CSC frames of experimental investigations. Figures 8 and 9 are showing hysteristic curve of cyclic loads of CC and CSC frames, respectively.

In case of lateral load CC frame has ultimate load capacity of 60 kN with 18.9 mm deflection and CSC frame has ultimate load capacity of 40 kN with 50.1 mm deflection. Under lateral load CC performance was better than CSC frame. For cyclic push load CC and CSC frame has ultimate load capacity of 40 kN and 38 kN and maximum deflection 53.72 mm and 52.59 mm, respectively. For cyclic push load CC and CSC frame

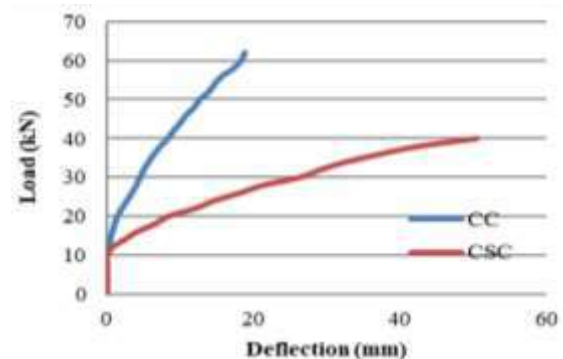


Figure 5. Load-deflection curve under a lateral load

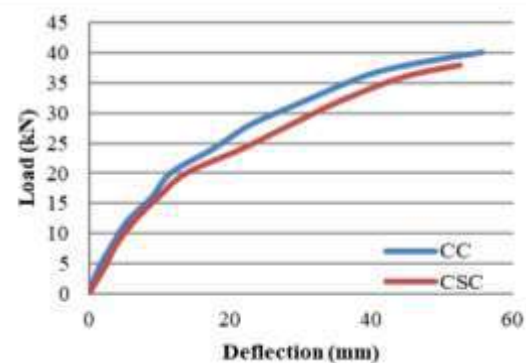


Figure 6. Load-deflection curve under a cyclic push load

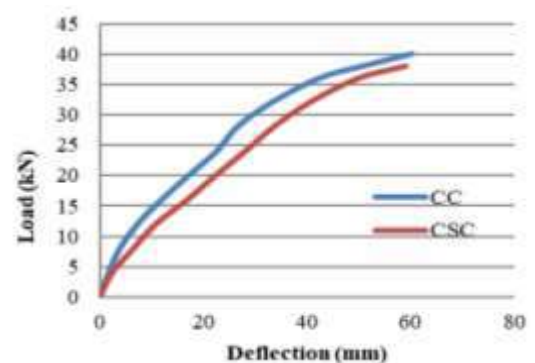


Figure 7. Load-deflection curve under a cyclic pull load

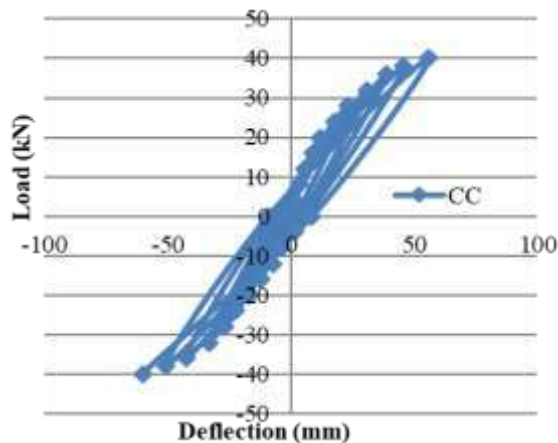


Figure 8. Hysteretic curves of cyclic load (CC)

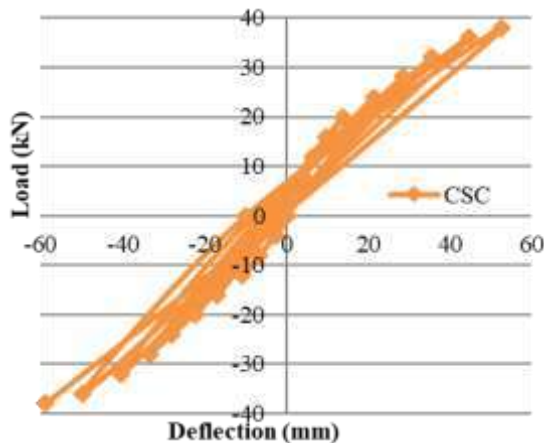


Figure 9. Hysteretic curves of cyclic load (CSC)

has ultimate load capacity of 40 kN and 38 kN and maximum deflection 60.18 mm and 50.72 mm, respectively. Cyclic loading ultimate load for CSC is 5% lesser compared to CC portal frame. It shows that CSC frames are having similar behaviour like CC frames under cyclic loads. But in both loading cases deflection was found more in CSC frame compared to the CC portal frame at the same amount of load. CSC frames are showing more deflection than CC frames and hence more ductility. There are some advantages and disadvantages of the coconut shell concrete mix compared to the traditional concrete mix. The advantage is coconut shell concrete density is less compared to conventional concrete density because of less coconut shell density (550-650 kg/m³) compared to the conventional stone aggregate density (1600-1800 kg/m³). Also, due to the fibrous nature of coconut shell aggregate compared to conventional stone aggregate, naturally, the ductility of coconut shell concrete is more compared to conventional concrete and it is more

advantageous especially in the case of seismic resistance. A disadvantage of using coconut shells in urban areas is transportation cost. Therefore, it is most advantageous the coconut shell is used in rural areas where it is dumped as waste.

3. 3. Cracking Patterns

Cracks are formed in frames after certain application loads. Loads are noted when the corresponding cracks occur and marking was done during the start to the end of the test. The cracks usually form on the beam-column joint and column base junctions. Initial cracks are formed in the column joints than mostly cracks occur in the upper and lower portion of the columns of the frame. In the case of the lateral load, an initial crack occurs in CC portal frame at the load of 16 kN which is 26% of its ultimate failure load. In the CSC portal frame initial crack occurs at the load of 14 kN which is 35% of its ultimate failure load. Figure 10 shows of cracks occurred in the CC frame on both side of the columns and beam at the load of 14, 18, 24, 26, 28, 34, 38, 42, 48, 54, 60, and 62 kN, and cracks occur in the CSC frame on both sides of the columns and beam at the load of 10,16,22,26,28,34,38, and 40 kN. Similarly, like the CC frame, the ultimate cracks have occurred in the beam-column connection.

Most of the cracks are formed in the horizontal and vertical directions both in CC and CSC frames in column and beam components, respectively. This shows that the bonding between the reinforcement and the coconut shell concrete is also similar to that of conventional concrete. Because if there is no bonding exist between the reinforcement and the concrete then along the length of the reinforcement crack will form. In this study, column reinforcement is normally placed vertical and beam reinforcement is placed horizontally which shows that the good compatibility exists between CSC and reinforcements is essential for any kind of structural element.

In the case of the cyclic push-pull load, an initial crack occurs in the CC portal frame at the pull load of 12 kN which is 30% of its ultimate failure load. Similarly for the CSC portal frame, the initial crack occurs at the load of 10 kN which is 26% of its ultimate failure load. Figure 11 shows of cracks are occurred in the CC frame on both side of the columns and beam at the load of 16 kN then 16 to 40 kN at the interval of 4 kN. Figure 12 shows of cracks occur in the CSC frame on both side of the columns and beam at the load of 12 kN and then 16 to 40 kN at the interval of 4 kN.

3. 4. Strains

Strain values are measured for every increment of load. Figures 13, 14 and 15 are showing the tension and compression strain values for both CC and CSC frames for each load type. Concrete surface strains for CSC frames are found more than CC frames.



Figure 10. Cracks in CC and CSC frames after lateral load



Figure 11. Cracks in CC frame after cyclic load



Figure 12. Cracks in CSC frame after cyclic load

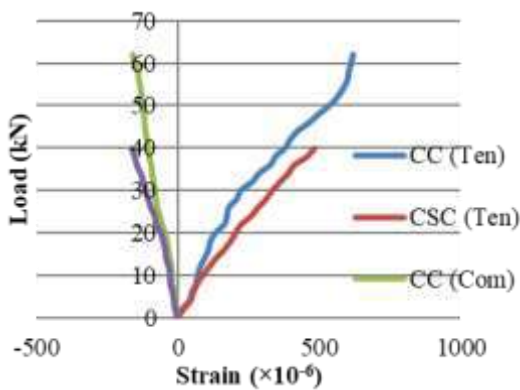


Figure 13. Load - strain curve under lateral

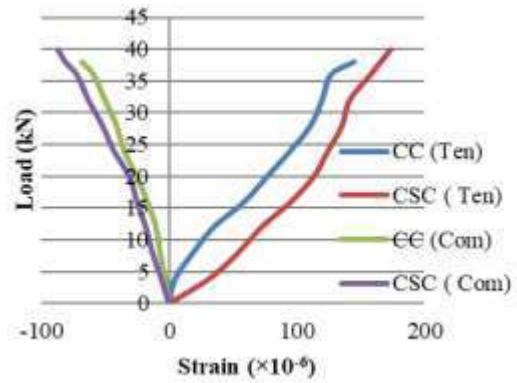


Figure 14. Load - strain curve under cyclic push load

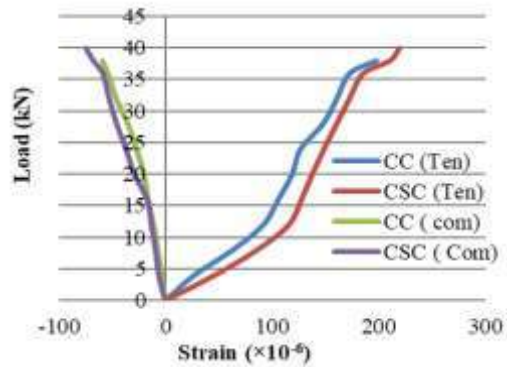


Figure 15. Load - strain curve under cyclic pull load

It is because of the replacement of coarse aggregate as coconut shell, and coconut shells having less strength and stiffness as compared to crushed granite. Granite aggregates are having more characteristics and properties than coconut shells. And hence there is more deflection in CSC frame compared to CC frame. These obtained strain values are similar to the previous work done on CSC [11]. From this study we can say CSC is efficient to attain its strain capacity.

3. 5. Stiffness Stiffness for both CC and CSC frames are calculated and compared with each other. The stiffness characteristics of both bare frames at the beam-column joint level calculated as a ratio of the difference of yield point load, ultimate load and the difference of yield point deflection and ultimate load deflection [16]. Figure 16 showing the stiffness for both CC and CSC frames. The stiffness at the beam-column joint of the frame under lateral loading for CC and CSC are 2.6 kN/mm, 0.56 kN/mm, respectively. Stiffness under cyclic push load for CC and CSC are 0.51 kN/mm, 0.56 kN/mm, respectively. Similarly, stiffness under cyclic pull load for CC and CSC is 0.49 kN/mm, 0.54 kN/mm, respectively. In the case of lateral load, CSC frames are showing less stiffness than CC frames. For

cyclic push-pull load, CSC frames are showing more stiffness than CC frames.

3. 6. Ductility Factor Ductility factors of both portal frames are calculated as the ratio between displacement at ultimate load and displacement at yield load and compared as recommended in the literature [16]. The ductility factor at the beam-column joint of CC and CSC frames under lateral loading are 23.63 and 20.16, respectively. Ductility factors for CC and CSC frame under cyclic push-load are 6.03, 8.4, and under cyclic pull-load is 5.03, and 5.5, respectively. In the case of lateral load, CSC is a little less ductile than CSC frames. But it is found that under cyclic push-pull load CSC frames are a little bit more ductile compared to CC frames. In Figure 17 ductility factors for both CSC and CC frames are shown for both types of loading.

4. CONCLUSIONS

The ultimate failure load in lateral loading is found approximately 34% lesser in CSC than CC portal frame.

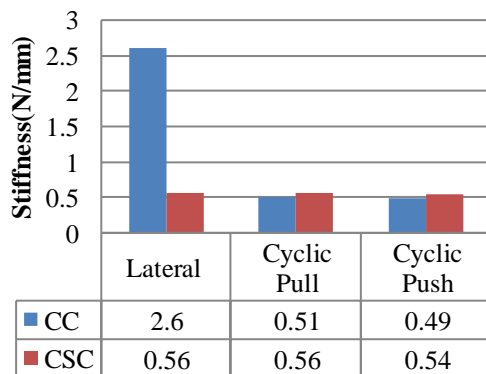


Figure 16. Stiffness in CC and CSC frames

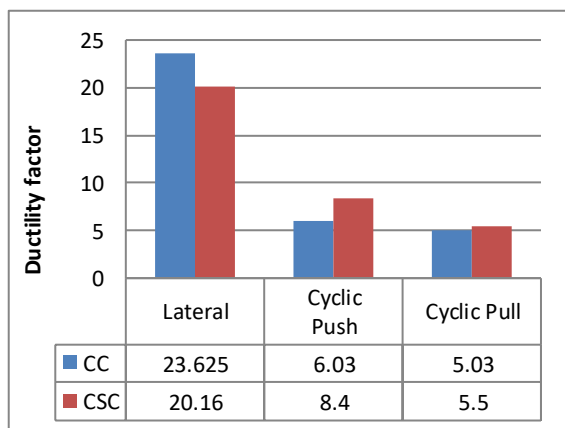


Figure 17. Ductility factor of in CC and CSC frames

Under lateral load, CC performance was better than CSC frame. Cyclic loading ultimate load for CSC is 5% lesser compared to the CC portal frame. It shows that CSC frames are having similar strength as CC frames under cyclic loads rather than lateral loading. But in both loading cases deflection was found more in the CSC frame compared to the CC portal frame on a similar amount of load. CSC frames are showing more deflection than CC frames. Concrete surface strains to the corresponding loads for CSC frames are found more than CC frames. It is because CS, and CS having less strength and stiffness as compared to CSA. Hence there is more deflection in the CSC frame compared to the CC frame. In the case of lateral load, CC frames are showing more stiffness than CSC frames. But for cyclic push-pull CSC frames are showing more stiffness than CC frames. In the case of lateral load, CSC is a little less ductile than CSC frames. But It is found that under cyclic push-pull load CSC frames are a little bit more ductile compared to CC frames. Overall it was observed that in the case of cyclic loads performance of CSC frames is preferable as a structural element and has a reliable comparison with CC frames.

CSC frames are showing more deflection than CC frames and hence more ductility. coconut shell concrete density is less compared to conventional concrete density because of less coconut shell density (550-650 kg/m³) compared to the conventional stone aggregate density (1600-1800 kg/m³). The use of coconut shells in urban areas would lead to higher transportation cost compared to conventional aggregate. Therefore, it is most advantageous the coconut shell is used in rural areas where it is dumped as waste. The crack pattern formed on CSC frames shows that the good compatibility of CSC exists with reinforcements like conventional concrete which is essential for any kind of structural element.

5. REFERENCES

1. Jumaat, M.Z., Alengaram, U.J. and Mahmud, H., "Shear strength of oil palm shell foamed concrete beams", *Materials & Design*, Vol. 30, No. 6, (2009), 2227-2236, <https://doi.org/10.1016/j.matdes.2008.09.024>
2. Gunasekaran, K., Kumar, P. and Lakshmiathy, M., "Mechanical and bond properties of coconut shell concrete", *Construction and Building Materials*, Vol. 25, No. 1, (2011), 92-98, <https://doi.org/10.1016/j.conbuildmat.2010.06.053>
3. Gunasekaran, K., Annadurai, R. and Kumar, P., "Long term study on compressive and bond strength of coconut shell aggregate concrete", *Construction and Building Materials*, Vol. 28, No. 1, (2012), 208-215, <https://doi.org/10.1016/j.conbuildmat.2011.08.072>
4. Shafiqh, P., Mahmud, H.B. and Jumaat, M.Z., "Oil palm shell lightweight concrete as a ductile material", *Materials & Design* (1980-2015), Vol. 36, (2012), 650-654, <https://doi.org/10.1016/j.matdes.2011.12.003>

5. Shafigh, P., Jumaat, M.Z., Mahmud, H.B. and Alengaram, U.J., "A new method of producing high strength oil palm shell lightweight concrete", *Materials & Design*, Vol. 32, No. 10, (2011), 4839-4843, <https://doi.org/10.1016/j.matdes.2011.06.015>
6. Gunasekaran, K., Annadurai, R. and Kumar, P., "Study on reinforced lightweight coconut shell concrete beam behavior under flexure", *Materials & Design*, Vol. 46, (2013), 157-167, <https://doi.org/10.1016/j.matdes.2012.09.044>
7. Gunasekaran, K., Annadurai, R. and Kumar, P., "Study on reinforced lightweight coconut shell concrete beam behavior under shear", *Materials & Design*, Vol. 50, No., (2013), 293-301, <https://doi.org/10.1016/j.matdes.2013.03.022>
8. Gunasekaran, K., Ramasubramani, R., Annadurai, R. and Chandar, S.P., "Study on reinforced lightweight coconut shell concrete beam behavior under torsion", *Materials & Design*, Vol. 57, (2014), 374-382, <https://doi.org/10.1016/j.matdes.2013.12.058>
9. Bolea, O., "The seismic behaviour of reinforced concrete frame structures with infill masonry in the bucharest area", *Energy Procedia*, Vol. 85, No., (2016), 60-76, doi: <https://doi.org/10.1016/j.egypro.2015.12.275>
10. Salihovic, A. and Ademovic, N., "Nonlinear analysis of reinforced concrete frame under lateral load", *Coupled Systems Mechanics*, Vol. 6, No. 4, (2017), 523-537, <https://doi.org/10.12989/csm.2018.7.3.281>
11. Standard, I., "Plain and reinforced concrete-code of practice", New Delhi: Bureau of Indian Standards, (2000).
12. Sirimontreea, S., Keawsawasvong, S., Thongchom, C., Jongvivatsakul, P. and Noroozinejad Farsangi, E., "Experimental investigations on strengthened reinforced concrete columns under monotonic axial loading", *International Journal of Engineering, Transactions B: Applications*, Vol. 34, No. 5, (2021), 1124-1131, doi: 10.5829/ije.2021.34.05b.06.
13. Shaiksha Vali, K., Murugan, B., Reddy, S. and Noroozinejad Farsangi, E., "Eco-friendly hybrid concrete using pozzolanic binder and glass fibers", *International Journal of Engineering, Transactions A: Basics*, Vol. 33, No. 7, (2020), 1183-1191, doi: 10.5829/IJE.2020.33.07A.03.
14. Mohammadhassani, M., Zarrini, M., Noroozinejad Farsangi, E. and Khadem Gerayli, N., "Prediction of structural response for hsscc deep beams implementing a machine learning approach", *International Journal of Coastal and Offshore Engineering*, Vol. 2, No. 1, (2018), 35-43, doi: 10.29252/ijcoe.2.1.35.
15. FARSANGI, E., "Connections behaviour in precast concrete structures due to seismic loading", *Gazi University Journal of Science*, Vol. 23, No. 3, (2010), 315-325, <https://dergipark.org.tr/tr/download/article-file/83157>

Persian Abstract

چکیده

به عنوان یک سنگ دانه سنگ طبیعی، منابع به دلیل استفاده زیاد از بتن، با سرعت بالایی کاهش می یابند. برای جستجوی مواد جایگزین برای سنگدانه های طبیعی، در سال های اخیر از پوسته های نارگیل در زمینه بتن استفاده می شود. قاب های پورتال بتن سیمان مسلح (RCC) یک عنصر ساختاری بسیار رایج است و برای مقاومت در برابر بارهای جانبی استفاده می شود. در این خلیج تحقیقاتی، قابهای پورتال RCC ساخته شده با بتن پوسته نارگیل (CSC) تحت بار جانبی و فشار فشار کششی چرخشی آزمایش می شوند. نتایج با فریم های ساخته شده با بتن معمولی (CC) مقایسه می شود. چهار قاب اولیه لخت در دو قاب ساخته شده با CSC و دو قاب با CC ساخته شده است. رفتار و خصوصیات مانده ظرفیت بار، انحراف، تشکیل ترک، کرنش بتن، سختی و شکل پذیری مورد مطالعه قرار می گیرد. مشخص شد که در زیر فشار فشار کششی چرخه های CSC با فریم های CC قابل مقایسه هستند تا زیر بار جانبی. میزان انحراف و فشارهای مشاهده شده در قاب CSC نسبتاً بیشتر از فریم های CC است. سختی و شکل پذیری نیز در فریم های CSC بیشتر از فریم های CC مشاهده شده است.



A Study on the Modified Algorithm for Image Processing in Tracking Seam Welding

Y. Pourasad^a, A. Afkar^b

^a Faculty of Electrical Engineering, Urmia university of Technology, Urmia, Iran

^b Technology and Engineering Research Center, Standard Research Institute, Karaj, Iran

PAPER INFO

Paper history:

Received 10 November 2020

Received in revised form 23 December 2020

Accepted 04 January 2021

Keywords:

Morphological Filter

Welding Robot

Non-destructive Tests

Feature Extraction

Ultrasonic

Least Squares

Image Processing

ABSTRACT

For robot path planning the weld seam positions need to be known in advance as the industrial robots generally work in teach and playback mode. Since the welding of the pipe is not done completely on the straight line (the nature of the pipe) and the test tube under the machine is moving, the symmetry of the two probes in relation to the welding site is very important during the test and quick tracking is required to set the probes. The use of image processing and machine vision techniques is very efficient in optimizing seamless welding radii. In designing the algorithms used, an attempt has been made to reduce the environmental conditions and unstable industrial situation well in order to track the weld seam with an acceptable speed. New approach has been used to access the central line of the weld seam area. The algorithm is designed to be implemented in a real environment and has very good results. One of the advantages of this method is the reduction of measurement error and the elimination of mechanical and electrical sensors in non-destructive tests.

doi: 10.5829/ije.2021.34.08b.13

1. INTRODUCTION

In the area of connecting the welding parts, the edges of the pieces are tangled together and close together to form a weld joint [1-3]. Another notion of welding is the boiling area after the welding operation on the piece. For inspecting imperfections, welding seals are designed to accurately and precisely control the head of the system at the center of the gun, which can be used for welding purposes such as a welding torch and a welding inspection of the head, a test and inspection device probe assembly. Figures 1 and 2 present the weld seam before and welded area after weldings, respectively.

Extensive research was carried out by Xizhang et al. [4], Yong et al. [5] and Xu et al. [6] on seamless welding detector system, which was based on the active method. The use of Laplacian Gaussian function, thresholding using the maximum squared difference method, use of the tagging technique, thin work and

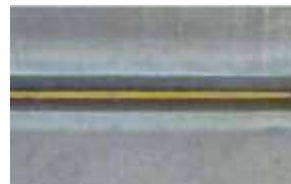


Figure 1. Weld seam before welding



Figure 2. Welded area after welding operation

find skeletons, the extraction of feature regions in this study is first partitioned using the image Laplacian of Gaussian (LoG) filter and the laser profile is extracted, then, to remove the discontinuities, the average filter is used. Continuation of the algorithm is based on the tagging technique. By calculating the meters and considering that the largest meter (label) is the weld profile. The largest label is left with the calculation of the length of the labels, and the remaining labels are deleted. To gain access to the characteristics of the weld profile property, this should be done using a weld profile sketch, the feature points in this way are the corners of the laser profile, which calculates the spatial coordinates of those points, and the center of the profile

Corresponding Author Institutional Email: y.pourasad@uut.ac.ir (Y. Pourasad)

with one geometric relationship is obtained. Another algorithm for detection of edge techniques for image segmentation that was announced by Dhankhar and Sahu [7]. The algorithm also operates on an active basis [8], believes that interpolation and hack conversion and pattern recognition algorithms are very costly and reduce the speed of tracking operations, instead offering a new algorithm. They defined the concept as the second central disagreement, which is expressed as follows:

$$2CD(x)=(f(x3)-f(x1))/2 \tag{1}$$

X1 pixel edge profile before the current pixel and X3 is the next pixel on the laser profile. An algorithm developed by Bender et al. [9] to detect the weld seam at the edges of the wound based on the active method. In this method, he defined the location of the intersection of the laser and the weld seam as this feature point. In fact, the laser beam was perpendicular to the weld seam and reflected in the segment. In the first step, for extracting the ROI region, the seam image (sum of intensities) calculated the weld in a vertical direction (column wise) and with respect to the difference in the intensity of the image on the edges of a region, $[UC-dy UC + dy]$ is defined as a column that $UC = \text{Min}(p(j))$ and $p(j)$ is also the image of the j -th row. Therefore, extracting the laser profile also performed the above operation in a row; then sketching and interpolating the feature points. Figure 3 shows the steps of this algorithm on an image of welding.

Noise reduction and smoothing conducted with middle filter, thresholding, skill and thin work, Huff conversion.

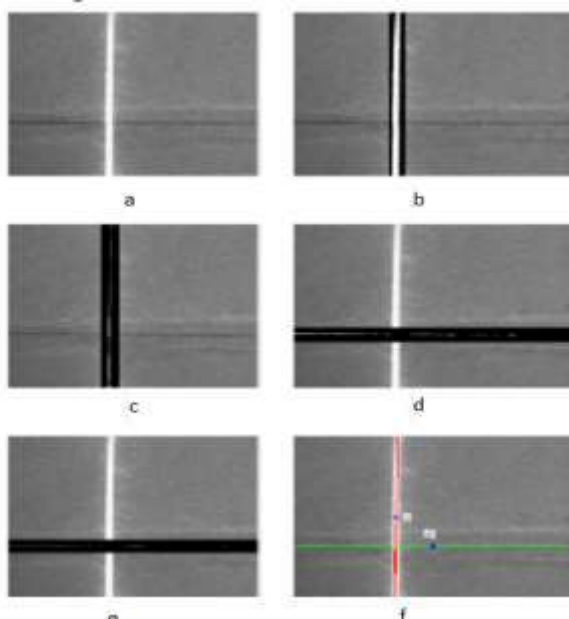


Figure 3. a (initial image), b (ROI region), c (image B), d (f points of the feature), e (Noise reduction), f (f1 and f2 points)

2. METHOD

2. 1. Algorithm Expressed by Tavlin Recently, an algorithm was developed by Bender [9] to detect the welding seam using arc-imaging, similar to the previous methods of its algorithm, including the steps of using the middle filter, manual thresholding, the removal of small areas, the edge detection. Using Robert's algorithm is an interpolation with a quadratic polynomial method, he unlike the previous methods considers seam edges to be two second-order curves.

2. 1. 1. Using Neural Networks and Fuzzy Logic The instability of industrial systems and turmoil in the industrial environment has led many research into the use of neural networks. In many cases, this has improved sustainability and increased reliability of these systems [10-12]. In some studies also, the combination of neural networks and fuzzy logic has been used [13]. But the problems with these methods are the strong dependence of these systems on the design environment, as these systems do not function in other environments, and depend on one special environment.

2. 1. 2. Proposed Algorithm for Seam Welding Detection Due to the problems of the existing vision systems of the existing machine and the use of the active method used in most of the research, our proposed algorithm is based on the method of inactivity, and the hardware and equipment required are also seen, the effects of using inactive method. The complexity of the algorithm is the extraction of the feature and the sensitivity to the removal of environmental conditions. Due to the use of the inactive hardware method in this article and the close relationship between hardware and the machine vision algorithm, the hardware platform of the system is also briefly examined. As shown in Figure 4, the seamless sewage detection system structure consists of several basic components, including: cross-axis, camera (sight sensing), system head (which

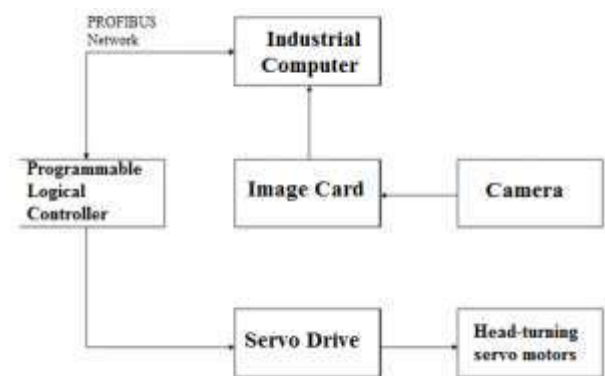


Figure 4. The hardware structure of the seam welding detector to detect the welding seam

includes a tube test tube probe assembly) camera image conversion cards, central controller system, analog-to-digital signal converter cards, head-turning servo motors and an industrial computer.

The crossover axes are controlled by two servomotor 1 controllers. Horizontally controlled motion by the servomotors, along with the control of the welding seam and the precise guidance of the system on the center line of the welding, is carried out by the gearbox to the horizontal axis coupling system, driving the axes in a horizontal direction. The amount of movement and speed of these servomotors depends on the amount of deviation of the system head from the central line, and the goal of the central controller is to minimize this difference so that it can maintain the system head with acceptable error along the center of the system. The mounted motors in the vertical direction also control the height to the pipe surface and vary according to the size of the pipe diameter, which does not need a controller and is manually controlled by the user. The camera sends per second 30 frames from the pipe surface into the computer [14]. In order to increase the reliability of the system for image segmentation and extraction of welder lines, the cutoff technique has been used in two steps, and the edge cutting technique has been used, as well as different edging methods have been evaluated and appropriate mask has been selected. With the characteristics and characteristics of boiling images, different thresholds have been applied to different images. A vertical histogram analysis has also been used for comparative thresholds, the proposed algorithm stages are shown in Figure 5.

2. 1. 3. Sharp Seam Welding Image Smoothing

The use of middle nonlinear filtering is very effective in eliminating random noise as well as pulsed noise, and has less negative effects on the removal of the edges of the weld than linear filters as well as gaseous filters. In order to smoothing and eliminating noise in the proposed algorithm, we used the middle filter, we used

three techniques to eliminate noise in practical studies, the aforementioned techniques are the mean, the mean, and the Gaussian filter. The size of the filter, the smaller the filter is, the less the weld edges disappear and the segmentation accuracy of the image increases. The results of the experiments on different images and the different conditions of welding inspection, the badge; it was mention that the use of the mid-filter is better than the Gaussian filter [15]. It can be said that the average strength of the middle filter is rather resistant to the Gaussian resistance to the momentary changes in intensity in pixels (the amount of pulse intensity is not displayed as a result) as well as the absence of the production of new edges when processing the edges. However, it should be noted that Gaussian filter has a stronger effect in Gaussian noise, unlike the middle filter [16].

2. 2. Detecting the Tube Movement in the Image

In order to increase the speed of the control of the system head and to accurately detect the welding seam, it is necessary to reduce the additional processing and the use of the current image properties. In this way, in extracting successive frames, the current frame difference is used with a new frame, and if a change is made, the new image will be processed. Otherwise, the current system parameters will be changed unchanged to the system head controller as input to the control system.

$$f = \text{median} (f(t+1) - f(t)) \tag{2}$$

where, f (t) is the image extracted at the moment t, also used to remove possible noise from the middle filter, as well as the second soft value of the resulting image difference with a constant threshold (empirically obtained) compared with the larger image. From a threshold, the new image is processed.

$$\text{motion}(t) = \begin{cases} \text{motion} & \|f\|_2 > T \\ \text{no motion} & \|f\|_2 \leq T \end{cases} \tag{3}$$

$$\|f\|_2 = \sqrt{\sum_{i=1}^n \sum_{j=1}^m |f(x_i, y_j)|^2} \tag{4}$$

A fixed threshold, and motion (t) is a function of image change detection, and the dimensions of the image are n * m; if the square matrix is a second, the second soft matrix is actually the largest singular point of the image matrix, in addition to using the soft two image matrices, we could Use the Accumulative Difference Image method to determine the change in image frames, the ADI matrix is created for a sequence of consecutive frames {f (x, y, t1), f (x, y, t2), ..., f (x, y, tn)}, by comparing each frame with a reference frame count for

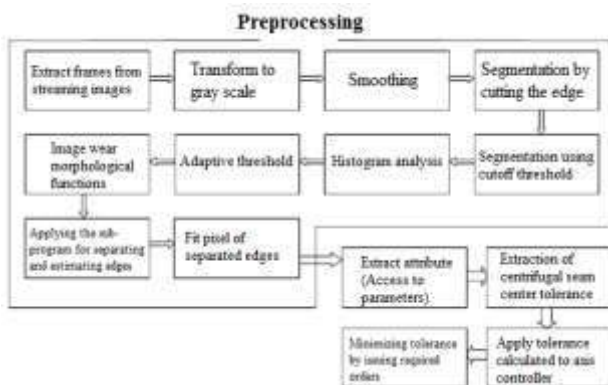


Figure 5. Image processing steps in the proposed algorithm

each location. The pixel in the growing image, however, is added where the difference in the pixel location between the reference image and the video frame (of the sequence) occurs. Therefore, when the k frame is compared with the reference frame, the desired value of the ADI indicates the number of times the pixel changes, Equation (5) shows an ADI matrix, which is an absolute ADI type.

$$A_k(x,y) = \begin{cases} A_{k-1}(x,y) + 1, & |R(x,y) - f(x,y,k)| > T \\ A_{k-1}(x,y), & \text{Otherwise} \end{cases} \quad (5)$$

R (x, y) is a reference image, k is the image at time tk, the above relation can be considered as the reference image as the current image, and as long as the ADI layers are no more than a threshold value, this image is considered as a reference, one of the problems of this method The volume of its calculations is high, therefore, we use the first method (soft second of the image difference matrix) in this paper; in none of the previous algorithms of this method (determination of image changes) is not considered, and according to the percentage of low-dimensional changes in consecutive images in some industrial environments, the application of this method can lead to a reduction in the volume of computation in the next steps.

2. 3. Separation of the Seam of the Weld The use of segmentation techniques in the separation of the weld area from the tube body in real conditions can be very difficult. In ideal images, the intensity of the weld regions is greater than the areas around it, but in actual images, the intensity of the images in the two welding regions (starting and finishing areas). Therefore, the choice of a criterion (such as a threshold) is often difficult in the segmentation of welding images. The tests showed that district growth methods and the use of clustering cannot meet our needs, because they are both cost-effective methods and the similarity criterion well, we cannot define it, we discuss the methods in this article that we have used the edges and thresholds, the severe changes on the edges represent the welding seam, and this feature is used to extract the edges.

2. 3. 1. Proposed Method for Weld Seam Segmentation

The results of practical experiments on a seamless weld image showed that the interval of the Sobel algorithm is wider than other algorithms, then the gradient calculations of the image are made to access a suitable seam welding extract using the matrices of Figure 6, given that the welding seam is parallel with the horizon axis, these matrices compute well the horizontal and vertical seams. Gradient image resulting from the application of a twist. 1 Image of a welder is a gray scale image taken from the sum of the two horizontal and vertical components of Figure 7. The resulting image has negative pixels, which

is due to a change in the intensity at the weld septum and the tube body. In these areas, where the intensity of the tube body is less than the intensity of the seam area, the result of applying the matrices is negative, since these areas must be extracted, in this algorithm, the total second power of the pixels is used to reduce the effect of the negative intensity pixels.

2. 4. Segmentation with Cut off Threshold

The resulting gradient image may have noises due to the strengthening of weak edges or unintended edges, one of the problems with the edges obtained is the probability that these edges are real, in other words, the probability of the edges being real To check, the boundary between real and unreal edges should be estimated as a threshold. Several methods have been used for segmentation of images with thresholds. We used this threshold algorithm in two stages of segmentation of images using thresholds. Probability density functions can be used to detect the actual weld seams. In Equation (6), the likelihood of the edge is shown.

$$P_D = \int p(G|edge)dG \quad (6)$$

where PD is the probability of the realities of the edges, and P (G|edge) is a gradient conditional probability function, provided that the edges are real and t is the



Figure 6. Matrix (mask) horizontal and vertical seam extraction $im=dx^2+dy^2$ where, im gradient image, dx is the vertical component and dy is the vertical component.

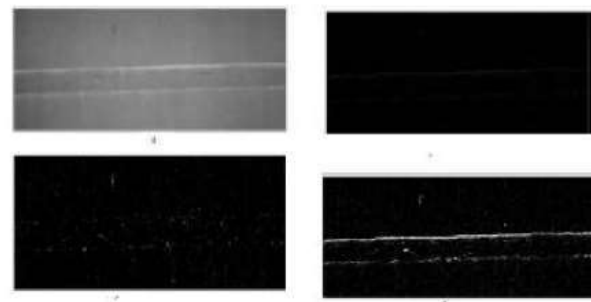


Figure 7. a: Input Image and b: Horizontal Component Image: c: Image of the vertical component; and d: The result of applying the $im = dx^2 + dy^2$

threshold, and the probability of the unrealized and unmerited edges extracted by Equation (7) can be displayed.

$$P_f = \int_1^{\infty} p(G | \text{no-edge}) dG \tag{7}$$

F is the probability of the unreality of the seams, and $P(G | \text{no-edge})$ is the conditional probability of the unreality of the edges. Using the above relations, the probability of the error in the actual welding seam extraction can be written as Equation (8).

$$P_E = (1 - P_D)P(\text{edge}) + (P_f)P(\text{no-edge}) \tag{8}$$

In fact, we can draw the density function as Figure 8 and examine the threshold state.

Selecting a suitable threshold t can be used to reduce the actual PE faces by reducing the actual edges. In fact, if the conditional probability ratio of the real edges is higher than the non-edges; one can hope that a good threshold has been chosen. In other words, if we can establish the relation 10, it can be concluded that the threshold is a useful and appropriate threshold.

$$\frac{p(G + \text{edge})}{p(G | \text{no-edge})} \geq \frac{p(G | \text{no-edge})}{p(G | \text{edge})} \tag{9}$$

The above relations show that the proper threshold selection statistic process requires having information about the probability density and probability functions of the conditional condition of the gradient function, which requires gradient image analysis, which will not be efficient in the real-time system of ours. The parameter shown in the above table is the signal-to-noise ratio defined as follow:.

$$SNR = \left(\frac{h}{\sigma}\right)^2 \tag{10}$$

where, h is the height of the edges of the gradient image and σ is the standard deviation of the image noise, the review of the above table shows that if the noise is low, the SNR of the optimum threshold decreases, as well as in the case of intense noise in the images and low signal

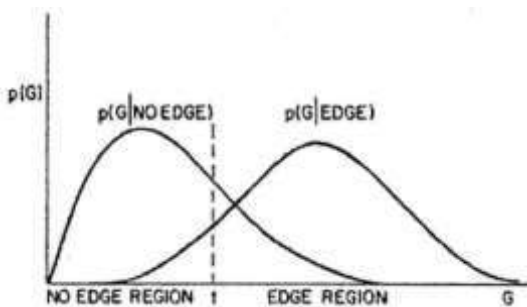


Figure 8. Graph of gradient probability density function

ratio to noise increases the optimum threshold. In addition, as a general rule in cases where $PD = 1 - PF$, in this case the threshold can estimate the signal-to-noise ratio, for example, if $SNR = 100$, the optimal threshold can be approximately 10% of the maximum gradient (William K. Pratt). However, in cases where the signal-to-noise ratio (SNR) is clear in optimum threshold estimates, the SNR parameter calculation is also not easy and costly in most cases, but it can be said that the average normalized gradient image is roughly estimated from SNR and the threshold properly can be an approximation of the root mean square, so you can write the optimal threshold as follows [6].

$$T \cong \sqrt{4 * \text{mean}(fx^2 + fy^2)} \tag{11}$$

By choosing this threshold, they are eliminated as an approximation of the optimal threshold for non-oblique edges. It is more successful in extracting real edges than other images, and very small changes (up to a thousandth) (in the choice of threshold eliminating the real edges or adding a wide range of unreal edges in the binary image. Although, the image obtained from applying an optimum threshold removes a significant portion of the non-edged edges, still has edges and unnecessary noise, which is due to the choice of a threshold instead of several thresholds and should be removed with further methods.

3. RESULTS

3. 1. Histogram Analysis

The choice of the appropriate threshold for separating the weld from the tube body is a key step in seamless tracking. After segmentation by cutting the edge, thresholding for the final seam cut is used, but as mentioned in some images still have many unobtrusive edges that should be removed, histogram analysis, and the use of variance. Atoso method has been used in many seam welding tracking methods [12]. In the practical test, the above methods did not succeed in weld images of all of the above methods, and practically eliminated a large part of the useful edges or created many unnecessary edges that, in the process of processing the extraction algorithm, faced the characteristics with a fundamental problem, one of the factors of the failure of the above methods is due to this feature that the difference in intensity between the seam and the bottom of the tube is not very high and the histogram of the images does not have distinct peaks and in spite of the uncertainty of the correctness of the operation of the above algorithms in the correct segmentation of all the image. The methods rely on repetition, which are very costly, for these reasons, we have to look for a new method for the proper placement of the seamless images.

3. 1. 1. The Proposed Threshold Method

Due to seamless welding images, which is almost parallel to the horizontal axis, this feature can be used to calculate the total intensity of the pixels along horizons (horizontal histogram) along the horizontal axis, so the histogram of each pixel. The row is computed, equation 12 defines the definition of the horizontal histogram (histogram projection). By this definition, for each row, i represents the total number of pixels in that row, which is equal to one (binary image) to that row.

$$hist(i) = \sum_{j=1}^M d(xi, yi), P(A) = \sum_{k=1}^N his(k) \quad (12)$$

A is a binary image of $N \times M$ dimension, N is the image length of the pixel unit, and M is the image width of the pixel unit. By checking the histogram obtained from equation 14 in different welding images, it was found that this histogram has two different peaks with suitable intervals. Observation, the accumulation of pixels in the weld seams will be higher, and these are the same pixels of seamless welding, so the pixels of our areas around the histogram peaks where the pixels are more focused. Therefore, if you can reconstruct the image by separating these pixels and eliminating the intensity of other pixels away from the peaks, then a successful segmentation has taken place. It is noteworthy to reach a number to estimate the margins of these peaks, by performing numerous experiments on practical images, we conclude that the use of peak (max) (histogram) and applying a coefficient can improve fractional percentages, so the desired threshold relationship that we define it as equation 13.

$$T = a \cdot \text{Max}(P(A)) \quad (13)$$

where, a is a coefficient and $P(A)$ is a histogram of the binary image A , which is a coefficient of a to adapt to a very flexible environment. A sample image with histogram and segmental image is shown in Figure 9.

3. 2. Investigating the Algorithm

In dealing with the type of welding, the surface of the pipes in practice there are two basic types of problems that must be considered as a solution for it. Distribution of pixels at two-edged points due to the accumulation of points in

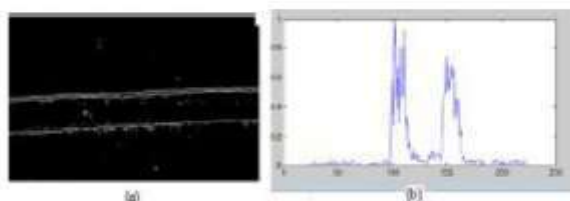


Figure 9. A: A binary image of the welding seam, a: a sectioned image with the proposed method, b: Histogram image

the edges: ruggedness of the welded area. Investigation of welding images in practical tests shows that the disturbances due to the lack of proper welding and the fluctuations of the welding parameters cause the damaged and deformed areas of the weld at the pipe level. Therefore, the extraction of the characteristic in this type of pouring is encountered with difficulty and if there is no proper welding surface, many boundaries, whether real or unrealistic, are created and this creates sharp changes in the histogram of the image, which makes it difficult to detect the maximum points, so the algorithm must be able to correctly and in a user-friendly environment to trace all of these poorly-formed welds.

In Figure 10, the purple spot is the center of the system, calibrated at the beginning of the test, and the point is red in the center of the weld seams, and dr is the distance between these two points.

3. 3. Automatic Ultrasonic Testing

This machine consists of three sections of pipe transfer, seam welding detection and monitoring system at the time of tube testing. The central controller includes the PLC of the Siemens S7 model, and the motor controllers and local sensors are connected to the profibus network to the CPU. The position of the pipe is connected to the plunger connected to the motor by the anchor and controlled by the speed and location of the pipe for the up and down of the ultrasonic levels. The advanced monitoring system provides real-time monitoring and monitoring of ultrasonic signals through profibus and opc communications, providing a data bank for data storage. The transfer of the pipe from the inlet to the outlet and follow the welding seam to detect the ultrasonic probes, as well as the automatic monitoring of the system. To simulate the positioning of two probes in relation to the welding site during the test of a seamless sewage detector system, which is based on image processing techniques and machine-design techniques used in this system. This test consists of two subsections: the tube transfer part and the computer-based monitoring part as shown in Figures 11 and 12, respectively.

3. 3. Evaluation of the Accuracy of the Algorithm (Implementation Method)

In evaluating the accuracy of the system, the amount of deviation from



Figure 10. Position of the center of the seam and the head of the system

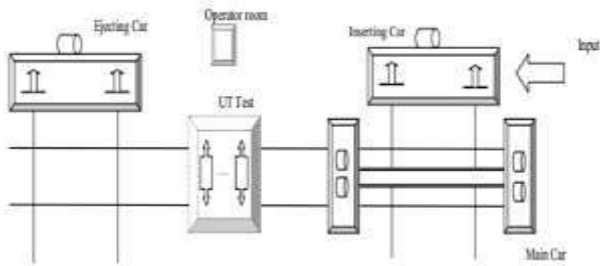


Figure 11. General diagram of pipe transfer



Figure 12. Monitoring system

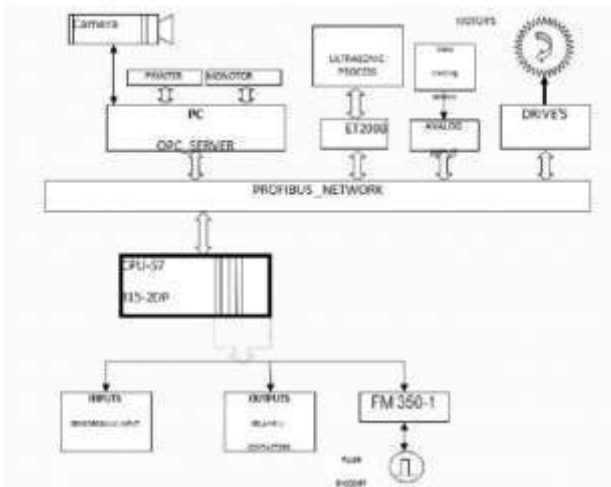


Figure 13. General structure of the automation system of the proposed ultrasonic testing machine

the center of the weld is considered from the center point of the device. The results of this test are presented in Table 1. In order to achieve these results, the system is implemented in a laboratory, and with the installation of hardware and software, the tracking operation. In order to calculate the amount of leakage deviation from the center of the system, a point-of-contact laser source was introduced into the coupler system, which is beamed to the welding seam at the output of the

machine, along with the deviation of the seams. This luminous point also diverged, at the same time, from the surface of the films, the deviation from the centerline was calculated by measuring the amount of distortion in the obtained frames. Considering that the algorithm is designed to extract the two edges of the weld seam, in the two windows execute the seamless pixel thinning operations. Therefore, the final accuracy depends on the accuracy of the algorithm in welding seam welding on both sides. In order to access the criteria for comparing the accuracy of the system, several different images at different intervals from the pipe surface and in different environmental conditions. It was tested with different contrast and resolution, resulting in a seamless deviation. By the proposed algorithm, the actual seam is calculated. According to Equation (13), the system error can be written as Equation (14).

$$d_r \leq 0.5(d_{low} + d_{hi})$$

$$\bar{e} = (\sum_{i=1}^N |e|) / N, i = 1, 2, \dots, N \tag{14}$$

e: The mean error of the system is calculated from Equation (27), if the magnitude of the relation is neglected, the mean of the arithmetic is obtained.

d r: The error rate of the center point of the weld seam is calculated from the actual center of the welding seam.

d low: The low seam extraction error is due to the boiling point of the lower seam.

d hi: The magnitude of the extracted extraction seams exceeds the actual boiling point of the seams.

Of course, due to different sources of error, computational errors and rounding errors of numbers are ignored.

3. 4. Calibration Operations

The precision and accuracy of the results of the algorithm in the industrial environment. In addition to the specific environmental conditions, depends on the visual distance of the machine as well as its viewing angle from the surface of the piece, the more the distance between the sensor (CCD) is less than the surface of the tube; the accuracy of the sampling operation increases in practice. Also, the angle of view of the sensor in the geometric coordinates of the image has a great impact. In the real world, the real coordinates of objects must conform to their coordinates in the image; in practice, there are usually angles between the Cartesian coordinates and in systems that are used for measurement. The relationships between the axes of the coordinates in the image and their actual axes in the environment must be calculated. In this, research we have set the angle between the axes of the coordinates in the image and the real coordinates of the system and set the sensor perpendicular to the direction of the tube movement. So that the axes are inconsistent and the only parameter to be calculated is the scale factor.

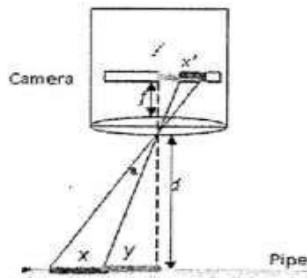


Figure 14. Connection between the camera and its distance from the pipe surface

$$\frac{x}{x'} = \frac{d}{f} \tag{15}$$

where, f is the focal length of the sensor lens and d is the distance between the camera and the tube and x is the part of the image and x' is the image of this section in the sensor x, f, d in length unit (mm), x picture size in the real world is the need to know the resolution of the pixel to calculate it.

$$x' = h(\text{count}(\text{pixel})) \tag{16}$$

where, h is the pixel factor. To calculate, h we use a standard ruler and, at a specified distance, by imaging a sample tube (pipe pipe), which is created in accordance with the standard pipe production, a pipe, and throughout the project that the calibration of different devices is used and the relationship (5) to determine the value of h .

$$s' = \text{pixel count for } S; \quad s = 10\text{mm}, \quad \frac{s}{s'} = h \tag{17}$$

In Table 1, in the first column, the value of h is calculated for different images at different intervals, depending on equation 3. The image size in the visual sensor is related to the distance from the image of the image. Therefore, at different intervals, different numbers for h is obtained. In Tables 1 and 2, the result of the algorithm's execution on fifty different frames shows the test of a pipe after calibration, in this $d_{r,low}, d_{hi}, h = 0.168\text{mm} / \text{pixel}$ test. The point in examining the results of the tables is that since the weld seam center error is computed, in most cases, the final error of the seam welding center has decreased, which increases the accuracy of the algorithm.

Given that the direction of movement along the y -axis is evaluated, only the spatial coordinates of this direction are evaluated; in Figure 16, on the number of frames of an analytical tube, the center of the welding seam in each frame is calculated by the proposed algorithm. The error rate is also measured from the actual boiling point. In section (a), this difference is in millimeters, and in (b) the difference is in pixels, since

TABLE 1. Sampling from the result of the algorithm implementation on fifty frames of the test of a pipe (I)

No.	d_{hi} (pixel)	d_{low} (pixel)	d_r (pixel)	d_r (mm)
P5	3	3	3	0.504
P10	-1	2	1	0.168
P15	1	-4	-2	-0.336
P20	-3	1	-2	-0.336
P25	-2	-6	-4	-0.672

TABLE 2. The result of the algorithm implementation on fifty frames of the test of a pipe (Part II)

No.	d_{hi} (pixel)	d_{low} (pixel)	d_r (pixel)	d_r (mm)
P5	-2	2	-4	-0.672
P10	-3	2	-1	0.168
P15	2	3	2	0.336
P20	4	2	3	0.504
P25	1	3	1	0.168

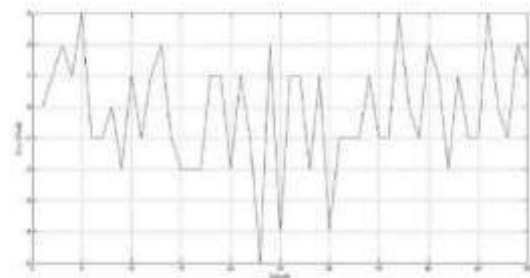


Figure 15. Tolerance diagram (deviation) of weld seam center calculated by the proposed algorithm from the actual center of weld seam in pixels

the deviation from the center is dependent on the value of h ($h = 0.168\text{mm} / \text{pixel}$) the accuracy of the algorithm is also based on the number of pixel deviation per millimeter.

$$\begin{aligned} \bar{x} &= 1.5 \text{ pixel} = 1.5 * 0.168 = 0.252 \text{ mm} \\ \bar{E} &= -0.2 \text{ pixel} = -0.2 * 0.168 = 0.0336 \text{ mm} \\ \sigma &= 1/50 \sqrt{\sum_{i=1}^{50} (|x_i| - 1.5)^2} = 6.4807 \text{ pixel} \end{aligned} \tag{18}$$

4. CONCLUSION

In the field of machine vision in nondestructive welding, there are many things that can be the basis for future research, these can be very effective in improving the efficiency of existing algorithms, such as the following.

- The use of multilayer neural networks for machine training in the estimation of the weld seam at the pipe inspection. It should be noted that neural network research in the welding section has been performed on the calculation of the welding arc, however, much research can be pursued in the area of welding inspection.
- Using fuzzy controllers to design a seam welding detection controller using fuzzy logic ++ software and Siemens systematic software.
- Development and design of integral and derivative controllers to improve the accuracy and speed of seam welding center detection.
- Designing algorithms for detecting non-parallel welds with the axis of motion of the welding machine.
- Development of techniques for eliminating all kinds of actual noise in industrial environments.
- Designing algorithms to draw a three dimensional polygonal pattern (pool welding) for more accurate tracing of the weld seam.
- Development of segmentation techniques for identifying the typical welds type of welds activated in weld inspection.
- Designing algorithms for tracking asymmetric welds.
- Using Kalman's algorithm (Kalman Filter) to detect and track the seam welding center.
- Providing combined methods for improving the mineral method and Atos method in welding seam extraction.
- Evaluating the effectiveness of methods such as active contour.

5. REFERENCES

1. Fang, Z.J. and Xu, D., "Application of vision sensor to seam tracking of butt joint in container manufacture", *Embedded Visual System and Its Applications on Robots*, (2010), 56-82.
2. Fang, Z., Xu, D. and Tan, M., "Visual seam tracking system for butt weld of thin plate", *The International Journal of Advanced Manufacturing Technology*, Vol. 49, No. 5, (2010), 519-526, doi: 10.1007/s00170-009-2421-0.
3. Gao, X., Ding, D., Bai, T. and Katayama, S., "Weld-pool image centroid algorithm for seam-tracking vision model in arc-welding process", *IET Image Processing*, Vol. 5, No. 5, (2011), 410-419, doi: 10.1049/iet-ipr.2009.0231.
4. Chen, X., Chen, S., Lin, T. and Lei, Y., "Practical method to locate the initial weld position using visual technology", *The International Journal of Advanced Manufacturing Technology*, Vol. 30, No. 7, (2006), 663-668, doi: 10.1007/s00170-005-0104-z.
5. Wu, Y.Q., Yuan, Z.H. and Wang, J.H., "A fuzzy controller design of seam tracking for welding robot", in *Advanced Materials Research, Trans Tech Publ.* Vol. 442, (2012), 370-374.
6. Xu, P., Xu, G., Tang, X. and Yao, S., "A visual seam tracking system for robotic arc welding", *The International Journal of Advanced Manufacturing Technology*, Vol. 37, No. 1-2, (2008), 70-75, doi: 10.1007/s00170-007-0939-6.
7. Dhankhar, P. and Sahu, N., "A review and research of edge detection techniques for image segmentation", *International Journal of Computer Science and Mobile Computing*, Vol. 2, No. 7, (2013), 86-92.
8. Fattahzadeh, M. and Saghaei, A., "A statistical method for sequential images-based process monitoring", *International Journal of Engineering*, Vol. 33, No. 7, (2020), 1285-1292.
9. Bender, G. and Simonsen, R.R., "Photography's materialities: Transatlantic photographic practices over the long nineteenth century, Leuven University Press, (2021).
10. Devanathan, R., Chan, S.P. and Chen, X., Techniques of automatic weld seam tracking, in *Advanced automation techniques in adaptive material processing*. 2002, World Scientific.125-166.
11. Kheradmandan, H. and Barati, F., "Modeling width of weld in saw with adding nano material", *Journal of Research in Science, Engineering and Technology*, Vol. 5, No. 02, (2017), 1-7.
12. Mashadi, B., Mahmoodi-K, M., Kakaee, A.H. and Hosseini, R., "Vehicle path following control in the presence of driver inputs", *Proceedings of the Institution of Mechanical Engineers, Part K: Journal of Multi-body Dynamics*, Vol. 227, No. 2, (2013), 115-132, doi: 10.1177/1464419312469755.
13. Fakoor, M., Kosari, A. and Jafarzadeh, M., "Humanoid robot path planning with fuzzy markov decision processes", *Journal of Applied Research and Technology*, Vol. 14, No. 5, (2016), 300-310, doi.
14. Meyghani, B., Awang, M. and Wu, C., "Thermal analysis of friction stir welding with a complex curved welding seam", *International Journal of Engineering, Transactions A: Basics*, Vol. 32, No. 10, (2019), 1480-1484, doi: 10.5829/ije.2019.32.10a.17.
15. Salehpour, F., Nematifard, V., Maram, G. and Afkar, A., "Experimental investigation of tig welding input parameters effects on mechanical characteristics", *International Journal of Engineering, Transactions B: Applications*, Vol. 34, No. 2, (2021), 564-571, doi: 10.5829/ije.2021.34.02b.30.
16. Xue, B., Chang, B., Peng, G., Gao, Y., Tian, Z., Du, D. and Wang, G., "A vision based detection method for narrow butt joints and a robotic seam tracking system", *Sensors*, Vol. 19, No. 5, (2019), 1144, doi: 10.3390/s19051144.

Persian Abstract

چکیده

برای برنامه ریزی مسیر ربات ، موقعیت درز جوش باید از قبل شناخته شود زیرا ربات های صنعتی معمولاً در حالت آموزش و پخش کار می کنند. از آنجا که جوشکاری لوله به طور کامل بر روی خط مستقیم (ماهیت لوله) انجام نمی شود و لوله آزمایش در زیر دستگاه در حال حرکت است ، تقارن دو پروب نسبت به محل جوشکاری در هنگام آزمایش بسیار مهم است و برای تنظیم کاوشگرها ردیابی سریع لازم است. استفاده از تکنیک های پردازش تصویر و بینایی ماشین در بهینه سازی شعاع جوشکاری بدون درز بسیار کارآمد است. در طراحی الگوریتم های مورد استفاده ، سعی شده است شرایط محیطی و وضعیت ناپایدار صنعتی به خوبی کاهش یابد تا درز جوش با سرعت قابل قبول ردیابی شود. روش جدیدی برای دسترسی به خط مرکزی ناحیه درز جوش استفاده شده است. الگوریتم طراحی شده است تا در یک محیط واقعی اجرا شود و نتایج بسیار خوبی دارد. یکی از مزایای این روش کاهش خطای اندازه گیری و حذف حسگرهای مکانیکی و الکتریکی در آزمایش های غیرمخرب است.



Strengthening of Reinforced Concrete Beams using Self-consolidating Concrete Jacket Consisting of Glass Fiber and Fiber-silica Fume Composite Gel

S. Mohsenzadeha, A. Maleki^{a*}, M. A. Lotfollahi-Yaghin^b

^a Department of Civil Engineering, Maragheh branch, Islamic Azad University, Maragheh, Iran

^b Faculty of Civil Engineering, University of Tabriz, Tabriz, Iran

PAPER INFO

Paper history:

Received 15 May 2021

Received in revised form 02 July 2021

Accepted 04 July 2021

Keywords:

Reinforced Concrete Jacket

Fiber-Silica Fume Composite Gel

Glass Fiber Reinforced Polymer Sheet

Reinforced Concrete Beam

Strengthening

Glass Fiber

ABSTRACT

In this paper, strengthening of RC beams with self-consolidating concrete (SCC) jacket containing glass fiber (GF) and fiber-silica fume composite gel (FSCG) were investigated. FSCG can use as a substitute for a part of the cement that contains silica fume powder, polypropylene fibers, superplasticizer, concrete waterproof, and some other admixtures. In order to evaluate the performance of the proposed jacket, twelve beams were strengthened and a control beam was made. The variables included the amount of glass fibers consumed in the jacket (0, 0.25, 0.5, 0.75, 1 and 1.25% by volume) and the amount of FSCG gel (0 and 7%), respectively. Fresh and hardened concrete properties and flexural capacity of RC beams were investigated. The use of FSCG in RC jackets can compensate well for the deficiency in strength due to the GF entry into the concrete matrix. High affinity of these materials improve the cohesion between cement and GFs. RC jackets containing GF and FSCG increased the beams' energy absorption capacity by about 89 to 463%, depending on the percentages of GFs. RC jacket containing GF and FSCG delays the growth of the primary crack and it can significantly increase the maximum load. Also, Glass Fiber Reinforced Polymer (GFRP) sheets have poor performance compared to the proposed method due to separation from the surface of the strengthened beams, and their load-bearing capacity and energy absorption are lower.

doi: 10.5829/ije.2021.34.08b.14

1. INTRODUCTION

In recent years, strengthening of existing structures and repair of damaged buildings has increased widely. Changes in structure occupancy require strengthening with increasing bearing capacity of their members [1-3]. The strengthening method's choice depends on strength, amount of damage, type of members and connections, access to materials, and economic aspects [4, 5]. These methods can include methods such as changing the lateral-resisting system (brace or shear wall), adding steel plates (steel jacket), using concrete jackets, using reinforced polymer fiber, using fiber concrete, shotcrete, and using near-surface mounted composite rebars, etc. [6-9]. Nowadays, strengthening and rehabilitation of beams, which are essential members of structural frames, have been investigated. Increasing flexural or shear

capacity, control of deformation, and cracking are the main goals of strengthening these members [10-12].

Monir et al. [13] analyzed RC beams using concrete jackets. The slip in the analysis was ignored and the jacket overall behavior was examined, which results in higher estimates of stiffness or capacity. Aldhafairi et al. [14] used steel jackets to retrofitting normal concrete beams, high strength and self-compacting. For this purpose, steel plates and angles were used and it was shown that steel angles have better performance compared to steel plates [14]. Tayeh et al. [15] investigated the flexural performance of RC beams retrofitted with self-compacting concrete jackets containing welded steel wire mesh. The results showed that the proposed method significantly increased the beams bearing capacity [15]. Yuan et al. [16] evaluated the strengthened beams using basalt sheets and a new epoxy was used. They showed that basalt fiber sheets

*Corresponding Author Email: Maleki.ah@yahoo.com (A. Maleki)

with the proposed epoxy can improve the behaviour of the RC beams and delay the debonding of the fiber [16]. Shadmam et al. [10] showed that the combined use of steel plate and steel reinforced fiber can improve the flexural toughness of RC beams by about 89 to 119%. Rahmani et al.[11] conducted a laboratory study on strengthening of RC with RC jackets containing steel fibers. They showed that steel fiber can decrease the cracks and improve the performance of the RC jacket [11]. Faez et al. [12] examined the strengthened beams with RC jacket. They used aluminum oxide nanoparticles and silica fume in jacket. The proposed method enhanced the bearing load about 155 to 447% [12]. Maraq et al. [17] investigated the flexural behavior of reinforced concrete beams with steel wire mesh and self-compacting concrete jacket. The proposed method increased the bearing capacity of the beam by about 110 to 163% [17]. Ghalehnavi et al. [18] investigated the retrofitting of concrete beams made from recycled materials using reinforced concrete jackets made of steel fibers. The results showed that the use of 2% steel fibers can play an effective role in improving the bearing capacity of beams made with recycled materials [18]. According to studies, tensile, compressive, and flexural concrete strengths can be significantly increased using fiber [6, 19, 20]. In a number of mentioned studies, it has been observed that steel fibers have been used in concrete jackets. One of the problems with steel fibers is that they rust in the long run, which can affect its performance. To overcome this weakness, in the proposed method, glass fibers are used in jackets, which in addition to not having the problem of corrosion, its weight is less compared to steel fiber. The use of FSCG is also expected to improve the adhesion between the fibers and the cement. In this paper, strengthening of the beams was investigated using SCC jackets containing glass fiber (GF) and fiber-silica fume composite gel (FSCG). FSCG and GF can compensate for tensile weakness of concrete. It should be noted that the concrete used in the concrete jacket is SCC, so that there will be no problem with vibration for obtaining the required compacting. In this method, RC beams' peripheral surface is first reinforced with longitudinal and transverse reinforcement rebars. The distance between steel reinforced rebars and the peripheral surface of beams is filled with SCC containing GF in which FSCG is used. Considering the use of GFRP plates is being developed as a conventional strengthening method, comparing the newly presented method with strengthening of RC beams using GFRP sheets in new aspects. Using a concrete jacket reinforced with GF and FSCG is more effective in strengthening irregular outer beams that do not have suitable concrete covering than GFRP sheets. Moreover, in many cases, tensile forces of concrete are not precisely known. Since reinforcement rebar forms a small part of the section, the concrete section's assumption is a homogenous and isotropic

section is incorrect. Therefore, GF and FSCG in the concrete jacket can create isotropic conditions and reduce fragility weakness and concrete brittle.

2. EXPERIMENTAL PROGRAM

2. 1. The Variables The studied variables are strengthening method type (strengthening by SCC jacket containing GF, strengthening by SCC jacket containing GF and FSCG, strengthening by GFRP sheets, without strengthening), the content of the used GF in RC jacket (0, 0.25, 0.5, 0.75, 1, and 1.25 % by total volume of concrete), presence or absence of FSCG in RC jacket (0 and 7% by weight of cement) and the number of GFRP layers (1, 2 and 3 layers). Thus, according to the study variables, 16 RC beams were constructed in different modes and were evaluated using a four-point bending test. The considered beams were introduced in Table 1.

TABLE 1. Introducing the investigated beams

Name	Strengthening method	AR-GF used in jacket (%)	FSCG	Number of GFRP layers
CB	Without strengthening	-	-	-
F0	RC Jacket	0	0	-
F-0.25	RC Jacket	0.25	0	-
F-0.5	RC Jacket	0.5	0	-
F-0.75	RC Jacket	0.75	0	-
F-1	RC Jacket	1	0	-
F-1.25	RC Jacket	1.25	0	-
F0-FS	RC Jacket	0	7	-
F-0.25-FS	RC Jacket	0.25	7	-
F-0.5-FS	RC Jacket	0.5	7	-
F-0.75-FS	RC Jacket	0.75	7	-
F-1-FS	RC Jacket	1	7	-
F-1.25-FS	RC Jacket	1.25	7	-
GFRP-1L	GFRP wrapping	-	-	1 Layer
GFRP-2L	GFRP wrapping	-	-	2 Layers
GFRP-3L	GFRP wrapping	-	-	3 Layers

CB: Control beam F: Glass fiber, FSCG: Fiber silica fume composite gel
 RC Jacket: Reinforced concrete jacket
 GFRP-1L: Glass-fiber reinforced polymer - 1 Layer
 GFRP-2L: Glass-fiber reinforced polymer - 2 Layers
 GFRP-3L : Glass-fiber reinforced polymer - 3 Layers

2. 2. Material Mixture details of the original beams and RC Jacket are presented in Table 2. Materials for constructing the 13 beams were gravel, sand, cement, water, GF, FSCG, and reinforcement rebars (Figure 1).

FSCG can be used as a substitute for a part of the cement that contains silica fume powder, polypropylene fibers, superplasticizer, concrete waterproof, and some other admixtures. According to the manufacturer's

TABLE 2. Mixture details of the original beams and RC Jacket

Member	Mix code	$\frac{W}{C}$	C (kg/m ³)	G (kg/m ³)	S (kg/m ³)	GF (kg/m ³)	FSFGe (kg/m ³)	SP (%)
Original Beam	S-OB	0.625	320	900	850	-	-	-
	S-0-0	0.27	760	480	414	0	0	1.52
	S-0.25-0	0.27	760	478	412	6.75	0	1.52
	S-0.50-0	0.27	760	475	410	13.5	0	1.52
	S-0.75-0	0.27	760	474	408	20.25	0	1.52
	S-1.00-0	0.27	760	471	406	27	0	1.52
RC Jacket	S-1.25-0	0.27	760	480	414	33.75	0	1.52
	S-0-0	0.27	703	478	412	0	57	1.49
	S-0.25-7	0.27	703	475	410	6.75	57	1.50
	S-0.50-7	0.27	703	474	408	13.5	57	1.51
	S-0.75-7	0.27	703	471	406	20.25	57	1.51
	S-1.00-7	0.27	703	480	414	27	57	1.52
	S-1.25-7	0.27	703	478	412	33.75	57	1.53



Figure 1. Used material a: Coarse aggregates b: Fine aggregates c: Cement d: GF e: Superplasticizer f: FSCG g: GFRP plates h: Paste

information, this product is following ASTM C1240 [21]. Properties of this gel are presented in Table 3. The consumption amount of this product in this study is considered 7% by the weight of cement. This product should be thoroughly mixed with about 200 g of water, and after mixing, it should be added to all concrete components, and then the mixing process should be continued for 5 minutes. The density of FSCG is 1.6 g/cm³. These materials are pasty and dissolve in water, and their color is gray.

The size range of the aggregates and their comparison with the values of the ASTM-C33 [22] are presented in Figure 2. The used cement was produced following ASTM C150 [23] (Table 4). Drinking water was used following ASTM C190 [24]. The plasticizer was liquid, and the density was 1.1 g/cm³. AR-GFs were used in this study (Length: 30 mm, Diameter: 5 to 20 mm). The reason for using this size is their better results in experiments conducted by other researchers. Although fibers whose size is smaller than optimum have better

TABLE 3. The attributes of FSCG

Physical state	Colour	Density (gr/cm ³)
Elastic paste	Gray	1.6
PH	Percent elongation	Tensile strength (MPa)
Neutral	4.8	3300

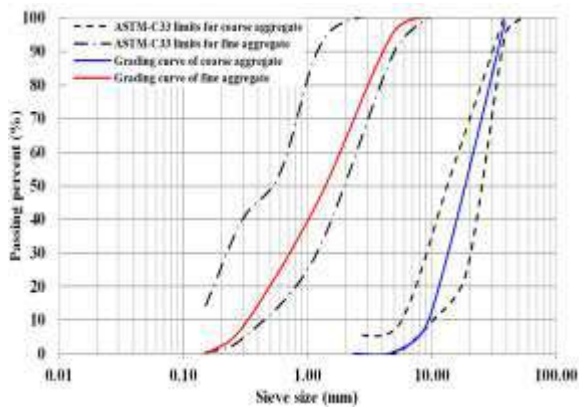


Figure 2. The size range of the aggregates and their comparison with the values of the ASTM-C33

TABLE 4. Chemical attributes of the used cement

Components	Cement type II%
SiO ₂	21.27
Al ₂ O ₃	4.95
Fe ₂ O ₃	4.03
CaO	62.95
MgO	1.55
SO ₃	2.26
K ₂ O	0.65
Na ₂ O	0.49

composition ability, they reduce strength; Larger fibers also have composition ability [25]. The properties of GF are presented in Table 5.

GFRP plates were cut into rectangles with 12 cm width and required length. And after smearing with the paste, the beams were carefully installed. Properties of the GFRP plates are presented in Table 6. The paste used for sticking GFRP plates on the beam is obtained from a mixture of resin and hardener in the ratio of 100 to 15. The mix of these two materials was performed concurring to the method suggested by the FRP producer. All resin components were mixed at a sufficient temperature until the mixing and stirring of materials reached a uniform and complete mix. Resin composite materials usually have different colors and must be mixed enough to achieve a uniform color (Table 7) [26].

TABLE 5. The attributes of the used GF

Type	Length (mm)	Density(g/cm ³)
A-Glass	30	2.44
Fiber diameter (mm)	Percent elongation	Tensile strength (MPa)
5-20	4.8	3300

TABLE 6. Properties of GFRP sheets

GFRP Type	Thickness (mm)	Tensile strength (MPa)
E-Glass	0.16	2200
Tensile modulus (GPa)	Young,s Modulus (MPa)	Density (kg/m ³)
70	72000	2550

TABLE 7. Properties of resin and hardener

Properties	Amount	Unit
Type	EPL1012	-
Compressive Strength	97.4	MPa
Flexural Strength	96	MPa
Tensile Strength	76.1	MPa
Impact resistance	7.850	kJ/m ²

According to the mentioned proportion, the two resin and hardener materials were mixed in the laboratory when the GFRP sheet was being pasted to the beam. After a short time, GFRP plates were installed on the beam.

2. 4. Preparation of the Beams before Strengthening

Geometric properties of the original beams are shown in Figure 3. Four reinforcement rebars are used in the beams (Diameter: 12 mm). Rebars with diameters and intervals of 10 and 100 mm were used as stirrups. Wooden molds were built according to the beams' measurements. The beams samples were expelled from molds 24 hours after concrete pouring and put away in a water tank for 28 days. After curing, the beams were arranged for strengthening by SCC jackets and GFRP sheets. The preparation steps of the original beams is shown in Figure 4.

2. 4. Preparation of RC Jackets

Three types of RC jackets were constructed in the present study. GF and FSCG weren't used in the first group. GF was used in the second group, and GF and FSCG were used in the third group. The beams' strengthening was conducted on three sides of the beams (bottom and lateral sides of the beam up to 2/3 height of beam). The distances and diameters of the reinforcement rebars were 50 mm and 10 mm, respectively. The beam surface preparation process is one

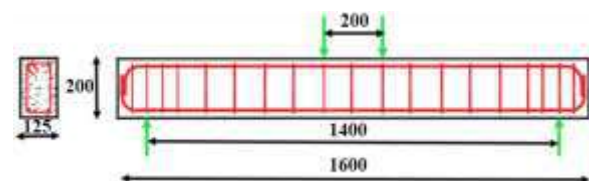


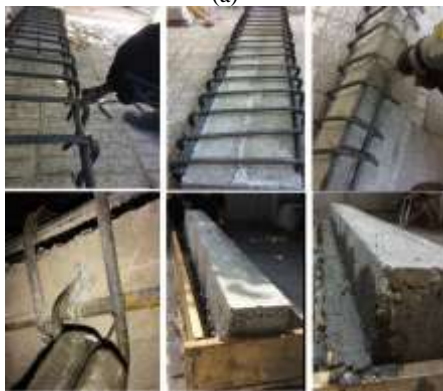
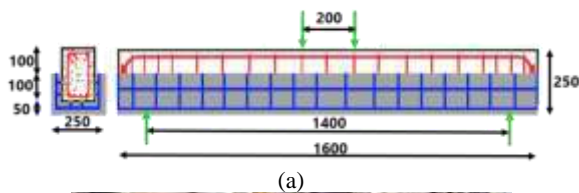
Figure 3. Geometric properties of original beams



Figure 4. Preparation of original beams

of the important parts of the experiment. For occurring no debonding during the test, a full bond must be made between the surface of the prior concrete, concrete jacket, and GFRP. The steps of preparing concrete jackets are shown in Figure 5.

2. 5. Installation of GFRP Plates Pollution, dust, oil, and anything else that may interfere with the FRP system's cohesion and concrete should be eliminated [27]. One of the significant failures of retrofitted RC beams with FRP plate is deboning from the beam surface, known as deboning. Much work has recently been done to prevent this phenomenon. Mostofinejad and Shameli [28] proposed a groove method to avoid this phenomenon. In this experiment, the beams considered for strengthening were reinforced with GFRP after preparing the concrete surface and making longitudinal grooves. It should be noted that these grooves were filled with paste. The GFRP plate was cut into the desired size,



(b)

Figure 5. Preparation of RC jackets a: Geometric properties and steel reinforcement arrangement b: Preparation

and the resin was scattered evenly to the surface using a brush. Fibers were put on the surface using rolling brushes that rotate and move in the direction of the fibers, the fibers were pasted to the resin, and air bubbles which were a detrimental factor for bonding, were removed. The time required for setting and curing the resin at temperatures above 7 ° C is 72 hours. The steps of pasting the GFRP plate onto the beam surfaces are shown in Figure 6.

2. 6. Experimental Tests Table 8 provides a list of tests performed to determine the attributes of fresh concrete and hardened concrete. Compressive strength and splitting tensile strength tests were performed in accordance with ASTM-C39 [29] and ASTM-C496, respectively. Slump flow, T50, V-funnel and L-box tests were also performed in accordance with EFNARC Standards. The beams supports were simple and the loads were applied to the center of the beam. Since four beam points (two support points and two loading points) are subjected to load, this method is called four-point loading. In many studies [30-34] that have been done in the field of beam retrofitting, this method is used for loading and is similar to ASTM-C293 [35] except that it has more load points.

The bending test machine used has an increasing bearing capacity of 200 tons. Loading was continued until the beam fails. The center distance to the support center is 140 cm, and the load span is 20 cm. Loading device and schematic image of loading is shown in Figure 7. Mid-span deflection were measured using a displacement gauge located just below the load site.



Figure 6. Installation of GFRP plates

TABLE 8. A list of tests performed to determine the attributes of fresh concrete and hardened concrete

Test	Standard	Properties type	Specimen dimension (cm)
Slump flow			
T50	EFNARC	Fresh properties	--
V-funnel			
L-box			
Compressive strength	ASTM-C39 [29]	Hardened properties	15×15×5
Splitting tensile strength	ASTM-C496 [37]		

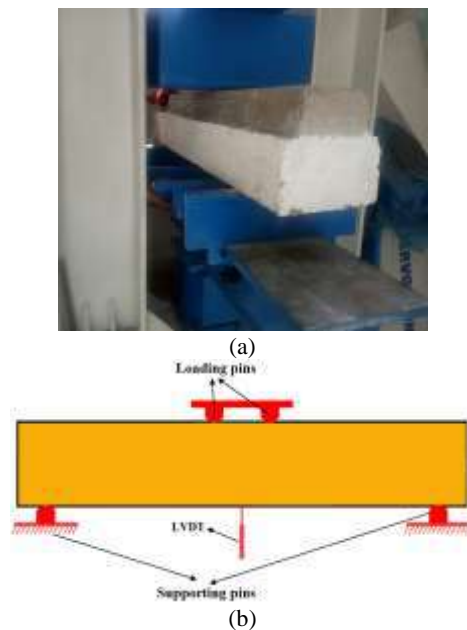


Figure 7. Details of loading a: Loading device b: Schematic image of loading

4. RESULTS AND DISCUSSION

4. 1. Fresh Concrete Results

Table 9 presents controlling fresh properties of SCC according to EFNARC Standards and ASTM C293 [35, 36]. The results show that all specimens meet SCC requirements and fall within the EFNARC standard range.

TABLE 9. Fresh concrete properties

Mix code	Slump flow		V-funnel flow time (s)	L-box (H_2/H_1)
	D (mm)	T_{50} (s)		
S-0-0	669	3.78	8.6	0.99
S-0.25-0	668	4.24	10.2	0.99
S-0.50-0	667	4.83	10.9	0.97
S-0.75-0	653	4.91	11.5	0.95
S-1.00-0	651	4.95	11.8	0.95
S-1.25-0	650	4.98	11.9	0.92
S-0-0	781	2.98	6.7	0.94
S-0.25-7	773	3.15	7.9	0.93
S-0.50-7	761	3.45	8.3	0.93
S-0.75-7	751	3.65	9.1	0.92
S-1.00-7	743	3.98	9.5	0.89
S-1.25-7	738	4.21	10.1	0.89
EFNARC recommended values				
Min.	650	2	6	0.8
Max.	800	5	12	1

The slump flow diameter decreases slightly by adding GF to concrete (Figure 8). The slump flow diameter of specimens containing 0, 0.25, 0.5, 0.75, 1 and % GF were decreased 0.14, 0.29, 2.4, and 2.7 %. Fibers prevent the flowability of cement paste [38, 39]. Güneyisi et al. [40] showed that using 1% GF reduces the slump flow diameter by about 6% [40]. Decreasing slump flow and T50 in fiber concrete was detailed in the study of Faraj et al. [41]. On the other hand, the slump flow diameter of specimens containing FSCG with GF was significantly higher than specimens containing GF. So, the slump flow diameter of specimens containing 0.25, 0.5, 0.75, 1 and 1.25% GF and 7% FSCG were 16.7, 15.5, 13.8, 12.3, 11.1 and 10.3% more than control specimen. The reason for this is that FSCG increases the viscosity and flowability of the concrete. In other words, the addition of FSCG increases the plastic viscosity of cement paste due to higher inter-particle friction. Studies by Hosseinpour et al. [42] also showed that increasing the paste's plastic viscosity increases with increasing the volume ratio of the binder.

As shown in Figure 8 and Table 9, the T50 range in specimens containing GF is between 4.24 to 4.98 seconds, and the T50 range in specimens containing GF and FSCG is between 2.98 to 4.21 seconds. Accordingly, the T50 slump flow time in all mixtures is between 2 and 5 seconds. In this range, the mixture viscosity is high enough to increase strength against segregation and limit excessive pressure to mold [43]. Figure 8 also shows that increasing GF can increase T50 slump flow time. Increasing T50 time in concrete specimens containing GF has also been reported in Güneyisi et al. [40] and Faraj et al. [41] studies.

The effect of GF and FSCG on the V-funnel flow time and blocking ratio (L-box test) is shown in Figure 9 and Table 8. The results show that fibers' presence in SCC increases the plastic viscosity of the concrete and the V-funnel flow time increases with increasing fiber percentage. Moreover, all obtained times from the V-funnel test correspond to EFNARC considerations (6 to 12 seconds). The V-funnel flow time for each specimen

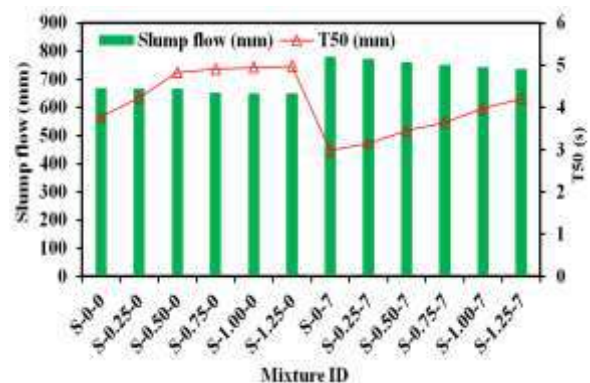


Figure 8. Slump flow and T50 results

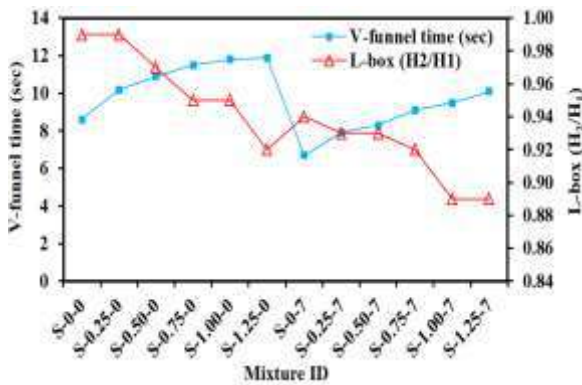


Figure 9. Fresh concrete results (V-funnel and L-box tests)

containing 0.25, 0.5, 0.75, 1, and 1.25% GF and 7% FSCG was 34, 27, 27, 22, 20, and 50% lower than corresponding specimens without FSCG, respectively.

L-box test results indicate that all mixtures have a good filling ability. But observations suggest that an increase in GF percentage has decreased the H1/H2 ratio. In other words, fibers' presence reduces the passing ability between rebars, and the passing ability is more reduced by increasing fiber percentage. According to the results obtained by Liu et al. [43], Chen et al. [44], and Kina et al. [45] fibers decrease the flowability. Fiber had adverse effects on the rheological properties of SCC. The studies above can confirm the fresh concrete results of the present study.

ACI has divided the viscosity of the SCC based on T50 and V-funnel flow time into two groups VS1/VF1 and VS2/VF2. According to the Figure 10 most of the specimens in the present study are classified into VS2/VF2 group. A good relationship is estimated by Equations (1) and (2) between the V-funnel flow time (V_f) and the T50 slump flow time (T50) for concrete containing GF without FSCG and concrete containing GF and FSCG.

$$V_f = 2.4878T_{50} + 0.6644(\text{Without fiber-silica gel}) \quad (1)$$

$$V_f = 2.5111T_{50} + 0.3647(\text{With fiber-silica gel}) \quad (2)$$

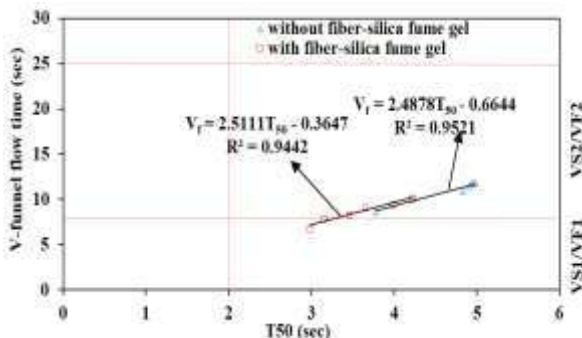


Figure 10. Variation of T50 versus V-funnel time for SCC with and without FSCG

4. 2. Hardened Concrete Results

The effect of GF and FSCG at 28-day compressive strength is also presented in Figure 11 and Table 10. GF's use has no significant impact on increasing compressive strength. GFs in concrete increased the porosity and entrapped air in concrete, thereby reducing the compressive strength [46]. Changes in compressive strength of GFRC specimens are presented in Figure 12 by Swami et al. [47], Ghorpade [48] and, Hilles and Ziara [49]. The rate of change in compressive strength of specimens containing GFs is within the range of similar studies.

The compressive strength of specimens containing 7% of FSCG with 0, 0.25, 0.5, 0.75, 1, 1.25% GF increased by 13, 19, 17, 20, 24 and 20 %, respectively. FSCG increases compressive strength due to prevent cracks, reduction of cracks growth, the contact surface, and further fiber-mortar interaction. The compressive strength of specimens containing GF and FSCG is higher than specimens containing GF. Increasing GF percentage

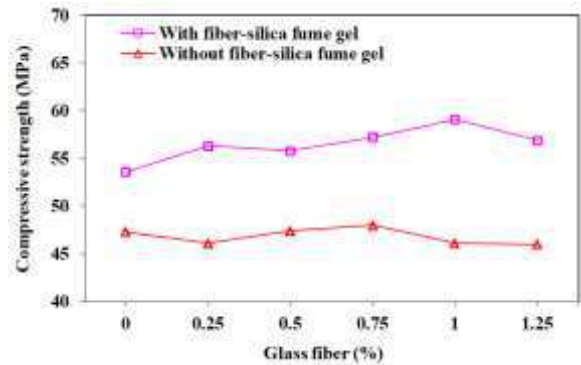


Figure 11. Compressive strength of the concrete specimens

TABLE 10. The hardened concrete results

Mix code	Compressive strength (MPa)	Splitting strength (Mpa)
S-0-0	47.3	3.11
S-0.25-0	46.1	3.26
S-0.50-0	47.4	3.39
S-0.75-0	48	3.46
S-1.00-0	46.1	3.49
S-1.25-0	46	3.53
S-0-7	53.6	3.43
S-0.25-7	56.3	3.95
S-0.50-7	55.8	4.02
S-0.75-7	57.2	4.13
S-1.00-7	59.1	4.17
S-1.25-7	56.9	4.21

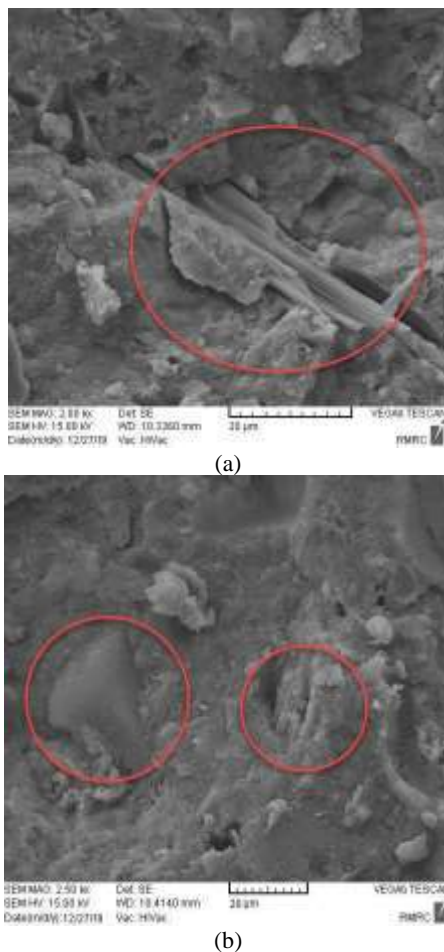


Figure 12. SEM images (a) 1% GF (b) 1% GF and 7% FSCG

in concrete increases the percentage of entrapped air in concrete. The higher the percentage of entrapped air is, the higher the porosity of the concrete will be, and consequently, the strength of concrete decreases. The SEM images shown in Figure 12 exhibit that the use of FSCG, which replaces a part of the cement, can greatly improve the strength reduction caused by GF entry into the concrete matrix. Due to their high affinity, these materials improve the cohesion between cement paste and GF. On the other hand, their fine particles and high filling ability caused them to penetrate through the pores created by an increase in the percentage of entrapped air in concrete and cover them.

Adding 0.25, 0.5, 0.75, 1, and 1.25% GF to the specimens without FSCG increased the splitting tensile strength by 4.8, 9, 11.3, 12.2, and 13.5%, respectively (Figure 13). Due to their high tensile resistance, the fibers prevent crack propagation by holding the cement matrix or forming a bridge between cracks. As a result, cracks do not grow in length, thickness (width). However, fibers will increase the volume of voids in concrete by forming defects at the microscale in the cement matrix.

The splitting tensile strength of the specimens containing 7% FSCG with 0.25, 0.5, 0.75, 1, and 1.25 % GF was increased by 43.1, 51.8, 58.5, 64%, and 68.8%, respectively. The use of FSCG compensates for the disadvantages of using only GF, thereby increasing the growth of concrete to a great extent and causing more tensile strength against deformation. The lack of proper cohesion and interaction between fibers and coarse aggregate reduces the tensile strength of concrete containing GF over concrete containing GF and FSCG; so the interaction between fibers and coarse aggregate can be considered a hairline crack, which accelerates concrete failure.

Lack of cohesion between cement paste, fibers, and coarse aggregates compared to cohesion between cement pastes, fibers, and fine aggregate causes this matrix not to work consistently against tensile load [50]. specimens containing FSCG increase the cohesion between fibers and coarse aggregates and increase bonding. Thus, the tensile strength of the concrete has more growth. The use of GF depending on the concrete grade in all the studies presented in Figure 14 resulted in increasing tensile strength of the concrete. As in the study of Ghorpad [48] and Swami et al. [47], the tensile strength of concrete containing 1% GF increased by 22% and 41%, respectively, compared to the control sample.

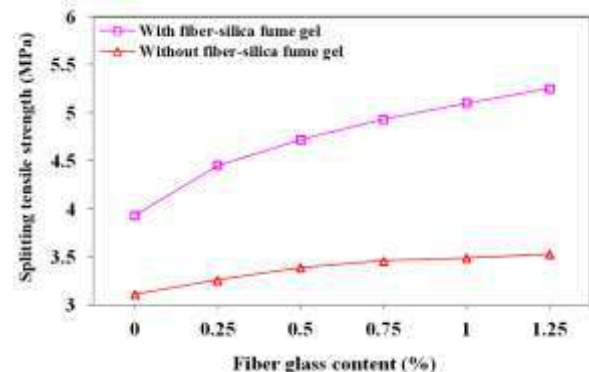


Figure 13. Splitting tensile strength

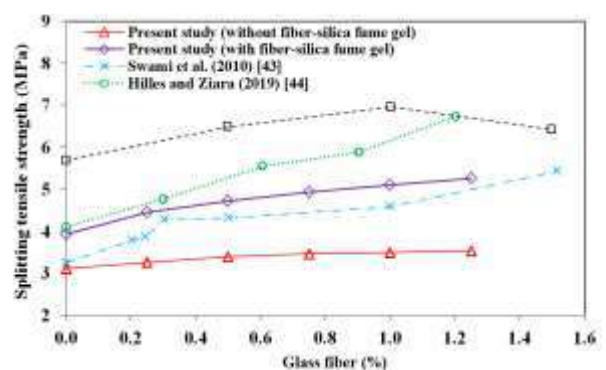


Figure 14. Comparison of 28-days tensile strength results with similar studies

Evaluating and determining the relationship predict concrete tensile strength based on its compressive strength has always been of interest to the concrete and construction industry researchers. The changes of cylindrical compressive strength versus tensile strength are shown in Figure 15. Based on this, Equations (3) and (4) for SCC containing GF and FSCG can be presented. Figure 16 shows the proposed relationship of CEB-FIP for high, low, and average tensile strength variations based on cylindrical compressive strength. As it can be seen, the results obtained in this study are within the range recommended by CEB-FIP.

However, the CEB-FIP [51] average range relationship to investigate changes in cylindrical compressive strength versus tensile strength provides a higher estimate of tensile strength at a given compressive strength.

$$f_t = 0.0015f_c^{2.0675} \tag{3}$$

$$f_t = 25.844f_c^{-0.562} \tag{4}$$

4. 3. Four-point Loading Results

Figure 16 shows load-mid span deflection curves of retrofitted beams with RC jackets and GFRP plates. Parameters extracted from the load-displacement curve are presented in Table 11. These curves have three separate linear parts. The first part consists of the un-cracked section and the linear elastic behavior.

Load and deflection corresponding to the first crack for the control beams were 19 kN and 2.1 mm, respectively. However, jackets containing GF and FSCG increased the crack load and decreased the crack deflection. The second part of curve is the interval between the first concrete crack and yield point.

The yield deflection and yield load of the control beam were 53 kN and 13.1 mm, respectively. However,

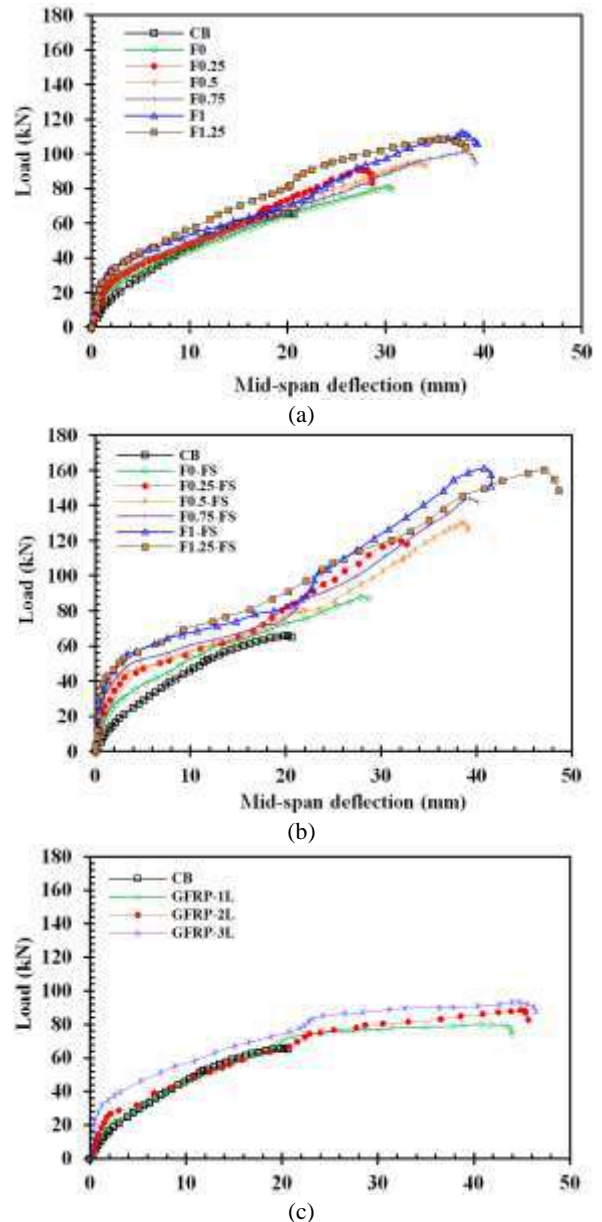


Figure 16. Load-deflection curves a: Strengthening of the beam with concrete jackets containing GF b: Strengthening of the beam with concrete jackets containing GF and FSCG c: Strengthening of the beam with GERP plates

concrete jackets containing 1.25% GF and 7% FSCG increased the yield load by approximately 102%. The third part of the load-deflection curve is the interval between yield point and ultimate failure. In this part, the deflection of beams decreased rapidly due to the decrease in stiffness. The performance of the proposed concrete jackets caused cracks to grow at a slower speed and significantly increased the bearing capacity of beams compared to the control specimen. The three different phases mentioned in the load-deflection diagrams are illustrated in the hypothetical diagram in Figure 17.

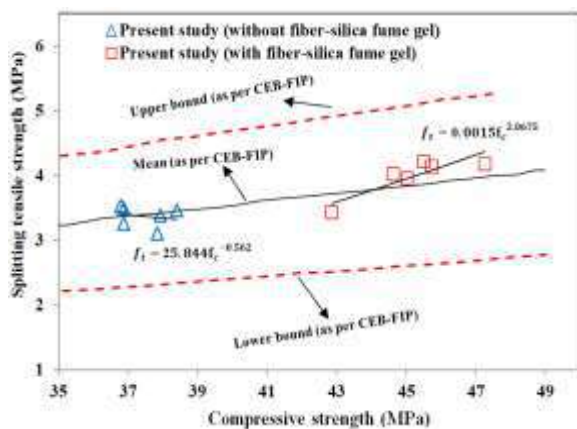


Figure 15. Comparison of the results of the relationship between compressive strength and tensile strength of SCC specimens at 28 days with the limits specified by CEB-FIP [51]

TABLE 11. Parameters extracted from the load-displacement curve

Beam	Crack Load (kN)	Yield Load (kN)	Ultimate Load (kN)	Crack deflection (mm)	Yield deflection (mm)	Ultimate Deflection (mm)	Deflection Ductility	Stiffness (kN/mm)	Energy absorption (J)
CB	19.0	53.0	64.0	2.10	13.10	20.0	1.53	7.5	896
F0	25.0	69.0	81.0	2.25	20.10	34.0	1.69	10.6	1636
F-0.25	28.0	63.0	91.0	2.61	16.00	28.6	1.79	10.2	1656
F-0.5	28.0	68.0	91.0	2.24	19.00	34.0	1.79	10.7	2106
F-0.75	29.0	69.0	101.0	2.37	21.00	39.0	1.86	10.8	2582
F-1	34.0	75.0	112.0	2.41	22.00	39.0	1.77	12.3	2859
F-1.25	34.0	82.0	108.0	2.51	20.00	38.0	1.90	12.0	2922
F-0-FS	29.0	61.0	88.0	2.52	13.00	28.7	2.21	10.8	1689
F-0.25-FS	40.0	71.0	117.0	2.58	17.00	33.0	1.94	13.9	2370
F-0.5-FS	42.0	78.0	128.0	2.45	20.40	39.0	1.91	14.8	2677
F-0.75-FS	45.0	85.0	144.0	2.60	21.00	40.0	1.90	16.0	3400
F-1-FS	46.4	101.0	160.0	1.78	23.00	41.6	1.81	16.3	4006
F-1.25-FS	47.0	107.0	157.0	2.00	24.80	48.6	1.96	16.6	5036
GFRP-1L	22.4	72.0	79.0	2.71	21.00	44.0	2.10	8.0	2677
GFRP-2L	21.8	74.0	87.0	1.73	22.90	45.8	2.00	9.5	2948
GFRP-3L	35.5	83.0	93.0	2.27	23.00	46.5	2.02	13.4	3424

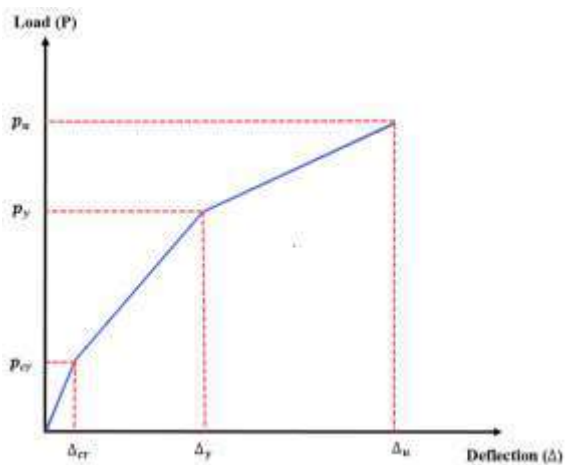


Figure 17. Hypothetical diagram of load-deflection and representation of points of cracking, yield, and ultimate failure

4. 3. 1. Crack Load Crack propagation of the beams is shown in Figure 18. As can be seen, the use of FSCG in concrete jackets increases the adhesion between the fibers and the aggregates and increases the cohesion between them. In fact, the connection between the fibers and the coarse part can be considered as a hair crack that accelerates the failure of concrete. Lack of adhesion between cement paste and fibers and coarse aggregates compared to adhesion between cement paste and fibers

and fine aggregates, has caused this matrix not to act continuously and coherently against tensile loads and stresses are evenly distributed in cement paste. This will reduce the tensile strength and create more cracks. However, the use of FSCG in reinforced concrete jackets improved the behavior of the beams and limited the distribution of cracks.

Corresponding points to the crack loads that give rise to the formation of the first cracks in RC sections are those points where maximum tensile strength is reached at the furthest tensile axis of the section. The concrete loses its tensile strength and the section cracks. The load in which cross-section cracking occurs is called "crack load" (P_{cr}).

The amounts and the increasing percentage of cracking load for all beams are shown in Figure 19. These amounts are derived from the diagram in Figure 16 and correspond to the first breakpoint in the load-deflection curves related to specimens. The corresponding crack load with retrofitted beams using jackets containing 0, 0.25, 0.5, 0.75, 1, and 1.25% GFs increased by 32, 47, 47, 53, 79 and 79%, respectively.

Moreover, the corresponding crack load with retrofitted beams using jackets containing 0, 0.25, 0.5, 0.75, 1 and 1.25% GF and 7% FSCG increased by 53, 111, 121.1, 137, 144 and 147%, respectively. The corresponding crack load with retrofitted beams using one, two, and three layers of GFRP plates increased by

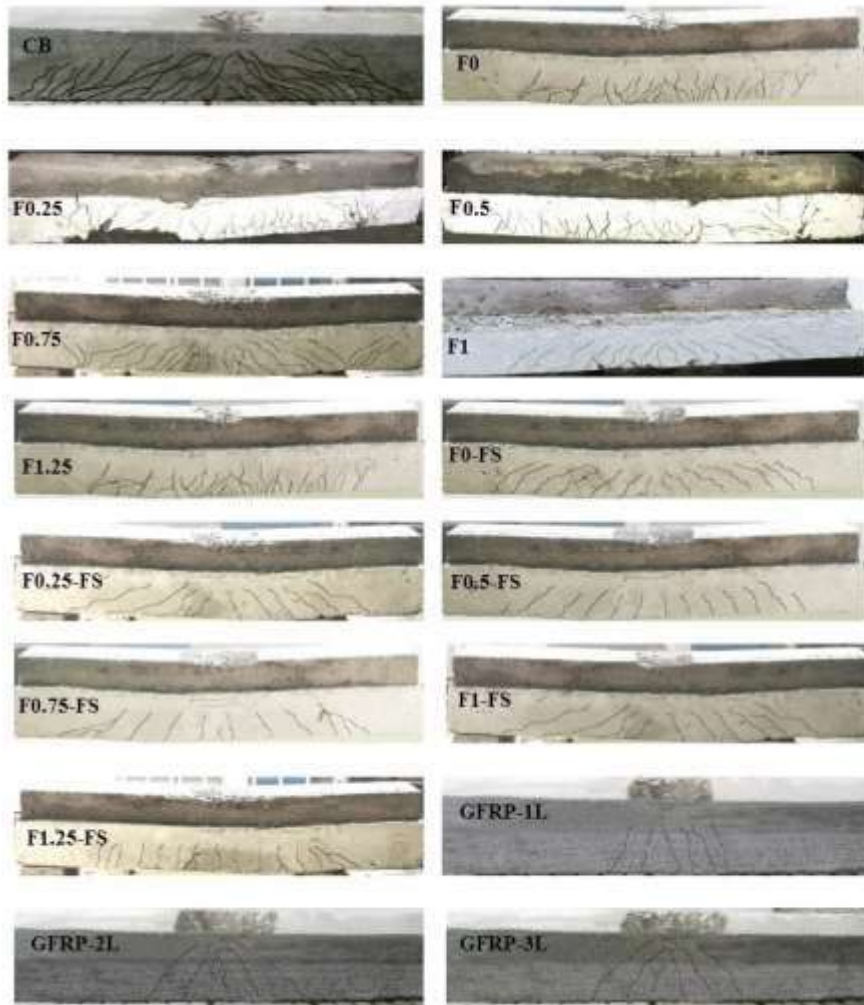


Figure 18. Crack propagation

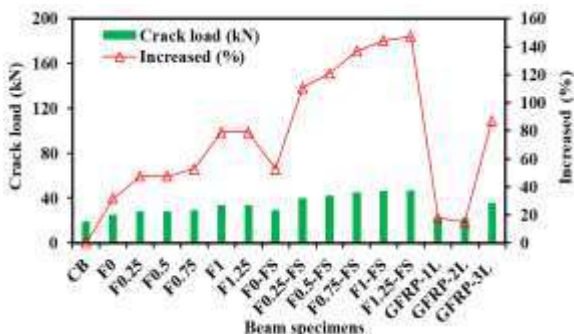


Figure 19. Cracking Load of beams

48, 60, and 71%, respectively. The jackets containing FG and FSCG has more effect on increasing the cracking load of the beams compared to the other two methods, and the first cracking is more delayed. Adding FSCG to the concrete composition, the lime produced in the

cement hydration process reacted to silica fume, produced calcium silicate hydrate, and increased concrete strength. In contrast, silica fume particles filled the space between aggregates, prevented them from interlocking, and increased the concrete workability.

4. 3. 2. Yield Load Figure 20 presents the amounts of yield load and the increasing percentage of yield load of the beams. In all cases, the proposed jackets increased yield load; the corresponding yield load of retrofitted beams with jackets containing 0, 0.25, 0.5, 0.75, 1, and 1.25 % of GF increased by 30, 19, 28, 30, 42 and 55 %, respectively. Also, the corresponding yield load to retrofitted beams with jackets containing 0, 0.25, 0.5, 0.75, 1 and 1.25% GF and 7% of FSCG increased by 15, 34, 47, 60, 91 and 102%, respectively. The corresponding yield load to retrofitted beams using one, two, and three layers of GFRP sheets increased by 17, 14, and 86%, respectively. The combination of fiber and silica fume

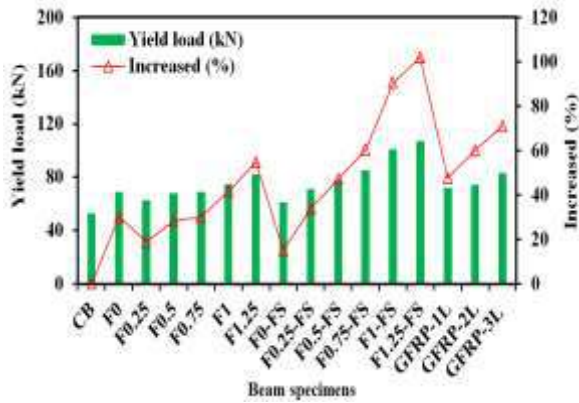


Figure 20. Comparison of the yield load of beams

made the rebars yield later and increased the yield strength of the beams. By creating more consistency, the superplasticizer used in FSCG caused the fine particles of silica fume powder to move into the concrete and move into the voids between the larger aggregates, which filled the void between them increased the concrete strength.

4. 3. 3. Ultimate Bearing Capacity (Ultimate Load)

Figure 21 shows the amounts of maximum bearing capacity. Concrete jackets containing GF increased the maximum load from 27% to 75%, depending on GF amount. Also, concrete jackets containing GF and FSCG enhanced the the maximum load from 82% to 150%, depending on the consumed amount of GF. On the other hand, using GFRP sheets also increased the final bearing capacity by 47 to 71 %, depending on the number of used layers. The reason for improving bearing capacity in reinforced specimens with GF and FSCG compared to specimens without fiber is that GF does not allow for further separation of the concrete by increasing the tensile strength and inhibition in crack generation and by creating a bridge between the two sides of the crack. FSCG improves the ultimate load by enhancing the

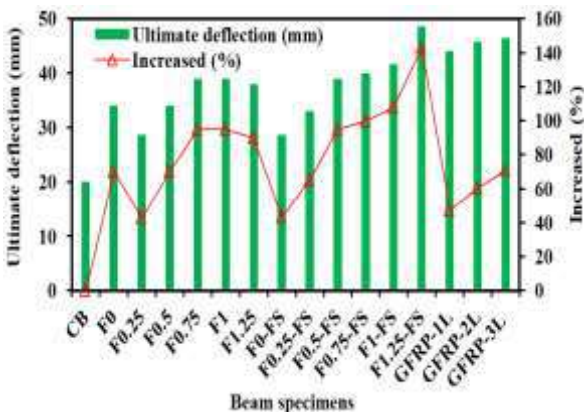


Figure 21. Comparison of ultimate bearing capacity

tensile strength. In both types of the studied jackets, increasing GF amount affects increasing flexural capacity, so the highest increase in bending capacity of beams was achieved using 1% of GF (Figure 22).

4. 3. 4. Deflection Ductility

To calculate the deflection ductility, the ultimate deflection (Δ_u) and yield deflection (Δ_y) values need to be available [52-55]. These parameters are obtained from the load-displacement curve. Deflection ductility is calculated by Equation (5).

$$\mu = \frac{\Delta_u}{\Delta_y} \tag{5}$$

Concrete jackets containing GF and FSCG shows greater bending stiffness, greater flexural capacity compared to jackets containing GF and GFRP. They also have a much better performance in ductility. The ductility of strengthened beam with jackets comprising of GF, jackets comprising of FSCG, and GFRP increased by about 11 to 17%, 18 to 28% and 31 to 36%, respectively. The strengthened beams with RC jackets comprising of GF and FSCG have more strength. The GFRP debonded

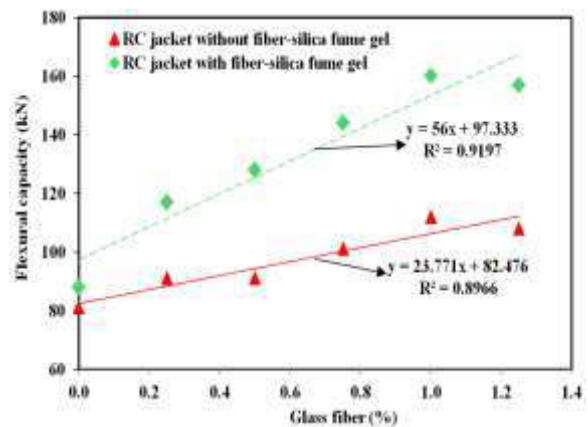


Figure 22. The effect of GFs on bending capacity of RC beams retrofitted with concrete jackets

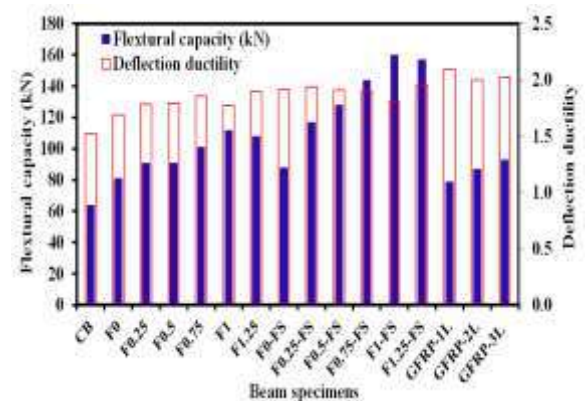


Figure 23. Comparison of flexural strength and deflection ductility of the beams

from the beams surfaces and this led to bear less forces. The RC jacket can have better performance in seismic zones in compared to the GFRP method.

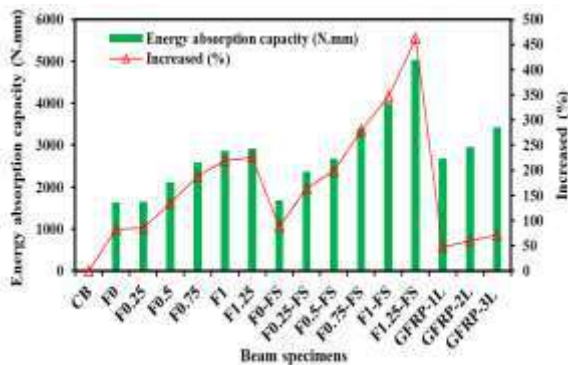
4. 3. 6. Energy Absorption Capacity (Flexural Toughness)

Energy absorption capacity is one of the parameters to be analyzed for the loading performance of RC members (Figure 24). RC jackets containing GF and FSCG increased the beams' energy absorption capacity by about 89 to 463%, depending on the percentages of GFs. RC jacket containing GF and FSCG delays the growth of the primary crack and it can significantly increase the maximum load. Also, GFRP sheets have poorer performance compared to the proposed method due to separation from the surface of the strengthened beams, and their load-bearing capacity and energy absorption are lower. Also, the energy absorption capacity of retrofitted beams with RC jackets containing GFs increased from 83 to 226%, depending on GFs contents. On the other hand, the energy absorption capacity of retrofitted beams with GFRP plates increased from 47 to 71%, depending on the number of layers.

Considering each of the parameters of bearing capacity, ductility, stiffness, energy absorption capacity and deformation, the use of 7% FSCG and 1.25% GF in the proposed self-compacting reinforced concrete jacket had a better performance compared to the other percentages.

4. 3. 7. Comparison of the Proposed Strengthening Method with Similar Studies

Figure 25 compares the proposed strengthening method with similar studies. The ultimate load (flexural capacity) of the retrofitted beams with concrete jackets to the flexural capacity of control beams and the $(A_c f_c A_s f_y)_{jacketed} / (A_c f_c A_s f_y)_{original}$ are shown in Figure 25. In $(A_c f_c A_s f_y)_{jacketed}$, A_c is the RC cross-sectional area, f_c is the original beam compressive strength and the concrete compressive strength of the jacket, A_s is the area of the longitudinal bars used in the jacket, and the main beam and the f_y is the yield stress of



concrete will be, and consequently, the strength of concrete decreases.

- The SEM images showed that the use of FSCG, which replaces a part of the cement, can significantly improve the strength reduction caused by GF entry into the concrete matrix. Due to their high affinity, these materials improve the cohesion between cement paste and GF, and, on the other hand, their fine particles and high filling ability caused them to penetrate through the pores created by an increase in the percentage of entrapped air in concrete and cover them. This increases the strength and improves the mechanical properties of concrete containing GF.
- The splitting tensile strength of the specimens containing 7% FSCG with 0.25, 0.5, 0.75, 1 and 1.25 % GF were increased by 43.1, 51.8, 58.5, 64% and 68.8%, respectively, compared to the control specimen. The lack of proper cohesion and interaction between fibers and coarse aggregate reduces the tensile strength of concrete containing GF over concrete containing GF and FSCG; so the interaction between fibers and coarse aggregate can be considered as a hairline crack, which accelerates concrete failure. Lack of cohesion between cement paste, fibers, and coarse aggregates compared to cohesion between cement pastes, fibers, and fine aggregate causes this matrix not to work consistently against tensile load.
- GFs in the proposed RC jackets increased the crack, yield, and ultimate loads by 79, 55, and 75%. The combined use of GFs and FSCG increased the crack, yield, and maximum loads by 147, 102, and 150%, respectively. On the other hand, the use of GFRP sheets increased by 71%, 86%, and 71%, respectively, depending on the number of layers.
- Using RC jackets containing FG and FSCG has more effect on increasing the cracking load of the beams compared to the other two methods, and the first cracking is more delayed. Adding FSCG to the concrete composition, the lime produced in the cement hydration process reacted to silica fume, produced calcium silicate hydrate, and increased concrete strength. In contrast, silica fume particles filled the space between aggregates, prevented them from interlocking, and increased the concrete workability.
- The combined use of GF and FSCG has a more influential role in increasing the yield load of rebars. In other words, using the combination of fiber and silica fume made the rebars yield later and increased the yield strength of the beams. By creating more consistency, the superplasticizer used in FSCG caused the fine particles of silica fume powder to move into the concrete and move into the voids between the larger aggregates. This filled the void

between them and thus increased the concrete strength.

- In both types of the studied jackets, increasing GF amount affects increasing flexural capacity, so the highest increase in bending capacity of beams was achieved using 1% of GF.
- The use of RC jackets containing GF and FSCG shows greater bending stiffness, greater flexural capacity compared to jackets containing GF and GFRP sheets.
- RC jackets containing GF and FSCG increased the beams' energy absorption capacity by about 89 to 463%, depending on the percentages of GFs. RC jacket containing GF and FSCG delays the growth of the primary crack and it can significantly increase the maximum load. Also, GFRP sheets have poorer performance compared to the proposed method due to separation from the surface of the strengthened beams, and their load-bearing capacity and energy absorption are lower.

The combined use of FSCG and GF in reinforced concrete jackets can be effective in improving the flexural behavior of concrete beams. Examination of the use of this method in other members of reinforced concrete structures (slabs, columns and foundations) can be evaluated in future studies

6. REFERENCES

1. Reza, S., Khan, MK., Menegon, SJ., Tsang, HH., and Wilson, JL., "Strengthening and repairing reinforced concrete columns by jacketing State-of-the-art review" *Sustainability*, Vol. 11, No. 11, (2019), 3208. doi: org/10.3390/su11113208
2. Siddika, A., AlMamun, MA., Alyousef, R., and Arman, YM., "Strengthening of reinforced concrete beams by using fiber-reinforced polymer composites: A review" *Journal of Building Engineering*, Vol. 25, (2019), 100798. doi: org/10.1016/j.jobbe.2019.100798
3. Elsanadedy, HM., Abbas, H., Almusallam, TH., and Al-Salloum, YA., "Organic versus inorganic matrix composites for bond-critical strengthening applications of RC structures-State-of-the-art review" *Composites Part B: Engineering*, Vol. 30, No. 10, (2019), 106947. doi: org/10.1016/j.compositesb.2019.106947
4. Gentile, R., and Galasso, C., "Optimal retrofit selection for seismically-deficient RC building based on simplified performance assessment" In COMPDYN 2019 7th ECCOMAS Thematic Conference on Computational Methods in Structural Dynamics and Earthquake Engineering., (2019). doi:10.7712/120119.6986.19675
5. Kheyroddin, A., Sepahrad, R., Saljoughian, M., Kafi, MA., "Experimental evaluation of RC frames retrofitted by steel jacket, X-brace and X-brace having ductile ring as a structural fuse" *Journal of Building Pathology and Rehabilitation*, Vol. 4, No. 1, (2019), 11. doi:10.1007/s41024-019-0050-z
6. Shafei, B., Kazemian, M., Dopko, M., Najimi, M. "State-of-the-Art Review of Capabilities and Limitations of Polymer and Glass Fibers Used for Fiber-Reinforced Concrete". *Materials*, Vol. 14, No. 2, (2021), 409. doi: 10.3390/ma14020409

7. Yu, R. "Development of sustainable protective ultra-high performance fibre reinforced concrete (UHPFRC): design, assessment and modeling". Technische Universiteit Eindhoven.
8. Hassanean, Y. A., Assaf, K. A., Raheem, S. E. A., Arafa, A. N. "Flexural behavior of strengthened and repaired RC beams by using steel fiber concrete jacket under repeated load". *International Journal of Civil and Structural Engineering*, Vol. 3, No. 3, (2013), 564. doi: 10.6088/ijcser.201203013052.
9. Hassanean, Y., Assaf, K. A., Abdel Raheem, S. E., Arafa, A. N. "Behavior of repaired RC beams by using steel fiber concrete jacket and subjected to short time repeated loading". *Journal of Engineering Sciences*, Vol. 40, No. 5, (2012), 1309-1324. doi: 10.21608/jesaun.2012.112111
10. Shadmand, M., Hedayatnasab, A., Kohnehpooshi, O. "Retrofitting of reinforced concrete beams with steel fiber reinforced composite jackets". *International Journal of Engineering, Transactions B: Applications*, Vol. 33, No. 5, (2020), 770-783. doi: 10.5829/ije.2020.33.05b.08
11. Rahmani, I., Maleki, A., Lotfollahi-Yaghin, M. A., "A laboratory study on the flexural and shear behavior of rc beams retrofitted with steel fiber-reinforced self-compacting concrete jacket". *Iranian Journal of Science and Technology, Transactions of Civil Engineering*, (2020), 1-17. doi:org/10.1007/s40996-020-00547-x
12. Faez, A., Sayari, A., Manei, S. "Retrofitting of RC beams using reinforced self-compacting concrete jackets containing aluminum oxide nanoparticles". *International Journal of Engineering, Transactions B: Applications*, Vol. 34, No. 5, (2021), 1195-1212. doi: 10.5829/ije.2021.34.05b.13
13. Monir A. M., Maged A. Youssef A 2017. Analysis of reinforced concrete beams strengthened using concrete jackets, *Engineering Structures*, Vol. 132: 172-187. doi: 10.1016/j.engstruct.2016.11.014
14. Aldhafairi, F., Hassan, A., Abd-EL-Hafez, L. M., Abouelezz, A. E. Y. (2020). Different techniques of steel jacketing for retrofitting of different types of concrete beams after elevated temperature exposure. *Structures*, Vol. 28, (2020), 713-725. Elsevier. doi: org/10.1016/j.istruc.2020.09.017.
15. Tayeh, B. A., Maraq, M. A. A., Ziara, M. M. "Flexural performance of reinforced concrete beams strengthened with self-compacting concrete jacketing and steel welded wire mesh". *Structures*, Vol. 28, (2020), 2146-2162. doi:org/10.1016/j.istruc.2020.10.035
16. Yuan, C., Chen, W., Pham, T. M., Hao, H., Chen, L., Wang, J. "Experimental and analytical study of flexural behaviour of BFRP sheets strengthened RC beams with new epoxy anchors". *Engineering Structures*, (2021), 241, 112441. doi: org/10.1016/j.engstruct.2021.112441
17. Maraq, M. A. A., Tayeh, B. A., Ziara, M. M., Alyousef, R. "Flexural behavior of RC beams strengthened with steel wire mesh and self-compacting concrete jacketing-experimental investigation and test results." *Journal of Materials Research and Technology*, Vol. 10, (2021), 1002-1019. doi: org/10.1016/j.jmrt.2020.12.069
18. Ghalehnovi, Mansour, Arash Karimipour, Ali Anvari, and Jorge de Brito. "Flexural strength enhancement of recycled aggregate concrete beams with steel fibre-reinforced concrete jacket." *Engineering Structures*, Vol. 240, (2021), 112325. doi: org/10.1016/j.engstruct.2021.112325
19. Falliano, D., De Domenico, D., Ricciardi, G., Gugliandolo, E. "Improving the flexural capacity of extrudable foamed concrete with glass-fiber bi-directional grid reinforcement: An experimental study." *Composite Structures*, Vol. 209, (2019), 45-59. doi: org/10.1016/j.compstruct.2018.10.092
20. Ali, B., Qureshi, L. A., Khan, S. U. "Flexural behavior of glass fiber-reinforced recycled aggregate concrete and its impact on the cost and carbon footprint of concrete pavement." *Construction and Building Materials*, Vol. 262, (2020), 120820. doi: org/10.1016/j.conbuildmat.2020.120820
21. ASTM C1240-15 "Standard Specification for Silica Fume Used in Cementitious Mixtures", ASTM International, West Conshohocken, PA, (2015).
22. ASTM Standard C33/C33M-18 (2018) Standard specification for concrete aggregates. ASTM International West Conshohocken PA.
23. ASTM C150-02 "Standard Specification for Portland Cement" ASTM International West Conshohocken PA, (2002).
24. ASTM C190-85 "Method of Test for Tensile Strength of Hydraulic Cement Mortars" ASTM International West Conshohocken PA, (1990).
25. Kafeel, A., Ahmad, R., Uzma, K., and Sherif, K., "Effect of compressive strength on bond behaviour of steel reinforcing bar in fiber reinforced concrete" *International Journal of Current Engineering and Technology*, Vol. 4, No. 1, (2014), 325-331.
26. MPO., "The guideline for design specification of strengthening reinforced concrete building using fiber reinforced polymers (frp)" *Office of Technical Affairs Deputy*, (2006).
27. ACI 440.3R-12 Guide Test Methods for Fiber-Reinforced Polymer (FRPs) Composites for Reinforcing or Strengthening Concrete Structures, *American Concrete Institute*. (2012), 23.
28. Mostofinejad, D., and Shemali, SM., "Externally bonded reinforcement in grooves (EBRIG) technique to postpone debonding of FRP sheets in strengthened concrete beams" *Construction and Building Materials*, Vol. 38, (2013), 751-758, doi: org/10.1016/j.conbuildmat.2012.09.030.
29. ASTM Standard C39/C39M-18 "Standard test method for compressive strength of cylindrical concrete specimens", *ASTM International West Conshohocken PA*, (2018).
30. Murad, Y., Abu-ElHaj, T. "Flexural strengthening and repairing of heat damaged RC beams using continuous near-surface mounted CFRP ropes". *Structures*, Vol. 33, (2021), 451-462. doi: org/10.1016/j.istruc.2021.04.079
31. Haddad, R. H., Yaghamour, E. M. "Side NSM CFRP strips with different profiles for strengthening reinforced concrete beams." *Journal of Building Engineering*, Vol. 32, (2020), 101772. doi: org/10.1016/j.jobeb.2020.101772
32. Bouziadi, F., Boulekbache, B., Haddi, A., Hamrat, M., Djelal, C. "Finite element modeling of creep behavior of FRP-externally strengthened reinforced concrete beams." *Engineering Structures*, Vol. 204, (2020), 109908. doi: org/10.1016/j.engstruct.2019.109908
33. Chen, C., Yang, Y., Yu, J., Yu, J., Tan, H., Sui, L., Zhou, Y. (2020). Eco-friendly and mechanically reliable alternative to synthetic FRP in externally bonded strengthening of RC beams: Natural FRP. *Composite Structures*, Vol. 241, 112081. doi: org/10.1016/j.compstruct.2020.112081
34. De Domenico, D., Urso, S., Borsellino, C., Spinella, N., Recupero, A. "Bond behavior and ultimate capacity of notched concrete beams with externally-bonded FRP and PBO-FRCM systems under different environmental conditions." *Construction and Building Materials*, Vol. 265, (2020), 121208. doi: org/10.1016/j.conbuildmat.2020.121208
35. ASTM C293/ C293M-16, Standard Test Method for Flexural Strength of Concrete (Using Simple Beam With Center-Point Loading), ASTM International, West Conshohocken, PA, (2016), www.astm.org
36. Self-Compacting Concrete European Project Group The European guidelines for self-compacting concrete: Specification, production and use. *International Bureau for Precast Concrete (BIBM)*, (2005).

37. ASTM Standard C496/C496M-17 "Standard test method for splitting tensile strength of cylindrical concrete specimens", *ASTM International West Conshohocken PA*, (2017).
38. Mohammadi, Y., Singh, SP., and Kaushik, SK., "Properties of steel fibrous concrete containing mixed fibres in fresh and hardened state" *Construction and Building Materials*, Vol. 22, No. 35, (2008), 956-965. doi: org/10.1016/j.conbuildmat.2006.12.004.
39. Mohsenzadeh, S., Maleki, A., Yaghin, M. A. "Experimental and Numerical Study of Energy Absorption Capacity of Glass Reinforced SCC Beams." *International Journal of Engineering, Transactions C: Aspects*, Vol. 32, No. 12, (2019), 1733-1744. doi: 10.5829/ije.2019.32.12c.06
40. Guneyisi, E., Atewi, YR., and Hasan MF., "Fresh and rheological properties of glass fiber reinforced self-compacting concrete with nanosilica and fly ash blended" *Construction and Building Materials*, Vol. 211, (2019), 349-362. doi: org/10.1016/j.conbuildmat.2019.03.087.
41. Faraj, R. H., Sherwani, A. F. H., Jafer, L. H., Ibrahim, D. F. "Rheological behavior and fresh properties of self-compacting high strength concrete containing recycled PP particles with fly ash and silica fume blended." *Journal of Building Engineering*, Vol. 34, (2021), 101667. doi: org/10.1016/j.job.2020.101667
42. Hosseinpoor, M., Koura, B. I. O., Yahia, A. "Rheo-morphological investigation of static and dynamic stability of self-consolidating concrete: A biphasic approach." *Cement and Concrete Composites*, Vol. 121, (2021), 104072. doi: org/10.1016/j.cemconcomp.2021.104072
43. Liu, Y., Shi, C., Zhang, Z., Li, N., Shi, D. "Mechanical and fracture properties of ultra-high performance geopolymer concrete: Effects of steel fiber and silica fume." *Cement and Concrete Composites*, Vol. 112, (2020), 103665. doi: org/10.1016/j.cemconcomp.2020.103665
44. Chen, X., Shi, X., Zhou, J., Yu, Z., Huang, P. "Determination of mechanical, flowability, and microstructural properties of cemented tailings backfill containing rice straw." *Construction and Building Materials*, Vol. 246, (2020), 118520. doi: org/10.1016/j.conbuildmat.2020.118520
45. Kina, C., Turk, K., Atalay, E., Donmez, I., Tanyildizi, H. "Comparison of extreme learning machine and deep learning model in the estimation of the fresh properties of hybrid fiber-reinforced SCC." *Neural Computing and Applications*, (2021), 1-19. doi: org/10.1007/s00521-021-05836-8
46. Yuan, Z., Jia, Y. "Mechanical properties and microstructure of glass fiber and polypropylene fiber reinforced concrete: an experimental study." *Construction and Building Materials*, Vol. 266, (2021), 121048. doi: org/10.1016/j.conbuildmat.2020.121048
47. Swami, B., Asthana, A., and Masood, U., "Studies on glass fibre reinforced concrete composites-strength and behavior challenges" *Opportunities and Solutions in Structural Engineering and Construction*, Vol. 4, No. 5, (2010), 144-203.
48. Ghorpade, VG., "An experimental investigation on glass fibre reinforced high performance concrete with silicafume as admixture" In 35th conference on our world in concrete & structures, Singapore, (2010). doi: 10.15680/IJRSET.2017.0605117. 9167
49. Hilles, MM., and Ziara, MM., "Mechanical behavior of high strength concrete reinforced with glass fibre" *Engineering Science and Technology, an Internatinal Journal*, Vol. 22, No. 3, (2019), 920-928. doi: org/10.1016/j.jestch.2019.01.003
50. Zhang, K., Pan, L., Li, J., Lin, C. "What is the mechanism of the fiber effect on the rheological behavior of cement paste with polycarboxylate superplasticizer?" *Construction and Building Materials*, Vol. 281, (2021), 122542. doi: org/10.1016/j.conbuildmat.2021.122542
51. CEB-FIB model code, Committee Euro-International du Beton. Thomas Telford, London, (1993).
52. Miruthun, G., Vivek, D., Remya, P. R., Elango, K. S., Saravanakumar, R., Venkatraman, S. "Experimental investigation on strengthening of reinforced concrete beams using GFRP laminates". *Materials Today: Proceedings*, Vol. 37, (2021), 2744-2748. doi: https://doi.org/10.1016/j.matpr.2020.08.544
53. Kumar, M. V., Raj, S. J., Kumar, K. R., Gurumoorthy, N., Ganesh, A. C. "Flexural and shear performance of HFRC beams." *Materials Today: Proceedings*, Vol. 42, (2021), 816-820. doi: org/10.1016/j.matpr.2020.11.370
54. Du, Y. X., Shao, X., Chu, S. H., Zhou, F., Su, R. K. L. (2021, April). Strengthening of preloaded RC beams using prestressed carbon textile reinforced mortar plates. *Structures*, Vol. 30, (2021), 735-744. doi: org/10.1016/j.jstruc.2021.01.024
55. Al Nuaimi, N., Sohail, M. G., Hawileh, R., Abdalla, J. A., Douier, K. "Durability of reinforced concrete beams externally strengthened with CFRP laminates under harsh climatic conditions." *Journal of Composites for Construction*, Vol. 25, No. 2, (2021), 04021005. doi: org/0000-0002-1826-2741
56. Chalioris, CE., Kytinou, VK., Voutetaki, ME., Papadopoulos, NA. "Repair of heavily damaged rc beams failing in shear using u-shaped mortar jackets." *Buildings*, Vol. 9, No. 6, (2019), 146. doi: https://doi.org/10.3390/buildings9060146
57. Chalioris, CE., Thermou, GE., and Pantazopoulou, SJ. "Behaviour of rehabilitated RC beams with self-compacting concrete jacketing–Analytical model and test results." *Construction and Building Materials*, Vol. 55, (2014), 257-273. doi: https://doi.org/10.1016/j.conbuildmat.2014.01.031
58. Bousias, S., Spathis, A. L., Fardis, M. N. "Seismic retrofitting of columns with lap spliced smooth bars through FRP or concrete jackets." *Journal of Earthquake Engineering*, Vol. 11, No. 5, (2007), 653-674. doi: org/10.1080/13632460601125714
59. Altun F, Haktanir T. "Flexural behaviour of composite reinforce concrete elements." *Journal of Materials in Civil Engineering – ASCE*, Vol. 13, No. 4, (2001), 255-259, doi: org/10.1061/(ASCE)0899-1561(2001)13:4(255)

Persian Abstract

چکیده

در مطالعه حاضر به بررسی آزمایشگاهی مقاوم‌سازی تیرهای بتن مسلح با استفاده از ژاکت بتنی خود متراکم حاوی الیاف شیشه و ژل میکروسیلیس الیاف دار (FSCG) و مقایسه آن با ورق‌های پلیمری مسلح شده با الیاف شیشه (GFRP) پرداخته شده است. ژل میکروسیلیس الیاف‌دار، به عنوان جایگزین بخشی از سیمان است که دارای پودر میکروسیلیس، الیاف پلی‌پروپیلین، فوق روانساز، انواع آب‌بند بتن، و برخی افزودنی‌های دیگر می‌باشد. بدین ترتیب استفاده از ژاکت بتنی اشاره شده ضمن افزایش سطح مقطع و ممان اینرسی تیر، با توجه به مقاومت کششی نسبتاً بالای بتن‌های مسلح به الیاف، می‌تواند منجر به بهبود مقاومت خمشی تیر شود. مطالعات آزمایشگاهی در سه بخش بررسی خواص بتن تازه، بررسی خواص بتن سخت شده و بررسی ظرفیت خمشی تیرها انجام شد. مقدار الیاف شیشه مورد استفاده در ژاکت بتنی به ترتیب برابر ۰، ۰.۲۵، ۰.۵، ۰.۷۵، ۱ و ۱.۲۵ درصد حجمی بتن، مقدار FSCG در ژاکت بتنی به ترتیب برابر ۰ و ۷.۵ درصد وزنی سیمان و تعداد لایه‌های ورق‌های GFRP (۱، ۲ و ۳ لایه) در نظر گرفته شد. نتایج حاصل نشان داد استفاده از FSCG در ژاکت‌های بتنی، ضعف مقاومتی را که به علت ورود الیاف شیشه به ماتریس بتن ایجاد شده است را می‌تواند به خوبی جبران کند. این مصالح به علت میل ترکیبی بالایی که دارند، باعث بهبود چسبندگی بین خمیر سیمان و الیاف شیشه شده و از طرفی ریز بودن ذرات آنها و قابلیت پرکنندگی زیادی که دارند، باعث می‌شود تا در خلل و فرجی که به علت افزایش درصد هوای محبوس در بتن ایجاد شده، نفوذ کرده و آنها را بپوشاند که این امر باعث افزایش مقاومت و بهبود دیگر خصوصیات مکانیکی بتن حاوی الیاف شیشه می‌شود. از سوی دیگر افزودن ژاکت‌های بتنی حاوی الیاف شیشه و FSCG بسته به مقدار الیاف شیشه ظرفیت جذب انرژی تیرها در حدود ۸۹ تا ۴۶۳ درصد افزایش یافته است. دلیل این موضوع آن است که ژاکت بتنی حاوی الیاف شیشه و ژل میکروسیلیس الیاف‌دار، تشکیل اولین ترک در بتن و تسلیم میلگردهای فولادی را به تاخیر می‌اندازد و سبب می‌شود که ظرفیت جذب انرژی به طور قابل توجهی افزایش یابد. همچنین ورق‌های GFRP به دلیل جدا شدن از سطح تیر ظرفیت جذب انرژی کمتری در مقایسه با سایر روش‌های مورد بررسی دارند.



Analysis of Under-reamed Piles Subjected to Different Types of Load in Clayey Soil

A. M. J. Alhassani*

Engineering Faculty, University of Kufa, Najaf, Iraq

PAPER INFO

Paper history:

Received 14 March 2021

Received in revised form 10 June 2021

Accepted 18 June 2021

Keywords:

Under-reamed Piles

Finite Element

Lateral Resistance

Uplift Capacity

Drucker-prager

ABSTRACT

Under-reamed piles with one or more bulbs have been widely used in almost all types of soil to support a range of structures. In some cases, in addition to vertical compressive or uplift loads, piles must withstand a considerable lateral load. A 3-D finite element study using ABAQUS software was conducted to examine the behavior of under-reamed piles in clay soil under pure lateral, pure uplift, and combined uplift and lateral loads. In this study, pile (L/D) ratios of 11.66, 15, 20, and 25 were considered by adjusting the pile length to simulate the behavior of rigid and flexible piles. The piles were modeled as a linear elastic material, and the soil behavior was simulated using the Drucker-Prager constitutive model. The findings show that the lateral resistance of piles with (L/D) ratios of 11.66 and 15 increased slightly when under-reamed piles were used. However, no change in lateral resistance was observed for under-reamed piles with (L/D) ratios of 20 and 25 compared with straight piles. The uplift capacity of under-reamed piles was significantly greater than that of a straight pile. The lateral capacity was marginally influenced by the prior uplift loading, such that it decreased for a rigid under-reamed pile, and increased for a flexible under-reamed pile.

doi: 10.5829/ije.2021.34.08b.15

1. INTRODUCTION

Under-reamed piles are bored concrete cast-in situ piles with one or more bulbs created by widening the stem of the pile. These piles were first introduced in India for use in expansive soils. Under-reamed piles are commonly used to support a wide range of structures in almost all types of soil. When used for towers, shed structures, bridge abutments, and other high-rise structures, the piles are subjected to a significant lateral load. However, the guidelines available for their design under lateral loads are highly empirical [1, 2]. With bulbs, it has been suggested that short under-reamed piles act more like rigid piles, and analysis may be conducted accordingly. For simplification purposes, as conservative assumption, the effect of the bulb can be ignored.

Most previous studies have focused primarily on estimating the compression and tension capacities of under-reamed piles. However, few studies in the literature, have examined the behavior of under-reamed piles exposed to a lateral load. Shrivastava et al. [3] used

Hrennikoff's approach [4] to examine the behavior of a single and a group of under-reamed piles with a single bulb. A pile was considered as a rigid pole and rotated about the underream (bulb) center, and the soil was idealized as a nonlinear deformation spring. The soil above the bulb was thought to be lifted up on one side and pushed down on the other side, forming a couple. Soneja and Garg [5] reported that, the first bulb significantly increased the resistance of the lateral load, based on several field tests on RC piles in sandy soils. However, addition of a second bulb, did not result in any substantial increase in capacity over single under-reamed piles.

Parakash and Ramakrishna [6] proposed an analytical method to predict the ultimate lateral load capacity of under-reamed piles in both ϕ -soils and c-soils, including the effect of bulb size, bulb position, the number of bulbs, and pile (L/D) ratio. That study concluded that for c-soils, the bulb located closer to the ground surface provides greater resistance for single under-reamed piles. For ϕ -soils, a bulb located at a depth of 0.4–0.6 times the length

*Corresponding Author Institutional Email:

athraam.alhassani@uokufa.edu.iq (A. M. J. Alhassani)

of the pile provides the highest resistance. The study also showed that the lateral capacity of under-reamed piles increases significantly with an increase in the number of bulbs. However, as the number of bulbs increases, the improvement in lateral capacity decreases, remaining almost constant beyond three bulbs. This was observed in both soils. It was also found that, with an increase in (L/D) to a certain value, the lateral resistance of under-reamed piles also increased, but decreased beyond that. Prakash and Chandra [7] conducted field tests on single bulb piles in a sandy soil deposit and reported that a single bulb pile acts as a short, rigid pile. They also reported that the point of rotation was near the center of the bulb; the predicted ultimate capacities and deflection using different techniques were found to be in good agreement with the observed values.

Several studies have been conducted to assess the efficiency of under-reamed piles, particularly with uplift loads [8-12]. Martin and De Stephen [8] reported that for overconsolidated stiff clay, a foundation of under-reamed piles with two bulbs is an acceptable option. It was further reported that the distance between the bulbs should be (1.5–2) times greater than the diameter of the bulb.

Watanabe et al. [13] conducted studies on under-reamed piles in clay subjected to compression and tensile loads, demonstrating that, under-reamed piles have sufficient resistance to tensile and compressive loads. Niroumand et al. [14] showed that the uplift resistance of under-reamed piles in sandy soil depends on the relative undrained/drained shear strength of the soil and the number of bulbs. George and Hari [15] performed an FE analysis to estimate the compression and uplift capacity of under-reamed piles in homogeneous clay, reporting an improvement in uplift capacity of approximately 119% for a single under-reamed pile and 204% for a double under-reamed pile with a bulb diameter 2.6 times greater than the pile stem.

Although bulbs in under-reamed piles provide a good benefit, the analysis is more complex. The problem becomes more complicated because these piles may be subjected to a combination of axial and lateral loads, as well as moments. For such a problem, a complete solution can be obtained through a 3-D continuum analysis.

The idea of this study was deduced due to the lack of literature in studying the behavior of the under-reamed pile subjected to lateral loads. In this study, the behavior of under-reamed piles in clay was numerically examined under separate and combined uplift and lateral loads. Pile (L/D) ratios of 11.66, 15, 20, and 25 by adjusting the pile length were investigated. ABAQUS-3D software was used to model the interaction between the uplift and lateral loads on the piles.

2. PROBLEM STATEMENT

This study examined straight and under-reamed piles with single or double bulbs embedded in a clay layer. The piles were subjected to lateral loads, uplift loads, and combined lateral and uplift loads. The loads were applied at a pile head 1 m above the ground surface. The diameter of the pile stem (D) was chosen as 0.3 m; the bulb diameter (D_u) was taken as 2.5D ($D_u = 0.75$ m), according to Indian standards [1]. The location of the lower bulb relative to the pile tip, and the distance between the bulbs also followed the standard requirements [1]. The diameter of the pile stem for straight and under-reamed piles with single or double bulbs was 0.3 m, and the pile length ranged from 3.5–7.5 m to achieve an embedment pile ratio of 11.66, 15, 20, and 25.

In this study, P, SURP, and DURP refer to the straight pile, the single under-reamed pile, and the double under-reamed pile, respectively. The soil properties used for the FE analysis were taken from Helwany's book [16] and considered as a thick homogeneous saturated clay layer under drained conditions, with the groundwater table level coinciding with the top surface of the soil. The properties of the soil and the piles are presented in Table 1. The constitutive model used to simulate the behavior of the soil mass was the Drucker–Prager/cap failure criterion, and the pile was considered as an elastic material.

3. NUMERICAL MODEL

A full 3-D finite element model using ABAQUS software was used to assess the behavior of P, SURP, and DURP under pure lateral, pure uplift, and combined lateral and uplift loads. To prevent any significant boundary effects, the locations of the bottom and lateral sides of the domain were chosen sufficiently far from the pile. Karthikeyan et al. [17] suggested that the lateral sides should be located 20D from the pile axis (the lateral domain for this study was calculated with respect to the diameter of the bulb

TABLE 1. Properties of soil and piles

Part	Soil	Pile
Model	Drucker-Prager	Linear elastic
E (kPa)	68900	30E6
Density (kN/m ³)	19	24
Cohesion (kPa)	0	-
Poisson's ratio	0.3	0.2
Angle of friction (°)	30	-
Length (m)	-	3.5, 4.5, 6, 7.5

D_u), and the total thickness of the soil stratum was $(L_{pile} + 20D)$. The boundary condition was set such that the bottom of the domain was restrained in three directions; at the lateral sides of the domain, movement was prevented horizontally but allowed vertically. Contact between the soil and pile surfaces was simulated using the basic Coulomb friction model, with penalty tangential contact and normal hard contact.

Figure 1(a-d) shows the schematic 3-D finite element mesh discretization of the pile–soil continuum.

4. MODEL VALIDATION

To ensure reliable results from the numerical analysis, the model and software must be validated. Validation can be performed by comparing the numerical data with the experimental data or the prescribed computed data. In this analysis, the model was validated for two cases of loading, lateral and uplift loads. To verify the pile model subjected to lateral load, the piles foundation for a high-speed railway in Taiwan were employed. In this project, two pile groups and several single piles were subjected to full-scale load testing [18]. The tested piles were either driven or bored. The findings of a lateral loading test performed on a single pile symbolized as B7 are considered in this study. The details of loading test and the computations by LPILE program using constant EI were stated in details by Huang et al. [18]. Pile B7 was a 34.9 m long bored reinforced concrete pile with a diameter of 1.5 m. The structural properties of the pile used in this analysis are shown in Table 2. According to the site exploration, the soil within the first 80 m depth may be described as a silty sand with layers of sandy silt. As illustrated in Figure 2, the soil strata is subdivided into six layers. It is found that the groundwater was at a depth 1m with buoyant unit weight of the soil $\gamma' = 9 \text{ kN/m}^3$ [18]. Table 3 lists the other soil properties utilized in the study.

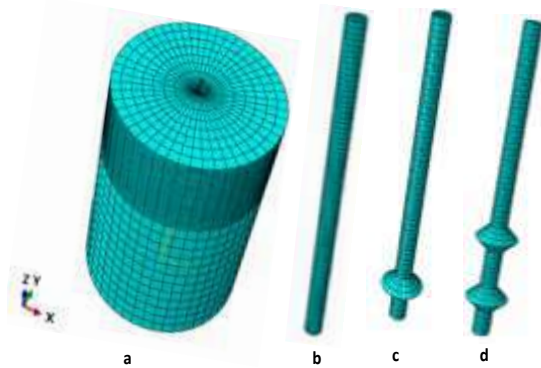


Figure 1. FE mesh for; a. soil domain, b. straight pile, c. single bulb under-reamed pile, d. double-bulb under-reamed pile adopted for current analysis

TABLE 2. Structural properties of the pile considered for simulating the pile model subjected to lateral load

γ (kN/m ³)	E (kPa)	Poisson's ratio	Dia. (m)	Length (m)
25	30E6	0.2	1.5	34.9

“To evaluate the initial field stress in the subsoil before the loading test, the coefficient of earth pressure at rest is estimated on the basis of the values of the stress index K_p provided by the DMTs which were performed after pile installation, using an empirical relationship published in the literature [19], was found that a value of $k_o = 0.72$ can be assumed for any soil layer” [20]. Due to the fact that the soil in front of the pile is freely to move, the dilation effect may be not important in the situation under consideration. Taking this into account, the angle of dilatancy is assumed zero [20] (nominally taken 0.1). Figure 3 displays the obtained findings compared with the measured results in terms of the (lateral deflection-lateral load) curve and also involving the computed results by LPILE. As can be seen, the simulation and observation findings are in good agreement.

The pile model subjected to uplift load was validated using the model presented by George and Hari [15]. The soil and pile properties used in this validation are shown in Table 4. The uplift load–pile head deflection curve of the numerical model obtained by using ABAQUS compared with that presented by George and Hari indicates a good agreement, as shown in Figure 4.

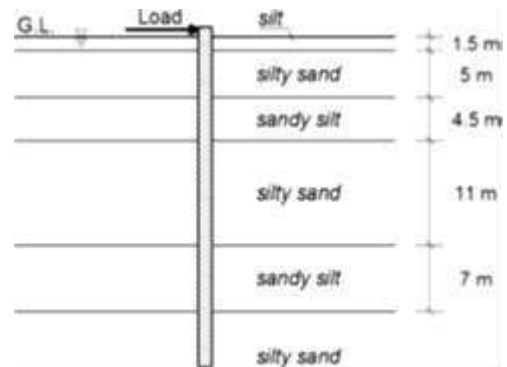


Figure 2. Subsoil layers as documented by Huang et al. [18]

TABLE 3. Soil properties as reported by Conte et al. [20]

Layer No.	G (kPa)	ν'	c'	ϕ' (°)	ϕ' (°)
1	30800	0.3	0	33	0
2	57700	0.3	0	34	0
3	57800	0.3	0	28	0
4	87700	0.3	0	33	0
5	87700	0.3	0	28	0
6	87700	0.3	0	30	0

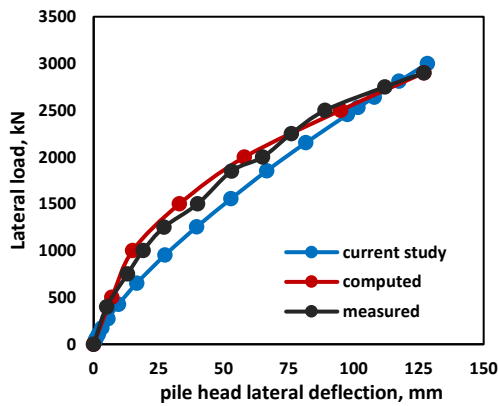


Figure 3. Comparison of measured and predicted findings involving the computations by LPILE program using constant EI

TABLE 4. Properties of soil and piles used for validation model pile subjected to uplift load [15]

Part	Soil	Pile
Model	Mohr–Coulomb	Linear elastic
E (kPa)	15000	31E6
Density (kN/m ³)	16	27
Cohesion, (kPa)	15	-
Poisson's ratio	0.35	0.15
Angle of friction (°)	1	-
Length (m)	-	4.5

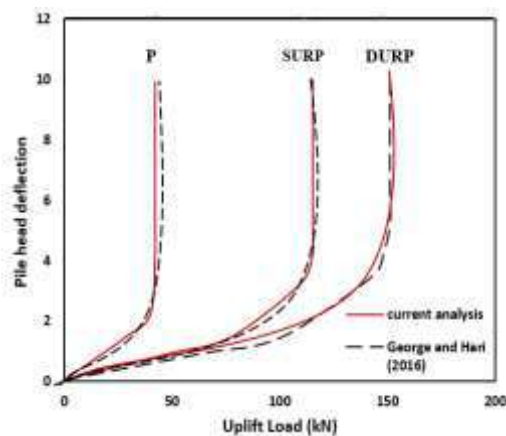


Figure 4. Validation of proposed model with results documented by George and Hari [15]

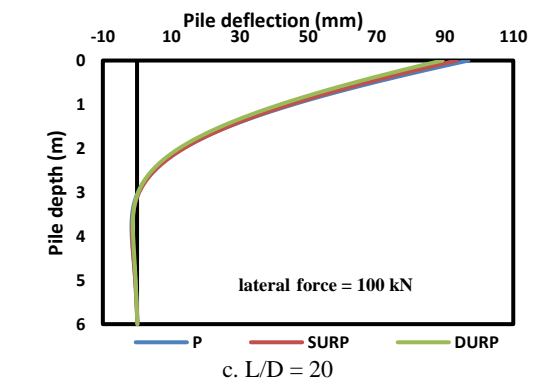
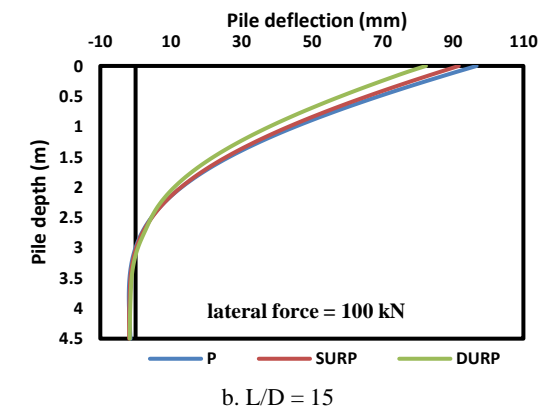
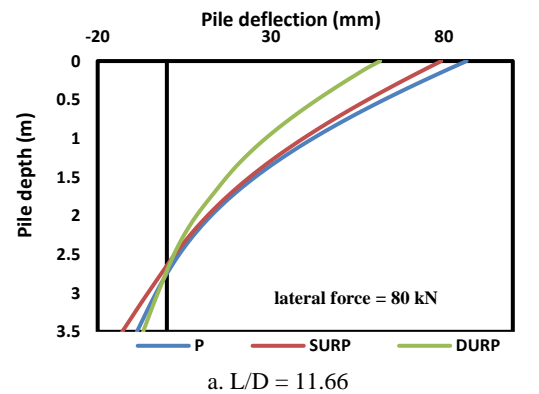
5. RESULTS AND DISCUSSIONS

A series of 3-D FE models were used to study the behavior of under-reamed piles with single and double bulbs. Three cases of loading were considered in this

analysis, pure lateral loads, pure uplift loads, and combined uplift and lateral loads. In this study, pile (L/D) ratios of 11.66, 15, 20, and 25 were investigated. The findings for different loading cases are summarized as follows:

5. 1. Behavior of Piles Subjected to Lateral Load

Figure 5(a-d) shows the computed lateral deflection along the pile depth for SURP and DURP compared with straight piles (P) for pile ratios of 11.66, 15, 20, and 25. From Figure 5, it can be concluded that piles 4.5 m, 6 m, and 7.5 m in length behave as flexible piles according to the shape of pile deflection. At the initial depth, the pile deflection is large; at a depth of approximately 3 m, the



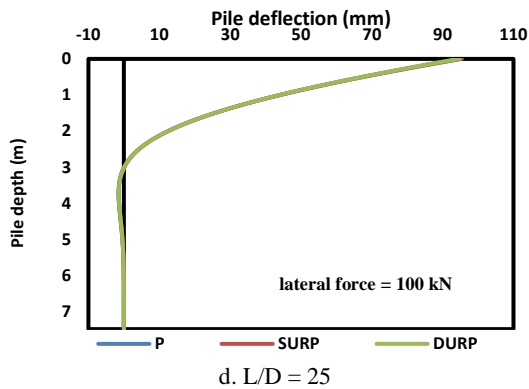


Figure 5. Lateral deflection along the piles

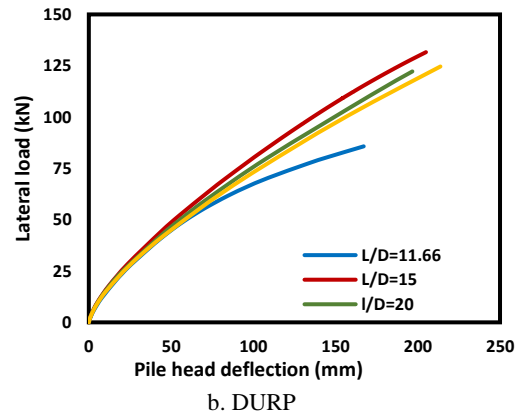
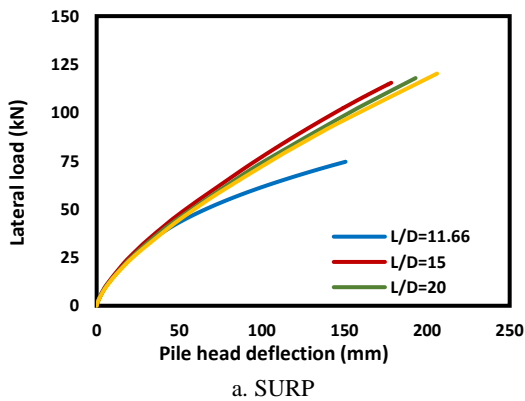


Figure 6. Distribution of lateral load vs. pile head deflection for different L/D ratios

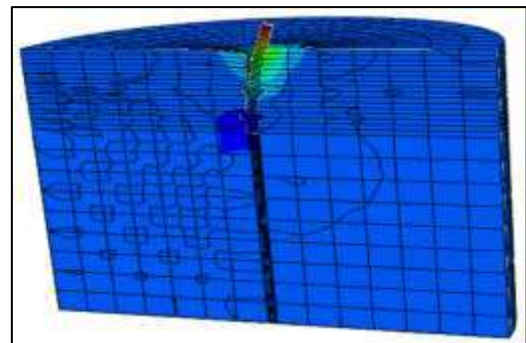
deflection is nearly zero. In addition, the piles do not rotate around a point.

For 3.5 m piles, there is rotation around a point at a depth of approximately 2.7 m, indicating rigid behavior. For shorter piles ($L/D = 11.66, 15$) under a certain lateral force, under-reamed piles noticeably reduced the pile deflection. For longer piles ($L/D = 20, 25$), no change in lateral pile resistance was observed using under-reamed piles with single or double bulbs.

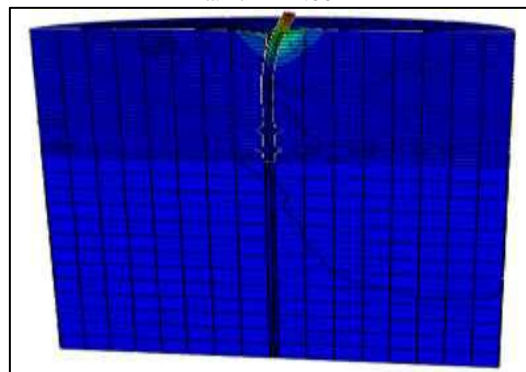
Figures 6(a) and 6(b) show the lateral load-deflection curves for single and double under-reamed piles with different (L/D) pile ratios subjected to pure lateral loads. It is observed that the lateral resistance of under-reamed piles with single and double bulbs increases considerably as the (L/D) pile ratio increases to 15. Further increasing of (L/D) ratio decreases the lateral resistance. This may be because initially, as the pile length increases, the passive pressure also increases. However, decreasing the lateral resistance with increasing pile length ($L/D > 15$) may be because “the soil resistance mobilized along the effective pile length and the ultimate moment of pile material governed the capacity of the long flexible piles” [21]. Figures 7(a) and 7(b) show viewport clarify the lateral displacement for short and long DURP.



a. SURP



a. $L/D=11.66$



b. $L/D=25$

Figure 7. lateral displacement for DURP. (This viewport was magnified five times)

5. 2. Behavior of Piles Subjected to Uplift Load

The behavior of P, SURP, and DURP subjected to pure uplift loads was examined. The variation of uplift load vs. pile head deflection for P, SURP, and DURP with different (L/D) pile ratios is shown in Figure 8 (a-d). As expected, the uplift pile capacity is greatly improved for SURP and DURP compared with a straight pile for all (L/D) pile ratios.

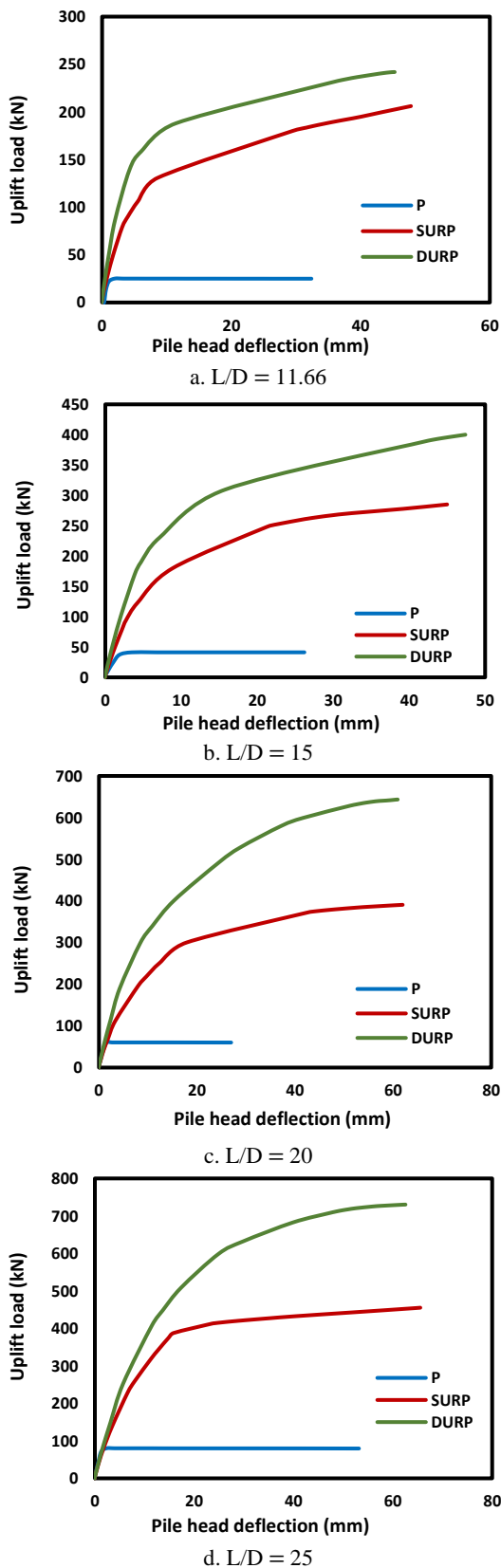


Figure 8. Distribution of uplift load vs. pile head deflection for P, SURP, and DURP

Table 5 presents the ultimate uplift capacity for P, SURP, and DURP for (L/D) pile ratios of 11.66, 15, 20, and 25. The double tangent method suggested by Shanker et al. [22] was used for interpreting the ultimate uplift pile capacity. The ultimate uplift capacity for SURP increased by a factor of (3.8, 4.24, 4.33, and 4.38) from the ultimate uplift capacity of the corresponding P pile, for (L/D) pile ratios of (11.66, 15, 20, and 25), respectively. The ultimate uplift capacity for DURP increased by a factor of (5.8, 6.07, 6.25, and 6.43) for (L/D) pile ratios of (11.66, 15, 20, and 25), respectively.

It is also observed from Table 5 that the ultimate uplift capacity increases significantly with increasing the (L/D) ratio. In addition, for a specific (L/D) pile ratio, there is an improvement in the ultimate uplift capacity of the DURP from that of the SURP.

Figures 9(a) and 9(b) show the influence of the (L/D) pile ratio on the uplift pile capacity; the uplift pile capacity increases considerably with increasing (L/D) ratio for SURP and DURP.

5. 3. Behavior of Piles Subjected to Combined Uplift and Lateral Loads

To investigate the effect of an uplift load on the lateral response of the SURP and DURP, the loading was applied in two steps. First, the pre-quantified uplift load was subjected to the pile head, which is represented in this study as the uplift load prior to lateral load (UPL). Second, the uplift load from the first step was maintained, and the lateral load was added. The lateral load was applied using displacement control; the displacement was specified as 0.5D. Uplift loads (here, UPLs) were chosen as a percentage of the previously evaluated ultimate uplift capacity (V_{ult}). The

TABLE 5. Ultimate uplift pile capacity of P, SURP, and DURP for different (L/D) ratios

L/D	Pile type	Ultimate uplift pile capacity	Increase factor
	P	25	
11.66	SURP	120	3.8
	DURP	170	5.8
	P	41	
15	SURP	215	4.24
	DURP	290	6.07
	P	60	
20	SURP	320	4.33
	DURP	435	6.25
	P	78	
25	SURP	420	4.38
	DURP	580	6.43

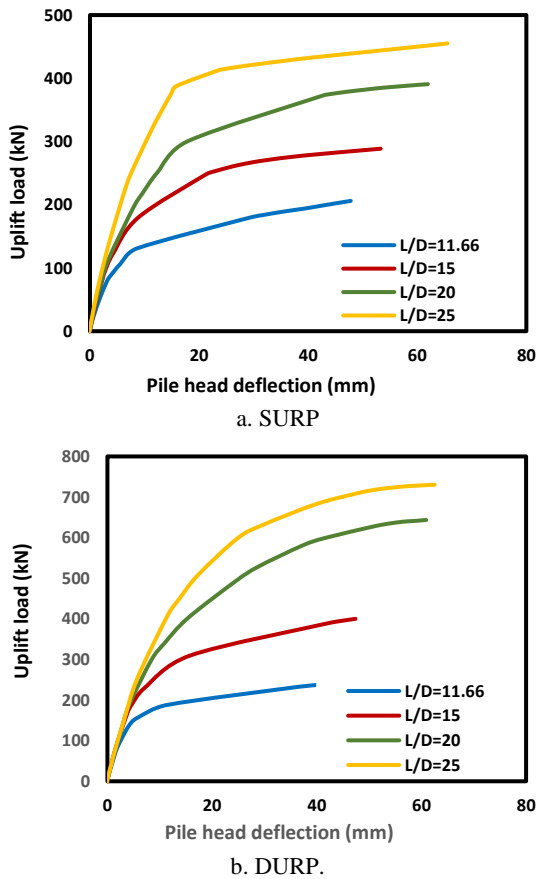


Figure 9. Influence of L/D ratio on the uplift pile capacity

uplift load was chosen as $(UPL = 0, 0.4 V_{ult}, 0.6 V_{ult}, \text{ and } 0.8 V_{ult})$.

The lateral load vs. pile head deflection for SURP and DURP subjected to combined uplift and lateral loads is shown in Figure 10 (a–d). Due to the similarity in the response of SURP and DURP, only SURP is shown. When the lateral load is extremely low, the lateral load–pile head deflection response is not significantly influenced by the pre-uplift load. It is clear from the figures that the load–deflection response is still nonlinear, even with UPL.

It is also observed that the influence of $(UPL = 0.4, 0.6, \text{ and } 0.8 V_{ult})$ on the lateral pile capacity depends on the embedment pile ratio. For an under-reamed pile with a (L/D) pile ratio of 11.66, the lateral pile capacity decreases with the UPL. For under-reamed piles with a (L/D) pile ratio of 15, uplift loading has no significant effect on the lateral pile capacity. However, for under-reamed piles with embedment pile ratios of 20 and 25, the lateral capacity increases marginally with increasing UPL. It can be concluded that the UPL reduces the lateral capacity of rigid Under-reamed piles and increases the lateral capacity of flexible under-reamed piles.

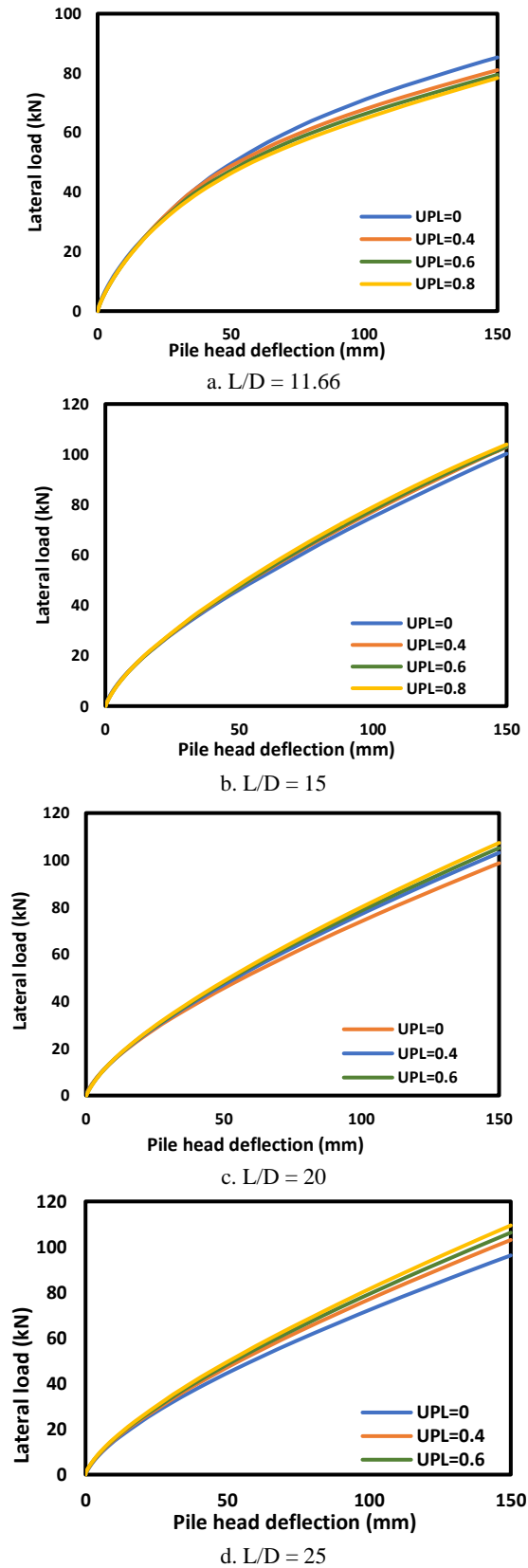


Figure 10. Distribution of lateral load vs. pile head deflection under pre-uplift load for SURP

6. CONCLUSIONS

In this study, a numerical analysis for a straight pile (P) and under-reamed piles with a single bulb (SURP) or a double bulb (DURP) was conducted to investigate their response under lateral, uplift, and combined lateral and uplift loads. Based on the results, the following conclusions can be drawn.

1. The lateral resistance was affected slightly by using under-reamed piles with single or double bulbs. P, SURP, and DURP with pile (L/D) ratios greater than 20 had nearly the same lateral resistance.
2. The ultimate uplift capacity for the under-reamed piles (SURP, DURP) was (3.8, 5.8), (4.24, 6.07), (4.33, 6.25), and (4.38, 6.43) times greater than the ultimate uplift capacity for the corresponding P pile, for pile (L/D) ratios of (11.66, 15, 20, and 25), respectively.
3. The lateral load–deflection behavior was nonlinear under both pure and combined loading.
4. For a specific (L/D) pile ratio, there was an improvement in the ultimate uplift capacity of the DURP compared with that of the SURP.
5. The lateral resistance of under-reamed piles with single and double bulbs increased considerably as the (L/D) pile ratio increased up to a certain value, beyond which the lateral resistance decreased.
6. The lateral capacity was marginally influenced by the uplift loading; it decreased for rigid under-reamed piles and increased for flexible under-reamed piles.

6. REFERENCES

1. I. 2911 P. III, "Indian Standard Code of Practice for Design and Construction of Pile Foundations, Under-reamed Piles." Bureau of Indian Standard, 1980.
2. Sharma, D., Jain, M. P., and Prakash, C., Handbook on under-reamed and bored compaction pile foundations. Jain, 1978.
3. Shrivatsava, S. P., Garg, K. G., and Sonoga, M. R. "Under-reamed pile group subjected to lateral loads," Proc. 3rd Symposium on Application of Soil Mechanics and Foundation Engineering in Eastern India, feb., Calcutta, 1972.
4. Hrennikoff, A., "Analysis of pile foundations with Batter Piles", *Transactions of the American Society of Civil Engineers*, Vol. 115, No. 1, 351-374, (1950), doi.org/10.1061/taceat.0006372.
5. M. R. Soneja and K. G. Garg, "Under-ream piles under lateral loads", *Indian Geotechnical Journal*, Vol. 10, No. 1, 232-244, 2013.
6. Prakash C. and Ramakrishna, V., "Lateral Load Capacity of Under-reamed Piles: An Analytical Approach," *Journal of Soils and Foundation*, Vol. 44, No. 5, 51-65, (2004), doi.org/10.3208/sandf.44.5_51.
7. Prakash, C. and Chandra, R., "Lateral Resistance of Single Under-reamed Piles in Silty Sand," proc. Indian Geotechnical Conference, IGC-83, Madras, India, (1983).
8. Martin, R. E. and DeStephen, R. A., "Large Diameter Double Under-reamed Drilled Shafts", *Journal of Geotechnical Engineering*, Vol. 109, No. 8, 1082-1098, (1983), doi.org/10.1016/01489062(83)90779-9.
9. Peter, J. A., Lakshmanan, N., and Devadas Manoharan, P., "Investigations on the Static Behavior of Self-Compacting Concrete Under-reamed Piles," *Journal of Materials in Civil Engineering*, Vol. 18, No. 3, 408-414, (2006) doi.org/10.1061/(asce)08991561(2006)18:3(408).
10. Shrivastava, N. and Bhatia, N., "Ultimate Bearing Capacity of Under-reamed Pile–Finite Element Approach," in *The 12th International Conference of International Association for Computer Methods and Advances in Geomechanics (IACMAG)*, 1-6, (2008).
11. Farokhi, A. S., Alielahi, H., and Mardani, Z., "Optimizing the Performance of Under-reamed Piles in Clay using Numerical Method," *Electronic Journal of Geotechnical Engineering*, Vol. 19, 1507-1520, (2014).
12. Vali, R., Mehrinejad Khotbehsara, E., Saberian, M., Li, J., Mehrinejad, M., and Jahandari, S., "A Three-Dimensional Numerical Comparison of Bearing Capacity and Settlement of Tapered and Under-reamed Piles," *International Journal of Geotechnical Engineering*, Vol. 13, No. 3, 236-248, (2019) doi.org/10.1080/19386362.2017.1336586.
13. Watanabe, K., Sei, H., Nishiyama, T., and Ishii, Y., "Static Axial Reciprocal Load Test of Cast-in-Place Nodular Concrete Pile and Nodular Diaphragm Wall," *Geotechnical Engineering Journal of the SEAGS & AGSSEA*, Vol. 42, No. 2, 11-19, (2011).
14. Niroumand, H., Kassim, K. A., Ghafooripour, A., and Nazir, R., "Uplift Capacity of Enlarged Base Piles in Sand," *Electronic Journal of Geotechnical Engineering*, Vol. 17, 2721-2737, (2012).
15. George, B. E., and Hari, G., "Numerical Investigations of Under-reamed Piles." Proceedings of Indian Geotechnical Conference, IGC-2016, IIT Madras, Chennai, India (2016).
16. Helwany, S., Applied soil mechanics with ABAQUS applications. John Wiley & Sons, 2007.
17. Karthigeyan, S., Ramakrishna, V., and Rajagopal, K., "Numerical Investigation of the Effect of Vertical Load on the Lateral Response of Piles," *Journal of Geotechnical and Geoenvironmental Engineering*, Vol. 133, No. 5, 512-521, (2007) doi.org/10.1061/(asce)10900241(2007)133:5(512).
18. Huang, A.B., Hsueh, C.K., O'Neill, M.W., Chern, S., Chen, C., "Effects of construction on laterally loaded pile groups". *Journal of Geotechnical and Geoenvironmental Engineering*. ASCE;127(5):385-97, (2001).
19. Marchetti, S., "The flat dilatometer: design applications". In: Proc III geotechnical Engineering Conference, Keynote Lecture, Cairo University; 1-26, (1997).
20. Conte, E., Troncone, A., Vena, M., "Nonlinear three-dimensional analysis of reinforced concrete piles subjected to horizontal loading", *Journal of Computers and Geotechnics*, Vol. 49 (2013)123–133, doi.org/10.1016/j.compgeo.2012.10.013.
21. Madhusudan Reddy, K. and Ayothiraman, R., "Experimental Studies on Behavior of Single Pile under Combined Uplift and Lateral loading," *Journal of Geotechnical and Geoenvironmental Engineering*, Vol. 141, No. 7, p. 4015030, (2015) doi.org/10.1061/(asce)gt.1943-5606.0001314.
22. Shanker, K., Basudhar, P. K., and Patra, N. R., "Uplift Capacity of Single Piles: Predictions and Performance," *Geotechnical and Geological Engineering*, vol. 25, no. 2, pp. 151–161, (2007) doi.org/10.1007/s10706-006-9000-z.

Persian Abstract

چکیده

شمعهای زیر ریم شده با یک یا چند حباب تقریباً در همه انواع خاک برای پشتیبانی از طیف وسیعی از ساختارها به طور گسترده ای استفاده شده است. در بعضی موارد، شمع ها علاوه بر بارهای فشاری عمودی یا صعودی، باید در برابر بار جانبی قابل توجهی مقاومت کنند. یک مطالعه ۳-D عنصر محدود با استفاده از نرم افزار ABAQUS برای بررسی رفتار شمعهای تحت اصلاح در خاک رس تحت بارهای جانبی خالص، صعودی خالص، و صعودی جانبی و جانبی خالص انجام گردید. در این مطالعه با تنظیم طول شمع برای شبیه سازی رفتار شمع های سفت و سخت و انعطاف پذیر، نسبت های شمع $(L/D) 11/66$ ، ۱۵، ۲۰ و ۲۵ در نظر گرفته شد. شمع ها به عنوان ماده الاستیک خطی مدل سازی شدند و رفتار خاک با استفاده از مدل سازنده دراکر-پراگر شبیه سازی شد. یافته ها نشان می دهد که مقاومت جانبی شمع هایی با نسبت $(L/D) 11.66$ و ۱۵ هنگامی که از شمع های تحت ریم استفاده می شود کمی افزایش می یابد. با این حال، هیچ تغییری در مقاومت جانبی برای شمعهای تحت ریم با نسبت $(L/D) 20$ و ۲۵ در مقایسه با شمع های مستقیم مشاهده نشد. ظرفیت صعودی شمعهای زیر ریمینگ به طور قابل توجهی بیشتر از یک شمع مستقیم بود. ظرفیت جانبی تحت تأثیر بارگذاری قبل از بالا بردن تحت تأثیر قرار گرفت، به طوری که برای یک شمع سفت و سخت تحت ریشه کاهش یافته و برای یک شمع قابل انعطاف تحت ریش افزایش می یابد.



Effect of Pin Geometry and Tool Rotational Speed on Microstructure and Mechanical Properties of Friction Stir Spot Welded Joints in AA2024-O Aluminum Alloy

Tiwan^{a,b}, M. N. Ilman^{*a}, Kusmono^a

^a Department of Mechanical and Industrial Engineering, Faculty of Engineering, Universitas Gadjah Mada, Yogyakarta, Indonesia

^b Department of Mechanical Engineering Education, Yogyakarta State University, Indonesia

PAPER INFO

Paper history:

Received 24 April 2021

Received in revised form 19 May 2021

Accepted 01 July 2021

Keywords:

Friction Stir Spot Welding

AA2024-O Aluminum Alloy

Pin Geometry

Tool Rotational Speed

Shear Strength

ABSTRACT

In the present study, the effects of pin geometry and tool rotational speed on the microstructure and mechanical characteristics of the AA2024-O friction stir spot welding (FSSW) joint were investigated. Two different types of pin geometries, namely cylindrical and step pins, and three different rotational speeds of 900, 1400, and 1800 rpm were used in the friction stir spot welding joint. The microstructure observation, hardness measurements, and shear tests were conducted. Results showed that both pin geometry and rotational speed gave a remarkable effect on the microstructure and maximum shear load of the weld joints. For both pin geometries, the hook height and width of the fully bonded region (FBR) increased by increasing the rotational speed. The weld joint produced by a cylindrical pin exhibits higher values in the hook height and width of the FBR than using a step pin. Furthermore, the highest value in a maximum shear load was obtained at a rotation speed of 1400 rpm for both cylindrical and step pins. Another finding is that the maximum shear loads of FSSW joints produced with a cylindrical pin are higher than that made using a step pin.

doi: 10.5829/ije.2021.34.08b.16

1. INTRODUCTION

The application of aluminum alloys in automotive industries is mainly intended to produce lightweight vehicles which leads to fuel savings, high speed, and a reduction in exhaust emission. Today, aluminum and its alloys are produced in various series and treatments. One of the aluminum alloys that is widely used in engineering applications, especially for aircraft structures is AA2024 aluminum alloy which is composed of copper (Cu) around 3.8-4.9 wt% as the main alloying element. This aluminum alloy has the potency to replace steel in the manufacture of the vehicle body. In general, AA2024 aluminum alloy is used in the aircraft industry due to its beneficial properties, i.e. the alloy has high strength at room temperature to high temperature up to 150 °C and good toughness [1]. In addition, it has a very good damage tolerance and high fatigue crack resistance [2] which is suitable for aircraft materials.

Apart from its excellent properties, AA2024 aluminum alloy together with its 2XXX series are, however, considered to be unweldable [3] so that AA2024 aluminum alloy is commonly fabricated by riveting. The invention of friction stir welding (FSW) at The Welding Institute (TWI), UK in 1991 followed by its variant, i.e. friction stir spot welding (FSSW) allows the unweldable materials such as AA2024 to be welded using these solid-state welding processes [4-6]. The FSSW process has similarities with FSW in which both of them use a rotating cylindrical tool equipped with a shoulder and a pin to produce weld joints but they are different in term of the tool movement that is the rotating tool in FSW moves along a weld line in the butt plane of the plates whilst the rotating tool in FSSW is operated in a stationary condition [7]. FSSW is performed by plunging the rotating tool into the sheets in the lap joint configuration. The heat generated by frictional forces leads to softening in the materials to be welded. As a

*Corresponding Author Institutional Email: ilman_noer@ugm.ac.id
(M. N. Ilman)

result, the softened materials of upper and lower sheets are mixed due to stirring action by the pin, and under such a condition, the weld joint is formed.

Since the invention of FSSW by Mazda's car manufacturer in 2003 [8], research in FSSW has been conducted extensively to improve mechanical characteristics of FSSW joints by considering factors affecting the mechanical properties of FSSW joints including process parameters and tool geometry in various metals. The influence of shoulder and pin geometries of a tool on the microstructure and mechanical characteristics of the FSSW joint in AA2024-T3 aluminum alloy has been studied by Paidar et al. [9]. According to the authors, at a low tool rotational speed, the grain size in the stirring zone is influenced by the pin geometry while at a high tool rotational speed, there is no significant difference in the grain size. Badarinarayan et al. [10] showed that the shape of the tool pin affects the hook, weld strength, and failure mode of the FSSW joint. Enami et al. [11] investigated the influences of welding parameters (plunge depth, dwell time, and tool rotational speed) and addition of alumina nanopowder on the FSSW joint strength and found that the normal plunge depth, dwell time, and tool rotational speed effectively affect the joint strength of AA2024 alloy. In addition, the optimum welding parameters are achieved at a speed of 1120 rpm, 5s dwell time, and normal plunge depth of 2.75, and the joint strength increased by 23% by the addition of alumina nanopowder. Subsequently, Klobčar et al. [12] have investigated the effect of process parameters on the strength of AA5754 FSSW joint with the results showed that axial force and torque increased with increasing plunge rate but they decreased with increasing dwell time and tool rotation speed. Other FSSW process parameters such as plunge depth have been investigated by Baek et al. [13] and according to the authors, plunge depth affects the shear strength of the FSSW galvanized steel joint. The effects of both plunge rate and dwell time on the joint strength of AA1100 sheets under micro FSSW were studied by Baskoro et al. [14]. They found that the dwell time gives a remarkable effect on the tensile shear strength but the plunge rate has a minor effect. Other studies on the effect of FSSW process parameters on the shear strength of FSSW joint have been conducted to optimize FSSW process parameters to produce the high quality of the joints [15-18]. Recently, Tiwan et al. [19] studied the effects of pin geometry and rotational speed on the microstructure and mechanical characteristics of the AA5052-H112 FSSW joint. They found that both pin geometry and rotational speed have a significant effect on the hook height and width of FBR of the FSSW joints. Moreover, the strength of the weld joints produced by a cylindrical pin is higher than that of a step pin. The effect of tool rotating speed (700, 900, and 1100 rpm) on the microstructures and mechanical characteristics of the AA6061 FSSW joints welded in air and water was also

demonstrated by Shekhawat et al. [20]. They found that the load-bearing capacity improved and also a slight increase in hardness when the rotational speed increases from 700 to 1100 rpm, irrespective of the welding medium. This increase is attributed to the grain size refinement in the weld nugget zone. In addition, the FSSW in water is obtained to be beneficial as compared to that in air.

The quality characteristics of FSSW joints formed in the metal alloy are strongly influenced by design and welding parameters. One of the most important factors influencing the quality of the FSSW joints is the design of the tool used for producing the friction and stirring action [21]. It seems that research works related to the FSSW in AA2xxx series aluminum alloys have been studied extensively, but there have been limited published data on the influences of pin geometry and rotational speed on the microstructure and strength of the FSSW AA2024-O aluminum alloy joints. Therefore, it is the subject of the present work. Two different types of pin geometries, i.e., cylindrical and step pins, and three different rotational speeds of 900, 1400, and 1800 rpm were selected for the AA2024-O FSSW joint.

2. MATERIAL AND EXPERIMENTAL

The materials used in this work were AA2024-O aluminum alloy plates with the chemical composition is given in Table 1. In this investigation, the plates with the dimension of 3 x 30 x 120 mm were welded using the FSSW process in lap joint configuration. The plates to be welded were tightly clamped using a jig. The tools having two different tool pin geometries, namely cylindrical and step pins were made of H13 steel as shown in Figure 1. The FSSW joints were produced using various tool rotational speeds (RS) of 900 rpm, 1400 rpm, 1800 rpm whereas other FSSW parameters including plunge depth, plunge rate, and dwell time were maintained constant at 0.1 mm, 4 mm/min and 5s, respectively.

The temperatures during welding were measured using K-type thermocouples attached at various distances of 0, 4, 5, 6, 7, 8 mm from the center of the weld hole as shown in Figure 2. Microstructure examinations were performed on the cross-section of the FSSW joints using optical microscopy. The samples were prepared

TABLE 1. Chemical compositions of AA2024-O aluminum alloy

Chemical composition (wt.%)								
Cu	Mg	Si	Fe	Zn	Ti	Mn	Cr	Al
4.4	1.11	0.12	0.14	0.08	0.01	0.40	0.01	Bal.

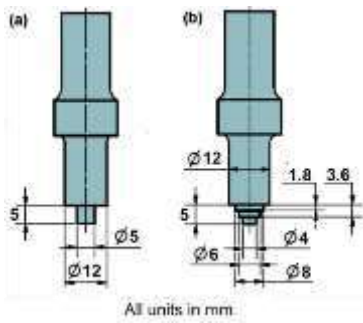


Figure 1. FSSW tools type:(a) Cylindrical pin (b) Step pin

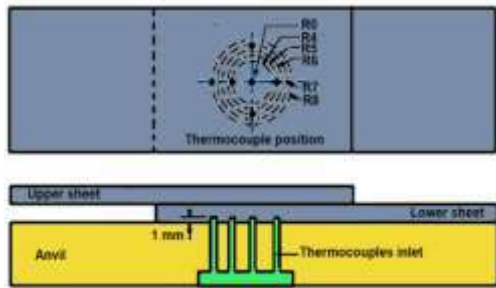


Figure 2. A schematic illustration of the FSSW process

following standard metallographic procedures with etchant used was Keller's reagent.

Furthermore, hardness distributions were assessed using Vickers microhardness along with the upper and lower plates around the FSSW joints as shown in Figure 3 with the load of 100 g for 10 s. The strength of FSSW joints was assessed using shear tests with the dimensions of shear test specimens are presented in Figure 4 as suggested by Kim et al. [22]. Following these shear tests, fractographic studies were conducted.

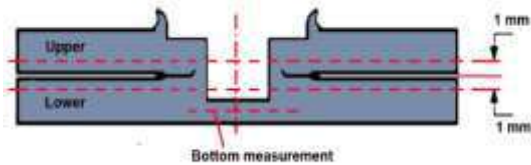


Figure 3. Position of hardness measurement

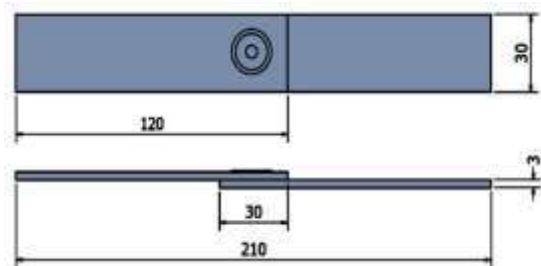


Figure 4. Tensile-shear test specimens

3. RESULT AND DISCUSSION

3. 1. Weld Thermal Cycles

The thermal cycles taken at various distances of 0, 4, 5, 6, 7, and 8 mm from the center of the exit hole (designated as R0, R4, R5, R6, R7 and R8, respectively) during friction stir spot welding (FSSW) of AA2024-O aluminum alloy plates at two different tool pin geometries are demonstrated in Figures 5 and 6.

Referring to Figures 5 and 6, it can be seen that each thermal cycle under study shows similar behaviors marked by rapid heating as the shoulder surface penetrates the workpiece. Furthermore, the maximum temperature is achieved when the distance between the tool tip and the bottom surface of the lower plate is

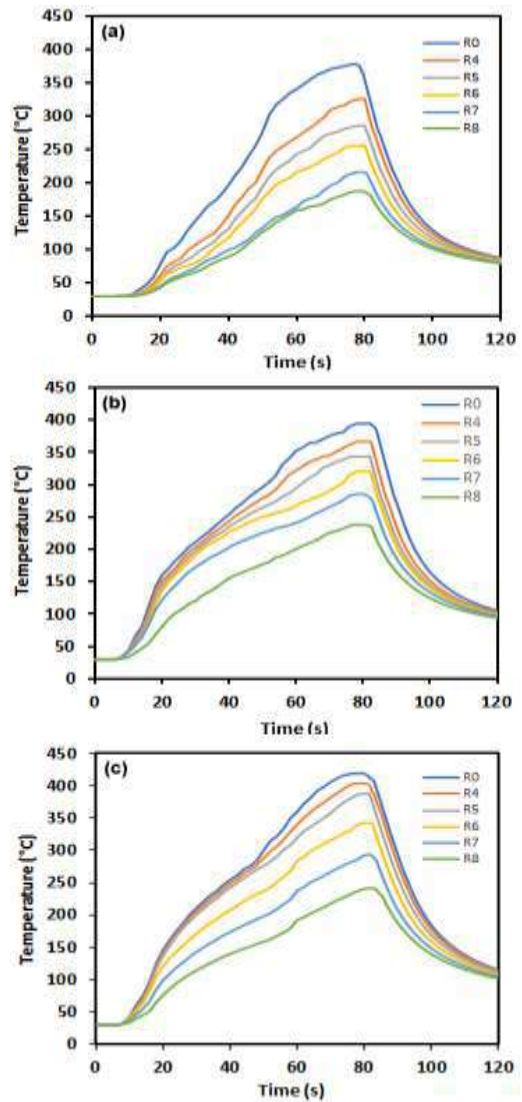


Figure 5. Thermal cycles of FSSW AA2024 using a cylindrical pin with variation in RS: (a) 900 rpm (b) 1400 rpm (c) 1800 rpm

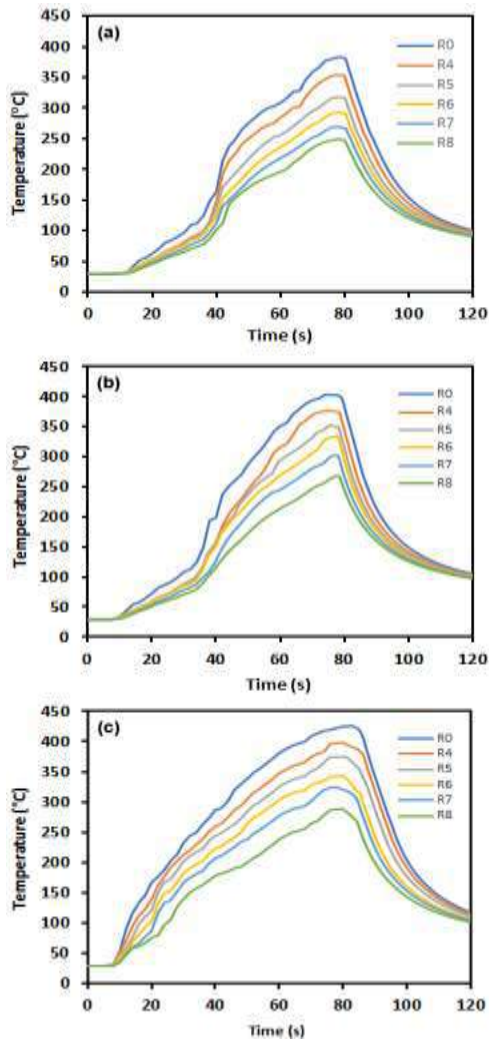


Figure 6. Thermal cycles of FSSW AA2024 using a step pin with variation in RS: (a) 900 rpm (b) 1400 rpm (c) 1800 rpm

the closest, typically 0.1 mm. At this condition, the maximum temperature is maintained constant for 5s then followed by continuous cooling towards the ambient temperature as the tool is lifted. Referring to Figures 5 and 6, it can be seen that increasing distance from the center of the keyhole decreases the peak temperature and the position of the peak temperature is shifted to a slightly longer time. Of note is that the peak temperatures resulted by cylindrical and step at the distance of R0 are slightly the same but as the distance, the significant differences are observed with the peak temperatures resulted from step pin is higher than that of cylindrical spin.

This seems to suggest that FSSW having a step pin produces higher heat input than that of the cylindrical pin at the same tool rotational speed.

The effects of tool rotational speed on the weld thermal cycles can be studied by comparing the welds made at the tool rotational speeds of 900, 1400, and 1800

rpm for both cylindrical and step pins. As expected, an increase in tool rotational speed tends to increase the peak temperature and reduce the cooling rate. In comparison with the tool having cylindrical pin geometry, the peak temperatures for the FSSW joints produced using step pin are slightly higher at the same tool rotational speed. The possible explanation is summarized as follows. The heat generated, q by a conventional tool having a cylindrical pin is given by following expression [23, 24]:

$$q = \frac{2}{3} \pi \omega \tau (R_{shoul}^3 + 3R_{pin}^2 H_{pin}) \tag{1}$$

With τ is shear stress, ω is angular speed, H_{pin} is pin height whereas R_{pin} and R_{shoul} are the radius of pin and shoulder respectively. According to Equation (1), the use of a step pin will increase the shoulder area hence increasing the heat since the shoulder has more contribution to the total heat compared to other components such as pin side and pin tip.

3. 2. Macro and Microstructures Figure 7 shows typical macrostructural regions taken from a cross-section of FSSW joint prepared using a tool having a cylindrical pin. The hole shown in Figure 7a is formed when the rotating tool was retracted from the weld joint. It can be seen that the FSSW profile is symmetrical concerning the hole-axis. There are three types of interface bonds, namely fully bonded region (FBR), partially bonded region (PBR), and unbonded region (UBR) [25]. The closest region to the exit hole is known as FBR which is marked by the presence of a perfect bond as the result of stirring of the upper and lower plate materials. Subsequently, PBR is formed starting from FBR to the distance where the bonding no longer exists. PBR has an imperfect bond which occurs caused by the lack of a diffusion process between the surface of the upper and lower plates. At the distance away from the hole exit, the upper and lower plates are separated with no bond formation, and this region is called UBR.

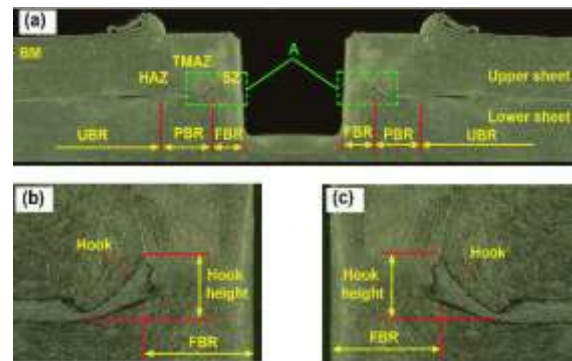


Figure 7. (a) Cross-section of FSSW joint, (b), (c) magnified region marked by A in Figure 6a showing various weld microstructures

Figures 8 and 9 show cross-sections of FSSW weld joints produced using a cylindrical pin and a step pin at various rotational speeds of 900 rpm, 1400 rpm, and 1800 rpm. It can be seen that all FSSW joints are characterized by the formation of hooks and microstructural regions with different dimensions. The hooks are formed when the interface is bent upward as the result of penetration and stirring of the tool which causes the bottom plate material to flow upward [26].

Details of the dimensions of FBR and the hooks under various tool rotational speeds at two different pin geometries are shown in Figures 10 and 11. In FSSW joints prepared using a cylindrical pin, the dimensions of the FBR increase with increasing rotational speed consistent with the previous report [25].

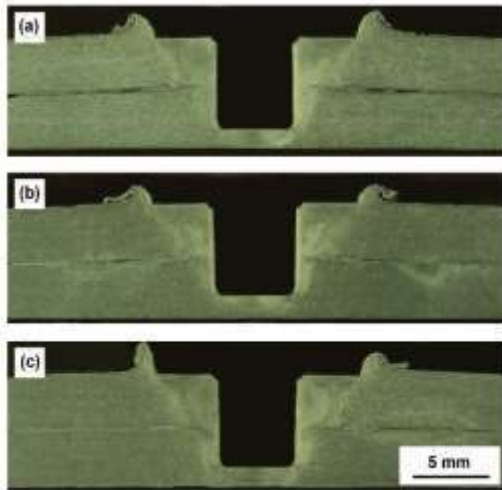


Figure 8. FSSW welded macrostructure by a cylindrical pin at RS: (a) 900 rpm, (b) 1400 rpm (c) 1800 rpm

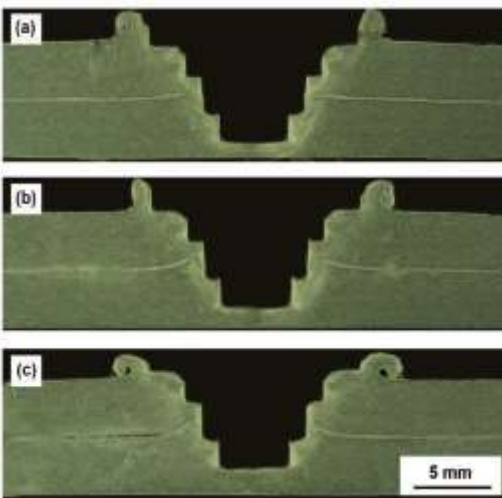


Figure 9. FSSW welded macrostructure by a step pin at RS: (a) 900 rpm, (b) 1400 rpm (c) 1800 rpm

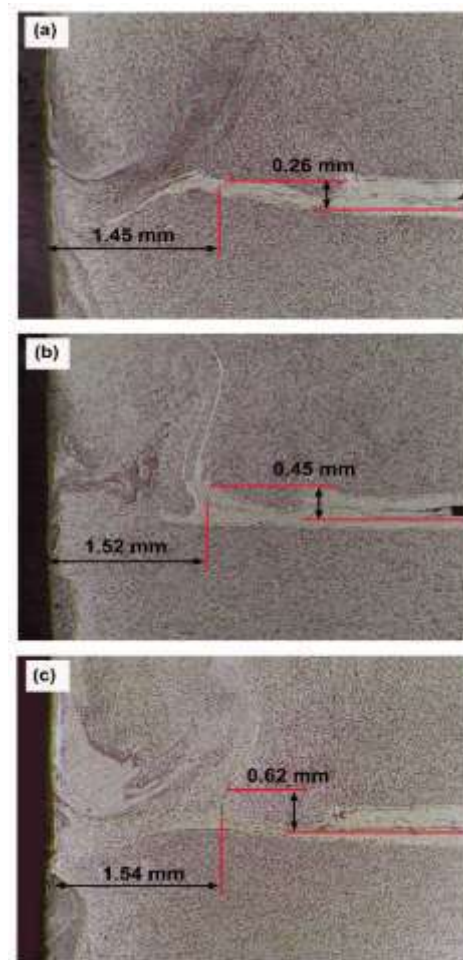


Figure 10. FBR dimension and height hook of FSSW by a cylindrical pin under different RS: (a) 900 rpm (b) 1400 rpm (c) 1800 rpm

The use of a rotational speed of 900 rpm produces FBR with a length of 1.45 mm. Subsequently, the length of FBR increases to 1.52 mm as the tool rotational speed is increased to 1400 rpm. On further increase in the tool rotational speed up to 1800 rpm, the dimension of FBR length continues to increase with the length of 1.54 mm. Similar behavior is also observed in the hook height. The hook height continuously increases from 0.26 mm to 0.45 mm and finally, 0.62 mm as the tool rotational speeds are increased to 900, 1400, and 1800 rpm, respectively.

In the step pin, there is a slight increase in the dimensions of the FBR from 1.31 mm to 1.33 mm as the tool rotational speed is increased from 900 to 1400 rpm. Further increase in the rotational speed to 1800 rpm does not increase the dimensions of FBR. Similar trends are observed in the hook heights under increasing tool rotational speeds marked by the hook heights of 0.23 mm, 0.25 mm, and 0.27 mm at increasing tool rotational speeds of 900, 1400, and 1800 rpm, respectively.

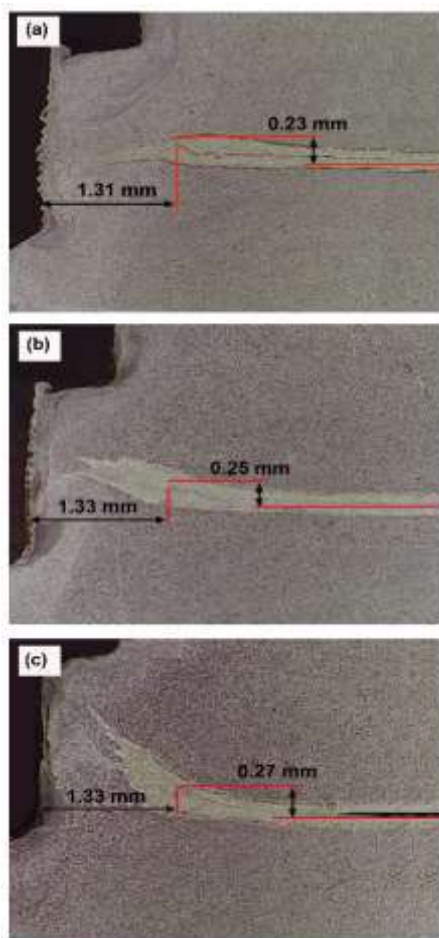


Figure 11. FBR dimension and height hook of FSSW by a step pin under different RS: (a) 900 rpm (b) 1400 rpm (c) 1800 rpm

Results of this investigation show that FBR dimensions (FBR length and hook height) of FSSW welds prepared using the step pin tool tend to be lower than the cylindrical pin which may be linked to material flow during welding. Based on the terminology used in FSSW [27, 28], microstructural regions in the FSSW can be classified into four regions, namely stir zone (SZ), thermomechanical affected zone (TMAZ), heat affected zone (HAZ), and base material (BM). Figures 12 and 13 show typical microstructures taken from various regions of FSSW joint produced using the tools having cylindrical and step pins at the tool rotational speed of 1400 rpm. The microstructure in SZ prepared using both cylindrical and step pins is characterized by the presence of fine equiaxed grains due to dynamic recrystallization of the material around the pins [29]. The microstructure of TMAZ has fine bent and deformed grains resulted from the combined effect of heat and plastic deformation [30].

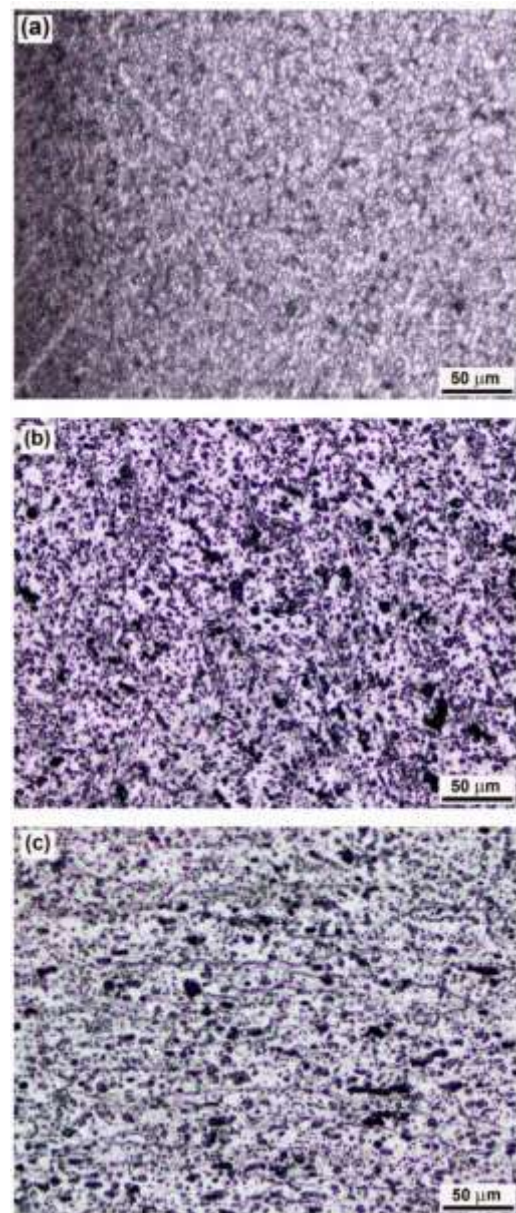


Figure 12. Microstructure of FSSW welded using a cylindrical pin at the RS of 1400 rpm: (a) SZ (b) TMAZ (c) HAZ

In HAZ regions, the microstructures are influenced by heat only and they are characterized by coarser polygonal grains [31]. In general, various microstructure present in both the welds prepared using the tools having cylindrical and step pins are the same but they are different in term of grain size with the tool equipped with step pin produces coarser microstructure.

Stir zone (SZ) microstructures of the FSSW joints produced using the cylindrical pin and step pin at various tool rotational speeds are presented in Figures 14

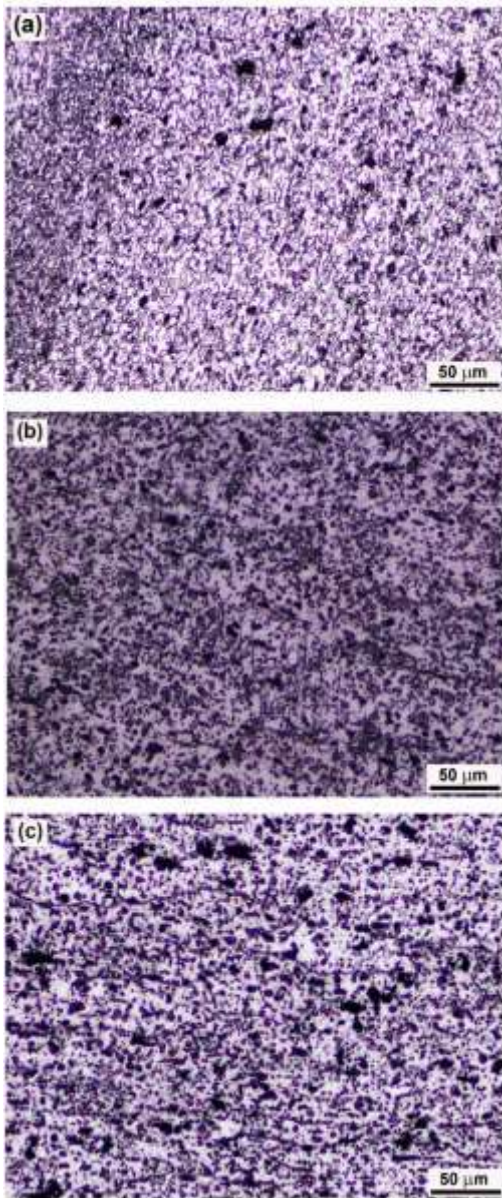


Figure 13. Microstructure of FSSW welded used a step pin at the RS of 1400 rpm: (a) SZ (b) TMAZ (c) HAZ

and 15. It can be seen that increasing tool rotational speed tends to grains coarsening the microstructures [32]. Referring to Figures 14 and 15, it can be seen the microstructures produced using the step pin are coarser than those produced using the cylindrical pin.

3. 3. Hardness Distributions

Results of microhardness measurements for all FSSW joints under study are shown in Figures 16 and 17.

It can be seen that the hardness profiles of all FSSW joints have the same behaviors, i.e. the maximum hardness occurs at the keyhole side for both upper and lower sheets which is likely to be associated with re-

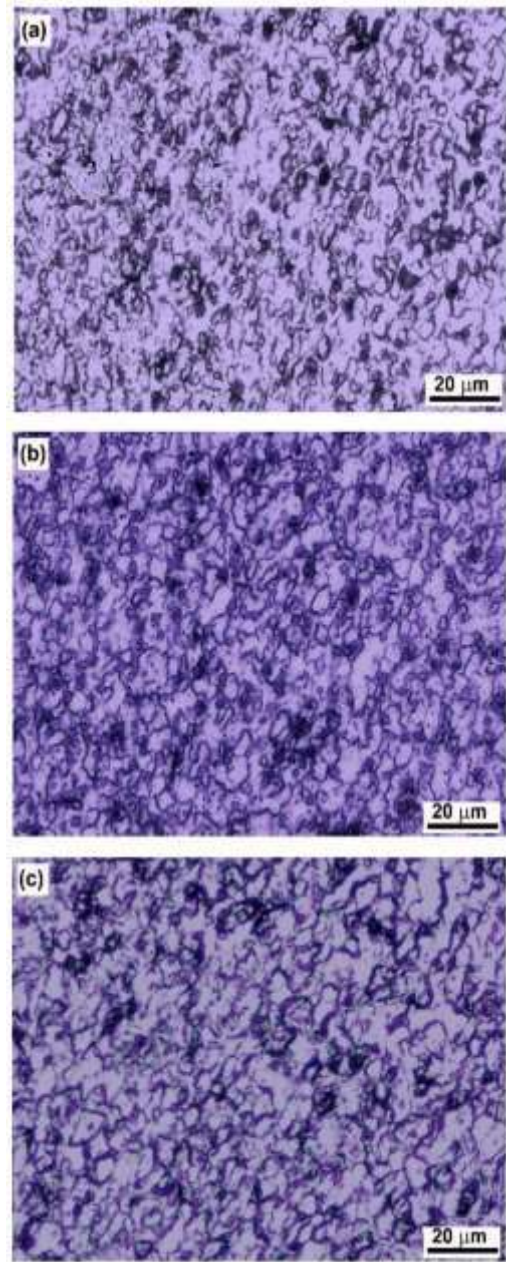


Figure 14. SZ microstructure of FSSW welded used a cylindrical pin in different RS: (a) 900 rpm (b) 1400 rpm (c) 1800 rpm

precipitation in SZ followed by continuous decrease along TMAZ and HAZ and the hardness values tend to constant at the BM as reported previously [9, 33]. However, they are different in terms of the magnitude of hardness, especially in the bottom of the exit hole due to variations in pin geometry and rotational speed.

In the FSSW joint produced using a cylindrical pin, the hardness curve in the upper sheet is higher than that measured in the lower sheet especially along the HAZ region but such a significant difference is not observed in

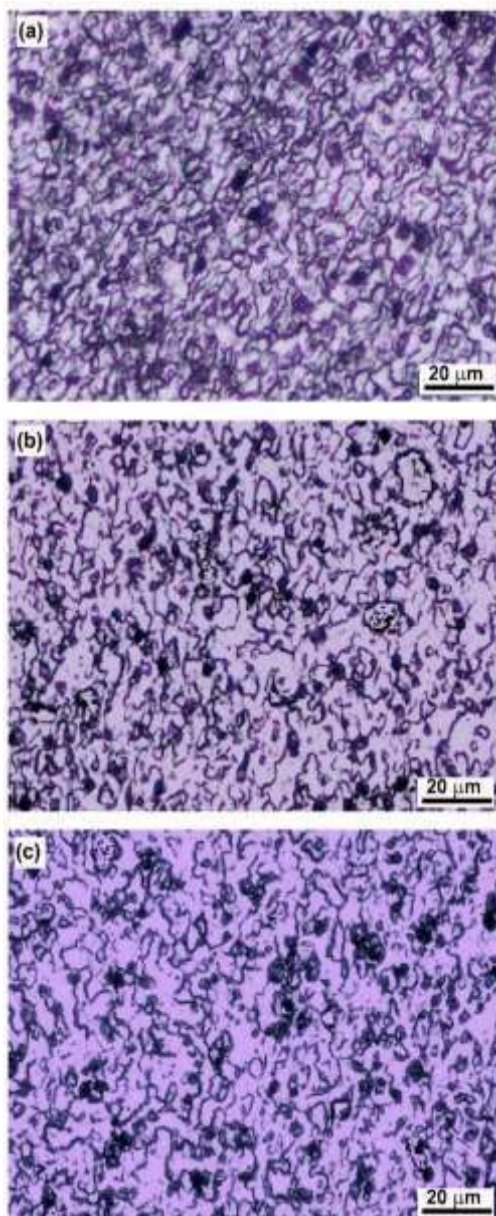


Figure 15. SZ microstructure of FSSW welded used a step pin in different RS: (a) 900 rpm (b) 1400 rpm (c) 1800 rpm

the FSSW joints produced using step pin. It is interesting to note that at the bottom of the keyhole, a continuous decrease in the hardness is observed with increasing tool rotational speed, especially in FSSW prepared using step pin. It may be argued that the use of step pin produced more heat which results in coarsening the precipitates hence softening [21, 34, 35].

3. 4. Strengths The maximum shear loads of the FSSW AA2024-O joints welded using different pin geometry and rotational speeds are shown in Figure 18. The maximum shear loads of FSSW joints that use

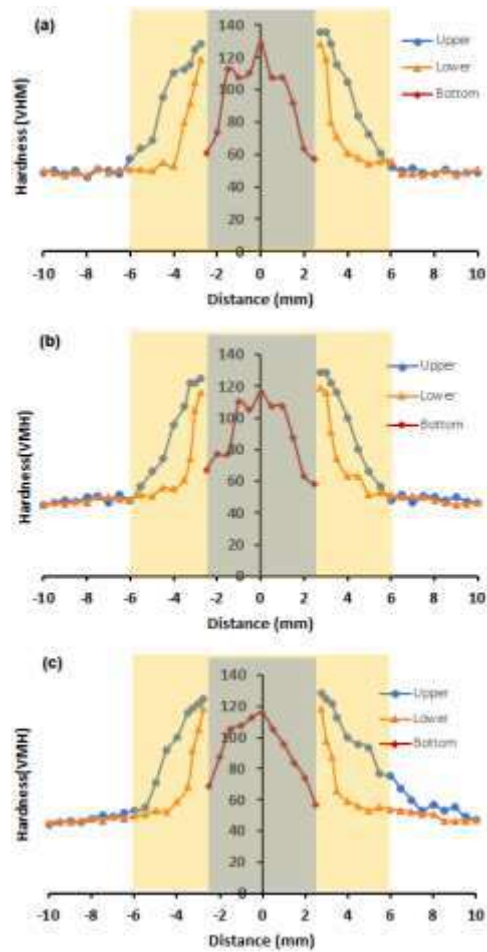


Figure 16. Microhardness distribution in a cross-section of FSSW welds used a cylindrical pin in different RS: (a) 900 rpm (b) 1400 rpm (c) 1800 rpm

cylindrical pin increase with increasing rotational speed until the highest value of the maximum shear load is achieved at 1400 rpm. On further increase in the rotational speed to 1800 rpm, the shear load decrease. Similar behaviors are observed in the FSSW joints produced using a step pin but with the lower magnitudes over a wide range of tool rotational speed, typically between 900-1800 rpm.

The strengths of the FSSW joints are determined by the structure of the welds, i.e. the FBR length and grain size in the SZ area [36].

The formation of FBR and grain size in SZ are influenced by the heat input which in turn tool rotational speed and pin geometry. The higher rotational speeds produce the higher strain and heat input making a wider FBR. Subsequently, the wider FBR results in a higher maximum fracture load. On the other hand, the strength of metallic materials including aluminum welded joints is controlled by grain size according to Hall-Petch as given by Mathers [37].

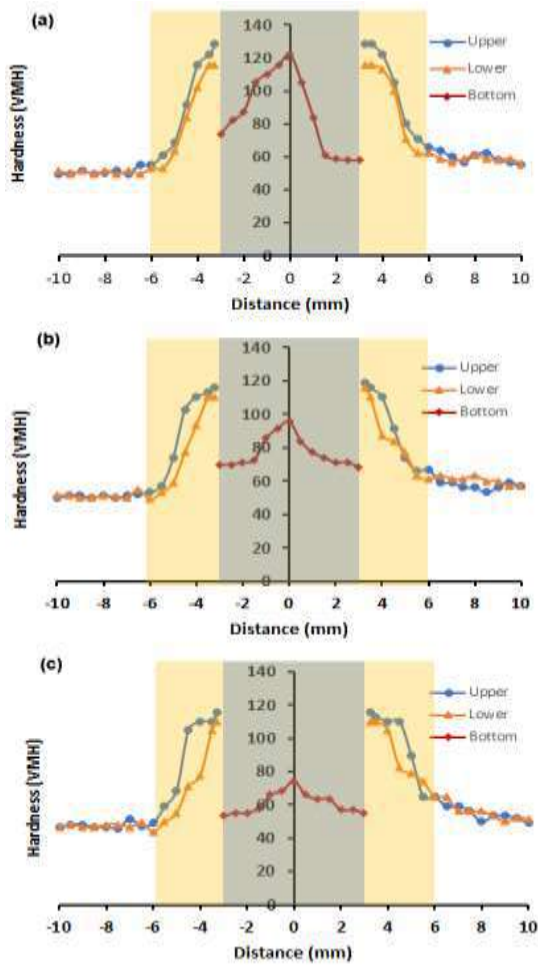


Figure 17. Microhardness distribution in a cross-section of FSSW welds used a step pin in different RS: (a) 900 rpm (b) 1400 rpm (c) 1800 rpm

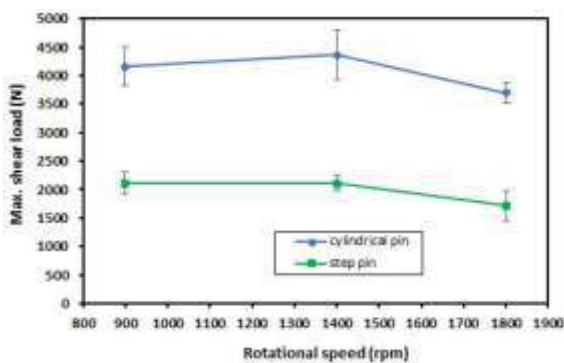


Figure 18. Maximum shear load in pin geometry and rotational speed tool variation

$$\sigma_y = \sigma_l + k_y d^{-\frac{1}{2}} \quad (2)$$

where d is the average diameter of the grains while σ_l and k_y are constants. It seems that increasing heat input due to

increased tool rotational has two conflicting effects. On one hand, high heat input increases the FBR length hence increasing the strength but it also causes coarsening of the microstructure resulting in reduced strengths. Therefore, the optimum tool rotational speed for both cylindrical and step pins seems to be achieved at the rotational speed of 1400 rpm owing to the balanced between these two factors.

Figures 19 and 20 show fractured surfaces of the FSSW joints under applied shear loads. It can be seen that

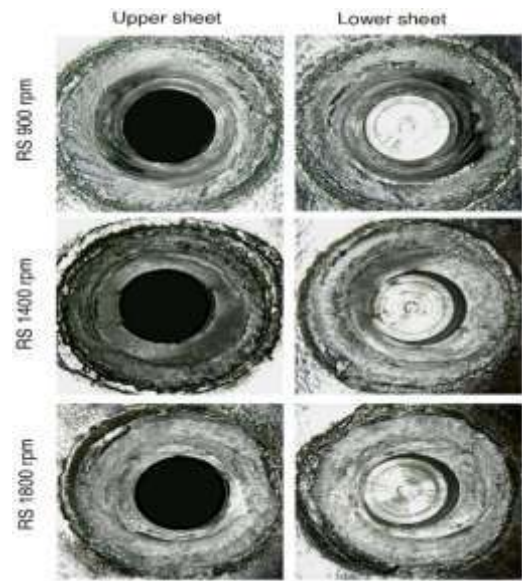


Figure 19. Fracture surfaces of FSSW joints under shear load using a cylindrical pin at different RS

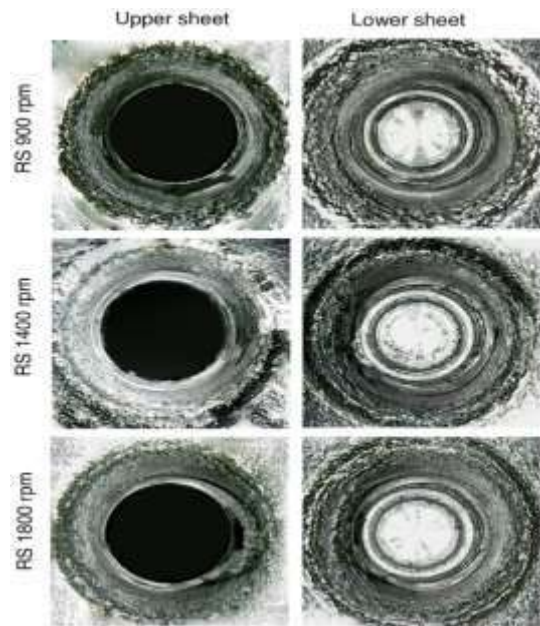


Figure 20. Fracture surfaces of FSSW joints under shear load using a step pin at different RS

at low tool rotational speed, typically of 900 rpm, the weld joints prepared using both cylindrical and step pins reveal failures correspond to shear mode. The failures are initiated by the formation of cracks at the hook tips which have high-stress concentrations. The cracks then propagate circumferentially along the stir zone (SZ) leading to final failure. At higher tool rotational speed, typically 1400 rpm or above, the failure mode change from shear to pullout in the nugget zone. The plausible explanation can be seen in Figure 21. As previously discussed, increasing tool rotational speed increases heat input and makes FBR wider. As a result, the working shear stress at the SZ under applied shear loads becomes lower so that the weakest part of the FSSW joints moves to the circumferential plane at the hook tip parallel to the exit hole. This condition combined with the moment of a couple due to eccentricity (misalignment) of the applied loads in the lap joints can cause nugget pullout.

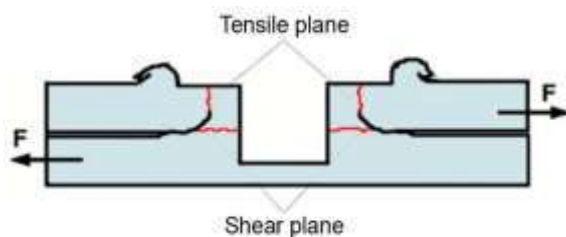


Figure 21. Schematic illustration of shear and tensile stresses around the SZ under applied shear stress

4. CONCLUSIONS

In this study, the effects of pin geometry and tool rotational speed on temperature profiles, microstructure, and mechanical properties of the FSSW joints aluminum alloy AA2024-O have been investigated and the following conclusions are drawn :

- Heat generated by the FSSW process is determined by the pin geometry and tool rotational speed. The tool has a step pin that produces more heat compared to the cylindrical pin due to the more frictional area in the step pin.
- The SZ region has the highest hardness probably due to re-precipitation then the hardness continuously decreases across TMAZ/HAZ and finally becomes constant along with BM.
- For the FSSW joints prepared using both cylindrical and step pins, the highest value of the maximum shear load is achieved at the tool rotational speed of 1400 rpm. It seems that this optimum tool rotational speed produces a proper combination of FBR length and grain size with the failure mode showing pullout nuggets.

5. REFERENCES

1. Rambabu P., N. Eswara Prasad, N.E., V.V. Kutumbarao, V.V., Wanhill, R.J.H., "Aluminium Alloys for Aerospace Applications", Aerospace Materials and Material Technologies, Indian Institute of Metals Series, Springer Science+Business Media Singapore, (2017). DOI: 10.1007/978-981-10-2134-3.
2. Rajan, R., Kah, P., Mvola, B., Martikainen, J., "Trends in Aluminium Alloy Development and their Joining Methods", *Annual Review of Material Science*, Vol. 44, (2015), 383-397.
3. Kaushik, N., Singhal, S., "Experimental Investigations on Microstructural and Mechanical Behavior of Friction Stir Welded Aluminum Matrix Composite", *International Journal of Engineering, Transactions A: Basics*, Vol. 32, No. 1, (2019), 162-170. DOI: 10.5829/ije.2019.32.01a.21.
4. Thomas, W.M., "Friction stir welding and related friction process characteristics", Inalco, International conference joint in aluminium Cambridge, UK., (1998).
5. Karthikeyan, R., Balasubramanian, V., "Predictions of the optimized friction stir spot welding process parameters for joining AA2024 aluminum alloy using RSM", *International Journal of Advanced Manufacturing Technology*, Vol. 51, No. 1-4, (2010), 173-183. DOI: 10.1007/s00170-010-2618-2.
6. Song, X., Ke, L., Xing, L., Liu, F., Huang, C., "Effect of plunge speeds on hook geometries and mechanical properties in friction stir spot welding of A6061-T6 sheets", *International Journal of Advanced Manufacturing Technology*, Vol. 71, No. 9-12, (2014), 2003-2010. DOI: 10.1007/s00170-014-5632-y
7. Khatami, H., Azdast, T., Mojaver, M., Hasanzadeh, R., Rafiei, A., "Study of Friction Stir Spot Welding of Aluminum/Copper Dissimilar Sheets using Taguchi Approach", *International Journal of Engineering, Transactions B: Applications*, Vol. 34, No. 05, (2021), 1329-1335. DOI: 10.5829/ije.2021.34.05b.28
8. Sprovieri, Jhon, "Friction Stir Spot Welding", *Assembly Magazine*, (2016), 1-6. <http://www.assemblymag.com/articles/93337>
9. Paidar, M., Sadeghi, F., Najafi, H., Khodabandeh, A. R., "Effect of Pin and Shoulder Geometry on Stir Zone and Mechanical Properties of Friction Stir Spot-Welded Aluminum Alloy 2024-T3 Sheets", *Journal of Engineering Materials and Technology*, Vol. 137, No. 031004, (2015), 1-6. DOI: 10.1115/1.4030197.
10. Badarinarayan, H., Yang, Q., Zhu, S., "Effect of tool geometry on static strength of friction stir spot-welded aluminum alloy", *International Journal of Machine Tools & Manufacture*, Vol. 49, (2009), 142-148. DOI: 10.1016/j.ijmactools.2009.06.001.
11. Enami, M., Farahani, M., Farhang, M. "Novel study on keyhole less friction stir spot welding of Al 2024 reinforced with alumina nanopowder.", *The International Journal of Advanced Manufacturing Technology*, Vol. 101, (2019), 3093-3106. DOI: 10.1007/s00170-018-3142-z
12. Klobear, D., Tu, J., Smolej, A., Simon, S., "Parametric study of FSSW of aluminium alloy 5754 using a pinless tool", *Weld World*, Vol. 59, (2015), 269-281. DOI: 10.1007/s40194-014-0208-x
13. Baek, S., Choi, D., Lee, C., Ahn, B., Yeon, Y., Song, K., Jung, S., "Microstructure and Mechanical Properties of Friction Stir Spot Welded Galvanized Steel", *Materials Transactions*, Vol. 51, No. 5, (2010), 1044-1050. DOI: 10.2320/matertrans.M2009337.
14. Baskoro, A.S., Hadisiswojo, S., Kiswanto, G., Winarto, Amat, M.A., Chen, Z.W. "Influence of welding parameters on macrostructural and thermomechanical properties in micro friction stir spot welded under high-speed tool rotation.", *The International Journal of Advanced Manufacturing Technology*, Vol. 106, (2020), 163-175. DOI:10.1007/s00170-018-3142-z.
15. Alheta, S., Zayan, S., Mahmoud, T., Gomaa, A., "Optimization of Friction Stir Spot Welding Process Parameters for AA6061-T4

- Aluminium Alloy Plates”, *American Scientific Research Journal for Engineering, Technology, and Sciences (ASRJETS)*, Vol. 20, (2016), 244-253.
16. Miles, M., Karki, U., Hovanski, Y., “Temperature and Material Flow Prediction in Friction-Stir Spot Welding of Advanced High-Strength Steel”, *JOM*, Vol. 66, No. 10, (2014), 2130-2136. DOI: 10.1007/s11837-014-1125-6
 17. D’Urso, G., “Thermo-mechanical characterization of friction stir spot welded AA6060 sheets: Experimental and FEM analysis”, *Journal of Manufacturing Processes*, Vol. 17, (2015), 108-119. DOI: 10.1016/j.jmapro.2014.08.004
 18. Chen, K., Liu, X., Ni, J., “Effects of Process Parameters on Friction Stir Spot Welding of Aluminum Alloy to Advanced High-Strength Steel”, *Journal of Manufacturing Science and Engineering*, Vol. 139, No. 8, (2017) 81016-1-9. DOI: 10.1115/1.4036225.
 19. Tiwan, Ilman, M.N., Kusmono, “Microstructure and mechanical properties of friction stir spot welded AA5052-H112 aluminum alloy”, *Heliyon*, Vol. 7, (2021), e06009. DOI: 10.1016/j.heliyon.2021.e06009
 20. Shekhawat, R.S., Nadakuduru, V.N., Nagumothu, K.B., “Microstructures and mechanical properties of friction stir spot welded Al 6061 alloy lap joint welded in air and water”, *Materials Today: Proceedings*, Vol. 41, (2021), 995-1000. DOI: 10.1016/j.matpr.2020.06.065.
 21. Ethiraj, N., Sivabalan, T., Sivakumar, B., Vignesh Amar, S., Vengadeswaran, N., Vetrivel, K., “Effect of Tool Rotational Speed on the *Tensile* and Microstructural Properties of Friction Stir Welded Different Grades of Stainless Steel Joints”, *International Journal of Engineering, Transactions A: Basics*, Vol. 33, No. 1, (2020), 141-147. DOI: 10.5829/ije.2020.33.01a.16
 22. Kim, J., Ahn, E., Das, H., Jeong, Y., Hong, S., Miles, M., Lee, K., “Effect of Tool Geometry and Process Parameters on Mechanical Properties of Friction Stir Spot Welded Dissimilar Aluminum Alloys”, *International Journal of Precision Engineering and Manufacturing*, Vol. 18, No. 3, (2017), 445-452. DOI: 10.1007/s12541-017-0053-0.
 23. Schmidt H., J. Hattel, J. Wert, “An analytical model for the heat generation in friction stir welding”, *Modelling and Simulation in Materials Science and Engineering*, Vol. 12, No. 1, (2004), 143-157. DOI: 10.1088/0965-0393/12/1/013
 24. Mijajlovic, M., Milcic, D., “Analytical Model for Estimating the Amount of Heat Generated During Friction Stir Welding: Application of plates Made of Aluminium Alloy 2024 T351”, *InTech, Welding Processes*, 247-274, (2012). DOI: 10.5772/53563
 25. Babu, S., Sankar, V. S., Ram, G. D. J., Venkitakrishnan, P. V., Reddy, G. M., Rao, K. P., “Microstructures and Mechanical Properties of Friction Stir Spot Welded Aluminum Alloy AA201”, *Journal of Materials Engineering and Performance*, Vol. 22, (2013), 71-84. DOI: 10.1007/s11665-012-0218-z
 26. Yang, Q., Mironov, S., Sato, Y. S., Okamoto, K., “Material flow during friction stir spot welding”, *Materials Science and Engineering A*, Vol. 527, No.16-17, (2010), 4389-4398. DOI: 10.1016/j.msea.2010.03.082
 27. Shen, Z., Yang, X., Zhang, Z., Cui, L., Yin, Y., “Mechanical properties and failure mechanisms of friction stir spot welds of AA 6061-T4 sheets”, *Materials and Design*, Vol. 49, (2013), 181-191. DOI: 10.1016/j.matdes.2013.01.066
 28. Mahmoud, T. S., Khalifa, T. A., “Microstructural and mechanical characteristics of aluminum alloy AA5754 friction stir spot welds”, *Journal of Materials Engineering and Performance*, Vol. 23, No. 3, (2014), 898-905. DOI: 10.1007/s11665-013-0828-0.
 29. Mishra, R.S., Ma, Z.Y., “Friction Stir Welding and Processing”, *Material Science and Engineering R: Reports*, Vol. 50, No. 1-2, (2005), 1-78. DOI: 10.1016/j.mser.2005.07.001
 30. Pathak, N., Bandyopadhyay, K., Sarangi, M., Panda, S. K., “Microstructure and Mechanical Performance of Friction Stir Spot-Welded Aluminum-5754 Sheets”, *Journal of Materials Engineering and Performance*, Vol. 22, No. 1, (2013), 131-144. DOI: 10.1007/s11665-012-0244-x
 31. Zhou, L., Luo, L. Y., Zhang, T. P., He, W. X., Huang, Y. X., Feng, J. C., “Effect of rotation speed on microstructure and mechanical properties of refill friction stir spot welded 6061-T6 aluminum alloy”, *International Journal of Advanced Manufacturing Technology*, Vol. 92, No. 9-12, (2017), 3425-3433. DOI: 10.1007/s00170-017-0359-1
 32. Li, Z., Gao, S., Ji, S., Yue, Y., Chai, P., “Effect of Rotational Speed on Microstructure and Mechanical Properties of Refill Friction Stir Spot Welded 2024 Al Alloy”, *Journal of Materials Engineering and Performance*, Vol. 25, No. 4, (2016), 1673-1682. DOI: 10.1007/s11665-016-1999-2
 33. Ji, S., Li, Z., “Microstructure and Mechanical Properties of Friction Stir Lap Welded Mg / Al Joint Assisted by Stationary Shoulder”, *Metals and Materials International*, Vol. 23, No. 6, (2017), 1158-1167. DOI: 10.1007/s12540-017-7065-2
 34. Chen, Y., Ding, H., Li, J., Zhao, J., Fu, M., Li, X., “Effect of welding heat input and post-welded heat treatment on hardness of stir zone for friction stir-welded 2024-T3 aluminum alloy”, *Transactions of Nonferrous Metals Society of China*, Vol. 25, No. 8, (2015), 2524-2532. DOI: 10.1016/S1003-6326(15)63871-7
 35. Sonne, M. R., Tutum, C. C., Hattel, J. H., Simar, A., De Meester, B., “The effect of hardening laws and thermal softening on modeling residual stresses in FSW of aluminum alloy 2024-T3”, *Journal of Materials Processing Technology*, Vol. 213, No. 3, (2013), 477-486. DOI: 10.1016/j.jmatprotec.2012.11.001
 36. Zhou, L., Zhang, R. X., Li, G. H., Zhou, W. L., Huang, Y. X., Song, X. G., “Effect of pin profile on microstructure and mechanical properties of friction stir spot welded Al-Cu dissimilar metals”, *Journal of Manufacturing Processes*, Vol. 36, No. 7, (2018), 1-9. DOI: 10.1016/j.jmapro.2018.09.017
 37. Mathers, Gene, “The welding of aluminium and its alloys,” First published, Woodhead Publishing Ltd and CRC Press LLC, (2002).

Persian Abstract

چکیده

در مطالعه حاضر، اثر هندسه پین و سرعت چرخش ابزار بر ریزساختار و مشخصات مکانیکی اتصال AA2024-O FSSW بررسی شد. از دو نوع هندسه پین متفاوت، یعنی پایه های استوانه ای و پله ای و سه سرعت چرخش متفاوت 1400، 900 و 1800 دور در دقیقه در اتصال جوشکاری نقطه اصطکاک استفاده شده است. مشاهده ریزساختار، اندازه گیری سختی و آزمایش برشی انجام شد. نتایج نشان می دهد که هندسه پین و سرعت چرخش تأثیر قابل توجهی بر ریزساختار و حداکثر بار برشی اتصالات جوش دارند. برای هر دو هندسه پین، با افزایش سرعت چرخش، ارتفاع و عرض قلاب منطقه کاملاً باند شده (FBR) افزایش می یابد. اتصال جوش توسط یک پین استوانه ای تولید می شود که مقادیر بیشتری از ارتفاع و عرض قلاب FBR نسبت به استفاده از پایه پله ای نشان می دهد. بعلاوه، بالاترین مقدار در حداکثر بار برشی با سرعت چرخش 1400 دور در دقیقه برای هر دو پایه استوانه ای و پله ای بدست می آید. یافته دیگر این است که حداکثر بارهای برشی اتصالات FSSW تولید شده با یک پین استوانه ای بیشتر از آن است که با استفاده از پین استپ ساخته شده است.



Comparative Experimental Study of Different Types of Fiber Reinforced Polymer Wrapping in Repairing of Reinforced Concrete Deep Beams with Circular Openings

S. Behzad Rahimi^a, A. Jalali^{*a,b}, S. Mohammad Mirhosseini^b, E. Zeighami^a

^a Department of Civil Engineering, Arak Branch, Islamic Azad University, Arak, Iran

^b Department of Civil Engineering, Faculty of Engineering, University of Kyrenia, Grine, Mersin 10, Turkey

PAPER INFO

Paper history:

Received 05 May 2021

Received in revised form 19 June 2021

Accepted 25 June 2021

Keywords:

Reinforced Concrete Deep beam

Retrofitting

Opening

Reinforced Concrete

Aramid Fiber Polymer

Glass Fiber Polymer

Carbon Fiber Polymer

Load-displacement

ABSTRACT

Openings of reinforced concrete (RC) deep beams can be used to pass electrical, mechanical, and architectural equipment. A comparative experimental study of fiber reinforced polymer (FRP) type on the performance of deep RC beams with the circular opening was the most important purpose of this study. The variables were FRP type (carbon, glass, and aramid) and the number of layers (1, 2, and 3). The geometric and rebar characteristics of the beams were considered constant in all cases. Deep RC beams were constructed, and their response to four-point loading was evaluated. Depending on the layers (1, 2 and, 3), aramid, carbon and glass fiber reinforced polymers (AFRP, CFRP, and GFRP) sheets increased the maximum load by about 65 to 94%, 87 to 130%, and 133 to 196%, respectively. In RC deep beams retrofitted with GFRP sheets, the sheet separation from the beam surface decreased with expanding the number of layers. The CFRP sheets debonded from the beam surface at the supports along the center of the circular opening. CFRP showed much better performance in energy absorption capacity and load capacity than AFRP and GFRP. The CFRP were debonded from the beam surface at the moment of rupture. However, no significant separation was observed in RC deep beams retrofitted with AFRP and GFRP sheets. SEM images of the cores specimens showed that the fracture surface of the specimens extracted from the beam retrofitted with GFRP and CFRP sheets was much rougher than the control specimen, which indicates a stronger bond between the concrete components.

doi: 10.5829/ije.2021.34.08b.17

1. INTRODUCTION

One of the topics that construction industry experts have considered in recent years is repairing existing structures that are still in operation after their lifetime. Errors in construction and execution, the weakness of old regulations, increasing the number of storys, and the impact of destructive environmental factors are among the reasons for the need for retrofitting computational errors [1-3].

On the other hand, many RC structures are damaged by cracking or excessive rising, caused by various factors such as earthquakes, excessive vibrations, corrosion of rebars, etc. One of the materials used in Europe since 1960 to strengthen or repair RC structures

is fiber reinforced polymer (FRP) installed on the concrete from the outside [4-6].

Extensive research has been conducted on retrofitting RC beams using FRP in the past decades [7-10]; most of which have been to achieve the maximum capacity of FRP and thus maximize the bearing capacity of existing beams.

In RC structures, deep beams are used as load-bearing beams and coupling shear walls of tall buildings. Openings must be designed in deep RC beams for electrical and computer network cables, mechanical installations, or commuting from room to room [11-14]. These openings interrupt the transfer of compressive forces from the place of application of the load to the abutment and cause it to collapse, and many cases requiring retrofitting [15-21]. Zhang et al. [22] investigated RC deep beams. Half of the beams were tested with an effective shear-depth ratio of 1.875 and

*Corresponding Author Email: Jalali.abdolrahim@kyrenia.edu.tr (A. Jalali)

the other half with 1.25. The beams were retrofitted with FRP sheets with different arrangements by the EBR method. Retrofitting with the FRP sheet increases the bearing capacity of the deep beam. The shear contribution of FRP sheets increases horizontally at a 45-degree angle [22]. Di Ludovico et al. [23] examined the effect of retrofitting prestressed beams by CFRP sheets. Retrofitting using CFRP sheets is structurally adequate and can play a significant role in recovering the capacity of damaged specimens [23]. Hussain and Pimanmas [24] investigated RC deep beams retrofitted using GFRP. With increasing the thickness of the GFRP, the shear strength would increase [24]. Chin et al. [25] studied various methods and issues related to retrofitting RC beams with the opening. It was stated that studies on retrofitting of beams around the opening are necessary [25]. Rahim et al. [26] examined the behavior of RC deep beams with CFRP. Their behavior was assessed using load-displacement curves. CFRP increases the capacity of the beams by about 10 to 40% [26]. Al-Bdari et al. [27] examined the performance of deep beams retrofitted with CFRP sheets. The CFRP sheets with vertical arrangement could increase the ultimate strength of the beam by about 20 to 32.6% [27]. Kumari and Nayak [28] evaluated the crack and maximum loads of the retrofitted deep beams using GFRP. The relationships were presented and compared with the relationships introduced in the regulations [28].

In our literature review, it has been pointed out that the openings diminish RC deep beams' bearing capacity [29-31]. Openings of RC deep beams can be used to pass electrical, mechanical, and architectural equipment. These openings can reduce the bearing capacity. Previous studies showed that carbon fiber reinforced polymer (CFRP) sheets could influence RC deep beams' ductility and bearing capacity. In this laboratory research, the impact of aramid and glass fiber reinforced polymer (AFRP and GFRP) sheets on the retrofitting of RC deep beams with the circular opening was investigated. Their response was compared with CFRP sheets. Another distinguishing feature of this study compared to other studies is that a comparative study of three different types of polymer sheets in retrofitting of RC deep beams with circular openings was conducted in this study. The results of this study can be used as validation of numerical analysis.

2. LABORATORY PROGRAM

2.1. Variables The RC deep beams with circular openings retrofitted with three types of FRP sheets were investigated. Aramid, glass, and carbon fiber reinforced polymers (AFRP, GFRP, and CFRP) sheets were used. The number of layers was considered 1, 2, and 3, respectively. Two beams with and without openings

were constructed as control beams to evaluate the variables' parameters. Table 1 summarized the investigated beams. An abbreviation was given to each of the beams. According to the variables, eleven RC deep beams were built.

2.2. Geometric Characteristics of Beams

Iranian national building code (part 9) [32] and the American concrete institute (ACI) [33] introduced deep beams as high-bending members. According to these regulations, the rules of flexural members with high height can be applied for beams that have the following conditions:

- Span to length ratio is less than four ($l \leq 4h$).
- It is possible to create pressure handles from the load side to the support. Deep beams are used as load-bearing beams that load from the top columns and transfer them to the supporting columns. These beams are placed in areas where removing several columns is necessary, such as parking entrances.
- In RC deep beams, openings are sometimes made to perform essential services such as air ducts, access to electrical and computer network cables, mechanical installations, or commuting from room to room. These openings interrupt the transfer of compressive forces from the place of application of the load to the abutment and cause it to become distorted, causing a severe reduction in the resistance of the beams.

The effective length was considered 320 mm. The beams' ratio of effective length to width is 2.13, and this value is less than 4. Therefore, beams are considered a deep type. The cover on the rebars was considered 40 mm. Steel plates were utilized to avoid the concentrating stress on top of the beams. The geometric characteristics of the beams and the arrangement of the steel reinforcement are shown in Figure 1.

TABLE 1. Introduction of variables

No.	Beam name	FRP type	Number of FRP layers
1	CB	Control beam without opening	-
2	CB-O	Control beam with opening	-
3	1AFRP	Aramid	1
4	2AFRP	Aramid	2
5	3AFRP	Aramid	3
6	1GFRP	Glass	1
7	2GFRP	Glass	2
8	3GFRP	Glass	3
9	1CFRP	Carbon	1
10	2CFRP	Carbon	2
11	3CFRP	Carbon	3

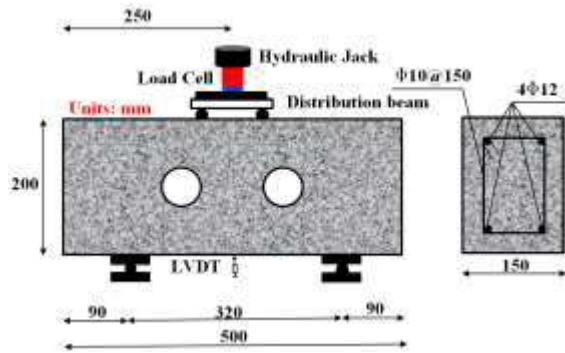


Figure 1. Geometric characteristics

The design of deep beams was done according to the ninth topic of the national building regulations of Iran. For this purpose, a six-story concrete building was first modeled and designed in Etabs software, and the details of the rebar and its geometric dimensions were extracted. Due to laboratory limitations, the beam was made on a 1:6 scale and subjected to four-point loading. The geometric properties of the beam and the characteristics of the rebars used in all cases were considered constant. The effect of FRP sheet type and number of layers on the response of deep beams with opening was considered as the most important objective of the research.

Four rebars with a diameter of 12 mm were used. Also, stirrups with a diameter of 10 mm were used with intervals of about 105 mm. There are two circular openings in the center of the beams. The distances between the two openings and their diameter were 150 mm and 60 mm, respectively.

2. 3. Materials

The materials used to make the main RC deep beams (without reinforcement) were sand, gravel, cement, water, and superplasticizer. Cement specifications are presented in Table 2. The aggregates used were fine river sand as filler and crushed gravel. The grading curve according to ASTM C33-87 [34]. The saturation density with the dry surface

of the gravel and sand is 2.62 and 2.54 g/cm³, respectively. The superplasticizer was obtained in each mixing design based on achieving acceptable performance and preventing the phenomenon of aggregate separation. A carboxylate-based superplasticizer (brand name WRM-TPP) was used. The slump, compressive and tensile strength were determined [35-37].

The amount of materials used to make the beams and the test results are presented in Table 2. RC deep beams and cylindrical and cubic specimens were poured together. Three samples were made for compressive and tensile strength tests, and their mean at 28 days of age was obtained. The beams vibrated adequately. Samples were cured in a water tank for 28 days.

Two rebars with diameters of 12 and 10 mm were used to make the RC beams (Table 4).

FRP sheets, with high resistance to corrosion (It can be easily used as a layer to protect reinforced concrete structures), have attracted many researchers' attention in recent years. Acceptable modulus of elasticity, high tensile strength, and corrosion resistance are among the characteristics of the FRP [38-40]. FRP is made using

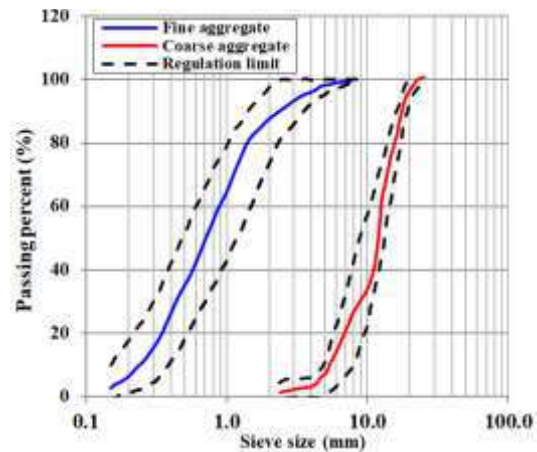


Figure 2. Coarse and fine aggregates grading curves

TABLE 2. Cement Specifications

Components	Cement type II
SiO ₂ %	21.27
Al ₂ O ₃ %	4.95
Fe ₂ O ₃ %	4.03
CaO %	62.95
MgO %	1.55
SO ₃ %	2.26
K ₂ O %	0.65
Na ₂ O %	0.49

TABLE 3. Mixture design and the test results

Cement (kg/m ³)	Water-Cement ratio	Sand (kg/m ³)	Gravel (kg/m ³)	Slump (mm)	Compressive strength (MPa)	Splitting tensile strength (MPa)
400	0.50	900	900	47	27.1	2.41

TABLE 4. Specifications of steel rebars

Rebar diameter (mm)	Yield stress (MPa)	Ultimate stress (MPa)
10	381	340
12	577	524

various fibers, the most famous of which are carbon, glass, and aramid fibers, together with a special epoxy resin adhesive. In this study, three types of sheets, AFRP, GFRP, and CFRP, were used to strengthen the beams (Table 5). The thicknesses of AFRP, GFRP, and CFRP sheets were considered 0.193, 1.3, and 11 mm, respectively.

The adhesive utilized to bond the FRP sheets was a two-part adhesive consisting of hardener and resin. According to the manufacturer's catalog, this adhesive's density and tensile strength are equal to 1.11 g/cm^3 and 76.1 MPa, respectively.

2. 4. Construction of the Beams Wooden molds were used to make the beam. The lower part of the molds was connected to the ground to prevent the molds from moving during vibration. The thickness of the wooden molds was considered 70 mm, and in addition to glue, special screws were used to connect the woods to each other. PVC pipes were used to create the circular opening of the beams. Figure 2 shows the steps for formatting and processing specimens. A mixing machine was used to mix the materials. The specimens were moisture treated at 20°C from molding to the moment of testing and kept in a water tank and a non-vibration environment. Figure 3 shows the steps of fabrication and curing of samples.

TABLE 5. Specifications of FRP sheets

FRP type	Ultimate strain (MPa)	Tensile strength (MPa)	Density (kg/m^3)
AFRP	0.026	1800	1250
GFRP	0.020	1800	2000
CFRP	0.015	2250	1900



Figure 3. Construction and curing of the beams a: Formwork and reinforcement b: Concreting c: Curing

2. 5. Installation of FRP Sheets First, the concrete surface of the RC deep beams was sanded to remove the weak surface with a Grinding Stone, and then a wire brush was pulled to clean the surfaces. Before applying the adhesive on the concrete surface, the concrete surface at the installation site and the surface of the FRP sheet were cleaned with a special solution. Then the two-component adhesive was mixed and spread by the spatula in the desired places, and then FRP sheets were placed on the adhesive and installed under a certain pressure. FRP sheets were cut to the desired size with scissors with fine teeth. FRPs were impregnated with an adhesive to install and execute the next layers, and the layering operation was started. FRP contains coatings that are removed after bonding to the surfaces, and the fibers attached to the surface are again impregnated with epoxy resin by a roller. The installation operation should be started from the middle part and continue to both ends to prevent bubbles. After smoothing the fiber surface by hand, a small hand roller should be pressed firmly onto the FRP surface. In all cases, the surfaces of the beams were painted, and the crack distribution could be observed. Figure 4 shows images of RC deep beams with circular openings before painting.

2. 6. Loading The beams were tested with simple two-end support conditions. The forces were applied to the specimens in four points by the hydraulic jack in specific locations (Figure 1). This method is one of the most common methods used in many studies [41-43] related to the study of bending and shear behavior of beams. In the studies that have used this method, no specific standard has been announced. It has been stated that this method is similar to the three-point load test (according to ASTM-C293) in some references. The only difference is the number of supports and the type of placement. Applying a load to more points causes the wider points of the beam to be stressed, and this method is usually used for more brittle materials such as concrete. The load-displacement values are extracted in this method. The loading continued at a constant speed with specific steps until the failure stage.

3. LABORATORY RESULTS

In this section, the results obtained from the experiments are presented, and the behavior of the beams is discussed.

3. 1. Laboratory Observations and Load-displacement Curves The load-deflection values of the control beams and the beams retrofitted with AFRP sheets are presented in Figure 6. The first crack of the control beam with openings (CB-O) was recorded

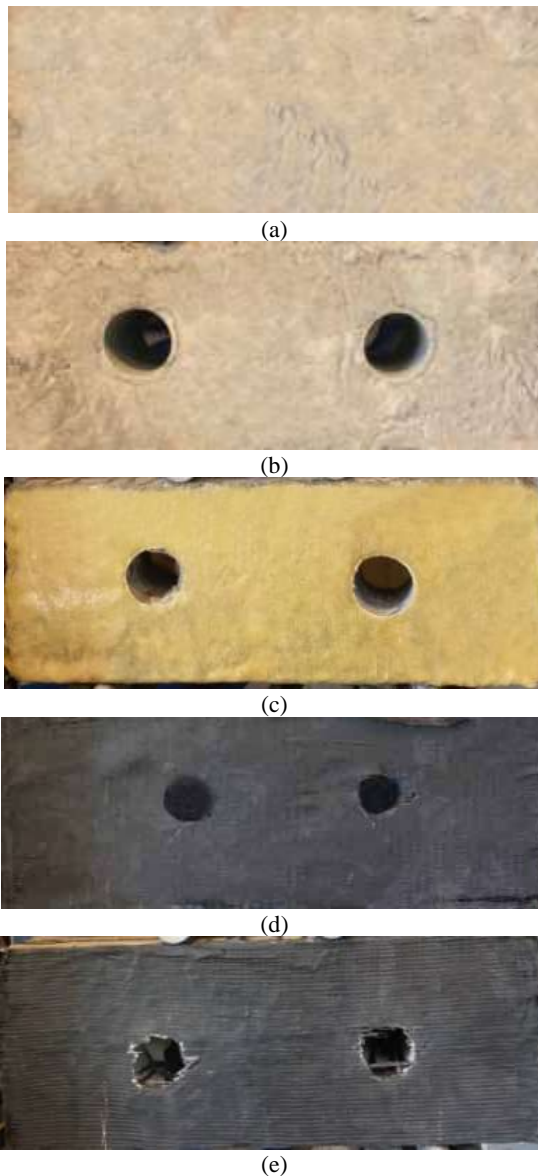


Figure 4. The investigated RC deep beams with circular openings a:CB b:CB-O c:AFRP d:GFRP e:CFRP



Figure 5. Loading device used

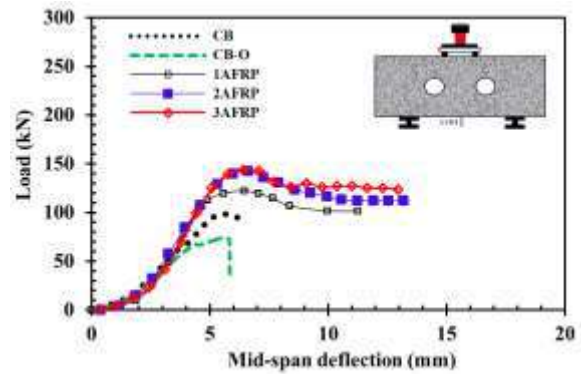


Figure 6. The results of four-point loading for the control beams and the beams retrofitted with AFRP

at 48 kN. These cracks were primarily observed in the loading area. With increasing load, shear-flexure cracks were watched within the lower regions of the beam. The yield load and yield deflection of the CB-O were 67 kN and 4.6 mm, respectively. As the load expanded, the cracks on the beam expanded and inevitably failed at a load equivalent to 74 kN. Figure 9 shows the deformable shape of the control beam after loading.

Adding a layer of AFRP sheet increases the maximum bearing capacity of the RC deep beam. The maximum load corresponding to 1AFRP, 2AFRP, and 3AFRP beams is 122, 143.1, and 143.2 kN, respectively. In retrofitted beams with AFRP sheets, many diagonal shear cracks occurred before flexural cracks. After hardening, the cracking patterns were similar, but the number and width of cracks by visual inspection were smaller. At the boundary of the AFRP material, no signs of debonding were observed at the boundary of the adhesive reinforced material in the attached AFRP sheet. For 1AFRP, 2AFRP, and 3AFRP beams, initial cracks of about 84, 124, and 126 kN were observed. Figure 9 shows the failure of beams retrofitted with AFRP sheets.

The load-deflection values of the controls and the beams retrofitted with GFRP sheets are presented in Figure 7. In beams using one, two, and three layers of GFRP, the primary flexural cracks were recorded at loads of about 98.3, 98.4, and 99.1 kN. In a beam using a layer of GFRP sheet, the cracks developed in shear. As the layers of GFRP increased, the width of the cracks decreased.

The maximum bearing capacity of RC deep beam with one, two, and three layers of GFRP sheets was 138, 164, and 170.5 kN, respectively. Images of 1GFRP, 2GFRP, and 3GFRP beams after failure are shown in Figure 9. Most of the cracks are flexural and were associated with rupture of GFRP sheets that adhered to deep beams in a U-shape. GFRP sheets as a reinforcing element in RC deep beams delayed the compression crushing, which increased the beam capacity and increased the beams' ductility.

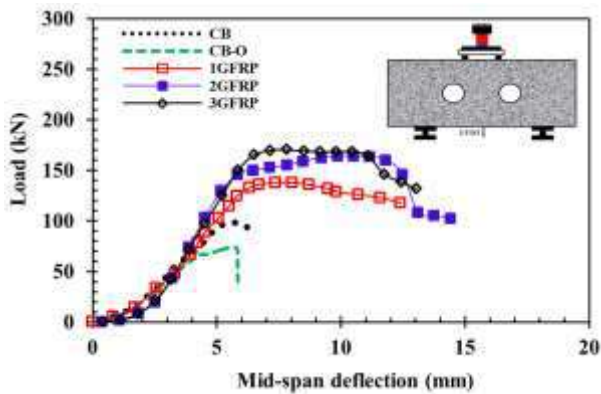


Figure 7. The results of four-point loading for the control beams and the beams retrofitted with GFRP

The load-deflection values of the control beam and the beams retrofitted with CFRP sheets are presented in Figure 8. In the 1CFRP beam, the first flexural crack occurred under a load of 98.3 kN, then the number of flexural cracks increased with continued loading. With increasing load, the number of cracks and the height of flexural and shear cracks increased until 172.5 kN load. The beam failed by separating the CFRP sheet from the concrete and crushing the concrete in the compressive zone between the two loads. After the formation of diagonal shear cracks, these cracks were restrained by CFRP sheets that are perpendicular to the crack and prevent the expansion of diagonal cracks and their increase in width. This prevented the premature shear failure of the beam and increased the bearing capacity of the RC deep with the opening.

After the start of the nonlinear part of the load-deflection curve, the RC deep Beams retrofitted with CFRP sheets showed more stiffness than beams retrofitted with GFRP and AFRP sheets. But with the sudden rupture of CFRP sheets, the ductility of these beams has been significantly reduced compared to the other two groups.

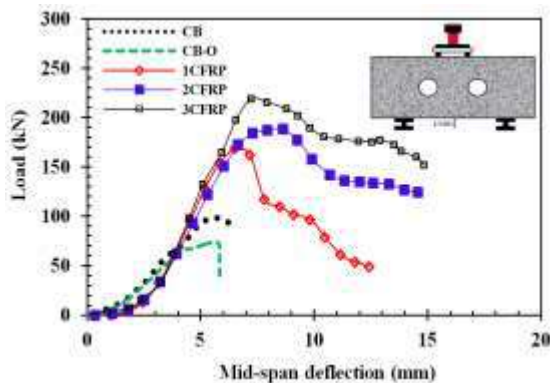


Figure 8. The results of four-point loading for the control beams and the beams retrofitted with CFRP



CB



CB-O



1AFRP



2AFRP



3AFRP



1GFRP

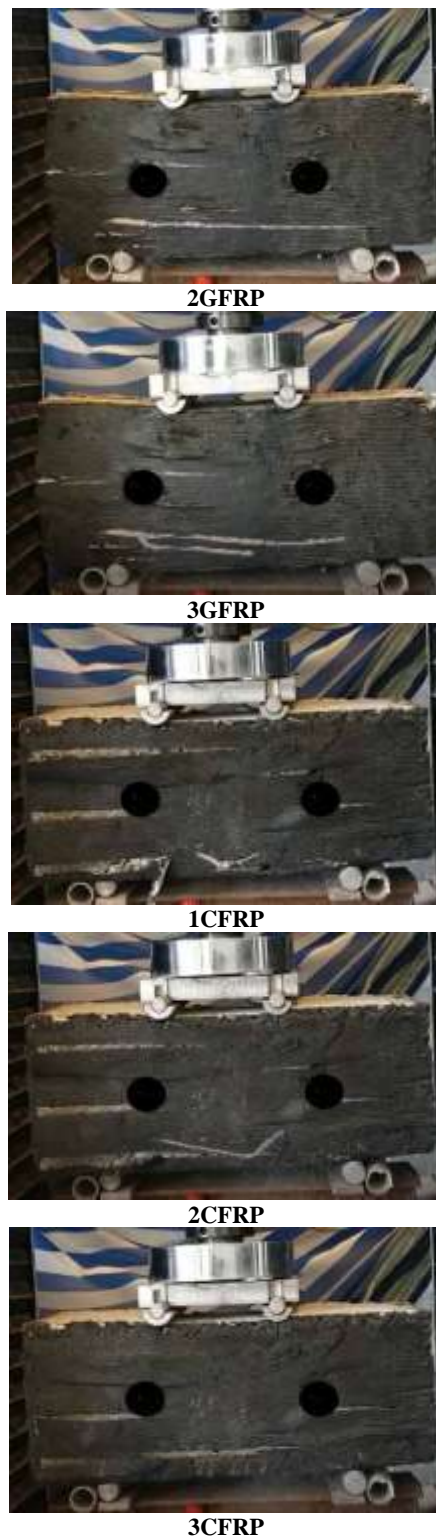


Figure 9. Crack distribution and deformable shapes

The load-deflection curves of the beams retrofitted with CFRP sheets have a relatively sharp drop compared to the beams retrofitted with AFRP and

GFRP sheets. The reason is the separation of the FRP sheet; before the maximum bearing capacity of FRP is used, the sheet is separated from the beam surface. The glue used was the same in all cases; AFRP and GFRP sheets have much better adhesion to the concrete surface.

Figure 9 shows the images of RC deep beams retrofitted after loading. In 2CFRP and 3CFRP RC deep beams, in which 2 and 3 layers of CFRP sheet were used for retrofitting, respectively, the first flexural cracks occurred under loads of 98.4 and 99.1 kN, then the number of flexural cracks increased with continued loading. As the load increased, the number of cracks and the height of the flexural and shear cracks increased until 188.2 and 219 kN loads, 2CFRP and 3CFRP beams failed when the concrete was crushed in the compressive zone between the two loads. The cracking loads of RC deep beams with 2 and 3 layers were significantly increased than the reference beam. As the number of layers increases, separation does not occur due to the greater involvement of the CFRP sheet with the concrete.

According to the load-deflection curves, CFRP sheets showed much better energy absorption capacity and flexural capacity than AFRP and GFRP sheets. But the important point here is that the CFRP sheets were detached from the beam surface at the moment of rupture. However, no significant separation was observed in deep beams reinforced with AFRP sheets.

In RC deep beams retrofitted with GFRP sheets, the sheet separation from the beam surface decreased with increasing layers. CFRP sheets detached from the beam surface at the lateral abutment and along the circular openings. The crack path expanded from the lateral abutment to the points of concentrated load application.

Table 5 summarizes the results of the four-point loading test. This table presents crack load, yield load, maximum load, crack displacement, yield displacement, ultimate displacement, ductility, and energy absorption capacity. In the following, each of these parameters is examined using various comparative diagrams.

3. 2. The Bearing Capacity of RC Deep Beams with Openings

The maximum load that each RC deep beam can withstand is called the bearing capacity of the beams. The comparative diagram of Figure 10 compares the bearing capacity of RC deep beams with openings. In this figure, the increased percentage in bearing capacity compared to the control beam is also presented. As can be seen in all cases, the addition of FRP sheets has increased the bearing capacity of RC deep beam beams compared to the control sample. The circular cavities created on the reinforced concrete deep beams have reduced the bearing capacity of the beam by about 24%.

TABLE 5. The test results

Name	Crack point		Yield point		P_{max} (kN)	Δ_U (mm)	Ductility	Energy absorption (N.mm)
	Δ_{cr} (mm)	P_{cr} (kN)	Δ_y (mm)	P_y (kN)				
CB	3.97	67	4.93	85	98	6.5	1.32	333
CB-O	3.3	48	4.60	67	74	5.52	1.2	234
1AFRP	3.95	84	4.61	107	122	11.3	2.45	894
2AFRP	5.1	124	5.76	139	143.1	13.20	2.31	1223
3AFRP	5.3	126	5.81	139	143.2	12.97	2.23	1836
1GFRP	4.49	97.1	5.82	125	138	12.4	2.13	1141
2GFRP	5.20	124	5.84	150	164	14.43	2.47	1887
3GFRP	5.22	125	5.86	151	170.5	13.03	2.22	1769
1CFRP	4.5	98.3	5.93	165	172.5	12.43	2.10	971
2CFRP	4.51	98.4	6.67	172	188.2	14.59	2.18	1609
3CFRP	4.58	99.1	6.56	198	219	14.90	2.27	1989

Δ_{cr} : Crack deflection, Δ_y : Yield deflection, Δ_u : Ultimate deflection
 P_{cr} : Crack load, P_y : Yield load, P_{max} : Maximum load

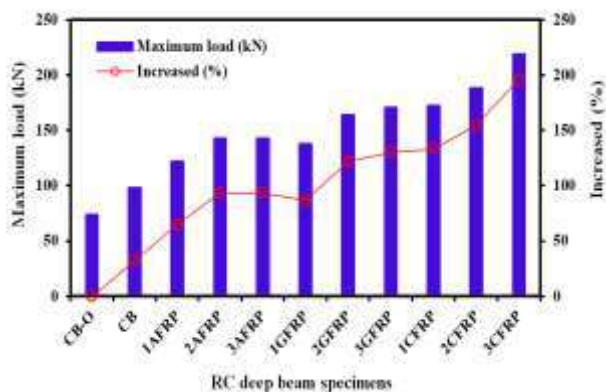


Figure 10. Comparison of bearing capacity and percentage increase

However, addition of AFRP, GFRP, and CFRP sheets to the deep beam with openings has increased the bearing capacity in most cases by 94, 130, and 196 percent, respectively, compared to the control beam with openings.

The addition of one, two, and three layers of AFRP sheet has improved the bearing capacity by 65%, 93%, and 94%, respectively. One, two, and three layers of the GFRP sheet have increased the bearing capacity by 87, 121, and 130%, respectively. One, two, and three layers of the CFRP sheet have increased the bearing capacity by 133, 154, and 196%, respectively. According to the changes, CFRP sheets in deep reinforced concrete beams in load-bearing capacity have a much better performance than AFRP and GFRP sheets.

3. 3. The Energy Absorption Energy absorption capacity is one of the parameters that can be used to evaluate the efficiency of the desired retrofitting method. This parameter is obtained using the area under the load-deflection curve [1-3, 44, 45]. Figure 11 compares the energy absorption of RC deep beams made in eleven different modes. As expected, FRP in RC deep beams with openings played an influential role. They increased the energy absorption capacity depending on the type and number of layers by 3.8 to 8.5 times. The highest energy absorption capacity was obtained in RC deep beams in which three layers of CFRP sheet were used. Although the beams retrofitted with one and two layers of GFRP sheets had less load-bearing capacity, their energy absorption capacity has increased compared to beams retrofitted with one and two layers of CFRP sheets. This is because GFRP sheets

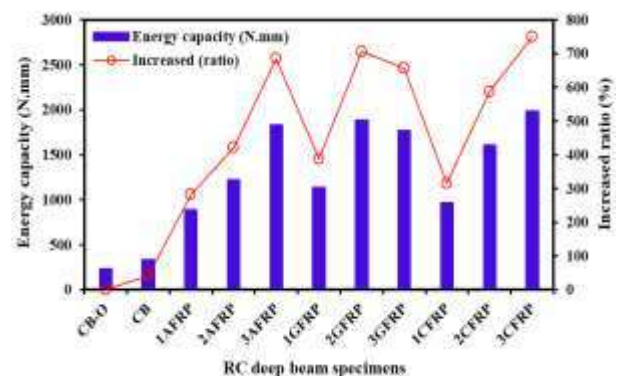


Figure 11. Comparison of energy absorption

had more adhesion than CFRP sheets and increased their energy absorption capacity. However, by increasing the number of sheets to three layers, the retrofitted beams with CFRP sheets performed better and showed more energy absorption capacity. The use of more layers in all cases has led to an increase in the energy absorption of RC deep beams with the opening.

For example, the energy absorption of three-layer retrofitted beams with CFRP, GFRP and AFRP is 17, 24, and 27% higher than single-layer retrofitted beams with CFRP, GFRP, and AFRP, respectively.

3. 4. Comparison of Deflection Ductility One of the most important considerations in addition to strength and serviceability in concrete beams is the issue of ductility. The important point is that the structure exhibits malleable behavior in a sudden damage close to the failure load. This means that the structure will not be damaged by a sudden brittle failure but will withstand large deformations near its maximum bearing capacity. Making large displacements near the maximum load will cause the residents to be informed before it breaks down, and as a result, the necessary safety will be achieved. The members' ductile behavior also provides the basis for the redistribution of bending moment and the design. In cases where design is required to load an earthquake, ductility is one of the most important parameters. The structure has sufficient ductility to absorb and dissipate seismic energy because the structure's performance against earthquake load is beneficial [46]. The ductility coefficient is obtained by dividing the ultimate deflection by the yield deflection of the beams. The ductility of the made beams is presented in Figure 12. This diagram also shows the bearing capacity (Maximum load).

The ductility of the retrofitted RC beams is about 1.75 to 2 times higher than the control sample, depending on the FRP type and layer numbers. AFRP sheets are much more ductile than CFRP and GFRP sheets. The ductilities of retrofitted beams with one, two, and three layers of AFRP sheet are 2.45, 2.31, and

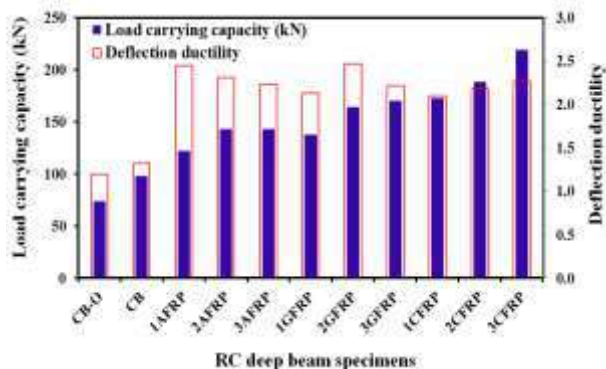
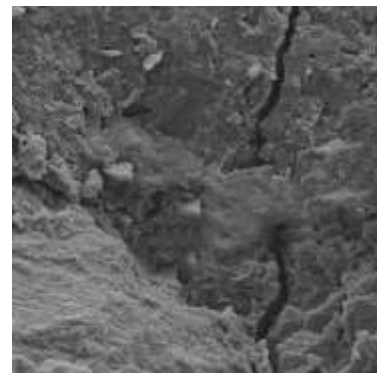


Figure 12. Comparison of deflection ductility

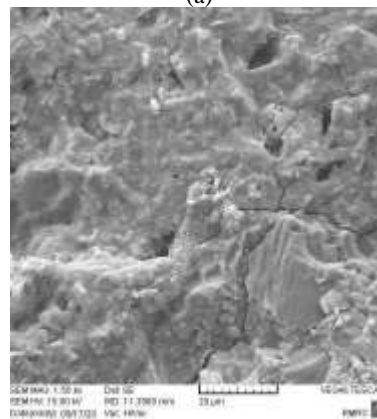
2.23, respectively. Meanwhile, the ductilities of RC deep beams retrofitted with one, two, and three layers of CFRP sheet are 2.1, 2.10, and 2.18, respectively. In the RC deep beams retrofitted with AFRP sheets, increasing the number of layers has reduced the ductility. However, in the RC deep beams retrofitted with CFRP sheets, increasing the number of layers has increased ductility. Also, in RC deep beams retrofitted with GFRP sheets, increasing the number of sheets first reduced the ductility and then increased it. Therefore, according to the changes made, it can be concluded that the type of FRP sheet has an impact on the ductility of RC deep beams with openings.

3. 5. Investigation of the Scanning Electron Microscope (SEM)

The microstructure of several specimens was evaluated using SEM images. This was done to investigate the specimens' general failure after four points loading and compare them with the state without retrofitting. For this purpose, cores were taken from the lower part of the loading area and within the openings of the control beam and retrofitted beams with three layers of AFRP, GFRP, and CFRP, and their SEM images were prepared. Figure 13 shows the SEM images of the mentioned specimens. After cracking, there was no factor to control and prevent crack growth



(a)



(b)

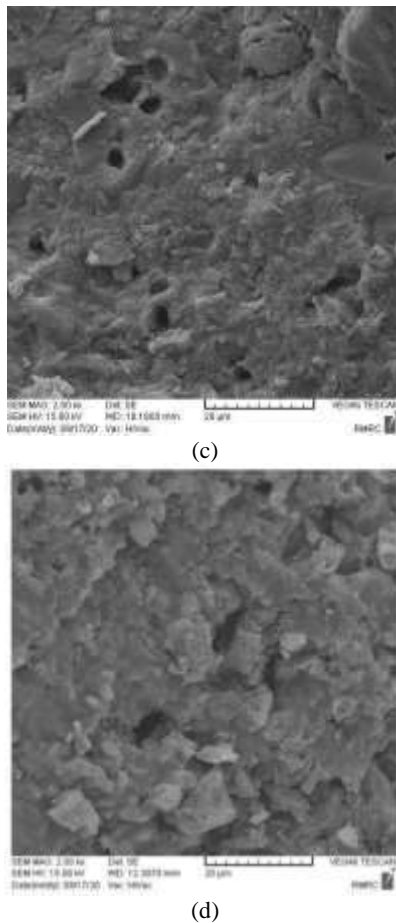


Figure 13. SEM images of core specimens of a number of investigated RC deep beams

in the control beam specimen. The crack in this specimen grew easily, and its width increased rapidly. Figure 13a shows that the concrete specimen has cracked and broken after withstanding the stress. The crack created in the sample is fully developed, and the width of the crack is considerable.

The core specimen of the 3AFRP beam cracked after withstanding its ultimate stress. The cracks due to stress in this specimen have a very small width and have not grown much. This sample has cracked after enduring its maximum stress. However, the crack created in this specimen has a much smaller width even than the control specimen, and its growth and development have been very low. More closely in these images, it can be seen that the fracture surface of the specimens extracted from the beam retrofitted with GFRP sheets is much rougher than the control sample, which indicates a stronger bond between the concrete components in the retrofitted beams with GFRP sheets. In the core specimen of the 3GFRP beam, after crack formation, the cracks did not grow much, and their width is much less than the control specimens. The use of CFRP sheets in

concrete beams significantly increases flexural strength and energy absorption. The CFRP sheets lead to the enclosure of the perimeter surfaces of the beam, which makes the internal structure of the concrete more compact and can have a higher load-bearing capacity.

4. CONCLUSION

In the present experimental study, retrofitting of deep beams with the opening was investigated using three types of sheets: AFRP, GFRP, and CFRP. For this purpose, the behavior of ten RC deep beams with openings against four-point loading was evaluated. A summary of the most important results is provided in this section.

- In retrofitted beams with AFRP sheets, many diagonal shear cracks occurred before flexural cracks. After hardening, the cracking patterns were similar, but the number and width of cracks by eye inspection were smaller.
- In retrofitted beams with CFRP sheets, diagonal shear cracks were restrained by CFRP sheets that are perpendicular to the crack, and the expansion of diagonal cracks and their increase in width was prevented.
- Beams retrofitted with CFRP sheets after the start of the nonlinear part of the load-deflection curve showed more stiffness than beams retrofitted with GFRP and AFRP sheets. But with the sudden rupture of CFRP sheets, the ductility of these beams has been significantly reduced compared to the other two groups.
- The crack loads of RC deep beams with 2 and 3 layers were significantly increased compared to the reference beam. As the number of layers increased, separation did not occur due to the greater involvement of the CFRP sheet with the concrete.
- According to the load-deflection curves, CFRP sheets showed much better load capacity than AFRP and GFRP sheets. But the important point here is that the CFRP sheets were detached from the beam surface at the moment of rupture. However, no significant separation was observed in deep retrofitted beams with AFRP sheets.
- The corresponding curves with four-point loading of CFRP retrofitted beams have a relatively sharp drop compared to beams retrofitted with AFRP and GFRP sheets. The reason is the separation of the FRP sheet; Before the maximum bearing capacity of FRP is used, the sheet is separated from the beam surface. The glue used was the same in all cases; AFRP and GFRP have much better efficiency in adhesion to the concrete surface.
- FRP sheets in RC deep beams with opening had an influential role and increased the bearing capacity by

3.8 to 8.5 times depending on the type and number of layers. The highest energy absorption capacity was obtained in deep reinforced concrete beams in which three layers of CFRP sheet were used. Beams retrofitted with one and two layers of GFRP sheet. Although they had more load-bearing capacity, their energy absorption capacity has increased compared to beams retrofitted with one and two layers of CFRP sheet. This is because GFRP sheets had more adhesion than CFRP sheets and increased their energy absorption.

- In RC deep beams retrofitted with GFRP sheets, the separation from the beam surface decreased with increasing the layers number. The CFRP sheets debonded from the beam surface at the lateral support and along with the circular opening. The crack path expanded from the lateral supports to the concentrated load points.
- By increasing the layers number, the retrofitted beams with CFRP sheets performed better and showed more energy absorption capacity. The bearing capacity of three-layer retrofitted beams with CFRP, GFRP and AFRP are 17, 24, and 27% higher than single-layer retrofitted beams with CFRP, GFRP, and AFRP, respectively.
- Adding all three types of FRP sheets used has increased the ductility of the beams. This increase is about 1.75 to 2 times higher than the control sample, depending on the FRP type and layer number.
- In the beams retrofitted with AFRP sheets, increasing the number of layers has reduced the ductility. However, in RC deep beams retrofitted with CFRP sheets, increasing the number of layers has increased ductility. Also, in RC deep beams retrofitted with GFRP sheets, increasing the number of sheets first reduced the ductility and then increased it. Therefore, according to the changes made, it can be concluded that the type of FRP sheet has an impact on the ductility of deep beams.

5. REFERENCES

1. Shadmand, M., Hedayatnasab, A., and Kohnehpooshi, O. "Retrofitting of reinforced concrete beams with steel fiber reinforced composite jackets" *International Journal of Engineering, Transactions B: Applications*, Vol. 33, No. 5, (2020), 770-783. DOI: 10.5829/IJE.2020.33.05B.08
2. Rahmani, I., Maleki, A., and Lotfollahi-Yaghin, MA. "A laboratory study on the flexural and shear behavior of RC beams retrofitted with steel fiber-reinforced self-compacting concrete jacket" *Iranian Journal of Science and Technology, Transactions of Civil Engineering*, (2020), 1-17. DOI: org/10.1007/s40996-020-00547-x
3. Faez, A., Sayari, A., and Manie, S. "Retrofitting of RC beams using reinforced self-compacting concrete jackets containing aluminum oxide nanoparticles" *International Journal of Engineering, Transactions B: Applications*, Vol. 34, No. 5, (2021). DOI: 10.5829/ije.2021.34.05b.13.
4. Kianoush, M., Esfahani, M. (2005). Axial Compressive Strength of Reinforced Concrete Columns Wrapped with Fiber Reinforced Polymers (FRP). *International Journal of Engineering, Transactions A: Basics*, Vol. 18, No. 1, (2005), 9-19.
5. Kim, TK., Park, JS., Kim, SH., and Jung, WT. "Structural behavior evaluation of reinforced concrete using the fiber-reinforced polymer strengthening method" *Polymers*, Vol. 13, No. 5, (2021), 780. DOI:10.3390/polym13050780
6. Fayyadh, MM. "Modified models to predict the ultimate flexural and shear capacities of CFRP repaired RC beams" (2021). DOI:10.12989/acd.2021.6.2.99
7. Maghsoudi, A., Rahgozar, R., and Hashemi, S. "Flexural testing of high strength reinforced concrete beams strengthened with CFRP sheets" *International Journal of Engineering, Transactions B: Applications*, Vol. 22, No. 2, (2009), 131-146.
8. Mahmoud, AS., and Ali, ZM. "Behaviour of reinforced GFRP bars concrete beams having strengthened splices using CFRP sheets" *Advances in Structural Engineering*, (2021), 13694332211001515. DOI: org/10.1177/13694332211001515
9. Zeng, Y., Li, X., Ali Ahmad, AH., and Wu, G. "Comparative study on the flexural strengthening of RC beams using EB CFRP bars, NSM CFRP bars, P-SWRs, and their combinations" *Advances in Structural Engineering*, Vol. 24, No. 5, (2021), 1009-1023. DOI: org/10.1177/1369433220971729
10. Dais, SJ., Silva, JR., and Barros, J. "Flexural and shear strengthening of reinforced concrete beams with a hybrid CFRP solution" *Composite Structures*, Vol. 256, (2021), 113004. DOI: org/10.1016/j.compstruct.2020.113004
11. Ghali, M., Said, M., Mustafa, TS., and El-Sayed, A. "Behaviour of T-shaped RC deep beams with openings under different loading conditions" *In Structures*, Vol. 31, (2021), 1106-1129. DOI: org/10.1016/j.istruc.2021.01.091
12. Arabzadeh, A., Hizaji, R. (2019). A Simple Approach to Predict the Shear Capacity and Failure Mode of Fix-ended Reinforced Concrete Deep Beams based on Experimental Study. *International Journal of Engineering, Transactions A: Basics*, Vol. 32, No. 4, 474-483. DOI: 10.5829/ije.2019.32.04a.03
13. Kumari, A., and Nayak, A. "Strengthening of shear deficient RC deep beams using GFRP sheets and mechanical anchors" *Canadian Journal of Civil Engineering*, Vol. 48, No. 1, (2021), 1-15. DOI:10.1139/cjce-2019-0333
14. Abdul-Razzaq, K., Jalil, A., and Dawood, A. "Reinforced concrete continuous deep beams under the effect of different parameters" *In AIP Conference Proceeding*, Vol. 2213, No.1, (2020), 020127. DOI: org/10.1063/5.0000055
15. Liu, J., and Mihaylov, B. "Shear strength of RC deep beams with web openings based on the two-parameters kinematic theory" *Structural Concrete*, Vol. 21, No. 1, (2020), 349-361. DOI: org/10.1002/suco.201800356
16. Jasim, WA., Tahnat, Y., and Halahla, A. "Behavior of reinforced concrete deep beam with web openings strengthened with (CFRP) sheet" *In Structures*, Vol. 26, (2020), 785-800. DOI: org/10.1016/j.istruc.2020.05.003
17. Khalaf, M., and Al-Ahmad, A. "Shear strength of reinforced concrete deep beams with large openings strengthened by external prestressed stands" *In Structures*, Vol. 28, (2020), 1060-1076. DOI: 10.1016/j.istruc.2020.09.052
18. Abdelaal, A., Askar, S., and E El-zoghiby, M. "Strength characteristics of lightweight reinforced concrete deep beams with web openings" *Engineering Research Journal*, Vol. 166, (2020), 262-283. DOI: 10.21608/erj.2020.138834

19. El Maaddawy, T., and Sherif, S., "FRP composites for shear strengthening of reinforced concrete deep beams openings" *Composite Structures*, Vol. 89, No.1, (2009), 60-69. DOI:10.1016/j.compstruct.2008.06.022
20. Abdul-Razzaq, K., Ali, H., and Abdul-Kareem, M. "A new strengthening technique for deep beam openings using steel plates" *International Journal of Applied Engineering Research*, Vol. 12, No. 24, (2017), 15935-15947.
21. Khalaf, M., and Al-Ahmad, A. "Shear strength of reinforced concrete deep beams with large openings strengthened by external prestressed strands" *In Structures*, Vol. 28, (2020), 1060-1076. DOI: org/10.1016/j.istruc.2020.09.052
22. Zhang, Z., Hsu, C., and Moren, J. "Shear strengthening of reinforced concrete deep beams using carbon fiber reinforced polymer laminates" *Journal of Composite for Construction ASCE*, Vol. 8, No. 5, (2004), 403-414. DOI:10.1061/(ASCE)1090-0268(2005)9:2(158)
23. Di Ludovico, M., Nanni, A., Protta, A., and Cosenza, E., (2005), "Repair of bridge girders with composites: experimental and analytical validation" *ACI Structural Journal*, V. 102, No. 5.
24. Hussain, Q., and Pimanmas, A. "Shear strengthening of RC deep beams with openings using sprayed glass fiber reinforced polymer composites (SGFRP): part 1: Experimental study" *KSCE Journal of Civil Engineering*, Vol. 19, No. 7, (2015), 2121-2133. DOI: org/10.1007/s12205-015-0243-1
25. Chin, SC., Shafiq, N., and Nuruddin, MF. "FRP as strengthening material for reinforced concrete beams with opening" *KSCE Journal of Civil Engineering*, Vol. 19, (2015), 213-219. DOI: org/10.1007/s12205-011-0162-8
26. Rahim, N., Mohammad, B., Al-Fakih, A., Wahab, M., Liew, M., Anwar, A., and Amran, Y. "Strengthening the structural behavior of web openings in RC deep beam using CFRP" *Materials*, Vol. 13, No. 12, (2020), 2804. DOI:10.3390/ma13122804
27. Al-Bdari, W., Al-Bayati, N., and Al-Shaarbaf, A. "Structural behavior of SCC continuous deep beam strengthening and retrofitting with carbon fiber reinforced polymer strips" *In IOP Conference Series: Materials Science and Engineering*, Vol. 737, No. 1, (2020), 012023. DOI: 10.1088/1757-899X/737/1/012023
28. Kumari, A., and Nayak, A., "Behaviour of RC deep beams, strengthened with externally bonded GFRP fabrics: an experimental study" *In Recent Development in Sustainable Infrastructure*, Vol. 75, (2021), 279-289. DOI: org/10.1007/978-981-15-4577-1_23
29. Arabzadeh, A., and Karimizadeh, H. "Experimental study of RC deep beams with opening and FRP composites installed by means of EBR and EBROG methods" *Construction and Building Materials*, Vol. 208, (2019), 780-791. DOI: doi.org/10.1016/j.conbuildmat.2019.03.055
30. Smarzewski, P. "Analysis of failure mechanisms in hybrid fiber-reinforced high-performance concrete deep beams with and without openings" *Materials*, Vol. 12, No. 1, (2019), 101. DOI: org/10.3390/ma12010101
31. Al-Shaarbaf, I., and Abdulridha, A. "Experimental and numerical investigation of high strength reinforced deep concrete beams with web openings under repeated loading" *Al-Nahrain Journal for Engineering Sciences*, Vol. 20, No. 2, (2017), 31-325.
32. MHUD "Iranian national building code (part 9)": Concrete structure design, Ministry of Housing and Urban Development, Tehran, Iran, (2009).
33. ACI Committee, Building Code Requirements for Structural Concrete and Commentary (ACI 318). Farmington Hills, MI: American Concrete Institute, (2014).
34. ASTM C33 / C33M-18, Standard Specification for Concrete Aggregates, ASTM International, West Conshohocken, PA, 2018.
35. ASTM C143 ASTM C143 / C143M-20, Standard Test Method for Slump of Hydraulic-Cement Concrete, ASTM International, West Conshohocken, PA, (2020).
36. ASTM Standard C39/C39M-18 "Standard test method for compressive strength of cylindrical concrete specimens", ASTM International West Conshohocken PA, (2018).
37. ASTM Standard C496/C496M-17 "Standard test method for splitting tensile strength of cylindrical concrete specimens", ASTM International West Conshohocken PA, (2017).
38. Abedini, M., Khlaghi, E., Mehrmashhadi, J., Mussa, M., Ansari, M., and Momeni, T. "Evaluation of concrete structures reinforced polymers bars: A review" *Journal of Asian Scientific Research*, Vol. 7, No. 5, (2017), 165. DOI:10.18488/journal.2.2017.75.165.175
39. Arpitha, G., and Yogesha, B. "An overview on mechanical property evaluation of natural fiber reinforced polymers" *Materials Today*, Vol. 4, No 2, (2017), 165. DOI: org/10.1016/j.matpr.2017.02.153
40. Alsubari, S., Zuhri, M., Sapuan, S., Ishak, M., Ilyas, R., and Asyraf, M. "Potential of natural fiber reinforced polymer composites in sandwich structures: a review on its mechanical properties" *Polymers*, Vol. 13, No. 3, (2021), 423. DOI: org/10.3390/polym13030423
41. Hassan, H. M., Arab, M. A. E. S., and Ismail el-kassas, A. (2019). "Behavior of high strength self compacted concrete deep beams with web openings". *Heliyon*, Vol. 5, No. 4, (2019), e01524. DOI: org/10.1016/j.heliyon.2019.e01524
42. Jumaat, M. Z., Shukri, A. A., Obaydullah, M., Huda, M., Hosen, M., & Hoque, N. "Strengthening of RC beams using externally bonded reinforcement combined with near-surface mounted technique". *Polymers*, Vol. 8, No. 7, (2016), 261. DOI: 10.3390/polym8070261.
43. Aykac, S., Kalkan, I., Aykac, B., Karahan, S., and Kayar, S. "Strengthening and repair of reinforced concrete beams using external steel plates". *Journal of Structural Engineering*, Vol. 139, No. 6, (2013), 929-939. DOI: 10.1061/(ASCE)ST.1943-541X.0000714.
44. Huang, L., Yan, B., Yan, L., Xu, Q., Tan, H., and Kasal, B. "Reinforced concrete beams strengthened with externally bonded natural flax FRP plates." *Composites Part B: Engineering*, Vol. 91, (2016), 569-578. DOI: org/10.1016/j.compositesb.2016.02.014
45. Imjai, T., Setkit, M., Garcia, R., & Figueiredo, F. P. (2020). "Strengthening of damaged low strength concrete beams using PTMS or NSM techniques." *Case Studies in Construction Materials*, Vol. 13, (2020), e00403. DOI: org/10.1016/j.cscm.2020.e00403.
46. Oudah, F., and El-Hacha, R. "A new ductility model of reinforced concrete beams strengthened using fiber reinforced polymer reinforcement." *Composites Part B: Engineering*, Vol. 43, No. 8, (2012), 3338-3347, DOI: org/10.1016/j.compositesb.2012.01.071

Persian Abstract

چکیده

حفرات ایجاد شده در تیرهای عمیق می‌تواند برای عبور تجهیزات برقی، مکانیکی و نیازهای معماری مورد استفاده قرار گیرد. این حفرات می‌توانند ظرفیت باربری تیرها را کاهش دهند. یکی از راه‌های تقویت چنین تیرهایی استفاده از ورق‌های FRP می‌باشد. در مطالعات گذشته گزارش شده است که ورق‌های پلیمری کربنی (CFRP) می‌تواند نقش تأثیرگذاری بر شکل پذیری و ظرفیت باربری تیرهای عمیق بتن مسلح داشته باشد. در مطالعه آزمایشگاهی حاضر تأثیر ورق‌های پلیمری آرامیدی (AFRP) و ورق‌های پلیمری شیشه‌ای (GFRP) در مقاوم سازی تیرهای عمیق بتن مسلح با بازشو مورد بررسی قرار گرفته و پاسخ آنها با کارایی ورق‌های CFRP مقایسه شده است. تعداد لایه‌های FRP ۱، ۲ و ۳ لایه در نظر گرفته شد. ابعاد هندسی، مشخصات فولادگذاری و مقاومت فشاری بتن در تمامی حالت‌ها ثابت فرض شد. افزودن ورق‌های CFRP، AFRP و GFRP بسته به تعداد ورق‌ها، ظرفیت باربری تیرها را به ترتیب ۶۵ تا ۹۴ درصد، ۸۷ تا ۱۳۰ درصد و ۹۶ تا ۱۳۳ درصد افزایش داد. منحنی‌های بار - جابجایی تیرهای مقاوم سازی شده با ورق‌های CFRP به دلیل جداشدگی زودتر، دارای افت بیشتری در مقایسه با تیرهای مقاوم سازی شده با ورق‌های AFRP و GFRP بودند. بطوریکه قبل از آن که از حداکثر ظرفیت باربری FRP استفاده شود، ورق از سطح تیر بتن مسلح عمیق جدا شد. بنابراین می‌توان نتیجه گرفت که ورق‌های AFRP و GFRP از جنبه چسبندگی با سطح بتن عملکرد بهتری دارند. همچنین تصاویر SEM از مغزه‌های تهیه شده از تیرها نشان داد که سطح شکست حاصل از نمونه‌های استخراج شده از تیر مقاوم سازی شده با ورق‌های GFRP و CFRP نسبت به نمونه شاهد بسیار زبرتر و خشن‌تر است که این امر نشان از پیوند قوی تر میان اجزای بتن در تیرهای مقاوم سازی شده با ورق‌های GFRP می‌باشد. در بتن تهیه شده از تیرهای مقاوم سازی شده با ورق‌های GFRP پس از تشکیل ترک، ترکها زیاد رشد نکرده و عرض آنها نسبت به نمونه شاهد بسیار کمتر است. افزودن ورق‌های CFRP به تیرهای عمیق بتن مسلح دارای بازشو منجر به محصور شدگی سطوح پیرامونی تیر می‌شود و این موضوع سبب می‌شود که ساختار داخلی بتن متراکم‌تر شود و بتواند ظرفیت باربری بیشتری داشته باشد.



A Neural Network Approach to Estimate Non-Newtonian Behavior of Nanofluid Phase Change Material Containing Mesoporous Silica Particles

S. Motahar*

Department of Mechanical Engineering, Shahreza Campus, University of Isfahan, Iran

PAPER INFO

Paper history:

Received 29 April 2021

Received in revised form 07 July 2021

Accepted 09 July 2021

Keywords:

Nanofluid

Non-Newtonian

Dynamic Viscosity

Rheological Properties

Artificial Neural Network

ABSTRACT

Neural networks are powerful tools for evaluating the thermophysical characteristics of nanofluids to reduce the cost and time of experiments. Dynamic viscosity is an important property in nanofluids that usually needs to be accurately computed in heat transfer and nanofluid flow problems. In this paper, the rheological properties of nanofluid phase change material containing mesoporous silica nanoparticles are predicted by the artificial neural networks (ANNs) method based on the experimental database reported in literature. Experimental inputs include nanoparticle mass fractions (0-5 wt.%), temperatures (35-55°C), shear rates (10-200 s⁻¹), targets include dynamic viscosities and shear stresses. A multilayer perceptron feedforward neural network with Levenberg-Marquardt back-propagation training algorithm is utilized to predict rheological properties. The optimal network architecture consists of 22 neurons in the hidden layer based on the minimum mean square error (MSE). The results showed that the developed ANN has an MSE of 6.67×10^{-4} and 6.55×10^{-3} for the training and test dataset, respectively. The predicted dynamic viscosity and shear stress also have the maximum relative error of 6.26 and 0.418%, respectively.

doi: 10.5829/ije.2021.34.08b.18

1. INTRODUCTION

Heat transfer enhancement techniques are widely used in many heating and cooling processes to improve the thermal performance of energy systems. With the development of nanotechnology, dispersing high conductive nanostructured materials in a transport medium such as conventional fluids has been considered as a promising method to enhance heat transfer [1]. The fabricated materials are usually called nanofluids which exhibit unique features especially in thermal conductivity and viscosity. Due to the unusual behavior of nanofluids, investigation of nanofluid flow and heat transfer [2] has always been challenging. Nanofluids can be used in many engineering applications including solar collectors [3], automotive [4], heat exchangers [5], and so on.

The rheological properties of nanofluids play an important role in the flow pressure drop inside the ducts, increasing the pumping power and the convective heat transfer [6]. To determine the rheological properties, the relationship between shear stress, shear rate and apparent

viscosity is investigated, the result of which determines the Newtonian or non-Newtonian behavior of the nanofluid. Various parameters such as temperature, nanoparticle concentration, nanoparticle size, type of base fluid, surfactant addition, shear stress and shear rate affect the rheological behavior of nanofluids. The viscosity of nanofluids and the effect of various parameters have been measured by many researchers and various models have been proposed for it, some of which are mentioned here. Experimental analysis of more than 30 nanofluids based on water, engine oil and ethylene glycol with the dispersion of Al₂O₃, TiO₂, ZrO₂, CuO, Fe₂O₃, Fe₃O₄, and nanodiamond nanoparticles was performed by Minakov et al. [7]. They investigated the effect of temperature, nanoparticle concentration, nanoparticle size and surfactant addition. The results indicated that the higher the viscosity of the base fluid, the higher the viscosity of the nanofluid. Adding more nanoparticles can also make the nanofluid behavior non-Newtonian. Garoosi [8] presented an experimental model based on a large number of laboratory data. In this model,

*Corresponding Author's Email: s.motahar@shr.ui.ac.ir (S. Motahar)

the viscosity of the nanofluids was investigated in terms of volume fraction, type and diameter of nanoparticles, temperature and thermophysical properties of the base fluid. This model gives more accurate output than conventional models such as Brinkman and Maxwell-Garnett models. Bardool et al. [9] developed a model for predicting the viscosity of nanofluids using friction theory and available equations of states. 711 experimental data were used in this study and the error of the developed model was less than 8.1%.

One of the most accurate methods for estimating the thermophysical characteristics of nanofluids is the use of artificial neural networks (ANNs). This method is a machine learning algorithm that has been utilized in thermal applications [10]. Ramezanizadeh et al. [11] have been recently reviewed machine learning methods used in modeling the viscosity of nanofluids. Toghraei et al. [12] experimentally studied the dynamic viscosity of Ag-EG nanofluid. The experiments were performed at the temperature of 25-55°C and a volume fraction of 0.2-2% which 42 experimental data were obtained. These data were used to estimate the dynamic viscosity of the nanofluid by ANN and correlation method. The accuracy of the ANN method compared to correlation was high and its MSE was equal to 0.0012 and the maximum error was 0.0858. Ahmadi et al. [13] evaluated the dynamic viscosity of SiO₂/EG-water nanofluid using the ANN intelligent method. In their study, 160 experimental data extracted from the literature were used. The developed ANN used Multilayer Perceptron (MLP) and Radial Basis Function (RBF) algorithms. Their results demonstrated that the MLP-RNB neural network accurately predicted the dynamic viscosity of the nanofluid and that the MSE and the correlation coefficient were obtained 5.5 and 0.998, respectively. Ali et al. [14] reported the viscosity of EG-water nanofluid and TiO₂ nanotubes in the temperature range of 25-65°C, mass fraction of 0-1% and shear stress of 150-500 s⁻¹. ANN and multivariable correlation methods were used to predict viscosity based on experimental data. The results showed that the ANN method has an accuracy of 0.1981 AAD% and 0.999 R² which is very accurate in comparison with the correlation method. Chen et al. [15] utilized 145 measured experimental data to evaluate the viscosity of MWCNTs-TiO₂/SAE50 hybrid nanofluids at different volume fractions, temperatures and shear rates using ANN. In their study, non-Newtonian nanofluid was considered, which follows the power-law model. They used another ANN to predict consistency index and power-law index using temperature and volume fraction. The neural networks used had a hidden layer and a *tansig* activation function whose number of neurons was obtained by trial and error. Hemmat-Esfe et al. [16] proposed an ANN model to compute the viscosity of MWCNT-Al₂O₃/5W50 hybrid nanofluid as a nano lubricant. 174 experimental data in the temperature range

of 5°C to 55°C and volume fraction of 0.05 to 1% were used as network inputs. The ANN network was MLP which its accuracy was measured by R² and MSE criteria. The results showed that temperature has a greater effect on nanofluid viscosity than other parameters. Ansari et al. [17] proposed a model for predicting the relative viscosity of nanofluids using a feedforward backpropagation network and using various algorithms including Levenberg-Marquardt (LM), Scaled Conjugate Gradient (SCG), Bayesian Regulation backpropagation (BR), and Resilient backpropagation (RP). They used 1620 laboratory data for network training. Shear rate, temperature, nanoparticle density, nanoparticle size, and volume fraction were considered as neural network inputs. The optimized ANN has a hidden layer consisting of 23 neurons and a *tansig* activation function that uses the LM algorithm. MSE and R² of this network were 0.00901 and 0.9954, respectively. The viscosity of Tungsten Oxide - MWCNTs/Engine Oil was measured at various temperatures, volume fraction and shear rates by Toghraie et al. [18]. They used an ANN model to predict the dynamic viscosity. The best accuracy was obtained by selecting 39 neurons in their proposed structure. For all data, MSE was 2.409 and MAE was 9.349.

A review of recent researches showed that many researchers have studied the rheological properties of different nanofluids using the ANN predictive method. In this study, the ANN method is used to predict the rheological properties of n-octadecane containing mesoporous SiO₂ nanofluid using 193 experimental measured data. This nanofluid can be considered as a nano-enhanced phase change material (nano-PCM) that can be used for thermal energy storage applications. To the best of our knowledge, no such study has been conducted so far for this material. Moreover, the power-law behavior of this phase change nanofluid is precisely estimated by ANN. An MLP neural network trained by the LM algorithm is used to predict the viscosity and shear stress. Temperature, mass fraction and shear rate are input parameters of the ANN. The ANN structure, i.e. the number of hidden layers and the neurons of each network layer, are optimized based on the minimum MSE and the maximum R. Due to the non-Newtonian behavior of nanofluids in some mass fractions, consistency index and power-law index at various temperatures and mass fractions are obtained according to the network results.

2. EXPERIMENTAL DATABASE

In the present paper, liquid n-octadecane (C₁₈H₃₈) with melting point of 27.5°C was utilized as the base fluid. Mesoporous SiO₂ particles with the average diameter of 280nm were dispersed into the n-octadecane to fabricate nanofluid samples. The nanoparticle mass fractions were.

1%, 3% and 5%. The rheological properties of nanofluids were measured in the temperatures range of 35-55°C and shear rates from 10 s⁻¹ to 200 s⁻¹. This includes 193 experimental data were previously reported by Motahar et al. [19]. In this study, these experimental data are used for designing an ANN. Figure 1 shows the viscosity of nanofluids at various mass fractions, temperatures and shear rates.

A fluid is Newtonian if the shear stress is proportional to shear rate, where the viscosity (μ) is the constant of proportionality:

$$\tau = \mu \dot{\gamma} \quad (1)$$

It was reported a non-Newtonian behavior for nanofluid samples with mass fractions of mesoporous SiO₂ greater than 3% [19], the liquid nanofluid can be considered as power-law liquid which is expressed as follows [19]:

$$\tau = K \dot{\gamma}^n \quad (2)$$

where K is the consistency index (in Pa·sⁿ), and the exponent n , is the power-law index. For $n=1$ and $K=\mu$, Equation (2) corresponds to Equation (1), and the fluid behaves Newtonian.

Figure 2 displays shear stress variations with shear rates at different temperatures and nanoparticle mass fractions. It is reported 193 experimental data in Figure 2.

3. ARTIFICIAL NEURAL NETWORKS APPROACH

Artificial neural networks (ANNs) are mathematical tools made by imitating the biological nervous system. The fundamental units of a nervous system are neurons. In solving engineering problems with several inputs, using one neuron is not enough and several neurons should be used. Several parallel neurons form a layer that

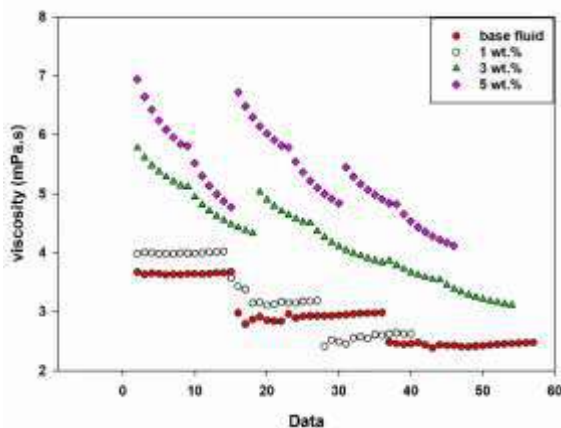


Figure 1. Experimental viscosity data

includes the weight matrix, the bias vector, the transfer function, and the output vector. An ANN consist of several layers. The layer whose output is the network output is called the output layer and the rest of the layers are called hidden layers. If the computing units are interconnected forward, the network is feedforward [20].

In this paper, a multilayer perceptron (MLP) is used, which is a common type of feedforward ANN. In general, MLP consists of a hidden layer and an output layer. This network operates very powerfully in regression applications [21].

The transfer function used for the hidden layer is the hyperbolic tangent function (*tansig*) ($f(m) = (e^m - e^{-m}) / (e^m + e^{-m})$) and the transfer function applied to the output layer is linear (*purline*) ($f(m) = m$) [20].

The LM backpropagation algorithm is utilized for solving non-linear least squares problems [22]. In multilayer neural networks, the back-propagation LM algorithm is used for network training. This algorithm has high accuracy and convergence speed in regression problems [23].

To design the structure of the ANN, the number of layers and the number of neurons in each layer are selected by trial and error. The amount of weights and biases is adjusted using the learning algorithm so that the MSE is minimal.

The value of MSE, the correlation coefficient (R) and mean relative error (MRE) used to evaluate the network performance are obtained from the following equations [24, 25]:

$$MSE = \frac{1}{N} \sum_{j=1}^N (\mu_j^{Exp} - \mu_j^{ANN})^2 \quad (3)$$

$$R = \frac{\sum_{j=1}^N (\mu_j^{Exp} - \bar{\mu}^{Exp})(\mu_j^{ANN} - \bar{\mu}^{ANN})}{\sqrt{\sum_{j=1}^N (\mu_j^{Exp} - \bar{\mu}^{Exp})^2 \sum_{j=1}^N (\mu_j^{ANN} - \bar{\mu}^{ANN})^2}} \quad (4)$$

$$MRE = \frac{100}{N} \sum_{j=1}^N \left| \frac{\mu_j^{Exp} - \mu_j^{ANN}}{\mu_j^{Exp}} \right| \quad (5)$$

where N is the number of experimental data, and the superscript *Exp* and *ANN* refer to the experimental measured data and the output predicted by ANN, respectively.

4. RESULTS AND DISCUSSIONS

In this work, 193 experimental measured data reported previously [19] are used to predict the rheological properties of n-octadecane/mesoporous SiO₂ nanofluid. These data include nanofluid temperature, mass fraction of nanoparticles and shear rate, which are considered as input parameters of the ANN. The output parameters of the network are viscosity and shear stress, which are used to obtain power-law indices. This data is randomly split

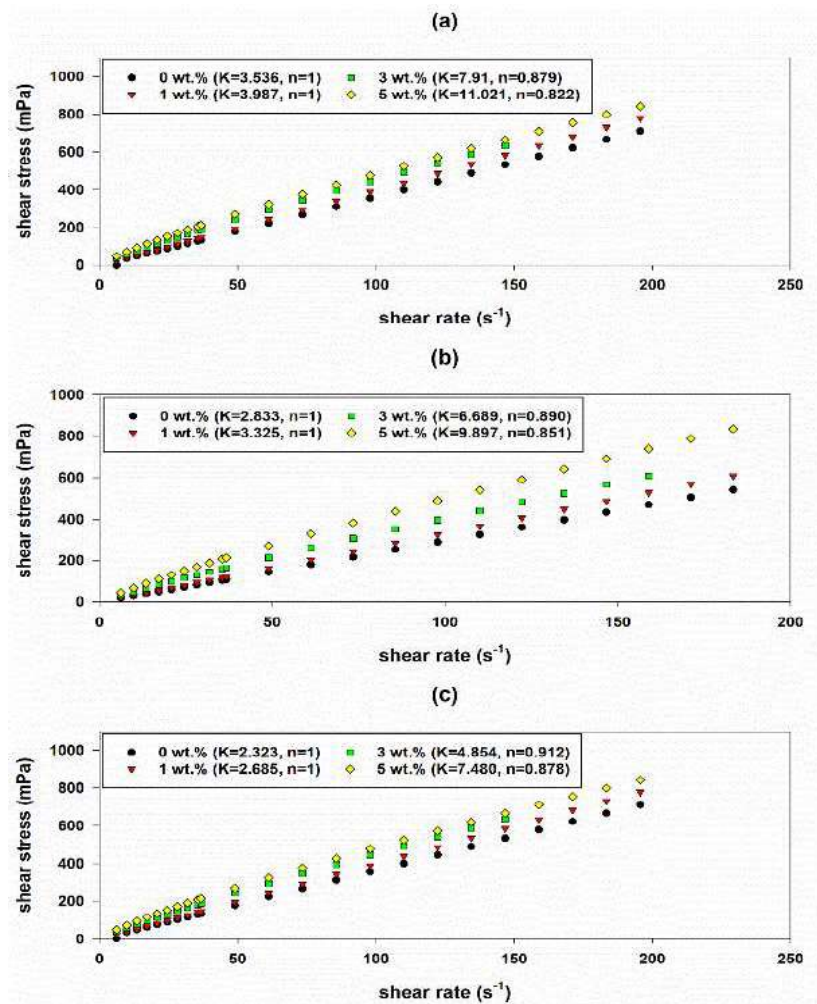


Figure 2. Experimental shear stress-shear rate diagrams (a) 35°C (b) 45°C (c) 55°C

into three categories: training, test, and validation. In the present study, 70% of the data (135 data) are used for training, 15% (29 data) for testing and 15% (29 data) for validation. The trial and error method is used to specify the optimal network structure.

A neural network with a hidden layer whose transfer function is a hyperbolic tangent (*tansig*) is considered. The number of hidden layer neurons varies from 2 to 30. The backpropagation LM algorithm is used to train the network. To increase network reliability and reproducibility, the training cycle is repeated 10 times for each neuron. Network error analysis is performed using MSE and R criteria. In an optimally structured network, the number of neurons in the hidden layer results in the lowest MSE and the highest R. Table 1 lists the MSE and R values of ANNs with various numbers of neurons in the hidden layer. As can be seen, when the number of neurons is equal to 22, the least MSE occurs which is bold in Table 1. For the optimal structure, the MSE of training, validation and test data are 6.67×10^{-4} , 4.90×10^{-3}

, and 6.55×10^{-3} , respectively. The correlation coefficient for all data is $R=0.99999$.

Figure 3 shows the optimal network structure. This optimal structure has 3 input parameters (temperature, mass fraction and shear rate). In the hidden layer, there are 22 neurons are delivered to the output layer by multiplying the weights and adding the biases with the input parameters and applying the *tansig* transfer function. There are two neurons in output layer that calculate the targets (dynamic viscosity and shear stress) by applying the *purline* function to its input signal.

Figure 4 shows the measured viscosity and the viscosity calculated by ANN in terms of data number. As can be seen, there is a great compromise between neural network results and experimental measurements. The maximum relative error value between the measured viscosity of n-octadecane/mesoporous SiO₂ nanofluid and the viscosity predicted by the proposed ANN is 6.26%.

Figure 5 compares the amount of laboratory shear stress with the shear stress calculated from the developed neural network. According to Figure 5, it is noted that a very small difference between the experimental values and the values predicted by the ANN can be found, so that the maximum relative error of 0.418% is obtained.

TABLE 1. MSE and R for various neurons numbers

No. of neurons	MSE		R	
	Train	Test	Train	Test
2	31.21446	50.86929	0.999599	0.999373
4	28.81507	47.33163	0.999622	0.999286
6	20.3478	43.0721	0.99974	0.999246
8	1.87313	8.29652	0.999974	0.999914
10	1.57532	2.66298	0.999979	0.999964
12	1.27434	1.82589	0.999982	0.999972
14	1.48E-02	2.14E-02	0.999735	0.999962
16	4.61E-03	1.10E-02	0.999987	0.999973
18	1.17E-02	6.26E-02	0.999992	0.999996
20	2.64E-03	4.10E-02	0.999999	0.999999
22	6.67E-04	6.55E-03	0.999999	0.999999
24	3.61E-03	2.45E-02	0.999998	0.999989
26	2.06E-02	2.27E-01	0.999999	0.999999
28	1.68E-02	1.51E-01	0.999894	0.999889
30	1.38E-01	1.50E+01	0.999998	0.999986



Figure 3. Optimal neural network structure

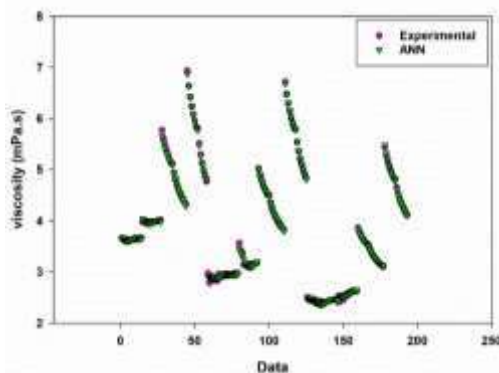


Figure 4. Comparison between experimental viscosity data and ANN results

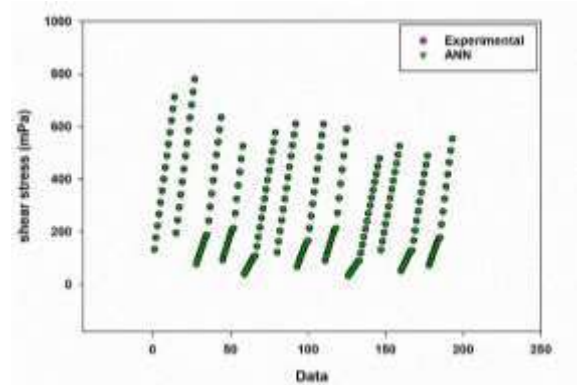


Figure 5. Experimental and ANN results of shear stress vs. number of data

Figure 6 depicts the measured viscosity values of n-octadecane/mesoporous SiO₂ nanofluids in terms of viscosity calculated by the neural network proposed in this study in a parity plot. This diagram compares the distribution of experimental values and modeling results. The line $y = x$ is plotted as a reference. Given the short distance between these points and the reference line, it can be concluded that ANN has made a satisfactory prediction. For all data, the MRE was 0.695 and $R=0.99999$.

Figure 7 shows the parity plot for comparing experimental shear stress and predicted shear stress by ANN. As evidenced, the points are completely on or near the reference line. The MRE of 0.0177 and $R = 0.99999$ are obtained for all shear stress data.

As can be seen from the results, the ANN method predicts the viscosity of nanofluid with high accuracy. A comparison between the results of nanofluid viscosity estimated by the ANN and other prediction methods is given in Table 2.

The rheological properties of n-octadecane/mesoporous SiO₂ nanofluids at different temperatures and mass fractions using shear stress calculated with ANN compared to experimental values are given in Table 3. According to the results, there is a

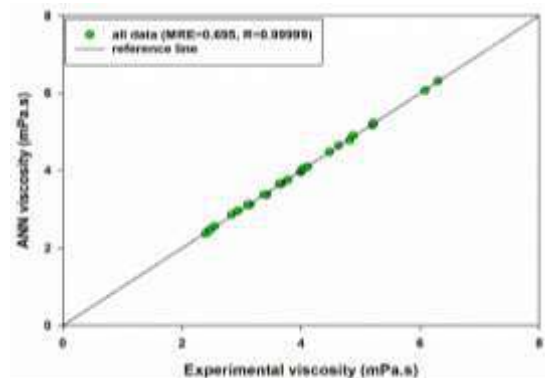


Figure 6. Experimental viscosity in comparison with ANN predicted viscosity

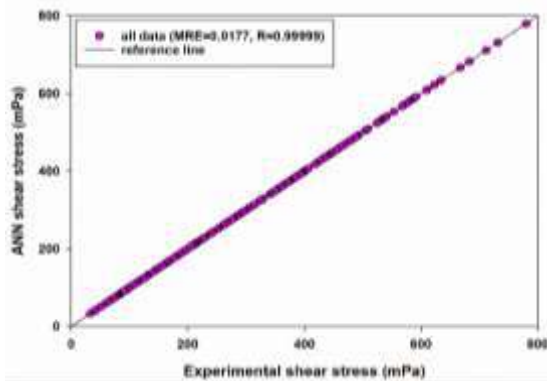


Figure 7. Experimental values shear stress in comparison with ANN shear stress

TABLE 2. Comparison between the ANN and other prediction methods for nanofluid viscosity

Ref.	Nanofluid	T (°C)	Particle loading	Method	Error
[12]	Ag/EG	25-55	0.2- 2 vol%	ANN	0.0314
				Correlation	0.0858
[15]	MWCNTs-TiO ₂ /SAE50	25-50	0.125-1 vol%	ANN	0
				Curve fitting	12.25%
[26]	MWCNT/paraffin	5- 65	0.005-5 wt.%	ANN	0.998 (R ²)
				RSM	0.988 (R ²)

TABLE 3. Rheological parameters predicted by ANN vs. experimental results

T (°C)	ϕ_m (%)	Experimental [19]		Predicted by ANN	
		K (mPa.s ^{n})	n	K (mPa.s ^{n})	n
35	0	3.536	1.000	3.636	1.000
	1	3.987	1.000	3.987	1.000
	3	7.91	0.879	7.937	0.878
	5	11.021	0.822	11.049	0.821
45	0	2.833	1.000	2.949	1.000
	1	3.325	1.000	3.325	1.000
	3	6.689	0.890	6.697	0.889
	5	9.897	0.851	9.882	0.851
55	0	2.323	1.000	2.446	1.000
	1	2.685	1.000	2.685	1.000
	3	4.854	0.912	4.854	0.910
	5	7.480	0.878	7.479	0.878

very good agreement between power-law index (n) and consistency index (K) coming from ANN method results

and experimental results. It is clear, the maximum relative error of consistency index (K) (or apparent viscosity) is 5.29%, which occurs at 55°C for the base fluid. For non-Newtonian nanofluids, the maximum relative error is 0.341%, which occurs for $\phi_m = 3\%$ and $T=35^\circ\text{C}$. Also, the maximum relative error for power-law index (n) is related to non-Newton nanofluid of $\phi_m = 3\%$ and $T=55^\circ\text{C}$ which is equal to 0.219%.

5. CONCLUSIONS

In this study, the rheological properties of n-octadecane/mesoporous SiO₂ nanofluids were predicted using experimental data and the ANN method. The proposed neural network is a feedforward MLP that uses the Levenberg-Marquardt backpropagation algorithm to predict targets. Network input parameters include temperature, mass fraction and shear rate, and network outputs are dynamic viscosity and shear stress. The optimal network architecture was obtained concerning the minimum MSE, which included one hidden layer, 22 neurons in the hidden layer, and a hyperbolic tangent transfer function. The MSE of training, validation and test data were 6.67×10^{-4} , 4.90×10^{-3} , and 6.55×10^{-3} , respectively. The correlation coefficient for all data was obtained as $R=0.9999$. The proposed ANN predicted dynamic viscosity and shear stress with the maximum relative error equal to 6.26% and 0.418%, respectively. Using the predicted shear stress, power-law index and consistency index were computed for non-Newtonian nanofluids, with a maximum relative error of 0.341% and 0.219%, respectively.

6. REFERENCES

- Adibi, T., Razavi, S.E., Adibi, O., "A Characteristic-based Numerical Simulation of Water-titanium Dioxide Nano-fluid in Closed Domains", *International Journal of Engineering, Transactions A: Basics*, Vol. 33, No. 1, (2020), 158-163. DOI: 10.5829/IJE.2020.33.01A.18
- Zhong, D., Zhong, H., Wen, T., "Investigation on the thermal properties, heat transfer and flow performance of a highly self-dispersion TiO₂ nanofluid in a multiport mini channel", *International Communications in Heat and Mass Transfer*, Vol. 117, (2020), 104783. DOI: 10.1016/j.icheatmasstransfer.2020.104783.
- Kundan, L., AJAY, K. "Performance Evaluation of Nanofluid (Al₂O₃/H₂O-C₂H₆O₂) Based Parabolic Solar Collector Using Both Experimental and CFD Techniques" *International Journal of Engineering, Transactions A: Basics*, Vol. 29, No.4, (2016), 572-580. doi: 10.5829/idosi.ije.2016.29.04a.17
- Akbarzade, S., Sedighi, K., Farhadi, M., ebrahimi, M. "Experimental Investigation of Force Convection Heat Transfer in a Car Radiator Filled with SiO₂-Water Nanofluid", *International Journal of Engineering, Transactions B: Applications*, Vol. 27, No.2, (2014), 333-340. doi: 10.5829/idosi.ije.2014.27.02b.17

5. Zamanian, M., "Factor Effect Estimation in the Convective Heat Transfer Coefficient Enhancement of Al₂O₃/EG Nanofluid in a Double-pipe Heat Exchanger", *International Journal of Engineering, Transactions B: Applications*, Vol.26, No.8, (2013), 837-844. doi: 10.5829/idosi.ije.2013.26.08b.05
6. Kheiri, M., Davarnejad, R. "Numerical Comparison of Turbulent Heat Transfer and Flow Characteristics of SiO₂/Water Nanofluid within Helically Corrugated Tubes and Plain Tube", *International Journal of Engineering, Transactions A: Basics*, Vol. 28, No. 10, (2015), 1408-1414. doi: 10.5829/idosi.ije.2015.28.10a.02
7. Minakov, A.V, Rudyak, V.Y., Pryazhnikov, M.I., "Systematic Experimental Study of the Viscosity of Nanofluids", *Heat Transfer Engineering*, (2020) DOI: 10.1080/01457632.2020.1766250.
8. Garoosi, F., "Presenting two new empirical models for calculating the effective dynamic viscosity and thermal conductivity of nanofluids", *Powder Technology*, Vol. 366, (2020), 788-820. DOI: 10.1016/j.powtec.2020.03.032.
9. Bardool, R., Bakhtyari, A., Esmailzadeh, F., Wang, X., "Nanofluid viscosity modeling based on the friction theory", *Journal of Molecular Liquids*, Vol. 286, (2019), 110923. DOI: 10.1016/j.molliq.2019.110923.
10. Motahar, S., Bagheri-Esfah, H., "Artificial neural network based assessment of grid-connected photovoltaic thermal systems in heating dominated regions of Iran", *Sustainable Energy Technologies and Assessments*, Vol. 39, (2020), 100694. DOI: 10.1016/j.seta.2020.100694.
11. Ramezanizadeh, M., Ahmadi, M.H., Nazari, M.A., Sadeghzadeh, M., Chen, L., "A review on the utilized machine learning approaches for modeling the dynamic viscosity of nanofluids", *Renewable and Sustainable Energy Reviews*, Vol.114, (2019), 109345. DOI: 10.1016/j.rser.2019.109345.
12. Toghraie, D., Sina, N., Adavoodi Jolfaei, N., Hajian, M., Afrand, M., "Designing an Artificial Neural Network (ANN) to predict the viscosity of Silver/Ethylene glycol nanofluid at different temperatures and volume fraction of nanoparticles", *Physica A: Statistical Mechanics and its Applications*, Vol.534, (2019), 122142. DOI: 10.1016/j.physa.2019.122142.
13. Ahmadi, M.H., Sadeghzadeh, M., Maddah, H., Solouk, A., Kumar, R., Chau, K.W., "Precise smart model for estimating dynamic viscosity of SiO₂/ethylene glycol-water nanofluid", *Engineering Applications of Computational Fluid Mechanics*, Vol. 13, No. 1, 1095-1105. DOI: 10.1080/19942060.2019.1668303
14. Ali, A., Ilyas S., Garg, S. et al. "Dynamic viscosity of Titania nanotubes dispersions in ethylene glycol/water-based nanofluids: Experimental evaluation and predictions from empirical correlation and artificial neural network". *International Communications in Heat and Mass Transfer*, Vol.118, (2020), 118:104882. DOI: 10.1016/j.icheatmasstransfer.2020.104882.
15. Chen, Z., Zarenezhad Ashkezari, A., Thili, I., "Applying artificial neural network and curve fitting method to predict the viscosity of SAE50/MWCNTs-TiO₂ hybrid nanolubricant", *Physica A: Statistical Mechanics and its Applications*, Vol.549, (2020), 123946. DOI: 10.1016/j.physa.2019.123946.
16. Hemmat Esfe, M., Reiszadeh, M., Esfandeh, S., Afrand, M., "Optimization of MWCNTs (10%)–Al₂O₃ (90%)/5W50 nanofluid viscosity using experimental data and artificial neural network", *Physica A: Statistical Mechanics and its Applications*, Vol.512, (2018), 731-744. DOI: 10.1016/j.physa.2018.07.040.
17. Ansari, H.R., Zarei, M.J., Sabbaghi, S., Keshavarz, P., "A new comprehensive model for relative viscosity of various nanofluids using feed-forward back-propagation MLP neural networks", *International Communications in Heat and Mass Transfer*, Vol. 91, (2018), 158-164. DOI: 10.1016/j.icheatmasstransfer.2017.12.012.
18. Toghraie, D., Aghahadi, M.H., Sina, N. et al. "Application of Artificial Neural Networks (ANNs) for Predicting the Viscosity of Tungsten Oxide (WO₃)-MWCNTs/Engine Oil Hybrid Nanofluid", *International Journal of Thermophysics*, Vol.41, No.163, (2020). DOI: 10.1007/s10765-020-02749-x.
19. Motahar, S., Nikkam, N., Alemrajabi, A., Khodabandeh, R., Toprak, M., Muhammed, M., "A novel phase change material containing mesoporous silica nanoparticles for thermal storage: A study on thermal conductivity and viscosity", *International Communications in Heat and Mass Transfer*, Vol.56, 114-120. DOI: 10.1016/j.icheatmasstransfer.2014.06.005.
20. Hagan, M.T., Demuth, H.B., Beale, M.H., De Jesús, O., *Neural Network Design*, 2nd Edition, 2014, available April 29 2021, <https://hagan.okstate.edu/NNDesign.pdf>
21. Motahar, S., Jahangiri, M., "Transient heat transfer analysis of a phase change material heat sink using experimental data and artificial neural network", *Applied Thermal Engineering*, Vol.167, (2020), 114817. DOI: 10.1016/j.applthermaleng.2019.114817.
22. Marquardt, D.W., "An algorithm for least-squares estimation of nonlinear parameters", *Journal of the Society for Industrial and Applied Mathematics*, Vol.11, (1963), 431-441. DOI: <https://doi.org/10.1137/0111030>
23. Oraon, M., Sharma, V. "Predicting Force in Single Point Incremental Forming by Using Artificial Neural Network", *International Journal of Engineering, Transactions A: Basics*, Vol.31, No.1, (2018), 88-95. doi: 10.5829/ije.2018.31.01a.13
24. Motahar, S., "Experimental study and ANN-based prediction of melting heat transfer in a uniform heat flux PCM enclosure", *Journal of Energy Storage*, Vol. 30, (2020), 101535. DOI: 10.1016/j.est.2020.101535.
25. Motahar, S., Sadri, S., "Applying artificial neural networks to predict the enhanced thermal conductivity of a phase change material with dispersed oxide nanoparticles", *International Journal of Energy Research*, (2021), 1-18. DOI: 10.1002/er.6785
26. Abu-Hamdeh, N.H., Golmohammadzadeh, A., Karimipour, A., "Performing regression-based methods on viscosity of nano-enhanced PCM-Using ANN and RSM", *Journal of Materials Research and Technology*, Vol. 10, (2021), 1184-1194, <https://doi.org/10.1016/j.jmrt.2020.12.040>

Persian Abstract

چکیده

شبکه های عصبی مصنوعی، ابزاری قدرتمند برای پیش بینی خواص ترموفیزیکی نانوسیالات و کاهش هزینه و زمان انجام آزمایش هستند. لزجت دینامیکی یک خاصیت مهم در نانوسیالات است که معمولاً نیاز به پیش بینی دقیق آن در مسائل انتقال حرارت و جریان نانوسیالات است. در این مقاله، خواص رئولوژیکی نانوسیال ان-اکتادکان حاوی نانوذرات مزوپروس سیلیکا به عنوان ماده تغییر فاز دهنده بر اساس داده های آزمایشگاهی موجود در مراجع، توسط یک شبکه عصبی پیش بینی شده است. داده های آزمایشگاهی ورودی شبکه شامل کسر جرمی در بازه صفر تا ۵٪، دماهای مختلف در بازه 35°C تا 55°C و نرخ کرنش برشی از ۱۳ تا ۱۹۶ بر ثانیه و خروجی شامل لزجت دینامیکی و تنش برشی است. گزارش شده است که رفتار نانوسیال با افزایش کسر جرمی به غیرنیوتنی میل می کند. یک شبکه عصبی پرسپترون چندلایه با الگوریتم آموزش لونیگ-مارکوات برای پیش بینی خواص رئولوژیکی نانوسیال بکار رفته است. بر اساس کمترین خطای میانگین مربعات، ساختار بهینه شبکه شامل ۲۲ نورون در لایه پنهان بدست می آید. نتایج نشان داد شبکه عصبی توسعه داده شده دارای خطای $0/00667$ و $0/00655$ برای داده های آموزش و آزمایش است. همچنین، لزجت دینامیکی و تنش برشی پیش بینی شده دارای بیشترین خطای نسبی به ترتیب برابر $6/26\%$ و $0/418\%$ است.



Price and Service Competition between Two Leader-follower Retailer-Stackelberg Supply Chains

S. Valizadeh, A. Mahmoodi*, I. NakhaiKamalabadi

Department of Industrial Engineering, University of Kurdistan, Sanandaj, Iran

PAPER INFO

Paper history:

Received 20 April 2021

Received in revised form 07 June 2021

Accepted 07 July 2021

Keywords:

Supply Chain

Price Competition

Service Competition

Stackelberg Game

ABSTRACT

In this paper, two leader-follower supply chains consisting of one manufacturer and one retailer are considered. In-chain competition is addressed besides the chain-to-chain competition in which the retailer is the leader and the manufacturer is the follower. The competition elements are price and service, which are investigated in three different scenarios: decentralized leader-decentralized follower, integrated leader-decentralized follower, and decentralized leader-integrated follower. Using the backward induction, we start the solving process from the follower supply chain and derive the follower's best response function. Then the leader strategies are examined after the substitution of the follower's best response function in leader profit function. Finally, we analyzed the effects of the price competition intensity and service investment coefficient of both chains on the equilibrium values in all three scenarios. The results show that increasing the price competition intensity will decrease the profit of the leading supply chain. In contrast, small values of price competition intensity are beneficial for the follower supply chain. Moreover, the service investment coefficient of both supply chains has a direct impact on follower optimal values and an inverse impact on the leader ones.

doi: 10.5829/ije.2021.34.08b.19

NOMENCLATURE

c_m	the unit production cost, which is assumed equal for both manufacturers	γ_s, γ_p	The intensity of competition between two retailers to the retailer's service and price, $\gamma_s, \gamma_p \geq 0$
α_i	the potential market demand for supply chain i	S_i	the service level of retailer i
p_i	the retail price of supply chain i	π^{ri}	The profit function of retailer i
w_i	the wholesale price of supply chain i	π^{mi}	The profit function of manufacturer i
η_i	the coefficient of service investment efficiency for retailer i .	π^{Ti}	Total profit of supply chain i
β_s, β_p	the sensitivity of retailer's market demand to the retailer's service and retailer's price, $\beta_s, \beta_p \geq 0$		

1. INTRODUCTION

Pricing is one of the critical components of the success of an organization and one of the most significant parts of business behaviors. Therefore, competing companies are involved in price competition to attract more customers and earn a fair market share. Along with the price, the

service level is also considered a crucial factor affecting customer purchasing decisions. In recent years, competition between supply chains has been considered not only on price but also on the service level. This is because services provided to the customers play an important role in attracting customers and the acquired share of the market.

* Corresponding Author Institutional Email: Anwar.mahmoodi@uok.ac.ir
(A. Mahmoodi)

In a competitive market, there are supply chains with different power structures. In most businesses, there is a chain that has more leadership power in the market because of its superior brand, position, or higher quality of products which has a competitive advantage to reach more customers. Such structures are modeled as a Stackelberg game, in which the chain with more power acts as a leader and the others as followers. In addition, unlike chain-to-chain competition in which two or more distinct supply chains compete with each other. There is the in-chain competition which is among the members of a supply chain.

There are some novelty and contributions which make this article different from other research. First, we examine an industry composed of two competing supply chains in which the retailers play a leading role in each chain. A case that has received less attention while being used in many retail industries. This paper is the first to examine both chain-to-chain and in-chain competitions over service and price between two leader-follower retailer-led supply chains. In addition to the leading retailers in both chains, a supply chain has more power in the market, and the competition is discussed from two perspectives of price and service level. Furthermore, the effect of integration or decentralization of each supply chain is investigated through different scenarios.

The remainder of the paper is organized as follows. In section 2, a brief description of the relevant literature is presented. Next, the model along with the assumptions and notations are provided in section 3. Section 4 is devoted to analyzing the model in which three different scenarios are addressed to examine the various structures of the model. Section 5 investigates the effect the main parameters on the equilibrium solutions in all three scenarios through numerical analysis. Eventually, in section 6, the study is concluded, and the main findings and some future research direction are described.

2. LITERATURE REVIEW

Price and service competition have attracted many researchers in recent decades. Most studies considered the price as the only factor of competition [1-4]. For example, Mahmoudi and Tofigh [5] considered five competitive firms using the game-theoretic approach in a dynamic competitive market. Amin-Naser and Azari-Khojasteh [6] examined two supply chains with risk-averse retailers and uncertain demand (one leader and one follower) competing on price. Mahmoudi [7] addressed the simultaneous pricing and replenishment policy in a duopoly environment with a unique Nash equilibrium. Sadjadi and Alirezaee [8] examined how different pricing strategies and cooperative advertising have influenced a two-echelon supply chain. Khanlarzade, Zegordi and Nakhai Kamalabadi [9] considered the price contest of two multi-echelon supply chains under two different

scenarios. In the first scenario, there was a Nash game between both supply chains, and in the second one, there was an imbalance power structure between supply chains. Lou et al. [10] assessed a supply chain consisting of two levels, including a manufacturer and a retailer. Finally, Widodo and Januardi [11] considered a dual-channel supply chain and obtained the Nash equilibrium solution. The above studies and the references therein show that price competition attracts much attention in the literature. However, none of the above papers considered the service as a factor of competition.

Another stream of relevant literature is one focused on service competition [12-16]. Jamshidi et al. [17] studied the impact of manufacturers and retailers' service level on customers' demand. They applied a game-theoretic approach in a supply chain consist of one manufacturer and a common retailer. Wu et al. [18] investigated optimal service decisions of two supply chains with a leading manufacturer under horizontal Stackelberg structure. In another study, Wu et al. [19] addressed the impact of competition on optimal decisions in a network of two supply chains. They applied the game theory deciding on green or non-green production under different competitive situations.

Several studies considered the competition from the perspective of both price and service level [20-23]. Xiao and Yang [24] studied an uncertain market that includes two supply chains competing on both the price and service level. At the same time, the manufacturer is risk-neutral, and the retailer is risk-averse. They found that when the retailers are more sensitive to risk, the optimal values equivalent to price and service level would be less. Chen et al. [25] investigated the problem of optimal price, service level, and quality decisions in a supply chain under different structures. Using the backward induction and a two-stage optimization game, they formulated the integrated and decentralized models.

Based on literature review, price and service competitions exist among researchers. In supply chain literature, vertical and horizontal competition between the industry members and the competition between supply chains is one of the growing areas in supply chain management. However, the leader-follower structure has received less attention from previous studies. Meanwhile, there has always been a supply chain with more leadership power in the actual competitive market that influences the decision of other supply chains.

Furthermore, in most studies, a manufacturer-Stackelberg structure is assumed, and none of the previous studies has addressed price and service competition for two leader-follower supply chains with the retailer-Stackelberg system. However, the retailer-Stackelberg system is widely used in retail industries like Walmart and Kmart. In this supply chains, retailer plays the leading role in determining the wholesale price of the manufacturer. Therefore, considering two competing

leader-follower supply chains, we examine the interaction between manufacturer and retailer in each chain and the competition between the supply chains. This paper covers the shortcomings in this area and extends the literature by formulating the leader-follower supply chains under the retailer-Stackelberg structure. Moreover, both price and service competition exists between market members.

The most related papers to our study are Amin-Naser and Azari-Khojasteh [6] and Xiao and Yang [24]. Amin-Naser and Azari-Khojasteh [6] investigated the price competition between two leader-follower supply chains. However, they did not consider the service competition, and they did not investigate the various centralization scenarios for the supply chains in their study. In contrast, we considered price and service competition in this paper and analyzed different centralization scenarios for the supply chains. On the other hand, Xiao and Yang [24] examined price and service competition. However, they did consider neither the leader-follower supply chains nor the retailer-led structure for the supply chains. However, we addressed price and service competition for two leader-follower supply chains with a retailer-led structure.

3. MODEL DESCRIPTION

We consider a market of two rival chains, where each of them contains a manufacturer (she) and a retailer (he) selling substitutable products to a common market. There is no cross-selling between the members of the supply chains, which means that each manufacturer offers her product only to the retailer in her supply chain, and at the same way, the retailer offers it to the end customers. The leader-follower relationship is considered not only among the supply chains but also between the members of a supply chain. We assume that Supply chain 1 has the role of leader and Supply chain 2 has the role of follower. In addition, the retailer is known as the leader and the manufacturer as the follower inside each supply chain. The decision variables of each retailer are the service level and the retail price, while the decision variable of each manufacturer is her wholesale price. Each agent aims to set his/her decision variable(s) to maximize his/her profit considering the strategy of the other agents. It is presumed that both chains have similar conditions in production cost and demand sensitivity to their price and service level. However, one of them has a bigger potential market size. These assumptions are rational because an incumbent may have a higher market share in a business environment compared to a new entrant.

The demand function of retailer i is a linear function of retail price and service level of both retailers as follows:

$$d_i = \alpha_i - \beta_p p_i + \gamma_p (p_j - p_i) + \beta_s s_i - \gamma_s (s_j - s_i) \quad (1)$$

Using $\beta'_s = \beta_s + \gamma_s$ and $\beta'_p = \beta_p + \gamma_p$, the demand function is better to be expressed as follows:

$$d_i = \alpha_i - \beta'_p p_i + \gamma_p p_j + \beta'_s s_i - \gamma_s s_j \quad (2)$$

This demand function is common in the literature; for example, Xiao and Yang [24], Tsay and Agrawal [20], and many other researchers have employed similar demand functions in their papers. Furthermore, as mentioned in the model of Xiao and Yang [24], the retailers in both chains will provide customers' services. Moreover, retailer i 's cost of providing service level s_i is $\frac{1}{2} \eta_i \cdot s_i^2$.

Therefore, the profit functions of the retailers and manufacturers could be written as follows:

$$\pi^{ri} = (p_i - w_i) (\alpha_i - \beta'_p p_i + \gamma_p p_j + \beta'_s s_i - \gamma_s s_j) - \frac{1}{2} \eta_i s_i^2; i=1,2; j=3-i \quad (3)$$

$$\pi^{mi} = (w_i - c_m) (\alpha_i - \beta'_p p_i + \gamma_p p_j + \beta'_s s_i - \gamma_s s_j) \quad (4)$$

$i=1,2; j=3-i$

The total profit of a supply chain will be

$$\pi^{Ti} = \pi^{mi} + \pi^{ri}; i=1,2; \quad (5)$$

The assumption that the retail price is bigger than the wholesale price in both chains can be defined by $p_i = w_i + v_i$. Therefore, after determining the wholesale price, the retailer could decide on his retail price by setting v_i .

In this study, the following three scenarios are analyzed.

Scenario 1: Both leader and follower supply chains are decentralized. Thus, each agent aims to maximize his/her profit, setting his/her decision variable(s) independently without any cooperation.

Scenario 2: The leading supply chain is integrated, and the follower is decentralized. The manufacturer and retailer of the leader chain cooperate and set their decision variables to maximize the total profit. However, the members of the follower supply chain do not cooperate and make their decisions independently.

Scenario 3: The follower supply chain is integrated while the leader is decentralized.

4. MODEL ANALYSIS

In this section, the equilibrium solution is provided for the scenarios mentioned above. Due to the leader-

follower relation of supply chains, each scenario is analyzed employing the concepts of the Stackelberg game in which the leader chooses his/her strategy, and then the follower determines his/her strategy given the leader's decision. Thus, the leader can predict the follower's next move. Effectively, the backward induction technique is employed to obtain the optimal values.

4. 1. Decentralized Leader-decentralized Follower

In the first scenario, the members of both leader and follower supply chains make their price and service level decisions independently. We use the backward induction technique based on which the solving process would be:

Stage 1: Considering the leader supply chain's decision variables as constant, we determine the decision variables of the follower supply chain in terms of the leader's variables. Furthermore, concerning the leader-follower relationship inside of the follower supply chain, the following sub-stages are used to determine its decision variables.

Sub Stage 1.1: The wholesale price of the follower chain's manufacturer is determined as a subordinate of the leader chain's decision variables and the follower chain's retailer decision variables.

Sub Stage 1.2: Considering the wholesale price of the follower chain's manufacturer, the retail price and service level of the follower chain's retailer are obtained as functions of the leader chain's decision variables.

Stage 2: Considering the equations obtained for the follower supply chain's decision variables as the response function, we determine the leader supply chain's decision variables. The following sub-stages are used to determine its decision variables regarding the leader-follower relationship within the leader supply chain.

Stage 2.1: The wholesale price of the leader chain's manufacturer is defined as a function of the leader chain's retailer decision variables.

Stage 2.2: Regarding the equations obtained as the best responses, the decision variables of the leader chain's retailer are determined;

Stage 3: Eventually, in a back-substitution process, all of the variables are determined.

Therefore, the solving process starts from the manufacturer of the follower chain whose profit function is

$$\pi^{m2} = (w_2 - c_m)(\alpha_2 - \beta'_p(w_2 + v_2) + \gamma_p p_1 + \beta'_s s_2 - \gamma_s s_1) \quad (6)$$

Since $\partial \pi^{m2} / \partial w_2 < 0$, the best response of Manufacturer 2 could be obtained from the first-order condition. Accordingly, we have

$$w_2 = \frac{1}{2}(c_m - v_2) + \frac{(\alpha_2 + \gamma_p p_1 + s_2 \beta'_s - \gamma_s s_1)}{2\beta'_p} \quad (7)$$

The profit function of Retailer 2 is:

$$\pi^{r2} = (p_2 - w_2)(\alpha_2 - p_2 \beta'_p + \gamma_p p_1 + \beta'_s s_2 - \gamma_s s_1) - \frac{1}{2} \eta_2 s_2^2 \quad (8)$$

Retailer 2 anticipates the best response of Manufacturer 2; therefore, his profit function is obtained by substitution of Equation (7) in Equation (8) as below.

$$\pi^{r2} = v_2 \left(\frac{\alpha_2 + \gamma_p p_1 + \beta'_s s_2 - \gamma_s s_1 - (c_m + v_2) \beta'_p}{2} \right) - \frac{1}{2} \eta_2 s_2^2 \quad (9)$$

LEMMA 1. In the first scenario, for given values of Chain 1's decision variables, the profit function of Retailer 2 is concave, if and only if, $0 \leq 1/\eta_2 \leq 4\beta'_p/\beta'_s$.

All proofs are presented in Appendix A.

We assume that the condition of Lemma 1 holds; therefore, the first-order condition of Equation (9) gives the equivalent values of v_2 and s_2 .

$$v_2 = 2\eta_2 (\alpha_2 + \gamma_p p_1 - \gamma_s s_1 - \beta'_p c_m) / (4\eta_2 \beta'_p - \beta'^2_s) \quad (10)$$

$$s_2 = \beta'_s (\alpha_2 + \gamma_p p_1 - \gamma_s s_1 - c_m \beta'_p) / (4\eta_2 \beta'_p - \beta'^2_s) \quad (11)$$

Based on leader-follower relation, Manufacturer 2 can anticipate the best response of Manufacturer 1 and Retailer 1. Therefore, the profit function of Manufacturer 1 is obtained by substitution of Equations (7), (10), and (11) in Equation (4).

$$\pi^{m1} = (w_1 - c_m) \left(\alpha_1 - (v_1 + w_1) \beta'_p + \gamma_p \left(\frac{(\alpha_2 + \gamma_p (v_1 + w_1) - \gamma_s s_1)}{2\beta'_p} + \left(\frac{\alpha_2 + \gamma_p (v_1 + w_1) - \gamma_s s_1 - \beta'_p c_m}{D} \right) R + \frac{1}{2} c_m \right) + \beta'_s s_1 - \gamma_s \left(\frac{\beta'_s}{D} (\alpha_2 + \gamma_p (v_1 + w_1) - \gamma_s s_1 - \beta'_p c_m) \right) \right) \quad (12)$$

where for simplification, we define the following notations;

$$D = 4\eta_2 \beta'_p - \beta'^2_s, A = \frac{\gamma_p^2}{2\beta'_p}, B = \frac{\gamma_s \gamma_p \beta'_s}{D}, E = \frac{\gamma_s \beta'_s}{D}$$

$$C = -\frac{\gamma_s \gamma_p}{2\beta'_p}, R = \eta_2 + \frac{\beta'^2_s}{2\beta'_p}, H = \beta'_p - A + B - R \frac{\gamma_p^2}{D}$$

It is easy to show that $\partial^2 \pi^{m1} / \partial w_1^2 \leq 0$, therefore, the best response of Manufacturer 1 is calculated by the first-order condition.

$$\frac{\partial \pi^{m1}}{\partial w_1} = 0 \Rightarrow w_1 = \frac{1}{2}(c_m - v_1) + \left(C + E\gamma_s + \beta'_s - \frac{RB}{\beta'_s} \right) s_1 / 2H + G \quad (13)$$

where

$$G = \left(\alpha_1 + \left(\frac{A}{\gamma_p} + R \frac{\gamma_p}{D} - E \right) \alpha_2 + \left(-R \left(\frac{\gamma_p \beta'_p}{D} \right) + \frac{\gamma_p}{2} + \frac{B\beta'_p}{\gamma_p} \right) c_m \right) / (2H)$$

Next, considering the best responses of Retailer 2 and Manufacturers 1 and 2, the profit function of Retailer 1 can be expressed as follows.

$$\pi^{r1} = (v_1) + \gamma_p \left(\begin{array}{l} \alpha_1 - \left(\frac{1}{2}(c_m + v_1) + Ks_1 + G \right) \beta'_p \\ \left(\frac{1}{2}c_m + \frac{\alpha_2 + \gamma_p \left(\frac{1}{2}(c_m + v_1) + Ks_1 + G \right) - \gamma_s s_1}{2\beta'_p} \right) \\ + \left(\frac{\alpha_2 + \gamma_p \left(\frac{1}{2}(c_m + v_1) + Ks_1 + G \right) - \gamma_s s_1 - \beta'_p c_m}{D} \right) R \\ + \beta'_s s_1 - \gamma_s \left(\frac{\beta'_s}{D} \left(\alpha_2 + \gamma_p \left(\frac{1}{2}(c_m + v_1) + Ks_1 + G \right) - \gamma_s s_1 - c_m \beta'_p \right) \right) \end{array} \right) - \frac{1}{2} \eta_1 s_1^2 \quad (14)$$

where $K = \left(C + E\gamma_s - \frac{RB}{\beta'_s} + \beta'_s \right) / 2H$.

LEMMA 2. In the first scenario, the profit function of Retailer1 is concave, if and only if,

$$0 \leq \frac{1}{\eta_1} \leq 4 \left(\beta'_p + B - A - \frac{R\gamma_p^2}{D} \right) / \left(C + E\gamma_s + \beta'_s - \frac{\gamma_p^2 R}{D} \right)^2$$

and $\frac{3\gamma_p}{\gamma_s \beta'_s + \beta'_p} \leq \frac{1}{\eta_2} \leq \frac{4\beta'_p}{\beta'^2_s}$

Regarding the conditions of Lemma 2 is correct, v_1 and s_1 could be obtained from the first-order conditions.

$$\frac{\partial \pi^{r1}}{\partial v_1} = 0 \text{ and } \frac{\partial \pi^{r1}}{\partial s_1} = 0 \Rightarrow$$

$$v_1^* = \left(G - \frac{c_m}{2} \right) \eta_1 / \eta_1 - K^2 H \quad (15)$$

$$s_1^* = \left(\frac{KH}{\eta_1} \right) \left(G - \frac{c_m}{2} \right) \eta_1 / \eta_1 - K^2 H \quad (16)$$

Now, all of the other decision variables could be obtained using the back-substitution process, which their equations are presented as follows.

$$w_1^* = \frac{1}{2}(c_m - O) + \frac{HK^2}{\eta_1} O + G \quad (17)$$

$$v_2^* = \frac{2\eta_2 X}{D} \quad (18)$$

$$s_2^* = \frac{\beta'_s X}{D} \quad (19)$$

$$w_2^* = c_m + \left(\frac{1}{2\beta'_p} + \frac{\beta'^2_s}{2D\beta'_p} - \frac{\eta_2}{D} \right) X \quad (20)$$

where in addition to the previous notations, we define the following notations to simplify the equations.

$$O = \frac{\left(G - \frac{c_m}{2} \right) \eta_1}{\eta_1 - K^2 H}, X = \alpha_2 + \gamma_p \left(\frac{1}{2}(c_m + O) + \frac{HK^2}{\eta_1} O + G \right) - \gamma_s \left(\left(\frac{KH}{\eta_1} \right) O \right) - \beta'_p c_m$$

4. 2. Integrated Leader-decentralized Follower

As stated in previous sections, the leader chain is integrated in the second scenario, which means that the manufacturer and retailer decide together on pricing and determine the service level based on profit maximization. However, the manufacturer and retailer act as two distinct agents in the follower chain to maximize their profit independently. Therefore, the decision variables in the leader supply chain are retail price and service level, while in the follower supply chain, they are wholesale price, retail price, and service level.

The solving sequence is the same as that of the first scenario, however, in stage 2, there are no sub-stages, and the leader chain decision variables are obtained in one step. Furthermore, the profit functions of the manufacturers and the retailers are similar to the functions expressed in the first scenario. Moreover, the total profit of the integrated chain is represented as below.

$$\pi^{r1} = (p_1 - c_m) (\alpha_1 - \beta'_p p_1 + \gamma_p p_2 + \beta'_s s_1 - \gamma_s s_2) - \frac{1}{2} \eta_1 s_1^2 = (w_1 + v_1 - c_m) (\alpha_1 - \beta'_p (w_1 + v_1) + \gamma_p (w_2 + v_2) + \beta'_s s_1 - \gamma_s s_2) - \frac{1}{2} \eta_1 s_1^2 \quad (21)$$

The follower chain's profit function is similar to the previous case; therefore, the best response of the follower chain is the same as the first scenario. As was discussed in the first scenario, the retail price and service level are as follows:

$$p_2 = \frac{1}{2}c_m + \frac{\alpha_2 + \gamma_p (w_1 + v_1) - \gamma_s s_1}{2\beta'_p} + \left(\frac{(\alpha_2 + \gamma_p (w_1 + v_1) - \gamma_s s_1 - \beta'_p c_m)}{D} \right) R \quad (22)$$

$$v_2 = \frac{2\eta_2 (\alpha_2 + \gamma_p p_1 - \gamma_s s_1 - \beta'_p c_m)}{D} \quad (23)$$

$$s_2 = \frac{\beta'_s (\alpha_2 + \gamma_p p_1 - \gamma_s s_1 - \beta'_p c_m)}{D} \quad (24)$$

$$w_2 = \frac{1}{2}(c_m - v_2) + \frac{\alpha_2 + \gamma_p p_1 + \beta'_s s_2 - \gamma_s s_1}{2\beta'_p} \quad (25)$$

Consequently, with substitution of the above best responses, the leader chain profit will be

$$\pi^{r1} = (v_1 + w_1 - c_m) \left(\begin{array}{l} \alpha_1 - \beta'_p (w_1 + v_1) \\ \left(\frac{1}{2}c_m + \frac{\alpha_2 + \gamma_p (w_1 + v_1) - \gamma_s s_1}{2\beta'_p} \right) \\ + \left(\frac{\alpha_2 + \gamma_p (w_1 + v_1) - \gamma_s s_1 - \beta'_p c_m}{D} \right) R \\ + \beta'_s s_1 - \gamma_s \left(\frac{\beta'_s (\alpha_2 + \gamma_p (w_1 + v_1) - \gamma_s s_1 - \beta'_p c_m)}{D} \right) \end{array} \right) - \frac{1}{2} \eta_1 s_1^2 \quad (26)$$

LEMMA 3. In the second scenario, the total profit function of the integrated chain is concave, if and only if,

$$0 \leq \frac{1}{\eta_1} \leq 2 \left(\beta'_p + B - A - \frac{\gamma_p^2 R}{D} \right) / \left(C + E\gamma_s + \beta'_s - \frac{BR}{\beta'_s} \right)^2 \quad \text{and}$$

$$\frac{3\gamma_p}{\gamma_s \beta'_s + \beta'_p} \leq \frac{1}{\eta_2} \leq \frac{4\beta'_p}{\beta_s'^2}$$

Assuming the conditions of Lemma 3 are held, the equilibrium equations for w_1 , v_1 and s_1 are obtained from the first-order conditions of Eq. (26). Then, the variables of Chain 2 are obtained using the back-substitution process. After all, the equilibrium equations in the second scenario are obtained as follows:

$$s_1^* = M \tag{27}$$

$$p_1^* = \frac{c_m}{2} + KM + G \tag{28}$$

$$v_2^* = \frac{2\eta_2 X'}{D} \tag{29}$$

$$s_2^* = \frac{\beta'_s X'}{D} \tag{30}$$

$$w_2^* = c_m - \frac{\eta_2 X'}{D} + \frac{X'}{2\beta'_p} \left(\frac{\beta_s'^2}{D} + 1 \right) \tag{31}$$

$$p_2^* = c_m + \frac{X'}{2\beta'_p} + \frac{X'R}{D} \tag{32}$$

where

$$M = \frac{2KH \left(-\frac{c_m}{2} + G \right)}{\eta_1 - 2K^2H} \quad \text{and}$$

$$X' = \alpha_2 + \gamma_p \left(\frac{c_m}{2} + K \left(\frac{2KH \left(-\frac{c_m}{2} + G \right)}{\eta_1 - 2K^2H} \right) + G \right) - \gamma_s \left(\frac{2KH \left(-\frac{c_m}{2} + G \right)}{\eta_1 - 2K^2H} \right) - \beta'_p c_m$$

4. 3. Decentralized Leader- Integrated Follower

In the third scenario, in contrast to the second scenario, the leader chain is decentralized, and the follower is integrated, which means that the retailer and manufacturer make their maximization decisions on price and service level cooperatively.

The solving sequence is similar to that of the first scenario; however, in stage 1, there are no sub-stages, and the follower chain decision variables are obtained in one step. Furthermore, the profit functions of the manufacturers and the retailers are similar to the functions expressed in the first scenario. Moreover, the total profit of the integrated follower chain is stated as:

$$\pi^{T2} = (p_2 - c_m - c_r) (\alpha_2 - \beta'_p p_2 + \gamma_p p_1 + \beta'_s s_2 - \gamma_s s_1) - \frac{1}{2} \eta_2 s_2^2 =$$

$$(w_2 + v_2 - c_m) (\alpha_2 - (w_2 + v_2) \beta'_p + \gamma_p p_1 + \beta'_s s_2 - \gamma_s s_1) - \frac{1}{2} \eta_2 s_2^2 \tag{33}$$

LEMMA 4. In the third scenario, for given values of Chain 1's decision variables, the total profit function of chain 2 is concave, if and only if $0 \leq \frac{1}{\eta_2} \leq \frac{2\beta'_p}{\beta_s'^2}$.

It is assumed that the condition of Lemma 4 is held; therefore, the best response of Chain 2 is obtained from the first-order condition:

$$\frac{\partial \pi^{T2}}{\partial v_2} = 0, \quad \frac{\partial \pi^{T2}}{\partial s_2} = 0, \quad \text{and} \quad \frac{\partial \pi^{T2}}{\partial w_2} = 0; \quad \text{which together gives}$$

$$s_2 = \frac{\beta'_s (\alpha_2 + \gamma_p p_1 - \gamma_s s_1 - \beta'_p c_m)}{2\eta_2 \beta'_p - \beta_s'^2} \tag{34}$$

$$p_2 = \frac{\beta'_s (\alpha_2 + \gamma_p p_1 - \gamma_s s_1 - \beta'_p c_m)}{2\beta'_p (2\eta_2 \beta'_p - \beta_s'^2)} + \frac{\alpha_2 + \gamma_p p_1 - \gamma_s s_1 + \beta'_p c_m}{2\beta'_p} \tag{35}$$

Manufacturer 2 could anticipate the above best responses; consequently, her profit function converts to

$$\pi^{m1} = (w_1 - c_m) + \gamma_p \left(\alpha_1 - \beta'_p (w_1 + v_1) + \frac{\beta_s'^2 (\alpha_2 + \gamma_p (w_1 + v_1) - \gamma_s s_1 - \beta'_p c_m)}{2\eta_2 \beta'_p - \beta_s'^2} + \frac{\alpha_2 + \gamma_p (w_1 + v_1) - \gamma_s s_1 + \beta'_p c_m}{2\beta'_p} + \beta'_s s_1 - \gamma_s \left(\frac{\beta'_s (\alpha_2 + \gamma_p (w_1 + v_1) - \gamma_s s_1 - \beta'_p c_m)}{2\eta_2 \beta'_p - \beta_s'^2} \right) \right) \tag{36}$$

Since $\frac{\partial^2 \pi^{m1}}{\partial w_1^2} < 0$, the best response of Manufacturer 1 is obtained from the first-order condition.

$$\frac{\partial \pi^{m1}}{\partial w_1} = 0 \Rightarrow w_1 = \frac{1}{2} (c_m - v_1) + \frac{(CQ + C + \beta'_s + \frac{I\gamma_s}{\gamma_p})}{2H} s_1 + G' \tag{37}$$

In which the following notations are used to simplify the presentation.

$$N = 2\beta'_p (2\eta_2 \beta'_p - \beta_s'^2), Q = \frac{\beta_s'^2}{2\eta_2 \beta'_p - \beta_s'^2}, I = \frac{\gamma_s \gamma_p \beta'_s}{2\eta_2 \beta'_p - \beta_s'^2},$$

$$H' = \beta'_p - AQ - A + I, G' = \left(\alpha_1 + \left(\frac{A}{\gamma_p} + \frac{AQ}{\gamma_p} - \frac{I}{\gamma_p} \right) \alpha_2 + \left(-\frac{\gamma_p Q}{2} + \frac{\gamma_p}{2} + \frac{I\beta'_p}{\gamma_p} \right) c_m \right) / 2H'$$

Furthermore, by substitution of the above best responses, the profit function of Retailer 1 would be:

$$\pi^1 = v_1 + \gamma_p \left(\begin{array}{l} \alpha_1 - \beta'_p \left(\frac{1}{2}(c_m + v_1) + N's_1 + G \right) \\ \left(\frac{\beta'_s \left(\alpha_2 + \gamma_p \left(\frac{1}{2}(c_m + v_1) + N's_1 + G \right) - \gamma_s s_1 - \beta'_p c_m \right)}{2\beta'_p (2\eta_2 \beta'_p - \beta'^2_s)} \right) \\ \left(\frac{\alpha_2 + \gamma_p \left(\frac{1}{2}(c_m + v_1) + N's_1 + G \right) - \gamma_s s_1 + \beta'_p c_m}{2\beta'_p} \right) \\ + \beta'_s s_1 - \gamma_s \left(\frac{\beta'_s \left(\alpha_2 + \gamma_p \left(\frac{1}{2}(c_m + v_1) + N's_1 + G \right) - \gamma_s s_1 - \beta'_p c_m \right)}{2\eta_2 \beta'_p - \beta'^2_s} \right) \end{array} \right) - \frac{1}{2} \eta_1 s_1^2 \quad (38)$$

where $N' = \left(CQ + C + \beta'_s + \frac{I\gamma_s}{\gamma_p} \right) / 2H'$

LEMMA 5. In the third scenario, the profit function of Retailer 1 is concave, if and only if, $0 \leq \frac{1}{\eta_2} \leq \frac{2\beta'^2_p - \gamma_p^2}{\beta'^2_s \beta'_p - \beta'_p \gamma_s \gamma_p}$ and $0 \leq \frac{1}{\eta_1} \leq \frac{1}{2H' N'^2}$.

Suppose that the conditions of Lemma 5 are held; the equilibrium equations are obtained by setting the gradient to zero.

$$\partial \pi^1 / \partial s_1 = 0 \text{ and } \partial \pi^1 / \partial v_1 = 0 \Rightarrow$$

$$s_1^* = N' H' M' / (\eta_1 - N'^2 H') \quad (39)$$

where to simplify the writing, we define the following abbreviation.

$$X'' = (\eta_1 - 4N'^2 H') c_m / (4(\eta_1 - N'^2 H')) + 3\eta_1 G' / (2(\eta_1 - N'^2 H')), \quad M' = G' - \frac{c_m}{2}$$

Eventually, using the back-substitution process, the equilibrium equation of other previous decision variables would be as follows.

$$v_1^* = M' \eta_1 / (\eta_1 - N'^2 H') \quad (40)$$

$$w_1^* = X'' + (2\eta_1 / (4(\eta_1 - N'^2 H'))) (c_m - 2G') \quad (41)$$

$$p_1^* = X'' \quad (42)$$

$$p_2^* = (Q + 1) \left(\left(\frac{\gamma_p}{2\beta'_p} \right) X'' - \frac{\gamma_s}{2\beta'_p} \left(\frac{N' H' M'}{\eta_1 - N'^2 H'} \right) \right) + \frac{Q(\alpha_2 - \beta'_p c_m) + \alpha_2}{2\beta'_p} + \frac{c_m}{2} \quad (43)$$

$$s_2^* = \frac{I}{\gamma_s} X'' - \frac{I}{\gamma_p} \left(\frac{N' H' M'}{\eta_1 - N'^2 H'} \right) + \frac{\beta'_s (\alpha_2 - \beta'_p c_m)}{2\eta_2 \beta'_p - \beta'^2_s} \quad (44)$$

5. NUMERICAL ANALYSIS

This section is devoted to numerically investigate the impact of main parameters on the equilibrium points and the profit of players. The base example is considered as follows.

$$\beta_p = 0.1, \gamma_p = 0.1, \beta_s = 0.1, \gamma_s = 0.1, \alpha_1 = 12, \alpha_2 = 10, c_m = 10, \eta_1 = \eta_2 = 0.3$$

We are interested in assessing the influence of price competition intensity and service investment efficiency on the optimal values. Therefore, we vary their related parameters in each scenario to explore their impacts and find some managerial insights.

5. 1. Effects of Price Competition Intensity

Since γ_p represents price competition intensity, the base example is analyzed for a various amount of γ_p , the results of which are reported in Table 1 for the first scenario. The analysis is done for second and third scenarios as well; however, their results are not reported due to the similarity. In all three scenarios, the market with more considerable price competition intensity has a smaller wholesale price, retail price, and service level in both supply chains. By increasing the intensity of competition, the retailers in all three scenarios try to decrease the retail price to attract more customers and gain more market share. In addition, the leader supply chain always has higher retail and wholesale prices than the follower supply chain.

Thus, for small values of γ_p , a part of market demand is attracted to the follower supply chain because of the lower retail price. Figure 1 shows the behavior of the supply chains and the industry's profits in terms of the price competition intensity. The profit functions of the follower chain's manufacturer and retailer are first increasing and then decreasing to the price competition intensity. Therefore, the total profit of the follower supply chain has similar behavior. Consequently, the existence of a low degree of price competition is better for the follower chain compared to having no competition. Furthermore, the increase of price competition intensity results in the decrease of leader chain's manufacturer and retailer profits and the total profit of the supply chain.

Amin-Naser and Azari-Khojasteh [6] observed that when the competition intensity increases, the total profit of the leading supply chain decreases, while the total profit of the follower supply chain increases. Their result is partially consistent with our result. That is, for the small values of competition intensity, the results are the same. However, for a higher value of competition intensity, we observe that the total profit of both supply chains is decreasing with competition intensity. The difference is due to the difference between the considered demand functions. Amin-Naser and Azari-Khojasteh [6] assumed

the classical version of the linear demand function. At the same time, we considered a modified version of the linear demand function, which draws the competition behavior better than the classical model.

5. 2. Effects of Service Investment Coefficient

To investigate the relationship between equilibrium solutions and the service investment coefficient of the leading supply chain, we change its quantity in the base example and report the results for the first scenario in Table 2 (the second and third scenarios are similar). As can be seen, increasing the service investment coefficient (decreasing the service investment efficiency) will decrease the leader chain’s service level.

Decreasing the service investment efficiency means that investing in the service levels does not positively influence the profit of the supply chain as it should. Thus, the leader supply chain decreases the service level, and therefore, the retail price will be decreased. On the other hand, the follower supply chain increases its service level results in gaining more customers. As a result, the retail price of the follower supply chain will be enhanced,

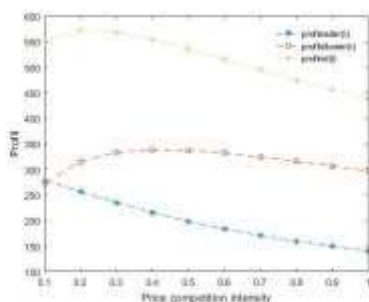
which directly impacts the chain’s whole profit. In addition, the profit functions of the follower chain’s manufacturer and retailer are increasing, and those of the leader chain are decreasing. Also, the industry’s total profit is decreasing because of the higher effect of the leading supply chain. The lower the service investment coefficient of one retailer, the lower the service level and retail price of his rival will be. This result is consistent with the result of Xiao and Yang [24], in which the authors considered two competing supply chains with manufacturer-Stackelberg structure.

5. 3. Comparison of Three Scenarios and Managerial Implications

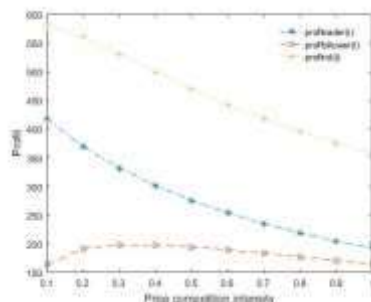
In all three scenarios, decentralization for both supply chains leads to having more retail prices in the leader and the follower supply chains. In the first scenario in which both chains are decentralized, the manufacturers and retailers try to increase their profit independently by increasing the retail price and wholesale price in both supply chains. In other words, centralization will decrease the retail price either in the follower or in the leading supply chain.

TABLE 1. Effect of varying γ_p in Scenario 1

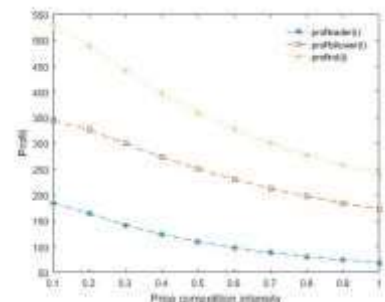
γ_p	p_1^*	s_1^*	p_2^*	s_2^*	w_1^*	w_2^*	π^{m1}	π^{r1}	π^{r1}	π^{m2}	π^{r2}	π^{r2}	$\pi^{r1} + \pi^{r2}$
0.1	84.57	13.67	77.90	15.09	34.85	32.63	101.95	175.86	277.81	102.46	170.78	273.25	551.06
0.2	74.13	10.68	68.38	12.97	31.37	29.46	91.41	165.68	257.10	113.62	201.99	315.61	572.72
0.3	66.88	9.04	61.46	11.43	28.96	27.15	82.52	152.76	235.28	117.70	215.79	333.50	568.79
0.4	61.24	7.93	56.13	10.25	27.08	25.37	75.02	140.61	215.63	118.22	220.69	338.92	554.55
0.5	56.66	7.09	51.85	9.30	25.55	23.95	68.68	129.82	198.51	116.80	220.62	337.42	535.93
0.6	52.86	6.42	48.33	8.51	24.28	22.77	63.29	120.38	183.67	114.30	217.72	332.03	515.71
0.7	49.64	5.88	45.37	7.86	23.31	21.79	58.65	112.11	170.77	111.25	213.23	324.48	495.25
0.8	46.88	5.43	42.85	7.30	22.29	20.95	54.64	104.85	159.50	107.92	207.85	315.77	475.28
0.9	44.48	5.05	40.66	6.81	21.49	20.22	51.13	98.44	149.57	104.50	201.04	306.55	456.13
1	42.37	4.72	38.76	6.39	20.79	19.58	48.04	92.74	140.79	101.10	196.07	297.17	437.96



Scenario 1



Scenario 2



Scenario 3

Figure 1. Profit versus the price competition intensity

TABLE 2. Effect of varying η_1 in Scenario 1

η_1	η_2	P_1^*	P_2^*	S_2^*	W_1^*	W_2^*	π^{m1}	π^{r1}	π^{f1}	π^{m2}	π^{r2}	π^{f2}	$\pi^{f1} + \pi^{f2}$	
0.1	0.3	119.47	60.22	72.66	13.92	46.49	30.88	219.73	258.18	477.91	87.27	145.46	232.73	710.65
0.2	0.3	91.03	22.28	76.93	14.87	37.01	32.31	120.37	191.09	311.47	99.56	165.94	265.50	576.98
0.3	0.3	84.57	13.67	77.90	15.09	34.85	32.63	101.95	175.86	277.81	102.46	170.78	273.25	551.06
0.4	0.3	81.71	9.86	78.33	15.18	33.90	32.77	94.28	169.12	263.41	103.76	172.94	276.71	540.12
0.5	0.3	80.10	7.71	78.57	15.23	33.36	32.85	90.09	165.32	255.41	104.50	174.17	278.67	534.09
0.6	0.3	79.06	6.33	78.73	15.27	33.02	32.91	87.45	162.88	250.33	104.97	174.96	279.93	530.27
0.7	0.3	78.34	5.37	78.83	15.29	32.78	32.94	85.63	161.18	246.81	105.30	175.51	280.11	527.63
0.8	0.3	77.81	4.66	78.91	15.31	32.60	32.97	84.31	159.93	244.24	105.55	175.91	281.46	525.71
0.9	0.3	77.40	4.11	78.97	15.32	32.46	32.99	83.30	158.96	242.27	105.73	176.22	281.96	524.24
1	0.3	77.08	3.68	79.02	15.33	32.36	33.00	82.50	158.20	240.71	105.86	176.47	282.36	523.08

On the contrary, centralization raises the service level. In the second scenario (integrated leader), the service level of the leading supply chain is more than the other two scenarios. Besides, in the third scenario (integrated follower), the service level of the follower supply chain is higher. Clearly, in the integrated structure, both the manufacturer and the retailer tend to maximize the total profit of the supply chain cooperatively. Subsequently, by decreasing the retail price and increasing the service level, more market share will be gain.

Comparing the results obtained from increasing the price competition intensity indicates that only for the small amount of price competition intensity, the centralization is the most sensible choice for the follower supply chain in the third scenario. In other words, for $\gamma_p \geq 0.3$, the total profit of the follower supply chain in the first scenario (decentralized leader and follower supply chains) has a higher total profit. Accordingly, the industry's total profit is the most in the first scenario, and only for $\gamma_p = 0.1$, the industry's total profit is the most in the second scenario. At the same time, changing the service investment coefficient of both the leader and follower supply chains, the integrated supply chain has the most profit among the three scenarios. It means that in the second scenario, the total profit of the leading supply chain is the most of the three scenarios, and in the third scenario, the follower supply chain has the same situation. Since the leader supply chain has a higher market share and more power, it has a more impressive impact on the market than the follower supply chain. Hence, the total profit of the industry is the most in the second scenario, and obviously, the centralization of the leading supply chain is the best choice for the total profit of the industry.

Some managerial implications of our findings could be elaborated on as follows. In a market with high price competition intensity, when the leader supply chain is

decentralized, the follower supply chain should choose the decentralized structure to maximize its profit. In contrast, centralization is more profitable for the follower supply chain in a market with low price competition intensity. Furthermore, when the leader supply chain is integrated, the best situation occurred for the entire industry when a low price competition intensity is introduced. Moreover, it is better for the entire industry in a market with a decentralized leader that the follower chain also has a decentralized structure. In addition, a market with an integrated follower is preferred from the costumers' point of view since both wholesale and retail prices have the least amount. In this case, customers who buy the product from the follower supply chain also have the advantage of receiving a higher service level.

6. CONCLUSION

This study considered the competition of two leader-follower supply chains where they compete on retail price and service level. Each supply chain consisted of a leading retailer and a follower manufacturer. Three scenarios with different structures were investigated to examine the impact of the competition intensity and the investment efficiency coefficient, on the optimal values of retail and wholesale prices, service levels, and profit functions of supply chain members.

The numerical analysis showed that if the price competition intensity increases, the retail price, the wholesale price, and the service level of both chains would decrease in all three scenarios. Furthermore, the profits of the leader chain and its members generally decrease by increasing the competition intensity. Moreover, in the follower supply chain, the manufacturer profits, the retailer profits, and the total profit in the first and second scenarios are first increasing and then decreasing as the price competition intensity increases.

However, this is not the case for the follower supply chain when a small competition intensity is introduced. In this scenario, the follower's retailer and manufacturer act the same as the leader ones, and by increasing the price competition intensity, the profit functions of the manufacturers and the retailers in both supply chains decrease. More specifically, the existence of limited price competition is beneficial for the follower supply chain. By increasing the investment efficiency coefficient of both chains, a rise happened in the follower chain's retail price, wholesale price, and service level, and a drop happened in leader's ones in all three scenarios. Therefore, having more investment efficiency coefficient both in the leader and follower supply chains is not profitable for the leading supply chain and will decrease its total profit while it leads to an increase in the follower's total profit.

Some directions less noted by researchers can be applied as a basis for future research. For example, one may consider a stochastic demand model that is more realistic. However, it is more complex than the current model. Another direction is to consider inventory decisions along with the price and service decisions.

7. REFERENCES

- Anderson, E. and Bao, Y., "Price competition with integrated and decentralized supply chains", *European Journal of Operational Research*, Vol. 200, No. 1, (2010), 227-234, DOI: 10.1016/j.ejor.2008.11.049.
- Sinha, S. and Sarmah, S.P., "Coordination and price competition in a duopoly common retailer supply chain", *Computers & Industrial Engineering*, Vol. 59, No. 2, (2010), 280-295, DOI: 10.1016/j.cie.2010.04.010.
- Ekici, A., Altan, B. and Özener, O.O., "Pricing decisions in a strategic single retailer/dual suppliers setting under order size constraints", *International Journal of Production Research*, Vol. 54, No. 7, (2016), 7, DOI: 10.1080/00207543.2015.1054451.
- Jafari, H., Hejazi, S.R. and Rasti Barzoki, M., "Pricing decisions in dual-channel supply chain with one manufacturer and multiple retailers: A game-theoretic approach", *RAIRO-Operations Research*, Vol. 51, No. 4, (2017), 1269-1287, DOI: 10.1051/ro/2017003.
- Mahmoudi, M. and Tofiqh, A.A., "Application of game theory in dynamic competitive pricing with one price leader and n dependant followers", *International Journal of Engineering, Transactions A: Basics*, Vol. 25, No. 1, (2012), 35-44, DOI: 10.5829/idosi.ije.2012.25.01a.03.
- Amin-Naser, M.R. and Azari-Khojasteh, M., "Price competition between two leader-follower supply chains under demand uncertainty", *The International Journal of Advanced Manufacturing Technology*, Vol. 79, (2015), 377-393, DOI: 10.1007/s00170-014-6728-0.
- Mahmoodi, A., "Joint pricing and inventory control of duopoly retailers with deteriorating items and linear demand", *Computers & Industrial Engineering*, Vol. 132, (2019), 36-46, DOI: 10.1016/j.cie.2019.04.017.
- Sadjadi, S.J. and Alirezaee, A., "Impact of pricing structure on supply chain coordination with cooperative advertising", *RRAIRO-Operations Research*, Vol. 54, No. 6, (2020), 1613-1629, DOI: 10.1051/ro/2019099.
- Khanlarzade, N., Zegordi, S. and Nakhai Kamalabadi, I., "Pricing in two competing supply chains based on market power and market size under centralized and decentralized structures", *Science Iranica*, Vol. 28, No. 1, (2021), 424-445, DOI: 10.24200/SCI.2019.50740.1845.
- Lou, Z., Lou, X. and Hou, F., "Competition and cooperation models for dynamic pricing of perishable products in a two-echelon supply chain", *RAIRO-Operations Research*, Vol. 55, No., (2021), 2619-2632, DOI: 10.1051/ro/2020097.
- Widodo, E. and Januardi, "Noncooperative game theory in response surface methodology decision of pricing strategy in dual-channel supply chain", *Journal of Industrial and Production Engineering*, Vol. 38, No. 2, (2021), 89-97, DOI: 10.1080/21681015.2020.1848932.
- Boyaci, T. and Gallego, G., "Supply chain coordination in a market with customer service competition", *Production and Operations Management Society*, Vol. 13, (2004), 3-22, DOI: 10.1111/j.1937-5956.2004.tb00141.x.
- Xiao, D. and Hao, Y.-H., "Customer service competition in crossed supply chain", *Management and Service Science*, Vol., (2009), DOI: 10.1109/ICMSS.2009.5301209.
- Kurata, H. and Nam, S.-H., "After-sales service competition in a supply chain: Does uncertainty affect the conflict between profit maximization and customer satisfaction", *International Journal of Production Economics*, Vol. 144, (2013), 268-280, DOI: 10.1016/j.ijpe.2013.02.014.
- Chiu, C.-H., Choi, T.M., Li.Y and Xu.L, "Service competition and service war: A game-theoretic analysis", *Service science*, Vol. 6, (2014), 63-76, DOI: 10.1287/serv.2014.0062.
- Giri, B.C. and Maiti, T., "Service competition in a supply chain with two retailers under service level sensitive retail price and demand", *International Journal of Management Science and Engineering Management* Vol. 9, No. 2, (2014), 133-146, DOI: 10.1080/17509653.2013.868079.
- Jamshidi, R., Asadi, H. and Ahmadvanda, A., "Impact of service on customer's demand and member's profit in supply chain", *International Journal of Engineering, Transactions C: Aspects*, Vol. 25, No. 3, (2012), 213-222, DOI: 10.5829/idosi.ije.2012.25.03c.05.
- Wu, Y., Wang, J. and Li, C., "Decisions of supply chain considering chain-to-chain competition and service negative spillover effect", *Sustainability*, Vol. 11, No. 6, (2019), 1612, DOI: 10.3390/su11061612.
- Wu, Y., Wang, J. and Chen, L., "Optimization and decision of supplychain considering negative spillover effect and service competition sustainability", *Sustainability*, Vol. 13, No. 4, (2021), 2320, DOI: 10.3390/su13042320.
- Tsay, A.A. and Agrawal, N., "Channel dynamics under price and service competition", *Manufacturing and Service Operations Management*, Vol. 4, (2000), 372-391, DOI: 10.1287/Msom.2.4.372.12342.
- Ali, S.M., Rahman, M.H., Tumpa, T.J., Rifat, A.A.M. and Paul, S.K., "Examining price and service competition among retailers in a supply chain under potential demand disruption", *Journal of Retailing and Consumer Services*, Vol. 40, (2018), 40-47, DOI: 10.1016/j.jretconser.2017.08.025.
- Bernstein, F. and Federgruen, A., "Coordination mechanisms for supply chains under price and service competition", *Manufacturing and Service Operations Management*, Vol. 9, (2006), 242-262, DOI: 10.1287/msom.1070.0159.
- Lu, J.C., Tsao, Y.-C. and Chatoensiriwath, C., "Competition under manufacturer service and retail price", *Economic Modeling*, Vol. 28, (2011), 1256-1264, DOI: 10.1016/j.econmod.2011.01.008.

- 24. Xiao, T. and Yang, D., "Price and service competition of supply chains with risk-averse retailers under demand uncertainty", *International Journal of Production Economics* Vol. 114, No. 1, (2008), 187-200, DOI: 10.1016/j.ijpe.2008.01.006.
- 25. Chen, J., Zhang, W. and Liu, Z., "Joint pricing, services and quality decisions in a dual-channel supply chain", *RAIRO-Operations Research*, Vol. 54, No. 4, (2020), 1041-1056, DOI: 10.1051/ro/2019024.

Appendix A: Proof of all lemmas

Proof of lemma 1.

The Hessian matrix of the follower chain's retailer is

$$H_2 = \begin{bmatrix} \frac{\partial^2 \pi^{r^2}}{\partial v_2^2} & \frac{\partial^2 \pi^{r^2}}{\partial v_2 \partial s_2} \\ \frac{\partial \pi^{r^2}}{\partial s_2 \partial v_2} & \frac{\partial \pi^{r^2}}{\partial s_2^2} \end{bmatrix} = \begin{bmatrix} -\beta'_p & \frac{\beta'_s}{2} \\ \frac{\beta'_s}{2} & -\eta_2 \end{bmatrix}$$

π^{r^2} is concave on retail price and service level if and only if H_2 is negative semi-definite. Therefore, the following two conditions must be held:

- 1) $-\beta'_p \leq 0$
- 2) $\begin{vmatrix} -\beta'_p & \frac{\beta'_s}{2} \\ \frac{\beta'_s}{2} & -\eta_2 \end{vmatrix} \geq 0 \rightarrow M_1 = \eta_2 \beta'_p - \left(\frac{\beta'_s}{2}\right)^2 \geq 0$

The first condition is correct by model assumptions, and the second condition is satisfied for the domain Lemma:

$$0 \leq \frac{1}{\eta_2} \leq \frac{4\beta'_p}{\beta'^2_s} \quad \square$$

Proof of lemma 2.

From the first condition of the leader's Hessian matrix, we know that:

$$-\beta'_p + A - B + \frac{\gamma_p^2 R}{D} \leq 0 \rightarrow \frac{\gamma_p}{D} (\gamma_s \beta'_s - \gamma_p \eta_2) \geq \frac{\gamma_p^2}{2\beta'_p} \left(1 + \frac{\beta'_s}{D}\right) - \beta'_p$$

Simplifying the equations above leads to:

$$\gamma_s \beta'_s + \beta'_p \geq 3\gamma_p \eta_2$$

According to the second condition of the follower's retailer hessian matrix:

$$0 \leq \frac{1}{\eta_2} \leq \frac{4\beta'_p}{\beta'^2_s} \quad \text{A-1}$$

Also, from the first condition of the leader's Hessian matrix:

$$\frac{1}{3\gamma_p \eta_2} \geq \frac{1}{\gamma_s \beta'_s + \beta'_p} \Leftrightarrow \frac{1}{\eta_2} \geq \frac{3\gamma_p}{\gamma_s \beta'_s + \beta'_p} \quad \text{A-2}$$

Therefore, according to A-1 and A-2, we can define an interval for the follower's investment efficiency at service level:

$$\frac{3\gamma_p}{\gamma_s \beta'_s + \beta'_p} \leq \frac{1}{\eta_2} \leq \frac{4\beta'_p}{\beta'^2_s}$$

We can change the second condition of the leader's retailer hessian matrix as follows:

$$H\eta_1 \geq (2KH - KH)^2 \Leftrightarrow 0 \leq \frac{1}{\eta_1} \leq \frac{1}{K^2 H}$$

Proof of lemma 3.

The leader's Hessian matrix is:

$$H_1 = \begin{bmatrix} \frac{\partial \pi^{T1}}{\partial v_1^2} & \frac{\partial \pi^{T1}}{\partial v_1 \partial s_1} \\ \frac{\partial \pi^{T1}}{\partial s_1 \partial v_1} & \frac{\partial \pi^{T1}}{\partial s_1^2} \end{bmatrix} = \begin{bmatrix} 2 \left(-\beta'_p + A - B + \frac{\gamma_p^2 R}{D} \right) C + E\gamma_s + \beta'_s - \frac{BR}{\beta'_s} & \\ C + E\gamma_s + \beta'_s - \frac{BR}{\beta'_s} & -\eta_1 \end{bmatrix}$$

If the Hessian matrix of the leader's chain is negative definite, the total profit function of the leader's chain will be concave with respect to price and service level. The determinant of the matrix is:

$$M_1 = 2\eta_1 \left(\beta'_p - A + B - \frac{\gamma_p^2 R}{D} \right) - \left(C + E\gamma_s + \beta'_s - \frac{BR}{\beta'_s} \right)^2$$

$$1) \left(-\beta'_p + A - B + \frac{\gamma_p^2 R}{D} \right) \leq 0$$

$$2) \begin{vmatrix} 2 \left(-\beta'_p + A - B + \frac{\gamma_p^2 R}{D} \right) C + E\gamma_s + \beta'_s - \frac{BR}{\beta'_s} & \\ C + E\gamma_s + \beta'_s - \frac{BR}{\beta'_s} & -\eta_1 \end{vmatrix} \geq 0 \rightarrow M_1 \geq 0$$

The first condition of the leader's chain in the second scenario is the first condition of the leader's chain in the first scenario. In other words, the follower's investment efficiency at the service level must be:

$$\frac{3\gamma_p}{\gamma_s \beta'_s + \beta'_p} \leq \frac{1}{\eta_2} \leq \frac{4\beta'_p}{\beta'^2_s}$$

The second condition of optimality can be identified as:

$$2\eta_1 H \geq K^2 \Leftrightarrow \eta_1 \geq \frac{\left(C + E\gamma_s + \beta'_s - \frac{BR}{\beta'_s} \right)^2}{2 \left(\beta'_p + B - A - \frac{R\gamma_p^2}{D} \right)} \Leftrightarrow$$

$$0 \leq \frac{1}{\eta_1} \leq \frac{2 \left(\beta'_p + B - A - \frac{\gamma_p^2 R}{D} \right)}{\left(C + E\gamma_s + \beta'_s - \frac{BR}{\beta'_s} \right)^2}$$

Proof of lemma 4.

The follower's hessian matrix of profit function is:

$$H_2 = \begin{bmatrix} \frac{\partial \pi^{T2}}{\partial v_2^2} & \frac{\partial \pi^{T2}}{\partial v_2 \partial s_2} \\ \frac{\partial \pi^{T2}}{\partial s_2 \partial v_2} & \frac{\partial \pi^{T2}}{\partial s_2^2} \end{bmatrix} = \begin{bmatrix} -2\beta'_p & \beta'_s \\ \beta'_s & -\eta_2 \end{bmatrix}$$

The two conditions of the Hessian matrix are:

$$1) -2\beta'_p \leq 0$$

$$2) \begin{vmatrix} -2\beta'_p & \beta'_s \\ \beta'_s & -\eta_2 \end{vmatrix} \geq 0 \rightarrow$$

$$M_2 = 2\beta'_p \eta_2 - \beta'^2_s \geq 0$$

β'_p is positive; therefore, the first condition is satisfied.

The second condition is satisfied if and only if the follower's retailer investment efficiency at service level will be $0 \leq \frac{1}{\eta_2} \leq \frac{2\beta'_p}{\beta'^2_s}$.

Proof of lemma 5.

The hessian matrix of leader's retailer profit function is:

$$H_1 = \begin{bmatrix} \frac{\partial \pi^1}{\partial v_1^2} & \frac{\partial \pi^1}{\partial v_1 \partial s_1} \\ \frac{\partial \pi^1}{\partial s_1 \partial v_1} & \frac{\partial \pi^1}{\partial s_1^2} \end{bmatrix} = \begin{bmatrix} -\beta'_p + AQ + A - I & (-\beta'_p + AQ + A - I)N' + \left(CQ + C + \beta'_s + \frac{I\gamma_s}{\gamma_p}\right) \\ (-\beta'_p + AQ + A - I)N' + \left(CQ + C + \beta'_s + \frac{I\gamma_s}{\gamma_p}\right) & -\eta_1 \end{bmatrix}$$

Moreover, the two conditions of the Hessian matrix are:

$$1) -(\beta'_p - AQ - A + I) \leq 0$$

$$2) \begin{vmatrix} (-\beta'_p + AQ + A - I) & (-\beta'_p + AQ + A - I)N' + \left(CQ + C + \beta'_s + \frac{I\gamma_s}{\gamma_p}\right) \\ (-\beta'_p + AQ + A - I)N' + \left(CQ + C + \beta'_s + \frac{I\gamma_s}{\gamma_p}\right) & -\eta_1 \end{vmatrix} \geq 0 \rightarrow$$

$$M_1 = \eta_1(\beta'_p - AQ - A + I) - \left[(-\beta'_p + AQ + A - I)N' + \left(CQ + C + \beta'_s + \frac{I\gamma_s}{\gamma_p}\right)\right]^2 \geq 0$$

The first condition is:

$$\beta'_p - AQ - A + I \geq 0 \Leftrightarrow$$

$$\frac{\beta'_p (2\eta_2 \beta'_p - \beta'^2_s) + \gamma_s \gamma_p \beta'_s}{2\eta_2 \beta'_p - \beta'^2_s} \geq \frac{\eta_2 \gamma_p^2}{(2\eta_2 \beta'_p - \beta'^2_s)} \Leftrightarrow$$

$$\eta_2 \geq \frac{\beta'^2_s \beta'_p - \beta'_s \gamma_s \gamma_p}{2\beta'^2_p - \gamma_p^2}$$

The first condition of the Hessian matrix of leader's retailer is satisfied if and only if the follower's retailer investment efficiency at service level will be:

$$0 \leq \frac{1}{\eta_2} \leq \frac{2\beta'^2_p - \gamma_p^2}{\beta'^2_s \beta'_p - \beta'_s \gamma_s \gamma_p}$$

By considering $\frac{CQ + C + \beta'_s + \frac{I\gamma_s}{\gamma_p}}{2H'} = N'$, the second

condition will be: $0 \leq \frac{1}{\eta_1} \leq \frac{1}{H' N'^2}$.

Persian Abstract

چکیده

رقابت یکی از فاکتورهای اساسی در تعیین استراتژی زنجیره های تامین است. به علاوه، با توجه به وجود عدم تعادل در سهم بازار، در اکثر موارد یک زنجیره دارای قدرت کنترل بیشتر در بازار بوده و نقش رهبر را در بازار رقابتی بازی می کند. در این تحقیق، دو زنجیره تامین رهبر-پیرو متشکل از یک تولیدکننده و یک خرده فروش مورد بررسی قرار می گیرند. علاوه بر رقابت بین زنجیره ای، رقابت درون زنجیره ای نیز مورد مطالعه قرار می گیرد که در آن خرده فروش نقش رهبر و تولیدکننده نقش پیرو را بازی می کند. دو عامل رقابتی قیمت و سطح سرویس در سه سناریوی مختلف مورد بررسی قرار می گیرند: رهبر غیرمتمرکز-پیرو غیرمتمرکز، رهبر متمرکز-پیرو غیرمتمرکز و رهبر غیرمتمرکز-پیرو متمرکز. با استفاده از رویکرد استنتاج بازگشتی، روند حل مسئله از زنجیره پیرو آغاز شده و توابع بهترین پاسخ زنجیره پیرو بدست می آیند. سپس استراتژی زنجیره رهبر پس از جایگذاری توابع بهترین پاسخ زنجیره پیرو در توابع سود زنجیره رهبر، تعیین می گردند. در نهایت، تاثیر شدت رقابت در قیمت و ضریب سرمایه گذاری در سطح سرویس هر دو زنجیره تامین را بر روی مقادیر بهینه در هر سه سناریو مورد تجزیه و تحلیل قرار می گیرد. نتایج بدست آمده نشان می دهد که افزایش شدت رقابت در قیمت موجب کاهش سود زنجیره رهبر می شود. در مقابل، مقادیر کم شدت رقابت در قیمت سودآوری بیشتری برای زنجیره پیرو در پی خواهد داشت. به علاوه، ضریب سرمایه گذاری در سطح سرویس در هر دو زنجیره رهبر و پیرو، تاثیری مستقیم بر روی مقادیر بهینه زنجیره پیرو و تاثیری معکوس بر روی زنجیره رهبر خواهد داشت. همچنین، سناریوی اول (رهبر غیرمتمرکز-پیرو غیرمتمرکز) بیشترین مقدار قیمت عمده فروشی و خرده فروشی را در بین هر سه سناریو دارد، در حالی که زنجیره متمرکز دارای بیشترین مقدار سطح سرویس در بین دو زنجیره خواهد بود.



Numerical Analyses of Manufacturing of an AA8111 Pin-shaped Bipolar Plate by Hot Metal Gas Forming

S. Esmaeili^a, S. J. Hosseinipour^{*a}, A. Shamsi-Sarband^b

^a Research Center for Advanced Processes of Materials Forming, Babol Noshirvani University of Technology, Babol, Iran

^b Department of Mechanical Engineering, Islamic Azad University-Sari Branch, Sari, Iran

PAPER INFO

Paper history:

Received 17 February 2021

Received in revised form 10 July 2021

Accepted 13 July 2021

Keywords:

Aluminium Alloy

Hot Metal Gas Forming

Finite Elements Simulation

Bipolar Plates

Pin-type Pattern

ABSTRACT

In this paper, fabrication of a pin-shaped bipolar plate for a proton exchange membrane fuel cell, the deformation behavior of a thin 8111 aluminum alloy sheet by the hot metal gas forming (HMGF) process was investigated. The effect of gas pressure, forming time, pin diameter, pin height, and die fillet radius on the specimen profiles, as well as the thickness distribution were analyzed by finite element method using ABAQUS 6.10 software. In addition, experimental tests were performed to validate numerical outputs. The results indicated that the sheet-thinning rate sharply grew by the gas pressure exceeding 4 MPa. The specimens were cracked following decreasing the die fillet radius to 0.1 mm. Furthermore, the die filling rate was high at the beginning of forming time and then diminished gradually after 1000 s. Moreover, the thickness reduced sharply by augmenting the ratio of pin height to diameter to over 0.4. Finally, perfect specimens were produced in experiments, which verified the feasibility of fabricating a pin-shaped bipolar plate out of a thin AA8111 sheet by the HMGF process.

doi: 10.5829/ije.2021.34.08b.20

1. INTRODUCTION

Nowadays, environmental issues and air pollution resulting from fossil fuels have led to a global attempt to replace traditional energy resources with clean ones. Fuel cells, which convert chemical potential energy to electrical power, can be considered among the best candidates. Bipolar plates play a remarkable role in the weight and price of the proton exchange membrane (PEM) fuel cell stacks [1, 2]. In this regard, metallic bipolar plates are widely used due to their low fabrication cost and desirable mechanical properties, [3]. Various methods, such as hydroforming, stamping, and rubber pad forming have already been investigated for forming metallic bipolar plates [4]. Koc and Mahabunphachai [5] used a two-stage hybrid process including hydroforming process and mechanical bonding to fabricate a multi-array micro-channel bipolar plate from the SS304 steel. These researchers showed that die filling increased with elevating internal pressure. Peng *et al.* [6] investigated

the shape of the flow channel by hydroforming the metallic bipolar plate. They showed that geometric parameters, such as the fillet radius, as well as the depth and width of the flow channel, were important in the performance of bipolar plates. Liu *et al.* [7, 8] studied the feasibility of the rubber pad forming process to make the SS304 steel bipolar plate containing multi-array micro-flow channels. Hung *et al.* [9] studied micro-channel forming using high-pressure hydroforming. They indicated that the height to width ratio of a flow channel has an essential impact on the performance of a fuel cell. Belali-Owsia *et al.* [10] fabricated a pin-shaped bipolar plate from the SS304 steel sheet using three different methods of hydroforming, stamping, and hybrid hydroforming-stamping. Mohammadtabar *et al.* [11] examined the feasibility of a double-step hydroforming process to make a bipolar plate with a serpentine channel flow field. Ghadikolaee *et al.* [12] constructed metallic bipolar plates out of the SS316 steel utilizing the rubber pad forming process. They investigated the contribution

*Corresponding Author Institutional Email: j.hosseini@nit.ac.ir (S. J. Hosseinipour)

of pressure, hardness, and thickness of a rubber pad in the maximum channel depth before fracture.

The applications of lightweight materials, such as aluminum alloys are being widely expanded in various industries, including the aerospace and transportation industries [13-17]. Aluminum alloys can be suitable as bipolar plates because of their desirable mechanical properties, corrosion resistance, thermal conductivity, and low electrical resistance. Lim *et al.* [18] studied the formability of AA1050 aluminum alloy to make a bipolar plate by the rubber pad forming process. They studied the influence of channel cross-sections on the velocity field of the bipolar plate. However, the formability of aluminum alloys at room temperature is limited, which can be resolved using high temperature forming processes [19, 20]. Therefore, Kwon *et al.* [21] used a warm progressive forming process to manufacture the micro-channel bipolar plates of AA5052 aluminum sheets. The latter researchers studied the effect of various parameters, namely forming speed and die temperature. In addition, Palumbo *et al.* [22] focused on the manufacturing of a bipolar plate from an AA6061 aluminum sheet using a warm hydroforming process. They analyzed both the channel profile and bipolar plate geometry by applying the finite element method (FEM). Taking advantage of the hot metal gas forming (HMGF) process, Esmaeili and Hosseinipour [23] experimentally studied the feasibility of forming a micro-channel bipolar plate out of AA8111 aluminum sheets with a serpentine channel flow field. Similarly, Kargar-Pishbijari *et al.* [24] experimentally investigated the fabrication of a micro-channel bipolar plate from an AA1070 aluminum alloy sheet with a thickness of 100 μm by the HMGF process.

As mentioned earlier, most research around the metallic bipolar plates has been performed on forming channel-shaped patterns through hydroforming, stamping, and rubber pad forming. The flow pattern of the bipolar plate has a significant impact on the fuel cell performance. The investigations showed that the performance of bipolar plates with a pin-shaped pattern did not decrease at high temperatures and the pressure drop was lower than with the channel-shaped flow field [6]. In this regard, little research has been conducted on the forming of pin-shaped bipolar plates. The fabrication of pin-shaped patterns from aluminum alloys is a considerable issue. Consequently, in this study, finite element simulations and experiments were carried out to evaluate the effects of various parameters on the deformation behavior of a thin AA8111 aluminum alloy sheet by the HMGF process to fabricate a pin-shaped bipolar plate.

2. MATERIALS AND METHODS

2. 1. Process description An AA8111 aluminum alloy sheet with 0.2 mm thickness was used for

experimental tests. Figure 1 shows the HMGF equipment, which consists of an argon gas container, a temperature sensor, a temperature controller, a heating element, a gas pressure valve, as well as upper and lower dies. First, a circular blank was fixed between the upper and lower dies, and then at a specified temperature, constant gas pressure was applied for a specified duration to form the sheet on the die. Figure 2 indicates the pin-type pattern die used in the experimental tests, in addition to the geometric parameters, including pin diameter (S), pin height (H), flow path width (W), and die fillet radius (R). Table 1 presents the values of parameters analyzed in the present study.

Figure 3 demonstrates diverse conditions of the formed bipolar plates, including partially formed, cracked, and perfect specimens. The specimens were cut and mounted with resin to measure the profile and thickness of specimens as illustrated in Figure 4. Next, images were taken from the cut sections of specimens with a Dewinter optical microscope (Figure 5). Dewinter material plus software was also used to analyze the images.

Free bulging tests were performed to obtain the mechanical properties of the material at a specific temperature. For this purpose, two distinct pressures were applied and the dome height changes were measured at various time points [25]. Figure 6 depicts the free bulged sample and its parameters.

The work hardening is negligible at high temperatures. As a result, the material behavior can be expressed by Equation (1) [26];

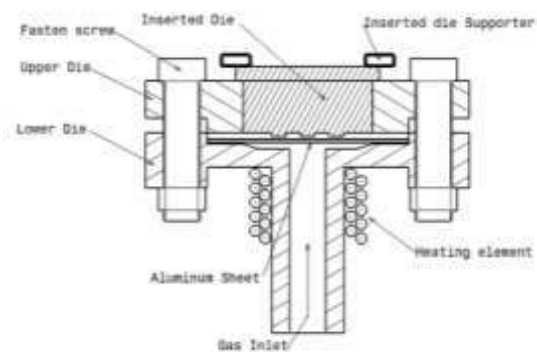


Figure 1. Experimental equipment

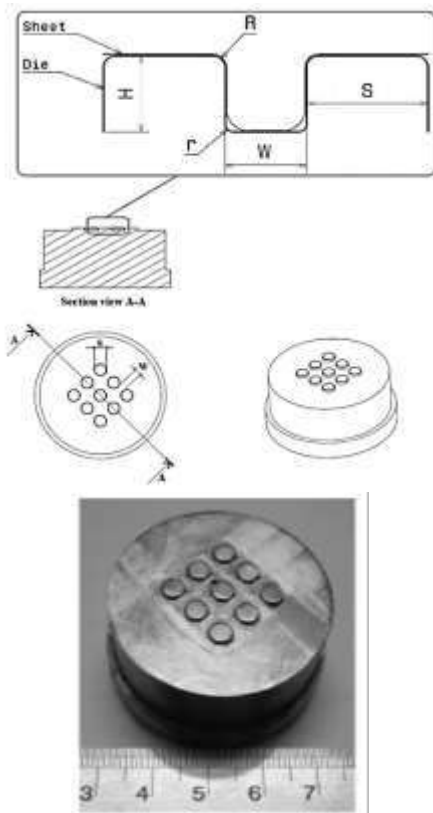


Figure 2. Pin-type die and the parameters

TABLE 1. Range of investigated parameters and the material property at 500 °C

Forming Parameters	Range
Temperature (°C)	500
Pressure (MPa)	1-5
Forming Time (s)	100, 1000, 2000
Pin diameter, S (mm)	2-4
Flow path width, W (mm)	2
Fillet radius, R (mm)	0.1, 0.2, 0.3
Pine height, H (mm)	0.8, 1
H/S	0.2-0.5
Strain rate sensitivity exponent, m	0.08
Coefficient of strength, C (MPa)	14

$$\sigma = C\dot{\epsilon}^m \tag{1}$$

where σ is the effective flow stress, $\dot{\epsilon}$ denotes the effective strain rate, m refers to the strain rate sensitivity exponent, and C represents the coefficient of strength. The strain rate sensitivity exponent, m , can be determined by Equation (2);

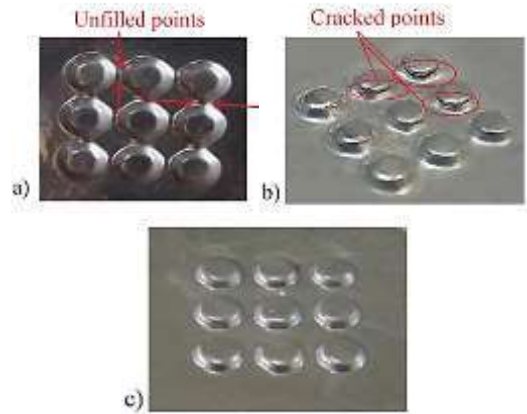


Figure 3. a) partially formed specimen, b) cracked specimen, and c) perfect specimen

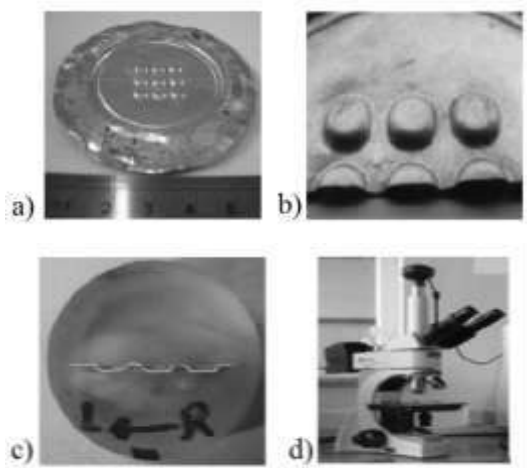


Figure 4. Preparation sequence to measure the profile and thickness of specimens

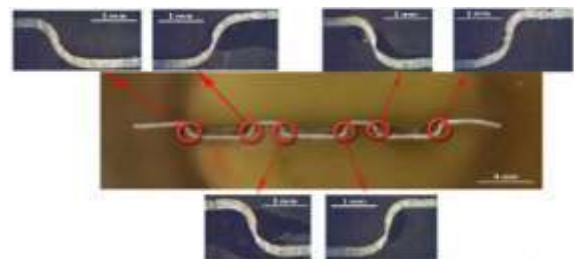


Figure 5. Cut a section of specimens

$$m = \frac{\ln(\frac{P_1}{P_2})}{\ln(\frac{t_1}{t_2})} \tag{2}$$

where t_1 and t_2 are the forming times to reach the same dome height at the constant pressures of P_1 and P_2 , respectively. The stress state at the dome is equal to the biaxial tension. Therefore, the stress σ is calculated using Equation (3);

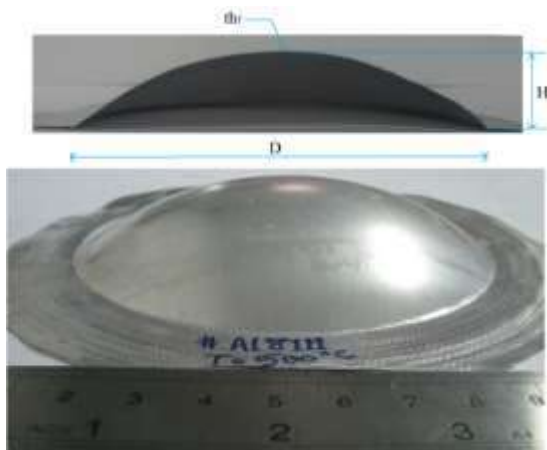


Figure 6. A free bulged specimen

$$\sigma = \frac{Pr}{2th_f} \tag{3}$$

where th_f denotes the thickness of sheet at the dome and r represents the dome radius calculated by Equation (4);

$$R = \frac{H^2 + (\frac{D}{2})^2}{2H} \tag{4}$$

where D refers to the die diameter, and H is the dome height. The strain ϵ and strain rate $\dot{\epsilon}$ can be calculated using Equations (5) and (6), respectively.

$$\epsilon = \ln \frac{th_f}{th_o} \tag{5}$$

$$\dot{\epsilon} = \frac{d\epsilon}{dt} \tag{6}$$

Table 1 represents the calculated values of C and m for the AA8111 at 500°C.

2. 2. Numerical Simulation The finite element software ABAQUS 6.10 was used to simulate the process. Both the die and sheet were geometrically symmetric. Consequently, a quarter of the whole process was modeled (Figure 7). The die was defined as a discrete rigid body and the blank was modeled as a deformable shell element. An isotropic behavior was assumed for the material flow because deformation was performed at high temperature.

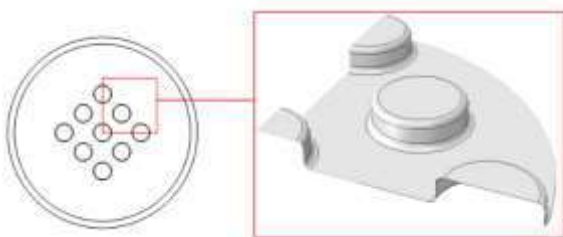


Figure 7. Die model in the finite element simulation

To enter the mechanical properties of the material into the software, a time-dependent deformation was described. Values of C and m at 500°C were also applied according to Table 1. Contact conditions were defined between the sheet and die surface [27, 28]. The die was fixed, and a constant uniform pressure was applied to the sheet during the forming process. The S4R element was used for meshing the blank model with the size of 0.02 mm based on the mesh convergence analysis depicted in Figure 8. **Error! Reference source not found.** According to the experimental results, the samples were cracked at the sheet thinning rate of 50% or more. Therefore, this level was considered as a failure limit in our finite element simulations. Figure 9 shows sheet deformation according to the geometry of the die in the simulation.

3. RESULTS AND DISCUSSION

3. 1. FEM Model Validation The simulation results were compared with the experimental tests to verify the accuracy of the FEM. To this aim, both the die filling profile and thickness distribution were examined. According to Figure 10, the die filling profile of the experimental method was highly matched with that of the simulation. Moreover, as could be seen in Figure 11, the thickness distributions of the formed plates were in agreement with each other in both experimental and simulation methods.

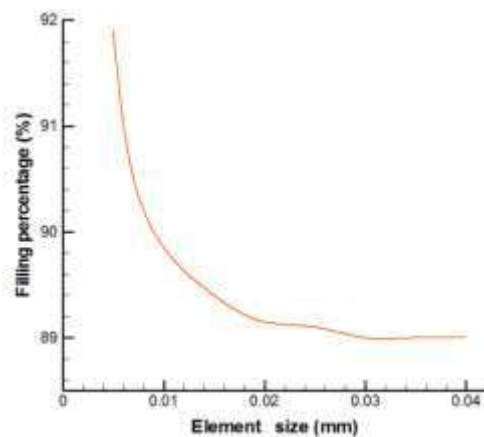


Figure 8. Mesh convergence diagram

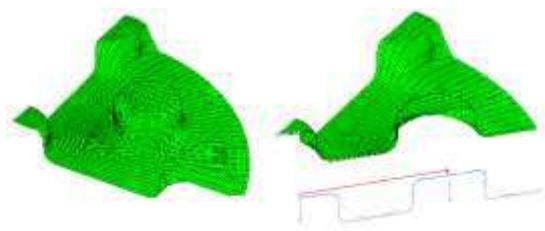


Figure 9. Deformed blank in the finite element simulation

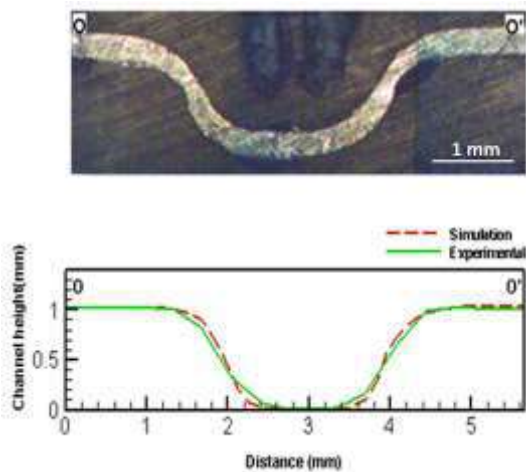


Figure 10 Die filling profile of a specimen (S=3mm, H=1mm, R=0.2mm, P=2MPa, t=1000s)

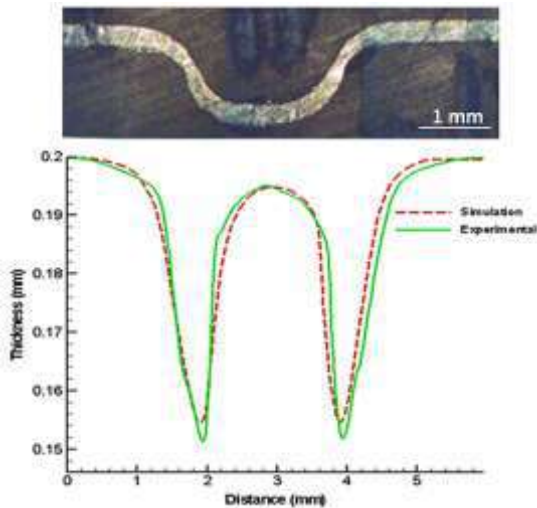


Figure 11 Thickness distribution of a specimen (S=3mm, H=0.8mm, R=0.2mm, P=1.6MPa, t=1000s)

3. 2. Effect of Forming Time

Figure 12 shows the rate of die filling as a percentage at various time points during the forming process. It was observed that at constant pressure, the filling rate increased with time, however, this behavior was not always uniform. At the initial time points, a considerable amount of the filling occurred with the rest of the deformation occurring gradually. When the pressure was 2 MPa, the filling rate 100 and 2000 s after the beginning of the experiment was 73 and 82%, respectively. The filling rate declined due to the contact of sheet with die surface, and as a result of high friction between the hot die and the sheet, it took more time to be filled.

Figure 13 demonstrates the sheet thinning rate during the forming period. A high thinning rate was observed at the beginning of the process, whereas it continued at a

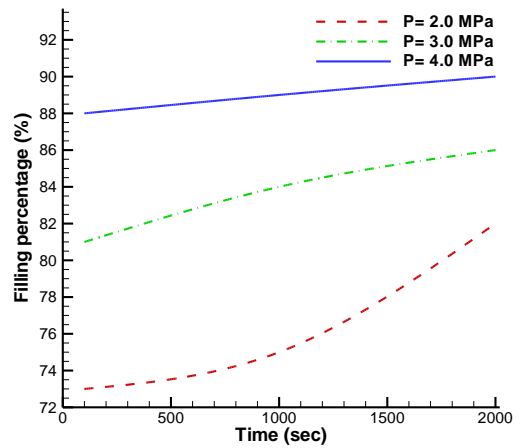


Figure 12. Effect of time on the filling rate (S=4mm, H=0.8mm, R=0.1mm)

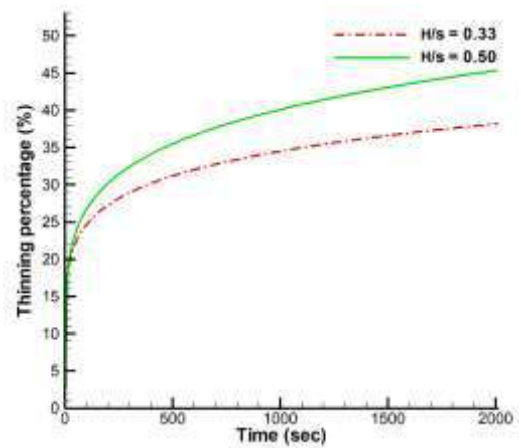


Figure 13. Effect of time on the thinning rate (R=0.2mm, P=2MPa)

slower rate during the rest of the experiment. Although the thinning rate was depicted for two different H/S values, it resulted in a similar thinning trend.

3. 3. Effect of Gas Pressure

Figure 14 indicates that the filling rate of the die cavity rises by elevating gas pressure. In order to obtain a perfect specimen, the sheet thinning rate should also be taken into consideration. According to Figure 15, the thinning rate grows by augmenting gas pressure. Moreover, the obtained results are shown for different H/S values. At lower pressures, the gas pushed the sheet to be drawn into the die cavity, and as a result, the thinning rate was not at critical values. By increasing the pressure, the sheet was forced to fill the corners of the die, and the thinning rate raised sharply. When H/S = 0.33 and P = 4 MPa, the thinning rate was 38%, which was below the threshold and acceptable. By increasing the pressure up to 5 MPa, the thinning rate reached 54%, which was beyond the failure limit.

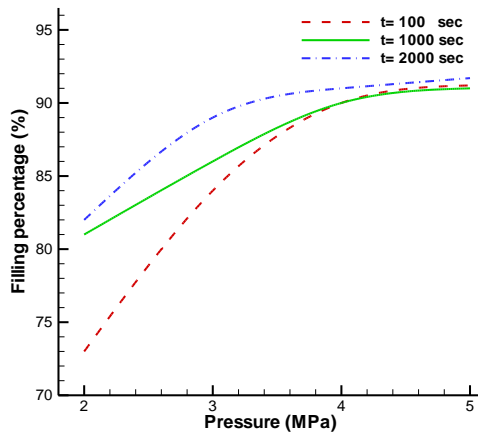


Figure 14. Impact of pressure on die filling rate ($S=3\text{mm}$, $H=0.8\text{mm}$, $R=0.1$)

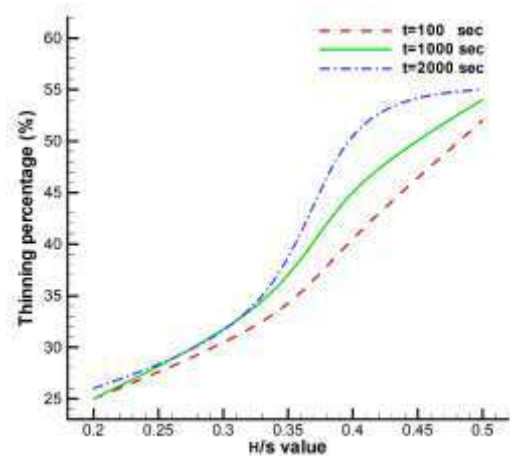


Figure 16. Effect of pressure on the thinning rate ($R=0.1$, $t=2000\text{s}$)

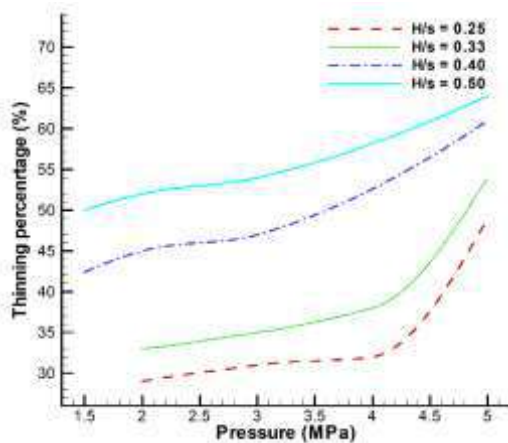


Figure 15. Effect of pressure on sheet thinning rate ($R=0.1$, $t=2000\text{s}$)

3. 4. Influence of Pin Height to Diameter Ratio (H/S)

Figure 16 shows the effect of different H/S values on sheet thinning rate, at three different time points. It should be noted that an increase in the H/S value led to increase in the thinning rate. The latter trend was consistent throughout the whole study period. Moreover, by augmenting the H/S value, the sheet needed to stretch more to fill the die cavity. This phenomenon raised the extension ratio of the sheet and resulted in a higher thinning rate. When H/S varied as 0.2-0.4, the thinning rate raised from 25 to 44%, which was still within an acceptable range. However, by increasing the H/S to 0.5, the thinning rate reached 54% or higher, at which a crack was likely to appear in the specimen. Overall, the H/S value was revealed to be an essential parameter in the forming process.

Therefore, the H/S value of 0.5 was observed to be a critical value, at which the thinning rate elevated significantly and the sheet cracked during the forming

process in a considerable number of experimental tests. This phenomenon can be explained by the contact area of the sheet and die during the forming process. As shown in Figure 17, at the same forming time, the first contact happened at the bottom of the die cavity for low H/S values. On the other hand, for high H/S values, it occurred on the vertical walls of the die before being drawn into the die cavity. Consequently, a considerable amount of the material was locked due to the friction in the contact area. Therefore, by continuing the forming process, the sheet was significantly prone to the experience of a high thinning rate.

3. 5. Effect of Fillet Radius (R)

Figure 18 demonstrates the die filling rate at various R values. As R increased from 0.1 mm to 0.2 mm, the filling rate at all applied pressures sharply augmented. However, by elevating the amount of R from 0.2 mm to 0.3 mm, the filling rate did not change considerably implying that higher R could facilitate the drawing of the sheet material into the die cavity. Consequently, a higher rate of die cavity will be filled by the sheet. Furthermore, R has a crucial impact on the thinning of the formed specimens. According to the experimental observations, cracks in all cracked specimens occurred in areas where the sheets were in contact with the die fillet of the pin (as could be observed in Figure 3). Figure 19 indicates that by rising the value of R, the thinning rate declined. When $R = 0.1$

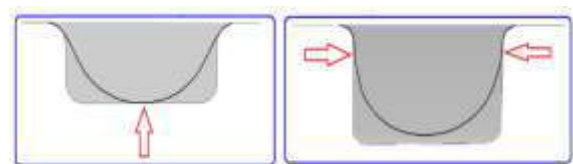


Figure 17. First contact area of sheet with die at a) low H/S value, and b) high H/S value

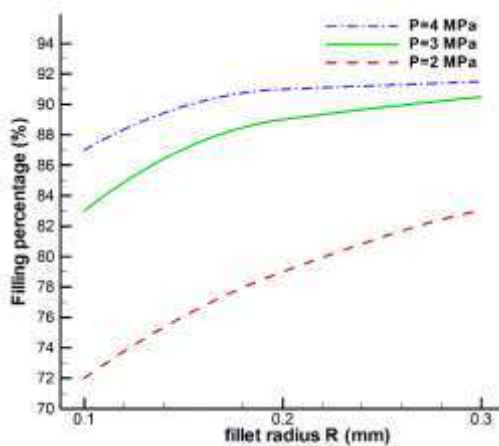


Figure 18. Influence of R on the filling rate ($S=4\text{mm}$, $H=1\text{mm}$, $t=1000\text{s}$)

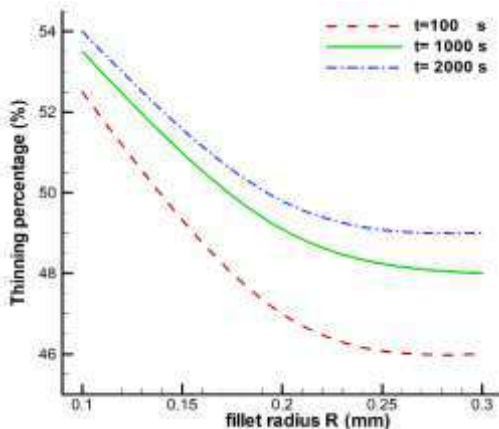


Figure 19. Effect of R on the thinning rate ($S=2\text{mm}$, $H=1\text{mm}$, $P=3\text{MPa}$)

mm, which was considered as a sharp fillet during all the forming periods, the thinning rate was higher than the critical limit (50%) and the samples were considered as cracked specimens. Finally, by selecting higher R values, such as 0.2 and 0.3 mm, the thinning rate diminished remarkably. However, this trend was not linear.

4. CONCLUSION

The current research studied the deformation behavior of a thin AA8111 alloy sheet by the HMGF process to fabricate a pin-shaped bipolar plate for PEM fuel cells. The effects of essential parameters, including forming time, gas pressure, die fillet radius, pin diameter, and pin height on die filling and sheet thinning rates were investigated.

It was found that gas pressure was an important parameter in the HMGF process. While the filling rate increased by applying high pressure, the thickness

reduced. Altogether, when $P > 4\text{ MPa}$, not only the filling rate did not change considerably but also the thickness sharply decreased.

Furthermore, reducing the die fillet radius led to decreased sheet material flow to the die cavity and significantly increased sheet thinning. Noteworthy, the specimen was cracked in a die fillet radius of 0.1 mm, while the fillet radius of about 0.2 mm was acceptable.

The sheet thickness extremely reduced with the growth of the pin height to diameter ratio, which was due to an elevation in the extension ratio. Based on the obtained results, the pin height to diameter ratio of 0.33 and 0.4 generated the most desirable outcomes.

The deformation mechanism by the HMGF process is time-dependent. As a result, augmenting the forming time could increase the die filling rate. It is observed that the forming time of 1000-2000 s could be suitable for forming AA8111 bipolar plates.

5. ACKNOWLEDGMENTS

The authors acknowledge the funding support provided by Babol Noshirvani University of Technology through Grant number BNUT/370203/97.

6. REFERENCES

- Hermann, A., Chaudhuri, T., Spagnol, P., "Bipolar plates for PEM fuel cells: A review", *International Journal of Hydrogen Energy*, Vol. 30, No. 12, (2005) 1297-1302. DOI: 10.1016/j.ijhydene.2005.04.016
- Li, X., Sabir, I., "Review of bipolar plates in PEM fuel cells: Flow-field designs", *International Journal of Hydrogen Energy*, Vol. 30, No. 4, (2005) 359-371. DOI: 10.1016/j.ijhydene.2004.09.019
- Weil, K. S., Xia, G., Yang, Z. G., Kim, J. Y., "Development of a niobium clad PEM fuel cell bipolar plate material", *International Journal of Hydrogen Energy*, Vol. 32, No. 16, (2007) 3724-3733. DOI: 10.1016/j.ijhydene.2006.08.041
- Mehta, V., Cooper, J. S., "Review and analysis of PEM fuel cell design and manufacturing", *Journal of Power Sources*, Vol. 114, No. 1, (2003) 32-53. DOI: 10.1016/S0378-7753(02)00542-6
- Koç, M., Mahabunphachai, S., "Feasibility investigations on a novel micro-manufacturing process for fabrication of fuel cell bipolar plates, Internal pressure-assisted embossing of micro-channels with in-die mechanical bonding", *Journal of Power Sources*, Vol. 172, No. 2, (2007) 725-733. DOI: 10.1016/j.jpowsour.2007.05.089
- Peng, L., Lai, X., Hu, P., Ni, J., "Flow channel shape optimum design for hydroformed metal bipolar plate in PEM fuel cell", *Journal of Power Sources*, Vol. 178, No. 1, (2008) 223-230. DOI: 10.1016/j.jpowsour.2007.12.037
- Liu, Y., Hua, L., "Fabrication of metallic bipolar plate for proton exchange membrane fuel cells by rubber pad forming", *Journal of Power Sources*, Vol. 195, No. 11, (2010) 3529-3535. DOI: 10.1016/j.jpowsour.2009.12.046
- Liu, Y., Hua, L., Lan, J., Wei, X., "Studies of the deformation styles of the rubber-pad forming process used for manufacturing

- metallic bipolar plates”, *Journal of Power Sources*, Vol. 195, No. 24, (2010) 8177–8184. DOI: 10.1016/j.jpowsour.2010.06.078
9. Hung, J. C., Lin, C. C., “Fabrication of micro-flow channels for metallic bipolar plates by a high-pressure hydroforming apparatus”, *Journal of Power Sources*, Vol. 206, (2012) 179-184. DOI: 10.1016/j.jpowsour.2012.01.112
 10. Belali-Owsia, M., Bakhshi-Jooybari, M., Hosseinipour, S. J., Gorji, A., “A new process of forming metallic bipolar plates for PEM fuel cell with pin-type pattern”, *International Journal of Advanced Manufacturing Technology*, Vol. 77, Nos. 5-8, (2015) 1281–1293. DOI: 10.1007/s00170-014-6563-3
 11. Mohammadtabar, N., Bakhshi-Jooybari, M., Hosseinipour, S. J., Gorji, A., “Feasibility study of a double-step hydroforming process for fabrication of fuel cell bipolar plates with slotted interdigitated serpentine flow field”, *International Journal of Advanced Manufacturing Technology*, Vol. 85, Nos. 1-4, (2016) 765–777. DOI: 10.1007/s00170-015-7960-y
 12. Ghadikolaee, H. T., Elyasi, M., Khatir, F. A., Hosseinzadeh, M., “Experimental investigation of Fracture in rubber pad forming of bipolar plate’s micro channels”, *Procedia Engineering*, Vol. 207, (2017) 1647-1652. DOI: 10.1016/j.proeng.2017.10.1093
 13. Oraon, M., Sharma, V., “Predicting Force in Single Point Incremental Forming by Using Artificial Neural Network”, *International Journal of Engineering, Transactions A: Basics*, Vol. 31, No. 1, (2018) 88-95. DOI: 10.5829/ije.2018.31.01a.13
 14. Tabatabaiea, S. M. R. Alasvand Zarasvand, K., “Investigating the Effects of Cold Bulge Forming Speed on Thickness Variation and Mechanical Properties of Aluminium Alloys: Experimental and Numerical”, *International Journal of Engineering, Transactions C: Aspects*, Vol. 31, No. 9, (2018) 1602-1608. DOI: 10.5829/ije.2018.31.09c.17
 15. Rahmania, F., Seyedkashi, S. M. H., Hashemi, S. J., “Experimental Study on Warm Incremental Tube Forming of AA6063 Aluminum Tubes”, *International Journal of Engineering, Transactions C: Aspects*, Vol. 33, No. 9, (2020) 1773-1779. DOI: 10.5829/ije.2020.33.09c.11
 16. Alijani Renani, H., Haji Aboutalebi, F., “Evaluation of Ductile Damage Criteria in Warm and Hot Forming Processes”, *International Journal of Engineering, Transactions A: Basics*, Vol. 29, No. 10, (2016) 1441-1449. DOI: 10.5829/ije.2016.29.10a.15
 17. Chausov, M., Pylypenko, A., Berezin, V., Volyanska, K., Maruschak, P., Hutsaylyuk, V., Markashova, L., Nedoseka, S., Menou, A., “Influence of dynamic non-equilibrium processes on strength and plasticity of materials of transportation systems”, *Transport*, Vol. 33, No. 1, (2018) 231-241. DOI: 10.3846/16484142.2017.1301549
 18. Lim, S. S., Kim, Y., Kang, C., “Fabrication of aluminum 1050 micro-channel proton exchange membrane fuel cell bipolar plate using rubber-pad-forming process”, *International Journal of Advanced Manufacturing Technology*, Vol. 65, Nos. 1-4, (2013) 231–238. DOI: 10.1007/s00170-012-4162-8
 19. Li, Z., Qu, H., Chen, F., Wang, Y., Tan, Z., Kopec, M., Wang, K., Zheng, K., “Deformation Behavior and Microstructural Evolution during Hot Stamping of TA15 Sheets: Experimentation and Modelling”, *Materials* Vol. 12, (2019), 223-236. DOI: 10.3390/ma12020223
 20. Roohi, A. H., Hashemi, S. J., Allahyari, M., “Hot metal gas forming of closed-cell aluminum foam sandwich panels”, *Transactions of the Indian Institute of Metals*, Vol. 73, (2020) 2231-2238. DOI: 10.1007/s12666-020-02027-2
 21. Kwon, H. J., Jeon, Y. P., Kang, C. G., “Effect of progressive forming process and processing variables on the formability of aluminum bipolar plate with microchannel”, *International Journal of Advanced Manufacturing Technology*, Vol. 65, Nos. 5-8, (2013) 681–694. DOI: 10.1007/s00170-012-4033-3
 22. Palumbo, G., Piccininni, A., “Numerical-experimental investigations on the manufacturing of an aluminum bipolar plate for proton exchange membrane fuel cells by warm hydroforming”, *International Journal of Advanced Manufacturing Technology*, Vol. 69, Nos. 1-4, (2013) 731–742. DOI: 10.1007/s00170-013-5047-1
 23. Esmaeili, S., Hosseinipour, S. J., “Experimental investigation of forming metallic bipolar plates by hot metal gas forming (HMGF)”, *SN Applied Science*, Vol. 1, No. 2, (2019) 187-191. DOI: 10.1007/s42452-019-0202-4
 24. Kargar-Pishbijari, H., Hosseinipour, S. J., Jamshidi Aval, H., “A novel method for manufacturing microchannels of metallic bipolar plate fuel cell by the hot metal gas forming process”, *Journal of Manufacturing Processes*, Vol. 55, (2020) 268-275. DOI: 10.1016/j.jmapro.2020.04.040
 25. Giuliano, G., Franchitti, S., “On the evaluation of superplastic characteristics using the finite element method”, *International Journal of Advanced Manufacturing Technology*, Vol. 47, Nos. 3-4, (2007) 471-476. DOI: 10.1016/j.ijmactools.2006.06.009
 26. Giuliano, G., Franchitti, S., “The determination of material parameters from superplastic free-bulging tests at constant pressure”, *International Journal of Machine Tools and Manufacture*, Vol. 48, Nos. 12-13, (2008) 1519-1522. DOI: 10.1016/j.ijmactools.2008.05.007
 27. Shamsi-Sarband, A., Hosseinipour, S. J., Bakhshi-Jooybari, M., Shakeri, M., “The effect of geometric parameters of conical cups on the preform shape in two-stage superplastic forming process”, *Journal of Materials Engineering and Performance*, Vol. 22, (2013), 3601-3611. DOI: 10.1007/s11665-013-0636-6
 28. Hojjati, M., Zoorabadi, M., Hosseinipour, S. J., “Optimization of superplastic hydroforming process of Aluminum alloy 5083”, *Journal of Materials Processing Technology*, Vol. 205, (2008), 482-488. DOI: 10.1016/j.jmatprotec.2007.11.208

Persian Abstract

چکیده

در این مقاله تغییر شکل یک ورق نازک از آلایز آلومینیوم AA ۸۱۱۱ برای ساخت صفحه دو قطبی برای پیل سوختی PEM با الگوی بین شکل با استفاده از فرایند شکل‌دهی داغ فلز با گاز (HMGF) بررسی شد. اثرات فشار گاز، زمان شکل‌دهی، قطر پین، ارتفاع پین و شعاع فیلت، بر پروفیل و توزیع ضخامت نمونه‌ها با استفاده از روش اجزای محدود با استفاده از نرم افزار ABAQUS 6.10 مورد مطالعه قرار گرفت. درستی شبیه‌سازی اجزای محدود با آزمایشات تجربی تایید گردید. نتایج نشان می‌دهد که با افزایش فشار گاز بیش از ۴ مگاپاسکال، سرعت نازک شدن به شدت افزایش یافت. با کاهش شعاع فیلت به کمتر از ۰/۲ میلی متر، نمونه شکسته شد. با افزایش زمان شکل‌دهی به بیش از ۱۰۰۰ ثانیه، نرخ افزایش پرشدگی کم می‌شود. علاوه بر این، کاهش ضخامت با افزایش نسبت ارتفاع به قطر پین به بیش از ۰/۴ به شدت افزایش یافت. سرانجام، نمونه‌های کاملی در آزمایشات تولید شد که امکان ساخت صفحات دو قطبی نازک بین شکل از آلایز آلومینیوم AA ۸۱۱۱ را با فرایند HMGF تأیید می‌کند.



Analysis of a New Linear Dual Stator Consequent Pole Halbach Array Flux Reversal Machine

N. Arish, H. Yaghobi*

Faculty of Electrical and Computer Engineering, Semnan University, Semnan, Iran

PAPER INFO

Paper history:

Received 27 February 2021

Received in revised form 15 June 2021

Accepted 10 July 2021

Keywords:

Finite Element Method

Halbach Array

Linear Machine

Magnetic Orientation

Pm Machine

ABSTRACT

The permanent magnet machine has attracted much attention due to its high torque density at low speed and simple configuration. This feature is due to many magnetic pole pairs that flux in the air gap can be significantly changed with the smallest motion of the moving. In this paper, a linear dual stator flux reversal permanent magnet machine (LDSFRPMM) with toroidal winding is presented, which magnets embedded with Halbach and simple array on the translator and stator, respectively. The innovation of this structure over a conventional machine is the addition of a magnet between the stator teeth with the appropriate magnetic orientation, and finding the best width of permanent magnet on the stator and a change of the type of winding from the concentrated to the toroidal. By implementing these changes on a conventional machine, the main parameters of the machine such as back electromotive force (EMF), thrust force, power factor and permanent magnetic (PM) flux are increased which improves the performance of the proposed machine.

doi: 10.5829/ije.2021.34.08b.21

1. INTRODUCTION

In recent years, linear flux reversal permanent magnet machine (LFRPMM) has received considerable research attention. Vernier machine is flag-bearer of this category due to generating high thrust force at the low speed [1, 2]. This feature exists because of numerous magnetic poles which are known as magnetic gearing effect [3, 4]. Generating a high thrust force at the low speed is very efficient in direct drive applications such as wave energy conversion and linear transportation [5, 6]. However, the first linear permanent magnet Vernier machine suffered from poor power factor due to high leakage flux [7]. During the years, scientists have reduced the weakness of the permanent magnetic Vernier machine with a different design. Dual stator spoke array permanent magnet (PM) is one of the most popular designs which is very effective to achieve high power factor, high thrust force and low leakage flux [8]. Recently, engineers by using special material such as superconductor and soft magnetic composite (SMC) improve performance of proposed LDSFRPMM. High-temperature superconductor (HTS) material has been used in electric machines because of

high-current tolerance and property of the shield leakage flux [9-12]. Also, SMC material has been used in the structures of PM machine to improve performance of proposed LDSFRPMM in terms of losses and temperature [13, 14]. Copper loss is an important parameter in electrical machine and is significantly related to the type of winding. Based on literature [15, 16], because of the particular type of winding, copper losses in the proposed LDSFRPMM remarkably reduced and thrust force increased. An increase in the volume of the PM and correct selection of the shape of magnet and magnetic direction can improve the performance of the proposed machine [17]. In the various types of structures, magnets are used in the form of simple [18], spoke array [19], skew [20], hybrid [21, 22] and Halbach array [23] to improve the main parameter of the proposed machine. A permanent magnet Vernier machine has been proposed Shi et al. [24] and Fan et al. [25]. So that, with an increase in the volume of the PM, air-gap magnetic field, back-EMF and power factor are increased in the proposed machine. Liu et al. [26] by integrating Halbach array leakage flux and the efficiency of the proposed machine have reduced and increased, respectively. Zhao et al. [27]

*Corresponding Author Email: yaghobi@semnan.ac.ir (H.Yaghobi)

by dividing the PM into the very small segment as Halbach array in various magnetic orientation back EMF, thrust force and flux density raised. Nematsaberi and Faiz [28] by changing the simple array to the spoke array PM and applying non-magnetic material the thrust force and PF have increased. The target of this paper is proposing a new LDSFRPMM with toroidal winding and a special arrangement of PM to improve the weaknesses of conventional LDSFRPMM. In the proposed LDSFRPMM magnet with Halbach array is mounted on the translator and simple magnet with correct width and effective orientation is embedded on the stator and winding has changed from concentrated to toroidal. So that, the magnetic orientation of the PM mounted on the stator is the same as the magnetic orientation of the middle part of the magnet with the Halbach array on the translator. In this structure PM flux, air gap flux density, thrust force, power factor and back-EMF are increased which causes the increase of the performance of the proposed LDSFRPMM.

2. MACHINE CONFIGURATION AND OPERATION

Ndfe35 PM with Halbach array is a specific arrangement that compound with several directions like vertical and horizontal. The conclusion of the combination of these two different magnetic directions, is that the intensity of the magnetic field on one side is highly stronger than the other side. All possible magnetic structures such as vertically, horizontally and Halbach are shown in Figure 1. As can be seen, the magnetic field vectors produced by the magnets are symmetric in structures (a) and (b), but in structure (c), they are asymmetric and the magnetic field is stronger on one side than on the other which using this feature properly can improve machine performance. By simultaneous use of magnets on stator and translator and proper combination of their magnetic orientation, the proposed LDSFRPMM can reach the ideal sinusoidal magnetic flux, which increases thrust force, PM flux and back-EMF. The proposed LDSFRPMM is designed based upon the conventional LDSFRPMM, which is shown in Figure 2. As can be seen, the main difference between conventional LDSFRPMM and the proposed LDSFRPMM is that there is no magnet on the stator of conventional LDSFRPMM and winding in the proposed LDSFRPMM turns into toroidal from concentrated. So that, in the toroidal winding, each phase consists of one coil, and in the concentrated winding, each phase comprises four coils. Translator is divided into three equal parts, which make the phases separated from each other, and each part consists of four major teeth which each of them are divided into three splits for modulation of the flux. The surface of the translator has been covered by a Halbach array composed of the same three magnets with different directions, the central one is vertically magnetized, and the two other sides are horizontally magnetized. PM applied between slots of the stator is

magnetized in perpendicular upward and downward directions. The main operation of both machines is based on the effect of the magnetic gear. Because of this effect, with a small displacement of the translator, the flux in the air gap changes rapidly and causes at the low speed to be able to generate high thrust force. The teeth of the stator modulate the PM field to provide an effective magnetic field so that a higher velocity of the field than that of the translator, improves the thrust force. The relation is illustrated by Arish et al. [11] and Yao et al. [29]:

$$\frac{p_{pm}}{s} = N_s \pm p \tag{1}$$

where P_{pm} , P and N_s are the number of pole pairs on the translator, the number of winding pole pairs and the

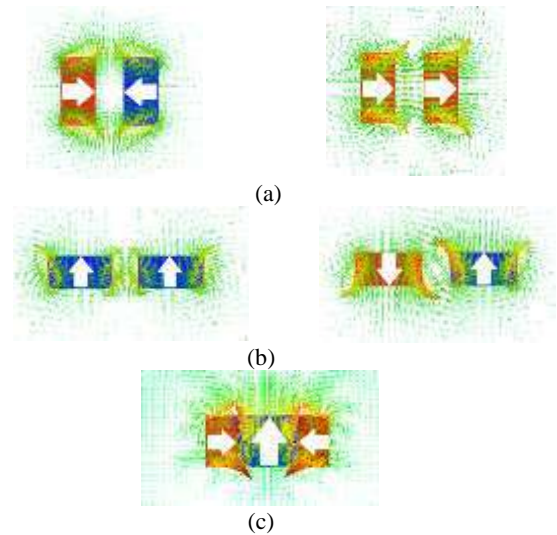


Figure 1. Magnet Structure. (a) Horizontal array, (b) Vertical array, (c) Halbach array

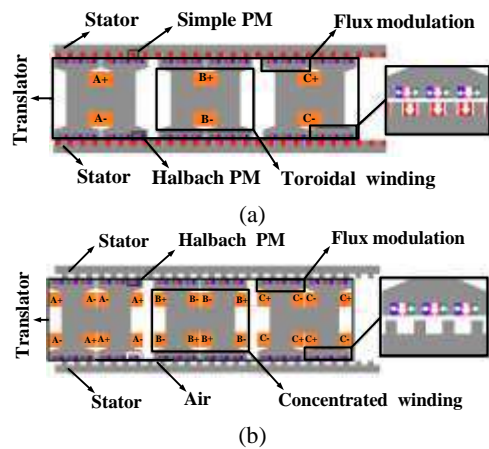


Figure 2. Machine structure. (a) Proposed LDSFRPMM, (b) Conventional LDSFRPMM

number of stator flux modulation teeth respectively in the proposed LDSFRPMM. Magnetic gear ratio is an important design index for the select of slot and pole combinations during the early stages of the machine design. Increasing gear ratio enhances thrust force and back-EMF capability. High thrust force can be achieved with the high number of poles, this typically causes higher leakage flux.

3. PERFORMANCE EVALUATION

In FEM for two machines, the permeability of the iron core is based on practical data, so iron core is laminated and the iron saturation is considered. Adding a magnet on the stator may cause the machine to saturate, which is why it is important to choose the correct magnet width added to the machine. Figure 3 shows the back-EMF and detent force variations based on the millimeter changes of the magnet's width. With magnet's width increases, the trend of detent force is increased too. The magnet width is chosen so that the proposed LDSFRPMM has the low detent force and the highest back-EMF. It should also be noted that the width of the selected magnet does not cause the saturation of the proposed LDSFRPMM. According to the description given, the best selection width is 7 mm. So that for high performance, the magnet width of the Halbach array should satisfy the following relation [3]:

$$w_v + 2w_h < \tau_s \tag{2}$$

$$w_h \leq w_v \tag{3}$$

where w_v , w_h and τ_s are the width of the bigger part of Halbach PM, width of the smaller part of Halbach PM and pole pitch, respectively. To generate a sinusoidal magnetic field in the air-gap, the width of horizontally magnetized PM should be smaller than vertically magnetized PM. The corresponding mesh of the proposed LDSFRPMM is shown in Figure 4. In order to obtain precise accuracy, more than 10000 meshes in several layers were created and calculated. All the design parameters of the proposed LDSFRPMM and the conventional LDSFRPMM are the same, including current density, translator pole pairs, magnetic gear ratio, the material of the core and air gap length. Design parameter of the proposed LDSFRPMM is shown in Figure 5 and listed in Table 1.

3. 1. Magnetic Field and Air Gap Flux Distribution

The air gap magnetic flux density is directly commensurate to the PM pole pairs in the Vernier machine and generate at the no load state. It is the interaction of the magnetic field generation with the teeth of stator and translator. Figure 6 depicts the waveforms of the air gap magnetic flux, the maximum of magnetic

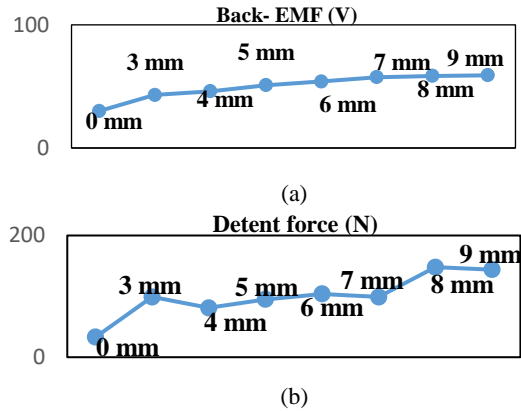


Figure 3. Variation of the back-EMF and detent force respect to width of PM. (a) Back-EMF. (b) Detent force

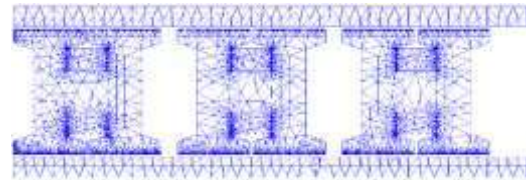


Figure 4. The corresponding mesh of the proposed LDSFRPMM

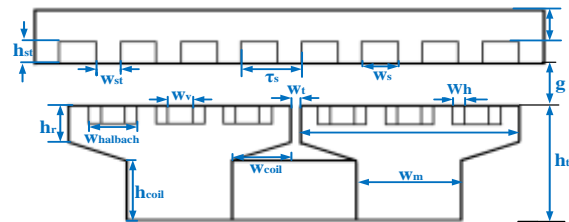


Figure 5. Design parameters of proposed LDSFRPMM

TABLE 1. The design parameter of the proposed LDSFRPMM

Items	Unit	LDSFRPMM
Speed	m/s	1.5
w_h	mm	3
w_v	mm	6
g	mm	2
w_y	mm	10
w_m	mm	26
w_{st}	mm	6
h_{st}	mm	6
h_r	mm	10
h_t	mm	32
w_s	mm	9
w_{coil}	mm	14
h_{coil}	mm	17
$w_{halbach}$	mm	12
τ_s	mm	15

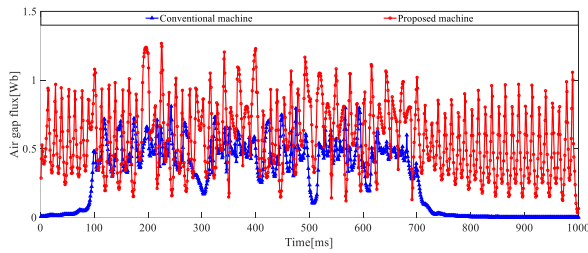


Figure 6. Comparison of the air gap magnetic flux

flux in the air gap for the proposed LDSFRPMM and conventional LDSFRPMM is 1.26 T and 0.81 T, respectively. Hence, the air gap magnetic flux in the proposed LDSFRPMM is 55% higher than the conventional LDSFRPMM. This increase is due to the increased volume of magnets used in the proposed LDSFRPMM. The air gap flux density waveform shows that there is 360 mm effective length, so it contains 24 numbers of the active teeth of the stator. Flux line distribution at the no-load is generated only by PM, and it is shown in Figures 7(a) and 7(b) for two models. It expresses that the flux lines of the three modules in the two models are autonomous. Thus, the field distributions in one phase do not affect relatively on the other phase, therefore the LDSFRPMM possess the excellent fault-tolerant capability. Density of the flux line due to adding the magnet on the stator and changing the type of winding in the proposed LDSFRPMM is higher magnetic flux distribution at full load for the two models generated by PM and armature current simultaneously. Figures 7(c) and 7(d) show magnetic flux distribution at full load for two models. It is evident that the magnetic flux distribution in the proposed LDSFRPMM is higher than conventional LDSFRPMM and maximum magnetic flux density for both models is less than 2. Figure 8 shows the PM flux of two models. PM flux in the proposed LDSFRPMM is generated by PM at the no-load. It is clear that the peak of the PM flux in the proposed LDSFRPMM is higher than the conventional LDSFRPMM, so RMS of the PM flux in the proposed LDSFRPMM and conventional LDSFRPMM are 0.057 Wb and 0.014 Wb, respectively. With an increase in PM flux, the back-EMF also increases accordingly and this improves the power factor and output power of the proposed LDSFRPMM.

3. 2. Back-EMF The relative motion between the translator and stator is caused by the external vibration and magnetic flux through in the air gap will change. Base on the Faraday’s law of the electromagnetic induction, the back-EMF will be generated in the coil. The phase’s back-EMF can be defined as:

$$EMF = \frac{d\psi}{dt} = \frac{d\psi}{dx}v \tag{4}$$

where, ψ and x are PM flux and displacement, respectively. It is obvious that back-EMF is derivation of PM flux relative to time or derivation of PM flux relative to displacement multiply to velocity. Thus, the back-EMF is only affiliated to the change of PM flux. Figure 9 shows no load back-EMF waveforms for two models. It is obvious which waveform of the back-EMF is purely sinusoidal and acceptable. Because back-EMF is derivation of PM flux, DC part of the PM flux is entirely omitted in the waveforms of back-EMF. The maximum

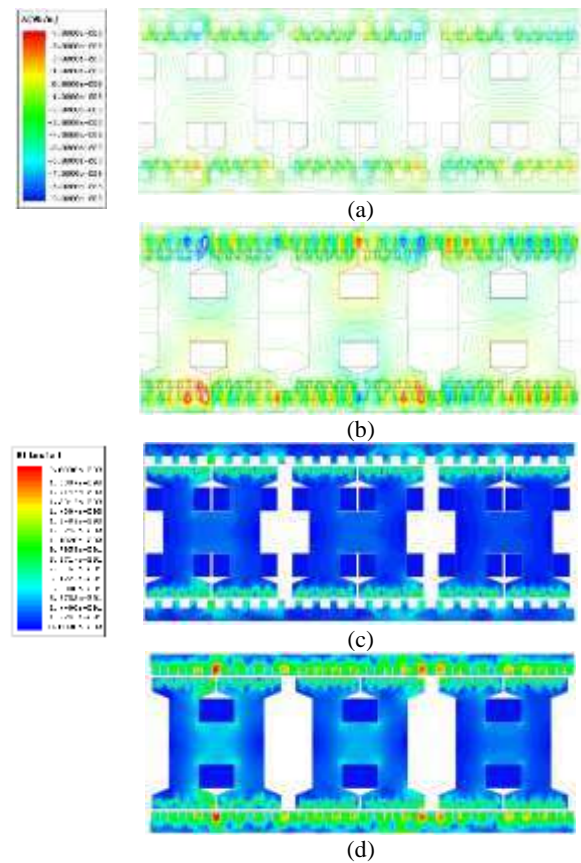


Figure 7. Comparison of the flux density distribution. (a) Flux line distribution in the conventional LDSFRPMM at no load, (b) Flux line distribution in the proposed LDSFRPMM at no load, (c) Magnetic flux distribution in the conventional LDSFRPMM at full load, (d) Magnetic flux distribution in the proposed LDSFRPMM at full load

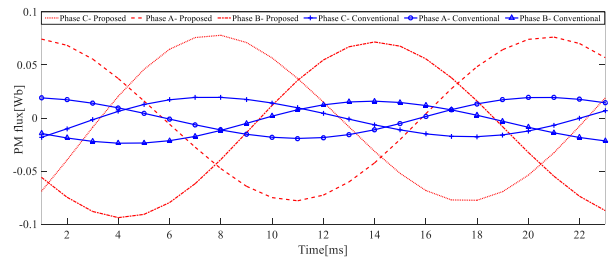


Figure 8. Comparison of the PM flux

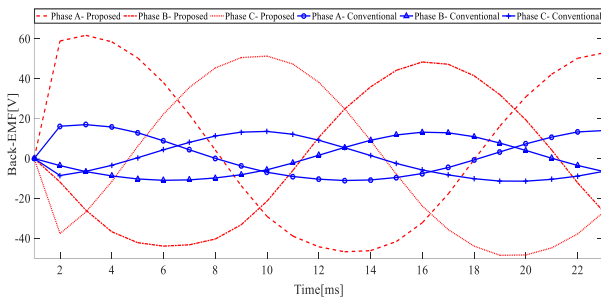


Figure 9. Comparison of the back-EMF

of the back-EMF at no load for the proposed LDSFRPMM and conventional LDSFRPMM is 61 V and 17 V, respectively.

In other words, maximum of the back-EMF for the proposed LDSFRPMM is significantly higher than the conventional LDSFRPMM, since the PM volume increases.

3. 3. Self-inductance and Mutual-inductance

Self inductance and mutual inductance of the proposed LDSFRPMM and conventional LDSFRPMM are shown in Figure 10. It is obvious that the self-inductance depends on the translator's position and type of winding.

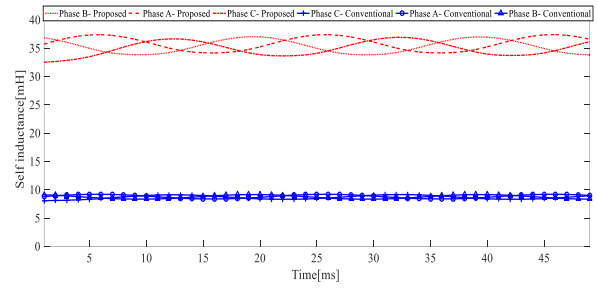
The average of three phases self inductance in the proposed LDSFRPMM and conventional is 35 mH and 8 mH, respectively. As can be seen, the average of three phases self inductance in conventional LDSFRPMM is much less than the proposed LDSFRPMM. Mutual inductance in the proposed LDSFRPMM and conventional LDSFRPMM is approximately equal to zero and mutual inductance between phase a and phase c is lower than two other phases. This is due to the distance between phase a and phase c is longer than two other phases. Because, three phases in both machines are separated and they do not have much impact on each others.

3. 4. Power Factor

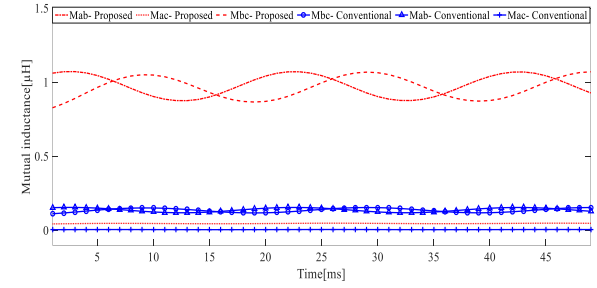
The classical approach of computing power factor is using phasor diagram which is employed in this paper with irrespective of the stator resistance. Power factor (PF) in LPMVM is given by with assuming that the current i_d is zero [8]:

$$PF = (1 + \frac{L_s I}{\psi})^{-0.5} \tag{5}$$

where I is the RMS of the phase current and L_s is the synchronous inductance. As can be seen, the major reason for low power factor according to the Equation (5) is high synchronous inductance and low PM flux. The proposed LDSFRPMM can reach high PM flux, because of the increase of volume of the PM and correct magnetic direction of PM. It is true that by converting the winding from the concentrated to the toroidal, the inductance



(a)



(b)

Figure 10. Comparison of inductance. (a) Self inductance. (b) Mutual inductance

increases and this reduces the power factor. But, an increase in the PM flux is much greater than the inductance increase, which according to Equation (5), since the flux is in the denominator of the fraction; generally the power factor is improved.

3. 5. Thrust Force and Detent Force

The electromagnetic force for all phases can be defined as follows [3]:

$$F_{ele} = i \frac{d\psi}{dx} + \frac{1}{2} i^2 \frac{dL}{dx} + \frac{d}{dx} (\frac{1}{2} i^2 L) \tag{6}$$

The first term in Equation (6) is the force generation by PM field and other terms are the forces arising from the position dependent inductances. Hence, the inductance variations with translator position in the proposed LDSFRPMM may give increase to fluctuating force. For both models, the thrust force can be given by Botha et al. [31]:

$$F_{thrust} = F_{ele} + F_{detent} \tag{7}$$

Detent force is a drawback for the linear machine which leads to mechanical vibration and noise for the machine. Then, minimizing detent force is an important requirement for linear machine design. Detent force in linear permanent magnet machine is appeared by two main reasons: 1- slot effect 2- end effect. Slot effect in the linear machine is caused by the interaction of PMs and the iron teeth. Also, the end effect is caused by the finite stator core length and has an impact on phase a and

phase c. Therefore, the electromagnetic parameters of phase b are higher than other phases. Figures 11(a) and 11(b) depict the detent force and thrust force for both models at the no-load and full load, respectively. As can be seen, the value of the detent force in the proposed LDSFRPMM is higher than conventional LDSFRPMM, but the average of thrust force in the proposed LDSFRPMM is higher than conventional LDSFRPMM and average of the thrust force for the proposed LDSFRPMM and conventional LDSFRPMM is 415 N and 50 N, respectively. High thrust force density of the proposed LDSFRPMM is due to the increase of volume of the PM and type of winding which causes flux density in yoke of the proposed LDSFRPMM be higher than yoke of conventional LDSFRPMM. High ripple force reduces machine performance, when the d-axis current is zero, the ripple of thrust force is obtained [32]:

$$F_{\text{thrust}} = \frac{F_{\text{max}} - F_{\text{min}}}{F_{\text{avg}}} \times 100\% \quad (8)$$

where, F_{max} is maximum thrust force, F_{min} is minimum thrust force, and F_{avg} is average thrust force. The ripple of thrust force in the proposed LDSFRPMM is a little higher than conventional LDSFRPMM which it is non-important at the low speed. It should be noted that with the increase of the PM volume, PM flux, back-EMF, thrust force, power factor and air gap flux density increase too. For a better comparison, the electromagnetic parameters of the proposed LDSFRPMM and conventional LDSFRPMM are presented in Table 2.

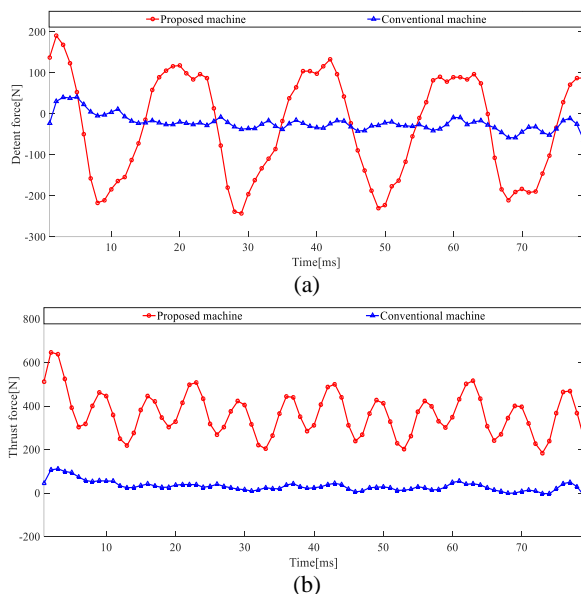


Figure 11. Comparison of force. (a) Detent force, (b) Thrust force

TABLE 2. Electromagnetic performance comparison

Item	Proposed LDSFRPMM	Conventional LDSFRPMM
Air gap flux density (T)	1.26	0.81
PM flux linkage (Wb)	0.057	0.014
Back-EMF (V)	61	17
Self-inductance (mH)	35	8
Thrust force (N)	415	50

4. CONCLUSION

This paper proposes a new LDSFRPMM topology with toroidal winding which simple PM with correct orientation and width is mounted on the stator and Halbach array PM is mounted on the translator. This paper shows the importance of width of magnet and winding arrangement. Electromagnetic performance of the proposed LDSFRPMM was compared to conventional LDSFRPMM by FEM in terms of back-EMF, thrust force, detent force, inductance, power factor, air gap flux density and PM flux. According to the obtained results of FEM, the novelty improved the performance of the proposed LDSFRPMM compared to conventional LDSFRPMM. So that, airgap flux density in the proposed LDSFRPMM and conventional LDSFRPMM is 1.26 T and 0.81 T, respectively. PM flux in the proposed LDSFRPMM and conventional LDSFRPMM is 0.057 Wb and 0.014 Wb, respectively. Back-EMF in the proposed LDSFRPMM and conventional LDSFRPMM is 61 V and 17 V, respectively. Inductance in the proposed LDSFRPMM and conventional LDSFRPMM is 35 mH and 8 mH, respectively. Thrust force, in the proposed LDSFRPMM and conventional LDSFRPMM, is 415 N and 50 N, respectively. In addition, the thrust force of the proposed LDSFRPMM has a significant increase compared to the conventional LDSFRPMM.

5. REFERENCES

1. Toba, A., and T. A. Lipo. "Novel Dual-Excitation Permanent Magnet Vernier Machine" Conference Record of the 1999 IEEE Industry Applications Conference. Thirty-Forth IAS Annual Meeting, Vol. 4, (1999), 2539-2544, doi:10.1109/IAS.1999.799197.
2. Raza, M., Zhao, W., Lipo, T.A. and Kwon, B.I., "Performance Comparison of Dual Airgap and Single Airgap Spoke-Type Permanent-Magnet Vernier Machines." *IEEE Transactions on Magnetics*, Vol. 53, No. 6, (2017), doi:10.1109/TMAG.2017.2669105.
3. Ji, J., Zhao, W., Fang, Z., Zhao, J. and Zhu, J., "A Novel Linear Permanent-Magnet Vernier Machine With Improved Force Performance" *IEEE Transactions on Magnetics*, Vol. 51, No. 8, (2015), doi:10.1109/TMAG.2015.2416123.
4. Ho, S.L., Niu, S. and Fu, W.N. "Design and Comparison of

- Vernier Permanent Magnet Machines" *IEEE Transactions on Magnetics*, Vol. 47, No. 10, (2011), 3280-83, doi:10.1109/TMAG.2011.2157309.
5. Faiz, J. and A. R. Nematsaberi. "Linear Electrical Generator Topologies for Direct-Drive Marine Wave Energy Conversion-an Overview" *IET Renewable Power Generation*, Vol. 11, No. 9, (2017), 1163-76, doi:10.1049/iet-rpg.2016.0726.
 6. Du, Y., Cheng, M., Chau, K.T., Liu, X., Xiao, F. and Zhao, W., "Linear Primary Permanent Magnet Vernier Machine for Wave Energy Conversion" *IET Electric Power Applications*, Vol. 9, No. 3, (2015), 203-212, doi:10.1049/iet-epa.2014.0138.
 7. Li, X., tong Chau, K., Cheng, M., Kim, B. and Lorenz, R.D. "Performance Analysis of a Flux-Concentrating Field-Modulated Permanent-Magnet Machine for Direct-Drive Applications" *IEEE Transactions on Magnetics*, Vol. 51, No. 5, (2015), doi:10.1109/TMAG.2014.2374553.
 8. Li, D., Qu, R. and Lipo, T.A., "High-power-factor vernier permanent-magnet machines" *IEEE Transactions on Industry Applications*, Vol. 50, No. 6, (2014), 3664-3674. DOI:10.1109/TIA.2014.2315443.
 9. Ardestani, M., Arish, N. and Yaghoobi, H., "A new HTS dual stator linear permanent magnet Vernier machine with Halbach array for wave energy conversion" *Physica C: Superconductivity and its Applications*, Vol. 567, No. 12, (2020). DOI:10.1016/j.physc.2019.1353593.
 10. Arish, N., "Electromagnetic performance analysis of linear vernier machine with PM and HTS-Bulk" *Physica C: Superconductivity and its Applications*, Vol. 579, (2020). doi.org/10.1016/j.physc.2020.1353751
 11. Arish, N., Ardestani, M., and Hekmati, A., " Study on the optimum structure of the rotor slot shape for a 20-kW HTS", *Physica C: Superconductivity and its Applications*, Vol. 567, (2021), doi.org/10.1016/j.physc.2021.1353829.
 12. Arish, N., Marignetti, F and Yazdani-Asrami, M. " Comparative study of a new structure of HTS-bulk axial flux-switching machine" *Physica C: Superconductivity and its Applications*, Vol. 584, (2021). doi.org/10.1016/j.physc.2021.1353854
 13. Marignetti, F., Colli, V.D. and Coia, Y., "Design of Axial Flux PM Synchronous Machines through 3-D Coupled Electromagnetic Thermal and Fluid-Dynamical Finite-Element Analysis" *IEEE Transactions on Industrial Electronics*, Vol. 55, No. 10, (2008), 3591-3601, doi:10.1109/TIE.2008.2005017.
 14. Kim, C.W., Jang, G.H., Kim, J.M., Ahn, J.H., Baek, C.H. and Choi, J.Y., "Comparison of Axial Flux Permanent Magnet Synchronous Machines with Electrical Steel Core and Soft Magnetic Composite Core" *IEEE Transactions on Magnetics*, Vol. 53, No. 11, (2017), 1-4., doi:10.1109/TMAG.2017.2701792.
 15. Bian, F. and Zhao, W., "A new dual stator linear permanent-magnet vernier machine with reduced copper loss", *AIP Adv*, Vol. 7, No. 5, (2017). DOI:10.1063/1.4978589.
 16. Arish, N., Ardestani, M. and Teymoori, V., "Comparison of Dual Stator Consequent-Pole Linear Permanent Magnet Vernier Machine with Toroidal and Concentrated Winding" 2020 11th Power Electronics, Drive Systems, and Technologies Conference, PEDSTC 2020, (2020), doi:10.1109/PEDSTC49159.2020.9088384.
 17. Arish, N. and Marignetti, F. "Evaluation of Linear Permanent Magnet Vernier Machine Topologies for Wave Energy Converters" *International Journal of Engineering, Transactions B: Applications*, Vol. 34, No. 2, (2021) 403-413, doi:10.5829/IJE.2021.34.02B.12
 18. Almoraya, A.A., Baker, N.J., Smith, K.J., and Raihan, M.A.H., "Design and Analysis of a Flux-Concentrated Linear Vernier Hybrid Machine with Consequent Poles", *IEEE Transactions on Industry Applications*, Vol. 55, No. 5, (2019), 4595-4604. DOI:org/10.1109/TIA.2019.2918499.
 19. Zhu, X., Ji, J., Xu, L. and Kang, M., "Design and Analysis of Dual-Stator PM Vernier Linear Machine with PMs Surface-Mounted on the Mover" *IEEE Transactions on Applied Superconductivity*, Vol. 28, No. 3 2018, doi:10.1109/TASC.2017.2786713.
 20. S. Khaliq, F. Zhao and B. Kwon, "Design and analysis of a dual stator spoke type linear vernier machine for wave energy extraction," 2015 IEEE International Magnetics Conference, (2015), doi: 10.1109/INTMAG.2015.7157480
 21. Arish, N., Teymoori, V., Yaghoobi, H. and Moradi, "Design of New Linear Vernier Machine with Skew and Halbach Permanent Magnet for Wave Energy Converters." 34th International Power System Conference, PSC 2019, (2019), doi:10.1109/PSC49016.2019.9081549.
 22. Arish, N and Teymoori, V., "Development of Linear Vernier Hybrid Permanent Magnet Machine for Wave Energy Converter" *International Journal of Engineering, Transaction B: Applications*, Vol. 33, No. 5, (2020), 805-813. doi.org/10.5829/ije.2020.33.05b.12.
 23. Ho, S.L., Wang, Q., Niu, S. and Fu, W.N., "A Novel Magnetic-Geared Tubular Linear Machine with Halbach Permanent-Magnet Arrays for Tidal Energy Conversion" *IEEE Transactions on Magnetics*, Vol. 51, No. 11, (2015), doi:10.1109/TMAG.2015.2450720.
 24. Shi, C., Li, D., Qu, R., Zhang, H., Gao, Y. and Huo, Y., "A Novel Linear Permanent Magnet Vernier Machine with Consequent-Pole Permanent Magnets and Halbach Permanent Magnet Arrays." *IEEE Transactions on Magnetics*, Vol. 53, No. 11, (2017), doi:10.1109/TMAG.2017.2696559.
 25. Fan, H., Chau, K.T., Cao, L. and Jiang, C., Machine." *IEEE Transactions on Energy Conversion*, Vol. 33, No. 4, (2018), 2081-2090, doi:10.1109/TEC.2018.2848545.
 26. G. Liu, H. Zhong, L. Xu and W. Zhao, "Analysis and Evaluation of a Linear Primary Permanent Magnet Vernier Machine With Multiharmonics," in *IEEE Transactions on Industrial Electronics*, Vol. 68, No. 3, (2021), 1982-1993, doi: 10.1109/TIE.2020.2973888.
 27. Zhao, W., Zheng, J., Wang, J., Liu, G., Zhao, J. and Fang, Z., "Design and analysis of a linear permanent- magnet vernier machine with improved force density", *IEEE Transactions Industrial Electronics*, Vol. 63, No. 4, (2016), 2072-2082. doi.10.1109/TIE.2015.2499165.
 28. Nematsaberi, A. and Faiz, J., "A Novel Linear Stator-PM Vernier Machine With Spoke- Type Magnets", *IEEE Transactions on Magnetics*, Vol. 54, No. 11, (2018), 1-5. doi.org/10.1109/iraniancee.2019.878640.
 29. Yao, T., Zhao, W., Bian, F., Chen, L. and Zhu, X., "Design and Analysis of a Novel Modular-Stator Tubular Permanent-Magnet Vernier Motor." *IEEE Transactions on Applied Superconductivity*, Vol. 28, No. 3, (2018), doi:10.1109/TASC.2018.2797948.
 30. Li, D., Qu, R. and Zhu, Z., "Comparison of Halbach and Dual-Side Vernier Permanent Magnet Machines" *IEEE Transactions on Magnetics*, Vol. 50, No. 2, (2014), doi:10.1109/TMAG.2013.2280760.
 31. Botha, C.D., Kamper, M.J., Wang, R.J. and Sorgdrager, A.J., "Force Ripple and Cogging Force Minimisation Criteria of Single-Sided Consequent-Pole Linear Vernier Hybrid Machines." Proceedings - 2020 International Conference on Electrical Machines, ICEM 2020, (2020), doi:10.1109/ICEM49940.2020.9270845.
 32. Davari, H., and Y. Alinejad-Beromi. "Torque Ripple Reduction in Switched Reluctance Motors by Rotor Poles Shape and Excitation Pulse Width Modification." *Iranian Journal of Electrical and Electronic Engineering*, Vol. 16, No. 1, (2020), 122-129, doi:10.22068/IJEEE.16.1.122.

Persian Abstract

چکیده

ماشین آهنربای دائمی به دلیل تراکم گشتاور بالا در سرعت کم و پیکربندی ساده توجه بسیاری را به خود جلب کرده است. این ویژگی به دلیل تعداد زیادی جفت قطب مغناطیسی است که شار در شکاف هوا می تواند با کوچکترین حرکت متحرک به صورت قابل توجهی تغییر کند. در این مقاله، یک ماشین آهنربای دائمی شار برگشت استاتور دوپل خطی با سیم پیچ تورونیدال ارائه شده است که آهن ربا ها به ترتیب با آرایش هالباخ و ساده روی متحرک و استاتور نصب شده است. نوآوری این ساختار بر روی یک ماشین معمولی افزودن آهنربا بین دندانهای استاتور با جهت گیری مغناطیسی مناسب و تغییر نوع سیم پیچ از متمرکز به تورونیدال است. با اجرای این تغییرات بر روی یک ماشین معمولی، پارامترهای اصلی دستگاه مانند نیروی الکتروموتور، نیروی رانش، ضریب توان و شار مغناطیسی دائمی افزایش می یابد که باعث بهبود عملکرد ماشین پیشنهادی می شود.



Vibration Analysis as Useful Domain for detection of Bearing Fault Signals in Induction Motors

M. Tabasi, M. Ojaghi*, M. Mostafavi

Department of Electrical Engineering, University of Zanjan, Zanjan, Iran

PAPER INFO

Paper history:

Received 2 Desember 2020

Received in revised form 08 June 2021

Accepted 23 June 2021

Keywords:

Induction Motor

Bearing Fault

Fault Detection

Vibration Analysis

Vibration Signal

ABSTRACT

Due to widespread usage of induction motor (IM) in various industries, the requirement for its condition monitoring have been considerably raised. It is essential to detect faults that happened in IMs in a short time with high accuracy because they may cause considerable financial losses. Bearing faults contribute to a large percentage of IM failures. In this paper, vibration signal is analyzed for getting reliable indicator for faulty modes of the bearings of the IMs. The proper direction for measuring the vibration signal is analyzed first. This analysis showed that the fault-related vibration frequency components along the Z-axis, i.e. the axis perpendicular to the motor's installing surface, usually have the largest magnitude. Thus, it is recommended to measure the vibration signal in the Z-axis. Then, the bearing fault diagnosis using the vibration signal is investigated in various scenarios. The results confirm that the vibration indicators are not sensitive to environmental parameters like temperature and also load variation of the IM but the severity of the fault has a considerable influence on them.

doi: 10.5829/ije.2021.34.08b.22

NOMENCLATURE

f_{IR}	The vibration characteristic frequencies for the defect in the inner race	φ	Ball contact angle
f_{OR}	The vibration characteristic frequencies for the defect in the outer race	D_c	Mean diameter of the bearing
f_{CF}	The vibration characteristic frequencies for the defect in the cage	D_1	Inner diameter of the outer race
f_{BF}	The vibration characteristic frequencies for the defect in the balls	D_2	Outer diameter of the inner race
f_r	shaft rotational speed	D_b	Diameter of the balls
N_b	number of balls		

1. INTRODUCTION

Today, the trend towards induction machines (IMs), especially in the industry, is growing due to its simple configuration and high reliability. Although induction machines are very reliable, but they may encounter a variety of mechanical or electrical defects. The defects may either stem from the operation or exist inherently and they cause financial losses [1]. Therefore, condition monitoring and fault detection of IMs is a major issue and hence recently, a lot of researches are conducted in this regard. Some research showed that about 41 percent of total failures of induction motors are due to their bearing faults [2]. The bearing fault may occur in the manufacturing process or operation of the IM and it is

vital to detect quickly and accurately. The bearing faults may be detected by acoustic measurements, vibration measurements, temperature measurements, wear debris analysis, etc. [3-4].

Vibration measurement and analysis is the oldest method which can detect not only mechanical but also electrical faults with high accuracy. Different faults usually cause vibration with different frequencies in the IM. Therefore, the faults are detected by determining major frequencies of the vibration signal using spectrum analysis. However, while the vibration analysis brings numerous advantages, it requires installation measuring transducers on the motor body. Moreover, some resonant frequencies may affect the main vibration signal [5].

*Corresponding Author Institutional Email: mojaghi@znu.ac.ir (M. Ojaghi)

Spectral analysis is used in order to analyze the vibration through its characteristic frequencies [6]. The vibration is a complex motion and it is analyzed by spectral modulation to detect the bearing failures [7]. In other words, IM failures like bearing fault can be investigated by analyzing special characteristic frequencies in its vibration signal [8]. Thus, this method can be considered as an accurate and fast approach for the fault detection. The vibration analysis is examined as an efficient method for diagnosing electromagnetic problems in induction motors [9, 10]. Also, in order to perfectly predict mechanical faults, it was confirmed by Gangsar and Tiwari [11] that the analysis of the vibration signal is an efficient method and there is no need to analyze the electrical current signal.

Many studies have confirmed the role of vibration analysis in fault detection of induction motor. A vibration detection system is designed by Kuspiani et al. [12] that can be used for online monitoring of an induction motor. Induction motor vibration data is read from two vibration sensors and the results are analyzed by using artificial intelligence-based analysis. The partially damaged rotor bar under load changes using wavelet transform analysis is investigated by Rangel-Magdaleno et al. [13] and the required features are extracted from the vibration signals at different levels of failure. A squirrel cage induction motor is selected to predict its sound based on the results obtained through FFT analysis [14]. In this paper, the FFT results are compared with ISO standard vibration charts in order to consider preventative condition. Two diagnosis techniques are presented which are based on the stator current and the vibration using FFT [15]. The result of vibration analysis was as accurate as that of current analysis. A novel method entitled EMD-FFT was proposed by Moiz et al. [16] for vibration analysis of an IM. According to this method, the signal is decomposed into its intrinsic mode functions (IMFs) and then each IMF is analyzed by FFT. In addition, a comparison between the current and vibration based techniques is performed for the bearing fault detection and analysis [17].

Induction motor fault detection is investigated on the basis of the acoustic sound and vibration signals by Delgado-Arredondo et al. [18]. On that work, a method that is called the Complete Ensemble Empirical Mode Decomposition is used for decomposing the signal. Spectral analysis was proposed by Novoa et al. [19] for various frequencies in the motor vibration by using of Compact RIO equipment, LabVIEW, triaxle accelerometers, and low-pass filters. Moreover, a simulation system for unbalanced loading condition of a three-phase induction motor was proposed by Salah et al. [20]. An experimental study has been presented by Marignetti et al. [21] that focused on the vibration as well as acoustic noise emitted by the inverter-fed induction

motor. In this paper, a control technique based on the SVPWM is performed for using vibration and acoustic noise experimental analysis in order to control the phase voltages of a three-phase induction motor. Despite previous methods that were based on the detection of bearing fault occurrence, the time and frequency features of construct regression models were extracted for predicting the bearing faults [22].

In this paper, the aim is to investigate vibration domain for the bearing fault detection in the IMs through comprehensive laboratory test results. As shown in Figure 1, the vibration signal may be measured along with three perpendicular axes that are the X-, Y- and Z-axes. The vibration signals experimentally sampled in the three axes are first evaluated using frequency spectrum analysis to identify the most reliable direction for the vibration measurement aiming the bearing fault detection. The evaluation showed that the Z-axis, i.e. the axis perpendicular to the motor's installing surface, is the most reliable direction for this purpose. Then, the vibration signals measured in the Z-axis are used for analyzing the bearing fault-related frequency components to determine their sensitivity to the different bearing faults intensities as well as the load torque change and the temperature rise. According to the investigation results, the vibration frequency components are sensitive enough to detect and discriminate different bearing faults, while they are almost insensitive to the temperature rise and load torque change. Therefore, the main contribution and advantages achieved by this paper are as follows:

- Collecting and analyzing comprehensive experimental vibration test results in the three axes under different bearing fault types and severities, load torques and temperatures.
- Using the test results to determine the most reliable direction for measuring the vibration signal aiming the bearing fault detection.
- Using the test results to determine the sensitivity of the vibration frequency components to detect different bearing fault types.
- Using the test results to determine the most insensitive vibration frequency components to the load torque and temperature rise.

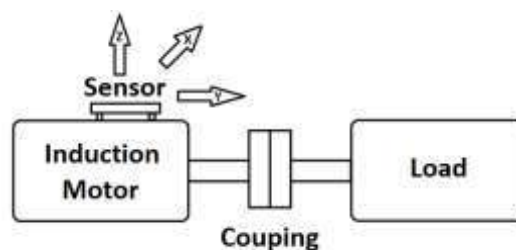


Figure 1. Three different directions on IM

The paper organization is as follows: Section 2 is dedicated to introduce various bearing fault types and their related vibration characteristic frequencies. The process of experimental test and its scenarios are explained in section 3. The examination and analysis of the experimental test results are presented in sections 4 and the conclusion is presented in section 5.

2. VIBRATION CHARACTERISTIC FREQUENCIES OF the BEARING FAULTS

Rolling-element bearings, which have radial loads, generate vibration even if they do not have any special defect geometrically. In fact, rolling motions in the bearing cause vibrational excitation in some frequencies [23]. However, geometrical defects, depending on their location, cause characteristic frequency components in the IM vibration. The values of the characteristic frequencies depend on the rotational frequency of the shaft as well as the geometrical parameters of the bearing, itself [2, 3]:

$$f_{IR} = \frac{f_r}{2} N_b \left(1 + \frac{D_b}{D_c} \cos \varphi\right) \quad (1)$$

$$f_{OR} = \frac{f_r}{2} N_b \left(1 - \frac{D_b}{D_c} \cos \varphi\right) \quad (2)$$

$$f_{CF} = \frac{f_r}{2} \left(1 - \frac{D_b}{D_c} \cos \varphi\right) \quad (3)$$

$$f_{BF} = \frac{D_c}{2D_b} f_r \left(1 - \left(\frac{D_b}{D_c} \cos \varphi\right)^2\right) \quad (4)$$

$$D_c = \frac{D_1 + D_2}{2} \quad (5)$$

φ is considered zero for deep groove ball bearings.

3. EXPERIMENTAL TEST SETUP AND PROCEDURE

In this section, the essential equipment for experimental tests is introduced and then the proposed research scenarios are explained. For getting laboratory test results, a 1-hp induction motor made by Motogen Co. (Tabriz, Iran) is used. Table 1 gives technical data of the IM. This IM incorporates two deep groove ball bearings with the code of 6204. In order to test with defective bearings, holes with different diameters are made on the inner race and outer race of similar bearings, and then these bearings are replaced, in turn, with the motor bearing at the drive end. Figure 2 shows two samples of such bearings. Besides, for investigation about the ball defect, a hole is created on one of the balls of another bearing as shown in Figure 3. Finally, to examine the faulty chain, the motor bearing at the drive end is replaced with a bearing in which a rupture is created on the chain as shown in Figure 4.

TABLE 1. Technical data of the induction motor

Parameter	Value	Unit
Motor Type	80-4B	---
Rated Power	1.0	Hp
Rated Voltage	220Δ/380Y	Volts
Rated Current	3.7Δ/2.15Y	A
Rated Speed	1385	Rpm
Rated Torque	5.17	Nm
Power Factor	0.76	---
Efficiency	70	%



Figure 2. Defective bearings with created holes of 2-mm diameter on the inner race and outer race



Figure 3. Defective bearing with a created hole of 2-mm diameter on a ball



Figure 4. Defective bearing with a rupture in the chain

In the first step, it is determined which axis gives a more reliable vibration signal to detect the proposed bearing defect. For this step, the vibration signal is measured on three different axes which are the X-axis, Y-axis, and Z-axis for various fault degrees. Then, in the second step, four scenarios are considered for analyzing the effectiveness of the vibration signal on the fault detection including the inner race fault with different intensities (hole diameters), the outer race fault with

different intensities, the chain fault, and the ball fault. There are three different sub-scenarios for every scenario which are focused on changes in the load level, temperature, and hole diameter size. For a comprehensive analysis, the desired IM is tested with a healthy bearing, too.

As the first sub-scenario, each state is performed at a constant temperature and a constant hole size for various loading including no-load condition, 1.5 Nm, 3 Nm, and 4.5 Nm load torques. In the second sub-scenario, each fault is tested and analyzed at a constant load as well as a constant hole size but various temperatures from 30°C to 75°C in order to evaluate the temperature effect on vibration indicators. In the final stage, the influence of the fault intensity on the vibration is evaluated by



Figure 5. Fault positions on the outer race of the bearing



Figure 6. The accelerometer module installed on the motor terminal box



Figure 7. The whole experimental test setup

increasing the hole diameter from 2 mm to 5 mm at a constant temperature and a constant load.

The efficient direction for measuring vibration is considered by evaluating three different axes in the first step. Vibration signals recorded at constant temperature, constant load torque and constant hole size for various fault positions are used in this stage. The considered positions of the fault for the outer race include 0 degrees, 60 degrees, 120 degrees, and 180 degrees as shown in Figure 5. In the second step, the analysis is conducted to investigate the advantage of the vibration signal to be used for the bearing faults detection.

In the experimental tests, the temperature is measured by an infrared thermometer type GM320 of Benetech Company, and the vibration is recorded by a tri-axial accelerometer type MMA7260Q. In addition, an intermediate circuit is built to connect the mentioned sensor output to the data acquisition card PCI-1716/L of Advantech Company. The sensor module is installed horizontally on the motor terminal box with two fixing screws. The accelerometer sensor module is shown in Figure 6. For the motor variable loading, its shaft is coupled to a magnetic powder brake system. Figure 7 indicates the whole experimental test setup.

To be used in the following section, using the bearing dimensions as well as the rotor speed at different loading, the characteristic frequencies of the motor vibration is calculated according to Equations (1)-(4) and presented in Table 2 for different bearing faults.

4. TEST RESULTS ANALYSIS

In this section, the results attained through experimental tests related to different scenarios are presented and analyzed in comparison with the corresponding results attained for the healthy condition. For this purpose, the frequency spectrum analysis is performed using the Fast Fourier Transform (FFT) and the MATLAB software on the recorded vibration signals.

4. 1. Most Efficient Direction for Measuring the Vibration Signal

As mentioned previously, in the first step, the most efficient direction for the vibration measurement is determined. The experimental tests for this step are performed at constant temperature of 50°C,

TABLE 2. The characteristic frequencies of the bearing defects under different loading

Load Torque	f_{IR} (Hz)	f_{OR} (Hz)	f_{BF} (Hz)	f_{CF} (Hz)
No load	122.2	77.8	49.3	9.8
1.5 Nm	120.2	76.4	48.7	9.7
3.0 Nm	118.2	74.8	47.9	9.5
4.5 Nm	115.4	73.2	47.2	9.4

constant load of 4.5 Nm, and fixed hole diameter of 5 mm for the inner and the outer race faults as well as the healthy condition. Vibration measurements are performed in three different directions corresponding to the X-axis, Y-axis, and Z-axis (Figure 1). The sample results related to this scenario in comparison to corresponding results in the healthy condition are presented in Figures 8 to 9.

In each figure, in comparison to the spectrum related to the healthy condition, the presence of the vibration characteristic frequencies (Table 2) and their integer

multiples are evident in all the three axes of the vibration. Table 3 gives exact amplitudes of the vibration frequencies produced by the inner race fault in different directions that are presenting in Figure 8. Similarly, Table 4 presents exact amplitudes of the vibration frequencies produced by the outer race fault in different directions as shown in Figure 9.

In addition, Table 4 includes the amplitudes of the same vibration frequencies for different positions of the defect on the outer race as indicated in Figure 5. By examining Tables 3 and 4, it is observed that among the

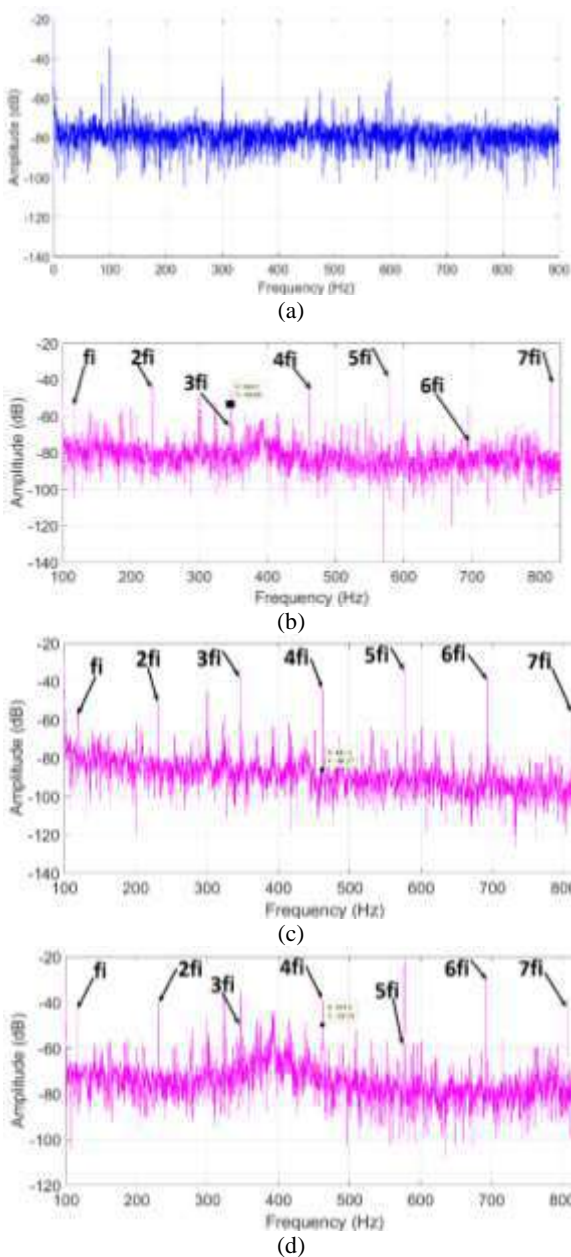


Figure 8. Motor vibration spectra under the: (a) healthy condition in Z-axis, and inner race fault condition in the: (b) X-axis, (c) Y-axis, (d) Z-axis

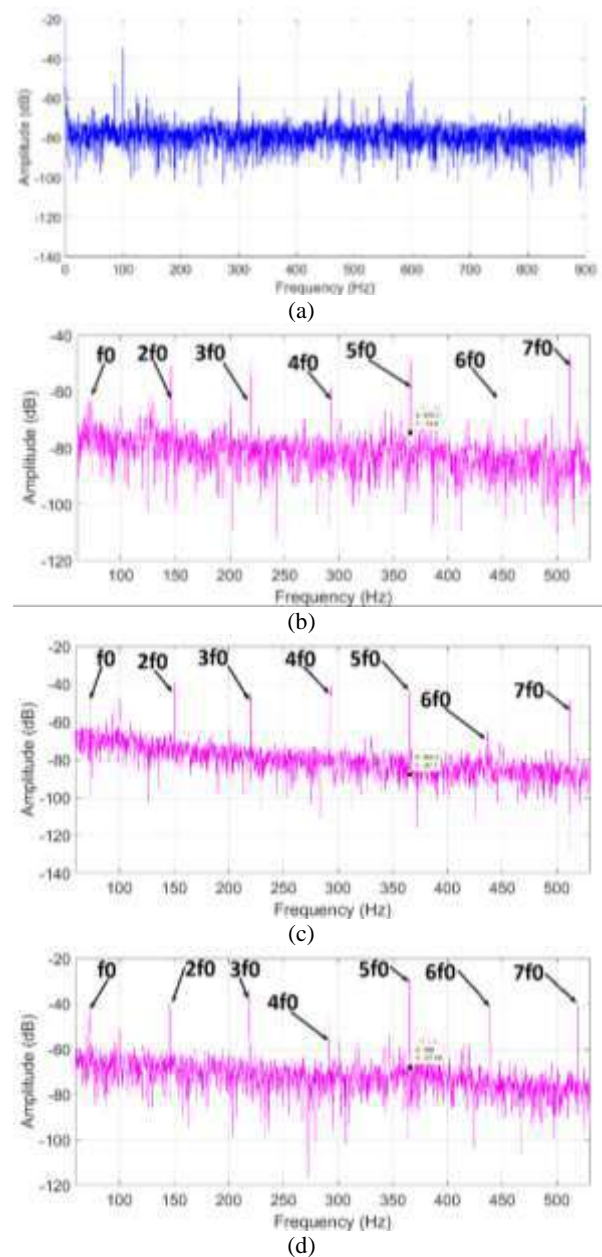


Figure 9. Motor vibration spectra under the: (a) healthy condition in Z-axis, and the outer race fault at 0 degree position in the: (b) X-axis, (c) Y-axis, (d) Z-axis

TABLE 3. Amplitudes of the vibration frequencies produced by the inner race fault (dB)

Direction	f_i	$2f_i$	$3f_i$	$4f_i$	$5f_i$	$6f_i$	$7f_i$
X-axis	-50	-43	-44	-40	-33	-53	-43
Y-axis	-54	-50	-36	-43	-30	-37	-55
Z-axis	-47	-44	-36	-42	-22	-31	-40

TABLE 4. Amplitudes of the vibration frequencies produced by the outer race fault in different position angles (dB)

Fault position	Direction	f_o	$2f_o$	$3f_o$	$4f_o$	$5f_o$	$6f_o$	$7f_o$
Zero Degree	X axis	-58	-	-	-	-	-	-
	Y axis	-48	-	-	-	-	-	-
	Z axis	-43	-	-	-	-	-	-
60 Degrees	X axis	-50	-	-	-	-	-	-
	Y axis	-47	-	-	-	-	-	-
	Z axis	-43	-	-	-	-	-	-
120 Degrees	X axis	-49	-	-	-	-	-	-
	Y axis	-33	-	-	-	-	-	-
	Z axis	-38	-	-	-	-	-	-
180 Degrees	X axis	-56	-	-	-	-	-	-
	Y axis	-48	-	-	-	-	-	-
	Z axis	-40	-	-	-	-	-	-

three axes, the fault characteristic frequency components in the Z-axis often have the highest amplitudes, and the position angle of the outer race failure has little effect on this fact.

Hence, when only the monitoring of the bearing status matters, usage of vibration sensor across all directions is not necessary and by monitoring the vibration of equipment along the Z-axis, the health or damage of the bearing can be reliably ensured. According to this result, it should be noted that all results in next subsections are measured on the Z-axis. In addition, it is observed that the fifth multiples of the characteristic frequencies ($5f_o$ and $5f_i$) have the maximum amplitude. Therefore, $5f_o$ and $5f_i$ frequencies can be harnessed for detecting the faults when the magnitudes of other related frequencies are rather low.

4. 2. Inner Race Fault In this subsection, the experimental results related to the inner race fault are investigated. Figure 10 demonstrates the frequency spectrum of the motor vibration under the healthy condition as well as the bearing inner race fault condition at the constant temperature of 50°C, hole diameter of 2-mm and no load. The related characteristic frequency of the vibration along with its integer multiples are marked with red arrows. Each of these frequencies can be used for the inner race fault detection, so they are called the fault indicator frequencies.

The amplitudes of the frequencies in the healthy condition as well as the inner race fault of the induction motor for different loading is presented in Table 5. According to this table, apart from the $7f_{IR}$ frequency, other frequencies in the defective bearing showed a significant increase compared to their corresponding value in the healthy condition. This fact confirms their high sensitivity to the bearing defect. Table 5 also indicates that the amplitudes of the frequencies vary slightly with changing the load level; however, the loading has the lowest effect on the $5f_{IR}$ and $6f_{IR}$ frequencies.

In the second stage, the influence of temperature on the frequency amplitudes produced by the inner race fault is examined. Thus, vibration sampling is performed at of 30°C, 50°C and 75°C temperatures with constant load (1.5 Nm) and hole diameter (2 mm). The vibration frequency amplitudes attained in this stage are presented in Table 6. What stands out from this table is that the temperature changes have minimal impact on the amplitudes of the frequencies.

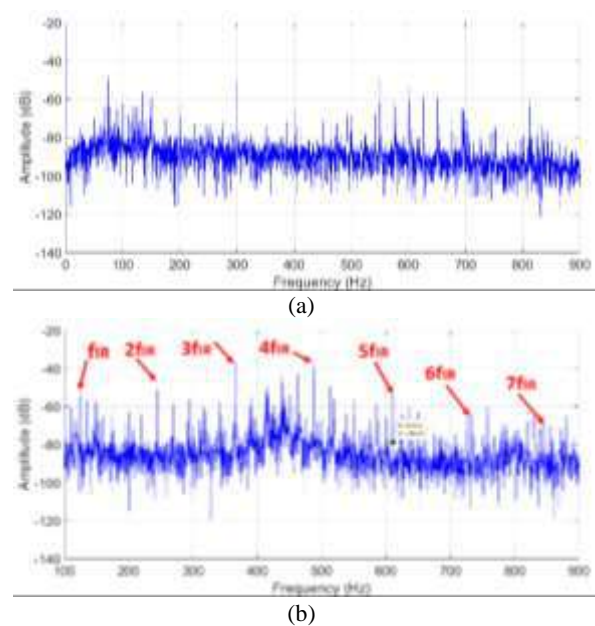


Figure 10. The vibration frequency spectra of induction motor at no load: (a) healthy condition, (b) inner race fault condition at 50°C and a hole diameter of 2-mm

In the third stage, the effect of the bearing fault severity is studied. To this end, the vibration frequencies are analyzed in the inner race fault condition with various hole diameters of 2 mm, 3 mm, 4 mm, and 5 mm at a constant load of 1.5 Nm and a constant temperature of 50°C. The results obtained for the vibration frequency amplitudes are demonstrated in Table 7. It can be seen that there is not any stable increase or decrease in amplitudes and hence they

showed fluctuation. Consequently, while the frequency amplitudes represent the bearing failure, the level of failure cannot be exactly estimated using them.

4. 3. Outer Race Fault In this subsection, the study results are presented for the outer race fault. Figure 11 illustrates the frequency spectra of the motor vibration under the outer race fault with 2 mm hole diameter, 50°C

TABLE 5. The vibration frequency amplitudes for inner race fault at the constant temperature of 50°C, fixed hole diameter of 2 mm and different load levels (dB)

Frequency component	No-load		1.5 N.m		3 N.m		4.5 N.m	
	Normal	Faulty	Normal	Faulty	Normal	Faulty	Normal	Faulty
f_{IR}	-64	-50	-62	-50	-73	-55	-74	-49
$2f_{IR}$	-77	-48	-77	-46	-75	-49	-72	-47
$3f_{IR}$	-82	-38	-82	-37	-70	-39	-72	-33
$4f_{IR}$	-84	-37	-70	-40	-73	-30	-75	-38
$5f_{IR}$	-81	-53	-74	-56	-81	-56	-70	-50
$6f_{IR}$	-76	-64	-79	-62	-72	-63	-71	-62
$7f_{IR}$	-82	-71	-87	-70	-75	-70	-74	-70

TABLE 6. The vibration frequency amplitudes for inner race fault at a constant load of 1.5 N.m, fixed hole diameter of 2mm and various temperatures (dB)

Frequency component	30° C	50° C	75° C
f_{IR}	-50	-50	-48
$2f_{IR}$	-47	-46	-47
$3f_{IR}$	-37	-37	-36
$4f_{IR}$	-36	-40	-37
$5f_{IR}$	-55	-56	-55
$6f_{IR}$	-61	-62	-61
$7f_{IR}$	-70	-70	-69

TABLE 7. The vibration frequency amplitudes of inner race fault at the constant temperature of 50°C, a constant load of 1.5 N.m and different hole diameters (dB)

Frequency component	2 mm	3 mm	4 mm	5 mm
f_{IR}	-50	-34	-40	-32
$2f_{IR}$	-46	-46	-37	-39
$3f_{IR}$	-37	-35	-29	-30
$4f_{IR}$	-40	-60	-40	-35
$5f_{IR}$	-56	-76	-57	-56
$6f_{IR}$	-62	-65	-60	-52
$7f_{IR}$	-70	-55	-57	-57

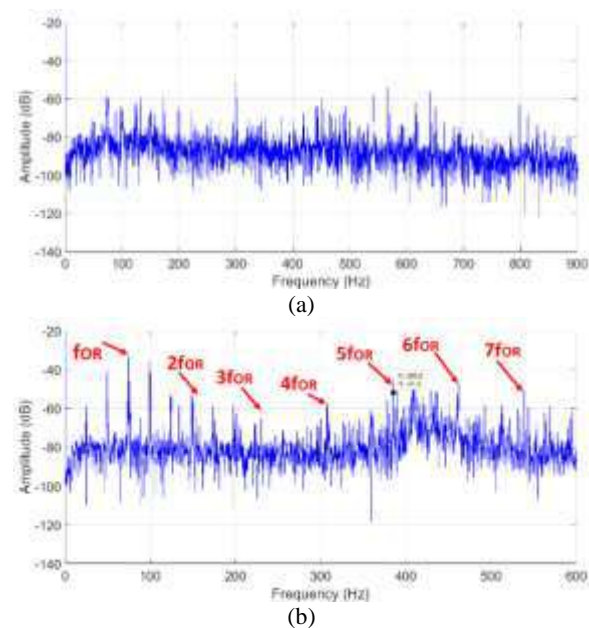


Figure 11. The vibration frequency spectra of induction motor under 1.5 Nm load torque: (a) healthy condition, (b) outer race fault condition at 50°C with 2 mm hole diameter

temperature of and 1.5 Nm load torque. The characteristic frequency f_{OR} and its integer multiples are distinguished by red arrows.

Table 8 demonstrates the frequencies amplitudes in the healthy condition as well as the outer race fault

condition under various loading. It is clear that the amplitudes of various frequencies in the outer race fault condition significantly increased in compare to the healthy condition. Moreover, the amplitudes of these frequencies are more stable than the inner race fault condition against the changes of load level especially for $2f_{OR}$ and $3f_{OR}$.

Similar to the previous subsection, the temperature influence on the amplitudes of the frequency indicators is considered. The motor vibration is sampled at a 2 mm

hole diameter, a constant load of 1.5 Nm and a variety of temperatures including 30°C, 50°C and 75°C. The results attained for the frequency amplitudes are demonstrated in Table 9. According to this table, the temperature variation has minor effect on the amplitudes.

In the last stage, the impact of the fault severity is investigated, so the experimental tests are performed at 1.5 Nm load torque, 50°C and different hole diameters of 2 mm, 3 mm, 4 mm, and 5 mm. The frequency amplitudes attained in this stage are presented in Table

TABLE 8. The vibration frequency amplitudes for outer race fault at the constant temperature of 50°C, fixed hole diameter of 2mm and different loads (dB)

Frequency component	No-load		1.5 N.m		3 N.m		4.5 N.m	
	Normal	Faulty	Normal	Faulty	Normal	Faulty	Normal	Faulty
f_{OR}	-81	-29	-57	-28	-57	-34	-54	-30
$2f_{OR}$	-75	-49	-65	-50	-64	-51	-62	-50
$3f_{OR}$	-78	-60	-73	-60	-74	-60	-72	-62
$4f_{OR}$	-81	-52	-84	-57	-60	-55	-71	-56
$5f_{OR}$	-70	-47	-70	-45	-71	-44	-71	-48
$6f_{OR}$	-73	-47	-65	-45	-71	-45	-70	-44
$7f_{OR}$	-67	-54	-73	-50	-76	-50	-69	-47

TABLE 9. The vibration frequency amplitudes of outer race fault at a constant load of 1.5 Nm, fixed hole diameter of 2-mm and various temperatures (dB)

	30° C	50° C	75° C
f_{OR}	-30	-28	-31
$2f_{OR}$	-50	-50	-51
$3f_{OR}$	-59	-60	-60
$4f_{OR}$	-54	-57	-55
$5f_{OR}$	-45	-45	-45
$6f_{OR}$	-46	-45	-45
$7f_{OR}$	-51	-50	-50

TABLE 10. The vibration frequency amplitudes of outer race fault at the constant temperature of 50°C, a constant load of 1.5 Nm and different hole diameters (dB)

	2 mm	3 mm	4 mm	5 mm
f_{OR}	-28	-25	-27	-10
$2f_{OR}$	-50	-35	-38	-28
$3f_{OR}$	-60	-47	-49	-45
$4f_{OR}$	-57	-40	-45	-55
$5f_{OR}$	-45	-33	-42	-37
$6f_{OR}$	-45	-37	-38	-31
$7f_{OR}$	-50	-42	-45	-41

10. It can be found that the amplitudes of the frequency indicators fluctuate with increasing the the fault intensity and hence there is not any uniform increase or decrease.

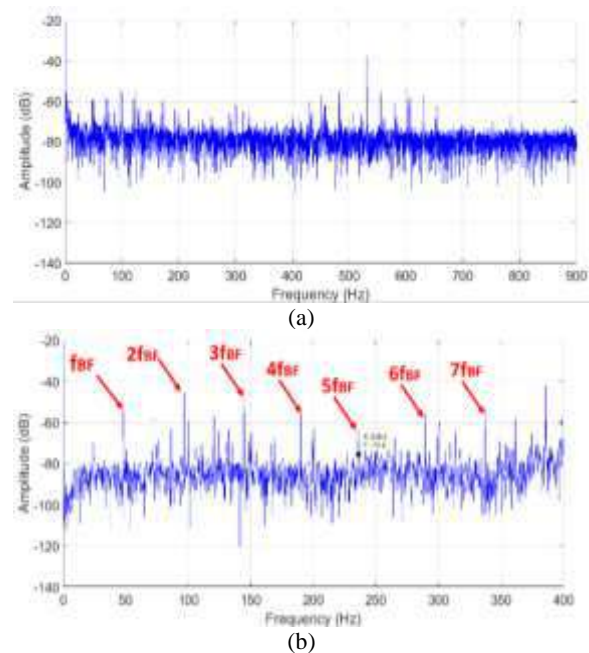


Figure 12. The vibration frequency spectra of induction motor under 3 Nm load torque: (a) healthy condition, (b) ball fault condition at 50°C with 2 mm hole diameter

Therefore, frequency indicator amplitudes may guide fault detection but the level of failure cannot be analyzed using them.

4. 4. Ball Fault In this subsection, the experimental study results for the ball fault in the bearing of the induction motor is presented. Figure 12 shows the frequency spectra of the motor vibration for the ball fault at a 2 mm hole diameter, 50°C and 3 Nm load torque. The red arrows are used to indicate the characteristic frequency f_{BF} and its integer multiples. Table 11 represents the vibration frequency amplitudes of the ball fault under various loads. According to Table 11, the amplitudes of the frequency indicators rapidly raised in compare to the healthy condition. Therefore, the indicators are useful for detecting the fault. The load variation shows a small effect on the amplitudes and it can be seen the influence is about ± 1 dB for f_{BF} and $4f_{BF}$, so, these frequencies are more stable against the load variations.

Similar to the frequency indicators of the inner race and outer race faults, the study showed that the ball fault

related frequency amplitudes have little sensitivity to the temperature variations. It should be noted that the creation of a bigger hole on the ball is so difficult due to its small size. Therefore, the experimental results regarding variation of the ball fault sesverity are not presented.

4. 5. Chain Fault The results related to the chain fault are presented in this subsection. Figure 13 shows the frequency spectra of motor vibration under the chain rupture condition at 50°C for different loads. The characteristic frequency of the chain fault along with its some integer multiples are distinguished by red arrows. However, some of the frequencies have rather small amplitudes. Table 12 gives exact amplitudes of the three strong frequencies at the healthy state and the chain fault condition. As seen, the amplitudes are increased in comparison to the healthy condition, so these frequencies can be used for the fault detection. The load changes have some impact on the frequency amplitudes but not the temperature changes.

TABLE 11. The vibration frequency amplitudes for ball fault at the constant temperature of 50°C, fixed hole diameter of 2 mm and different loads (dB)

Frequency component	No-load		1.5 N.m		3 N.m		4.5 N.m	
	Normal	Faulty	Normal	Faulty	Normal	Faulty	Normal	Faulty
f_{BF}	-70	-55	-70	-54	-59	-55	-64	-57
$2f_{BF}$	-62	-40	-64	-51	-53	-46	-54	-47
$3f_{BF}$	-58	-44	-76	-43	-74	-47	-56	-42
$4f_{BF}$	-79	-58	-66	-58	-76	-56	-66	-58
$5f_{BF}$	-78	-61	-76	-59	-70	-62	-72	-64
$6f_{BF}$	-77	-55	-85	-53	-73	-55	-70	-51
$7f_{BF}$	-85	-57	-75	-56	-76	-53	-67	-56

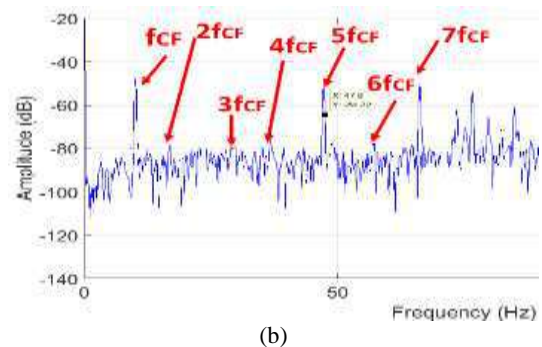
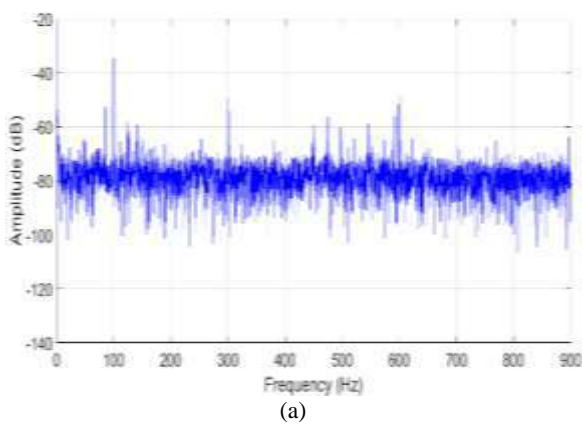


Figure 13. The vibration frequency spectra of induction motor under 4.5 Nm load torque: a) healthy condition, (b) chain fault condition at 50°C

TABLE 12. The vibration frequency amplitude for the chain fault at the constant temperature of 50°C and different loads (dB)

Frequency component	No-load		1.5 N.m		3 N.m		4.5 N.m	
	Normal	Faulty	Normal	Faulty	Normal	Faulty	Normal	Faulty
f_{CF}	-81	-58	-81	-51	-65	-49	-70	-48
$5f_{CF}$	-70	-46	-73	-44	-59	-50	-64	-52
$7f_{CF}$	-65	-45	-75	-31	-65	-41	-67	-51

5. CONCLUSION

The results attained through comprehensive experimental tests for healthy bearing as well as faulty ones demonstrate that for every bearing fault types, including the inner race fault, the outer race fault, the ball fault, and the chain fault, some specific frequencies appear in the motor vibration spectrum. These frequency indicators can be used for the fault detection. Further analysis confirms that for saving time as well as cost, vibrations amplitude can be measured only along the axis perpendicular to the motor installing surface, i.e. the Z-axis. This is because, regardless of the type and position of the fault, the related frequency amplitudes of the vibration usually have higher amplitudes along the Z-axis. In general, the temperature and load changes have minimal influence on the magnitudes of the frequency indicators. However, the amplitude of these frequencies vary with changing the fault severity.

6. REFERENCES

- Resendiz-Ochoa, E., Osornio-Rios, R. A., Benitez-Rangel, J. P., Romero-Troncoso, R. D. J. and Morales-Hernandez, L. A., "Induction Motor Failure Analysis: An Automatic Methodology Based on Infrared Imaging." *IEEE Access*, Vol. 6, (2018), 76993-77003. DOI: 10.1109/ACCESS.2018.2883988
- Saucedo-Dorantes, J. J., Miguel Delgado-Prieto, M., Ortega-Redondo, J. A., Osornio-Rios, R. A. and Romero-Troncoso, R. D. J., "Multiple-Fault Detection Methodology Based on Vibration and Current Analysis Applied to Bearings in Induction Motors and Gearboxes on the Kinematic Chain." *Shock and Vibration*, Vol. 2016, (2016), 1-13. DOI: 10.1155/2016/5467643
- Tandon, N. and Choudhury, A., "A review of vibration and acoustic measurement methods for the detection of defects in rolling element bearings." *Tribology International*, Vol. 32, No. 8, (1999), 469-480. DOI: 10.1016/S0301-679X(99)00077-8
- Chopade, S. A., Gaikwad, J. A. and Kulkarni, J. V., "Bearing fault detection using PCA and Wavelet based envelope analysis." in 2016 2nd International Conference on Applied and Theoretical Computing and Communication Technology (iCATccT), Bangalore, India, (2016). DOI: 10.1109/ICATccT.2016.7912031
- Heidari, M., "Fault Detection of Bearings Using a Rule-based Classifier Ensemble and Genetic Algorithm." *International Journal of Engineering, Transactions A: Basics*, Vol 30, No. 4, (2017), 604-609, DOI: 10.5829/idosi.ije.2017.30.04a.20
- Yuan, R., Lv, Y. and Song, G., "Fault Diagnosis of Rolling Bearing Based on a Novel Adaptive High-Order Local Projection Denoising Method." *Complexity*, Vol. 2018, (2018), 1-15, DOI: 10.1155/2018/3049318
- Mitra, S. and Koley, C., "Vibration signal analysis of induction motors used in process control operation." in 2013 IEEE 1st International Conference on Condition Assessment Techniques in Electrical Systems (CATCON). Kolkata, India, (2013). DOI: 10.1109/CATCON.2013.6737514
- Liu, J., Wu, H., and Shao, Y., "A theoretical study on vibrations of a ball bearing caused by a dent on the races." *Engineering Failure Analysis*, Vol. 83, (2018), 220-229. DOI: 10.1016/j.engfailanal.2017.10.006
- Tsytkin, M., "Induction motor condition monitoring: Vibration analysis technique — diagnosis of electromagnetic anomalies." in 2017 IEEE Autotestcon, Schaumburg, IL, USA, (2017). DOI: 10.1109/AUTEST.2017.8080483
- Attaran, B., Ghanbarzadeh, A. and Moradi, S., "A Novel Intelligent Fault Diagnosis Approach for Critical Rotating Machinery in the Time-frequency Domain." *International Journal of Engineering, Transactions A: Basics*, Vol 33, No. 4, (2020), 668-675. DOI: 10.5829/IJE.2020.33.04A.18
- Gangsar, P. and Tiwari, R., "Comparative investigation of vibration and current monitoring for prediction of mechanical and electrical faults in induction motor based on multiclass-support vector machine algorithms." *Mechanical Systems and Signal Processing*, Vol. 94, (2017), 464-481. DOI: 10.1016/j.ymssp.2017.03.016
- Kuspijani, K., Watiasih, R. and Prihastono, P. "Faults Identification of Induction Motor Based On Vibration Using Backpropagation Neural Network." in 2020 International Conference on Smart Technology and Applications (ICoSTA), Surabaya, Indonesia, (2020). DOI: 10.1109/ICoSTA48221.2020.1570615779
- Rangel-Magdaleno, J., Hayde Peregrina-Barreto, H., Ramirez-Cortes, J., Morales-Caporal, R., and Cruz-Vega, I., "Vibration Analysis of Partially Damaged Rotor Bar in Induction Motor under Different Load Condition Using DWT." *Shock and Vibration*, Vol. 5, (2016). DOI: 10.1155/2016/3530464
- Sudhakar, I., AdiNarayana, S. and AnilPrakash, M., "Condition Monitoring of a 3-Ø Induction Motor by Vibration Spectrum analysis using FFT Analyser- A Case Study." *Materials Today: Proceedings*, Vol. 4, No. 2, (2017), 1099-1105. DOI: 10.1016/j.matpr.2017.01.125
- Wissam Dehina, W., Boumehraz, M., Kratz, F. and Fantini, J., "Diagnosis and Comparison between Stator Current Analysis and Vibration Analysis of Static Eccentricity Faults in The Induction Motor." in 2019 4th International Conference on Power Electronics and their Applications (ICPEA). Elazig, Turkey, (2019). DOI: 10.1109/ICPEA1.2019.8911193
- Moiz, M. S., Shamim, S., Abdullah M., Khan, H., Hussain, I., Iftikhar, A. B. and Memon, T. D., "Health Monitoring of Three-Phase Induction Motor Using Current and Vibration Signature Analysis." in 2019 International Conference on Robotics and

- Automation in Industry (ICRAI), Rawalpindi, Pakistan, (2019). DOI: 10.1109/ICRAI47710.2019.8967356
17. Mahani, M. F. and Besanjideh, M., "Nonlinear and Non-stationary Vibration Analysis for Mechanical Fault Detection by Using EMD-FFT Method." *International Journal of Engineering, Transactions C: Aspects*, Vol. 25, No. 4, (2012), 363-372. DOI: 10.5829/idosi.ije.2012.25.04c.11
 18. Delgado-Arredondo, P. A., Morinigo-Sotelo, D., Osornio-Rios, R. A., Avina-Cervantes, J. G., Rostro-Gonzalez, H. and Romero-Troncoso, R. J., "Methodology for fault detection in induction motors via sound and vibration signals." *Mechanical Systems and Signal Processing*, Vol. 83, (2017), 568-589. DOI: 10.1016/j.ymsp.2016.06.032
 19. Novoa, C. G., Berríos, G. A. G. and Söderberg, R. A., "Predictive maintenance for motors based on vibration analysis with compact rio." in 2017 IEEE Central America and Panama Student Conference (CONESCAPAN), Panama, Panama, (2017). DOI: 10.1109/CONESCAPAN.2017.8277603
 20. Salah, M., Bacha, K. and Chaari, A., "Stator current analysis of a squirrel cage motor running under mechanical unbalance condition." in 10th International Multi-Conferences on Systems, Signals & Devices 2013 (SSD13), Hammamet, Tunisia, (2013). DOI: 10.1109/SSD.2013.6564078
 21. Marignetti, F., Rubino, G., Boukadida, Y., Conti, P., Gregorio, F., Iengo, E., Longobardi, V. G., "Noise and vibration analysis of an inverter-fed three-phase induction motor." in 2020 International Symposium on Power Electronics, Electrical Drives, Automation and Motion (SPEEDAM), Sorrento, Italy, (2020). DOI: 10.1109/SPEEDAM48782.2020.9161859
 22. Chang, S., Liu, M., Lan, C. and Hsu, W., "Lifetime Prediction for Bearings in Induction Motor." in 2019 IEEE International Conference on Industrial Cyber Physical Systems (ICPS), Taipei, Taiwan, (2019). DOI: 10.1109/ICPHYS.2019.8780366
 23. Marghitu, D. B. and Dupac, M., Machine Component Analysis with MATLAB, Butterworth-Heinemann. 2019.

Persian Abstract

چکیده

با توجه به استفاده گسترده از موتور القایی (IM) در صنایع مختلف، الزامات نظارت بر وضعیت آن به طور قابل توجهی افزایش یافته است. تشخیص عیوب موتور القایی در مدت زمان کوتاه و با دقت بالا ضروری است زیرا عدم توجه به این امر باعث خسارات مالی هنگفتی می شود. درصد بالایی از خرابی های موتور القایی ناشی از خطاهای یاتاقان است. در این مقاله، سیگنال ارتعاش برای به دست آوردن شاخص های قابل اعتماد در نظارت بر حالت های معیوب بلبرینگ موتورهای القایی به کار می رود. ابتدا جهت مناسب برای اندازه گیری ارتعاش تحلیل می شود. این تجزیه و تحلیل نشان می دهد که معمولاً مؤلفه های فرکانس ارتعاش مربوط به خطا در امتداد محور Z ، یعنی محور عمود بر سطح نصب موتور، بیشترین اندازه را دارند. بنابراین، توصیه می شود سیگنال ارتعاش در محور Z اندازه گیری شود. سپس، مانیتورینگ خطای یاتاقان با سیگنال ارتعاش در سناریوهای مختلف بررسی می شود. نتایج نشان می دهد که شاخص های ارتعاش به پارامترهای محیطی مانند دما و همچنین تغییر بار موتور حساس نبوده اما شدت خطا تأثیر قابل توجهی بر روی آن ها دارد.



Influence of Mould Thickness on Microstructure, Hardness and Wear of Al-Cu Cast Alloys

N. F. Soliman^a, D. O. Ramadan^{*b}, J. A. Yagoob^c

^a Mechanical Technical Department, Technical Institute of Kirkuk, Northern Technical University, Iraq

^b Mechanical and Energy Engineering Techniques Department, Erbil Technical Engineering College, Erbil Polytechnic University, Erbil, Kurdistan Region, Iraq

^c Technical College of Kirkuk, Northern Technical University, Iraq

PAPER INFO

Paper history:

Received 19 April 2021

Received in revised form 09 July 2021

Accepted 13 July 2021

Keywords:

Aluminium-Copper Alloys

Cooling Rate

Grain Size

Tribology

ABSTRACT

Aluminium-copper alloys have a wide range of industrial applications especially in military vehicles, rocket fins and aerospace. Solidification plays a vital role in controlling the mechanical and tribological properties, and influencing the microstructure of metallic alloys in general and aluminium alloys in particular. Therefore, the researchers have made many efforts to figure out the solidification behaviour of Al-Cu alloys. Despite all these endeavors, however, the behavior is not yet fully understood. This research aims to investigate the effect of cooling rate on the microstructure, mechanical and tribological properties of aluminium-copper cast alloys (Al-Cu alloys) under dry sliding conditions. Four cooling rates were achieved by using four various steel moulds made of different thicknesses and one of them was surrounded with green sand, to get a lower cooling rate, with the same respective mould hole geometries. The microstructure results showed that the grain size increases with decreasing the cooling rate. While the hardness increased largely due to the refinement of the microstructure. Finally, it was concluded that the wear rate increases with decreasing the cooling rate, and that is due to the reduction in hardness.

doi: 10.5829/ije.2021.34.08b.23

NOMENCLATURE

V	Linear sliding speed (m/min)	t	Running time (min)
r	Distance between the center of sample to the centre of the disc (m)	W_r	Wear rate
n	Disc rotational speed (RPM)	Greek Symbols	
S	Total Sliding distance (cm)	ρ	Density (g/cm ³)

1. INTRODUCTION

Aluminium and copper alloys are characterized by high strength, lightweight, resistance to high temperature, and high ductility which made them very important alloys in many industries such as military and aircraft industries as well as in transport applications and lightweight construction. Where high strength and ductility are highly needed in such kinds of applications [1]. Therefore, the mechanism of precipitation hardening in wrought and cast binary Al-Cu alloys is well understood and extensively recorded in the literature. Copper

element is considered as a great deposition-strengthening in aluminium. Adding copper improves machinability, toughness, tensile strength, and creep [2, 3]. Where, additions of about 0.05 wt.% of copper to aluminium results in good toughness and high strength alloys after subjected to different aging including at elevated temperature (artificial aging) or at room temperature (natural aging) [4, 5]. Aryshenskii et al. [6] studied the recrystallisation process in aluminium alloys.

It is well known that the microstructure of the material has a significant effect on the mechanical properties, where decreasing the grain size leads to

*Corresponding Author Institutional Email:

dlair.o.ramadan@epu.edu.iq (D. O. Ramadan)

improve mechanical properties, such as ductility and hardness [7] and resistance to corrosion [8]. In addition, decreasing in the size of the grains results in reducing the interface between the matrix and the phases and gives rise to a uniform distribution of solute components as well [9, 10]. The distribution of solute elements, supersaturated solid solution degree, morphologies of the secondary phases and the grain size are all affected by the rate of cooling [11]. The influence of cooling rate on the microstructure and properties of various alloys has been investigated previously using different experimental techniques for the design of high-efficiency materials [12]. Padmanabhan and Prabhub [13], studied the effect of cryogenic treatment on the mechanical and microstructure of different grades of aluminium. They found that the hardness increased with cryogenic coolant. Moulds of iron with different thicknesses, (5-50 mm), were made to get various cooling rates namely (2.3, 3.4, 9.8, and 24.1 Kelvin per second) [2]. The solidification rate has the greatest impact on the strength and the internal quality of the materials. Furthermore, it has an inverse relationship with the microstructure where increasing the solidification rate produces a refined microstructure [14,15]. Enhancing the mechanical properties of aluminium alloys that are susceptible to heat treatment is another advantage of refining the microstructure since the particles are smaller and need less time to dissolve during the heat-treating process [2, 5, 16]. Therefore, the aim of this study is to investigate the influence of cooling rate on the mechanical, microstructure, and the tribological properties of aluminium-copper cast alloys (Al-Cu alloys) under dry sliding conditions.

2. EXPERIMENTAL WORK

In this study, aluminium with a weight ratio of 95.5% was cast with copper with a weight ratio of 4.5 %. The purity of both materials was 99.9%. A digital scale was used for determining the weight of the materials. Tables 1 and 2 summarized the chemical compositions of pure aluminium and pure copper, respectively.

Aluminium without additives was put in a preheated crucible by using an electrical furnace of maximum temperature 1200°C. The aluminium was heated to 750°C and kept at this temperature for half an hour to ensure the homogeneity. Then, the copper was poured on the molting aluminium with fast continuous stirring by using a graphite rod, then poured into the four different permanent steel moulds with three different thickness range as shown in Figure 1.

The temperatures of inside the moulds were recorded using a thermocouple (K- type) with a range of (20-1400°C). The four cast specimens have the same dimensions which is 10 mm in diameter and length of 110 mm. The samples were prepared according to the required test including hardness, wear and microstructure. The following sections describe in detail how the samples prepared for each of the tests. Figure 2 shows the pouring process of the Al-Cu alloy inside the four different moulds.

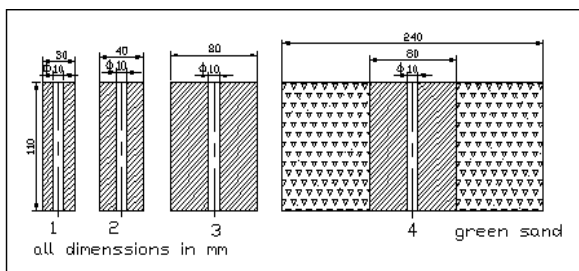
2. 1. Hardness Test The preparation procedure included cutting each specimen into three parts using a handsaw, each with dimension (10 mm diameter and 10 mm length), for hardness and microstructure test. The

TABLE 1. Chemical composition of pure aluminum [17]

Elements	Fe	Si	Mn	Cu	Mg	Zn	Ti	Zn	Na	Al
Weight %	0.09	0.05	0.001	0.005	0.004	0.008	0.004	0.008	0.005	balance

TABLE 2. Chemical composition of pure copper [18]

Elements	Sn	P	Mg	Zn	Pb	Se	Cu
Weight %	0.001	0.02	0.002	0.002	0.001	0.001	balance



(a) A schematic of the moulds



(b) The first three moulds



(c) The fourth mould which surrounded with green sand
Figure 1. A schematic and photographs of the utilized different moulds



Figure 2. Pouring the alloy inside the moulds

hardness tests were carried out according to ASTM E10-18 standard. The cast alloys were tested using a Brinell hardness tester.

2. 2. Microstructure Test The microstructural features of Al - Cu cast alloys were investigated using an optical microscope. To reduce the influence of the externalities on the specimens, the microstructure samples were taken between the mould wall and the centre of the mould. The microstructure samples were applied to a mechanical grind using wet emery papers with different grades of grit including 600, 800, and 1200 grits. For further surface finishing the grinded specimens were polished with a light cloth. To reveal the boundary conditions, the samples were etched, using a solution which prepared according to the ASTM E407 standard with (3 ml of Hydrochloric acid (HCl) + 5 ml of Nitric acid (HNO₃) + 2 ml of Hydrofluoric acid (HF) + 190 ml of distilled water] for 10 seconds [19].

2. 3. Wear Test In this study, a pin-on-disc tribometer was used to evaluate the wear behavior of Al - Cu alloys at dry conditions. The casting specimens were prepared, for wear test, according to the ASTM

G99-05 standard. The specimens' weight were measured before conducting the wear test using a digital scale having the least count of 0.1 mg. The wear tests were conducted at dry conditions under the dead weights of 10 N and a constant time of 5 min, and linear velocity of 626.74 m/min on the counter-face. The wear losses were calculated by measuring the difference between the weight of the specimens before and after the wear tests. An emery paper with a grit size of 1200 was used before the test to polish the contact surfaces of the test specimens.

The linear sliding speed (V) was calculated using Equation (1):

$$V = 2\pi rn \quad (1)$$

where r is the distance between the centre of the sample to centre of the disc which is equal to 0.07 m, and n is the rotational speed which is equal to 1425 RPM.

Equation (2) shows how the total sliding distance is calculated.

$$S = V \times t \quad (2)$$

where S is the total sliding distance in cm, and t is running time in minute. The wear rate was calculated using Equation (3).

$$W_r = \Delta W / \rho \times S \times 1000 \quad (3)$$

where ρ is the aluminium density ($\rho_{Al} = 2.7 \text{ g/cm}^3$), ΔW is difference in weight of the sample before and after testing (See Equation (4)).

$$\Delta W = W_0 - W_1 \quad (4)$$

3. RESULTS AND DISCUSSION

3. 1. Cooling Rates for Mould Castings Figure shows the relation between the temperature and time for the various moulds utilized in this study. The rapid drop in the temperature of the castings from (750-400)°C with an approximate duration of (60 seconds) is due to the very low temperature of the moulds inner wall surfaces, which were equal to room temperature. Hence the heat transfer from the poured Al-Cu castings toward the wall of the moulds will be with the rapid manner and because the moulds were made of steel, therefore, the heat transfer from the wall of the mould outward to the surrounding environment will also become rapidly, by continuity of the heat transfer process the moulds wall temperature will increase while the temperature of the castings will decrease, accordingly the differences between the two temperatures will be lower. From this point of view, the cooling rate will become slower with time. This action will affect the relation between temperature drop and required time. Thereafter in order to reach the moulds wall temperature to room or near room temperature, this

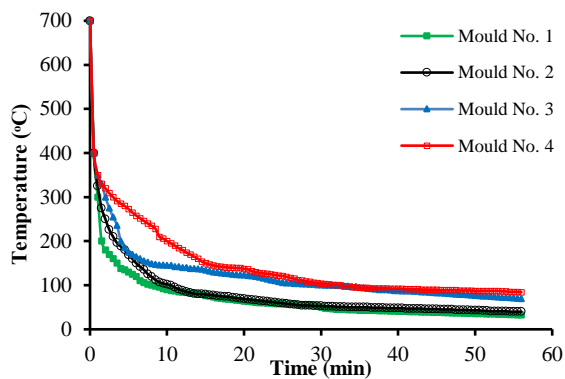


Figure 3. The relation between casting temperature and time for different wall thicknesses

will actually take place after prolonged time as explained at the lower portion of the cooling curves shown in Figure 2; particularly when the temperatures of moulds wall become less than 400°C. A digital camera and a thermocouple (K-type) were used to record the data of temperature changes during the solidification of the castings. It was then noticed that after (400°C), the temperature drop became gradually and data of the temperature detection and record can be performed by naked eye until it reaches room temperature. and the cause of rapid drop in temperature degree is due to using a mould casting material carbon steel in the experiment, and this what was proved by the researcher [20].

Figure 4 presents the cooling rates for Al-Cu castings poured in different used moulds at different temperature ranges including (640 to 200)°C, (640 to 150)°C, (640 to 100)°C and (640 to 50)°C. It is clearly shown that the cooling rates of the thinnest steel mould were greater at all temperature ranges listed above. While the cooling rates of the composite mould were the lowest at all temperature ranges listed above as shown in Figure 3. The cooling rates of the other steel moulds were decreased continually with an increase in the moulds wall thickness. It is important to note that the trend of the cooling rate decrease occurred with the highest manner

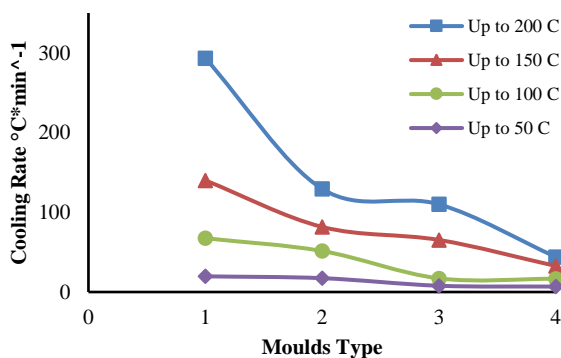


Figure 4. The relation between cooling rate and moulds type

for all used moulds at the temperature range (640 to 200)°C when compared with the three other temperature ranges. This result indicates that two cooling rate temperature ranges (640 to 200)°C and (640 to 150)°C have the most important effect on the microstructure, hardness, and wear resistance of the Al–Cu alloy because of their minimum temperatures (200 and 150) °C are near to the recrystallization temperature of the alloy which is approximately 122°C.

3. 2. Metallographic Examinations

The nucleation rate and the growth rate are the two most significant parameters that affect grain size. The rate of nucleation relies on the melting undercooling below the liquids and on the amount of energy required for the creation of a new phase structure. In this study, four moulds, made of steel with different wall thicknesses, were used to get different cooling rates. The results reveal that the cooling rate increases with decreasing the wall thicknesses of the steel moulds, as shown in **Error! Reference source not found.** This phenomenon is due to refining the grain size α - phase of (Al) and dark grains of (Cu Al₂) [10], and also can observe the grain size increase with decreasing the cooling rate as shown in Figure -8. This finding was also reported by the other researcher [19].

3. 3. Hardness Results

Figure 9 shows the variation of hardness with the steel mould types. The results showed that the hardness decreased as cooling rates decreased. It is likely that this is attributed to the grains size which is significantly affected by the cooling rate, where the size of the grains increases, thus decreasing the hardness, with decreasing the cooling rate. These results are in agreement with data reported in

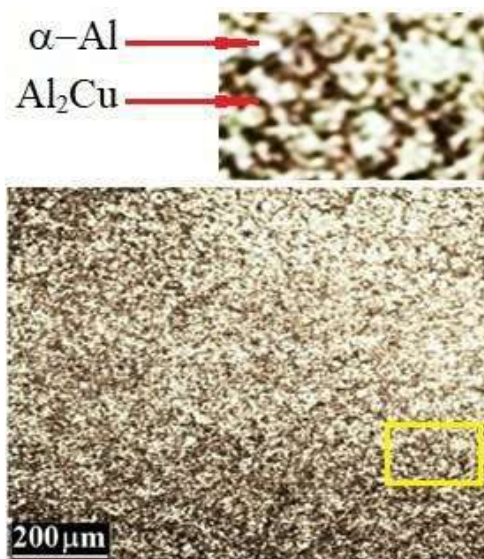


Figure 5. Microstructure of aluminium-copper alloys casted in steel moulds with wall thicknesses (10 mm)

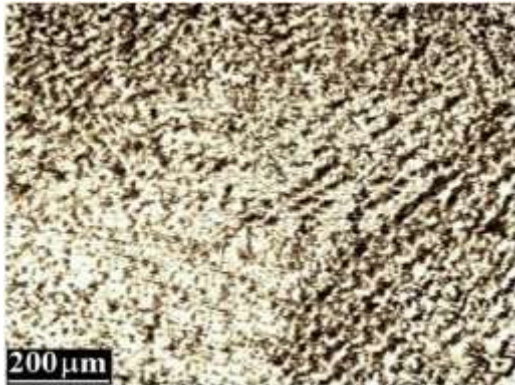


Figure 1: Microstructure of aluminium-copper alloys cast in steel mould with wall thicknesses (15mm)

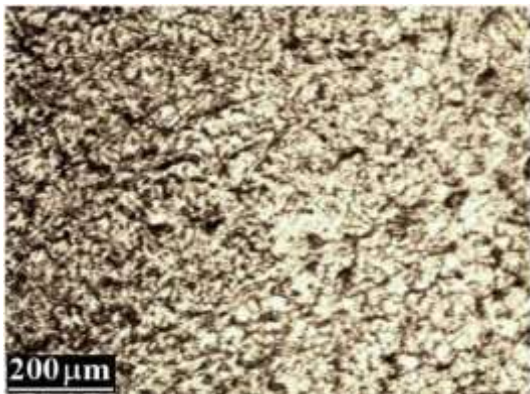


Figure 7: Microstructure of aluminium-copper alloys cast in steel mould with wall thicknesses (35mm)



Figure 8: Microstructure of aluminium-copper alloys casted in steel mould with wall thicknesses (35mm). surrounded with green sand grains

literature [8, 10, 12]. The amount of heat dissipated from the first mould (Mould No. 1) is more than that dissipated from the other moulds (i.e. Moulds No. 2, 3 and 4). The grains size in the moulds which are relatively fast heat dissipated are more smaller than the other moulds and

this caused increasing in hardness as shown in Figure 9. The results also reveal that the hardness of the first mould, which is the thinner, is about (83 Brinell hardness (BHN)) and that it relatively decreases with cooling rate. While the hardness in the thicker mould (Mould No. 4), which was surrounded with green sand grains, is about (73 BHN), and this what was proved by the other researcher [8], all these hardness numbers are in the range as reported in the literature [21].

3. 4. Wear Results The wear results reveal that the cooling rates are reversible in proportion with the wear rates, where the wear rate of the specimen number (1) (see Figure 10) was minimum (about $2.36 \times 10^{-8} \text{ cm}^3 \cdot \text{cm}^{-1}$) while the wear rate of the specimen number (2) which cast in the medium mould increased (about $3.5 \times 10^{-8} \text{ cm}^3 \cdot \text{cm}^{-1}$) and specimens (3 and 4) have the maximum

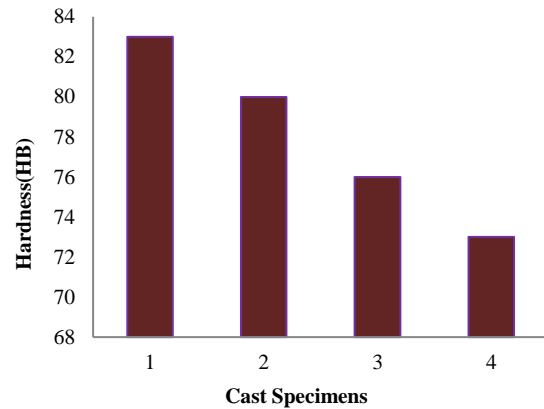


Figure 9. Brinell hardness (BHN) of the different specimens in different steel moulds.(1: Wall thickness=10 mm, 2: Wall thickness=15 mm, 3: Wall thickness=35 mm and 4: Wall thickness=35 mm surrounded with green sand grains)

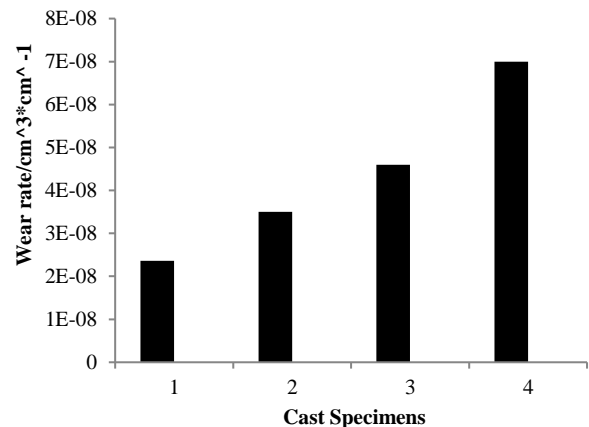


Figure 10. The relation between Wear rate with the cast specimens in different moulds (1: Wall thickness=10 mm, 2: Wall thickness=15 mm, 3: Wall thickness=35 mm and 4: Wall thickness=35 mm surrounded with green sand grains)

wear rate (about $4.6 \times 10^{-8} \text{ cm}^3 \cdot \text{cm}^{-1}$) and ($7 \times 10^{-8} \text{ cm}^3 \cdot \text{cm}^{-1}$), respectively. These results are due to the using low cooling rates, and the weight loss is due to mechanical wear at linear speeds of 626.74 m/min. The wear resistance increase for specimen cast in thin thickness wall mould (10 mm) this is the expected trend as it is supposed to increase wear resistance of specimen cast in steel mould with increasing of hardness, as shown in Figure 9. The wear resistance of cast alloys decreased gradually with increasing the wall thickness of the steel mould (2 and 3), especially steel mould which surrounded with sand grains (4) which means decreasing of the cooling rate due to increasing the wear, and these results are in agreement with the other researchers findings [21, 22].

4. CONCLUSION

The aim of the present research was to examine the effect of cooling rates on the tribological behaviour of Al-Cu alloys, namely the wear resistance. In addition, its effect on the hardness and microstructure have been examined as well. Four moulds of steel with the same length and diameter but varying thicknesses were made to attain four different cooling rates. The following conclusions can be drawn from the present study:

1. The cooling rate of the mould, particularly the composite mould, reduced as the wall thickness of the mould increased.
2. The grain size increased with decreasing the cooling rate.
3. The wear rate increased with an increase in the wall thickness of the mould, while the hardness decreased.

5. REFERENCES

1. Wierzbinska, M., Sieniawski, J. "Microstructural Changes of Al-Cu Alloys After Prolonged Annealing at Elevated Temperature." In: Recent Trends in Processing and Degradation of Aluminium Alloys., (2011), 155-174. doi: 10.5772/22195.
2. Rana, R.S., Purohit, R., Das, S. "Reviews on the Influences of Alloying elements on the Microstructure and Mechanical Properties of Aluminum Alloys and Aluminum Alloy Composites." *Internation Journal of Scientific and Research Publications*. Vol. 2, (2012), 1-7.
3. Sahoo, A.K., Behera, A., Behera, S., Senapati, S. "Development of Al Alloy (Al-Cu and Al-Cu-Tib2) and to Improve the Mechanical Properties of Al." *International Research Journal of Modernization in Engineering Technology and Science*, Vol. 3, (2021), 487-498.
4. Amoozraei, M., Gurevich, S., Provatas, N. "Spacing characterization in Al-Cu alloys directionally solidified under transient growth conditions." *Acta Materialia*, Vol. 58, (2010), 6115-6124. <https://doi.org/10.1016/j.actamat.2010.07.029>
5. Li, M., Wang, H., Wei, Z., Zhu, Z. "Effect of returns on microstructure and mechanical properties of AL-Cu based alloys." *China Foundry*, Vol. 7, No. 1, (2010), 37-42. doi:1672-6421(2010)01-037-06
6. Aryshenskii, E., Hirsch, J., Yashin, V., Konovalov, S., Chitnaeva, E. "Study of the Recrystallization Behaviour of the Aluminium 1565ch Alloy During Hot Rolling of the As Cast Structures." *Materials Research Express*, Vol. 6, No. 7, (2019). <https://doi.org/10.1088/2053-1591/ab13b6>
7. Xie, L., Wang, C., Wang, Y., Wu, G., Huang, X. "Grain Size Effect on the Mechanical Behavior of Metastable Fe-23Cr-8.5 Ni alloy." *Metals*, Vol. 9, No. 7, (2019). <https://doi.org/10.3390/met9070734>
8. Xu, Z., Wang, S., Wang, H., Song, H., Li, S., Chen, X. "Effect of Cooling Rate on Microstructure and Properties of Twin-Roll Casting 6061 Aluminum Alloy Sheet." *Metals*, Vol. 10, No. 9, (2020), 1-11. <https://doi.org/10.3390/met10091168>
9. Chausov, M., Pylypenko, A., Berezin, V., Volyanska, K., Maruschak, P., Hutsaylyuk, V., Markashova, L., Nedoseka, S., Menou, A. "Influence of Dynamic Non-Equilibrium Processes on Strength and Plasticity of Materials of Transportation Systems." *Transport*, Vol. 33, No. 1, (2018), 231-241. <https://doi.org/10.3846/16484142.2017.1301549>
10. He, C., Yu, W., Li, Y., Wang, Z., Wu, D., Xu, G. "Relationship between Cooling Rate, Microstructure Evolution, and Performance Improvement of an Al-Cu Alloy Prepared using Different Methods." *Materials Research Express*, Vol. 7, No. 11, (2020). <https://doi.org/10.1088/2053-1591/abc4f9>
11. Aryshenskii, E., Hirsch, J., Yashin, V., Sergei, K., Kawalla, R. "Influence of Local Inhomogeneity of Thermomechanical Treatment Conditions on Microstructure Evolution in Aluminum Alloys." *Journal of Materials Engineering and Performance*, Vol. 27, No. 12, (2018), 6780-6799. <https://doi.org/10.1007/s11665-018-3733-8>
12. Kordijazi, A., Weiss, D., Das, S., Behera, S., Roshan, H.M., Rohatgi, P. "Effect of Solidification Time on Microstructure, Wettability, and Corrosion Properties of A205-T7 Aluminum Alloys." *International Journal of Metalcasting*, Vol. 15, No. 1, (2021), 2-12. <https://doi.org/10.1007/s40962-020-00457-8>
13. Padmanabhan, K.K., Prabhub, G. "Experimental Investigation by Cryogenic Treatment of Aluminium 6063 and 8011 and NiCoW Coating to Improve Hardness and Wear." *International Journal of Engineering, Transactions C: Aspects*, Vol. 29, No. 6, (2016). <https://doi.org/10.5829/idosi.ije.2016.29.06c.12>
14. Dobrzański, L.A., Maniara, R., Krupiński, M., Sokolowski, J.H. "Microstructure and Mechanical Properties of AC AlSi9CuX Alloys." *Journal of Achievements in Materials and Manufacturing Engineering*, Vol. 24, No. 2, (2007), 51-54.
15. Talamantes-Silva, M.A., Rodríguez, A., Talamantes-Silva, J., Valtierra, S., Colás, R. "Characterization of an Al-Cu Cast Alloy." *Materials Characterization*. Vol. 59, No. 10, (2008), 1434-1439. <https://doi.org/10.1016/j.matchar.2008.01.005>
16. Li, J., Bourgeois, L., Tsalanidis, A., Weyland, M., Medhekar, N. V., Bourgeois, L. "The Enhanced Theta-prime (θ') Precipitation in an Al-Cu Alloy with Trace Au Additions." *Acta Materialia*, Vol. 125, 340-350 (2017). <https://doi.org/10.1016/j.actamat.2016.12.012>
17. Zaid, A.I.O., Allawi, G.T.A., Al-Haj-Ali, A. "Effect of Vanadium Addition to Aluminum and Aluminum Grain Refined by Titanium on Their Chemical Corrosion Rate in Acidic Solution, Hcl, at Different Temperatures." *Key Engineering Materials*, Vol. 510-511, No. 1, (2012), 481-486. <https://doi.org/10.4028/www.scientific.net/KEM.510-511.481>
18. Ebrahimi, M., Attarilar, S., Shaeri, M.H., Gode, C., Armoon, H., Djavanroodi, F. "An Investigation into the Effect of Alloying Elements on Corrosion Behavior of Severely Deformed Cu-Sn Alloys by Equal Channel Angular Pressing." *Archives of Civil and Mechanical Engineering*, Vol. 19, No. 3, (2019), 842-850.

<https://doi.org/10.1016/j.acme.2019.03.009>

19. Hu, X., Ai, F., Yan, H. "Influences of Pouring Temperature and Cooling Rate on Microstructure and Mechanical Properties of Casting Al-Si-Cu Aluminum Alloy." *Acta Metallurgica Sinica (English Letters)*, Vol. 25, No. 4, (2012), 272-278. <https://doi.org/10.11890/1006-7191-124-272>
20. Dobrzański, L., Maniara, R., Sokolowski, J. "The Effect of Cooling Rate on Microstructure and Mechanical Properties of AC AlSi9Cu Alloy." *Archives of Materials Science and Engineering*, Vol. 28, No. 2, (2007), 105-112.
21. Higgins, R. *Engineering Metallurgy: Applied Physical Metallurgy*. Printed in Great Britain, 1999.
22. Jabur, A.S. "Preparation and Characterization of Cast Aluminum Matrix-SiC Particulate Composite." PhD Thesis, University of Technology-Iraq, (2000).

Persian Abstract

چکیده

آلیاژهای آلومینیوم - مس کاربرد وسیع در صنعت به ویژه در وسایل نقلیه نظامی، باله موشکی و هوافضا دارند. انجاماد نقش مهمی در کنترل، خواص مکانیکی و تریبولوژیکی و تأثیر بر ریزساختار آلیاژهای فلزی (به طور کلی) و آلیاژهای آلومینیوم (به طور خاص) دارد. از این رو، تحقیقات بسیاری جهت کشف رفتار انجاماد آلیاژهای Al-Cu صورت گرفته است. با وجود همه این تلاش ها، این رفتار همچنان درک نشده است. هدف از این مقاله، بررسی تأثیر میزان خنک سازی بر ریزساختار، خواص مکانیکی و تریبولوژیکی آلیاژهای آلومینیوم مس (Al-Cu) در شرایط خشک متغیر است. چهار میزان خنک سازی با استفاده از چهار قالب فولادی مختلف با ضخامت‌های متفاوت به دست آمد و یکی از آنها با ماسه سبز احاطه شده بود تا سرعت خنک سازی پایین‌تری با سوراخ یکسان داشته باشد. نتایج ریزساختار نشان داد که با کاهش سرعت خنک سازی، اندازه ذره افزایش می‌یابد؛ در حالی که سختی بیشتر به دلیل تصفیه ریزساختار زیاد میشود. در آخر نتیجه گیری شد که با کاهش سرعت خنک کننده، میزان سایش افزایش یافته که علت آن، کاهش سختی است.



Holistic Persian Handwritten Word Recognition using Convolutional Neural Network

A. Zohrevand*, Z. Imani

Computer Engineering Department, Kosar University of Bojnord, Bojnord, Iran

PAPER INFO

Paper history:

Received 16 April 2021

Received in revised form 07 June 2021

Accepted 06 July 2021

Keywords:

Persian Handwritten Word Recognition

Convolutional Neural Network

End-to-end Learning Method

Transfer Learning

Persian Handwritten Dataset

ABSTRACT

Due to the cursive-ness and high variability of Persian script, the segmentation of handwritten words into sub-words is still a challenging task. These issues could be addressed in a holistic approach by sidestepping segmentation at the character level. In this paper, an end-to-end holistic method based on deep convolutional neural network is proposed to recognize off-line Persian handwritten words. The proposed model uses only five convolutional layers and two fully connected layers for classifying word images effectively, which can lead to a substantial reduction in the required parameters. The effect of various pooling strategies is also investigated in this paper. The primary goal of this article is to ignore handcrafted feature extraction and to attain a generalized and stable word recognition system. The presented model is assessed using two famous handwritten Persian word databases called Sadri and IRANSHAHR. The recognition accuracies were obtained at 98.6% and 94.6%, on Sadri and IRANSHAHR datasets respectively, and outperformed the state-of-the-art methods.

doi: 10.5829/ije.2021.34.08b.24

1. INTRODUCTION

Handwriting recognition refers to the process of converting handwritten images into their corresponding editable files [1, 2]. Unlike printed texts, due to significant changes in writing style and shape, the skew or slant automatic handwritten text recognition is still a debatable subject in the pattern recognition and computer vision community [1]. Handwriting recognition has several applications such as bank cheque processing [3], the recognition of notes [4, 5], postal address recognition [6] and historical documents [7, 8] in various scripts including Indian, Chinese, Latin, Arabic, and Persian. Compared to Latin/Roman, Chinese and Japanese scripts in which texts are written separately, in Persian script, the texts are usually written cursively, which further complicates the recognition process [9].

Handwritten recognition methods are divided into two major groups: on-line and off-line methods [10]. While on-line recognition depends on pen movement coordinates and the pen trajectory of the letter, off-line recognition is based on the analysis of the text image [1]. Also, there are two methods for word recognition:

segmentation-based and holistic methods [11]. In the segmentation-based, an input image is segmented into different sets of sub-words, and the word is recognized by its constituent units. In the holistic approach, however, an input image is recognized by its shape as a whole. Recently, Convolutional Neural Network (CNN) models have been widely used in various computer vision applications such as image segmentation, image classification, object detection and recognition due to their capability to directly extract high-level features from images [12]. In this article, attempts have been made to design a CNN model for holistic Persian off-line handwritten word recognition.

To the best of our knowledge, despite the excellent performance of CNN in a variety of computer vision applications, the use of CNN models for the holistic-based Persian off-line handwritten word recognition has received scant scholarly attention. Therefore, this study uses a novel CNN model to recognize Persian handwritten words. The main contributions of this article are as follows:

- Inspiring by [1], this paper proposed an end-to-end learning architecture that eliminates the need for

*Corresponding Author Institutional Email: a.zohrevand@kub.ac.ir
(A. Zohrevand)

handcrafted feature extraction in holistic Persian off-line handwritten word recognition.

- Presenting a new Transfer Learning (TL) approach for holistic Persian off-line handwritten word recognition.
- Analysing the proposed method on two popular Persian handwritten word datasets called IRANSHAHR [13] and Sadri [14].
- Analysing errors on Sadri dataset for the first time.

The rest of this paper is formed as follows. Section 2 reviews the related works about Persian handwritten word recognition. The proposed methodology is explained in Section 3. Sections 4 presents details of the experimental results. Error analysis is described in Section 5. Discussion and comparison are presented in Section 6. Finally, conclusions and future works are explained in Section 7.

2. LITERATURE REVIEW

Several important studies have explored the handwritten word recognition in Persian script, which are reviewed in this section. Dehghan et al. [15] proposed a vector quantization method based on Self-Organizing Feature Map (SOFM) in order to recognize Persian handwritten words. In this work, the contour image of each word is scanned from right to left to extract features. SOFM was utilized to prepare a codebook and smoothen the distribution of observation probabilities. Then, a distinct Hidden Markov Model (HMM) was trained on each word. The same authors [16] proposed a similar approach based on fuzzy C-means. The database used in both studies was 198 classes from IRANSHAHR dataset. For the first and second methods, the recognition accuracies were 65% and 67.2%, respectively. Mozaffari et al. [17] proposed a lexicon reduction method based on single, double and triple dots. In their approach, the words with different dot patterns are discarded prior to the classification. This strategy not only enhances accuracy but also the accelerate recognition process. As an experimental result, a recognition accuracy of 73.61% was obtained for 200 classes of IRANSHAHR dataset.

Broumandnia et al. [18] proposed rotation and scale invariant features for the recognition of holistic Arabic/Persian handwritten words. In their approach, M-band wavelet transform was used for features extraction and the Mahalanobis distance for classification. The experimental results showed a 12% improvement in the recognition accuracy on the database provided by themselves. Arani et al. [10] combine the output of Left-to-Right (LtR) and Right-to-Left (RtL) HMMs to recognize Persian handwritten words. In their approach, the LtR and RtL drew on complement rules for decreasing errors in recognition accuracy. Imani et al. [2] used a sliding window that sweeps vertically across a

word image for the extraction of intensity and directional gradient features. The features extracted from each window are then coded by the Self Organizing Map (SOM). Then, a distinct HMM was trained on each word. The recognition accuracy was obtained 69.07% on a database that contained 30,000 images from 300 formal words [19].

Arani et al. [11] extracted three feature groups including white-black transition, image gradient, and the chain code of contour from the input image. For each feature group, a discrete HMM was trained for each word. Finally, the outcomes of three HMMs are fused by a multilayer perceptron that is responsible for recognition classification. The recognition accuracy was obtained 89.06% on the 200 classes of IRANSHAHR dataset. Tavoli et al. [20] proposed new approach for extracting appropriate features to recognize Arabic/Persian handwritten words. In this method, the input image is divided into an $n \times m$ strip from which straight lines are extracted. Then, based on the location, number, angle, and straight line size, some geometrical features are extracted. The classification is conducted using the Support Vector Machine (SVM). Their proposed approach was evaluated on three databases: IBN SINA [21], IFN/ENIT [22] for Arabic and IRANSHAHR for Persian. Recognition accuracy of the proposed method was reported about 67.47, 86.22, and 80.78% for the IRANSHAHR, IBN-SINA, and IFN/ENIT dataset respectively. The above works are impressive, but since all of them employ manual methods for feature extraction, they are known as handcrafted features. The success of a recognition system primarily relies on the extraction of proper features from the word images. Generally, extracting handcrafted features are challenging, boring and in some case impossible for researchers. The end-to-end learning in the absence of handcrafted features is one of the remarkable characteristics of the CNN. Therefore, CNN-based models can be a good alternative for the recognition of Persian handwriting words.

LeCun et al. proposed the CNN architecture for the first time [23]. CNN models have been the subject of considerable attention in most computer vision applications [24-27]. These families of neural network, which fuse classification and feature extraction tasks, are intended to recognize images based on their scale, shift, and distortions. Safarzadeh et al. [28] proposed a novel approach according to the sequence labeling with CNN and Bidirectional Long Short Term Memory (LSTM). In this method, in order to ignore the segmentation step in segmentation-based methods, a Connectionist Temporal Classification (CTC) is used as the cost function. For feature extraction, the sequences of feature vectors are extracted by CNN model from an input word image. Then, the Recurrent Neural Network (RNN) model beside CTC cost function is utilized for input sequence

labeling as the classification task. According to the experimental results, the recognition accuracy was obtained 98.8% on the Sadri dataset, which contains 62,500 images from 125 word classes. Bonyani et al. [29] present ensemble method based on various CNN architectures for the recognition of handwritten Persian letters, digits and words. Specifically, an ensemble of various DenseNet [30] architectures and Xception [31] were utilized for word recognition. In experimental results, the recognition accuracy was reported 98.8% on Sadri dataset. These studies are summarized in Table 1.

3. PROPOSED METHODOLOGY

The general chart of the presented method is depicted in Figure 1. As shown in this figure, the presented approach consists of two major parts: preprocessing and training the CNN model. The preprocessing details and CNN model are explained in the following subsections.

3.1. Preprocessing In this paper, two databases called Sadri and IRANSHHR are used. There are word images of various sizes in the two datasets. Also, for

word images, the region of interest (i.e. handwritten area) in each class is different. However, the proposed CNN model needs 224×224 images as the input size in the first layer. There are several methods for image resizing [14]. The simplest one is the resizing of all images to 224×224 , but applying this method on all images with different sizes may deform structure of handwritten images. Sabzi at al. [32] proposed a simple approach for an efficient image scaling (resizing). In this approach, all images in each dataset are divided into two groups. In the first group, images with dimensions smaller than the standard size, are only padded with a background pixel. In the second group, for images with one or two dimensions greater than 224, ratio of the standard size to the bigger dimension is calculated, then the height and width of the input image are resized according to the ratio. The result of image resizing is shown in Figure 2. As shown in this figure, compared to the image resizing by normal scaling (middle column), this strategy (right column) does not change the structure of input images.

3.2. Proposed CNN Architecture Dealing with images directly reduces the performance of existing neural networks. Thus, a handcraft feature extraction step

TABLE 1. Some seminal works on the recognition of Persian handwritten words

Ref.	Method	Dataset	Recognition method	Year
[15]	Self-Organization Map, discrete HMM	IRANSHHR	Holistic	2001
[16]	Fuzzy vector quantization, discrete HMM	IRANSHHR	Holistic	2001
[17]	Lexicon reduction, discrete HMM	IRANSHHR	Segmentation-based	2008
[18]	M-band wavelet transform	Private	Holistic	2008
[10]	Fusion of Right-to-Left, Left-to-Right HMMs	IRANSHHR	Holistic	2018
[2]	Image gradient, discrete HMM	Private	Holistic	2014
[11]	Discrete HMM, classifier fusion	IRANSHHR	Holistic	2020
[20]	Statistical features, Support Vector Machine	IRANSHHR	Holistic	2018
[28]	Connectionist Temporal Classification (CTC), CNN	Sadri	Holistic	2020
[29]	Various CNN models	Sadri	Holistic	2020

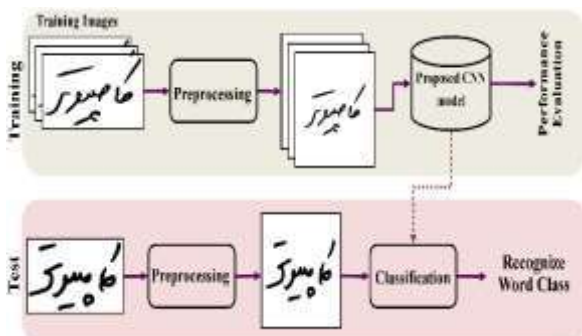


Figure 1. The general diagram for handwritten word recognition

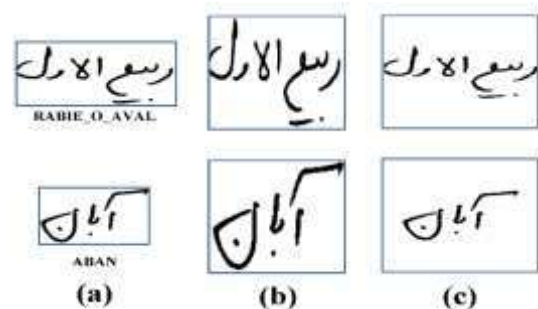


Figure 2. Left column(a): original image, Middle column (b): Resized image by normal scaling, and right column (c): Resized image by [32]

is utilized in most conventional approaches [1]. The end-to-end learning in the absence of handcrafted features is one of the remarkable characteristics of the CNN. Therefore in this paper, inspired by [1], a CNN model is adopted for holistic Persian off-line handwritten word recognition. As far as the authors are concerned, this is the first paper to focus on the effectiveness of CNN model for holistic recognition of Persian off-line handwritten. The architecture of the proposed CNN

model is depicted in Figure 3. As can be seen, the proposed CNN networks have one input layer, five convolutional blocks with corresponding four max-pooling ($L_1 \dots L_4$) and one average-pooling in the last block (L_5) for feature extraction, two fully-connected layers (L_6 and L_7) for classification, and finally one output layer. The details of the proposed architecture are listed in Table 2.

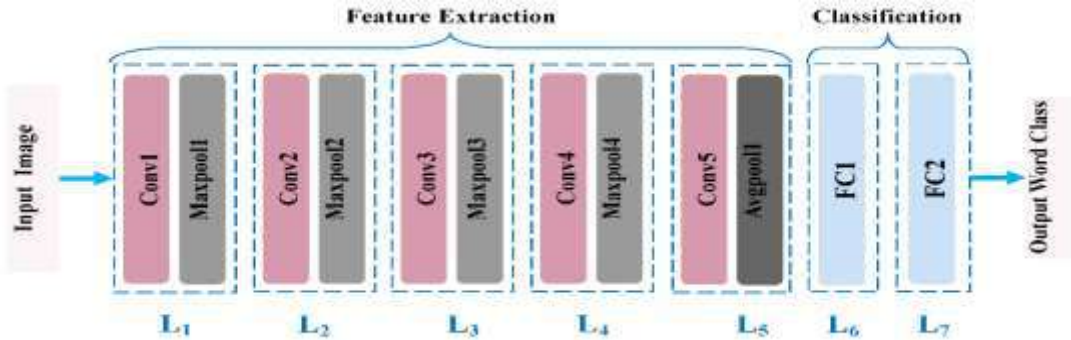


Figure 3. The proposed CNN model for Persian handwritten word recognition. This architecture contains seven layers ($L_1 \dots L_7$) for extracting feature and classification

TABLE 2. The details of the proposed CNN model shown in Figure 3

Layer Name	Layer Type	No. of Filters	Kernel Size	Stride	Input Features	Output Features	No. of Parameters
L ₁	Convolution (Conv1)	16	(7×7)	(1×1)	(1,224,224)	(16,218,218)	800
	Batch Normalization	---	---	---	(16,218,218)	(16,218,218)	32
	RELU	---	---	---	(16,218,218)	(16,218,218)	0
	Max Pooling (Maxpool1)	---	(2×2)	(2×2)	(16,218,218)	(16,109,109)	0
L ₂	Convolution (Conv2)	32	(5×5)	(1×1)	(16,109,109)	(32,105,105)	12,832
	Batch Normalization	---	---	---	(32,105,105)	(32,105,105)	64
	RELU	---	---	---	(32,105,105)	(32,105,105)	0
	Max Pooling (Maxpool2)	---	(2×2)	(2×2)	(32,105,105)	(32,52,52)	0
L ₃	Convolution (Conv3)	64	(3×3)	(1×1)	(32,52,52)	(64,50,50)	18,496
	Batch Normalization	---	---	---	(64,50,50)	(64,50,50)	128
	RELU	---	---	---	(64,50,50)	(64,50,50)	0
	Max Pooling (Maxpool3)	---	(2×2)	(2×2)	(64,50,50)	(64,25,25)	0
L ₄	Convolution (Conv4)	64	(3×3)	(1×1)	(64,25,25)	(64,23,23)	36,928
	Batch Normalization	---	---	---	(64,23,23)	(64,23,23)	128
	RELU	---	---	---	(64,23,23)	(64,23,23)	0
	Max Pooling (Maxpool4)	---	(2×2)	(2×2)	(64,23,23)	(64,11,11)	0
L ₅	Convolution (Conv5)	128	(3×3)	(1×1)	(64,11,11)	(128,9,9)	73,856
	Batch Normalization	---	---	---	(128,9,9)	(128,9,9)	256
	RELU	---	---	---	(128,9,9)	(128,9,9)	0
	Average Pooling (Avgpool1)	---	(2×2)	(2×2)	(128,9,9)	(128,2,2)	0
L ₆	Fully Connected (FC1)	---	---	---	512	256	131,328
	RELU	---	---	---	256	256	0
L ₇	Fully Connected (FC2)	---	---	---	256	125	32,125
Totally = 308,541							

According to Table 2, in general, the proposed CNN consists of 308,541 (≈ 0.3 million) parameters (weight) that must be trained in the training process. It is worth noting that the number of layers and characteristics of each layer have been adjusted experimentally. As shown in Figure 3, feature extraction and classification were conducted automatically. The main goal for the presented model design is to accomplish the best performance with the minimum number of layers.

4. EXPERIMENTAL RESULTS

This section explains experimental results after introducing the two datasets. All experiments were run on a machine with Intel® core i3 - 6300 CPU @3:70GHz, 16GB RAM, and NVidia® 1060Ti 6GB GPU. The experiments were implemented using PyTorch® framework installed on Microsoft® Windows 10. The back-propagation algorithm beside the Adam optimizeris were utilized to train the proposed CNN model. The proposed CNN model requires a number of hyper-parameters shown in Table 3. It should be noted that the hyper-parameter values were adjusted empirically.

4. 1. Dataset In the proposed method, two Persian handwritten word datasets including IRANSHAHR and Sadri was utilized. The Sadri dataset comprises text, dates and numbers, as well as words, numbers, signs, letters, and symbols. There are 62,500 words from 125 word classes in the Sadri dataset, which were collected randomly by 500 Persian authors, including 250 males and 250 females, of whom 10% were left-handed. IRANSHAHR is another dataset that contains 19,583 word images from 503 names of Iranian cities with approximately 38 sample images for each class. In this paper, to compare the proposed method with the state-of-the art, a subset of 200 out of the 503 city names was selected from IRANSHAHR. Figure 4 shows some samples of the two datasets.

4. 2. The First Experiment- Sadri Dataset In the first set of experiments, samples of Sadri dataset

TABLE 3. Hyper-parameter setting of the proposed CNN model

Hyper-parameter	value
Batch size	200
Number of epochs	100
Initial learning rate	0.001
L2regularization	0.001

including 62,500 words were divided into three categories, 70% ($0.7 \times 62,500 = 43,750$) for training, 15% ($0.15 \times 62,500 = 9,735$) for validation and 15% ($0.15 \times 62,500 = 9,735$) for testing. Figure 5 shows validation accuracy and validation cost in different epochs. For comparative investigation, Figure 6 shows the confusion matrix of each category for Sadri dataset. The rows and columns denote the 10 first classes in Sadri dataset. The last column represents the rest of 125 classes in Sadri dataset.

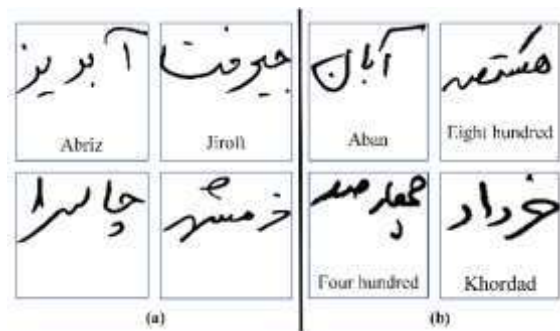


Figure 4. Several samples of the Persian handwritten word database, (a): IRANSHAHR dataset, (b) Sadri dataset

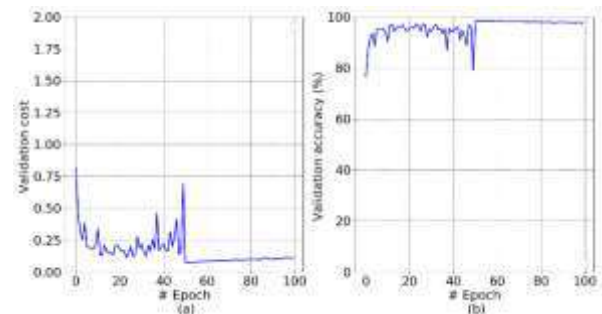


Figure 5. Performance of the proposed model in different epochs on Sadri dataset for validation set, (a) validation cost versus the number of epochs, (b) validation accuracy versus the number of epochs

	1	2	3	4	5	6	7	8	9	10	Other
1	0.97	0.00	0.00	0.00	0.01	0.00	0.00	0.00	0.00	0.00	0.02
2	0.00	0.97	0.00	0.00	0.00	0.00	0.00	0.00	0.00	0.00	0.03
3	0.00	0.00	1.00	0.00	0.00	0.00	0.00	0.00	0.00	0.00	0.00
4	0.00	0.00	0.00	0.99	0.00	0.00	0.00	0.00	0.00	0.00	0.01
5	0.00	0.00	0.00	0.00	0.99	0.00	0.00	0.00	0.00	0.00	0.01
6	0.00	0.00	0.00	0.00	0.00	1.00	0.00	0.00	0.00	0.00	0.00
7	0.00	0.00	0.00	0.00	0.00	0.00	0.99	0.00	0.00	0.00	0.01
8	0.00	0.00	0.00	0.00	0.00	0.01	0.00	0.99	0.00	0.00	0.00
9	0.00	0.00	0.00	0.00	0.00	0.00	0.00	0.00	0.99	0.00	0.01
10	0.00	0.00	0.00	0.00	0.00	0.00	0.00	0.00	0.00	1.00	0.00

Figure 6. Confusion matrix where rows and columns represent the 10 first classes in each Sadri dataset. The last column represents the rest of 125 classes in Sadri dataset

4. 3. Effects of Rotation on Performance of the CNN Model

This subsection attempts to assess stability of The presented CNN model in the presence of rotation errors. In this investigation, as shown in Figure 7, the test word samples are rotated in different angles (-15°, -10°, -5°, 0°, 5°, 10°, 15°) and their corresponding recognition accuracies are depicted in Figure 8. As can be seen, rotation errors affect performance of the proposed model. In fact, this experiment shows the proposed model isn't rotation invariant.

4. 4. Effects of Pooling Types on the Proposed CNN Model

The size of feature map in CNN is reduced by the pooling operation, which is invariant to image transformations [1]. Furthermore, research shows that pooling operations have a substantial effect on performance of the model [1]. The max pooling and average pooling are two pooling types widely used for designing CNN. Several studies [33] have sought to figure out the best one. In this paper, to design the proposed CNN, both pooling types have been utilized together: four max pooling operations in the first four

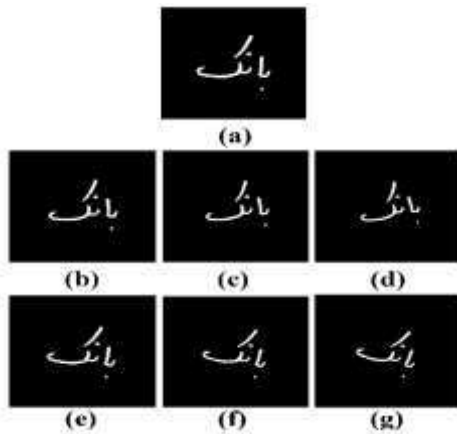


Figure 7. Different levels of rotation error (a) Original image, (b) Rotation angle = 5°, (c) Rotation angle = 10°, (d) Rotation angle = 15°, (e) Rotation angle = -5°, (f) Rotation angle = -10°, (g) Rotation angle = -15° respectively

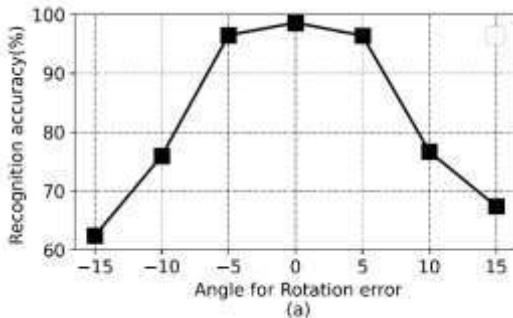


Figure 8. Performance evaluation for word images with various degrees of rotation

convolution blocks as well as one average-pooling operation in the last convolution block (see Figure 3). Performance of the proposed model is evaluated once with only max pooling in all five convolution blocks, then with only average pooling in all five convolution blocks, and the results are listed in Table 4. As depicted in this table, compared to the average pooling and max-pooling strategies alone, the combined max-average pooling not only shows higher performance in terms of recognition accuracy, but also has fewer trainable parameters and training time.

4. 5. The Second Experiment- Transfer Learning on IRANSHAHR

Compared to the Sadri dataset, IRANSHAHR has smaller samples, approximately about 38 samples per class. In this subsection, two approaches are used. First, the proposed CNN model is trained from scratch on IRANSHAHR dataset, then the Transfer Learning (TL) approach is used [34]. TL aims to leverage knowledge from a related domain (called source domain) to improve learning performance in a target domain, when there is a small number of labeled training data in the target domain. In fact, due to the over-fitting phenomenon, it is not common to train the CNN model from scratch on a small dataset. Instead, the CNN model is trained on a richer dataset (i.e. Sadri), and then the trained model is fine-tuned on a small dataset (i.e. IRANSHAHR). So in this experiment, the trained CNN architecture on Sadri dataset was considered as the backbone network. Then, the backbone network was fine-tuned on IRANSHAHR by re-training only the last two layers (L_6 and L_7 in Figure 3). In the two experiments of this sub-section, samples of IRANSHAHR dataset are divided into three categories, 70% ($0.7 \times 19,583 = 13,708$) for training, 15% ($0.15 \times 19,583 = 2,938$) for validation and 15% ($0.15 \times 19,583 = 2,938$) for testing. Figure 9 shows validation accuracy and validation cost in different epochs of the two approaches. As depicted in this figure, when training from scratch, the CNN network weights are randomly initialized, so the learning process shows a fluctuating behavior. In contrast, in the TL approach, CNN weights in the target domain are initialized based on the trained network's weights in the source domain. Thus, this initialization strategy triggers

TABLE 4. Evaluations of Different pooling types

Pooling Type	Training Time (minute)	# of Trainable Parameters	Test Accuracy (%)	
			Top 1	Top 5
Max-pooling	181.3	701,757	98.6	99.8
Average-pooling	183.4	308,541	97.9	99.8
Max-average pooling	175.1	308,541	98.6	99.8

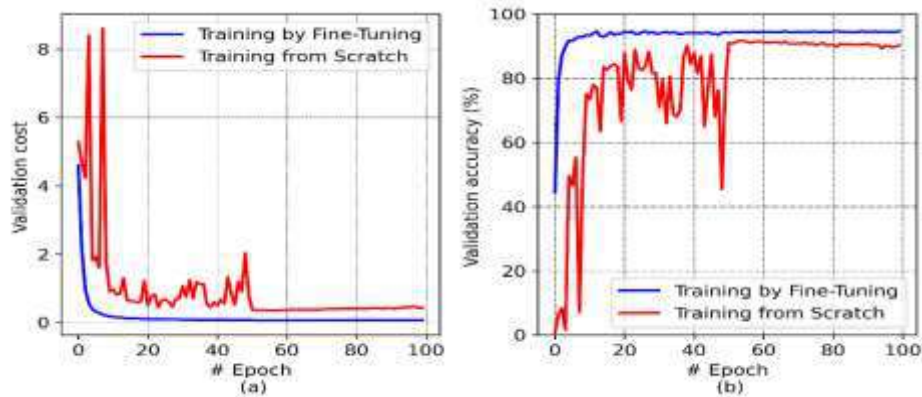


Figure 9. Performance of the proposed model in different epochs on IRANSHHR dataset, (a): cost value versus the number of epochs, (b): validation accuracy versus the number of epochs for validation set

a smoother behavior in the learning process. This difference is clearly shown in Figure 9. As shown in Table 5, the TL approach outperforms other approach with regard to the recognition accuracy, test cost, and training time.

5. ANALYSIS OF ERROR

This section presents an analysis of errors on the proposed method. In this article, CNN model is proposed for the holistic Persian off-line handwritten word. The proposed CNN models have hierarchical structures with many trainable kernels. The CNN model is essentially based on convolution operator, meaning that CNN kernels are convolved over the image for extracting meaningful information. While kernels in the primary layers extract common information like edge, line, etc., kernels in the later layers progressively extract more detailed and complex information from input sample

images. For error analysis, first the average of images in each class is calculated by summing the images of that class divided by the total number of images in the class. Figure 10 shows the average image in class “آبان” (Aban). In fact, Figure 10 shows how people usually write the word "آبان" on paper.

On the other hand, the intensity frequency in average images of each class indicates that the kernels of a CNN will attach great importance to these regions during the training process. It means that a CNN learns the general structure of the images in each class during the training. However, during the test, the test images distant from the overall structure of its corresponding class will have a greater probability of error and vice versa. Based on this analysis, the errors in the test stage were split into two main groups on Sadri dataset. The first group contains errors occurring during data collection. Table 6 shows some of these errors. In the second group, as shown in Table 7, the test image samples are distant from average images in the corresponding class. It should be noted that

TABLE 5. Details of the two different approaches on IRANSHHR dataset in the test phase

Database	Training Type	Test Accuracy (%)		Test Loss	Training Time (minute)
		Top1	Top5		
IRANSHHR	From Scratch	90.8	98.1	0.39	22.3
	Fine-Tuning	94.6	99.0	0.24	10.4



Figure 10. Image average for the class "آبان"

this distance can be due to differences between the beginning or end of test image and the average structure of the corresponding class.

6. DISCUSSION AND COMPARISON

This section compares our study with the most recent state-of-the-art works on these two datasets in terms of

TABLE 6. The number of errors during the collection of Sadri dataset

Word Image	Image Label in dataset	Word Image	Image Label in dataset
	Five		Forty
	Forty		Eleven

TABLE 7. The number of errors made by the proposed method on Sadri dataset

Word Image	Average Images in corresponding class	True Label	Predicted Label
		آبان ABAN	آذر AZAR
		چهارده Fourteen	چهارصد Four hundred
		تومان TOMAN	تلفن Phone
		خانم Miss	تمام End

TABLE 8. Comparing the performance of the proposed approach with the state-of-the-art methods

Dataset	Ref.	Method	Year	# of trainable parameters	# of classes	Accuracy (%)	
						Top1	Top5
IRANSHAHR	[15]	Self-Organization Map, discrete HMM	2001	----	198	69.0	----
	[11]	Image gradient, classifier fusion	2020	----	200	89.0	96.4
	[16]	Fuzzy vector quantization, HMM	2001	----	198	67.7	----
	[10]	Right to Left, Left to Right HMM	2018	----	200	84.4	97.9
	[17]	Lexicon reduction, discrete HMM	2008	----	200	73.6	89.0
	[20]	Statistical features, Support Vector Machine	2018	----	198	80.7	----
	---		Proposed Network		$\approx 0.3M$	200	93.0
Sadri	[28]	Connectionist Temporal Classification, bi-LSTM, CNN	2020	$\approx 0.7M$	125	98.8	99.3
	[29]	Various CNN models	2020	$\approx 7M$	125	98.8	----
	---		Proposed Network	----	$\approx 0.3M$	125	98.6

M : Million

recognition accuracy. To the best of our knowlwdge, few studies have explored CNN-based methods for the recognition of Persian handwritten off-line words.

Thus, motivated by [1], this paper adopted CNN architecture for holistic Persian handwritten word recognition. In addition, for the first time, this paper focuses on the effectiveness of CNN model for holistic Persian off-line handwritten word recognition. Compared to previous studies on IRANSHAHR dataset, the proposed model had a significantly higher improvement in recognition accuracy. Due to limited samples in each class of the IRANSHAHR dataset, all works had been selected from a limited subset of 503 classes for their analysis. In this paper, for the first time, we used the all 503 classes as shown in Table 8. As can be see, compared to IRANSHAHR, much fewer investigations have been conducted on Sadri dataset. As far as the authors are concerned, there are currently only studies based on Sadri dataset [28, 29]. The proposed method has several advantages over the existing methods. For example, the proposed method provides better results with fewer weights than the other methods. Moreover, compared to the work in literature [28], in which CNN was conducted for extracting a feature sequences and the RNN was used along with CTC for sequence labeling, the proposed method is end-to-end, meaning that feature extraction and classification are conducted automatically. Given the large size of trainable parameters, the method of Bonyani et al. [29] used data augmentation for data generation. In contrast, the proposed method eliminates the need for data augmentation due to efficient trainable parameters. In general the proposed holistic method has several critical advantages over other studies including:

- During the network training, appropriate features are extracted automatically. Hence, it eliminates the

manual feature extraction stage, which is a highly time-intensive and boring task in existing approaches.

- As the experimental results indicate, the presented method can be used as the backbone for other handwritten scripts with a reduced time complexity.

7. CONCLUSION AND FUTURE WORKS

In this article, an end-to-end method based on CNN architecture was adopted for holistic Persian off-line handwritten word recognition. To the best of our knowledge, this is the first paper to focus on the effectiveness of CNN model for holistic Persian off-line handwritten word recognition. For this purpose, two sets of experiments were carried out. In the first set of experiments, the presented method was assessed on the Sadri dataset. In the second experiment, two approaches were followed on IRANSHAHR dataset. In the first approach, the proposed CNN method was trained from scratch. In the second approach, the TL approach was adopted. The experimental results indicate that the presented method surpasses the state-of-the-art in term of recognition accuracy. The error analysis was conducted on the Sadri dataset for the first time. In the future, the authors would like to extend their model to other scripts like Arabic, Latin, etc.

8. ACKNOWLEDGEMENT

We would like to appreciate Sadri et al. [14] for providing the dataset.

9. REFERENCES

1. Das, D., Nayak, D.R., Dash, R., Majhi, B. and Zhang, Y.-D., "H-wordnet: A holistic convolutional neural network approach for handwritten word recognition", *IET Image Processing*, Vol. 14, No. 9, (2020), 1794-1805. DOI: [10.1049/iet-ipr.2019.1398](https://doi.org/10.1049/iet-ipr.2019.1398).
2. Imani, Z., Ahmadyfard, Z. and Zohrevand, A., "Holistic farsi handwritten word recognition using gradient features", *Journal of AI and Data Mining*, Vol. 4, No. 1, (2016), 19-25. DOI: [10.5829/idosi.JAIDM.2016.04.01.03](https://doi.org/10.5829/idosi.JAIDM.2016.04.01.03).
3. Akbari, Y., Jalili, M.J., Sadri, J., Nouri, K., Siddiqi, I. and Djeddi, C., "A novel database for automatic processing of persian handwritten bank checks", *Pattern Recognition*, Vol. 74, (2018), 253-265. DOI: <https://doi.org/10.1016/j.patcog.2017.09.011>.
4. Ye, M., Viola, P., Raghupathy, S., Sutanto, H. and Li, C., "Learning to group text lines and regions in freeform handwritten notes", in Ninth International Conference on Document Analysis and Recognition (ICDAR 2007). Vol. 1, (2007), 28-32. : [10.1109/ICDAR.2007.4378670](https://doi.org/10.1109/ICDAR.2007.4378670).
5. Razzak, I., Kamran, I. and Naz, S., "Deep analysis of handwritten notes for early diagnosis of neurological disorders", in 2020 International Joint Conference on Neural Networks (IJCNN). (2020), 1-6. DOI: [10.1109/IJCNN48605.2020.9207087](https://doi.org/10.1109/IJCNN48605.2020.9207087).
6. Vajda, S., Roy, K., Pal, U., Chaudhuri, B.B. and Belaid, A., "Automation of indian postal documents written in bangla and english", *International Journal of Pattern Recognition and Artificial Intelligence*, Vol. 23, No. 08, (2009), 1599-1632. DOI: <https://doi.org/10.1142/S0218001409007739>.
7. Venu, G. and Xue, H., "Fast handwriting recognition for indexing historical documents", in First International Workshop on Document Image Analysis for Libraries, 2004. Proceedings. (2004), 314-320. DOI: [10.1109/DIAL.2004.1263260](https://doi.org/10.1109/DIAL.2004.1263260).
8. Sánchez, J.A., Romero, V., Toselli, A.H., Villegas, M. and Vidal, E., "A set of benchmarks for handwritten text recognition on historical documents", *Pattern Recognition*, Vol. 94, (2019), 122-134. DOI: <https://doi.org/10.1016/j.patcog.2019.05.025>.
9. Bhowmik, S., Malakar, S., Sarkar, R., Basu, S., Kundu, M. and Nasipuri, M., "Off-line bangla handwritten word recognition: A holistic approach", *Neural Computing and Applications*, Vol. 31, No. 10, (2019), 5783-5798. DOI: [10.1007/s00521-018-3389-1](https://doi.org/10.1007/s00521-018-3389-1).
10. Abbaszadeh Arani, S.A.A., Kabir, E. and Ebrahimpour, R., "Combining rtl and ltr hmms to recognise handwritten farsi words of small-and medium-sized vocabularies", *IET Computer Vision*, Vol. 12, No. 6, (2018), 925-932. DOI: [10.1049/iet-cvi.2017.0645](https://doi.org/10.1049/iet-cvi.2017.0645).
11. Arani, S.A.A.A., Kabir, E. and Ebrahimpour, R., "Handwritten farsi word recognition using nn-based fusion of hmm classifiers with different types of features", *International Journal of Image and Graphics*, Vol. 19, No. 01, (2019), 1950001. DOI: <https://doi.org/10.1142/S0219467819500013>.
12. Guo, Y., Liu, Y., Oerlemans, A., Lao, S., Wu, S. and Lew, M.S., "Deep learning for visual understanding: A review", *Neurocomputing*, Vol. 187, (2016), 27-48. DOI: <https://doi.org/10.1016/j.neucom.2015.09.116>.
13. Bayesteh, E., Ahmadyfard, A. and Khosravi, H., "A lexicon reduction method based on clustering word images in offline farsi handwritten word recognition systems", in 2011 7th Iranian Conference on Machine Vision and Image Processing. (2011), 1-5. DOI: [10.1109/IranianMVIP.2011.6121550](https://doi.org/10.1109/IranianMVIP.2011.6121550).
14. Sadri, J., Yeganehzad, M.R. and Saghi, J., "A novel comprehensive database for offline persian handwriting recognition", *Pattern Recognition*, Vol. 60, (2016), 378-393. DOI: <https://doi.org/10.1016/j.patcog.2016.03.024>.
15. Dehghan, M., Faez, K., Ahmadi, M. and Shridhar, M., "Handwritten farsi (arabic) word recognition: A holistic approach using discrete hmm", *Pattern Recognition*, Vol. 34, No. 5, (2001), 1057-1065. DOI: [https://doi.org/10.1016/S0031-3203\(00\)00051-0](https://doi.org/10.1016/S0031-3203(00)00051-0).
16. Dehghan, M., Faez, K., Ahmadi, M. and Shridhar, M., "Unconstrained farsi handwritten word recognition using fuzzy vector quantization and hidden markov models", *Pattern Recognition Letters*, Vol. 22, No. 2, (2001), 209-214. DOI: [https://doi.org/10.1016/S0167-8655\(00\)00090-8](https://doi.org/10.1016/S0167-8655(00)00090-8).
17. Mozaffari, S., Faez, K., Märgner, V. and El-Abed, H., "Lexicon reduction using dots for off-line farsi/arabic handwritten word recognition", *Pattern Recognition Letters*, Vol. 29, No. 6, (2008), 724-734. DOI: <https://doi.org/10.1016/j.patrec.2007.11.009>.
18. Broumandnia, A., Shanbehzadeh, J. and Rezakhah Varnoosfaderani, M., "Persian/arabic handwritten word recognition using m-band packet wavelet transform", *Image and Vision Computing*, Vol. 26, No. 6, (2008), 829-842. DOI: <https://doi.org/10.1016/j.imavis.2007.09.004>.
19. Imani, Z., Ahmadyfard, A. and Zohrevand, A., "Introduction to database farsa: Digital image of handwritten farsi words (in persian)", in 11th Iranian Conference on Intelligent Systems in Persian, Tehran, Iran. (2013). DOI: <https://civilica.com/doc/214715/>.

20. Tavoli, R., Keyvanpour, M. and Mozaffari, S., "Statistical geometric components of straight lines (sgcsl) feature extraction method for offline arabic/persian handwritten words recognition", *IET Image Processing*, Vol. 12, No. 9, (2018), 1606-1616.
21. Moghaddam, R.F., Cheriet, M., Adankon, M.M., Filonenko, K. and Wisnovsky, R., "Ibn sina: A database for research on processing and understanding of arabic manuscripts images", in Proceedings of the 9th IAPR International Workshop on Document Analysis Systems, Boston, Massachusetts, USA, Association for Computing Machinery. (2010 of Conference), 11-18.
22. Pechwitz, M., Maddouri, S.S., Märgner, V., Ellouze, N. and Amiri, H., "Ibn/enit-database of handwritten arabic words", in Proc. of CIFED, Citeseer. Vol. 2, (2002), 127-136.
23. LeCun, Y. and Bengio, Y., "Convolutional networks for images, speech, and time series", *The Handbook of Brain Theory and Neural Networks*, Vol. 3361, No. 10, (1995), 1995.
24. Liu, L., Ouyang, W., Wang, X., Fieguth, P., Chen, J., Liu, X. and Pietikäinen, M., "Deep learning for generic object detection: A survey", *International Journal of Computer Vision*, Vol. 128, No. 2, (2020), 261-318. DOI: 10.1007/s11263-019-01247-4.
25. Zohrevand, A., Imani, Z. and Ezoji, M., "Deep convolutional neural network for finger-knuckle-print recognition", *International Journal of Engineering, Transactions A: Basics*, Vol. 34, No. 7, (2021), 1684-1693. DOI: 10.5829/ije.2021.34.07a.12.
26. Guo, G. and Zhang, N., "A survey on deep learning based face recognition", *Computer Vision and Image Understanding*, Vol. 189, (2019), 102805. DOI: <https://doi.org/10.1016/j.cviu.2019.102805>.
27. Zohrevand, A., Sattari, M., Sadri, J., Imani, Z., Suen, C.Y. and Djeddi, C., "Comparison of persian handwritten digit recognition in three color modalities using deep neural networks, Cham, Springer International Publishing. (2020), 125-136. DOI: 10.1007/978-3-030-59830-3_11.
28. Safarzadeh, V.M. and Jafarzadeh, P., "Offline persian handwriting recognition with cnn and rnn-ctc", in 2020 25th International Computer Conference, Computer Society of Iran (CSICC). (2020), 1-10. DOI: 10.1109/CSICC49403.2020.9050073.
29. Bonyani, M., Jahangard, S. and Daneshmand, M., "Persian handwritten digit, character and word recognition using deep learning", *International Journal on Document Analysis and Recognition (IJ DAR)*, Vol. 24, No. 1, (2021), 133-143. DOI: 10.1007/s10032-021-00368-2.
30. Huang, G., Liu, Z., Van Der Maaten, L. and Weinberger, K.Q., "Densely connected convolutional networks", in Proceedings of the IEEE conference on computer vision and pattern recognition. (2017), 4700-4708.
31. Chollet, F., "Xception: Deep learning with depthwise separable convolutions", in Proceedings of the IEEE conference on computer vision and pattern recognition. (2017), 1251-1258.
32. Sabzi, R., Fotoohinya, Z., Khalili, A., Golzari, S., Salkhorde, Z., Behraves, S. and Akbarpour, S., "Recognizing persian handwritten words using deep convolutional networks", in 2017 Artificial Intelligence and Signal Processing Conference (AISP). (2017), 85-90. DOI: 10.1109/AISP.2017.8324114.
33. Scherer, D., Müller, A. and Behnke, S., "Evaluation of pooling operations in convolutional architectures for object recognition", in Artificial Neural Networks – ICANN 2010, Berlin, Heidelberg, Springer Berlin Heidelberg. (2010), 92-101. DOI: https://doi.org/10.1007/978-3-642-15825-4_10.
34. Zhuang, F., Qi, Z., Duan, K., Xi, D., Zhu, Y., Zhu, H., Xiong, H. and He, Q., "A comprehensive survey on transfer learning", *Proceedings of the IEEE*, Vol. 109, No. 1, (2021), 43-76. DOI: 10.1109/JPROC.2020.3004555.

Persian Abstract

چکیده

به دلیل ماهیت پیوسته کلمات و تنوع زیاد نوشتاری در زبان فارسی، شکستن کلمات به زیر کلمات و حرف کار بسیار سختی است. روش‌های کلی‌نگر با در نظر گرفتن شکل کلی کلمه این قسمت را نادیده می‌گیرند. در این مقاله یک روش end-to-end و کلی‌نگر بر اساس شبکه‌های عصبی کانولوشنی عمیق برای بازشناسی کلمات دست‌نوشته فارسی به صورت برون خط ارائه شده است. مدل پیشنهادی تنها دارای پنج لایه کانولوشنی و دو لایه طبقه‌بندی است که منجر به کاهش محسوس در تعداد پارامترها می‌شود. در این مقاله همچنین تاثیر استراتژی‌های متفاوت برای pooling مورد مطالعه قرار گرفته است. هدف اصلی این مقاله معرفی یک روش جدید برای بازشناسی کلمات دست‌نویس فارسی است که در آن ویژگی‌ها به صورت خودکار استخراج می‌شوند. روش پیشنهادی روی دو پایگاه داده مشهور به نام ایران‌شهر و صدی مورد ارزیابی قرار گرفت و به دقت بازشناسی معادل ۹۴.۶٪ روی ایران‌شهر و ۹۸.۶٪ روی صدی رسید که نشان می‌دهد نسبت به روش‌های موجود کارایی بالاتری دارد.



Multi Objective Optimization of Multi-hole Orifices using Fluid-solid Interaction Analysis and Multi-objective Genetic Algorithm

M. Taheri^a, A. Mahdavi^{a,b}, H. Safikhani^{*a}

^a Department of Mechanical Engineering, Faculty of Engineering, Arak University, Arak 38156-88349, Iran

^b Department of Mechanical Engineering, 5-8 F Mech. Eng. Building, University of Alberta, Edmonton, AB, T6G 2G8 Canada

PAPER INFO

Paper history:

Received 22 April 2021

Received in revised form 14 May 2021

Accepted 29 May 2021

Keywords:

Multi-hole Orifices

Pressure Drop

Fluid Solid Interaction

Multi-objective Optimization

Sensitivity Analysis

ABSTRACT

Multi-hole orifices have better performance than single-hole orifices. In this paper, multi-objective optimization of multi-hole orifices is performed using a Fluid-Solid Interaction (FSI) analysis and multi-objective genetic algorithm (NSGA II). In all numerical analysis, the governing equations of the solid and the governing equations of the fluid are carried out for orifice and fluid around orifice, respectively. All calculations are made for a 16-hole orifice with circular holes. The design variable in the optimization process is the distance between the holes of the orifice and thus the amount of shrinkage or expansion of the orifice geometry. The objective functions are the pressure drop created on the sides of the orifice, the deformation and tension created in the orifice structure, which should be maximized, minimized and minimized, respectively. In the results section, the Pareto front are presented which represent useful information for designing the multi-hole orifices geometry, and five orifices are also introduced as final design options that have better performance. The results of the sensitivity analysis of the various parameters are also presented and discussed in detail in the multi-hole orifices.

doi: 10.5829/ije.2021.34.08b.25

1. INTRODUCTION

Orifice is a device for measuring the mass flow rate of fluid flow, which is a flat metal plate with one or more holes and is installed perpendicular to the flow direction. When the fluid passes through the orifice, due to the decrease in cross-section, its velocity increases and its pressure decreases. For different sizes of the orifice plates, there is a direct relationship between the current flow through the orifice plate and the pressure drop due to the flow through the orifice plate. The orifice plate usually has a thickness of about 1.61 to 1.4 inches, and is usually positioned between two flanges interfaced with two metal seals, and according to the diameter that is in plate, they pass through a range of mass flow rates of fluids. Figure 1 shows the location of the orifice in the pipeline, and also shows how to calculate the mass flow rates in the presence of orifice.

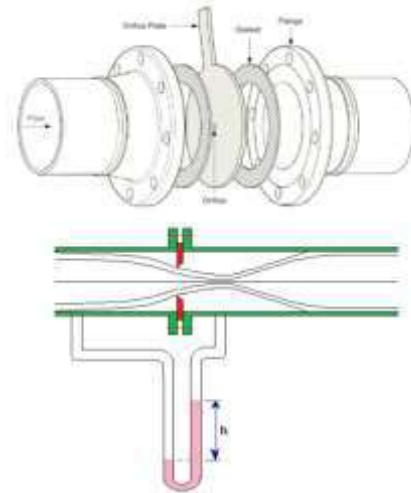


Figure 1. The location of orifice and the general overview of the fluid transition from orifice

*Corresponding Author Institutional Email: h-safikhani@araku.ac.ir
(H. Safikhani)

When the flow passes through the plate, its pressure suddenly drops and this pressure drop continues to the area called the lowest pressure (Vena Contracta). After passing through this area, the flow pressure gradually increases and after a distance of about 5 to 8 times the downstream area. Reducing fluid pressure during the passing through the orifice is because of increased velocity in this area, and when the velocity starts to decrease, the pressure begins to increase in proportion to this decrease.

For the first time, the Italian physicist Juan Venturi used a pressure drop system to measure flow rates in 1797, which resulted in the development of a more modern Venturi measuring system by Clemens in 1886 and from 1924 to 1935, laboratory experiments were carried out by the American Gas Association and the American Society of Mechanical Engineers (ASME) to develop the orifice measurement systems for coefficients and installation standards. Finally, in 1935, these two associations jointly published a report entitled calibration history, installation and performance of orifice measurement systems and in 1991, the American Petroleum Institute (API) published the standards for the measurement of petroleum in Chapter 14, Part 3, in terms of pressure difference method [1]. Krou and Sowa [2] optimized the geometry of orifices for the flow of mixtures in a cylinder in terms of the number of orifices, hole diameter, and angle of the holes of the orifice using experimental results. But, the behavior of the orifices has not been investigated in simulation and numerical solution. Also, the experimental results are not verified by numerical solution. Zhang and Bodony [3] reviewed numerical and linear acoustic modeling of flow in orifice to reduce noise by numerical solution using Navier Stokes equations and also using Fourier's law in heat transfer. Badr et al. [4] predicted the dynamical behavior of the flow of some orifices by calculating the fluid dynamics using the vortex viscosity model $k-\epsilon$. The flow characteristics were predicted and the effect of different parameters such as flow velocity and erratic distance they made it and the effects of various parameters such as flow velocity and distance of orifices were investigated. Gan and Riffat [5] conducted a study on the characteristics of pressure drop in perforated orifices and plates. They conducted experiments to determine the pressure drop for a thin plate in a square duct for a number of Reynolds numbers and investigated the effect of plate thickness on pressure loss for orifices using Computational Fluid Dynamics (CFD). Zhao and Zhang [6] presented a general structural design method for multi-hole orifices and its empirical application and said that in comparison to single-hole and multi-hole orifices, single-hole orifices have smaller sizes and different patterns of geometric shapes and are more complex. This method first introduces a comprehensive set of geometric architectures that include the orifice setup criteria and

geometric parameters such as the total number of orifice, the density of the distribution of orifice, and the equivalent diameter ratio. They investigated a series of different experiments with water flow to study the effect of different geometric properties on the pressure drop and finally presented an optimal model. Simpson and Ranade [7] presented results of computational investigation into cavitation in different orifice designs over a range of operating conditions. Rainsford et al. [8] presented high-speed photography to visualize fast-flame and detonation propagation through a transparent round tube equipped with repeating orifice plates, in stoichiometric hydrogen-oxygen mixtures at initial pressures up to 60 kPa. Yu et al. [9] presented experimental and numerical research on the internal flow and spray behaviors with biodiesel for elliptical orifice with large aspect ratio and circular orifice of diesel nozzles, under high injection pressure and backpressure conditions. Zhao and Zhang [10] investigated the influences of supply pressure, orifice diameter, film thickness and pressure ratio on the pressure depression. Shan et al. [11] investigated the effects of the orifice to pipe diameter ratio (defined as the β ratio) on the flow field behind a thin circular square-edged orifice plate. Moreover, some other researchers have studied about geometry of orifices [12-14], physical parameters of orifices [15-17], optimal conditions of orifices [18-21] and different algorithms for optimization methods [22-25] and numerical methods [26-28].

Based on available information, multi-objective optimization of multi-hole orifices in the form of a combination of FSI analysis and NSGA II algorithm has not been done so far. In this paper, multi-objective optimization of multi-hole orifices is performed using a Fluid-Solid Interaction (FSI) analysis and multi-objective genetic algorithm (NSGA II). In all numerical analysis, the governing equations of the solid and the governing equations of the fluid are carried out for orifice and fluid around orifice, respectively. All calculations are made for a 16-hole orifice with circular holes. The design variable in the optimization process is the distance between the holes of the orifice and thus the amount of shrinkage or expansion of the orifice geometry. The objective functions are the pressure drop created on the sides of the orifice, the deformation and tension created in the orifice structure, which should be maximized, minimized and minimized, respectively. In the results section, the Pareto front are presented which represent useful information for designing the multi-hole orifices geometry, and five orifices are also introduced as final design options that have high performance.

2. DESIGN VARIABLES AND OBJECTIVE FUNCTIONS

The orifice examined in this paper is a multi-hole orifice with 16 circular holes, shown in Figure 2.

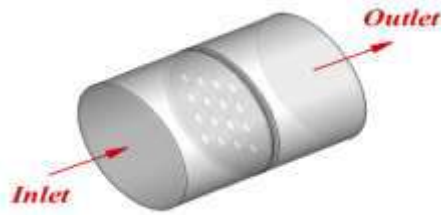


Figure 1. Overview of the 16-hole orifice and the fluid passing through it

The only design variable for optimization in this paper is the gap between the two holes of the orifice. The orifice geometry, as shown in Figure 3, is bounded in such a way that all the horizontal and vertical distances of the orifice holes are equal. Therefore, the orifice can be opened or folded symmetrically in an optimization process.

The objective functions are the pressure created on the sides of the orifice, the deformation and tension created in the orifice structure, which should be maximized, minimized and minimized, respectively.

Flowchart of MOO process is depicted in Figure 4.

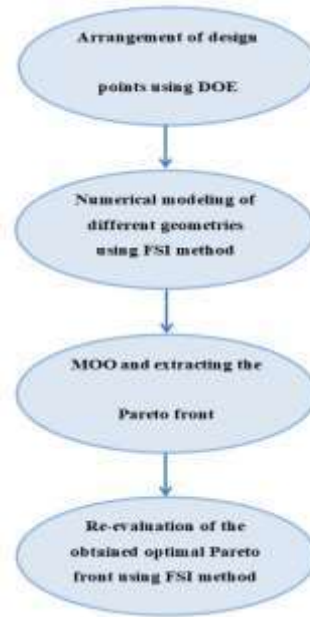


Figure 2. Flowchart of MOO process

3. NUMERICAL MODELING

3. 1. Grid Generation Due to the FSI analysis, the grid should be produced for separate fluid and solid. Figure 5 shows the view of the generated grid. It has been attempted to produce the best and most high-quality grid after conducting the grid independency test, especially in areas with high gradients. By changing the design variable, the grid can automatically adapt itself to the new geometry in the optimization process. There are approximately 800,000 elements in the produced grids.

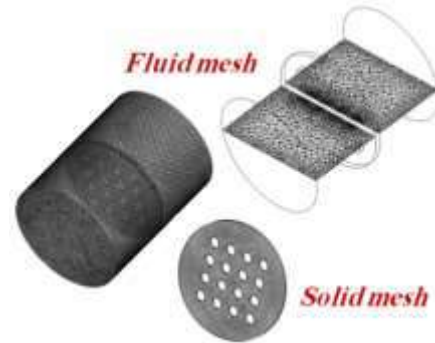


Figure 3. Mesh generation in FSI analysis

3. 2. Governing Equations The flow of fluid in the pipes is mainly turbulent. The governing equations in the turbulent flow in the fluid are as follows:

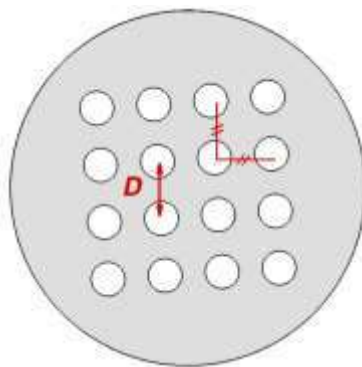


Figure 3. The distance between two orifice holes as an optimization design variable

Continuity:

$$\nabla \cdot (\rho V) = 0 \tag{1}$$

Momentum:

$$\nabla \cdot (\rho V V) = -\nabla p + \nabla \cdot (\tau - \tau_t) + \rho g \tag{2}$$

Kinetic energy of turbulence:

$$\nabla \cdot (\rho V k) = \nabla \cdot \left[\left(\mu + \frac{\mu_t}{\sigma_k} \right) \nabla k \right] + G - \rho \epsilon \tag{3}$$

turbulence loss rate:

$$\nabla \cdot (\rho V \epsilon) = \nabla \cdot \left[\left(\mu + \frac{\mu_t}{\sigma_\epsilon} \right) \nabla \epsilon \right] + \frac{\epsilon}{k} (C_1 G - C_2 \rho \epsilon) \tag{4}$$

3. 3. Boundary Conditions

Mass flow rate and the turbulence rate are specified at the inlet of the orifice, and there is a specific pressure at the output. The wall boundary condition is also used in walls. Fluid and solid

exchange data for the calculation of tension and displacement of the wall.

4. RESULTS

In this paper, multi-objective optimization of multi-hole orifices performance is performed using a FSI analysis and multi-objective genetic algorithm. In this section, the associated results, including the Pareto front, are presented. The optimization process can be expressed mathematically according to the following equation:

$$\begin{cases} \text{Maximize } \Delta P = f_1(D) \\ \text{Minimize } \sigma = f_2(D) \\ \text{Minimize } \varepsilon = f_3(D) \end{cases} \quad (5)$$

To validate numerical simulations, various data including pressure drop with the standard governing orifice, which is ISO 5167, were compared and a good agreement was observed with an error of less than 9%. Therefore, numerical simulations can be used to carry out a multi-objective optimization process of multi-hole orifices. Pressure drop contour in fluid and deformation and stress contour in the structure are shown in Figure 6 as a sample of numerical simulations performed.

After 250 numerical simulations, as shown in Figure 7, the Pareto front showing changes in pressure drop and deformation is shown in Figure 8. As is clear, all the results representing an independent and unique orifice, are completely non-dominant to each other, and when moving from an orifice to another orifice, one of the objective functions gets better and the other gets worse. In Figure 8, five points have unique characteristics. As shown in Figure 9, the front section of the deformation of the orifice is shown for points A to E. Orifices have the minimum and maximum deformation in A and E, respectively. Also for more recognition on the flow field, the way of fluid passing is shown in Figure 10 from 16-hole orifice for points A to E.

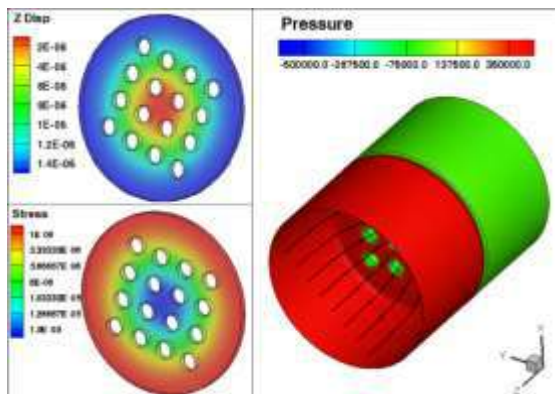


Figure 6. A sample of deformation and tension contours in the orifice and pressure drop in the fluid in a 16-hole orifice

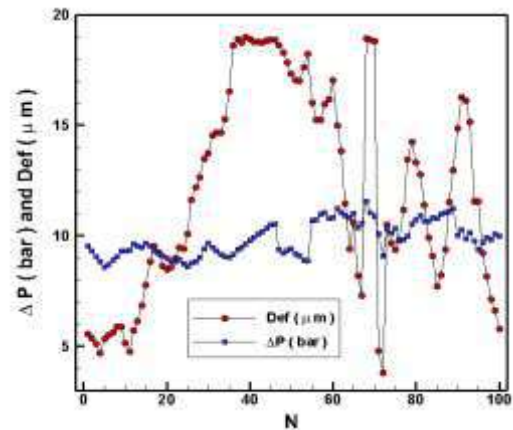


Figure 4. Sample of 250 numerical simulations performed in the multi-objective optimization process

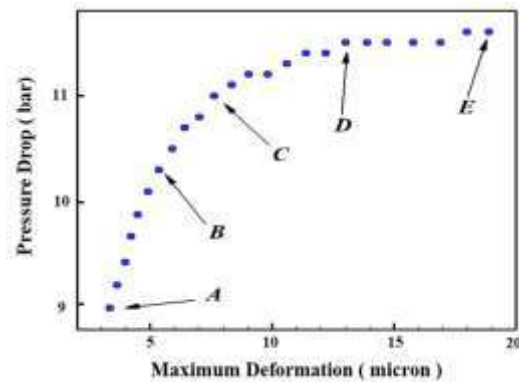


Figure 5. Pareto front: pressure drop vs. maximum deformation

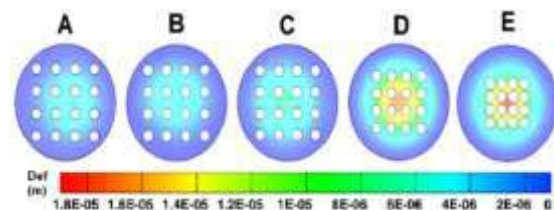


Figure 6. Deformation contour for the five points indicated in the Pareto front

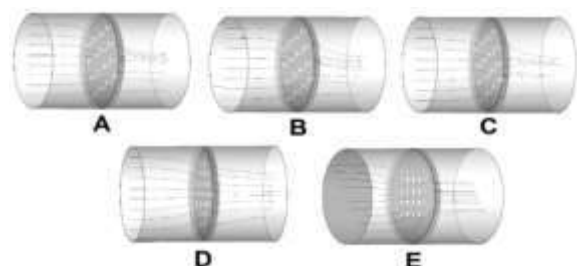


Figure 10. Fluid flow from orifice for the five points indicated in the Pareto front

In Figure 8, the design points *A* and *E* stand for the best ϵ (strain and deformation) and the best ΔP respectively. Moreover, the other optimum design points, *B* and *D* can be simply recognized from Figure 8. The design point, *B* presents important design concepts. In fact, optimum design point *B* obtained in this paper exhibits an increase in deformation (about 12.3%) in comparison with that of point *A* whilst its pressure drop improves about 43.9%, similarly optimum design point *D* exhibits a decrease in pressure drop (about 8.2%) in comparison with that of point *E* whilst its deformation improves about 38.3%. Points *B* and *D* which known as break points can only be identified by the multi-objective optimization approach used in this paper.

There are some interesting design facts which can be used in the design of multi-hole orifices. It is clear from these figures that *D* is constant from points *A* to *B* and from *D* to *E* and varies with quadratic relation between points *B* and *D*. These useful relationships that infeasible between the optimum design variables of multi-hole orifices cannot be discovered without the use of multi objective Pareto optimization process presented in this paper. It is now ideal to find optimal design points that are compatible with both functions. This can be achieved by the method employed in this study, namely, the mapping method [23]. In this method, the values of objective functions of all Pareto points are mapped range 0 and 1. Using the sum of these values for each Pareto point, the trade-off point simply is one having the minimum sum of those values. As a result, optimum design point *C* is the trade-off points which have been obtained from this method.

In a post CFD investigation, the design points of the Pareto front obtained by the optimization process are re-evaluated by CFD. The results of such CFD analysis re-evaluations have been compared with those of numerical results using the optimization method in Table 1. As seen the optimization process agree well with the CFD results with error less than 3%. This shows the accuracy of the optimization process from start to the end.

The Pareto front obtained from the optimization process (Figure 8) is mounted with the corresponding CFD simulation results in Figure 11. From this figure it is clear that such a Pareto front is the best possible combination of CFD data target values, which shows the effectiveness of this paper in obtaining the Pareto front.

Figure 12 shows the sensitivity analysis of the distance between the orifice holes on the functional functions of the orifice, such as pressure drop, deformation, tension and strain. As it is known, the highest sensitivity among the functional functions is the tension and strain and the low sensitivity is the pressure drop.

In the results section, the Pareto front, which represent useful information for designing the multi-hole orifice's geometry, were presented, and five orifices that

have better performance are also presented as final design options, with details of their flow in Table 2 and their figures were shown in Figures 8 and 9. The design points *A* and *E* were stand for the best ϵ and the best ΔP .

TABLE 1. Re-evaluation of the obtained optimal Pareto front using CFD

Point	Pressure drop (bar)			Deformation (μm)		
	Pareto	CFD	Error (%)	Pareto	CFD	Error (%)
<i>A</i>	8.86	8.96	1.18	3.15	3.24	2.88
<i>B</i>	10.03	9.81	-2.16	5.12	5.23	2.13
<i>C</i>	10.09	10.28	1.89	7.50	7.40	-1.32
<i>D</i>	11.30	11.63	2.92	12.99	13.38	2.98
<i>E</i>	11.52	11.73	1.82	19.11	18.90	-1.11

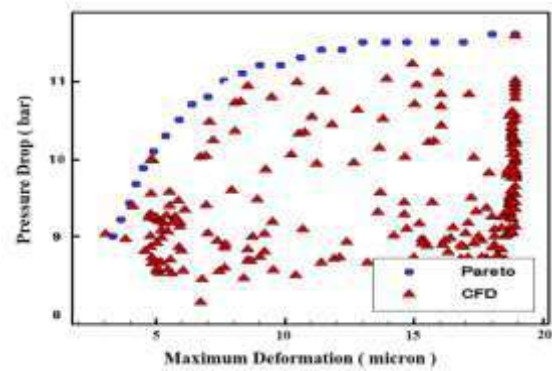


Figure 11. Overlapping of numerical results and the Pareto front that indicate the correctness of the optimization process

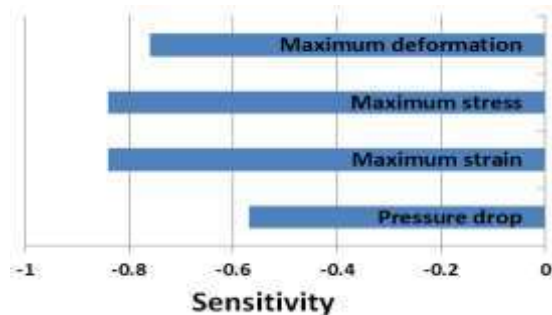


Figure 7. Sensitivity analysis results

TABLE 2. The values of objective functions and their associated design variables of the optimum points

Point	Design variable	Objective functions			
	<i>D</i> (mm)	Pressure drop (bar)	Maximum strain $\times 10^6$	Deformation (μm)	Maximum tension (N/m^2) $\times 10^6$
<i>A</i>	41.94	8.86	30.0	3.15	6.0

<i>B</i>	41.76	10.03	30.8	5.12	6.1
<i>C</i>	39.39	10.09	47.9	7.50	9.5
<i>D</i>	32.27	11.30	94.8	12.99	18.9
<i>E</i>	26.07	11.52	126.9	19.11	25.3

Moreover, optimum design point *B* obtained in this paper exhibits an increase in deformation (about 12.3%) in comparison with that of point *A* whilst its pressure drop improves about 43.9%, similarly optimum design point *D* exhibits a decrease in pressure drop (about 8.2%) in comparison with that of point *E* whilst its deformation improves about 38.3%.

5. CONCLUSION

Multi-hole orifices have better performance than single-hole orifices. In this paper, multi-objective optimization of multi-hole orifice function was performed using a FSI analysis and multi-objective genetic algorithm. In all numerical analysis, the governing equations of the structure for orifice and the governing equations for the fluid were carried out for the fluid around orifice. All calculations were made for a 16-hole orifice with circular holes. The design variable in the optimization process was the distance between the holes of the orifice and thus the amount of shrinkage or opening of the orifice geometry. The objective functions were the pressure drop created on the sides of the orifice, the deformation and tension created in the orifice structure, which should be maximized, minimized and minimized, respectively.

Also, the sensitivity analysis of the distance between the holes of orifice on the functional functions of the orifice was performed and it was observed that among the functional functions, the most sensitivity was tension and strain, and the least sensitivity was the drop in pressure relative to the changes in the distance between the holes of orifice.

6. REFERENCES

- Standardization, I.O.f., "Measurement of fluid flow by means of pressure differential devices inserted in circular cross-section conduits running full: Mesure de débit des fluides au moyen d'appareils déprimogènes. Inserés dans des conduites en charge de section circulaire. General principles and requirements, International Organization for Standardization, (2003).
- Sowa, W., Kroll, J., Samuelsen, G. and Holdeman, J., "Optimization of orifice geometry for cross-flow mixing in a cylindrical duct", in 32nd Aerospace Sciences Meeting and Exhibit. (1994), 219.
- Zhang, Q. and Bodony, D.J., "Numerical investigation and modelling of acoustically excited flow through a circular orifice backed by a hexagonal cavity", *Journal of Fluid Mechanics*, Vol. 693, (2012), 367-401, <https://doi.org/10.1017/jfm.2011.537>
- Araoye, A.A., Badr, H.M. and Ahmed, W.H., "Dynamic behaviour of flow through multi-stage restricting orifices", in Proceedings of the 3rd International Conference on Fluid Flow, Heat and Mass Transfer (FFHMT'16). Ottawa, Canada, Citeseer. (2016), 161.
- Gan, G. and Riffat, S.B., "Pressure loss characteristics of orifice and perforated plates", *Experimental Thermal and Fluid Science*, Vol. 14, No. 2, (1997), 160-165, [https://doi.org/10.1016/s0894-1777\(96\)00041-6](https://doi.org/10.1016/s0894-1777(96)00041-6)
- Zhao, T., Zhang, J. and Ma, L., "A general structural design methodology for multi-hole orifices and its experimental application", *Journal of Mechanical Science and Technology*, Vol. 25, No. 9, (2011), 2237, <https://doi.org/10.1007/s12206-011-0706-3>
- Simpson, A. and Ranade, V.V., "Modelling of hydrodynamic cavitation with orifice: Influence of different orifice designs", *Chemical Engineering Research and Design*, Vol. 136, (2018), 698-711, <https://doi.org/10.1016/j.cherd.2018.06.014>
- Rainsford, G., Aulakh, D.J.S. and Ciccarelli, G., "Visualization of detonation propagation in a round tube equipped with repeating orifice plates", *Combustion and Flame*, Vol. 198, (2018), 205-221, <https://doi.org/10.1016/j.combustflame.2018.09.015>
- Yu, S., Yin, B., Deng, W., Jia, H., Ye, Z., Xu, B. and Xu, H., "Internal flow and spray characteristics for elliptical orifice with large aspect ratio under typical diesel engine operation conditions", *Fuel*, Vol. 228, (2018), 62-73, <https://doi.org/10.1016/j.fuel.2018.04.156>
- Zhang, J., Zou, D., Ta, N. and Rao, Z., "Numerical research of pressure depression in aerostatic thrust bearing with inherent orifice", *Tribology International*, Vol. 123, (2018), 385-396, <https://doi.org/10.1016/j.triboint.2018.03.009>
- Shan, F., Liu, Z., Liu, W. and Tsuji, Y., "Effects of the orifice to pipe diameter ratio on orifice flows", *Chemical Engineering Science*, Vol. 152, (2016), 497-506, <https://doi.org/10.1016/j.ces.2016.06.050>
- Wang, L.-Q., Ma, H.-H., Deng, Y.-X. and Shen, Z.-W., "On the detonation behavior of methane-oxygen in a round tube filled with orifice plates", *Process Safety and Environmental Protection*, Vol. 121, (2019), 263-270, <https://doi.org/10.1016/j.psep.2018.11.002>
- Wen, J., Sun, Q., Sun, Z. and Gu, H., "The effect of multi-orifice plate configuration on bubble detachment volume", *Chinese Journal of Chemical Engineering*, Vol. 27, No. 1, (2019), 72-84, doi: <https://doi.org/10.1016/j.cjche.2018.09.024>
- Wang, L.-Q., Ma, H.-H. and Shen, Z.-W., "Effect of orifice plates on detonation propagation in stoichiometric hydrogen-oxygen mixture", *Experimental Thermal and Fluid Science*, Vol. 99, (2018), 367-373, <https://doi.org/10.1016/j.expthermflusci.2018.08.012>
- Golijanek-Jędrzejczyk, A., Świsulski, D., Hanus, R., Zych, M. and Petyka, L., "Uncertainty of the liquid mass flow measurement using the orifice plate", *Flow Measurement and Instrumentation*, Vol. 62, (2018), 84-92, doi: <https://doi.org/10.1016/j.flowmeasinst.2018.05.012>
- Araoye, A., Badr, H., Ahmed, W., Habib, M. and Alsarkhi, A., "Erosion of a multistage orifice due to liquid-solid flow", *Wear*, Vol. 390, (2017), 270-282, <https://doi.org/10.1016/j.wear.2017.07.010>
- Zhao, X., Wang, G., Lu, W., Chen, M., Yan, P. and Zhou, C., "Effects of close proximity underwater explosion on the nonlinear dynamic response of concrete gravity dams with orifices", *Engineering Failure Analysis*, Vol. 92, (2018), 566-586, <https://doi.org/10.1016/j.engfailanal.2018.06.016>
- Qiao, M., Wei, W., Huang, W., Li, J., Xue, Y. and Deng, C., "Flow patterns and hydrodynamic model for gas-liquid co-current downward flow through an orifice plate", *Experimental Thermal*

- and Fluid Science*, Vol. 100, (2019), 144-157, <https://doi.org/10.1016/j.expthermflusci.2018.09.005>
19. Zhao, D., Sun, Y., Ni, S., Ji, C. and Sun, D., "Experimental and theoretical studies of aeroacoustics damping performance of a bias-flow perforated orifice", *Applied Acoustics*, Vol. 145, (2019), 328-338, <https://doi.org/10.1016/j.apacoust.2018.10.025>
 20. Rydlewicz, W., Rydlewicz, M. and Pałczyński, T., "Experimental investigation of the influence of an orifice plate on the pressure pulsation amplitude in the pulsating flow in a straight pipe", *Mechanical Systems and Signal Processing*, Vol. 117, (2019), 634-652, <https://doi.org/10.1016/j.ymssp.2018.08.005>
 21. Araoie, A.A., Badr, H.M. and Ahmed, W.H., "Investigation of flow through multi-stage restricting orifices", *Annals of Nuclear Energy*, Vol. 104, (2017), 75-90, <https://doi.org/10.1016/j.anucene.2017.02.002>
 22. Khalkhali, A. and Safikhani, H., "Pareto based multi-objective optimization of a cyclone vortex finder using cfd, gmdh type neural networks and genetic algorithms", *Engineering Optimization*, Vol. 44, No. 1, (2012), 105-118, <https://doi.org/10.1080/0305215x.2011.564619>
 23. Safikhani, H., Akhavan-Behabadi, M., Nariman-Zadeh, N. and Abadi, M.M., "Modeling and multi-objective optimization of square cyclones using cfd and neural networks", *Chemical Engineering Research and Design*, Vol. 89, No. 3, (2011), 301-309, doi. <https://doi.org/10.1016/j.cherd.2010.07.004>
 24. Sanaye, S. and Hajabdollahi, H., "Thermal-economic multi-objective optimization of plate fin heat exchanger using genetic algorithm", *Applied Energy*, Vol. 87, No. 6, (2010), 1893-1902, doi. <https://doi.org/10.1016/j.apenergy.2009.11.016>
 25. Sanaye, S. and Dehghandokht, M., "Modeling and multi-objective optimization of parallel flow condenser using evolutionary algorithm", *Applied Energy*, Vol. 88, No. 5, (2011), 1568-1577, doi. <https://doi.org/10.1016/j.apenergy.2010.11.032>
 26. Yamini, O.A., Mousavi, S.H., Kavianpour, M.R. and Movahedi, A., "Numerical modeling of sediment scouring phenomenon around the offshore wind turbine pile in marine environment", *Environmental Earth Sciences*, Vol. 77, No. 23, (2018), 1-15, doi. <https://doi.org/10.1007/s12665-018-7967-4>
 27. Sengupta, A.R., Gupta, R. and Biswas, A., "Computational fluid dynamics analysis of stove systems for cooking and drying of muga silk", *Emerging Science Journal*, Vol. 3, No. 5, (2019), 285-292, doi. <https://doi.org/10.28991/esj-2019-01191>
 28. Dirbude, S.B. and Maurya, V.K., "Effect of uniform magnetic field on melting at various rayleigh numbers", *Emerging Science Journal*, Vol. 3, No. 4, (2019), 263-273, doi: 10.28991/esj-2019-01189.

Persian Abstract

چکیده

دهانه های چند سوراخ عملکرد بهتری نسبت به روزنه های یک سوراخ دارند. در این مقاله، بهینه سازی چند هدفه دهانه های چند سوراخ با استفاده از تجزیه و تحلیل متقابل سیال و جامد (FSI) و الگوریتم ژنتیک چند هدفه (NSGA II) انجام می شود. در تمام تحلیل های عددی، معادلات حاکم بر جامد و معادلات حاکم بر سیال به ترتیب برای روزنه و مایع در اطراف روزنه انجام می شود. تمام محاسبات برای یک روزنه ۱۶ سوراخ با سوراخ های دایره ای شکل انجام شده است. متغیر طراحی در فرایند بهینه سازی فاصله بین سوراخ های روزنه و در نتیجه مقدار جمع شدگی یا انبساط هندسه روزنه است. توابع هدف عبارتند از افت فشار ایجاد شده در کناره های روزنه، تغییر شکل و کشش ایجاد شده در ساختار روزنه، که باید به ترتیب حداکثر، به حداقل رسانده و به حداقل برسد. در بخش نتایج، جلو پارتو ارائه شده است که اطلاعات مفیدی را برای طراحی هندسه روزنه های چند سوراخ نشان می دهد و پنج روزنه نیز به عنوان گزینه های طراحی نهایی معرفی می شوند که عملکرد بهتری دارند. نتایج تجزیه و تحلیل حساسیت پارامترهای مختلف نیز در دهانه های چند سوراخ با جزئیات ارائه و بحث شده است.

AIMS AND SCOPE

The objective of the International Journal of Engineering is to provide a forum for communication of information among the world's scientific and technological community and Iranian scientists and engineers. This journal intends to be of interest and utility to researchers and practitioners in the academic, industrial and governmental sectors. All original research contributions of significant value focused on basics, applications and aspects areas of engineering discipline are welcome.

This journal is published in three quarterly transactions: Transactions A (Basics) deal with the engineering fundamentals, Transactions B (Applications) are concerned with the application of the engineering knowledge in the daily life of the human being and Transactions C (Aspects) - starting from January 2012 - emphasize on the main engineering aspects whose elaboration can yield knowledge and expertise that can equally serve all branches of engineering discipline.

This journal will publish authoritative papers on theoretical and experimental researches and advanced applications embodying the results of extensive field, plant, laboratory or theoretical investigation or new interpretations of existing problems. It may also feature - when appropriate - research notes, technical notes, state-of-the-art survey type papers, short communications, letters to the editor, meeting schedules and conference announcements. The language of publication is English. Each paper should contain an abstract both in English and in Persian. However, for the authors who are not familiar with Persian, the publisher will prepare the latter. The abstracts should not exceed 250 words.

All manuscripts will be peer-reviewed by qualified reviewers. The material should be presented clearly and concisely:

- *Full papers* must be based on completed original works of significant novelty. The papers are not strictly limited in length. However, lengthy contributions may be delayed due to limited space. It is advised to keep papers limited to 7500 words.
- *Research notes* are considered as short items that include theoretical or experimental results of immediate current interest.
- *Technical notes* are also considered as short items of enough technical acceptability with more rapid publication appeal. The length of a research or technical note is recommended not to exceed 2500 words or 4 journal pages (including figures and tables).

Review papers are only considered from highly qualified well-known authors generally assigned by the editorial board or editor in chief. Short communications and letters to the editor should contain a text of about 1000 words and whatever figures and tables that may be required to support the text. They include discussion of full papers and short items and should contribute to the original article by providing confirmation or additional interpretation. Discussion of papers will be referred to author(s) for reply and will concurrently be published with reply of author(s).

INSTRUCTIONS FOR AUTHORS

Submission of a manuscript represents that it has neither been published nor submitted for publication elsewhere and is result of research carried out by author(s). Presentation in a conference and appearance in a symposium proceeding is not considered prior publication.

Authors are required to include a list describing all the symbols and abbreviations in the paper. Use of the international system of measurement units is mandatory.

- On-line submission of manuscripts results in faster publication process and is recommended. Instructions are given in the IJE web sites: www.ije.ir-www.ijeir.info
- Hardcopy submissions must include MS Word and jpg files.
- Manuscripts should be typewritten on one side of A4 paper, double-spaced, with adequate margins.
- References should be numbered in brackets and appear in sequence through the text. List of references should be given at the end of the paper.
- Figure captions are to be indicated under the illustrations. They should sufficiently explain the figures.
- Illustrations should appear in their appropriate places in the text.
- Tables and diagrams should be submitted in a form suitable for reproduction.
- Photographs should be of high quality saved as jpg files.
- Tables, Illustrations, Figures and Diagrams will be normally printed in single column width (8cm). Exceptionally large ones may be printed across two columns (17cm).

PAGE CHARGES AND REPRINTS

The papers are strictly limited in length, maximum 6 journal pages (including figures and tables). For the additional to 6 journal pages, there will be page charges. It is advised to keep papers limited to 3500 words.

Page Charges for Papers More Than 6 Pages (Including Abstract)

For International Author ***	\$55 / per page
For Local Author	100,000 Toman / per page

AUTHOR CHECKLIST

- Author(s), bio-data including affiliation(s) and mail and e-mail addresses).
- Manuscript including abstracts, key words, illustrations, tables, figures with figure captions and list of references.
- MS Word files of the paper.



THOMSON REUTERS
WEB OF SCIENCE



Scopus®



CAS®
A DIVISION OF THE
AMERICAN CHEMICAL SOCIETY



 Crossref



Scientific Indexing Services

Google
Scholar